ANNUAL REPORT

University Research Initiative

Contract No.: N00014-92-J-1808

March 1993 - April 1994

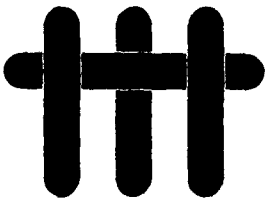

The Processing and Mechanical Properties of High Temperature/ High Performance Composites

by

A.G. Evans & F. Leckie
University of California,
Santa Barbara

University of Pennsylvania
Harvard University
Washington State University
Carnegie Mellon University
University of Virginia

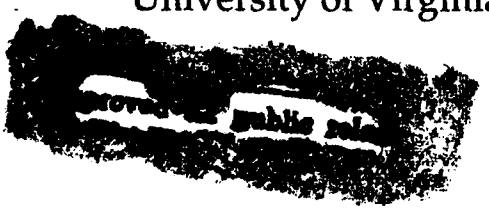

Book 3 of 7:

Fatigue and Creep

SUMMARY

OF

TABLE OF CONTENTS

KJS 4/27/94

KJS 4/27/94

BOOK 3

FATIGUE AND CREEP

43.	The Creep Anisotropy of a Continuous-Fiber-Reinforced SiC/CAS Composite	C. Weber J. Löfvander A. G. Evans
44.	Power Law Creep of a Composite Material Containing Discontinuous Rigid Aligned Fibers	R. M. McMeeking
45.	Diffusive Void Bifurcation in Stressed Solid	Z. Suo W. Wang

EXECUTIVE SUMMARY

The general emphasis for 1994 would be on increased software development, testing of subelements and design calculations. For these purposes, the constitutive law coding and development would be coordinated by Nick Aravas, and implemented in ABAQUS. The initial implementation would be the elastic/plastic model for MMCs with interface debonding developed in 1993 (Leckie). This would be extended in 1994 to include creep and some aspects of thermomechanical cycling. The code would be used for design calculations concerned with MMC rotors, actuators and vanes (Leckie). A plan is being formulated to collaborate with Pratt and Whitney to acquire MMC sub-elements representative of these components during 1994. Experimental tests on these subelements would be capable of providing a direct validation of the code capabilities.

Constitutive law and fatigue lifing software would be created for CMCs using continuum damage mechanics (CDM) approaches (Leckie, McMeeking). The approach has been motivated by micromechanics models developed in 1993 (Hutchinson, Zok, Evans). These codes would be used to calculate stress redistribution effects and fatigue life on simple sub-elements, such as center notched and pin-loaded plates. Comparison with experimental measurements needed to test the fidelity of the models will be based on moiré interferometry and thermoelastic emission. This effort is coordinated with the NASA EPM program through both General Electric and Pratt and Whitney. A plan for acquiring sub-elements from DuPont Lanxide is being formulated.

A new emphasis for 1994 would be on the transverse properties of CMCs. The measurements and calculations performed in 1993 have indicated a strategy for curved sections and junctions that would establish a consistent design approach. The basic approach for resisting failures from combinations of interlaminar shear and transverse tension involves the use of stitching and angle ply weaving patterns that inhibit major reductions in stiffness when matrix cracks are induced by transverse loads and bending moments. For this purpose, calculations would be performed that combine

the mechanics of delamination cracks with models of bridging by inclined fiber bundles (Hutchinson, Ashby, Evans, McMeeking). The insight gained from these calculations would be used to design and acquire sub-elements, such as C sections and T junctions.

Additional software development will be for creep and creep rupture (McMeeking). The models devised in 1993 and test data relevant to MMCs will be combined into a code that predicts the creep and rupture of unidirectional MMCs subject to multiaxial loads. Some aspects of this code will also be applicable to CMCs.

Two new activities will be introduced in 1994: thermal properties and damping. The thermal properties will be studied on both CMCs and MMCs (Ashby, Hutchinson). Measurements of thermal diffusivity will be made by the laser flash method and related to the properties of the interface and the density of matrix damage in the material. Thermal expansion measurements will also be performed with emphasis on determining hysteresis effects, which can be related to the temperature dependence of the interfaces properties, through cell models. The latter might evolve into a diagnostic for establishing relationships between the interface properties and thermomechanical fatigue.

The processing activities in the program will have newly established goals in 1994. The principal emphasis will be on concepts for affordable manufacturing. The issues selected for investigation will be consistent with manufacturing processes that allow near-net shape consolidation while still yielding reasonable combinations of longitudinal and transverse properties. Performance models developed in the program would be used as an initial test of concept viability.

Beyond these general trends, specific activities are planned for 1994. These are elaborated below. The status of understanding and development in each of these areas is summarized in Table I. Increasing magnitudes between 0 and 1 designate a knowledge range from limited to comprehensive.

TABLE 1A

Status of Design Knowledge for MMCs

	$[0°]_n$ MMC				$[0°/90°]_n$	
	LONG.		TRANS.			
	P	S	P	S	P	S
Tensile Strength	3/4	1	1	1/2	1/4	~0
Creep and Creep Rupture	3/4	0	1	0	0	0
Cyclic Flow (Isothermal, TMF)	1/4	0	1	1/2	0	0
Crack Growth (Isothermal Fatigue)	1	1	0	1/2	0	0
Crack Growth (TMF)	1/2	1/2	0	0	0	0
Compressive Strength	3/4	0	0	0	0	0

TABLE 1B

Status of Design Knowledge for CMCs

	[0/90]		[45/45]	
	P	S	P	S
Stress/Strain	3/4	1/4	1/2	0
Fatigue	3/4	0	0	0
TMF	1/4	0	0	0
Creep and Rupture	1/2	0	0	0
Compression Strength	3/4	1/4	0	0
Transverse Properties	3/4	1/2	—	—
Thermal Properties	1/4	0	—	—

P Primary Structure

S Secondary Structure

2. CONSTITUTIVE LAWS

Two approaches will be used to create a formulation capable of representing the in-plane properties of CMCs. One would be based on Continuum Damage Mechanics (CDM) (Leckie). The other would use concepts analogous to those used in plasticity theory (Hutchinson). The CDM approach uses damage parameters that relate explicitly to micromechanics models. A potential function has already been identified as the state variable which separately represents the strain from the elastic compliance change caused by the matrix cracks and the inelastic strains associated with the debonding and sliding interfaces. Derivatives of the potential with regard to strain and damage give the relationships between variables, such as stress, interface sliding resistance, matrix crack density, etc.

The first version of the CDM model would use the minimum number of damage variables potentially capable of representing the behavior of laminated or woven composites. Cross terms between the damage variables would not be considered at this stage. Moreover, matrix cracks would be introduced normal to the maximum principal tensile stress, consistent with the experimental observations.

The plasticity theory approach would seek a formulation based on matrix cracks occurring normal to the maximum principal tension. It would introduce parameters that reflect the inelastic strain caused by interface sliding upon off-axis loading which would be calibrated from tests performed in tension in 0/90 and 45/45 orientations.

The insight needed to characterize off-axis loading effects will be gained from cell models (Hutchinson) in a manner analogous to that previously used for axial loads. The principal objective will be to understand trends in matrix crack opening and interface debonding/sliding with applied loads. The stress on the fibers will be calculated with the intent of predicting effects of loading orientation on fiber failure. The models will be compared with measurements made in 45/45 tension, using various CMCs (Evans).

Calibration of the damage parameters for each material would be made from hysteresis loop measurements in accordance with procedures developed in 1993. Experimental results obtained in 0/90 tension, 45/45

tension and in-plane shear will be used. In future work, it is hoped that shear tests will not be necessary.

The validation of the constitutive laws will be achieved by comparing calculations with measurements made on sub-elements, especially pin-loaded holes (Evans). The experimental results include residual strains obtained by Moiré interferometry (Fig. 2.1), ultimate loads for either tensile or shear failure and principal strain trajectories delineated by matrix cracking patterns. Acoustic methods will also be developed to probe the local values of the elastic modulus (Clarke, Wadley) which could be compared directly with the CDM predictions.

3. FATIGUE LIFING

3.1 CMCs

A software program for isothermal low cycle fatigue (LCF) of CMCs, developed in 1993 (Fig. 3.1) will be extended in 1994. The present program asserts that fatigue is associated with cyclic degradation of the interface sliding resistance, τ, which can be characterized by analyzing hysteresis loops measured periodically during a fatigue test. With this methodology, S-N curves have been predicted for both unidirectional and woven 0/90 composites tested in cyclic tension as well as changes in compliance and permanent strain. Some additional effort is required to analyze data on 0/90 laminates in order to validate the model predictions. The extensions envisaged for 1994 include thermomechanical fatigue (TMF), strain controlled LCF and off-axis fatigue (Zok, Evans). Experiments are planned which would assess the effects of temperature cycling and of inclined fibers on τ degradation, measured from hysteresis loops. Various cell model calculations (Hutchinson) will be used to interpret the experiments. The results will be used to establish general *rules* for interface degradation in CMCs.

The off-axis experiments will also give insight into the fiber failure criterion that replaces the global load sharing (GLS) results successfully used for 0/90 loadings. This study will coordinate with the cell calculations described above, and the 45/45 tensile experiments.

Notch fatigue studies will be initiated. These will examine cyclic stress redistribution and notch sensitivity (Evans).

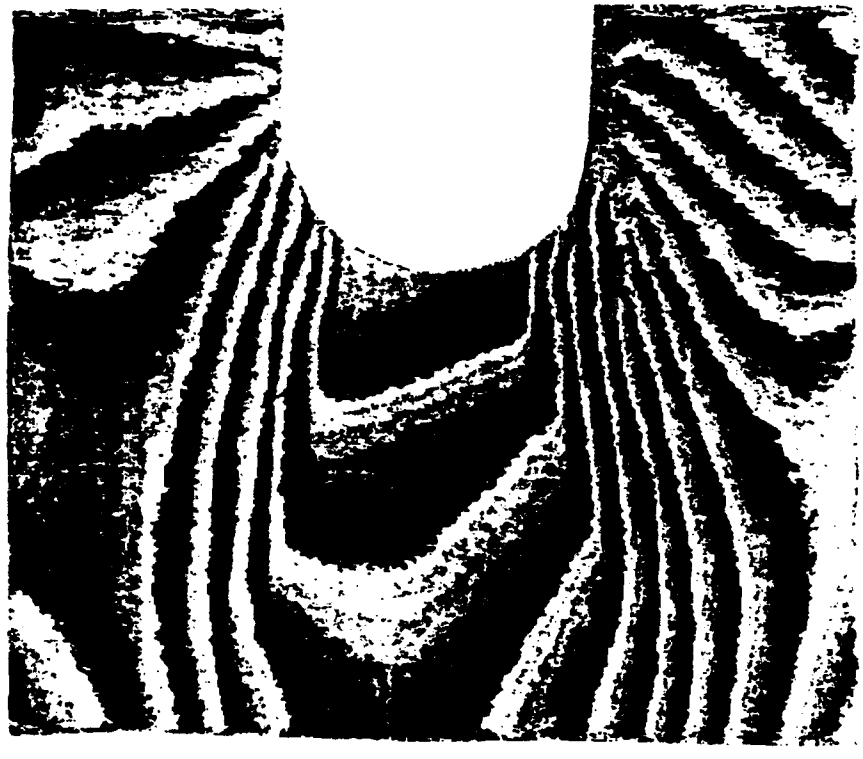

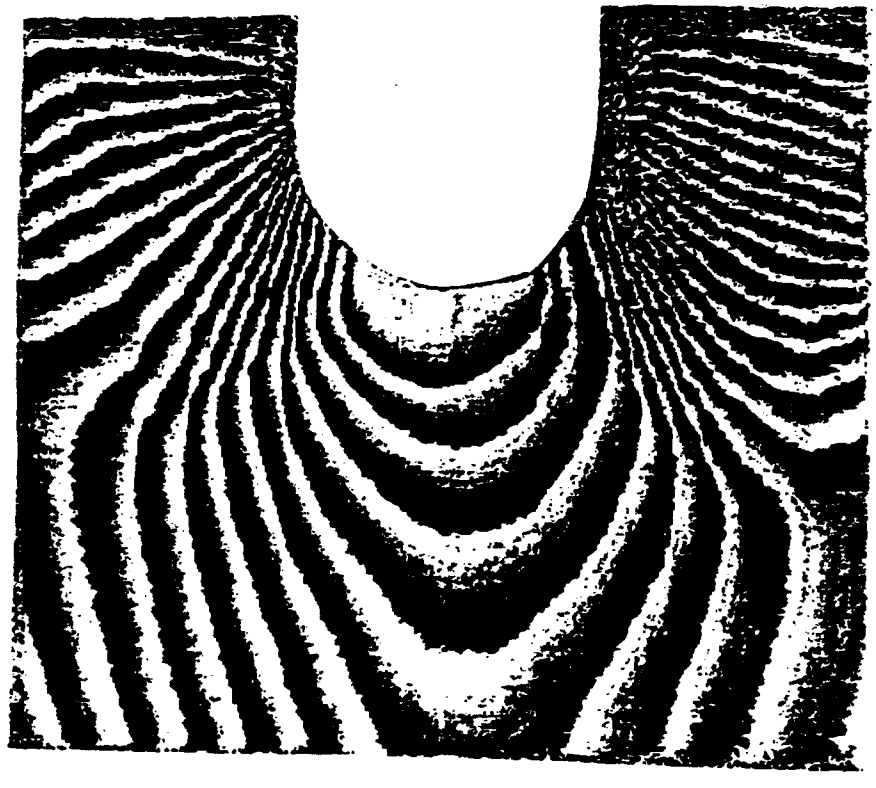

Figure 2.1

Fatigue Methodology

CMC Life Program

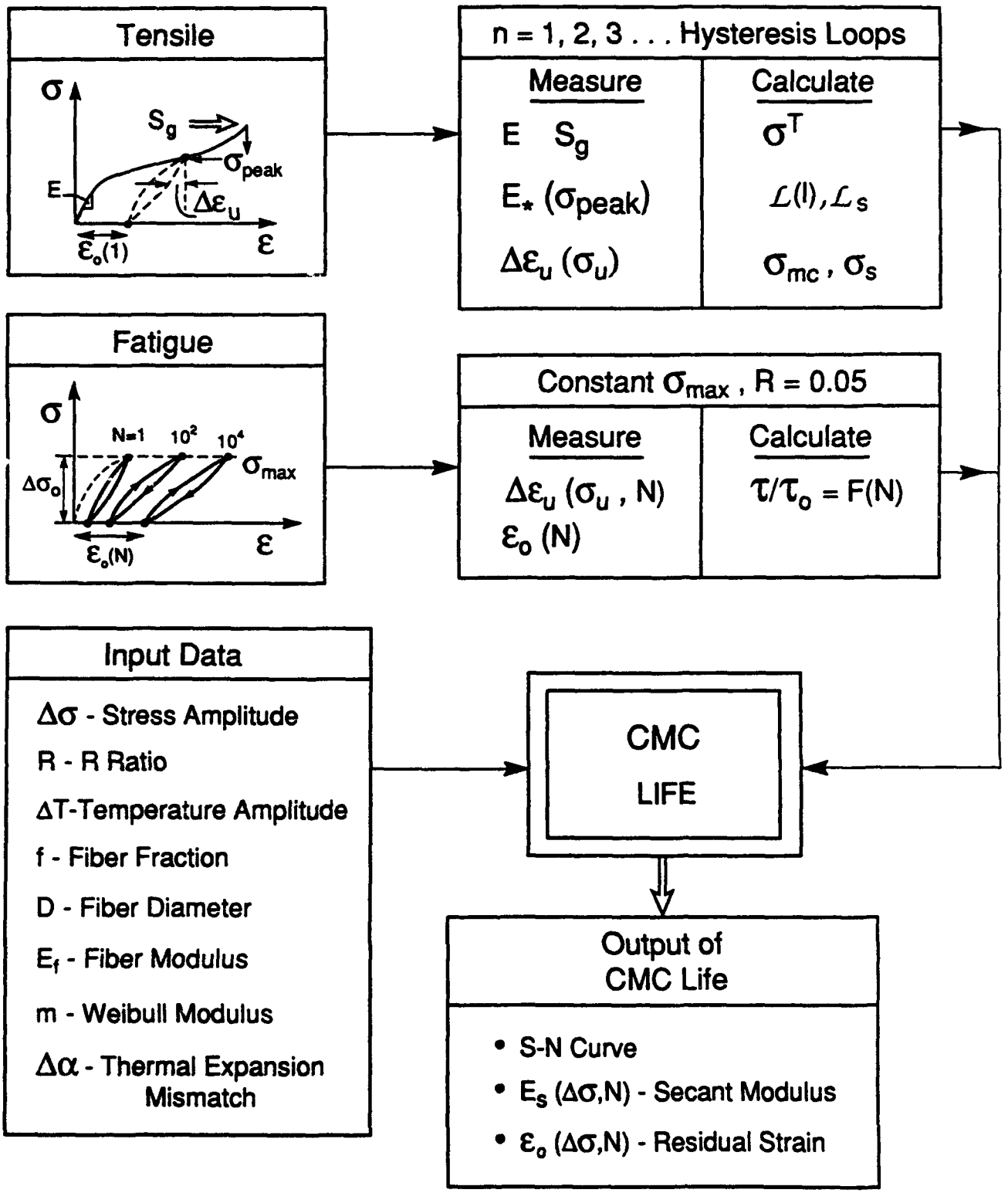

Figure 3.1

3.2 MMCs

Fatigue crack growth and notch strength studies in MMCs will be extended to 0/90 laminates (Zok, Suo). The experiments concerned with crack growth will be interpreted using crack bridging models. The utility of such models has been validated in previous years through studies on unidirectional MMCs. It is envisaged that the fatigue crack growth characteristics of the unidirectional and 0/90 configurations will be related through the volume fraction of fibers aligned with the loading direction. The notch strength behavior will also be interpreted using crack bridging models. Such models have been developed in 1993 and found to be useful in rationalizing the behavior of unidirectional materials (Zok, Suo). In all cases, the mechanical measurements will be augmented by *in-situ* observations to identify changes in damage mechanisms with temperature, fiber architecture, etc. Plans to study the influence of panel thickness on fatigue and fracture resistance are also being developed, as well as tests to understand the potential for crack growth in mixed mode loadings (Hirth, Zok).

Studies of the TMF response of MMCs loaded parallel to the fiber axis will be initiated (Zok, Leckie). Experiments will evaluate both in-phase and out-of-phase loadings. Models of load shedding (matrix-fibers) will be used to interpret the hysteresis loops and to develop fatigue life models applicable to low cycle, high strain TMF.

4. CREEP AND RUPTURE

4.1 MMCs

The considerable progress made in 1993 towards identifying and understanding the mechanisms of creep and rupture in unidirectional MMCs containing non-creeping fibers (McMeeking, Zok) will be used to develop creep rupture software. The longitudinal creep model to be used incorporates stochastic fiber fracture and interface sliding in a format amenable to the prediction of primary and tertiary creep in terms of matrix creep strength, interface sliding resistance, fiber strength, Weibull modulus, etc. The concepts would be visualized in a rupture mechanisms map

(Fig. 4.1). The transverse creep behavior would include interface debonding, which greatly accelerates the creep, leading to marked anisotropy. A constitutive law for creep that includes these effects will be developed (Aravas, McMeeking).

Additional experiments and calculations will be conducted to assess the effects of notches and holes on creep rupture (Zok, Suo). Experience with MMCs at ambient temperature indicates that the notch sensitivity is largely dictated by matrix properties (i.e., strength and ductility). The reduction in matrix properties at elevated temperatures may lead to a substantial elevation in notch sensitivity. However, this behavior may be complicated by the development of alternate damage processes, such as shear bands.

4.2 CMCs

Studies of the creep and rupture of CMCs will continue with emphasis on materials containing creeping fibers. A particular emphasis will be on matrix cracking that arises as fiber creep relaxes fiber bridging tractions (McMeeking, Evans). The experimental studies will be performed on SiC/SiC composites. Hysteresis loop measurements will be used to monitor matrix damage during composite creep, using procedures devised in 1993. Models will be developed based on time dependent fiber bridging concepts (McMeeking, Cox).

It is envisioned that the lifetime of some CMCs will be dictated by time-dependent rupture of the fibers. A lifetime prediction tool for such a composite *must* incorporate the knowledge of fiber strength degradation over time. A new activity will be initiated to address this problem (Suo, Evans). The initial work will involve a survey of data in the existing literature, and a comparison with available models. A new model is being developed for single crystal fibers. This model involves a residual pore inside a fiber which changes shape, under stress, via surface diffusion, to become a crack. These issues will be viewed in the broad context of fiber and composite manufacture.

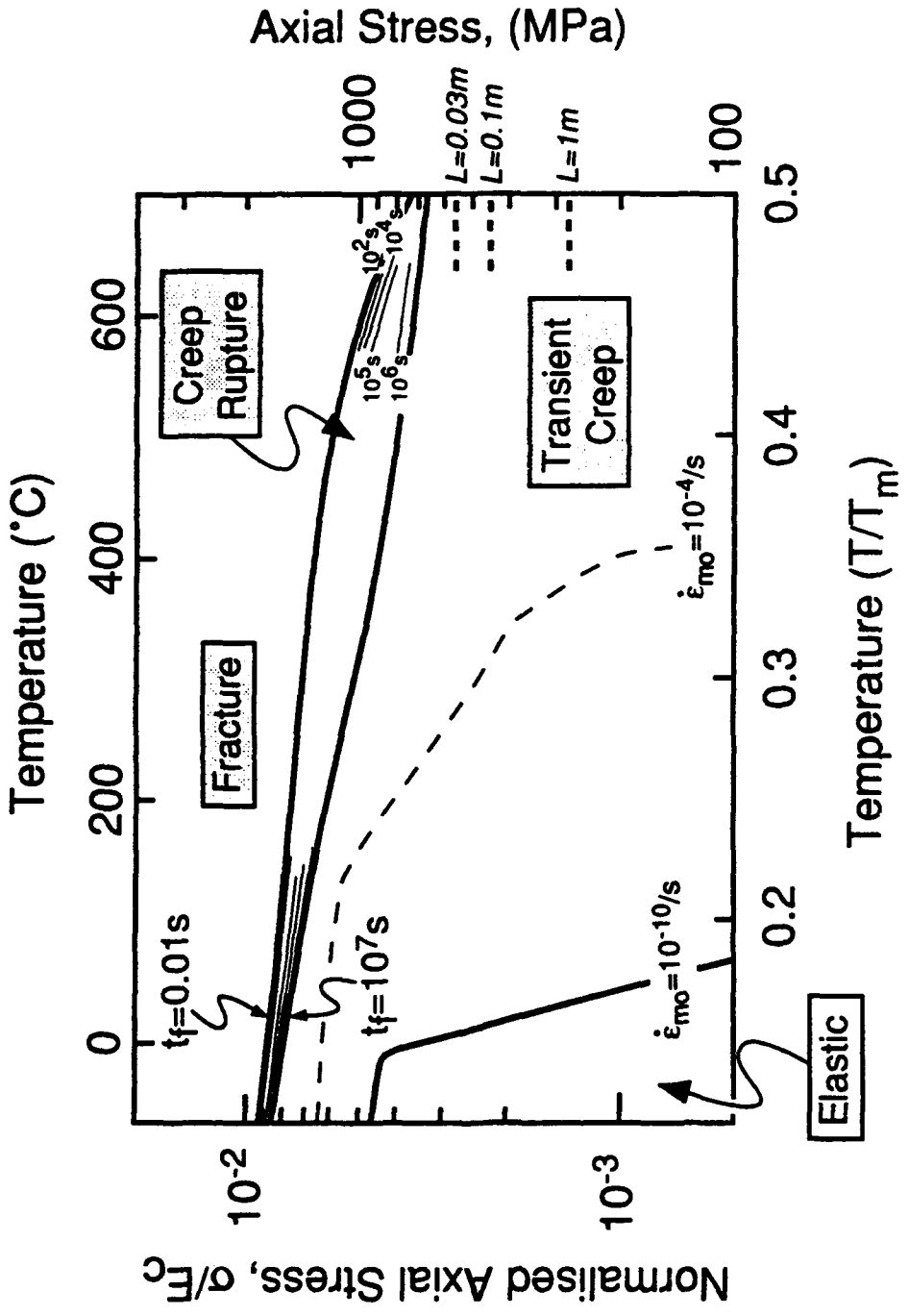
Axial Stress, (MPa)
1000
100
L=0.03m
L=0.1m
L=1m
Creep Rupture
Fracture
Transient Creep
Elastic
10^2s
10^4s
10^5s
10^6s
t_f=0.01s
t_f=10^7s
$\dot{\varepsilon}_{mo}$=10^{-4}/s
$\dot{\varepsilon}_{mo}$=10^{-10}/s
Temperature (°C)
0
200
400
600
Temperature (T/T_m)
0.2
0.3
0.4
0.5
Normalised Axial Stress, σ/E_C
10^{-2}
10^{-3}

Figure 4.1

5. TRANSVERSE PERFORMANCE OF CMCs

Analyses and tests performed in 1993 (Ashby, Hutchinson, Bao) have highlighted the essential issues related to components that experience combinations of transverse tension and interlaminar shear. In both loadings, matrix cracks form at manufacturing flaws at low stresses, of order 10-100 MPa. These cracks extend across the plies and interact minimally with the fibers. Although the crack configurations differ for transverse tension and interlaminar shear loadings, multiple cracks always form. This multiplicity of cracking causes a major reduction in stiffness, which can cause unacceptably large displacements and also redis te stress into other areas. The formation of the matrix cracks is probabili in nature and governed by the size distribution of manufacturing flaws. Design based on the prevention of such transverse cracks must rely on weakest link statistics, usually with a low Weibull modulus. Alternatively, it may be assumed that cracks *inevitably* form and, instead, reliance is placed on *controlling* the diminished modulus of the material, after matrix cracking has occurred. This approach relies on having 3-D architectures, with transverse fibers introduced locally either by stitching or by using angle plies. To explore this possibility, calculations will be performed (Hutchinson, Evans) to examine fiber architectures that lead to minimum stiffness loss, subject to acceptable in-plane properties. Based on these calculations, sub-elements will be designed that test out the concepts.

6. COMPRESSIVE BEHAVIOR

The studies completed in 1993 on the compressive failure of polymer matrix composites by the growth of kink bands (Budiansky, Fleck) will be extended to metal matrix composites, through a coordination with 3M. Compressive failure of Al and Ti MMCs with small diameter fibers has been observed by 3M to occur in accordance with the same kink band mechanism known to operate in PMCs and in C/C composites. The theory should thus extend to the MMCs, with the fiber misalignment, the shear yield strength of the matrix and its work hardening coefficient as the principal variables. A comparison between the theory and experimental

results would provide the basis for specifying the compressive properties of MMCs.

Compression failure of CMCs occurs by different mechanisms (Ashby). The dominant failure modes are similar to those that operate in porous brittle solids such as monolithic ceramics, concrete and rocks. The theory is well established and validated for these materials. Applications of the theory to various CMCs will be made and applied to the understanding of a behavior of pin-loaded holes (Evans, Ashby).

7. THERMAL PROPERTIES

A new focus on the thermal properties of CMCs and MMCs will be initiated in 1994. Calculations of the effects of matrix cracks in the thermal expansion of CMCs will be made (Hutchinson). These will be compared with data obtained from TMF testing (Zok). The effects of such cracks on the in-plane thermal conductivity will also be calculated (Hutchinson). Measurements will be performed using the laser flash method (Ashby).

Thermal conductivity measurements will be initiated on Ti MMCs (Ashby). These will be used to understand the effects of the fiber/matrix interphases and of matrix damage on the transverse and in-plane thermal conduction.

8. MATERIALS SELECTION

The Cambridge Materials Selector software will be expanded in 1994 to include high temperature creep design with the corresponding data base (Ashby). This expanded version will permit estimates to be made of temperature limits for MMCs based on creep controlled TMF and on the transverse creep of components with unidirectional reinforcements.

9. DESIGN CALCULATIONS AND SUB-ELEMENT TESTS

A larger fraction of the effort in 1994 will be on design and sub-element testing, particularly for MMCs. Discussions are now in progress with Pratt and Whitney, Textron and 3M to perform design calculations using the

constitutive equations developed at UCSB and to produce sub-elements for testing.

The design emphasis for MMCs will be on various diffusion bonded joints with Ti matrices and monolithic Ti attachments. Two specific subelements are envisaged. The first involves unidirectionally reinforced rods (or plates), clad with monolithic metal. The purpose of the cladding is to prevent exposure of the fibers to the environment and to mechanical abrasion. The design of clad MMC structures requires consideration of (i) the residual stresses resulting from thermal mismatch between the cladding and the composites section, (ii) the potential for fatigue cracks to initiate and grow through the monolithic material, and (iii) the interaction of such cracks with the composite section and their influence on the strength and life of the structure. The design and testing of such subelements (Zok, Leckie) will be augmented by calculations of crack growth and fracture, incorporating the effects of thermal and elastic mismatch between the cladding and the composite (McMeeking). The clad structures will also be used to initiate studies on the reinforcement of holes in composite sections with monolithic metal patches, as drawn in Fig. 9.1 (Zok, Suo). The second subelement involves the attachment of a MMC actuator rod to a pin-loaded monolithic section (Fig. 9.2). The critical design issues relate to the strength and fatigue resistance of the interfaces between the composite and monolithic matrices. Design studies shall also be completed on rotor rings with special efforts made to produce rule-based design procedures which would be used by industry at the conceptual level of design to determine sizes and the efficient disposition of material.

For CMCs, the sub-element studies would be based on the calculations described above in Section 5. These would include C sections and T junctions (Fig. 9.3) Negotiations for manufacturing these sub-elements will be initiated and tests performed at UCSB.

10. AFFORDABLE MANUFACTURING

As our understanding of composite mechanics and its interplay with design and performance has evolved, it has become increasingly evident that *cost* and *reproducibility*, are major constraints. Even as processing

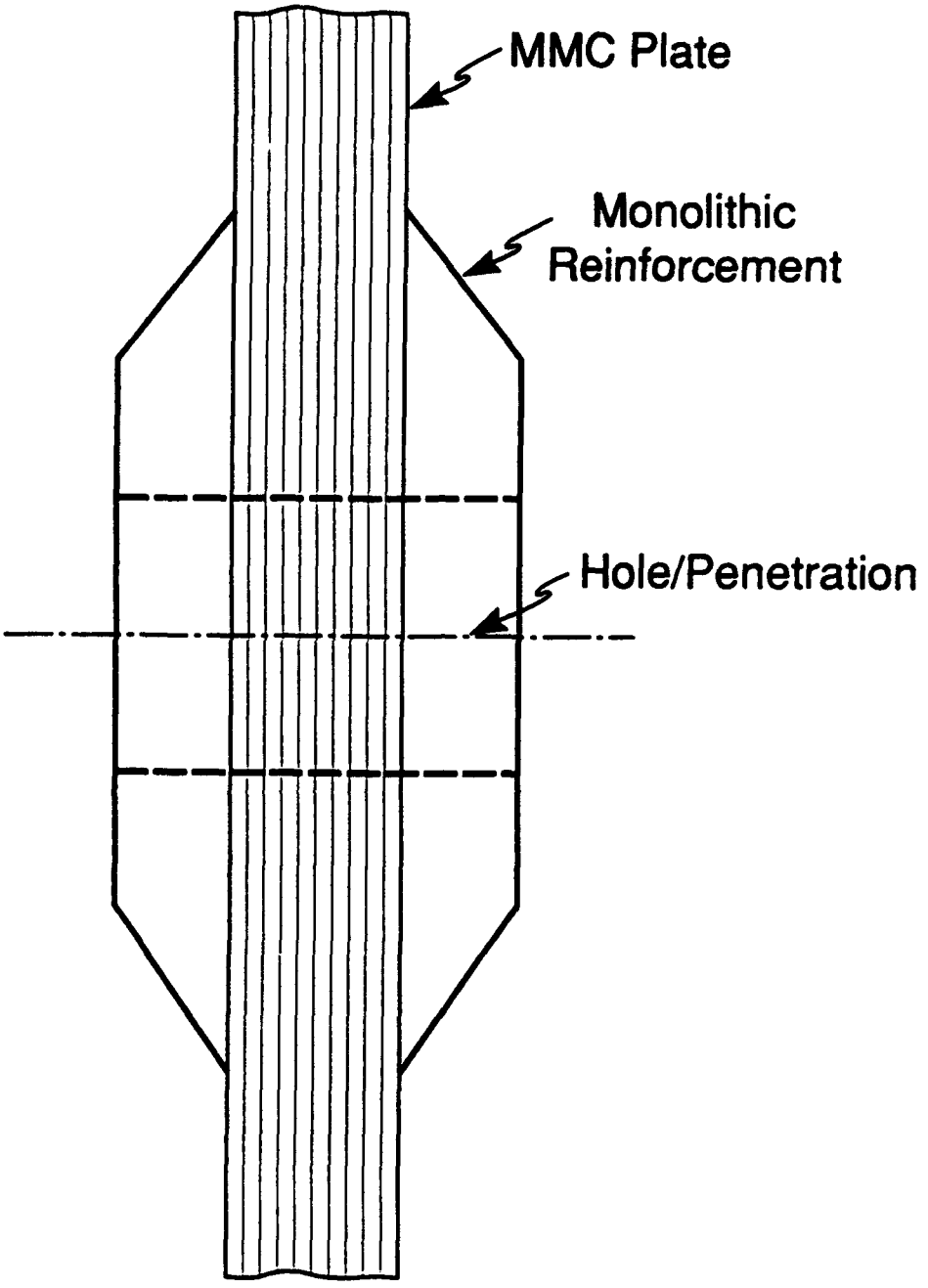

Figure 9.1

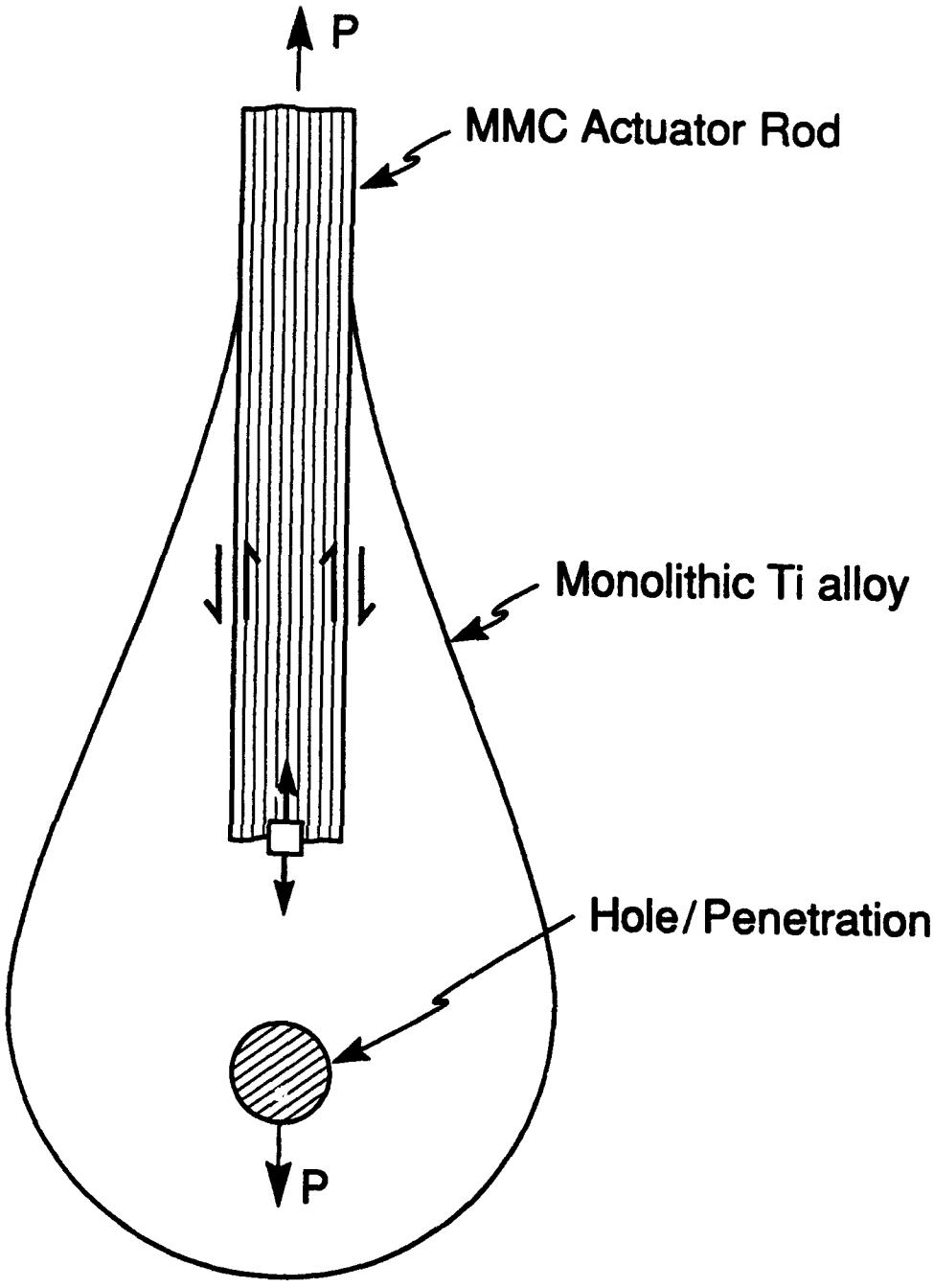

Figure 9.2

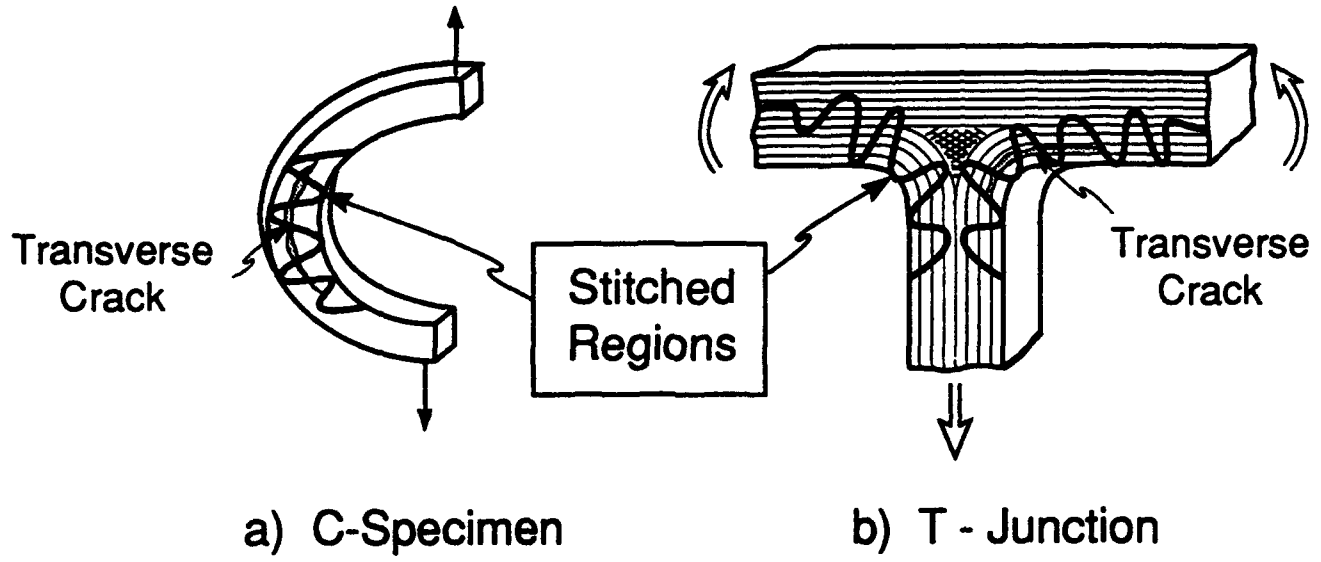
Transverse
Crack
Stitched
Regions
Transverse
Crack
a) C-Specimen
b) T - Junction

Figure 9.3

developments make the prospect of affordable high temperature fibers more realistic, evolving knowledge on the mechanical and thermochemical functions of interfaces have led to design concepts involving carefully tailored interphase layers, with unfavorable impact on cost. Moreover, if affordable coated fibers were available today, fabrication costs associated with consolidation and pressure densification would often remain prohibitive. Future processing and manufacturing activities are predicated on these issues, especially the need for new ideas, and the related knowledge base.

10.1 MMCs

Melt processing methods provide the more affordable options in composite synthesis with the added benefit of near-net shape capability. For continuous fiber composites melt infiltration also enables full density while minimizing the consolidation stresses that typically cause premature reinforcement failure in solid state processes. However, melt processing requires a high degree of thermochemical compatibility between matrix and reinforcement since deleterious diffusional interactions would be accelerated by the liquid phase. Conventional melt processing also exhibits limited ability to control the volume fraction and spatial uniformity of the reinforcements.

Among metal matrices, Ti alloys epitomize unsuitability for direct melt infiltration owing to aggressive reactivity. Fiber clustering is also a concern, even in solid state processes based on powder or foil matrices. Composite consolidation by vapor deposition (PVD) of the matrix on the fibers provides an avenue for improving *homogeneity of fiber spacing*. However, present schemes require expensive pressure densification with its many problems. A potential solution involves a hybrid manufacturing route wherein part of the matrix is first applied to the fibers by PVD. The pre-metallized fibers are then assembled into a preform having the desired shape and then infiltrated with the remaining matrix in liquid form.

Direct infiltration with Ti alloys could be feasible owing to the protection of the fiber by the PVD layer, but the high temperatures involved would exacerbate the diffusional interactions at the fiber-matrix interface. An alternate approach involves depositing the more refractory constituents of

the matrix (e.g., Ti, Nb, Mo, etc.) by PVD and then infiltrating with the lower melting point constituents (e.g. Al). Based on stoichiometric considerations, the latter approach would be suitable for matrices with $\geq$ 25 at.% Al, notably the orthorhombic and α_2 alloys. The obvious problem with this approach is the homogenization of the matrix after consolidation, which may require lengthy high temperature treatments in the solid state. However, a significant part of the matrix synthesis reaction could be effected in the presence of molten Al, followed by a final heat treatment in the solid state. While this lower temperature infiltration approach is evidently desirable from a manufacturing viewpoint, it is not clear that matrix homogenization can be achieved.

A program involving modeling and experimental work will be initiated in 1994 to generate the knowledge base appropriate to hybrid approaches for Ti matrix composites (Levi, Evans). Cell models (single fiber environment) would be developed to study diffusional interactions and remelting/solidification phenomena as a function of processing cycle (temperature-time history). Experiments would be performed to elucidate the relevant aspects of microstructural evolution and provide the reaction and interdiffusion kinetics needed to calibrate the models. Initial experiments would be performed by infiltrating pure Ti-wire preforms with molten Al and subjecting the "composite" to different treatments in the semi-solid state. Subsequent experiments would focus on developing a metallization route for Ti-Nb alloys on SiC fibers and on the relevant interactions with infiltrated Al. Larger scale modeling issues would be tackled in 1995 if the proposed approach appears promising.

Ongoing activities on the understanding of microstructure evolution and its relationship to properties in *in-situ* TMC systems based on TiB reinforcements would be continued (Levi). These are by nature affordable composites which exhibit inherent thermochemical stability and may be cast into shapes using conventional Ti processing techniques. A potential application of these materials would be in joints with unidirectionally reinforced composites, wherein their higher modulus and creep resistance combined with acceptable toughness and isotropic properties could be advantageous. It is also anticipated that these materials could be used for cladding in PVD or plasma-sprayed form, thereby reducing the potential for fatigue crack initiation in the cladding. Since TiB is thermochemically stable

with practically all Ti matrices of interest in fiber composites, such strengthening concepts may be readily implemented.

10.2 CMCs

Measurements and observations in 1993 have shown that strong, high strain to failure CMCs can be fabricated using an inexpensive method that involves a) packing a powder around fibers within a fiber preform using pressure filtration and b) making the powder matrix strong by heat treatment followed by infiltration with a liquid precursor that decomposes to an inorganic material. A composite made this way, with polycrystalline alumina fibers in a silicon nitride matrix, demonstrated that the *matrix* deflects the crack. This observation is significant since it suggest that a class of CMCs can be processed without needing weak fiber/matrix interfaces. The potential of this observation will be explored (Lange, Evans), by processing a composite with strong, polycrystalline alumina fibers in a mullite matrix because the thermomechanical properties of mullite minimize thermal stresses and resist creep. In addition, the thermal expansion mismatch is relatively small. Mixed Al, Si metal alkoxide precursors which can be gelled *in-situ*, prior to decomposition, will be used to strengthen the matrix.

Manufacturing studies would initiate with understanding the precursor infiltration into mullite power compacts. The densification of the matrix would be determined as a function of the cyclic infiltration. Microstructure changes would be controlled to avoid flaw populations during densification. The fracture toughness and the strength of the matrix would be determined as a function of the number of precursor infiltration cycles. Composite processing would initiate with precursor infiltration into alumina fiber preforms by pressure filtration, with emphasis on the colloidal aspects of this processing step. The goal would be to determine the processing conditions needed to produce a matrix that optimizes the ability to deflect cracks without degrading fiber strength. To optimize composite processing, panels for testing under conditions of both strain and stress control would be manufactured.

11. STRESS AND DAMAGE SENSORS

The extensive exploitation of the optical fluorescence method of measuring stresses in sapphire fiber and alumina-containing ceramic composites begun in 1993 will be continued in 1994 (Clarke, Wadley). The emphasis is on using the method to understand basic, unresolved issues in stress redistribution in composites by the direct measurement, with high spatial resolution, of the stresses themselves. Particular attention will be paid to determining the stress distribution associated with interfacial sliding. One of the problems to be addressed relates to new concepts for oxidation resistant interfaces within MMCs and CMCs, particularly the concomitant roles of fiber roughness and sintering on interface sliding and debonding, after exposure to high temperatures and cyclic loadings. For this purpose, fibers with fugitive, low modulus coatings will be explored and fluorescence measurements used to understand stress evolution and its connection with fiber durability within the composite. A second problem relates to the distinction between the line spring and large scale sliding models for fiber bridging (Budiansky, Hutchinson), so as to determine the range of applicability of the two models. The two competing models predict different distributions of stresses in the fibers within the bridging zone and hence are amenable to validation on the basis of the measured stress distribution.

Two approaches to measuring local damage are under development and will be the focus of the sensor activities. One is the use of acoustic methods (Wadley) to probe local variations in the elastic modulus of CMCs as a function of load. This should provide a means of mapping the distribution of damage which can be compared directly with the predictions of continuum damage mechanics models. The second approach (Clarke) is to detect the third harmonic signal generated by the presence of local damage. Preliminary experimental results obtained in 1993 concerned with the detection of crack-like voids in thin metal lines, together with computer simulation studies, have demonstrated the viability of the technique. This work will be extended in order to detect damage accumulation in CMCs and MMCs.

Acta metall. mater. Vol. 41, No. 7, pp. 2061–2071, 1993
Printed in Great Britain.

0956-7151/93 $6.00 + 0.00

MODE I FATIGUE CRACKING IN A FIBER REINFORCED METAL MATRIX COMPOSITE

D. P. WALLS†, G. BAO‡ and F. W. ZOK
Materials Department, University of California, Santa Barbara, CA 93106-5050, U.S.A.

(Received 8 June 1992; in revised form 20 January 1993)

Abstract—The mode I fatigue crack growth behavior of a fiber reinforced metal matrix composite with weak interfaces is examined. In the longitudinal orientation, matrix cracks initially grow with minimal fiber failure. The tractions exerted by the intact fibers shield the crack tip from the applied stress and reduce the rate of crack growth relative to that in the unreinforced matrix alloy. In some instances, further growth is accompanied by fiber failure and a concomitant loss in crack tip shielding. The measurements are compared with model predictions, incorporating the intrinsic fatigue properties of the matrix and the shielding contributions derived from the intact fibers. The magnitude of the interface sliding stress inferred from the comparisons between experiment and theory is found to be in broad agreement with values measured using alternate techniques. The results also indicate that the interface sliding stress degrades with cyclic sliding, an effect yet to be incorporated in the model. In contrast, the transverse fatigue properties are found to be inferior to those of the monolithic matrix alloy, a consequence of the poor fatigue resistance of the fiber/matrix interface.

1. INTRODUCTION

Fiber reinforced metal matrix composites exhibit a variety of damage modes under cyclic loading conditions [1–5]. In the presence of holes or notches, the damage may involve the propagation of a *single* mode I matrix crack perpendicular to the fibers [1–3]. Provided the fiber/matrix interface is sufficiently weak, cracking initially occurs without fiber failure. The tractions exerted on the crack face by the intact fibers shield the crack tip from the remote stress and thus reduce the crack growth rate relative to that of the matrix alone. Further growth may lead to fiber failure, both in crack wake and ahead of the crack tip, leading to an acceleration in crack growth. Alternatively, the damage may be in the form of a process zone comprised of *multiple* mode I cracks [4]. The mechanics of this process again involves issues of crack bridging and fiber failure, as well as an understanding of the role of the *interactions* between cracks. In yet other instances, failure occurs by splitting parallel to the fiber direction [4, 5]. The splitting mode is enhanced by the application of bending moments, as exemplified by tests conducted on compact tension specimens [5].

A comprehensive understanding of the material parameters governing the various damage modes and the role of the damage in fatigue lifetime is not yet available. However, the recognition that the damage modes have close analogies in fiber reinforced *ceramic* matrix composites (CMCs) under *monotonic* loading conditions suggests that the existing mechanics (developed from CMCs) may have applicability to MMCs, provided appropriate modifications are made to account for the cyclic nature of the imposed stress. The present article examines one of these fatigue mechanisms (mode I matrix cracking), and attempts to assess the utility of the mechanics formulisms [6–8] in describing fatigue crack growth. The study compares experimental measurements with model predictions, incorporating the effects of fiber bridging. The role of fiber failure in the fatigue cracking process is also examined.

The paper is organized in the following way. First, a summary of the mechanics of crack bridging by frictionally constrained fibers under cyclic loading is presented (Section 2). The mechanics identifies the important material properties and loading parameters governing fatigue, and provides guidance for the design and interpretation of the experiments. This is followed by a description of the materials and experimental methods employed (Section 3), and a summary of the measurements and observations, along with comparisons with model predictions (Sections 4 and 5).

2. MECHANICS OF CRACK BRIDGING

2.1. Shielding effects

The mechanics of crack bridging by frictionally constrained fibers in brittle matrix composites under monotonic tensile loading has been well established [9–11]. A fundamental assumption in the analysis is that the driving force for crack extension is the *crack tip* stress intensity factor, K_t, as governed by the

†Present address: United Technologies, Pratt and Whitney, West Palm Beach, FL 33410-9600, U.S.A.
‡Present address: Department of Mechanical Engineering, The Johns Hopkins University, Baltimore, MD 21218, U.S.A.

remote stress and the tractions acting in the crack wake. Equating K_t with the composite fracture toughness (which usually scales with the fracture toughness of the matrix itself), gives the stress required for matrix cracking in terms of the component geometry and various constituent properties.

These concepts have been extended to describe matrix cracking in fiber reinforced metal matrix composites under *cyclic* loading conditions [6–8]. By analogy with the monotonic loading problem, the driving force for crack extension is taken to be the crack tip stress intensity factor *amplitude*, ΔK_t

$$\Delta K_t = \Delta K_a + \Delta K_b \tag{1}$$

where ΔK_a is the component due to the applied stress amplitude, $\Delta\sigma_a$, and ΔK_b is the component due to the bridging tractions, $\Delta\sigma_b$, exerted by intact fibers in the crack wake. For an *infinite* center-cracked tensile panel, these components are given by [12]

$$\Delta K_a = \Delta\sigma_a\sqrt{\pi a} \tag{2}$$

and

$$\Delta K_b = -2\sqrt{\frac{a}{\pi}}\int_{a_0}^{a}\frac{\Delta\sigma_b(x)}{\sqrt{a^2-x^2}}\,dx \tag{3}$$

where $2a_0$ is the initial notch length, $2a$ is the current crack length and x is the distance from the crack center.

To evaluate the distribution of bridging tractions, $\Delta\sigma_b(x)$, it is first necessary to specify the contributions to the change in crack opening displacements Δu due to the applied stress Δu_a and that due to the bridging fibers Δu_b [12]

$$\Delta u_a = \frac{4}{E}\Delta\sigma_a\sqrt{a^2-x^2} \tag{4}$$

and

$$\Delta u_b = \frac{-4}{E}\int_{a_0}^{a}\Delta\sigma_b(t)H(t,x,a)\,dt \tag{5}$$

where E is an effective composite modulus (taking account of material orthotropy) and the Green's function H is [12]

$$H(t,x,a) = \frac{1}{\pi}\log\left|\frac{\sqrt{a^2-x^2}+\sqrt{a^2-t^2}}{\sqrt{a^2-x^2}-\sqrt{a^2-t^2}}\right|. \tag{6}$$

The sum of these components

$$\Delta u = \Delta u_a + \Delta u_b \tag{7}$$

is required to be consistent with the cyclic traction law (taking into account reverse slip during unloading) [6]

$$\Delta u = \frac{1}{2}\lambda\Delta\sigma_b^2. \tag{8}$$

Here λ is a material parameter defined by†

$$\lambda = \frac{D(1-f)^2E_m^2}{4E^2E_f\tau f^2} \tag{9}$$

where D is the fiber diameter, f is the fiber volume fractions, E_m and E_f are the matrix and fiber Young's moduli and E is the longitudinal composite modulus ($=fE_f+(1-f)E_m$). Combining equation (4)–(8) gives an integral equation of the form

$$\frac{1}{2}\lambda\Delta\sigma_b^2 = \frac{4}{E}\Delta\sigma_a\sqrt{a^2-x^2} - \frac{4}{E}\int_{a_0}^{a}\Delta\sigma_b(t)H(t,x,a)\,dt. \tag{10}$$

This equation is solved numerically for $\Delta\sigma_b$ using an iterative scheme, and the result combined with equations (1)–(3) to evaluate ΔK_t.

The effects of finite specimen width, $2w$, have also been studied through calculations based on finite element methods [7]. For specimens with a normalized notch size $a_0/w = 0.2$ (a value comparable to those used in the present experiments) and crack lengths in the range $a/w \leqslant 0.5$, the effects of finite width on the *crack tip* stress intensity amplitude can be approximated by the relation

$$\Delta K_t(a/w, \Delta\sigma) \cong Y(a/w)\,\Delta K_t(a/\infty, \Delta\sigma) \tag{11}$$

where $\Delta K_t(a/w, \Delta\sigma)$ and $\Delta K_t(a/\infty, \Delta\sigma)$ represents values for the finite and infinite specimens, respectively, and

$$Y(a/w) = \sqrt{\sec \pi a/2w} \tag{12}$$

(the usual finite width correction used in calculating the *applied* stress intensity [12]). The error introduced by this approximation is less than ~ 3%. As seen later, this range of crack lengths is consistent with the majority of values measured experimentally, making the approximate width correction [equations (11) and (12)] suitable for subsequent calculations.

2.2. Fatigue crack growth

By analogy to monolithic materials, it is expected that the rate of fatigue crack growth in composites can be described in terms of ΔK_t through an empirical relation of the form

$$da/dN = \beta(\Delta K_t)^n \tag{13}$$

where N is the number of loading cycles. The parameters β and n represents the behavior of a matrix crack propagating through an array of elastic fibers and are thus properties of the *composite*. However, in view of the lack of understanding of the effects of the fibers on the processes occurring at the crack tip, it seems adequate to select values of β and n that are representative of the *monolithic matrix alloy*. With this approach, the effects of the fibers *at the crack tip* are neglected.

†The parameter λ differs from that used in Refs. [6, 9] by a factor of $E_m(1-f)/E$. This modification provides consistency between the *steady-state* stress intensity factor and the value obtained from energy-based approaches [10]. A more detailed discussion of the origin of such effects can be found in [13].

2.3. Fiber failure

Once the fibers begin to fail, their contribution to crack tip shielding is reduced substantially. To incorporate such effects in the model, a deterministic criterion for fiber failure has been used [7]. The calculations are conducted by continuously adjusting the unbridged portion of the crack to maintain a stress at the tip of the unbridged segment equal to the fiber strength. Through this approach, the entire cracking history (a vs N) can be simulated.

The results of these calculations can also be used to develop a criterion for a "threshold" stress amplitude, $\Delta\sigma_{th}$, below which fiber failure does not occur for *any* crack length. Within such a regime, the crack growth rate approaches a steady-state value, with all fibers in the crack wake remaining intact. The variation in the "threshold" stress amplitude with fiber strength is plotted in Fig. 1. The maximum value of $\Delta\sigma_{th}$ occurs when there is no notch, i.e. $a_0 = 0$, whereupon

$$\Delta\sigma_{th}/fS(1-R) = 1 \tag{14}$$

where R is the ratio of the minimum to maximum applied stress. Increasing either the notch length or interface sliding stress (or, equivalently, decreasing the fiber strength or fiber diameter) has the effect of decreasing the quantity $\Delta\sigma_{th}/(1-R)fS$.

3. EXPERIMENTAL METHODS

3.1. Material

The material used in this study was a metastable β-titanium alloy (Ti–15V–3Cr–3Al–3Sn) reinforced with continuous, aligned SCS-6 (SiC) fibers. The fibers are 140 μm in diameter and are coated with a 3 μm graded C/Si layer. The purpose of the coating is to inhibit fiber/matrix interaction during consolidation. The composite was fabricated through a foil–fiber–foil technique, wherein Ti-alloy foils and fiber mats are alternately stacked and subsequently vacuum hot-pressed. During consolidation, a brittle reaction product consisting primarily of TiC forms are the interface between the Ti matrix and the C-rich fiber coating [14]. Prior studies have shown this system to exhibit the requisite properties for interface debonding and sliding to occur during matrix cracking [2, 15, 16]. A transverse cross section of the composite is shown in Fig. 2.

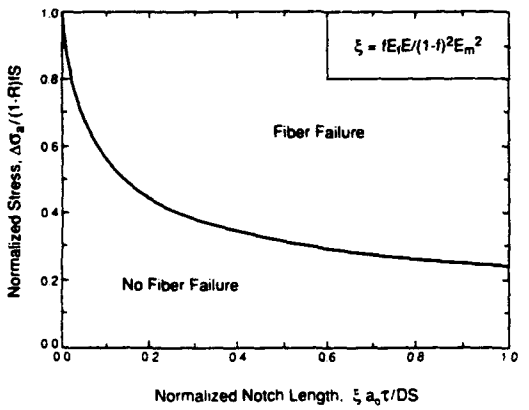

Fig. 1. A diagram showing the influence of notch length, $2a_0$, and material parameters (τ, D, f, S) on the applied stress $\Delta\sigma/(1-R)$ at which fiber failure is predicted to occur during fatigue cracking (adapted from Refs [7] and [22]).

3.2. Fatigue testing

Fatigue tests were conducted in the 0° orientation using center-notched tensile specimens. To minimize machining damage, the notches were formed using electrical discharge machining. The normalized notch lengths were in the range $0.23 \leqslant a_0/w \leqslant 0.35$. One face of each specimen was subsequently diamond polished to a 1 μm finish. Tests were conducted on a servohydraulic mechanical test system at fixed stress amplitude, $\Delta\sigma$. In all cases the stress ratio, R, was maintained at 0.1. Crack extension was monitored using two techniques: indirect potential drop (with thin foil crack gauges mounted at the notch tips), and with a traveling stereo-microscope. The loading parameters and specimen geometry were selected to elucidate the effects of stress amplitude, $\Delta\sigma_a$, and notch size, $2a_0$. The transverse fatigue behavior was measured using compact tension specimens, in accordance with the ASTM standards [17].

The extent of fiber failure during fatigue cracking was monitored using an acoustic emission (AE) system. The system consists of a 175 kHz resonant piezoelectric transducer, a variable gain amplifier, and a detector. The detector incorporates a variable threshold voltage with two counting techniques. *Ringdown* counting records each positive slope threshold crossing of a decaying acoustic signal, whereas *event* counting records the first crossing and ignores subsequent crossings within a fixed reset period (1 ms). The latter technique (employed in the present study) has the potential to resolve *individual* fiber fractures provided that three conditions are satisfied: (a) the acoustic signal decays below the threshold within the reset period; (b) multiple fiber

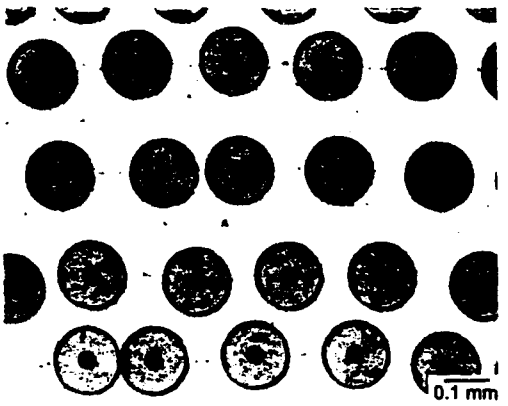

Fig. 2. At transverse section through the composite.

failures do not occur within the reset period; and (c) the system settings can be adjusted to prevent signals from alternate acoustic sources from crossing the threshold. To determine the system settings appropriate to the Ti/SiC composite, a series of preliminary tensile tests were conducted on *monofilament* composite specimens. The specimens were prepared by extracting individual SiC fibers from the composite and bonding fibers onto aluminium strips using an epoxy adhesive. Tensile tests were conducted with the transducer attached to the aluminum strip, and the number of acoustic events associated with fiber failure recorded. The system settings were systematically varied until individual fiber failures were consistently counted as *single* acoustic events. These settings were subsequently used during fatigue testing of the composite. Furthermore, the accuracy of the acoustic emission measurements was evaluated by examining the tested specimens following matrix dissolution, as described below.

3.3. Observations

Direct observations of fiber bridging and fiber fracture were also made. For this purpose, tested specimens were sectioned along a plane ~3 mm above the matrix crack plane, and the matrix subsequently dissolved down to a depth of ~6 mm. During matrix dissolution, the fractured fibers were removed, whereas the intact fibers continued to span the entire length of the specimen. A comparison of the spatial distribution of fractured fibers with the matrix crack prior to dissolution provided a direct measure of the length over which intact fibers had bridged the matrix crack. The fatigue fracture surfaces were also examined in a scanning electron microscopy (SEM).

4. LONGITUDINAL PROPERTIES

4.1. Measurements and observations

Figure 3(a–c) show representative trends in the crack growth behavior, plotted as crack extension, Δa, vs number of loading cycles, N, for tests conducted at various stress amplitudes. Here, the specimens had an initial notch size, $2a_0 = 3$ mm. The results are re-plotted as crack growth rate, da/dN, vs applied stress intensity range, ΔK_a, in Fig. 3(d). Similarly, Fig. 4(a–d) show trends with notch length at a fixed stress amplitude, $\Delta\sigma_a = 400$ MPa.

In all cases, the crack growth rates initially decreased with increasing crack length, despite the corresponding increase in ΔK_a. This behavior is a manifestation of crack tip shielding by intact fibers in

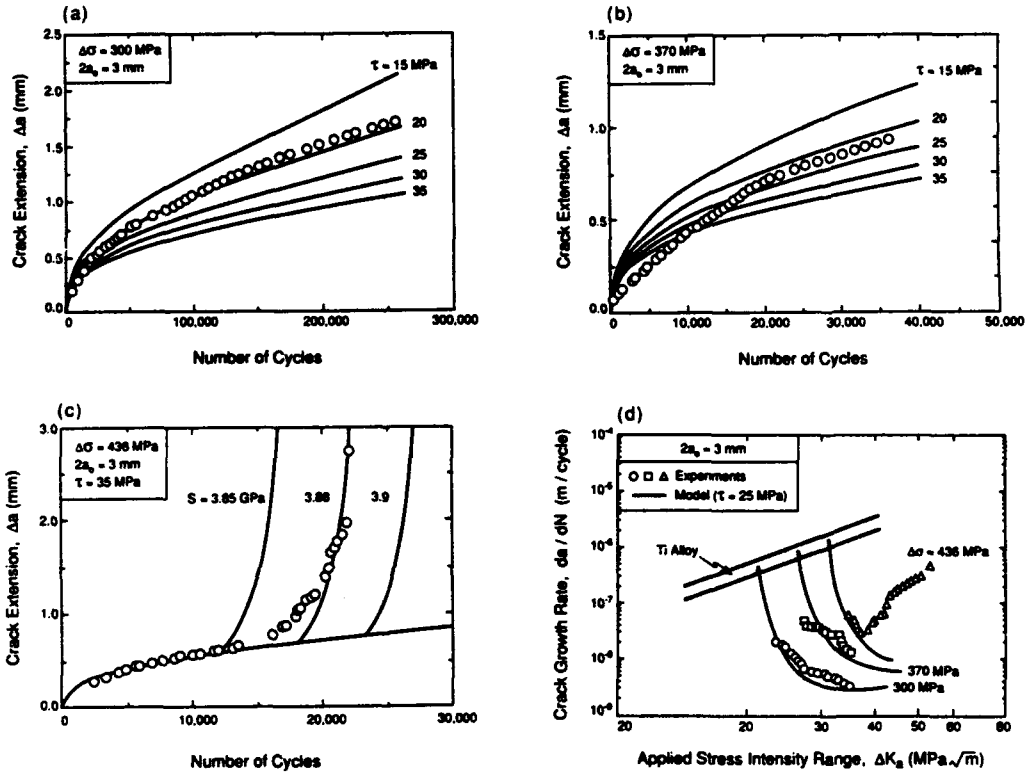

Fig. 3. The influence of stress amplitude on crack growth in the longitudinal orientation, for a notch length $2a_0 = 3$ mm: (a) $\Delta\sigma = 300$ MPa, (b) 370 MPa, (c) 436 MPa. The solid lines are model predictions, assuming no fiber failure in the crack wave. The additional lines in (c) show the model predictions incorporating fiber failure, using a sliding stress, $\tau = 35$ MPa, and 3 values of fiber strength. (d) The data of (a–c) replotted in the conventional format.

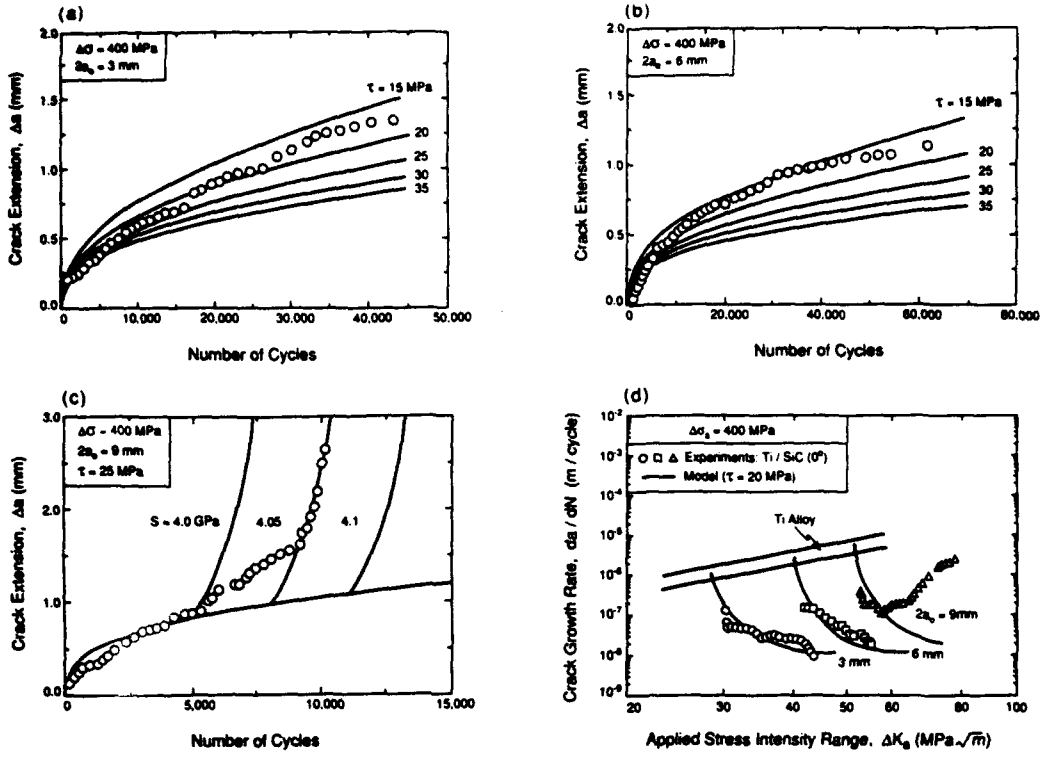

Fig. 4. The influence of notch length on crack growth in the longitudinal orientation, for a stress amplitude $\Delta\sigma_a = 400$ MPa ($R = 0.1$): (a) $2a_0 = 3$ mm, (b) 6 mm, (c) 9 mm. The solid lines are model predictions assuming no fiber failure. The additional lines in (c) show model predictions incorporating fiber failure, using a sliding stress $\tau = 25$ MPa, and 3 values of fiber strength. (d) The data in (a–c) replotted in the conventional format.

the crack wake. The presence of such fibers was confirmed through comparisons between the matrix cracks following fatigue testing and the distribution of underlying fibers following matrix dissolution: an example is shown in Fig. 5. For tests conducted at low stress amplitudes or with small notches, the deceleration in crack growth continued throughout the duration of the tests [Figs. 3(a, b) and 4(a, b)]. In contrast, tests conducted at high stress amplitudes or large notches exhibited a transition in which the growth rate accelerated rapidly with crack extension [Figs 3(c) and 4(c)]. The transition was correlated with the onset of fiber failure. The distribution of broken fibers following fatigue testing for one such test is shown in Fig. 6. [These observations correspond to the data in Fig. 3(c).] In this case, the zone of intact fibers at the end of the tests was only $\sim 300\,\mu$m (or ~ 2 fiber spacings).

The evolution of fiber failure during fatigue cracking was also confirmed by the acoustic emission measurements. For tests conducted at low stress amplitudes or with short notches, the total number of acoustic events was typically $\leqslant 10$. These measurements correspond to the failure of fibers that were partially cut during machining of the notch, an example of which is seen in Fig. 5. In contrast, tests conducted at high stress amplitudes or with long notches exhibited extensive acoustic activity, in accord with observations of fiber failure. Figure 7 shows one example of the evolution of the number, n_f, of failed fibers with crack extension, corresponding to the test results presented in Fig. 4(c). The parameters in this figure have been normalized such that a line of slope unity represents failure of *all* the fibers in the crack wake; the region above the line corresponds to the incidence of fiber failure *ahead* of the crack tip. In this case, fiber failure began at a relatively small amount of crack extension ($\Delta a/D = 2$–3). Further crack growth was accompanied by increasing fiber failure and a concomitant increase in crack growth rate. The acoustic emission measurements also indicate that, beyond $\Delta a/D \approx 12$, fiber failure occurs ahead of the crack tip. This point corresponds closely to the onset of rapid crack acceleration (at $N \approx 8000$), seen in Fig. 4(c). SEM examination of the specimen following matrix dissolution (Fig. 8) confirmed the number of failed fibers measured through acoustic emission (within $\sim 10\%$).

SEM examinations of the fracture surfaces revealed two notable features. Firstly, the amount of fiber pullout on the fatigue fracture surface was small; typically $\leqslant 2D$ (Fig. 9). This observation indicates that the fiber strength distribution is narrow, in

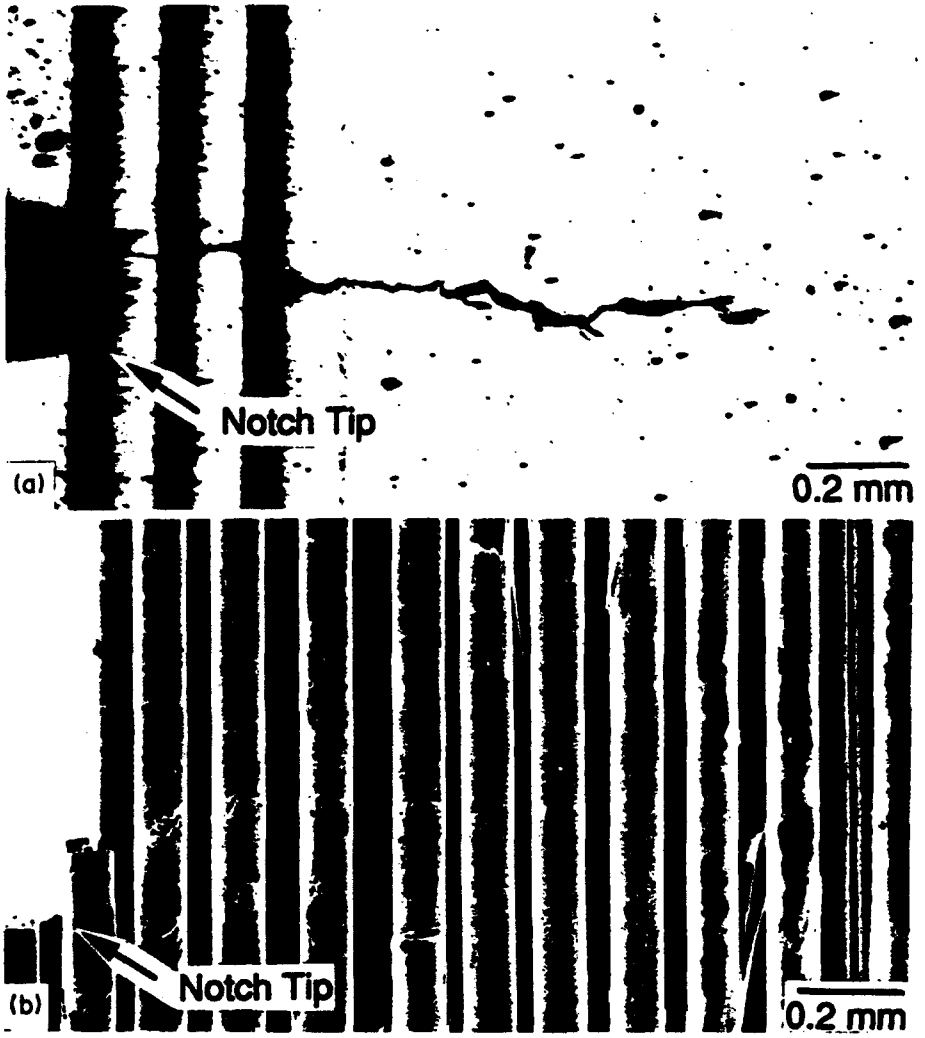

Fig. 5. Comparison between (a) a matrix fatigue crack, as seen on the external surface, and (b) the underlying fibers following matrix dissolution. The micrograph are at the same magnification and represent the identical region of the specimen. The fatigue test was conducted at $\Delta\sigma_0 = 300$ MPa, $R = 0.1$, and $2a_0 = 3$ mm.

accord with the reported values of Weibull modulus for the SCS-6 fibers (~ 10). Secondly, the fiber coatings exhibited extensive fragmentation following fatigue [Fig. 10(a)]. In contrast, the coatings on the fibers in the fast fracture region were left intact [Fig. 10(b)]. Evidently, the cyclic sliding leads to a degradation in the fiber coating.

4.2. *Comparison between experiment and theory*

The measured crack growth curves have been compared with model predictions [7], taking into account the effect of bridging fibers on ΔK_t. The parameters β and n in equation (13) were taken to be those for the matrix alloy [5] and are given in Table 1. The various elastic moduli [14] are also given in Table 1. The material parameter that is subject to the most uncertainty is the interface sliding stress, τ. Consequently, the approach adopted here was to compare the experimental data with model predictions for *a range of values* of τ and then assess whether consistency is achieved over the entire range of measurements. The model predictions also accounted for fiber failure, assuming a deterministic fiber strength, S. In this regime, the calculations were based on a fixed value of τ (chosen to be consistent with the data in the regime prior to fiber failure) and comparisons made for a range of values of S. The inferred value of S was then compared with values reported elsewhere.

Figures 3 and 4 show the comparisons between experiment and theory. In the regime prior to fiber failure, all the experimental data are consistent with the model for τ in the range of 15–35 MPa.

The values of τ inferred from the fatigue tests have been compared with those measured on both pristine and "fatigued" fibers using single fiber pushout

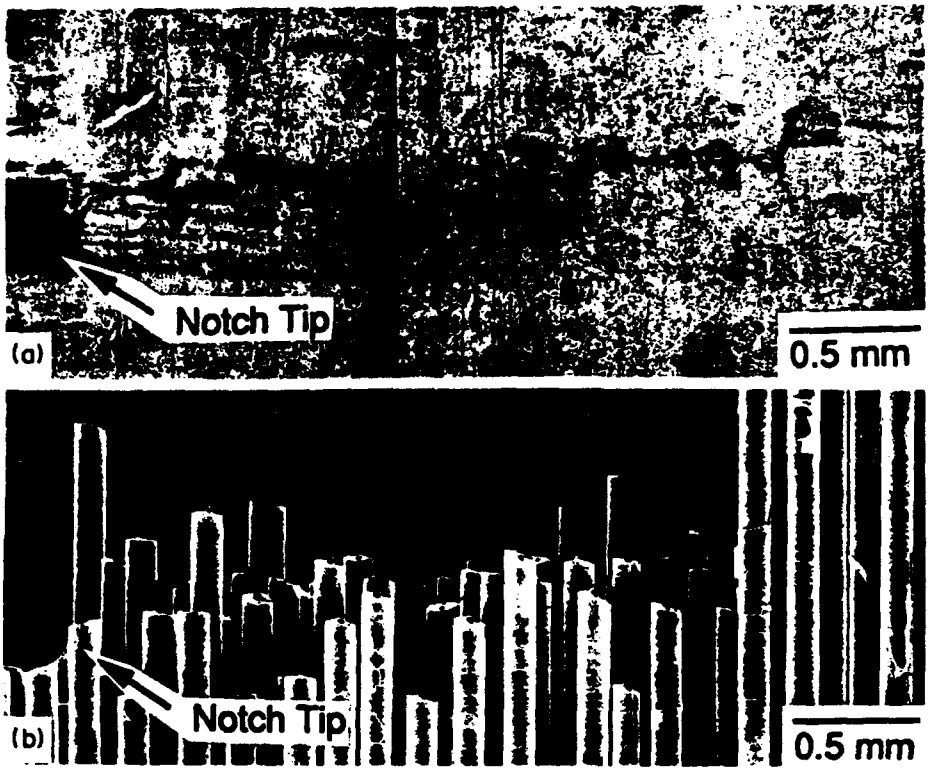

Fig. 6. A comparison similar to that shown in Fig. 6, for a specimen tested at $\Delta\sigma_a = 436$ MPa, $R = 0.1$ and $2a_0 = 3$ mm. Note the extent of fiber failure in the crack wake.

tests [18] (Fig. 11). Specimens with "fatigued" fibers were prepared by cutting composite sections $\sim 600\,\mu$m thick, adjacent to a matrix fatigue crack. The sections were then ground and polished to a final section thickness of $\sim 400\,\mu$m. The pristine specimens were prepared in a similar fashion, using undeformed material. The pushout tests show that the sliding resistance of the pristine fibers is initially ~ 90 MPa, but decreases as the fiber slides out of the composite. This trend has previously been rationalized in terms of the wear of asperities on the fiber coating during sliding [19]. In contrast, the sliding stress for the fatigued fiber is initially only ~ 20 MPa, but subsequently *increases* with pushout distance. This behavior is consistent with the extensive fragmentation of the fiber coating following fatigue (Fig. 10). Comparisons of the data with the range of values of τ inferred from the fatigue crack growth experiments shows broad agreement, providing additional confidence in the utility of the micromechanical model. However, it must be emphasized that the fiber coatings degrade during cyclic sliding, leading to changes in the interface sliding stress. Such effects have yet to be incorporated in the model.

The model predictions in the regime following fiber failure are consistent with a fiber strength of ~ 4 GPa [Figs 3(c) and 4(c)]: a value comparable to previous measurements of the strength of pristine SCS-6 fibers [20]†.

The present observations have also been used to assess the predictions of the "threshold" stress amplitude, described in Section 2.3. A comparison of the measurements and predictions is shown in Fig. 12. Here, the experimental data have been plotted for an average value of sliding stress, $\tau = 25$ MPa, with the error bars corresponding to the uncertainty in τ (15–35 MPa). Despite the rather broad uncertainty, the observations

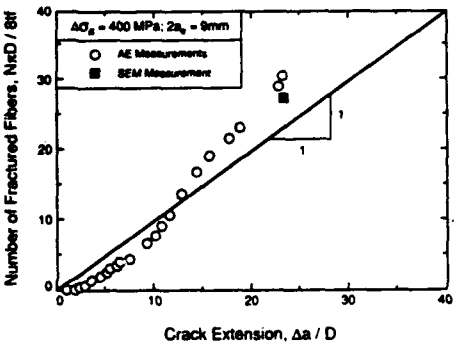

Fig. 7. Evolution of fiber failure with crack extension (t is the thickness of the composite panel).

†It is recognized that a deterministic fiber failure criterion is not, strictly speaking, applicable to ceramic fibers. However, in the present case, the range of fiber strength is narrow and thus the criterion appears to be adequate.

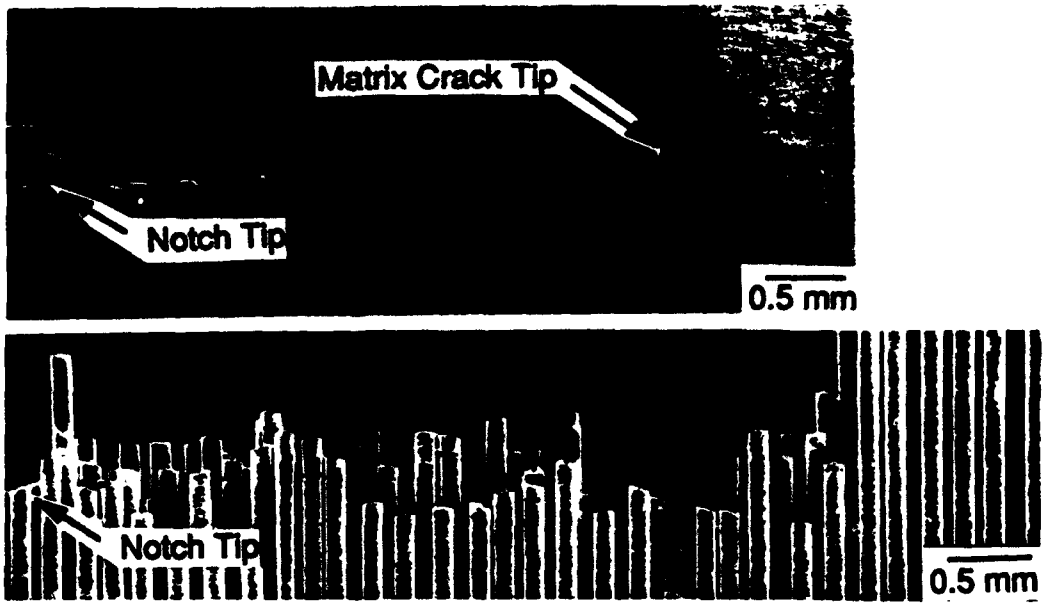

Fig. 8. Comparison of matrix crack and underlying fibers for test conducted at $\Delta\sigma_a = 400$ MPa, $R = 0.1$ and $2a_0 = 9$ mm. Note the absence of intact fibers in the crack wake and the extent of fiber failure *ahead* of the crack tip.

appear to be consistent with the predictions. Specifically, both the experiments and the theory indicate that a transition to the regime of fiber failure can be brought upon by increasing either $\Delta\sigma_a$ or a_0.

5. TRANSVERSE PROPERTIES

5.1. Measurements and observations

In contrast to the longitudinal behavior, fatigue crack growth in the transverse orientation was not

Fig. 9. SEM view of fatigue fracture surface, showing the extent of fiber pullout.

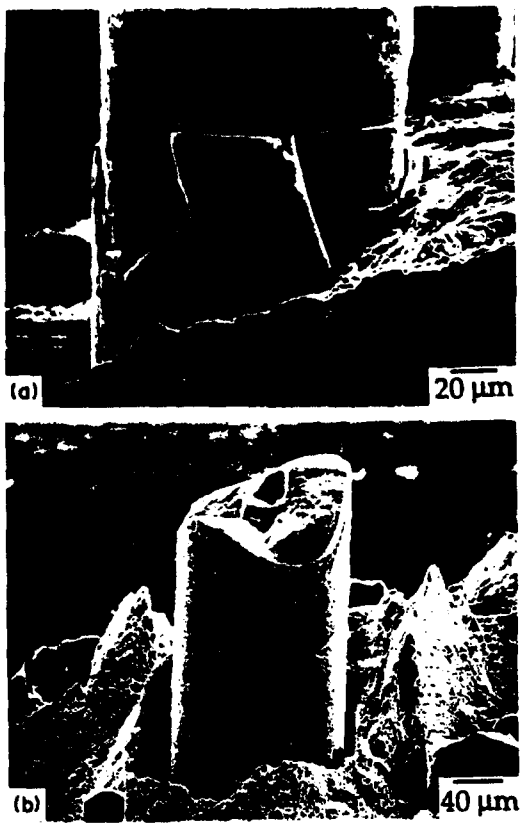

Fig. 10. SEM observations of failed fibers in (a) the fatigue region, and (b) the fast fracture region. Note the damage on the fiber coating in (a).

accompanied by crack bridging. Indeed, the fatigue resistance of the composite in this orientation was *inferior* to that of the matrix alloy. The trends in the crack growth rate with the *applied* stress intensity amplitude are shown in Fig. 13. The behavior of the composite closely parallels that of the matrix alloy, though the growth rates are somewhat higher in the composite. SEM examinations of the fatigue fracture surface indicate that the cracks propagate along the matrix ligaments between fibers, with no evidence of fiber bridging or fiber fracture in the crack wake (Fig. 14). These observations are consistent with the static tensile properties of the composite, wherein the transverse strength is lower than that of the matrix [14].

5.2. *Comparison between experiment and theory*

An upper bound estimate of the transverse crack growth rate in the composites can be obtained by

Table 1. Mechanical properties of fiber, matrix and composite

Matrix modulus	$E_m = 115$ GPa [14]
Fiber modulus	$E_f = 360$ GPa [14]
Longitudinal composite modulus	$E = 200$ GPa [14]
Effective composite modulus	$\bar{E} = 193$ GPa*
Coefficient in Paris law	$\beta = 5.5 \times 10^4$ (m$^{1-n/2}$) [5]
Exponent in Paris law	$n = 2.8$ [5]

*Calculated in Ref. [7].

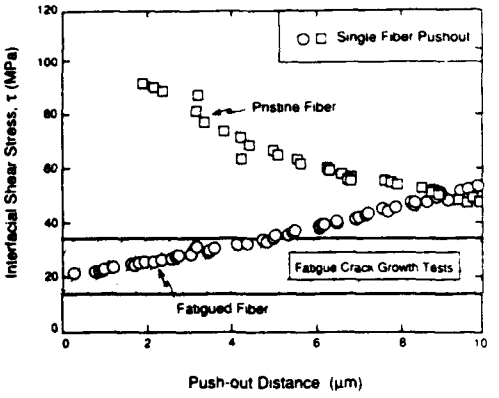

Fig. 11. Results of single fiber push out tests on pristine and fatigued fibers. Also shown is the range of τ inferred from the fatigue crack growth experiments.

neglecting the fatigue resistance of the fiber matrix interface. The driving force for crack extension in the composite is thus obtained through a net section correction of the form

$$\Delta K_t = \Delta K_a \cdot A_m \tag{15}$$

where A_m is the area fraction of matrix on the fracture surface. Measurements made on the fracture surface give $A_m \approx 0.38$. This value compares favorably with one calculated, assuming that the fibers are arranged in a square array and that the fatigue crack propagates along the narrowest matrix ligament between fibers, giving

$$A_m = 1 - (4\pi/f)^{1/2} \approx 0.33. \tag{16}$$

The model predictions based on this adjustment are shown by the dashed lines on Fig. 13. Evidently, the predictions lie above the measured data. This result suggests that either the fiber/matrix interface provides some fatigue resistance, or a closure effect arises from the presence of the debonded fibers in the crack wake. The latter effect is consistent with the thermal expansion mismatch in this composite system.

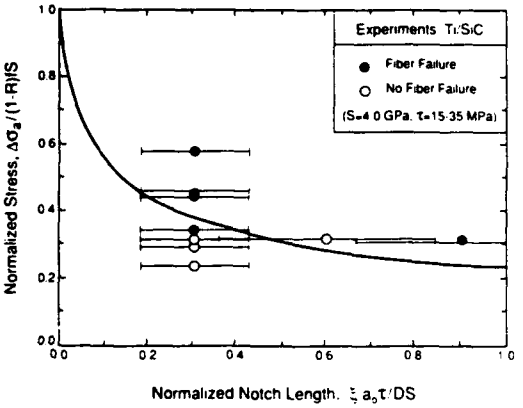

Fig. 12. A diagram showing the conditions under which fiber failure was observed during fatigue cracking. The line shows model prediction, based on the results of Fig. 3. (The parameter ξ is defined on Fig. 1.)

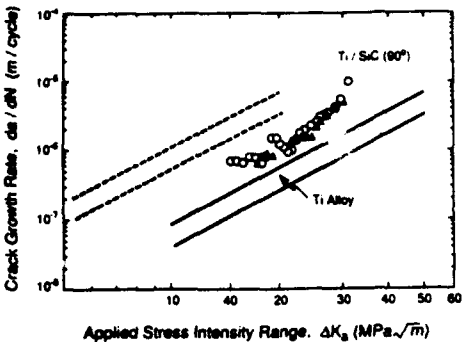

Fig. 13. Comparison of crack growth rates in composite in transverse orientation with that of the monolithic matrix alloy. The broken lines represent model predictions for the composite, based on a net section correction [equation (16), $A_m = 0.38$].

6. CONCLUDING REMARKS

The fatigue crack growth characteristics of a unidirectional, fiber reinforced metal matrix composite have been measured and the results compared with model predictions. The results indicate that the properties of the fiber/matrix interface play a central role. In the longitudinal orientation, matrix cracking initially proceeds with minimal fiber failure: the weak fiber/matrix interface allows debonding and sliding to occur, leaving the fibers intact in the crack wake. The bridging fibers provide substantial crack tip shielding during crack growth, as evidenced by the reductions in crack growth rate with increased crack extension. The measurements have been found to be consistent with the predictions of a micromechanical model in which the fibers are assumed to be frictionally coupled to the matrix, with a constant interface sliding stress. The values of the sliding stress inferred from such comparisons are in broad agreement with values measured from single fiber pushout tests on *fatigued* specimens. These values, however, are substantially lower than those measured on pristine fibers, suggesting that the fiber coatings degrade during cyclic sliding. The role of such degradation on the cyclic traction law will be addressed elsewhere [21]. In some instances, the fibers in the crack wake fail, leading to a loss in crack tip shielding and an acceleration in crack growth. The behavior in this regime is also consistent with the model predictions, using a deterministic value for fiber strength. In the transverse orientation, the weak fiber/matrix interface results in a degradation in the fatigue resistance of the composite relative to that of the matrix alloy alone.

An important conclusion derived from both the experimental measurements and the model predictions pertains to the use of the *applied* ΔK as a loading parameter in describing fatigue crack growth in this class of composite. It is apparent that the bridging effects in the longitudinal orientation are so pronounced that ΔK_a does not generally provide even a rough estimate of the crack tip stress field. Consequently, no unique relationship exists between da/dN

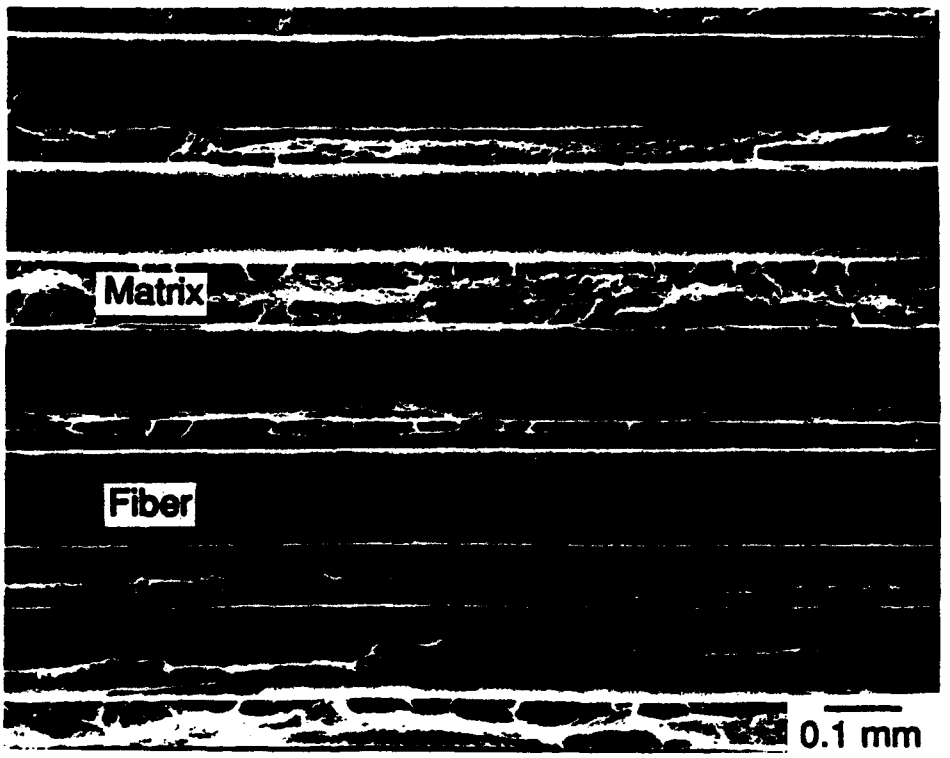

Fig. 14. Fatigue fracture surface of the composite in the transverse orientation.

and ΔK_a, except in the extreme cases where the crack extension into the composite is small, i.e. less than one fiber spacing, or when all the fibers in the crack wake have failed. Similar conclusions have been reached regarding the use of the applied stress intensity factor in characterizing matrix cracking in brittle matrix composites.

Acknowledgements—Funding for this work was supplied by the Defense Advanced Reseach Projects Agency through the University Research Initiative Program of UCSB under ONR Contract no. N-0014-86-K-0753, and the College of Engineering, UCSB.

REFERENCES

1. B. N. Cox and D. B. Marshall, *Fatigue Fract. Engng Mater. Struct.* **14**, 847 (1991).
2. M. D. Sensmeier and P. K. Wright, in *Fundamental Relationships Between Microstructure and Mechanical Properties of Metal Matrix Composites*, (edited by P. K. Liaw and M. N. Gungor), pp. 441–457. The Minerals Metals and Materials Society (1990).
3. P. K. Wright, R. Nimmer, G. Smith, M. Sensmeier and M. Brun, in *Interfaces in Metal–Ceramic Composites*, (edited by R. Y. Lin, R. J. Arsenault, G. P. Martins and S. G. Fishman), pp. 559–581. The Minerals, Metals and Materials Society (1989).
4. D. M. Harmon and C. R. Saff, in *Metal Matrix Composites: Testing, Analysis and Failure Modes*, ASTM STP 1032 (edited by W. S. Johnson). ASTM, Pa. (1989).
5. P. Kantzos, J. Telesman and L. Ghosn, NASA TM-103095 (1989).
6. R. M. McMeeking and A. G. Evans, *Mech. Mater.* **9**, 217 (1990).
7. G. Bao and R. M. McMeeking, to be published.
8. B. N. Cox and C. S. Lo, *Acta metall. mater.* **40**, 69 (1192).
9. D. B. Marshall, B. N. Cox and A. G. Evans, *Acta metall.* **33**, 2013 (1985).
10. B. Budiansky, J. W. Hutchinson and A. G. Evans, *J. Mech. Phys. Solids* **34**, 167 (1986).
11. D. B. Marshall and B. N. Cox, *Acta metall.* **5**, 2607 (1987).
12. H. Tada, P. C. Paris and G. R. Irwin, *The Stress Analysis of Cracks Handbook*. Del Research, St. Louis (1985).
13. M. D. Thouless, *Acta metall.* **37**, 2297 (1989).
14. S. Jansson, H. Deve and A. G. Evans, *Metall. Trans.* **22A**, 2975 (1991).
15. D. P. Walls, G. Bao and F. Zok, *Scripta metall. mater.* **25**, 911 (1991).
16. P. Bowen, A. R. Ibbotson and C. J. Beevers, in *Fatigue of Advanced Materials* (edited by R. O. Ritchie, R. H. Dauskardt and B. N. Cox), pp. 379–93. Materials and Component Engineering Pub. Ltd., Birmingham (1991).
17. ASTM E399, Annual Book of ASTM Standards, ASTM Pa (1988).
18. P. D. Warren, T. J. Mackin and A. G. Evans, *Acta metall. mater.* **40**, 1243 (1992).
19. T. J. Mackin, P. D. Warren and A. G. Evans, *Acta metall. mater.* **40**, 1251 (1992).
20. K. K. Chawla, *Composite Materials Science and Engineering*. Springer, New York (1987).
21. D. P. Walls and F. W. Zok, to be published.
22. L. Cui and B. Budiansky, to be published.

MATERIALS

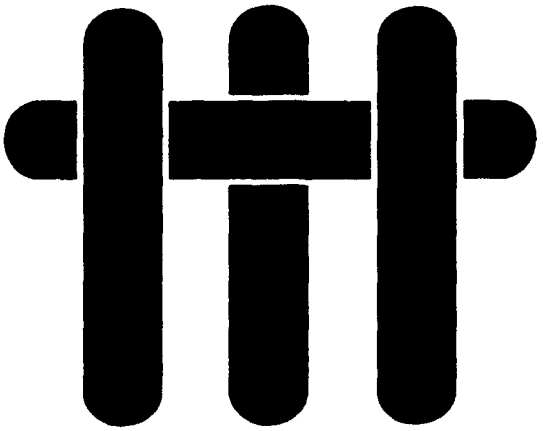

INTERFACIAL FATIGUE IN A FIBER REINFORCED METAL MATRIX COMPOSITE

by

D. P. Walls* and F. W. Zok

Materials Department
University of California
Santa Barbara, California 93106

*Presently at United Technologies, Pratt & Whitney
Mail Stop 707-22, PO Box 109600
West Palm Beach, FL 33410-9600

Submitted to Acta Metallurgica et Materialia, April 1993

7F:MS25(June 15, 1993)/3:07 PM/mef

ABSTRACT

An experimental investigation of interface fatigue in a fiber reinforced metal matrix composite has been conducted. For this purpose, the cyclic traction law (the relationship between the fiber stress and the pullout displacement) was measured using fiber pullout tests. On the first loading cycle, the traction law was found to be parabolic, in accord with predictions of a micromechanical model based on a constant interface sliding stress. Upon subsequent unloading and re-loading, the relationship changed, following trends which suggest that the sliding resistance degrades with cyclic sliding. Such effects have been confirmed through SEM examinations of the fiber coatings following fatigue testing. Furthermore, the degradation was found to be greatest near the plane of the matrix crack. The results are consistent with the notion that the degradation in sliding stress occurs most rapidly in regions where the relative sliding distance (fiber/matrix) is greatest. A phenomenological model incorporating such degradation is presented and compared with the experimental measurements.

1. INTRODUCTION

The growth of mode I matrix fatigue cracks in fiber reinforced metal matrix composites (MMCs) is frequently accompanied by interface debonding and sliding. This process allows the fibers to remain intact in the crack wake. The tractions exerted by the fibers reduce the crack tip stress intensity amplitude (relative to an unbridged crack) and thus reduce the rate of matrix cracking[1-5]. The fundamental composite property governing the fatigue resistance of such composites is the *cyclic traction law*: the relationship between the bridging stress amplitude and the crack opening amplitude[6,7]. Such laws have been combined with fracture mechanics analyses to predict crack tip stress intensity amplitudes for a variety of specimen geometries[6,7]. Through this approach, fatigue life predictions can be made, incorporating the relevant constituent properties.

The existing models of fiber bridging are based on the assumption that the sliding behavior of the interface is characterized by a constant shear stress, τ[6-11]. This approach has been validated for a variety of metal and intermetallic matrix composites, subject to monotonic tensile loading[11,14]. However, there is experimental evidence to suggest that the sliding behavior changes substantially during high cycle fatigue. Specifically, measurements of fatigue crack growth rates have been found to be consistent with the bridging models for values of τ that are substantially lower than those measured on pristine fibers[12]. Such trends have been confirmed by fiber push-out tests, conducted on specimens cut adjacent to a fatigue crack[13]. The purpose of the present article is to present experiments that provide more direct information about changes in the cyclic traction law in MMCs subject to high cycle fatigue, and make comparisons with predictions of the model based on constant τ.

2. MATERIALS AND EXPERIMENTAL TECHNIQUES

The composite used in the study was a metastable β-titanium alloy (Ti-15V-3Cr-3Al-3Sn) reinforced with continuous, aligned SCS-6 (SiC) fibers. The fibers had a 3 μm graded C/Si layer, in order to protect them from damage and inhibit fiber/matrix interaction during consolidation. The composite panel was ~2 mm thick and consisted of 9 fiber plies, with a fiber volume fraction of 35%. Fatigue studies on this composite have shown that interface debonding and sliding occurs during matrix cracking, resulting in substantial crack tip shielding[12]. The relevant properties of this composite are summarized in Table 1.

Pullout specimens suitable for fatigue testing were made by a process involving cutting, grinding and chemical dissolution (Fig. 1). First, long slender specimens, 6 mm wide by 50 mm long, were cut parallel to the fiber direction. Two coplanar notches were ground into each side of the specimens. The process was carefully monitored to ensure that the central 3 fiber layers were not damaged during grinding. In addition, shallow notches (~0.5 mm) were cut on either side of the central notch on one face, with a separation of 10.0 mm. These grooves were subsequently used for mounting an extensometer on the specimen. The section of the specimen away from the notch was masked with an epoxy and the matrix material within the notch dissolved using concentrated nitric acid, leaving a section consisting of only 3 rows of fibers.

Uniaxial fatigue tests were performed in a servohydraulic mechanical testing machine. The specimens were gripped over a length of ~10 mm on either end using hydraulic wedge grips. The load amplitude was selected to give a fiber stress range, $\Delta\sigma_f^o$, in the notch plane between 1500 and 2000 MPa, with an R ratio (minimum to maximum stress) of 0.1. The loading frequency was fixed at 5 Hz. The displacements were measured using a 10 mm clip-on extensometer. The knife edges of the extensometer were inserted snugly into the grooves, and the extensometer securely

attached to the specimen using rubber bands. Cycling was periodically interrupted and the load/displacement behavior recorded while loading the specimen at a rate of 0.2 μm/s.

Subsequent to testing, one of the specimens was fractured along a plane *perpendicular* to the notch plane, exposing the fiber/matrix interfaces (both pristine and cycled). This was accomplished by cutting a deep notch from the gripped region of the specimen and subsequently wedging the notch open. The specimen was broken in liquid nitrogen (-196°C) in order to minimize the effects of matrix plasticity on the exposed interfaces. The interfaces on both pristine and cycled fibers were examined in a scanning electron microscope (SEM).

3. MECHANICS OF FIBER PULLOUT

Prior to presenting the experimental results, the relevant mechanics associated with fiber pullout is briefly reviewed. The mechanics provides a framework within which the results are presented and interpreted.

The simplest model of fiber pullout is based on the assumption that the sliding resistance of the interface is characterized by a constant shear stress, τ. This approach has been used to study crack bridging in fiber-reinforced CMCs under monotonic loading and MMCs under cyclic loading. The relations pertinent to the present study are summarized below. Additional details of the mechanics can be found in Refs. 6-8.

Under monotonic tensile loading, the fibers slip past the matrix over a length, ℓ, given by

$$\ell = \frac{\sigma_f^0 (1-f) E_m D}{4\tau E} \qquad (1)$$

where D is the fiber diameter, f is the fiber volume fraction, σ_f^o is the fiber stress in the matrix crack plane, and E_m and E_f are the Young's moduli of the matrix and fiber, respectively. The *remote* displacement due to pullout, δ_p, is obtained by integrating the additional fiber strain due to sliding over the slip length, yielding

$$\delta_p = \frac{D\alpha^2 \sigma_f^{o\,2}}{4E_f \tau(1+\alpha)^2} \tag{2}$$

where $\alpha \equiv E_m(1\text{-}f) / E_f f$. During unloading, slip occurs in the reverse direction, whereupon the pullout displacement becomes[6]

$$\delta_p' = \delta_{p\max} - \frac{D\alpha^2 \left(\sigma_{f\max}^o - \sigma_f^o\right)^2}{8E_f \tau(1+\alpha)^2} \tag{3}$$

where $\delta_{p\,max}$ is given by Eqn. (2), evaluated at the stress maximum, $\sigma_{f\,max}$. The corresponding result for re-loading is[6]

$$\delta_p'' = \delta_{p\min} + \frac{D\alpha^2 \left(\sigma_f^o - \sigma_{f\min}^o\right)^2}{8E_f \tau(1+\alpha)^2} \tag{4}$$

where $\delta_{p\,min}$ is given by Eqn. (3), evaluated at the stress minimum, $\sigma_{f\,min}$. Figure 2 shows the predicted trends for the case where R = 0. A notable feature here is that the cyclic traction law remains the same beyond the first loading cycle, *provided τ remains constant*.

Application of these formulisms to the present experiments requires two modifications. First, because the notching process used to make the specimens reduces

the fiber volume fraction within the notched section, the matrix "crack" is not fully bridged. This effect can be treated through a modified shear lag analysis, assuming that load is transferred uniformly from the composite to the bridging fibers (Appendix). Following this approach, the relations between δ_p and σ_f become

$$\delta_p = \frac{D(\eta+\alpha)^2 \sigma_f^{o^2}}{4E_f \tau(1+\alpha)^2} \tag{5}$$

$$\delta_p' = \delta_{p\max} - \frac{D(\eta+\alpha)^2 \left(\sigma_{f\max}^o - \sigma_f^o\right)^2}{8E_f \tau(1+\alpha)^2} \tag{6}$$

$$\delta_p'' = \delta_{p\min} + \frac{D(\eta+\alpha)^2 \left(\sigma_f^o - \sigma_{f\min}^o\right)^2}{8E_f \tau(1+\alpha)^2} \tag{7}$$

where η is the number fraction of broken fibers. In the present geometry, $\eta = 2/3$. When η is zero, Eqns (5)-(7) reduce to Eqns. (2)-(4), as required.

The second problem involves interpretation of the measured displacement, δ. This displacement has two components. One is due to *elastic* extension, δ_e, both in the fibers within the notched section and in the composite, and the other is due to *pullout*, δ_p. The elastic component varies linearly with load, P, whereas the pullout component is proportional to the square of the load (subject to the constant τ assumption). The total displacement can thus be expressed as

$$\delta = C_1 P + C_2 P^2 \tag{8}$$

where C_1 represents the (elastic) compliance of the specimen and C_2 is a parameter that embodies the material properties given in Eqn. (4). Upon rearrangement, Eqn. (8) becomes

$$\delta / P = C_1 + C_2 P \tag{9}$$

The form of Eqn. (9) suggests that δ/P should vary linearly with P, with the slope being C_2 and the intercept C_1.

4. MEASUREMENTS AND OBSERVATIONS

The measured load-displacement curve for the first loading cycle of each test was used to determine the specimen compliance, C_1, and to assess the validity of the constant τ model. Figure 3 shows the variation in δ/P with P for one such test. In this case, the degree of linearity is high, with a correlation coefficient, r = 0.998. Two additional tests conducted at similar stress levels provided essentially the same results, with correlation coefficients consistently above 0.99. The values of τ, evaluated from the slopes of these plots, were in the range, τ = 55 to 60 MPa. This range is consistent with values measured on other metal and intermetallic matrices reinforced with the same fibers[11,14].

A series of hysteresis loops (stress vs. pullout displacement) for various numbers of loading cycles, N, is shown in Fig. 4. The pullout displacement was obtained by subtracting the elastic displacement, C_1P, from the measured displacement S, using the experimentally determined value of C_1. Two features are noteworthy. (i) The slope of the loops decreases with loading cycles, suggesting that the interface sliding resistance is diminished. Closer examination indicates that the first cycle (loading *and* unloading)

is consistent with the constant τ model (Fig. 5). Substantial deviations from the model predictions occur on the *second* loading cycle. (ii) Cyclic loading results in an increasing amount of permanent (zero-load) displacement, manifested in the translation of the hysteresis loops. The variation in permanent displacement with number of cycles is plotted on Fig. 6. This trend is also consistent with a diminishing sliding stress with loading cycles.

Further insight is obtained by plotting the results as the *change* in pullout displacement, $\Delta\delta_p$, during a single loading cycle with the *change* in fiber stress, $\Delta\sigma_f^o$, using logarithmic coordinates. Figure 7 shows one such plot. (For clarity, only the loading portion of each cycle is shown.) The linearity of the data suggests that the traction law can be represented by a power law, with the power law exponent, $d \log \Delta\delta_p / d \log \Delta\sigma_f^o$, varying with loading cycles, N. The exponent decreases rapidly from an initial value of 2 to a value of ~1.3 following ~100 loading cycles, and subsequently remains constant (Fig. 8). The change in the exponent from a value of 2 indicates that the degradation process occurs *non-uniformly* along the slip zone, i.e. the sliding stress varies along the fiber length.

SEM examinations of the fiber coatings confirmed that the coatings did indeed undergo changes during cyclic sliding. The surfaces of the pristine fibers, exposed by breaking the sample along the fiber length, exhibit a hillock morphology, with a roughness amplitude of ~0.3 μm and a wavelength of ~3 μm (Fig. 9). On the fatigued fibers, the hillocks are smeared out along the fiber length (Fig. 10). Furthermore, the degree of smearing varies along the length of the fiber, being highest near the notch plane. At distances ≥ 1mm from the notch plane, the surfaces appear to be essentially the same as those of the pristine fibers. The observations suggest that the degree of wear and the corresponding reduction in the sliding resistance depends on the amount of relative sliding between the fibers and the matrix: the amount of sliding being greatest near the notch plane.

The measurements and observations form the basis for a phenomenological degradation model that incorporates changes in the interface sliding stress. Details of the model and comparisons of the model predictions with the experimental measurements are presented below.

5. MODEL OF INTERFACE DEGRADATION

The change in the cyclic traction law was simulated using a simple interface degradation law. In this law, the sliding stress τ was assumed to vary *linearly* along the length of the fiber, being lowest at the notch plane (where the largest amount of wear had occurred) and highest at the end of the slip zone. Furthermore, the value of τ at the notch plane was assumed to be zero. This relation can be written as

$$\tau(x) = \tau_0 x/\ell_{max} \qquad (0 \le x/\ell_{max} \le 1) \tag{10}$$

where ℓ_{max} is the slip length at the stress maximum, x is the normal distance from the crack plane and τ_0 is the initial (pristine) sliding stress. Combining Eqn. (10) with the analysis presented in Section 3 yields the results for the cyclic traction law:

$$\delta_p = \frac{2D(\eta+\alpha)^2 \sigma_{fmax}^{o\,1/2} \sigma_f^{o\,3/2}}{3\tau_0 E_f (1+\alpha)^2} \tag{11}$$

$$\delta_p' = \delta_{pmax} - \frac{\sqrt{2}\, D(\eta+\alpha)^2 \sigma_{fmax}^{o\,1/2} \left(\sigma_{fmax}^{o} - \sigma_f^{o}\right)^{3/2}}{3E_f \tau_0 (1+\alpha)^2} \tag{12}$$

$$\delta_p'' = \delta_{p\min} + \frac{\sqrt{2}\, D(\eta+\alpha)^2\, \sigma_{f\max}^{o\,1/2} \left(\sigma_f^o - \sigma_{f\min}^o\right)^{3/2}}{3 E_f\, \tau_o\, (1+\alpha)^2} \tag{13}$$

In this case, the exponent on the cyclic traction law, $d \log \Delta \delta_p / d \log \Delta \sigma_f^o = 3/2$.

The predictions of the model are plotted in Figs. 6 and 8. The predicted permanent displacement was evaluated by setting $\sigma_f^o = 0$ in Eqn. (12). Evidently the predicted exponent is in reasonable agreement with the experimental measurements for $N \geq 100$ (1.5 vs. ~1.3). In contrast, the correlation between the measured and predicted permanent displacements is poor. However, the model correctly predicts the *direction* of such changes.

6. CONCLUDING REMARKS

The present results indicate that, on the first loading cycle, the traction law is consistent with the model based on constant τ. The value of τ inferred from the measurements (~60 MPa) is comparable to values measured in other fiber-reinforced composites[11,14], but somewhat lower than values measured on the same composite using fiber pushout tests (~90 - 100 MPa)[12]. This disparity may be attributed to the Poisson effect. During the pullout tests, the fibers contract laterally, reducing the radial thermal residual stress. Conversely, during pushout, the fibers expand, increasing the radial stress and the corresponding sliding stress.

Substantial changes occur in the traction law during subsequent cyclic loading. The changes in the shape of the loops (manifested in the reduction in traction law exponent) and the progressive increase in permanent displacement are consistent with the notion that the interface sliding stress degrades *non-uniformly* along its length, with the degradation being greatest near the matrix crack plane. SEM examinations of the

fiber coatings following testing have confirmed such non-uniformity. These trends have been qualitatively demonstrated using a simple interface degradation law wherein the sliding stress is assumed to vary linearly along the fiber length. However, a model of interface degradation incorporating explicitly the effects of the cyclic sliding amplitude is required.

The process of interface degradation is expected to play a dual role in the fatigue cracking behavior in this type of composite. First, the reduction in sliding stress will reduce the shielding associated with bridging fibers, resulting in an acceleration in the rate of matrix cracking. Second, this reduction will reduce the stress borne by the fibers in the crack wake, reducing the propensity for fiber fracture. The onset of fiber fracture during cyclic loading has been shown to lead to dramatic increases in the rate of matrix cracking[12]. The net effect of these two opposing trends on fatigue life is not yet clear.

ACKNOWLEDGMENTS

Funding for this work was supplied by the Defense Advanced Research Projects Agency though the University Research Initiative Program of UCSB under ONR Contract no. N-0014-86-K-0753, and by ONR 3M Contract no. N-00014-92-J-1991.

Table 1 Properties of the Ti/SiC Composite

Matrix Modulus, E_m	115 GPa
Fiber Modulus, E_f	360 GPa
Longitudinal Composite Modulus, $E = E_m (1-f) + E_f f$	200 GPa
Fiber Diameter, D	140 μm

REFERENCES

[1] M.D. Sensmeier and P.K. Wright, in Fundamental Relationships Between Microstructure and Mechanical Properties of Metal Matrix Composites, P.K. Liaw and M.N. Gungor (Eds.), The Minerals Metals and Materials Society, 1990, pp. 441-457.

[2] P. Kantzos, J. Telesman and L. Ghosn, NASA TM-103095 (1989).

[3] D.P. Walls, G. Bao and F. Zok, *Scripta Metall. Mater.*, **25** (1991), 911.

[4] P.Bowen, A.R. Ibbotson and C.J. Beevers, in Fatigue of Advanced Materials (Eds. R.O. Ritchie, R.H. Dauskardt and B.N. Cox), MCE Pub. Ltd., Birmingham, pp. 379-94 (1991).

[5] B.N. Cox and D.B. Marshall, *Fatigue Fract. Engg. Mater. Struct.*, **14** (1991), 847.

[6] R.M. McMeeking and A.G. Evans, *Mech. Materials*, **9** (1990), 217.

[7] B.N. Cox and C.S. Lo, *Acta Metall. Mater.*, **40** (1992), 69.

[8] D.B. Marshall, B.N. Cox and A.G. Evans, *Acta Metall.*, **33** (1985), 2013.

[9] B. Budiansky, J.W. Hutchinson and A.G. Evans, *J. Mech. Phys. Solids*, **2** (1986), 167.

[10] J.W. Hutchinson and H.M. Jensen, *Mech. Mater.*, **9** (1990), 139.

[11] D.B. Marshall, M.C. Shaw and W.L. Morris, *Acta Metall. Mater.*, **40** (1992), 443.

[12] D.P. Walls, G. Bao and F.W. Zok, *Acta Metall. Mater.*, in press (1993).

[13] P.D. Warren, T.J. Mackin and A.G. Evans, *Acta Metall. Mater.*, **40** (1992), 1243.

[14] D.B. Marshall, M.C. Shaw, W.L. Morris and J. Graves, to be published.

APPENDIX

The shear lag analysis presented in Refs. 6-8 is based on the assumption that all of the fibers in the crack wake are intact. In the present experiments, a significant fraction of the fibers are cut during preparation of the specimens. Below is a modification to the shear lag analysis that accounts for this effect. The analysis presented here assumes that τ is constant and that the load is increased monotonically, though it can be readily applied to cyclic loading as well as other traction laws.

Consideration of mechanical equilibrium requires that the fiber stress in the matrix crack plane be

$$\sigma_f^o = \varepsilon^\infty E / f(1-\eta) \tag{A1}$$

where η is the number fraction of broken fibers. Consequently, the fiber strain at this point is

$$\varepsilon_f^o = \sigma_f^o / E_f = \varepsilon^\infty E / f E_f(1-\eta) \tag{A2}$$

The additional remote displacement due to sliding is obtained by integrating the fiber strain distribution, whereupon

$$\delta_p = \ell(\varepsilon_f^o - \varepsilon^\infty) \tag{A3}$$

and the slip length, ℓ, is

$$\ell = \varepsilon^\infty D E_f(\eta + \alpha) / 4\tau(1-\eta) \tag{A4}$$

Combining Eqns. (A1) through (A4) gives Eqn. (5) in the text. For unloading and reloading, the expressions in Eqns. (3) and (4) are modified in a similar way, such that the term α in the numerator of these equations is replaced by $(\eta + \alpha)$. This modification lead to Eqns. (6) and (7).

LIST OF FIGURES

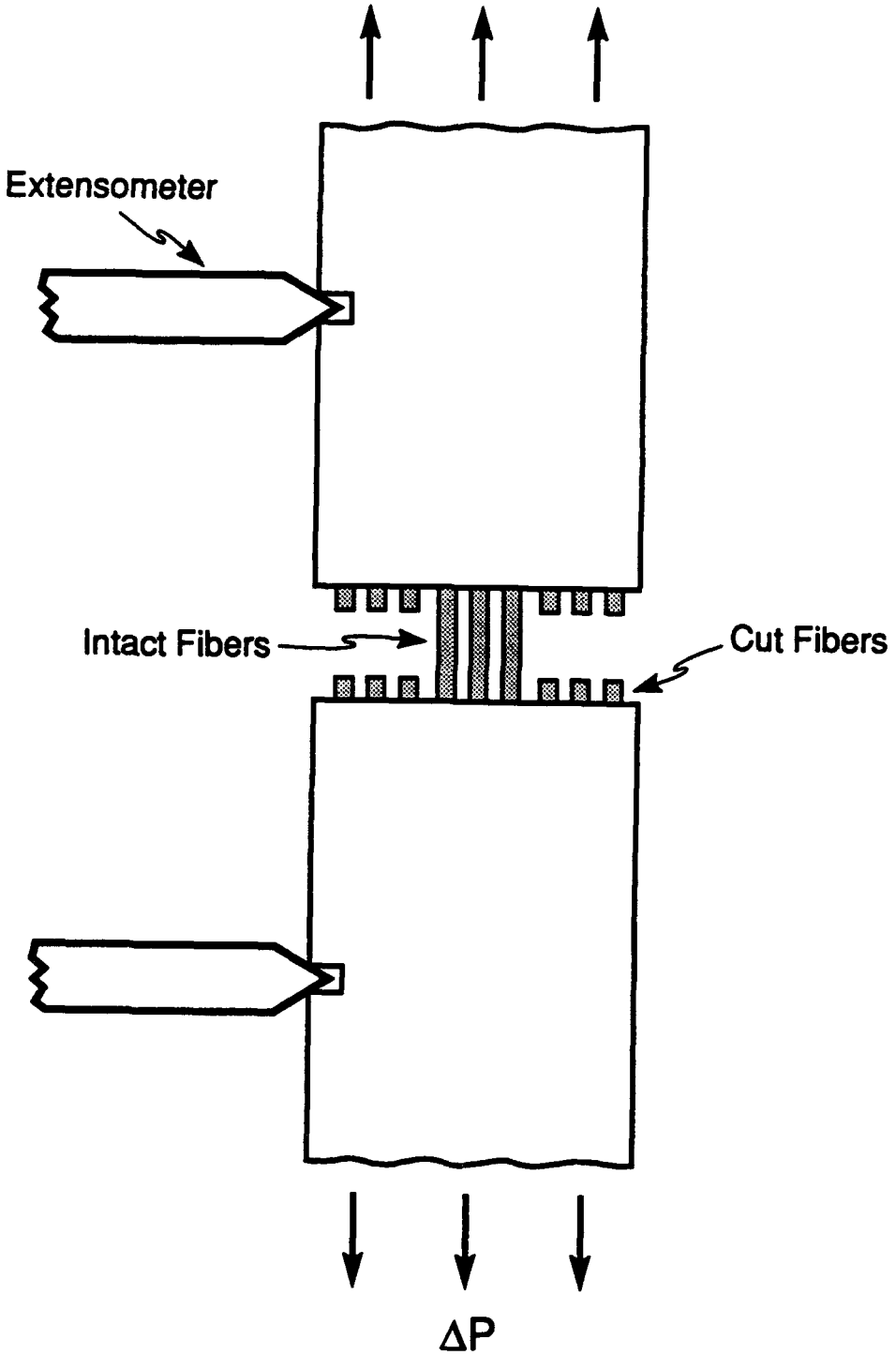

Figure 1

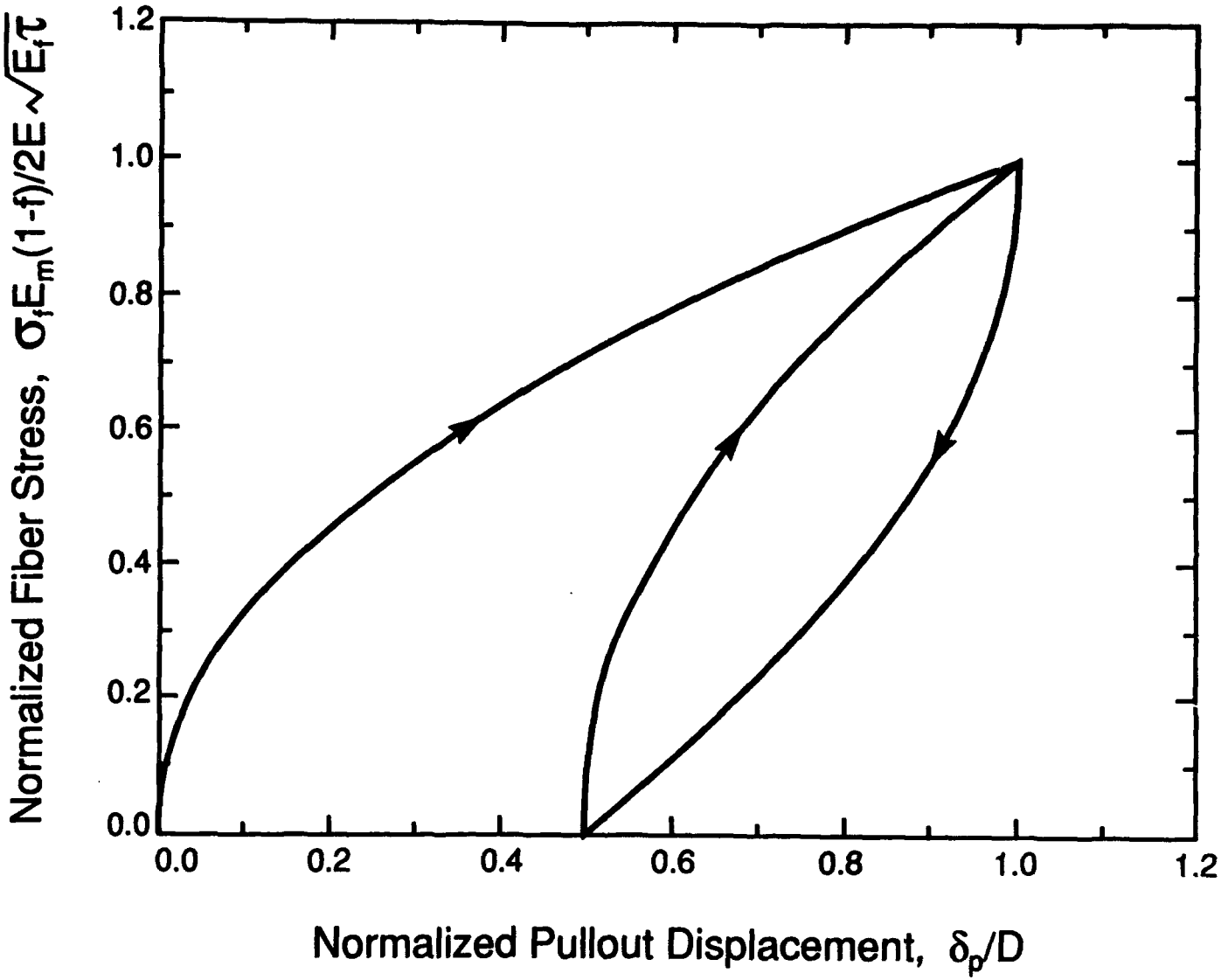
Normalized Fiber Stress, $\sigma_f E_m(1-f)/2E\sqrt{E_f\tau}$
1.2
1.0
0.8
0.6
0.4
0.2
0.0
0.0
0.2
0.4
0.6
0.8
1.0
1.2
Normalized Pullout Displacement, δ_p/D

Figure 2

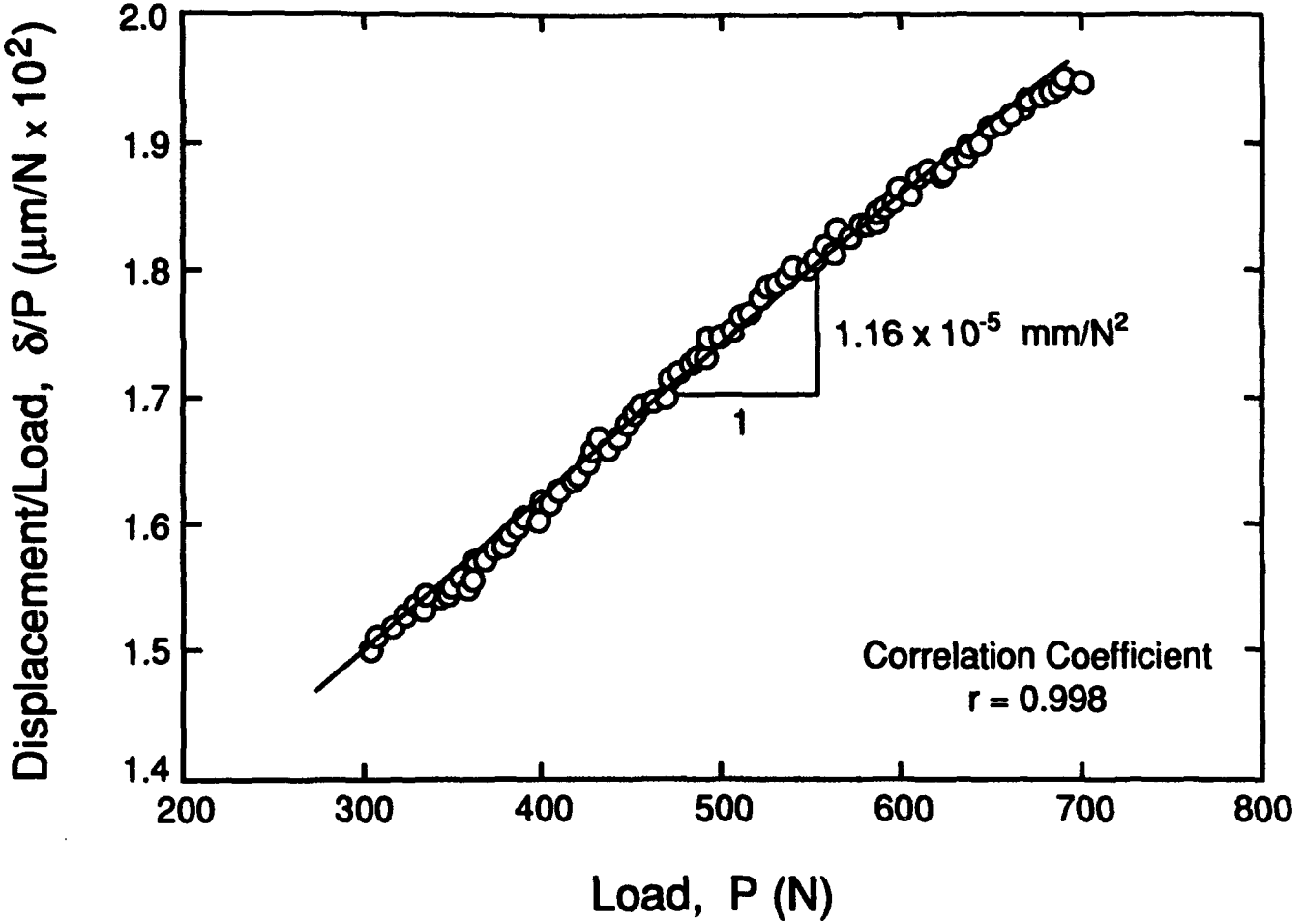
Displacement/Load, δ/P (μm/N x 10²)
2.0
1.9
1.8
1.7
1.6
1.5
1.4
200
300
400
500
600
700
800
Load, P (N)
1.16 x 10⁻⁵ mm/N²
1
Correlation Coefficient
r = 0.998

Figure 3

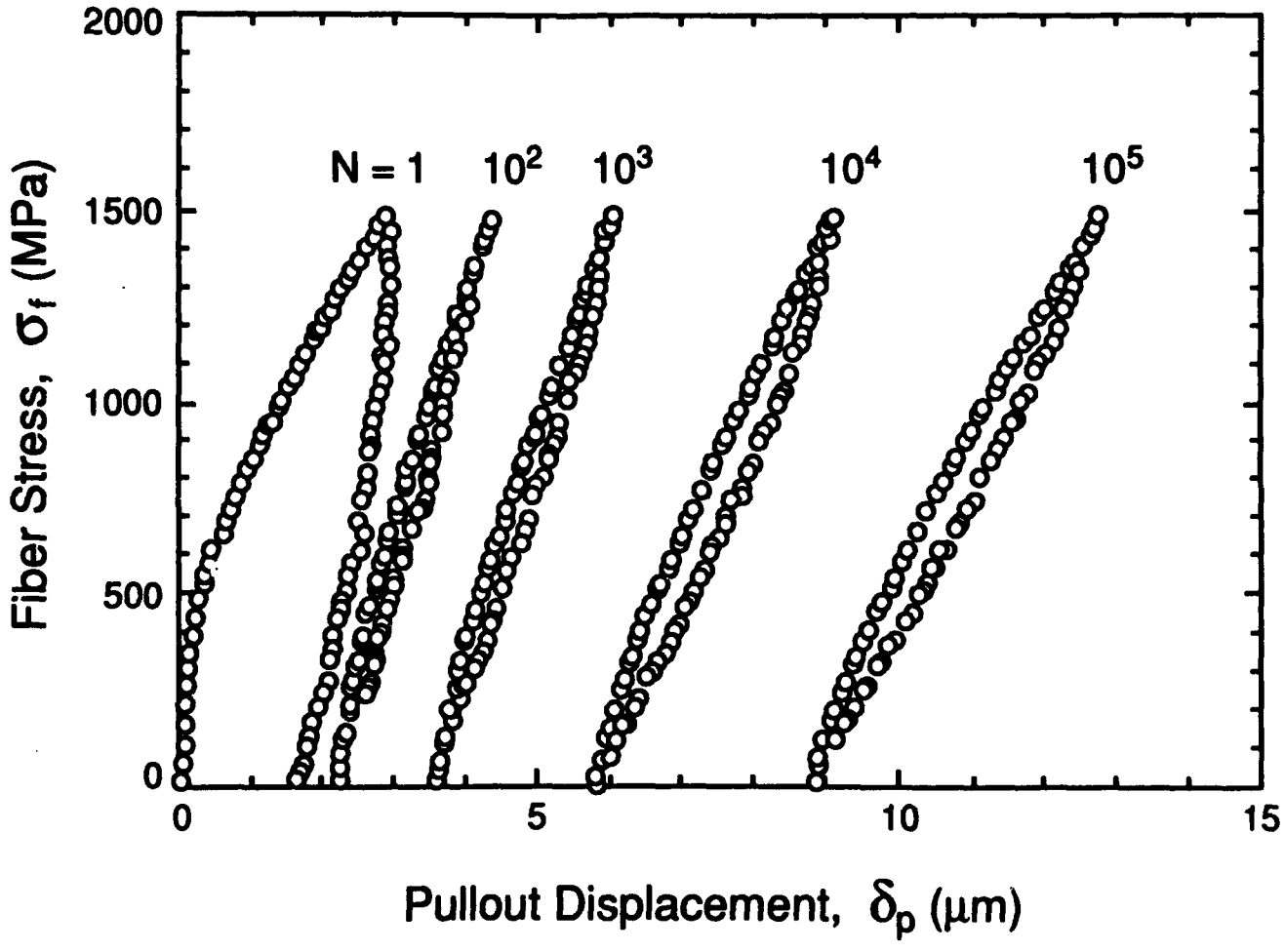
2000
1500
1000
500
0
Fiber Stress, σ_f (MPa)
N = 1
10^2
10^3
10^4
10^5
0
5
10
15
Pullout Displacement, δ_p (μm)

Figure 4

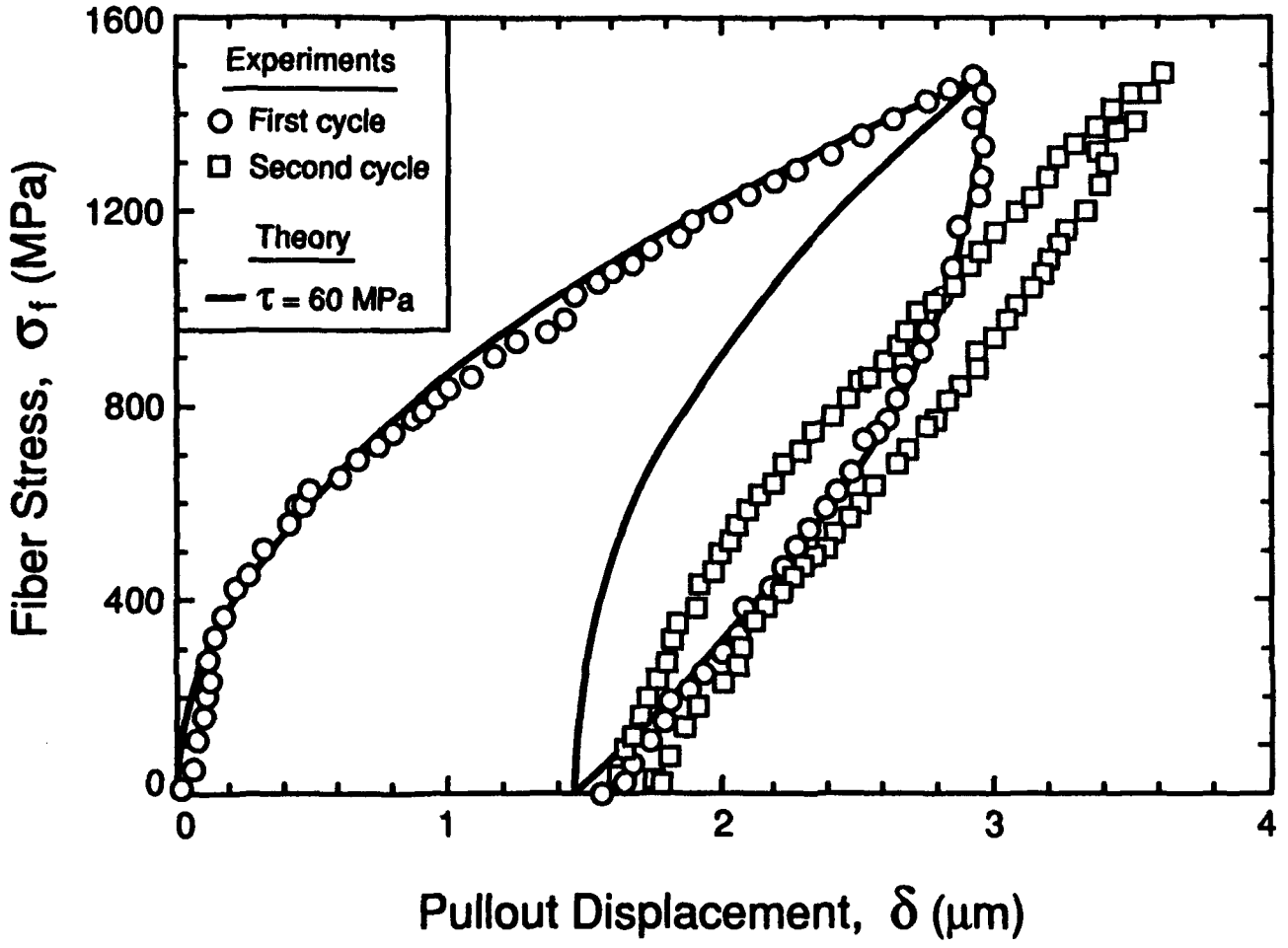
Experiments
First cycle
Second cycle
Theory
τ = 60 MPa
Fiber Stress, σ_f (MPa)
1600
1200
800
400
0
0
1
2
3
4
Pullout Displacement, δ (μm)

Figure 5

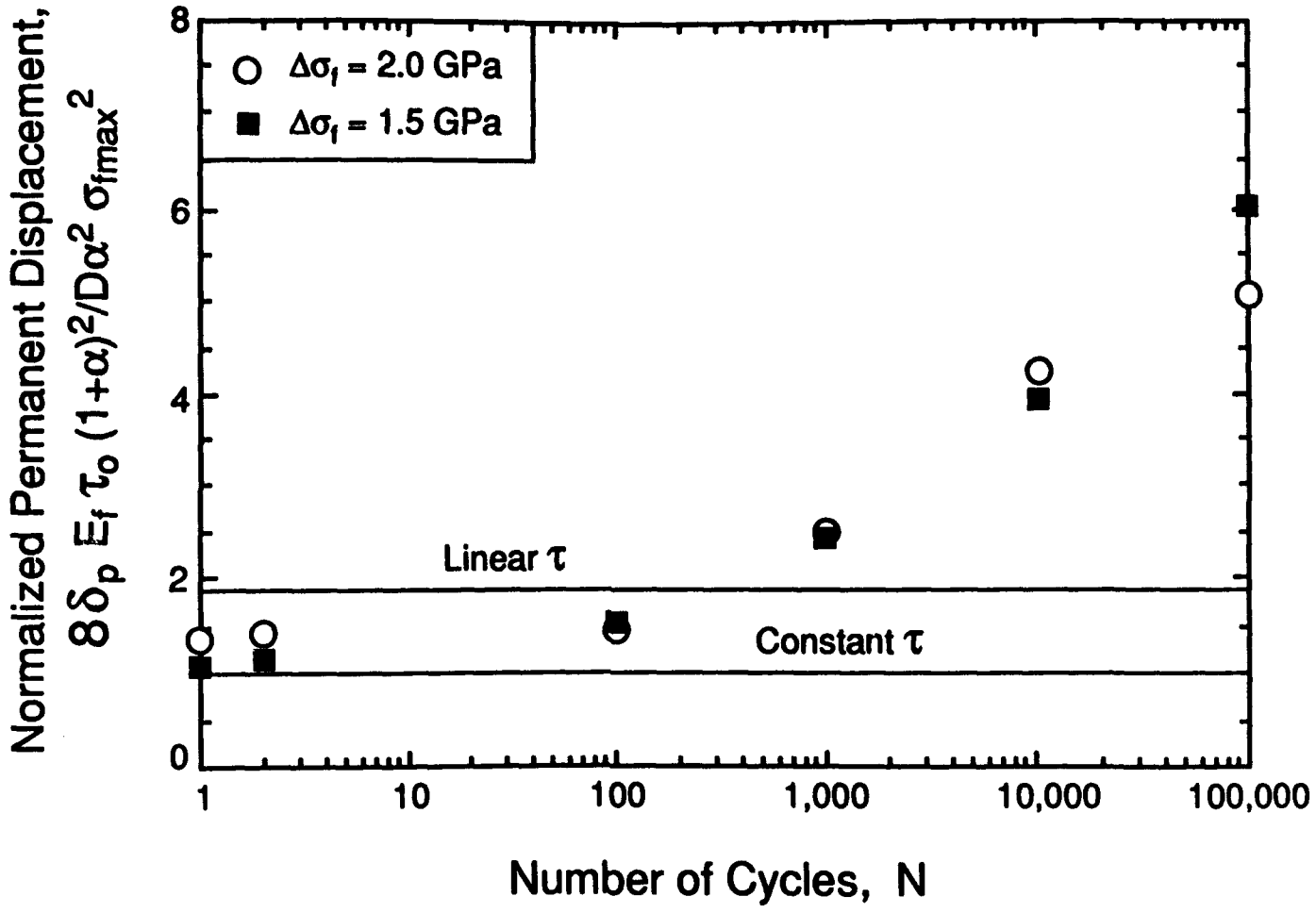
Normalized Permanent Displacement,
$8\delta_p E_f \tau_o (1+\alpha)^2/D\alpha^2 \sigma_{fmax}^2$
$\Delta\sigma_f$ = 2.0 GPa
$\Delta\sigma_f$ = 1.5 GPa
Linear τ
Constant τ
0
2
4
6
8
1
10
100
1,000
10,000
100,000
Number of Cycles, N

Figure 6

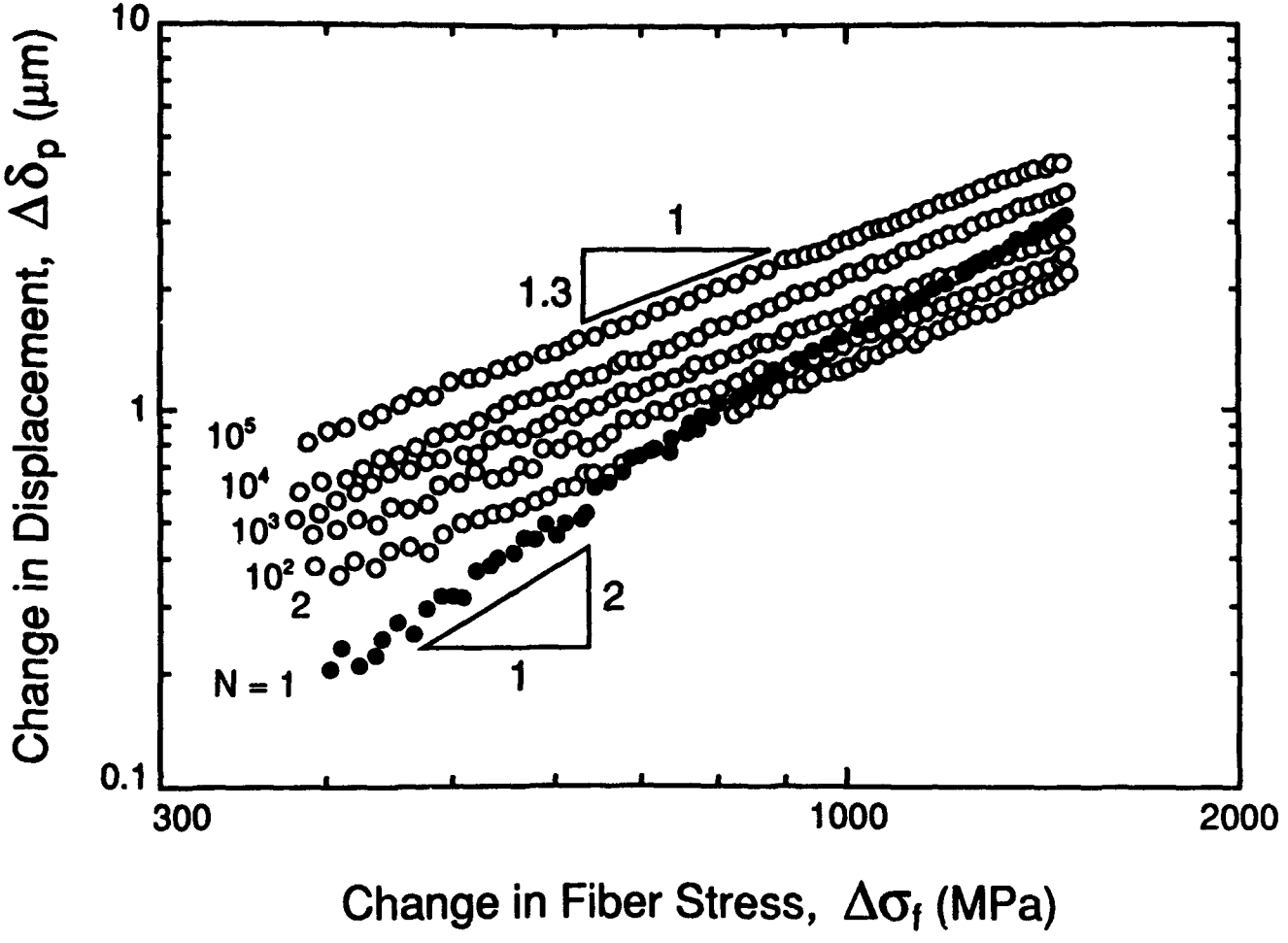
10
1
0.1
300
1000
2000
Change in Displacement, $\Delta\delta_p$ (μm)
Change in Fiber Stress, $\Delta\sigma_f$ (MPa)
1
1.3
10^5
10^4
10^3
10^2
2
N = 1
2
1

Figure 7

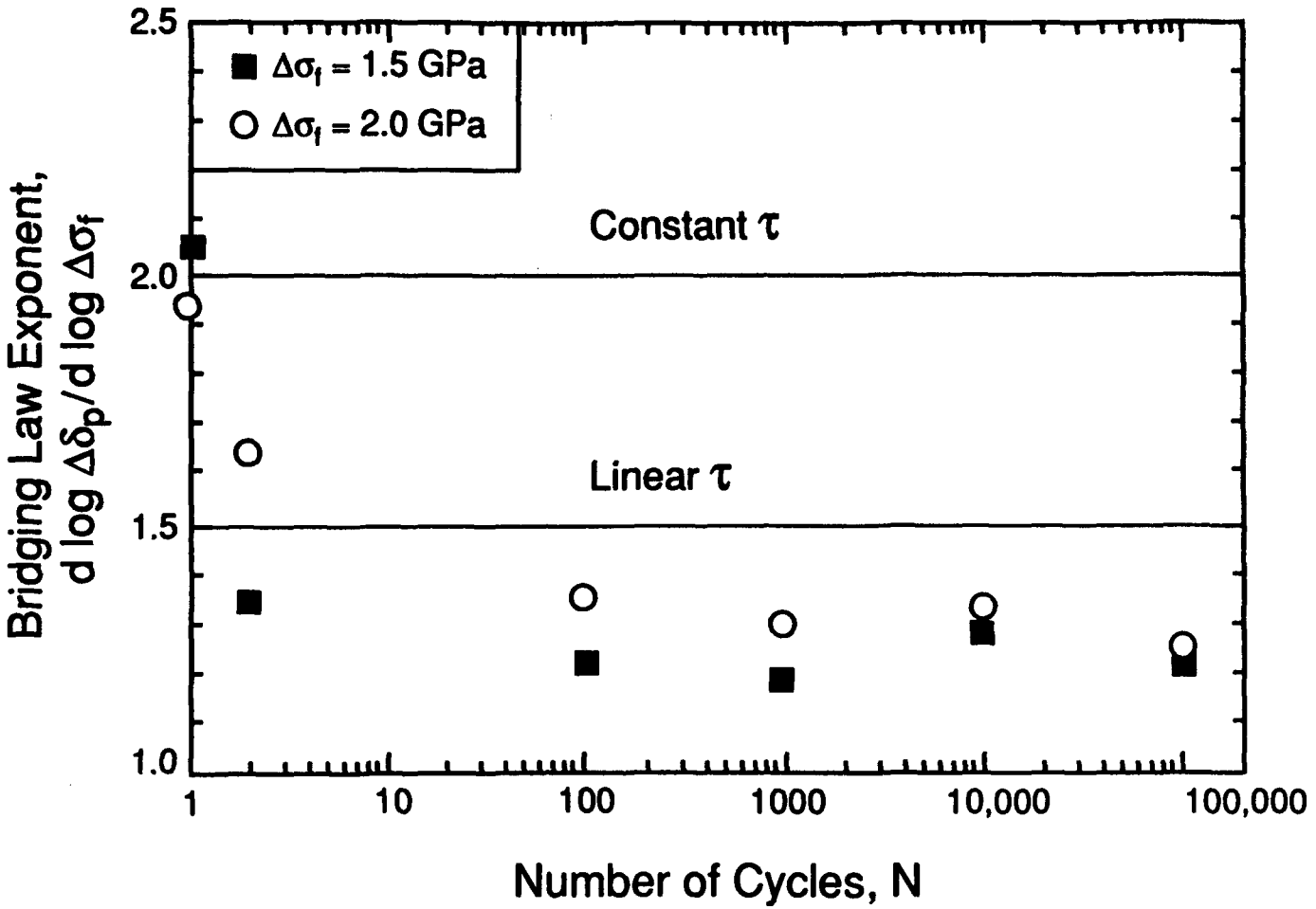
2.5
2.0
1.5
1.0
■ Δσf = 1.5 GPa
○ Δσf = 2.0 GPa
Constant τ
Linear τ
Bridging Law Exponent,
d log Δδp/d log Δσf
1
10
100
1000
10,000
100,000
Number of Cycles, N

Figure 8

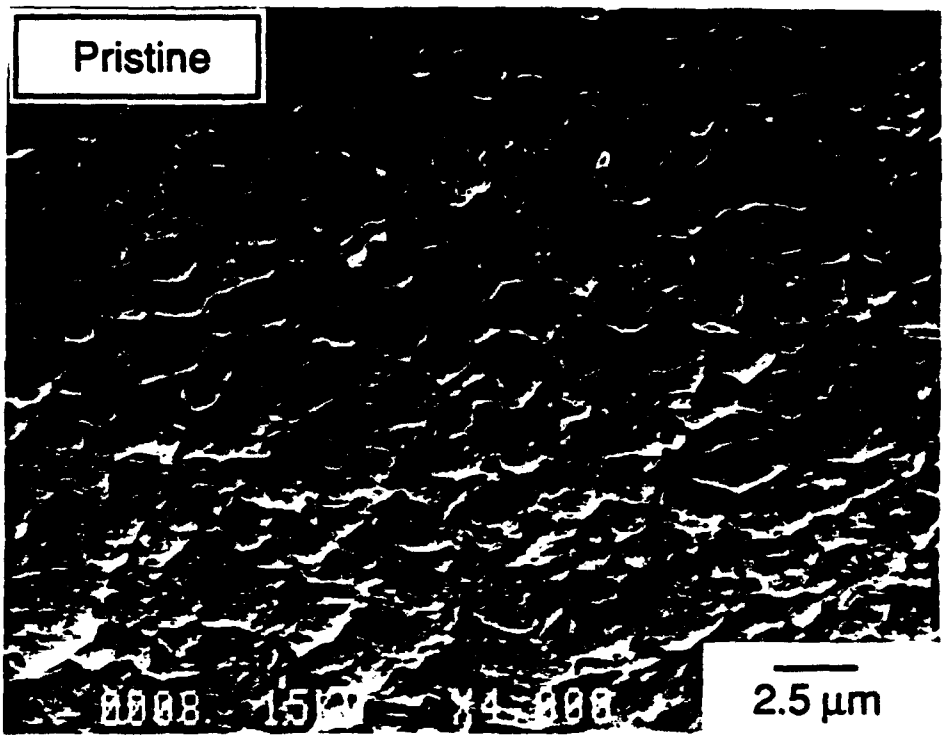

Figure 9

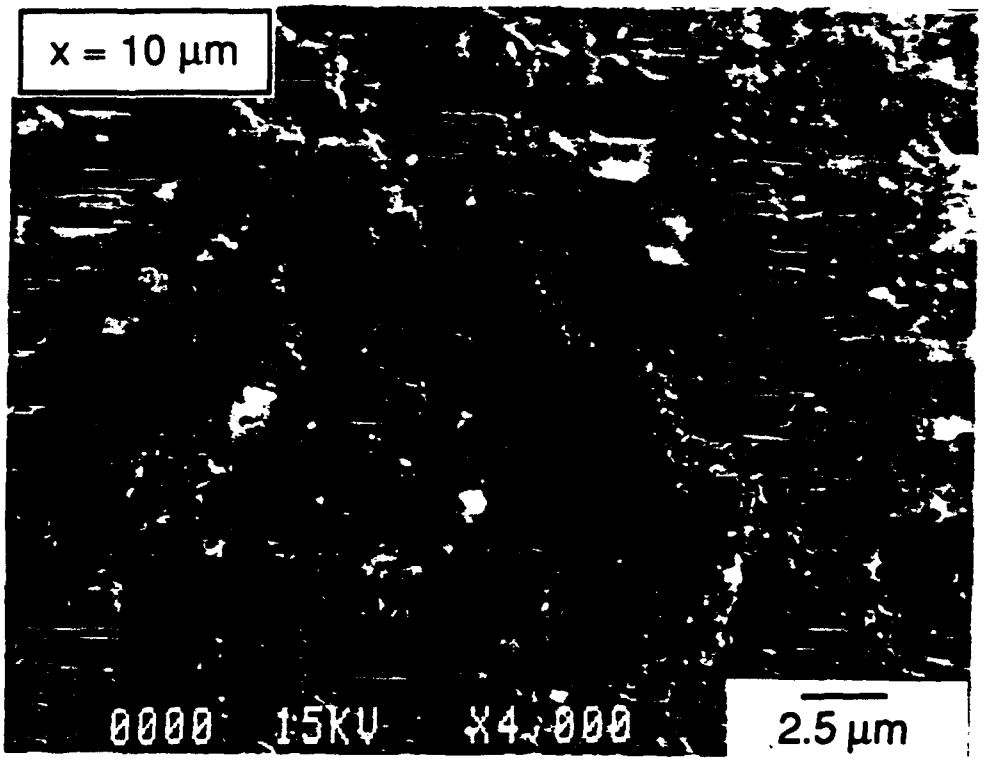

Figure 10 (a)

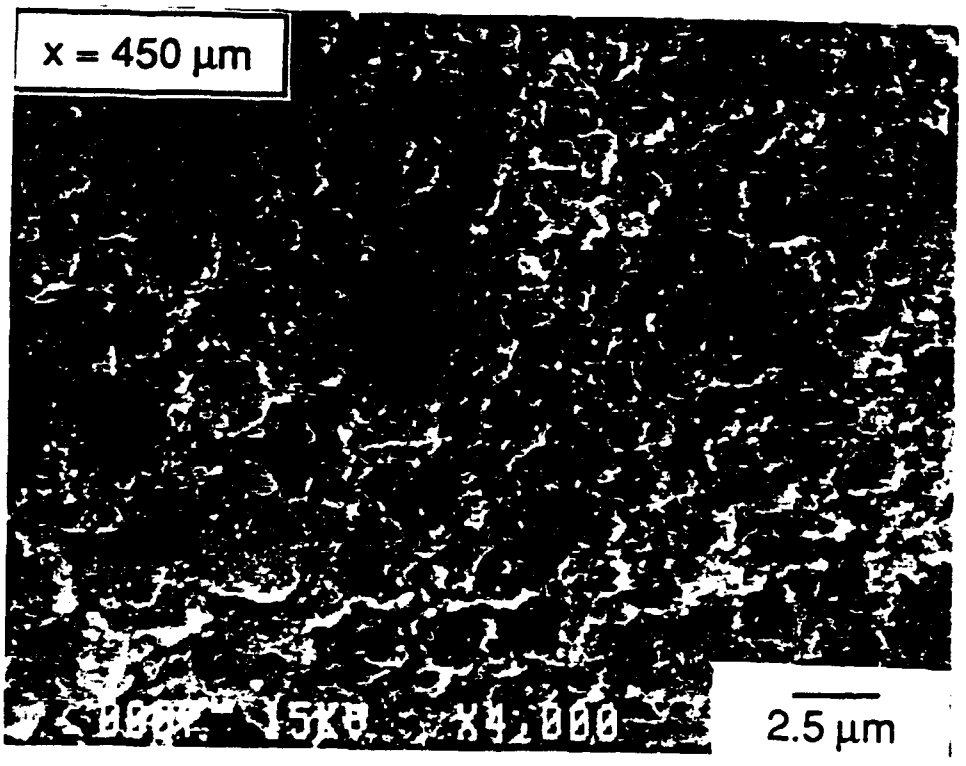

Figure 10 (b)

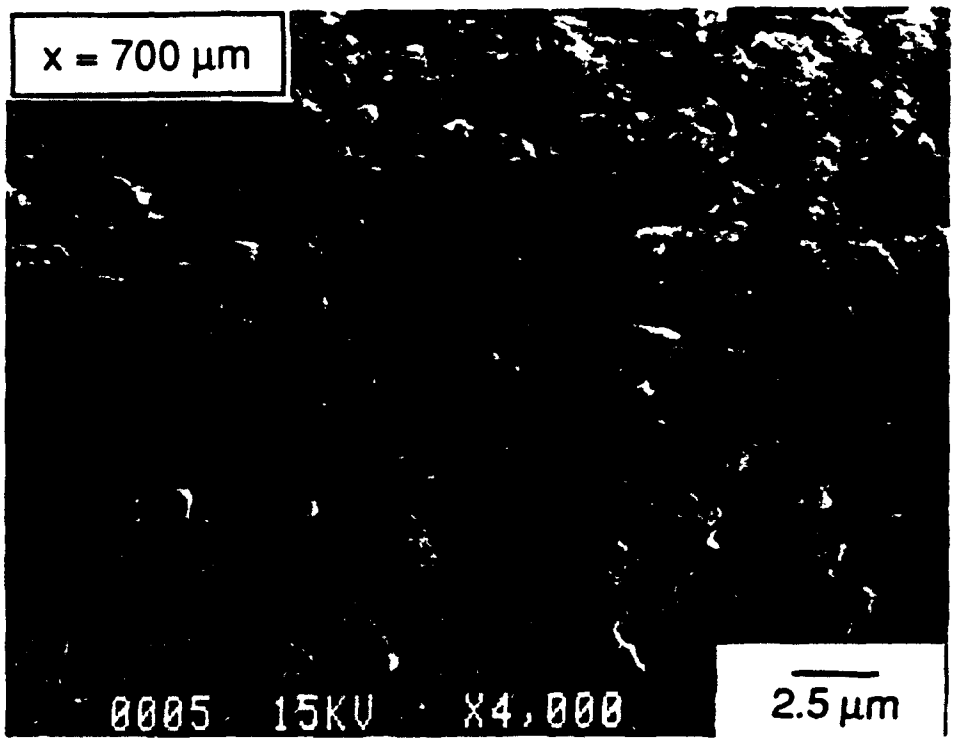

Figure 10 (c)

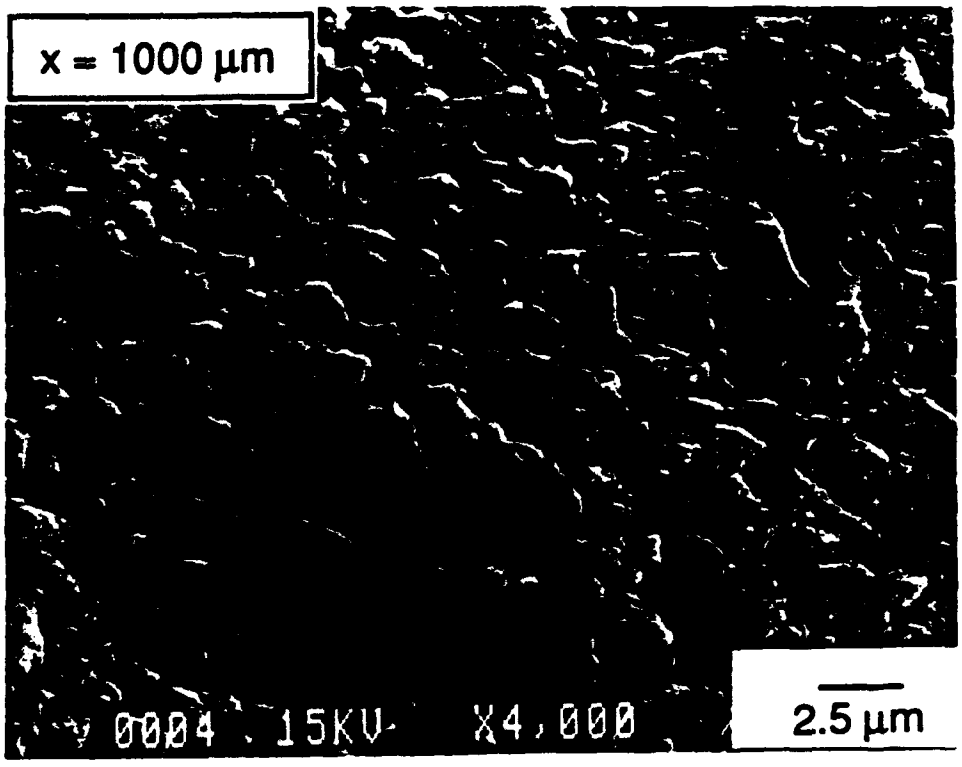

Figure 10 (d)

FATIGUE CRACK GROWTH IN FIBER-REINFORCED METAL-MATRIX COMPOSITES

G. Bao[†] and R.M. McMeeking[*]

[†]Department of Mechanical Engineering
The Johns Hopkins University, Baltimore, MD 21218

[*]Department of Mechanical and Environmental Engineering
University of California, Santa Barbara, CA 93106

April, 1993
Revised version, November, 1993

To appear in Acta Metallurgica et Materialia

ABSTRACT

Fatigue crack growth in fiber-reinforced metal-matrix composites is modeled based on a crack tip shielding analysis. The fiber/matrix interface is assumed to be weak, allowing interfacial debonding and sliding to occur readily during matrix cracking. The presence of intact fibers in the wake of the matrix crack shields the crack tip from the applied stresses and reduces the stress intensity factors and the matrix crack growth rate. Two regimes of fatigue cracking have been simulated. The first is the case where the applied load is low, so that all the fibers between the original notch tip and the current crack tip remain intact. The crack growth rate decreases markedly with crack extension, and approaches a "steady-state". The second regime occurs if the fibers fail when the stress on them reaches a unique fiber strength. The fiber breakage reduces the shielding contribution, resulting in a significant acceleration in the crack growth rate. It is suggested that a criterion based on the onset of fiber failure may be used for a conservative lifetime prediction. The results of the calculations have been summarized in calibrated functions which represent the crack tip stress intensity factor and the applied load for fiber failure.

NOMENCLATURE

a	matrix crack half length
a_o	initial notch half length
D	fiber diameter
E	Young's modulus of composites: $f E_f + (1-f)E_m$
$\bar{E}$	effective composite Young's modulus considering material orthotropy
E_f	Young's modulus of fiber
E_m	Young's modulus of matrix
f	volume fraction of fibers
$F(a/w)$	shape function for stress intensity factor: $\sqrt{\sec(\pi a/2w)}$
ℓ	unbridged segment half length
n	Paris law exponent
N	number of load cycles
S	fiber strength
w	finite panel width
α	non-dimensional bridge length: $(a-\ell)/a$
β	Paris law coefficient
δ	total crack opening displacement
δ_F	crack opening displacement induced by bridging fibers
δ_A	crack opening displacement caused by applied stress
$\Delta\kappa$	ratio of ΔK_{tip} to ΔK_a
ΔK_A	range in applied mode I stress intensity factor
ΔK_{tip}	range in mode I crack tip stress intensity factor
$\Delta\delta$	change in crack opening
$\Delta\Sigma$	non-dimensional measure of the stress amplitude/crack length: $2\lambda\bar{E}\Delta\sigma/a$
$\Delta\Sigma_o$	non-dimensional measure of the stress amplitude/notch length: $2\lambda\bar{E}\Delta\sigma/a_o$
$\Delta\sigma$	cyclic applied stress amplitude

$\Delta\sigma_s$	cyclic bridging stress amplitude
λ	bridging law coefficient: $D(1-f)^2(E_m)^2/4f^2\,E_f\,E^2\tau$
ν	Poisson's ratio
σ	applied stress
σ_{max}	maximum applied stress
σ_s	bridging stress due to fibers
Σ	non-dimensional measure of the maximum applied stress: $4\lambda\bar{E}\Delta\sigma_{max}/\ell$
τ	interface sliding stress
η	non-dimensional measure of fiber strength: $4\lambda\bar{E}\,f\,S/\ell$

INTRODUCTION

Fatigue crack growth in metal matrix composites reinforced with brittle fibers has been studied extensively (Naik and Johnson, [1]; Kantzos, Telesman and Ghosn, [2]: Sensmeier and Wright, [3]; McMeeking and Evans, [4]; Walls, Bao and Zok, [5, 6]). Experimental results (Sensmeier and Wright, [3]; Walls, Bao and Zok, [5, 6]) indicate the following fatigue cracking behavior. Under tensile cyclic loading of the composite in the fiber direction, the matrix undergoes mode I fatigue cracking normal to the fibers, while the fibers in the crack wake remain intact due to the frictional sliding at the fiber/matrix interface. These fibers bridge the crack and shield the crack tip from the applied stress. Consequently, a transient occurs in which the crack growth rate da/dN diminishes upon crack extension, and a steady-state regime follows in which da/dN is small. When the applied stress level is high, the stress in the fiber at the original notch tip may reach the fiber strength and then the fibers begin to fail. The crack growth thereafter accelerates again, leading to the final rupture. These features of fatigue cracking in fiber reinforced metal-matrix composites are shown in Fig. 1 in which a typical fatigue crack growth curve of a Ti matrix composite with SiC fibers is replotted from the work of Walls, Bao and Zok [5]. The composite tested contains 35% of unidirectional fibers, with fiber diameter D = 140μm (Jansson, Deve and Evans, [7]).

In this paper, the micromechanical model of McMeeking and Evans [4] is extended to predict the above fatigue crack growth behavior. The materials of particular interest for this model include Ti/SiC composites that have "weak" interfaces. Attention here is focused on mode I cracking that initiates from a sharp notch. Matrix fatigue cracking in metal matrix composites in the absence of a notch has been modeled recently by McMeeking and Evans [4]. The analysis of fiber stresses, interface sliding and crack bridging in their model is analogous to that conducted earlier for fiber-reinforced ceramics subject to monotonic tensile loading (Marshall, Cox and

Evans, [8]; Marshall and Cox, [9]; McCartney, [10]). Following the analysis of Marshall and Oliver [11] and Cox [12], McMeeking and Evans [4] considered the effect of reversal of the fiber interface sliding direction during cyclic loading. They found that the results for bridging during monotonic loading can be scaled simply to represent the effect of bridging during fatigue loading. The model is further developed here to include the effects of an initial sharp notch which is unbridged by fibers at the outset. This analysis permits the inclusion of the effect of breaking fibers which can increase the size of the unbridged segment. The influence of finite specimen width and, of greater importance, the role of fiber failure in fatigue cracking behavior is accounted for too. Fatigue crack growth curves, both with and without fiber fracture, are predicted for given values of the relevant parameters.

Calibrated functions have been devised to represent the results. One set of functions provides values for the crack tip stress intensity factor amplitude as a function of material parameters, the applied load, the matrix crack length and the size of the unbridged segment of the crack. Another set of functions gives the applied load sufficient to fail a fiber in terms of the fiber strength, material parameters, the matrix crack length and the extent of the unbridged segment.

The results in this paper are based on individual models (for bridging fibers, for their effect on crack tip stress intensities, for the incidence of fiber failure, for cyclic loading of bridging fibers and for matrix fatigue) which, in one way or another, have been developed and used previously. In addition, the basic method of analysis employed to solve integral equations in this paper has been used widely. However, the previous applications mostly have concerned monotonic loading of brittle matrix composites and only the work of McMeeking and Evans [4], Cox and Marshall [13] and Cox and Lo [14, 15] addressed the question of cyclic loading. Furthermore, the earlier modelling of fatigue in fiber-reinforced metals has not fully explored the phenomena when there are notches and failing fibers. In this paper, all of the individual model

elements are brought together in a treatment of matrix fatigue crack growth in conjunction with notches and fiber failure. The models have been shown to agree well with the available data for matrix fatigue growth with and without fiber failure (Walls et al., [6]). Therefore, the comprehensive model in this paper is suitable for studying in some detail the phenomena associated with this important damage mechanism in fiber-reinforced metals to augment the insights available from experimental data. Such features that can be studied are: the deceleration of the crack growth rate as the matrix crack grows; the relative influence of notches; the interplay play between applied load amplitude and the matrix crack length in controlling the crack growth rate; and the relatively sudden and dramatic transition from survival of fibers to failure of fibers leading to rapid crack growth as the load is increased or a critical matrix crack length is reached and exceeded. It is true that these features can be deduced directly or indirectly from results available in several different papers in the literature. However, we believe that it is important to bring the results and phenomena together and present them in a focused manner for the matrix fatigue crack growth problem.

The model presented in this paper is based on certain assumptions. Important ones are: the interface shear strength τ is uniform and does not degrade during fiber load cycling; the strength of the fibers is deterministic and not statistical; the matrix fatigue crack growth obeys the Paris law for fatigue crack growth in the monolithic matrix; the entire component or specimen, except for the fiber bridging, can be analyzed elastically which implies that crack tip plastic zones are small. Some assumptions are known to be inexact. For example, measurements have shown that the interface shear strength τ for a fatigued specimen with a matrix crack is lower than that for a pristine material (Warren, Mackin and Evans, [16]). This is known to influence the crack tip opening shape since the fiber constraint near the matrix crack tip on freshly exposed surfaces is relatively stronger than the fiber constraint far from the matrix crack tip on old and therefore fatigued surfaces (Kantzos et al., [2]). In some cases this influences the

fatigue crack growth rate. However, there has been significant success when the model with the fixed value for τ is compared with the data for matrix fatigue crack growth. There are some discrepancies in the transient behavior which can be attributed to the degradation of τ. However, even those discrepancies can be rationalized in terms of interpolation among models with a fixed τ (Walls et al., [6]).

The value of the interface shear strength τ which is used to compare the models to the experiments is usually chosen empirically to obtain one match to the steady state crack growth rate usually observed after some crack growth in large specimens with short cracks under modest load amplitudes. Furthermore, the fiber strength S is usually chosen empirically so that onset of fiber failure in the model agrees in one case with the initiation of fiber failure in an experiment. There is therefore an element of fitting in the model presented in this paper. However, it should be emphasized that with this minimal degree of fitting, the model is capable of capturing the rich interplay among phenomena as controlled by load amplitude, peak load level, matrix crack length and initial notch length. Furthermore, the pragmatic approach to choosing values for τ and S is made necessary by the fact that *in situ* properties are needed. In contrast to other empirical material constants such as fiber and matrix elastic moduli which are relatively unchanged *in situ*, it is well known that the interface shear strength τ and fiber strength S are sensitive to processing, treatment, handling and to fatigue cycling itself (Walls et al., [6]).

CRACK-TIP SHIELDING ANALYSIS

Consider the crack configuration depicted in Fig. 2. The center section of length ℓ is unbridged. The unbridged center section can represent the original notch of length $2a_0$ or a current unbridged segment after fiber failure. The bridged sections represent the growing, mode I, plane strain matrix fatigue crack in the infinite body. With the

possibility that fibers can break, the bridge segment can become unbridged. The current unbridged segment will then have a length $2\ell > 2a_o$. Both the fibers and the matrix are assumed to be linear elastic, with Young's modulus E_f and E_m respectively. Plasticity of the matrix is neglected in this study. The continuous reinforcing fibers are aligned normal to the plane of the matrix crack. The fracture energy of the fiber/matrix interface is assumed to be small, such that debonding and sliding occur readily during matrix cracking. The sliding behavior of the interface is characterized by a constant frictional shear stress τ, such that the bridging stress σ_s is related to the crack opening displacement δ during monotonic opening by (Aveston, Cooper and Kelly, [17]; McCartney, [10]; Hutchinson and Jensen, [18])

$$\delta = \lambda \sigma_s^2 \tag{1}$$

where λ is a material parameter given by

$$\lambda = D (1 - f)^2 E_m^2 / 4 E^2 E_f f^2 \tau. \tag{2}$$

The bridging stress σ_s is the force per unit surface area applied by the fibers to the crack surface and the opening δ is the additional displacement of the material on one side of the crack compared to the [illegible]r due to the presence of the crack and is measured on a gauge length larger than t[illegible]terface slip zones on the fibers at the crack. In eq. (2), D is the fiber diameter, f the fiber volume fraction and E the composite Young's modulus, $E = f E_f + (1\text{-}f) E_m$. Upon cyclic loading, the change in crack opening displacement $\Delta\delta$ after the first peak opening is related to the change in bridging stress $\Delta\sigma_s$ in a similar fashion (McMeeking and Evans, [4])

$$\Delta\delta = \pm \frac{1}{2} \lambda (\Delta\sigma_s)^2 \tag{3}$$

where the plus (+) and minus (–) signs correspond to the loading and unloading portions of the cycle, respectively.

The bridging law and the theory of elasticity and fracture mechanics can be used to solve the problem depicted in Fig. 2. Pertinent results are the distribution of fiber stresses within the bridged zone and the crack tip stress intensity factor. Such solutions have been obtained for both infinite and finite geometries previously by many workers (Marshall et al., [8]; Marshall and Cox, [9]; McCartney, [10]; Cox, [12]; Cox and Lo, [14]). A summary of the analytical method is provided in the Appendix. Values for the bridging stress amplitude have been computed for the applied load range $0 \leq \Delta\Sigma \leq 20$ where the dimensionless parameter $\Delta\Sigma$ is such that

$$\Delta\Sigma = 2\lambda\bar{E}\Delta\sigma/a \tag{4}$$

with $\bar{E}$ an effective elastic modulus for crack problems which takes the orthotropy of the material into account (see Appendix). A representative result for the bridging stress is shown in Fig. 3 where it is shown in dimensionless form as a function of position on the matrix crack. Each curve represents a result for a case with a different unbridged segment.

Two features in Fig. 3 are noteworthy. The peak stress in the bridging zone always occurs at the edge of the unbridged segment. This implies that if fiber failure occurs at a unique deterministic strength, it will always start at the original notch tip. In addition, when the crack length a becomes very large, for low values of $\Delta\sigma$ almost all the applied stress is transferred through the intact fibers (i.e., $\Delta\sigma_s \approx \Delta\sigma$), as indicated by the $\ell/a = 0$ curve. The bridging stress is then rather uniformly distributed except in the crack tip region where $\Delta\sigma_s$ falls well below $\Delta\sigma$. At higher values of $\Delta\sigma$, the fiber

stresses $\Delta\sigma_s$ are nonuniform even for long cracks and fall somewhat below $\Delta\sigma$, indicating that the shielding effect in that case is less effective.

The stress intensity factor range at the crack tip ΔK_{tip} is normalized by the stress intensity factor range which would occur in the absence of the bridging fibers. For an infinite body, this would be

$$\Delta K_A = \Delta\sigma \sqrt{\pi a}. \tag{5}$$

The resulting ratio is

$$\Delta\kappa = \frac{\Delta K_{tip}}{\Delta K_A}. \tag{6}$$

Numerical results for $\Delta\kappa$ for the problem shown in Fig. 2 are plotted in Fig. 4 against the non-dimensional bridge length $(a - \ell)/a$ for $\Delta\Sigma = 1, 2, 4, 8, 12$ and 20. For a small bridge, ΔK_{tip} is almost the same as ΔK_A, since the shielding effect is small. The stress intensity at the crack tip is reduced significantly as the crack length a is increased beyond the bridged segment to produce a large bridge. These general trends are shown clearly in Fig. 4.

For the purpose of investigating when a fiber will fail, it is of interest to determine the largest stress in the fibers in a given state of matrix crack length, unbridged segment and applied stress. The maximum fiber stress, which always occur in the fiber adjacent to the unbridged segment, is plotted in Fig. 5a against the normalized bridge length $(a-\ell)/a$. These calculations were carried out with the bridging law in eq. (1) and represent the stress in the fiber at maximum applied load. Results are presented in Fig. 5a for several values of the maximum applied load σ_{max}. The points in Fig. 5a were obtained by numerical calculation. The full lines were obtained by

fitting functions to the numerical results which will be discussed below. The results in Fig. 5a can be replotted to give the length ($a-\ell$) of the bridge which will have a maximum fiber stress exactly equal to S as a function of the maximum applied stress σ_{max}. This is shown in Fig. 5b. Since the unbridged segment ℓ will grow as fibers fail, the value of η (defined in (10b) below) will increase when fibers break. However, in the initial configuration with $\ell = a_o$, the curves can be used to predict when the first fiber will fail. At the beginning of fatigue crack growth, the bridge length $a-\ell$ is zero and gets bigger as fatigue cracking proceeds. Therefore, at a given maximum load, the state of the specimen starts at the bottom of the diagram and moves upwards at constant Σ (defined in (10c) below) since ℓ is fixed at a_o. This will proceed until the curve representing the fiber strength is reached at which point the first fiber will fail. Thus, the diagram predicts directly the amount of fatigue crack growth which can occur before fiber failure will occur. Note that if the fiber strength is high enough or the maximum applied stress is low enough, fatigue crack growth will proceed without fibers ever failing.

The numerical results for the maximum fiber stress just discussed can be augmented with an exact result due to Suo, Ho and Gong [19] for the situation where the maximum applied stress is low and the matrix crack is very long compared to the unbridged segment. In this situation, the unbridged segment will behave like an isolated crack since the stress transmitted through the bridge almost everywhere will be equal to the applied stress. Only near the tip of the matrix crack and near the edge of the unbridged segment will the bridge stress differ from the applied stress. However, the tip of the matrix crack is too far away from the unbridged segment to have any influence. Thus, the unbridged segment will behave like a finite crack in a uniform stress field. Furthermore, the smallness of the applied stress will ensure that the region of nonuniform bridge stress will be effectively small and the unbridged segment will behave as a crack with small scale yielding. Thus, the value of the J-integral (Rice, [20])

for the tip of the unbridged segment is just that for a finite elastic crack in a uniform tensile stress. Denoting the value of the J-integral to be J, we thus have

$$J = \frac{\sigma_{max}^2 \pi \ell}{\bar{E}} \tag{7}$$

when the maximum stress is being applied. An elementary result (Rice, [20]) gives the J-integral to be the energy per unit area absorbed by the bridging process and thus

$$J = \int_0^{\delta_o} \sigma_s(\delta) d\delta = \frac{2}{3} \lambda (fS)^3 \tag{8}$$

where δ_o is the crack opening displacement when $\sigma_s = f S$. Thus, eq. (7) & (8) can be combined to give

$$fS = \left(\frac{3\pi \sigma_{max}^2 \ell}{2\lambda \bar{E}} \right)^{\frac{1}{3}} \tag{9}$$

or $$\eta = (6\pi)^{\frac{1}{3}} \Sigma^{\frac{2}{3}} \tag{10a}$$

where $$\eta = \frac{D(1-f)^2 E_m^2 \bar{E} S}{E^2 E_f f \ell \tau} \tag{10b}$$

and $$\Sigma = \frac{D(1-f)^2 E_m^2 \bar{E} \sigma_{max}}{E^2 E_f f^2 \ell \tau}. \tag{10c}$$

As noted above, this result is valid for small Σ and large a/ℓ. The latter means that $(a-\ell)/a = \alpha$ in Fig. 5a is close to unity. The result for $\Sigma = 0.5$ in Fig. 5a agrees closely with eq. (10a) but for $\Sigma = 1$ the agreement is merely good. Thus, we conclude that the

asymptotic limit in eq. (10a) can be used when $\Sigma \leq 0.5$ and inspection of Fig. 5a suggests that it will be applicable for $\ell/a \leq 0.5$.

FINITE GEOMETRY

The crack tip shielding analysis performed in the previous section is based on a model geometry of a center crack in an infinite body. Clearly, fatigue tests on center-notched tensile specimens are conducted with finite widths. To justify the relevance of the model just developed for finite widths, finite element calculations have been carried out for such specimens using the ABAQUS code (Hibbitt et al., [21]). The specimen length 2h is much larger than the specimen width w (h/w = 10) and the non-dimensional original notch size, a_o/w is taken to be 0.2 for these calculations, as shown schematically inset in Fig. 6.

To simulate the intact fibers that bridge the matrix crack, non-linear springs are used, with a spring law identical to eq. (1). Crack tip stress intensity factors ΔK_{tip} are obtained through the J-integral, and normalized by the applied stress intensity, ΔK_A

$$\Delta K_A = \Delta\sigma \sqrt{\pi a}\, F(a/w) \tag{11a}$$

where F (a/w) is given in Tada et al., [22] to be approximately

$$F(a/w) = \sqrt{\sec\frac{\pi a}{2w}}\,. \tag{11b}$$

Plotted in Fig. 6 as the solid lines are finite element results for the normalized crack tip stress intensity amplitude $\Delta K_{tip}/\Delta K_A$ against the normalized crack extension $(a - a_o)/a$ for $\Delta\Sigma_o = 1$ and $\Delta\Sigma_o = 2$ where $\Delta\Sigma_o$ is the value of $\Delta\Sigma$ when $a = a_o$. The

corresponding results for the infinite body ($w \to \infty$) are shown as the dashed lines. Inspection of these results indicates that for $(a-a_o)/a < 0.6$, the values of $\Delta K_{tip}/\Delta K_A$ for finite width specimen are essentially the same as those given by the infinite body solution. Consequently for $(a-a_o)/a < 0.6$, the results in Fig. 4 can be used for the finite strip as long as ΔK_A is computed according to eq. (11). These findings imply that in general as long as $a/w < 0.5$, the results in Fig. 4 can be used to determine the stress intensity factor in the finite strip.

Following the argument leading to eq. (9), we infer that the maximum stress in the fiber adjacent to the unbridged segment is such that

$$fS = \left(\frac{3\pi F^2 (\ell / w) \sigma_{max}^2 \ell}{2\lambda \bar{E}} \right)^{\frac{1}{3}} \tag{12a}$$

or

$$\eta = (6\pi)^{\frac{1}{3}} \left[F(\ell / w) \Sigma \right]^{\frac{2}{3}} \tag{12b}$$

when σ_{max} is small and the matrix crack is very large compared to the unbridged segment. This result is valid for any value of ℓ/w as long as the applied stress is sufficiently low so that small scale "yielding" prevails in the bridge next to the unbridged segment (Suo et al., [19]).

CALIBRATED FUNCTIONS

It is convenient to approximate the numerical results in Fig. 4 by a set of functions. These functions can then be used to compute results without recourse to the numerical methods used to generate the curves in the first place. Calibration functions of this type were pioneered by Cox and Lo [15] including those for finite geometries with center notches as in this paper and for edge notches. The functions suggested here

serve the same purpose as those of Cox and Lo [15] and are presented as possible alternatives. We state the following expression for $\Delta\kappa = \Delta K_{tip}/\Delta K_A$:

$$\Delta\kappa(\Delta\Sigma, \alpha) = \exp\{-\sin\alpha\,[A(\Delta\Sigma) + B(\Delta\Sigma)\,\alpha + C(\Delta\Sigma)\,\alpha^2]/\alpha^{1/4}\}$$

where $\alpha = (a - \ell)/a$ (13)

$$A(\Delta\Sigma) = -0.049 + 3.0/\sqrt{\Delta\Sigma} - 0.027/\Delta\Sigma$$
$$B(\Delta\Sigma) = -0.399 + 2.504/\sqrt{\Delta\Sigma} - 3.207/\Delta\Sigma + 0.379/\Delta\Sigma^{3/2}$$
$$C(\Delta\Sigma) = 0.439 - 1.784/\sqrt{\Delta\Sigma} + 1.374/\Delta\Sigma - 0.04/\Delta\Sigma^{3/2}$$

This approximation is accurate to within a few percent of the numerical results depicted in Fig. 4 for the range $0.1 \le \Delta\Sigma \le 12$. It is similarly close to the function devised by Cox and Lo [15] for the case of the finite crack in tension. In addition, it should be noted that the expression in eq. (13) is valid for the finite strip with ΔK_A given by eq. (11) as long as $a/w < 0.5$.

In a similar manner, a function can be fitted to the peak fiber stresses shown in Fig. 5. This function finds its utility in predictions of fiber failure. The function is

$$\eta = \phi(\Sigma)\,\exp\left[-\frac{(1-\alpha)^{m(\Sigma)}}{\sqrt{\alpha}\,\psi(\Sigma)}\right] \qquad (14a)$$

where $\alpha = (a - \ell)/a$ as before,

$$\phi(\Sigma) = \sqrt{\Sigma^2 + \left(6\pi\,\Sigma^2\right)^{\frac{2}{3}}} \qquad (14b)$$

$$\psi(\Sigma) = 13.1 - 2.3\,\Sigma + 0.2\,\Sigma^2 \qquad (14c)$$

$$m(\Sigma) = 14.037 - 15.327\,\Sigma + 7.237\,\Sigma^2 - 1.5628\,\Sigma^3 + 0.1274\,\Sigma^4 \qquad (14d)$$

and η and Σ are given by (10b) and (10c) respectively. When $\alpha = 1$, the form given in eq. (14a) represents the relationship for an infinite body split by a bridged matrix crack with a center unbridged notch. The form given in eq. (14b) has been deduced from an expression of Cui and Budiansky [23] and is asymptotically exact both for small and large Σ. Cui and Budiansky [23] have shown that this expression compares well with their numerical results for Σ ranging from 0.4 to extremely large values. The function in eq. (14a) has been plotted and compared with the numerical results in Fig. 5a. It can be seen that the agreement is good. No comparison has been made between (14a) and numerical results for values of α not equal to unity for values of Σ other than those shown in Fig. 5a. Thus the accuracy of (14a) outside the range shown in Fig. 5a (apart from $\alpha = 1$) is not known.

The form in eq. (14a) is valid for the infinite body only and forms cannot as yet be given for the finite strip. However, based on the work of Suo et al. [19], in the case of the finite strip with the matrix crack extending across the entire width so that a = w, the form

$$\eta^2 = \Sigma^2/(1-\ell/w)^2 + [6\pi\, F^2(\ell/w)\,\Sigma^2]^{2/3} \qquad (15)$$

can be stated with $F(\ell/w)$ given by (11b). The form in eq. (15) is an interpolation between results for small and large Σ in the manner of Suo et al. [19] but using the findings of Cui and Budiansky [23] to give accuracy for small ℓ/w. For cases where the matrix extends over only a fraction of the width of the finite strip, it is possible that eq. (14a) can be used with $\phi(\Sigma)$ given by the right hand side of eq. (15), $(1-\alpha)$ replaced

by ℓ (w-a)/a(w-ℓ) but $\sqrt{\alpha}$ retained as it is. The resulting behavior takes η from zero in the absence of bridging to the known estimate for η when the matrix crack extends over the entire width of the finite strip. However, no attempt has been made to check whether this assertion is reasonable.

MATRIX FATIGUE CRACKING

The governing equation for matrix fatigue crack growth in fiber reinforced composite is assumed to be simply the Paris law (McMeeking and Evans, [4])

$$da/dN = \beta (\Delta K_{tip}/\bar{E}_m)^n \tag{16}$$

where β and n are material parameters for the matrix material. An underlying assumption here is that the fatigue crack growth rate in the matrix is governed by the crack tip stress intensity amplitude, ΔK_{tip}, *in accord with the Paris law for the matrix* alloy alone. Therefore, the intact fibers contribute to the composite fatigue behavior only through ΔK_{tip}. In the calculation of ΔK_{tip}, the composite is taken to be homogeneous and orthotropic, and the crack front is assumed to be straight. In practice, however, only the matrix is fatigue cracked when fibers remain intact, and the crack front adopts a rather complex shape. As a consequence, the local stress intensity factor amplitude will not generally be equal to the calculated ΔK_{tip} values established through idealized bridging calculations. One approximate model for the effect is that the average stress intensity factor amplitude at the matrix crack front is equal to $\Delta K_{tip}/\sqrt{(1\text{-}f)\,\bar{E}/E_m}$ (Budiansky Amazigo and Evans, [24]), accounting for the reduced area of material being cracked as well as the elastic inhomogeneity. To permit incorporation of this effect into the model, the modulus $\bar{E}_m$ has been used in eq. (16) instead of E_m. Thus, the Budiansky et al., [24] model would be accounted for by use of

$\bar{E}_m = \sqrt{(1\text{-}f)\,\bar{E}/E_m}$. However, in this paper, $\bar{E}_m$ will simply be assumed to be E_m and any effect of this assumption will be compensated for in the empirical choice of a value for τ.

The fatigue crack growth law of eq. (16) was integrated with ΔK_{tip} evaluated from the expression in eq. (13) with $\Delta K_A = \Delta\sigma\sqrt{\pi a}$ as for the infinite body. The calculation was carried out for exponents n = 2 and 4 and for 4 values of $\Delta\Sigma_o$ in each case where $\Delta\Sigma_o = \Delta\Sigma\, a/a_o$. Note that $\Delta\Sigma_o$ remains constant if $\Delta\sigma$ is held fixed during fatigue. The results for non-failing fibers are shown in Fig. 7a and 7b. The plots show that for the load amplitudes assumed, the crack does not have to extend very far compared to the original notch length for the rate of crack extension to diminish dramatically.

The theoretical predictions of fatigue crack growth in Fig. 7 have two of the features exhibited in the experimental results, i.e., a transient region in which da/dN diminishes upon crack growth, and a seemingly steady-state region in which da/dN remains almost constant. The non-dimensional parameter $\Delta\Sigma_o$ that governs the prediction is a combination of the original notch size, material properties and the fixed applied load amplitudes. Fatigue crack growth curves for situations with a varying load amplitude $\Delta\sigma$ have not been presented because there are too many possibilities. However, they can be pieced together in a rather complicated manner from the curves for constant $\Delta\Sigma_o$. The appropriate procedure can be deduced from integration of eq. (16).

It has been observed experimentally that at high values of applied stress amplitude $\Delta\sigma$, the crack growth rate decreases first due to the fiber shielding, reaches a minimum value and then increases with further crack extension, as exemplified by the crack growth curve shown in Fig. 1 (Walls et al., [5, 6]). The acceleration in crack growth rate has been attributed to the occurrence of fiber failure, as suggested by the

direct observations of fiber bridging and fiber fracture along the length of the matrix crack (Walls et al., [5, 6]).

In practice, there is a statistical characteristic to the fiber failure process. However, to incorporate the effects of fiber breaking into the fatigue crack growth model just developed, a deterministic approach is adopted. The fibers are assumed to have a unique strength S, such that they fail in the plane of the matrix crack when the stress on them there reaches S. Both the bridging law eq. (3) and the Paris law eq. (16) remain valid. The frictional pull-out effect of broken fibers on ΔK_{tip} is neglected since the deterministic fiber strength implies that fibers break at the matrix crack rather than inside the material. Once the fibers begin to fail, the unbridged notch length is continuously adjusted in the calculation to maintain a fiber stress at the unbridged notch tip equal to the fiber strength. The conditions giving rise to this have been presented and discussed already in connection with Fig. 5.

Of interest, however, is the relationship between the current unbridged segment length 2ℓ and the original notch length $2a_0$ for a given fatigue problem. For simplicity, attention will be confined to cases where $\Delta\sigma$ is fixed during fatigue. The function in eq. (14) can be used to predict ℓ vs. a_0 during fatiguing for given fiber strength. A particular result is shown in Fig. 8 for crack growth in an infinite body. The dashed line on the diagonal specifies $\ell = a_0$ and so depicts the relationship prior to first fiber failure. At the beginning of fatiguing, $a = a_0$ so the top right of Fig. 8 is the starting point for the process. As the fatigue crack grows at first without fiber failure, the state of the specimen will move down the dashed line on the diagonal towards the bottom as indicated by the arrow. The state departs from the dashed line when fibers begin to fail. The point of departure for several ratios of maximum applied stress to volume fraction reduced fiber strength are marked on Fig. 8. Thereafter, as the fatigue crack grows, the state of the specimen follows the relevant full line towards the top left of the diagram as

indicated by the arrow. Each full line in Fig. 8 represents the relationship for the fixed ratio of σ_{max}/fS noted at the intersection of that full line with the diagonal dashed line.

If the fibers are weak or the maximum applied stress is high, the fibers break close to the matrix crack tip (a_o/a is close to unity) and the bridging zone is always a small fraction of the crack length (ℓ/a remains close to unity as the crack grows). This means that fibers will continuously fail close to the matrix crack tip as the matrix crack grows. In this case there will not be much shielding and the fatigue crack growth rate will be similar to what would be expected in an unreinforced matrix. If the fibers are moderately strong or the maximum applied stress is moderately high, the fibers remain intact at first and a sizable bridging zone can develop. However when the first fiber fails, say when $a_o/a = 0.5$, subsequent fiber failure occurs fairly rapidly as the crack grows. The unbridged crack length increases faster than the matrix crack length. In that case the value of ΔK_{tip} will increase quite rapidly as the matrix crack grows after the first fiber fails. That means that the matrix crack growth rate will accelerate significantly after first fiber failure. When the fibers are strong or the maximum applied stress is modest, first fiber failure is delayed. However, after it occurs, say when $a_o/a = 0.1$, many fibers fail essentially simultaneously and the unbridged length increases very rapidly. This causes ΔK_{tip} to jump to a higher value with a corresponding sudden increase in the crack growth rate. As noted previously, when the fiber strength is higher than a threshold value, they will never break and the fatigue crack growth rate will persist at the low level associated with extensively bridged cracks. The annotation on Fig. 8 makes it clear that the sensitivity to fiber strength is quite marked, with the different types of behavior outlined in the last few sentences occurs over a very narrow range of fiber strengths, or equivalently over a very narrow range of maximum applied stress.

Plotted in Fig. 9 are the fatigue crack growth curves predicted from the Paris law eq. (18) for infinitely large specimens taking fiber fracture into account. Without fibers

breaking, the fatigue crack growth curves are the same as those in Fig. 7. In the presence of fiber fracture three matrix fatigue crack growth curves are presented corresponding to three different fiber failure strengths. If fibers are relatively weak, fiber failure occurs early on, and a gradual transition is predicted. For stronger fibers, however, the transition occurs later but becomes more abrupt as can be seen in Fig. 9. This sudden increase of crack growth rate is due to the sudden lengthening of the unbridged zone after first failure of stronger fibers as depicted in Fig. 8. Once the fiber failure process starts for strong fibers, it tends to continue rapidly until most of the fibers fail in the bridging zone that has been previously built up. As a consequence the crack growth rate increases suddenly and is comparable to the fatigue crack growth rate in the unreinforced matrix. This has been observed in experiments (Walls et al., [5, 6]).

FIBER FAILURE

The rapid growth of fatigue cracks after fibers have commenced failing, as depicted in Fig. 9, suggests that an important strategy for design and use of fiber reinforced metal components will be the avoidance of fiber failure. Once fibers begin to fail after significant crack growth, they will quickly break along the fatigue crack. In addition, further crack growth will be accompanied by more fiber failure. As a consequence, the benefits of fiber reinforcement will be partially lost and if there are many matrix fatigue cracks, fiber reinforcement may be significantly impaired. Therefore, it can be suggested that the end of useful life of the composite material can be considered to be the onset of fiber failure. It should be noted that fracture of the composite material after fatigue crack growth will depend on a combination of the matrix toughness and the fiber strength. This has been studied by Cui and Budiansky [23]. However for high toughness matrices such as titanium alloys, fracture of the composite material after matrix fatigue and fiber failure will depend primarily on

matrix toughness. A very approximate estimate for residual composite strength after fiber failure is therefore $K_{IC}/\sqrt{\pi a}$ where K_{IC} is the fracture toughness of the matrix alloy. A more exact assessment of residual strength can be carried out using the more accurate models of Cui and Budiansky [23]. However, an important point is that fiber failure is a necessary precursor before the residual strength of the composite material becomes a relevant consideration. Therefore, the life up to fiber failure is an important determinant and the time between first fiber failure and composite fracture is likely to be relatively short.

As noted previously, if the maximum applied stress is low enough, fibers will never fail during matrix fatigue crack growth. It is useful to investigate the circumstances which will ensure that fibers will remain intact throughout crack growth. As implemented by Walls et al. [6], this can be done by plotting the ratio of the maximum applied stress to the fiber strength against the intercepts of the curves in Fig. 5a with $\alpha = 1$ (where $\ell/a \rightarrow 0$). The result, shown in Fig. 10, is a map determining when fibers will fail and when they do not. The numerical results have been shown for the infinite body in which case $a_o/w = 0$. Below the line in the diagram, no fiber failure will occur no matter how much matrix fatigue crack growth occurs. However, if a component is highly stressed so that it operates above the line in the diagram, eventually fiber failure will occur during matrix fatigue crack growth. Walls et al. [6] have found this diagram to be effective in distinguishing the incidence of fiber failure from nonfailure in experiments.

For comparison with the numerical results, a relationship derived from eq. (15) has been plotted in Fig. 10. This is

$$\left[\frac{(1-a_o/w)fS}{\sigma_{max}}\right]^{\frac{4}{3}} - \left[\frac{\sigma_{max}}{(1-a_o/w)fS}\right]^{\frac{2}{3}} = \left[\left(1-\frac{a_o}{w}\right)^2 F^2\left(\frac{a_o}{w}\right)\frac{6\pi}{\eta}\right]^{\frac{2}{3}} \qquad (17)$$

where η is given by eq. (10b) and $F^2(a_o/w) = \sec(\pi a_o/2w)$. It can be seen that the prediction agrees well with the numerical results. Furthermore, the form of eq. (17) indicates that the map can be generalized to the finite strip without significant alteration. In view of this, the map in Fig. 10 has been presented in a form allowing for the notch to width ratio of a finite strip.

The map in Fig. 10 can be adapted to show the extent to which crack growth can occur in an infinite body prior to fiber failure. If the loading of a very large component is such that according to Fig. 10 fiber failure will eventually occur, the matrix crack will reach the length $2a_f$ and then fibers will commence failing. The ratio of this length to the original notch length is shown in Fig. 11 for various levels of loading and original notch length taking fiber strength and volume fraction into account. For a given notch length, the contours in Fig. 11 indicate the permissible maximum stress for a given extension of the matrix crack. For example, the contour marked $a_f/a_o = 2$ shows the relationship between maximum applied stress and notch length which will produce exactly a doubling of the flaw length before fiber failure will begin to occur. Similarly the contour for $a_f/a_o = 20$ shows the maximum stress which will exactly cause the matrix crack to reach 20 times the length of the initial notch before fiber breakage. The line with $a_f/a_o = \infty$ is the boundary between fiber nonfailure and failure from Fig. 10 and for a maximum stress lying on or below this contour, the matrix crack can extend to infinity without fiber failure. The plots in Fig. 7 can be used to predict how many cycles of constant load amplitude will occur before the matrix crack reaches the extent at which fiber failure will commence. Thus, for large components, Figs. 7 and 11 can be combined to provide a basis for life estimation up to fiber failure for values of $\Delta\Sigma_o$ ranging from 1 to 8.

CONCLUDING REMARKS

A model has been presented for matrix fatigue crack growth emanating from a finite notch. Predictions have been presented for the relationship between the matrix crack length and the number of load cycles of a given amplitude. In addition, the matrix crack length when fibers will begin to fail has been identified in terms of fiber strength, maximum applied stress and initial notch length. These predictions have been compared to experimental data for fatiguing of titanium/SiC fibrous composites and the model has been shown to work well (Walls et al., [6]). As mentioned in the introduction, the comparison between the model and the data has been based on a number of empirical steps. Over and above the use of empirical values for fiber and matrix elastic moduli, fiber volume fraction, fiber diameter and monolithic matrix fatigue crack growth rates, a single value for the interface shear stress τ is determined to ensure that the steady state fatigue crack growth rate in one experiment is accurately predicted. The transient prior to steady state matrix fatigue crack growth is then predicted accurately without any further empiricism. Furthermore, it is then found that when no fiber failure occurs, the model with the same value of τ can predict the results of other experiments carried out at different load amplitudes and with different notch lengths.

Fiber failure is treated in a similar way. A value of fiber strength S is determined that will cause the model to accurately predict the onset of fiber breakage in one experiment. Without further empiricism, the model then accurately predicts the rate of matrix fatigue crack growth after the initiation of fiber breakage in that experiment. In addition, without alteration to parametric values, the model accurately predicts the onset of fiber failure when different initial notch lengths and maximum applied stress magnitudes are used in the experiments. The value of τ used in the comparison of the model with experimental data is consistent with in situ measurements by push out of

fibers (Warren et al., [16]) after fatigue cycling of the specimen. In addition, the fiber strength used in the model is in good agreement with the strength of fibers tested after being removed from the composite by dissolution of the matrix. This strength is less than that for pristine fibers and the reduced value is thought to be due to processing of the composite material.

ACKNOWLEDGMENT

This work was supported in part by DARPA through the University Research Initiative at UCSB (ONR Prime Contracts N00014-86-K0753 and N–00014-93-1-0224). The work of GB was in addition supported by NSF through a Research Initiation Award MSS-9210250. Provision of the ABAQUS Finite Element Code by Hibbitt, Karlsson and Sorensen Inc. through an Academic User's License is gratefully acknowledged.

REFERENCES

1. Naik, R.A. and Johnson, W.S., Third Symposium on Composite Materials: Fatigue and Fracture, ASTM STP 1110 (edited by T.K. O'Brien), p. 753, American Society for Testing and Materials (1991).

2. Kantzos, P., Telesman, J. and Ghosn, L., NASA TM-103095 (1989).

3. Sensmeier, M.D. and Wright, P.K., in "Fundamental Relationships between Microstructure and Mechanical Properties of Metal Matrix Composites", (edited by P.K. Liaw and M.N. Gungor), p. 441, The Minerals Metals and Materials Society (1990).

4. McMeeking, R.M. and Evans, A.G., *Mech. of Materials*, **9**, 217 (1990).

5. Walls, D., Bao, G. and Zok, F., *Scripta Metall. Mater.*, **25**, 911 (1991).

6. Walls, D., Bao, G. and Zok, F., *Acta Metall. Mater.*, **41**, 2061 (1993).

7. Jansson, S., Deve, H. and Evans, A.G.,*Metall. Trans.*, **22A**, 2975 (1990).

8. Marshall, D.B., Cox, B.N. and Evans, A.G., *Acta Metall.*, **33**, 2013 (1985).

9. Marshall, D.B. and Cox, B.N., *Acta Metall.*, **35**, 2607 (1987).

10. McCartney, L.N., *Proc. Roy Soc. Lond.*, **A409**, 329 (1987).

11. Marshall, D.B. and Oliver, W.C., *J. Amer. Ceram. Soc.*, **70**, 542 (1987).

12. Cox, B.N., *Acta Metall. Mater.*, **38**, 2411 (1990).

13. Cox, B.N. and Marshall, D.B., *Fatigue Fract. Engng. Mater. Struct.*, **14**, 847 (1991).

14. Cox, B.N. and Lo, C., *Acta Metall. Mater.*, **40**, 69 (1992).

15. Cox, B.N. and Lo, C., *Acta Metall. Mater.*, **40**, 1487 (1992).

16. Warren, P., Mackin, T. and Evans, A.G., *Acta Metall. Mater.*, **40**, 1243 (1992).

17. Aveston, J., Cooper, G.A. and Kelly, A., in The Properties of Fiber Composites, IPC Science and Technology Press, p. 15 (1967).

18. Hutchinson, J.W. and Jensen, H.K., *Mech. of Materials*, **9**, 139 (1990).

19. Suo, Z., Ho. S. and Gong, X., Trans. ASME, Series H (*J. Eng. Mat. Tech.*) **115**, 319 (1993).

20. Rice, J.R., *J. App. Mech.*, **35**, 379 (1968).

21. Hibbitt, H.D., Karlsson, B.I. and Sorensen, E.P., ABAQUS User's Manual Version 4.8, Hibbitt, Karlsson and Sorensen, Inc., Providence, RI (1990).

22. Tada, H., Paris, P.C. and Irwin, G.R., The Stress Analysis of Cracks Handbook, Del Research, St. Louis (1985).

23. Cui, L. and Budiansky, B., to be published.

24. Budiansky, B., Amazigo, J. and Evans, A.G., *J. Mech. Phys. Solids*, **36**, 167 (1988).

25. Sih, G.C., Paris, P.C. and Irwin, G.R., *Int. J. Frac. Mech.*, **1**, 189 (1965).

26. Bao, G., Ho, S., Suo, Z. and Fan, B., *Int. J. Solids Struct.*, **29**, 1105 (1992).

APPENDIX

GOVERNING EQUATIONS

The equation governing the stress distribution along a bridged matrix crack subject to a monotonic applied stress σ_{max} and the bridging law eq. (1) is (McCartney, [10])

$$\bar{\Sigma}_s^2(\bar{x})/16 + \int_{1-\alpha}^{1} \bar{\Sigma}_s(\bar{x})\, H(t,\bar{x})\, dt = \bar{\Sigma}\sqrt{1-\bar{x}^2} \tag{A1}$$

where

$$\bar{\Sigma}_s = 4\lambda\bar{E}\sigma_s/a \tag{A2}$$

and σ_s is the stress transmitted through the matrix crack by the fibers defined as a traction on the crack area. Thus σ_s is equal to the actual stress in the fibers at the matrix crack multiplied by the volume fraction of fibers. In addition, λ is given by eq. (2),

$$1 - \alpha = \ell/a \tag{A3}$$

2ℓ is the length of the unbridged segment, 2a is the length of the matrix crack, $\bar{x} = x/a$ where x is the distance from the center of the notch,

$$H(t,\bar{x}) = \frac{1}{\pi}\log\left|\frac{\sqrt{1-\bar{x}^2} + \sqrt{1-t^2}}{\sqrt{1-\bar{x}^2} - \sqrt{1-t^2}}\right| \tag{A4}$$

$$\bar{\Sigma} = 4\lambda\bar{E}\sigma_{max}/a = \Sigma\ell/a \tag{A5}$$

with Σ given by eq. (10c) and $\bar{E}$ is an effective elastic modulus taking the material orthotropy into account.

Consider a plane strain, center crack running in the x-direction in an infinite, orthotropic body. Results from Sih, Paris and Irwin [25] for cracks in orthotropic bodies can be used to provide solutions for the point force on a crack surface and therefore for fully and partially bridged cracks. This justifies the use of $\bar{E}$ in (A1). For example, when the coordinates x and y coincide with the principal axes 1 and 2 of the orthotropic material, the crack opening displacement δ_A due to the remote applied tension σ is (Bao et al., [26])

$$\delta_A = \frac{4\sigma}{E_2'}\left[\frac{E_2'}{E_1'}\right]^{\frac{1}{4}} \sqrt{a^2 - x^2} \tag{A6}$$

provided that

$$\rho = \frac{\sqrt{E_1' E_2'}}{2G_{12}} - \left(\nu_{12}' \nu_{21}'\right)^{\frac{1}{2}} = 1 \tag{A7}$$

Consequently, the effective Young's modulus $\bar{E}$ is given by

$$\bar{E} = E_2'\left[E_1'/E_2'\right]^{\frac{1}{4}} \tag{A8}$$

where

$$
\begin{aligned}
E_1' &= E_1/(1-\nu_{13}\,\nu_{31}) \\
E_2' &= E_2/(1-\nu_{23}\,\nu_{32}) \\
\nu_{12}' &= (\nu_{12}+\nu_{13}\,\nu_{32})/(1-\nu_{13}\,\nu_{31}) \\
\nu_{21}' &= (\nu_{21}+\nu_{23}\,\nu_{31})/(1-\nu_{23}\,\nu_{32}).
\end{aligned} \tag{A9}
$$

In the cases where ρ is close to 1, $\bar{E}$ can be approximated by

$$
\bar{E} = \left(\frac{1+\rho}{2}\right)^{\frac{1}{2}} E_2' [E_1'/E_2']^{\frac{1}{4}}. \tag{A10}
$$

For more general situations Cui and Budiansky [23] have provided numerical values for orthotropy factors A which can be used to determine $\bar{E}$. The relationship between $\bar{E}$ and A is

$$
\bar{E} = \frac{A\,E}{1-\nu^2} \tag{A11}
$$

in which ν is the Poisson's ratio of fiber and matrix which are assumed to be the same. The orthotropic modulus $\bar{E}$ can be used to determine the opening of the crack due to the applied load and for the effect of fibers on the crack opening (Cui and Budiansky, [23]).

For a bridged matrix crack subject to load cycling such that the amplitude of the applied load is $\Delta\sigma$ the bridging behavior is given by eq. (3) and the governing is (Marshall and Cox, [9]; McMeeking and Evans, [4])

$$
\Delta\Sigma_s^2(\bar{x})/16 + \int_{1-\alpha}^{1} \Delta\Sigma_s(t)\, H(t,\bar{x})\, dt = \Delta\Sigma\sqrt{1-\bar{x}^2} \tag{A12}
$$

where $\Delta\Sigma$ is given by eq. (4) and

$$\Delta\Sigma_s = 2\lambda \bar{E} \Delta\sigma_s / a \qquad \text{(A13)}$$

and $\Delta\sigma_s$ is the amplitude of the stress cycle at the matrix crack surface. Note that as shown by McMeeking and Evans [4] $\bar{\Sigma}_s$ and $\Delta\Sigma_s$ obey exactly the same equation so that results for them can be interchanged.

The equations were solved by standard methods discussed by Marshall and Cox [9].

FIGURE CAPTIONS

Fig. 1 A typical fatigue crack growth curve for a Ti/SiC composite. The length Δa of the matrix fatigue crack beyond the original notch is plotted against N the number of load cycles. The actual dimensions of the specimen are shown in the insert.

Fig. 2 Schematic of a center crack in an infinite body under remote tension, with bridging fibers in the matrix crack wake.

Fig. 3 Distributions of the non-dimensional bridging stress for different unbridged lengths for $\Delta\Sigma = 1$.

Fig. 4 Non-dimensional stress intensity ranges versus normalized crack extension for different applied stress amplitudes.

Fig. 5 Plots giving the relationship among the length of the crack, a, the unbridged segment ℓ, the maximum stress in the fibers S and the maximum applied load σ_{max}.

Fig. 6 Full lines show the normalized stress intensity ranges versus normalized crack extension for a finite width specimen computed by finite elements. The dashed lines show the results for an infinite body computed by solution of the integral equation.

Fig. 7 Predicted fatigue crack growth curves when fibers do not fail. The normalized crack extension is plotted versus the normalized number of load cycles. (a) Paris law exponent n = 2; (b) Paris law exponent n = 4.

Fig. 8 Fiber breaking rate related to fiber strength, applied load and matrix crack growth rate; 2ℓ is the length of the current unbridged segment of the crack, whereas $2a_o$ is the length of the original unbridged notch.

Fig. 9 Predicted fatigue crack growth curves in the presence of fiber failure for n = 2 and different values of $\Delta\Sigma_o$.

Fig. 10 Map for fiber failure and non-failure in a finite strip with a central notch in which a matrix crack can grow by fatigue.

Fig. 11 Relationship between applied stress, fiber strength and notch length for a specified extension of the matrix crack before fiber failure will occur.

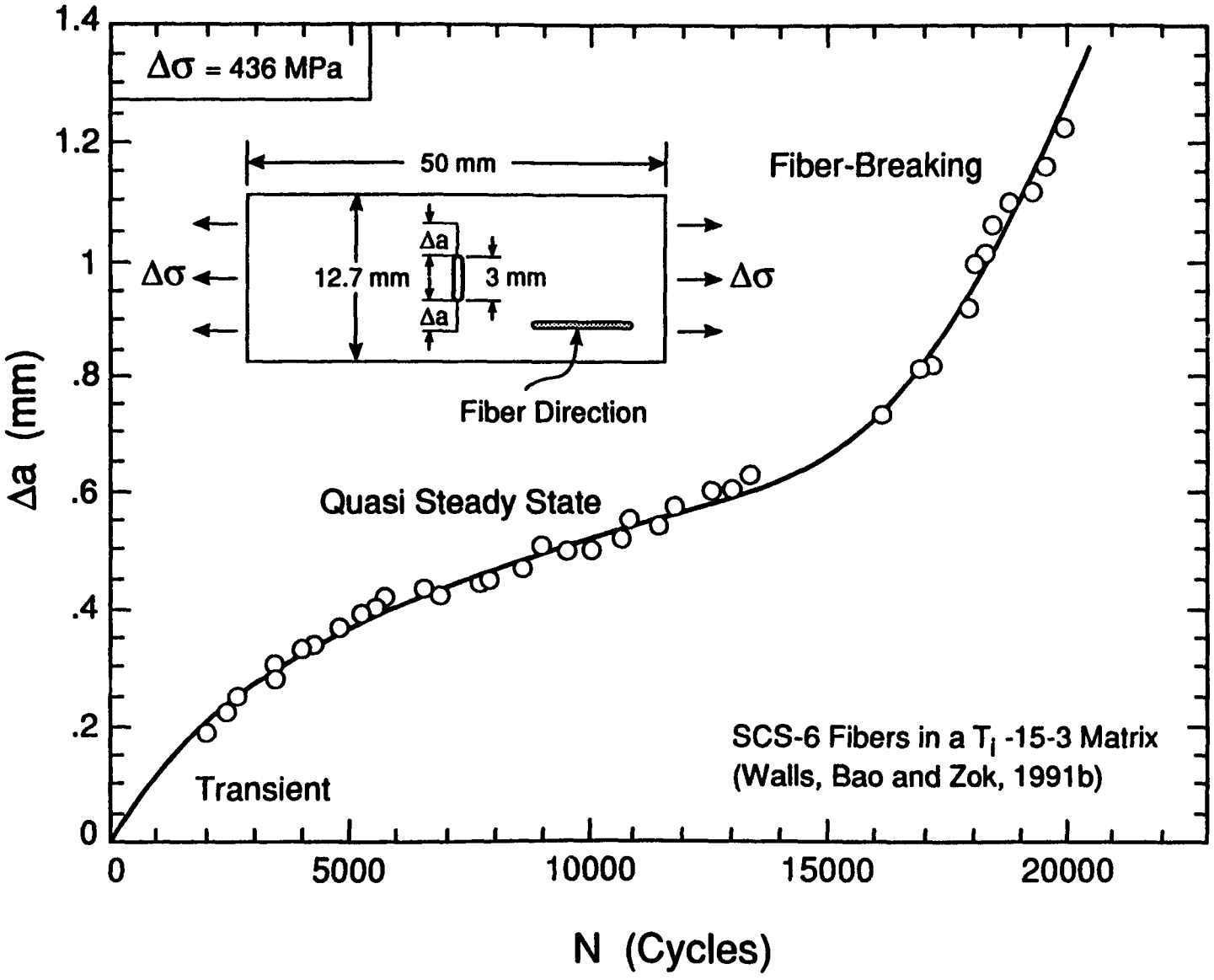
Δσ = 436 MPa
50 mm
Fiber-Breaking
Δa
12.7 mm
3 mm
Δa
Δσ
Δσ
Fiber Direction
Quasi Steady State
Transient
SCS-6 Fibers in a Ti -15-3 Matrix
(Walls, Bao and Zok, 1991b)
Δa (mm)
N (Cycles)
0
.2
.4
.6
.8
1
1.2
1.4
0
5000
10000
15000
20000

Fig. 1

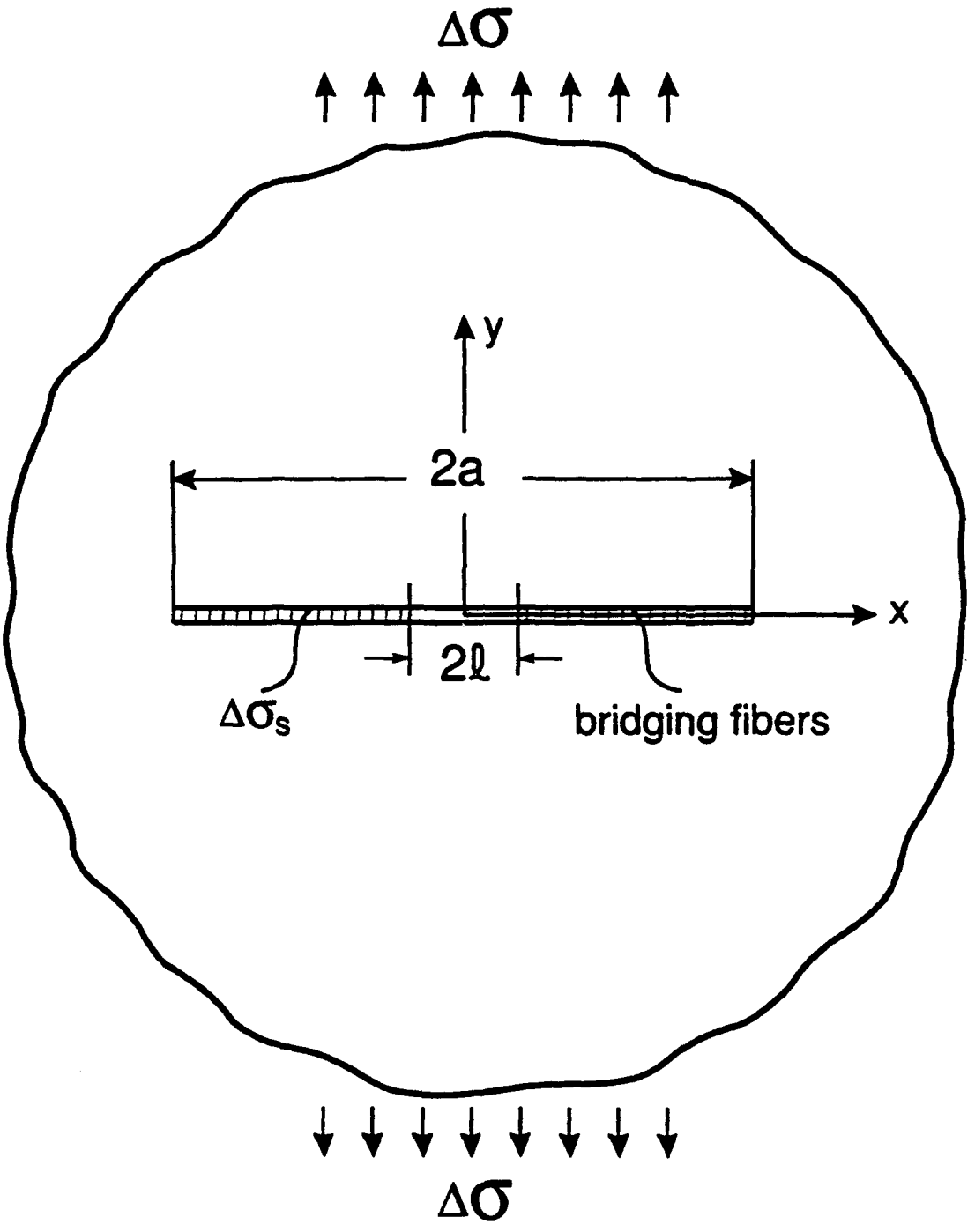

Fig. 2

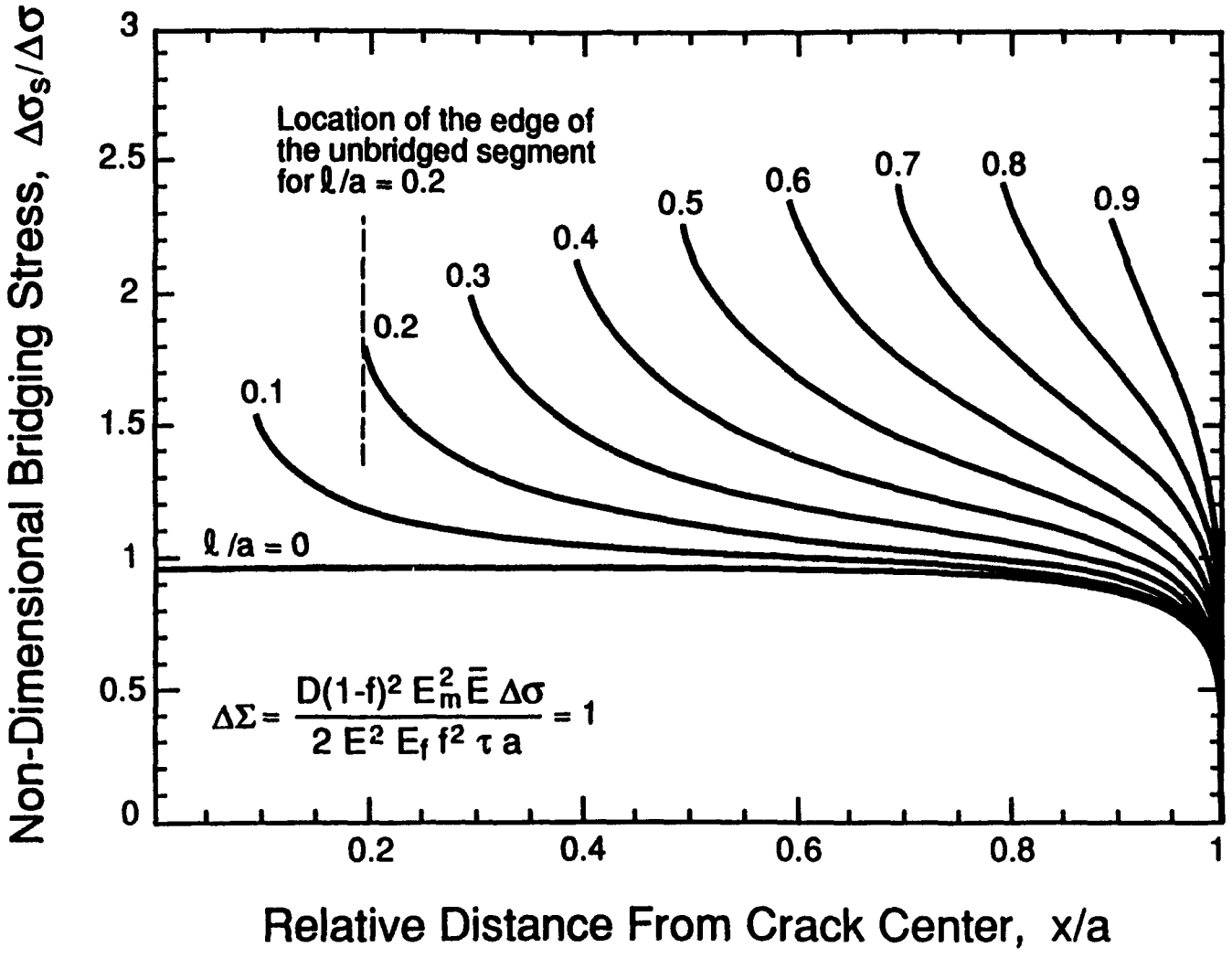
Non-Dimensional Bridging Stress, $\Delta\sigma_s/\Delta\sigma$
Relative Distance From Crack Center, x/a
Location of the edge of the unbridged segment for $\ell/a = 0.2$
0.1
0.2
0.3
0.4
0.5
0.6
0.7
0.8
0.9
$\ell/a = 0$
$\Delta\Sigma = \frac{D(1-f)^2 E_m^2 \bar{E} \Delta\sigma}{2 E^2 E_f f^2 \tau a} = 1$
0
0.5
1
1.5
2
2.5
3
0.2
0.4
0.6
0.8
1

Fig. 3

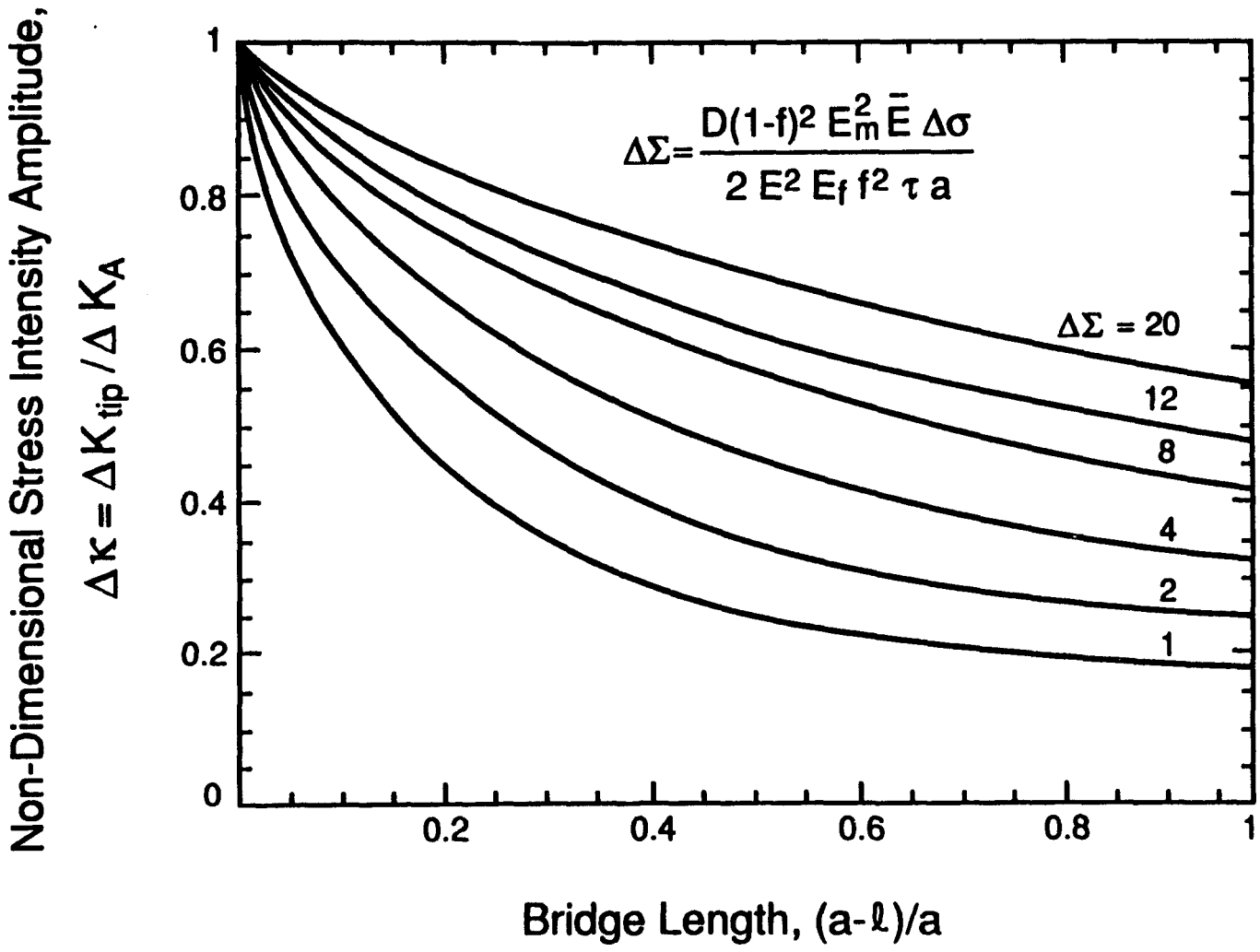
Non-Dimensional Stress Intensity Amplitude,
$\Delta\kappa = \Delta K_{tip} / \Delta K_A$
$\Delta\Sigma = \frac{D(1-f)^2 E_m^2 \bar{E} \Delta\sigma}{2 E^2 E_f f^2 \tau a}$
ΔΣ = 20
12
8
4
2
1
0
0.2
0.4
0.6
0.8
1
Bridge Length, (a-ℓ)/a

Fig. 4

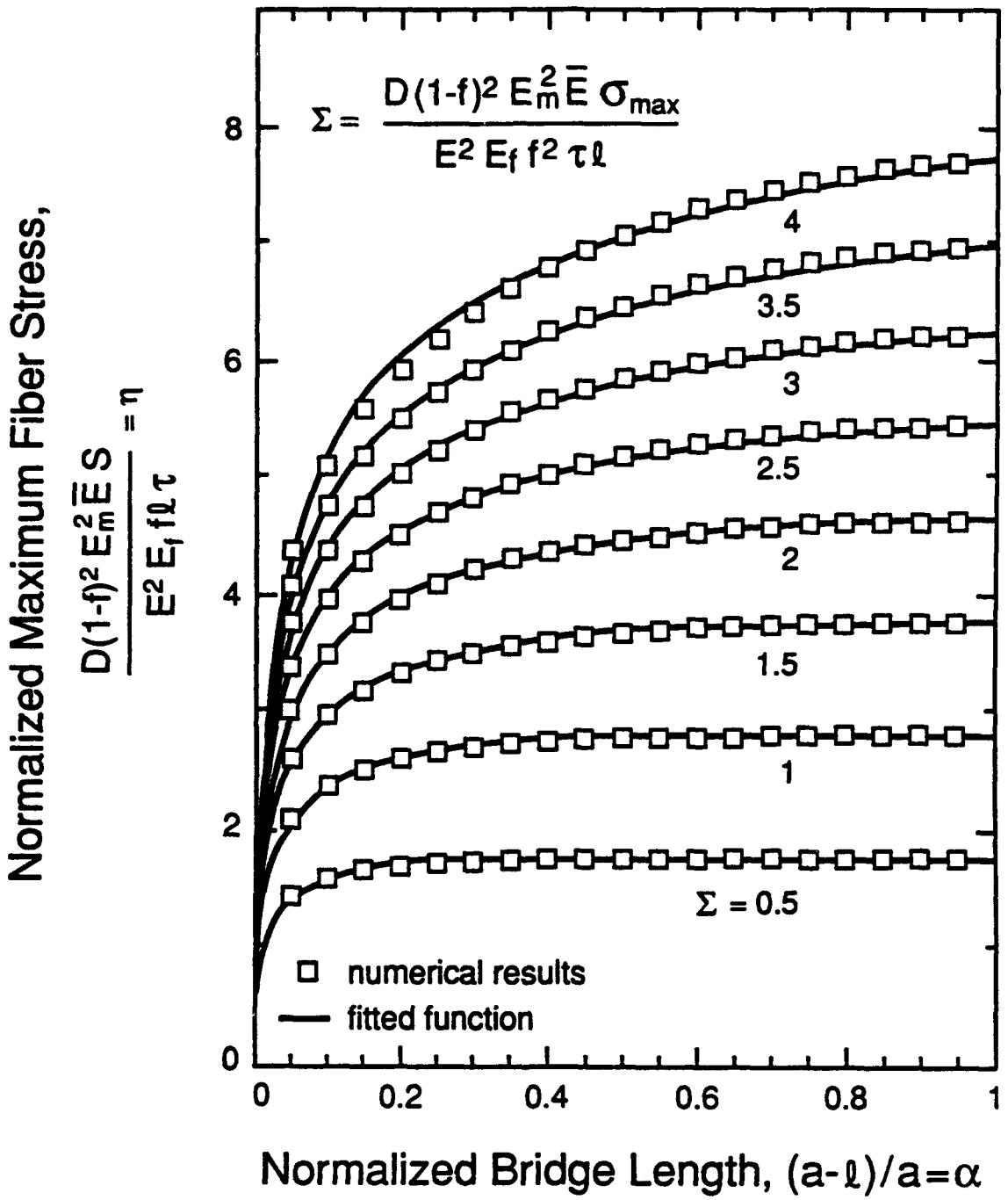
$\Sigma = \frac{D(1-f)^2 E_m^2 \bar{E} \sigma_{max}}{E^2 E_f f^2 \tau \ell}$
4
3.5
3
2.5
2
1.5
1
$\Sigma = 0.5$
numerical results
fitted function
0
2
4
6
8
0
0.2
0.4
0.6
0.8
1
Normalized Maximum Fiber Stress, $\frac{D(1-f)^2 E_m^2 \bar{E} S}{E^2 E_f f \ell \tau} = \eta$
Normalized Bridge Length, $(a-\ell)/a=\alpha$

Fig. 5a

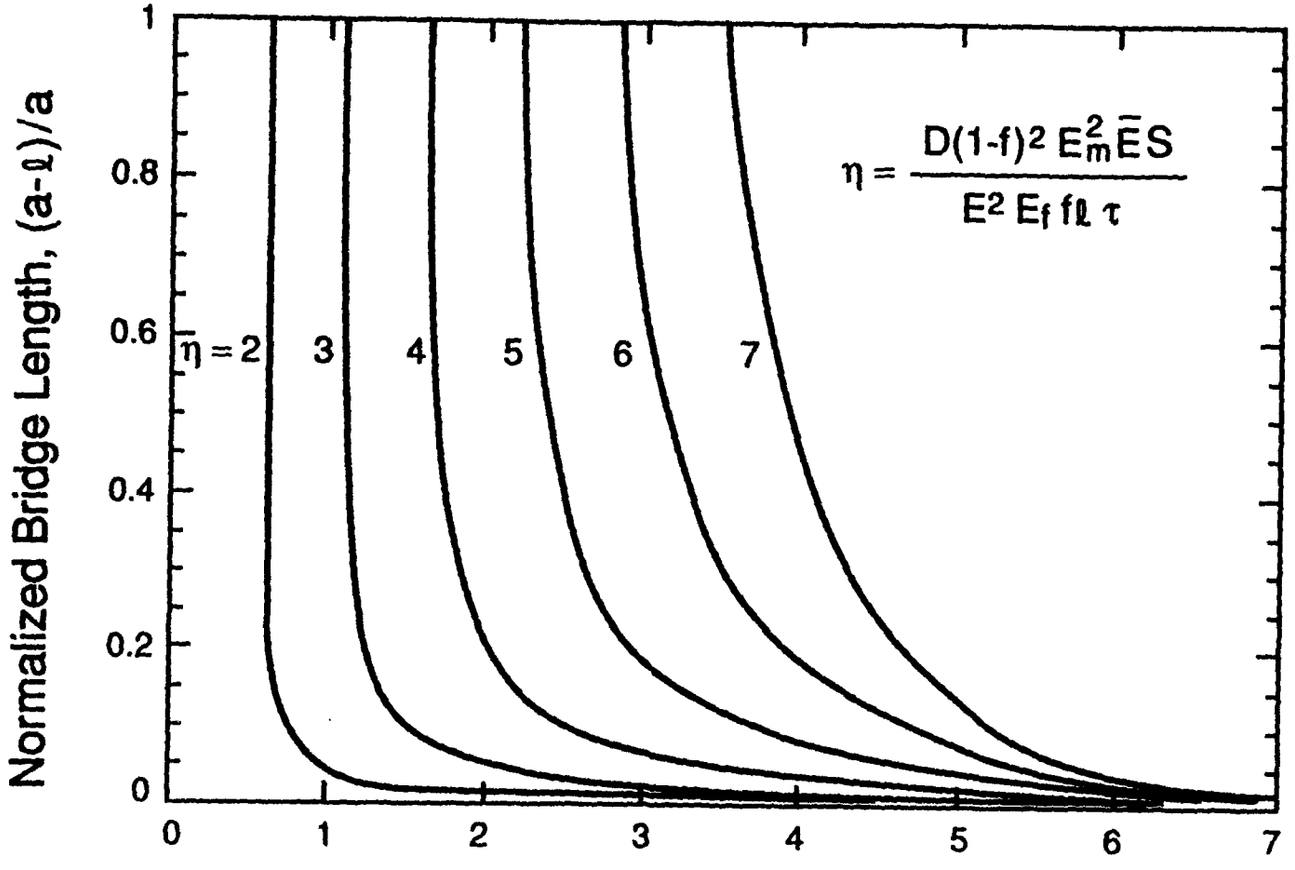
Normalized Bridge Length, (a-ℓ)/a
1
0.8
0.6
0.4
0.2
0
η = 2
3
4
5
6
7
$\eta = \frac{D(1-f)^2 E_m^2 \bar{E} S}{E^2 E_f f \ell \tau}$
0
1
2
3
4
5
6
7
Normalized Maximum Applied Stress,
$\frac{D(1-f)^2 E_m^2 \bar{E} \sigma_{max}}{E^2 E_f f^2 \ell \tau} = \Sigma$

Fig. 5b

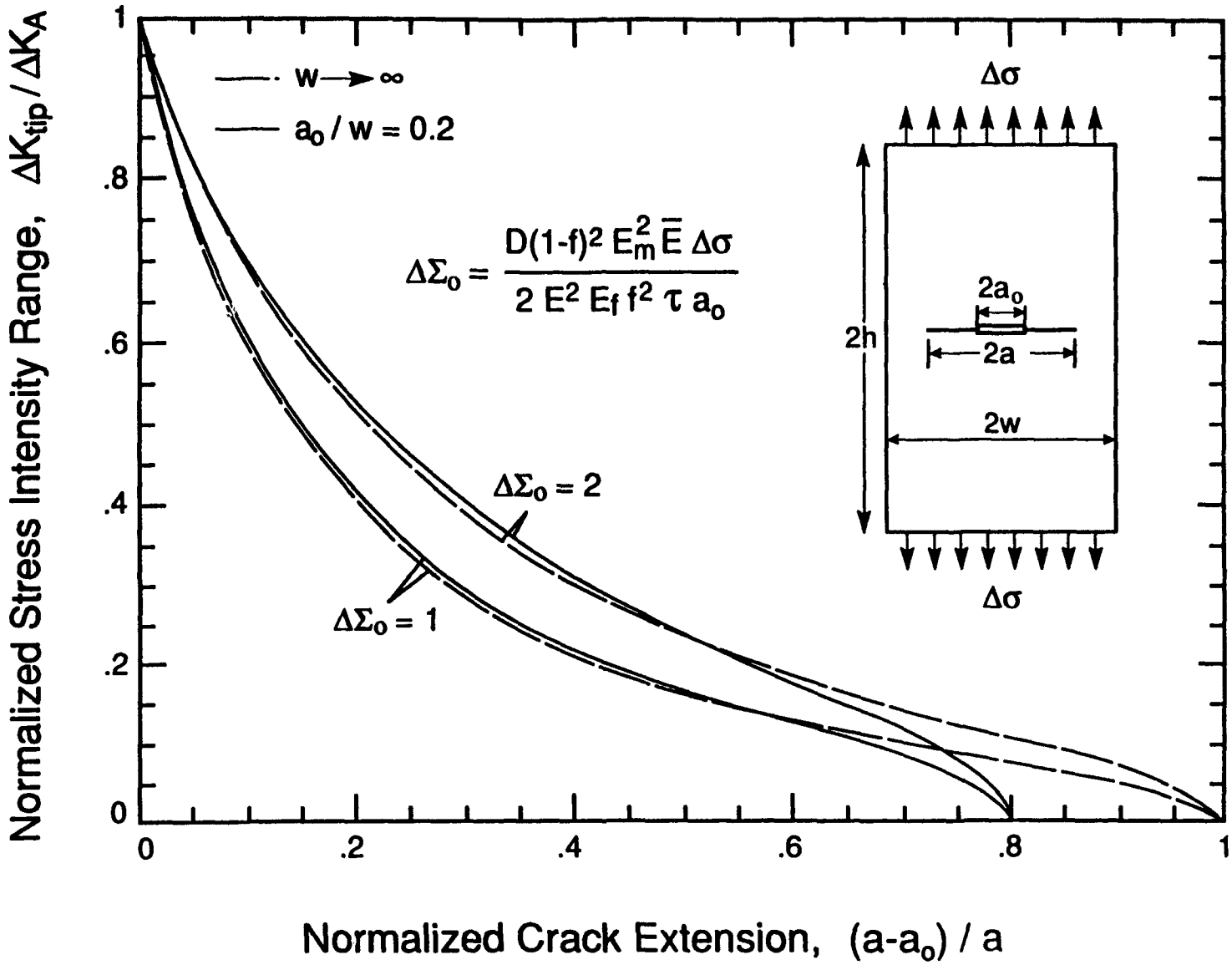
Normalized Stress Intensity Range, $\Delta K_{tip} / \Delta K_A$
Normalized Crack Extension, $(a-a_o) / a$
$w \rightarrow \infty$
$a_o / w = 0.2$
$\Delta\Sigma_o = \frac{D(1-f)^2 E_m^2 \bar{E} \Delta\sigma}{2 E^2 E_f f^2 \tau a_o}$
$\Delta\Sigma_o = 2$
$\Delta\Sigma_o = 1$
$\Delta\sigma$
$2a_o$
$2a$
$2h$
$2w$
$\Delta\sigma$
0
.2
.4
.6
.8
1

FIG. 6

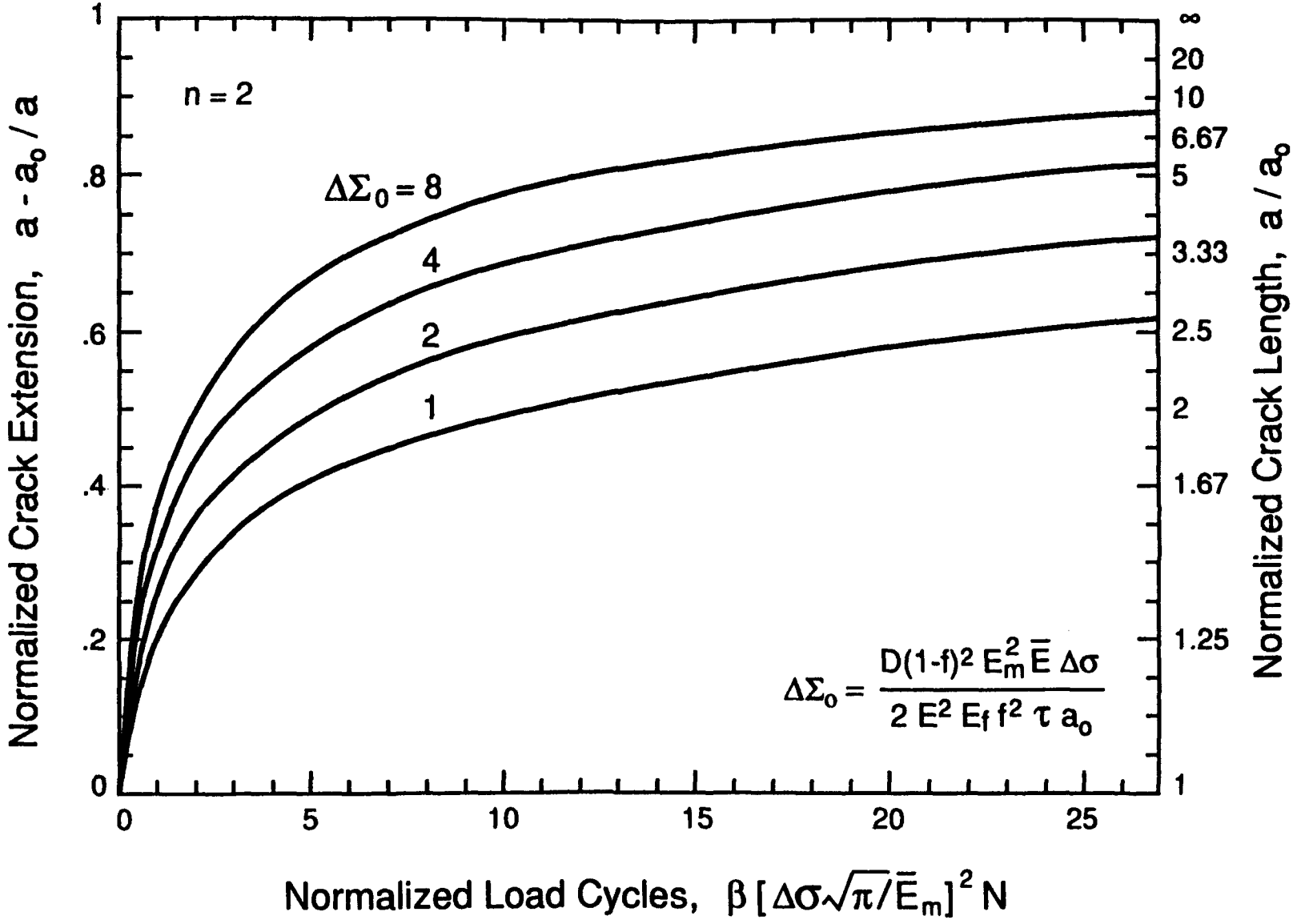
n = 2
$\Delta\Sigma_0 = 8$
4
2
1
$\Delta\Sigma_o = \frac{D(1-f)^2 E_m^2 \bar{E} \Delta\sigma}{2 E^2 E_f f^2 \tau a_o}$
Normalized Crack Extension, a - a_o / a
Normalized Crack Length, a / a_o
Normalized Load Cycles, $\beta [\Delta\sigma\sqrt{\pi}/\bar{E}_m]^2 N$
0
.2
.4
.6
.8
1
0
5
10
15
20
25
∞
20
10
6.67
5
3.33
2.5
2
1.67
1.25
1

FIG. 7a

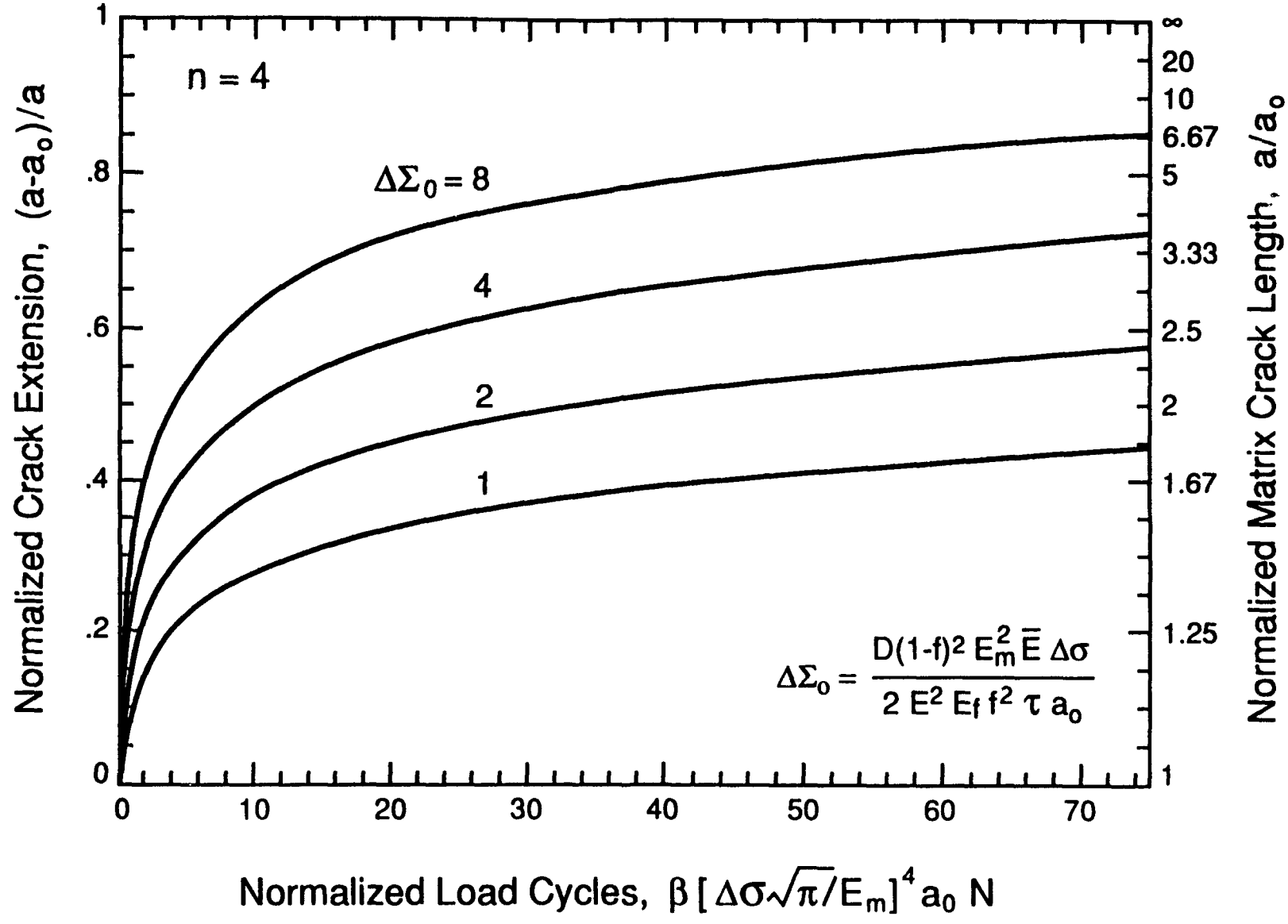
n = 4
$\Delta\Sigma_0 = 8$
4
2
1
$\Delta\Sigma_o = \frac{D(1-f)^2 E_m^2 \bar{E} \Delta\sigma}{2 E^2 E_f f^2 \tau a_o}$
Normalized Crack Extension, $(a-a_o)/a$
Normalized Matrix Crack Length, a/a_o
Normalized Load Cycles, $\beta [\Delta\sigma\sqrt{\pi}/E_m]^4 a_0 N$
0
.2
.4
.6
.8
1
0
10
20
30
40
50
60
70
∞
20
10
6.67
5
3.33
2.5
2
1.67
1.25
1

Fig. 7b

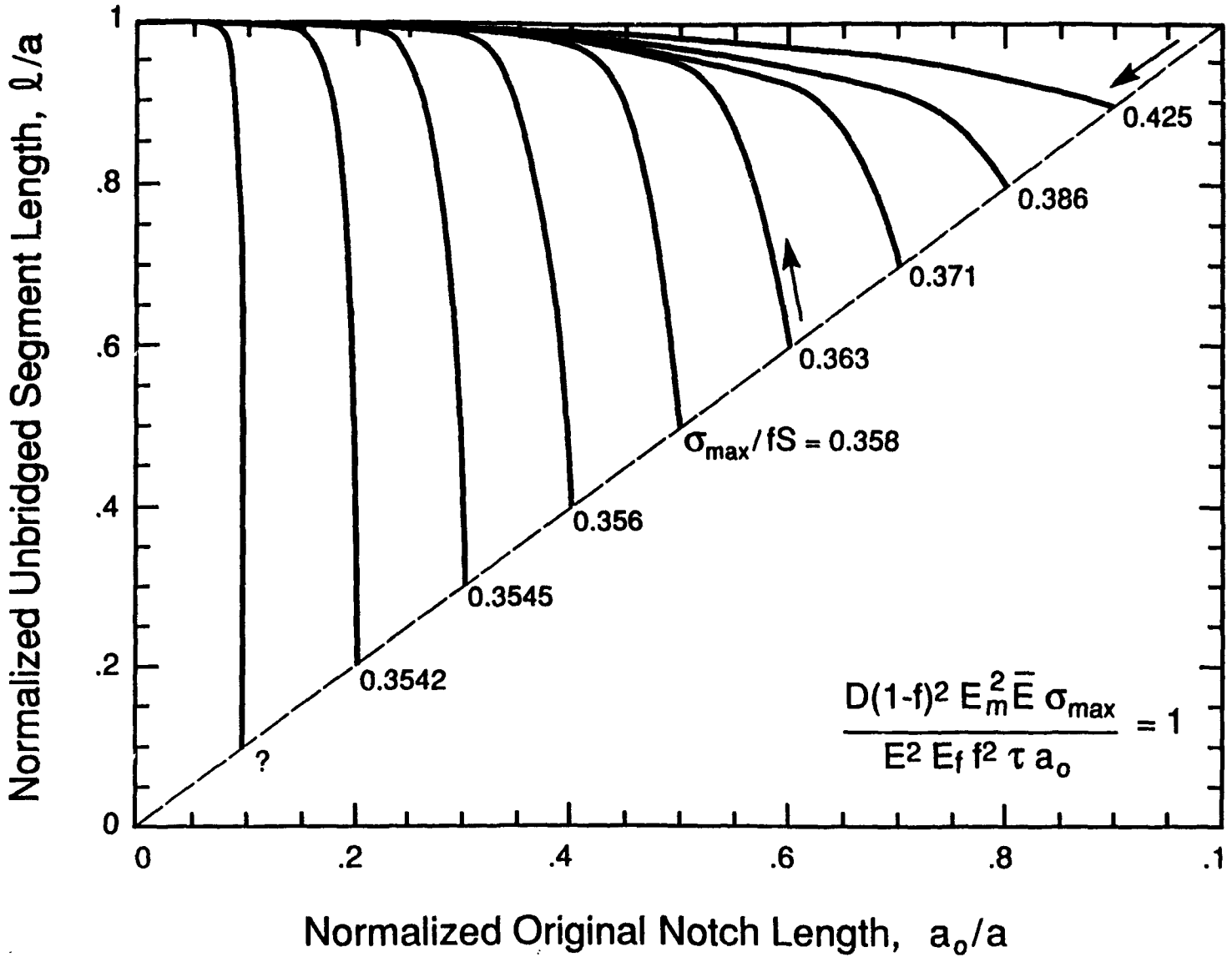
Normalized Unbridged Segment Length, ℓ/a
1
.8
.6
.4
.2
0
0
.2
.4
.6
.8
.1
Normalized Original Notch Length, a_o/a
0.425
0.386
0.371
0.363
$\sigma_{max}/fS = 0.358$
0.356
0.3545
0.3542
?
$\frac{D(1-f)^2 E_m^2 \bar{E} \sigma_{max}}{E^2 E_f f^2 \tau a_o} = 1$

Fig. 8

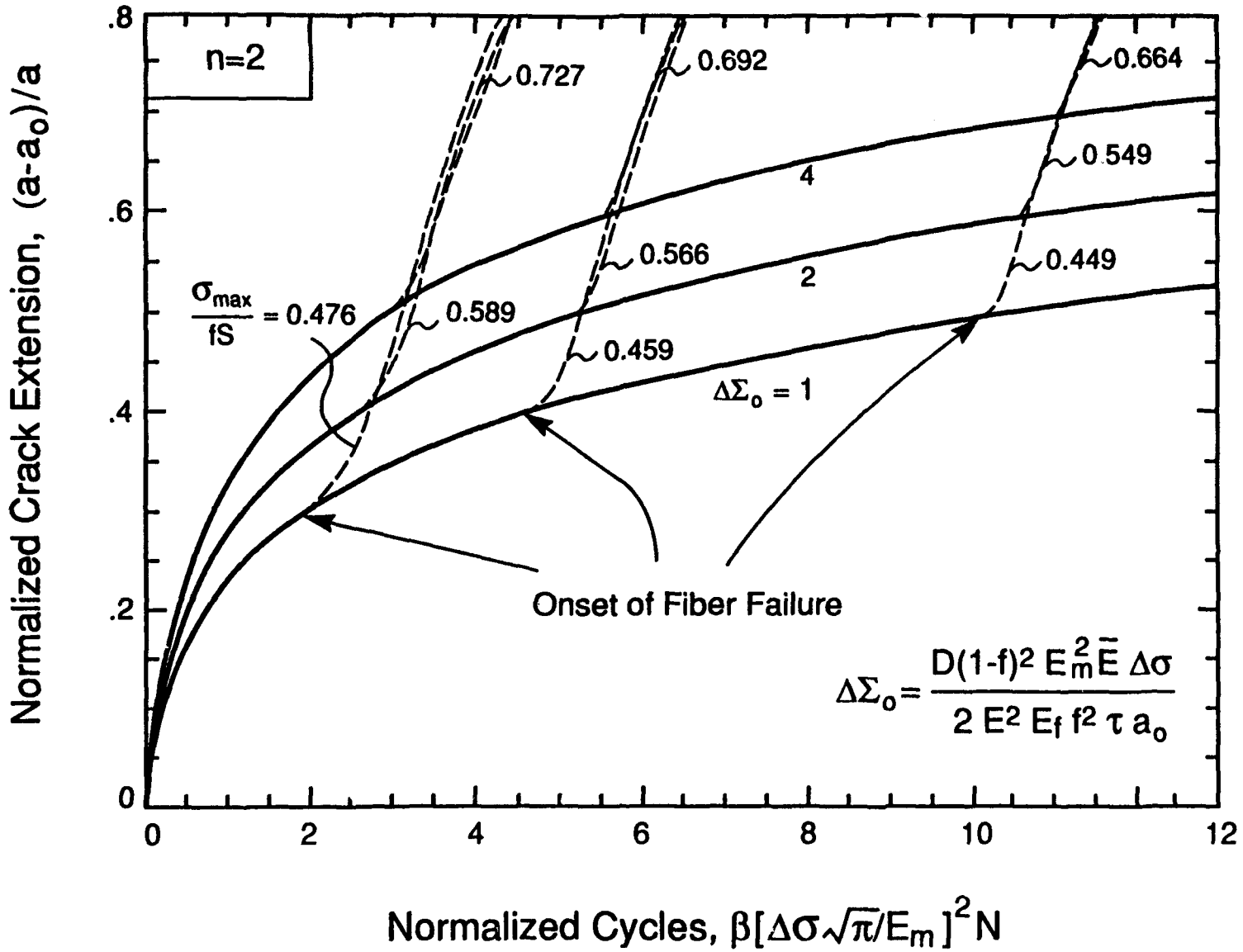
n=2
0.727
0.692
0.664
0.549
4
0.566
2
0.449
$\frac{\sigma_{max}}{fS}$ = 0.476
0.589
0.459
$\Delta\Sigma_o$ = 1
Onset of Fiber Failure
$\Delta\Sigma_o = \frac{D(1-f)^2 E_m^2 \tilde{E} \Delta\sigma}{2 E^2 E_f f^2 \tau a_o}$
Normalized Crack Extension, $(a-a_o)/a$
Normalized Cycles, $\beta[\Delta\sigma\sqrt{\pi}/E_m]^2 N$
0
.2
.4
.6
.8
0
2
4
6
8
10
12

FIG. 9

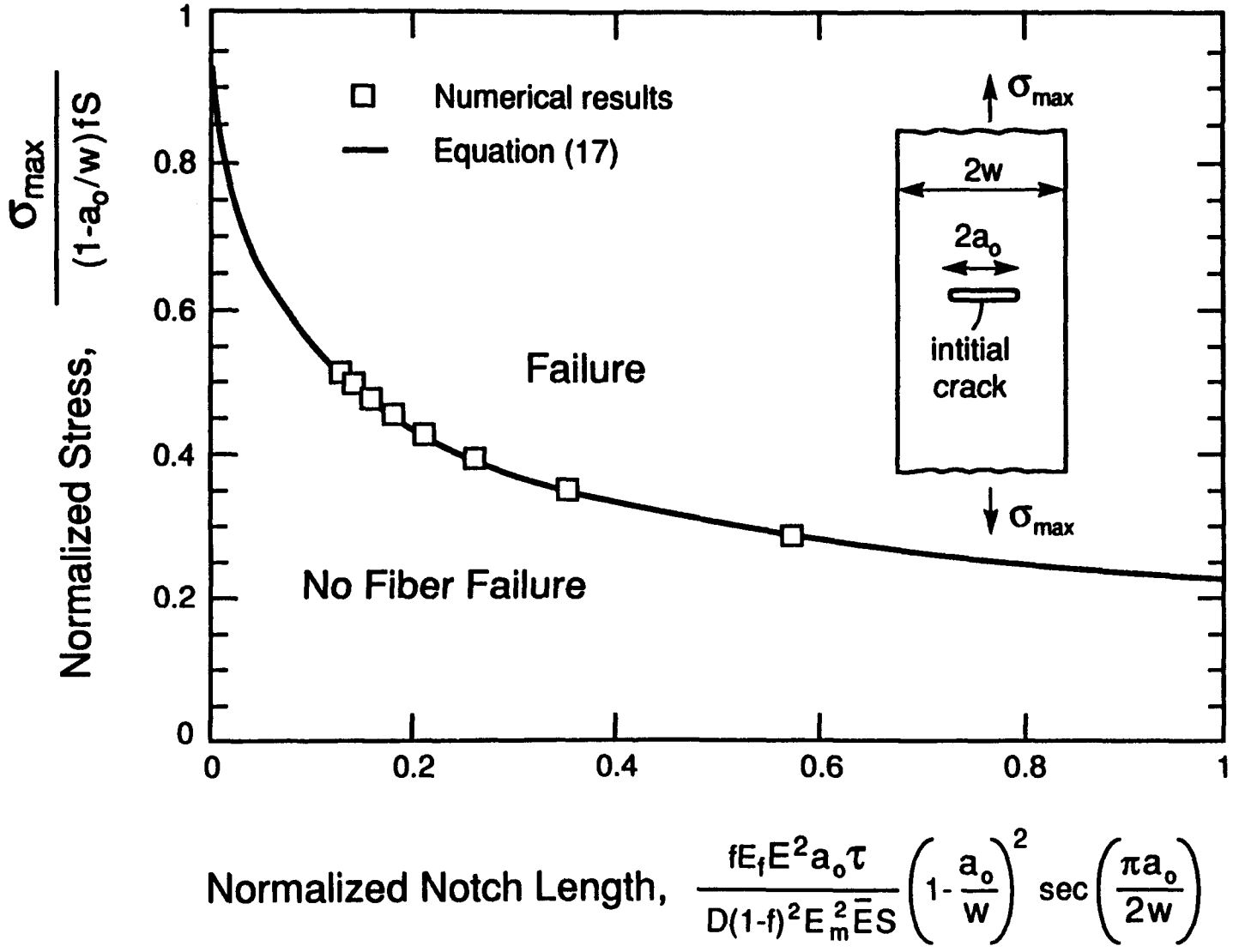
Numerical results
Equation (17)
Failure
No Fiber Failure
σ_{max}
2w
$2a_o$
intitial crack
σ_{max}
Normalized Stress, $\frac{\sigma_{max}}{(1-a_o/w)fS}$
Normalized Notch Length, $\frac{fE_f E^2 a_o \tau}{D(1-f)^2 E_m^2 \bar{E} S}\left(1-\frac{a_o}{w}\right)^2 \sec\left(\frac{\pi a_o}{2w}\right)$
0
0.2
0.4
0.6
0.8
1

FIG. 10

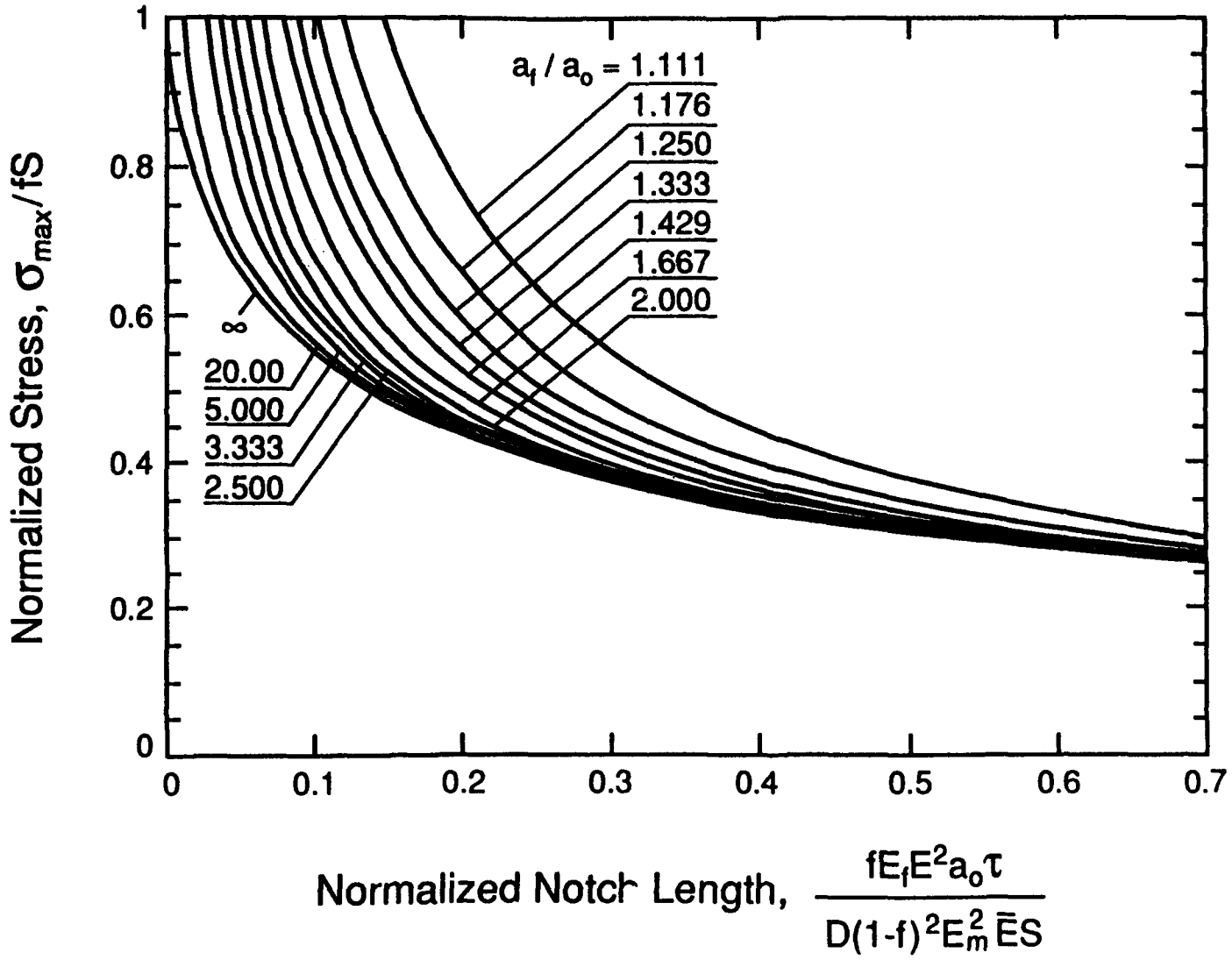

Fig. 11

McMeeking.NSF•4/93•amk• D11#1058-3

THERMOMECHANICAL FATIGUE CRACKING IN FIBER REINFORCED METAL MATRIX COMPOSITES

G. Bao‡ and R.M. McMeeking*

‡Department of Mechanical Engineering
The Johns Hopkins University, Baltimore, MD 21218

*Department of Mechanical and Environmental Engineering
University of California, Santa Barbara, CA 93106

Submitted to the Journal of the Mechanics and Physics of Solids

March, 1994

ABSTRACT

A theoretical model is developed for thermomechanical fatigue cracking in fiber reinforced metal matrix composites. Interfacial debonding is assumed to occur readily, allowing fibers to slide relative to the matrix resisted by a uniform shear stress. The fibers therefore bridge any matrix crack which develops. The crack bridging traction law is obtained, including the effect of thermal expansion mismatch between the fiber and the matrix and a temperature dependence of the frictional shear stress. Any combination of thermal and mechanical cycling is considered as long as the slip zone along the fiber increases in length monotonically during each increment of cycling. However, for clarity, the results are presented in terms of in phase and out of phase cycling of the thermal and mechanical loads at the same frequency. For each case, the stress distributions in the bridging zone as well as the stress intensity factors at the crack tip are computed for relevant regimes of the thermal and mechanical loading parameters. Predictions are made of the matrix fatigue crack growth under combined thermal and mechanical loading conditions. It is found that when the thermal expansion coefficient of the fiber is less than that of the matrix, a significant increase in the crack growth rate results in out-of-phase thermomechanical fatigue. On the other hand, there is decreased tendency for fibers to fail in this case. For in-phase thermomechanical fatigue, the crack growth rate is reduced but the stress in the fiber is larger than that due to mechanical loading alone, resulting in an increased tendency for fiber failure. The implications for life prediction for fiber reinforced metal matrix composites are discussed.

1. INTRODUCTION

Fiber reinforced metal matrix composites are designed and developed for high performance aerospace applications, including advanced gas turbine engines and supersonic airframes. A combination of cyclic thermal and mechanical loading in these applications may cause thermomechanical fatigue (TMF) cracking in the composite, perhaps reducing the load carrying capacity, and potentially leading to failure. Prediction of fatigue crack growth in fiber reinforced metal matrix composites under thermomechanical loading is therefore of critical importance in the safe design of composite structures.

In many fiber reinforced metal matrix composites, the fibers are made of ceramic with a coefficient of thermal expansion (CTE) α_f lower than that of the metal matrix α_m. Thus during cool down, axial tensile stress builds up in the matrix, while parallel compressive stress results in the fibers; the opposite is true when the composite is warming up. The thermal stresses and stress amplitudes due to CTE mismatch can be very high, possibly exceeding the applied mechanical stress and its range. The history of thermal stress and mechanical stress can be very complex, since both the applied load and the temperature can vary independently with time. However, for this initial study, two limiting cases are considered: the temperature change is completely in phase (IP) or completely out-of-phase (OP) with the mechanical loading, as shown in Fig. 1. However, certain of the results can be interpreted for arbitrary TMF cycling.

The most effective application of metal matrix fiber composites is for longitudinal stressing of uniaxially reinforced materials. To preserve good toughness and fatigue properties, the fiber/matrix interface is relatively weak. Debonding in shear occurs readily along the interface, allowing the fibers to slide relative to the matrix with drag provided by friction. Due to these phenomena, fibers remain intact in the tip region of a matrix crack as depicted in Fig. 2. This permits the fibers to bridge the matrix crack,

thus reducing the crack tip stress intensity. In the absence of thermal loading, crack bridging models have been developed (e.g., Marshall, Cox and Evans, 1985; Marshall and Cox, 1987; McCartney, 1987; Hutchinson and Jensen, 1990) based on the justifiable assumption that the frictional sliding shear stress τ is a constant along the interface. These models have been used extensively in fiber bridging calculations (Marshall et al., 1985; Marshall and Cox, 1987; McCartney, 1987; Marshall, 1991; Cox, 1991; Cox and Lo, 1992). Corresponding mechanical fatigue crack growth analyses have been performed for metal matrix composites by McMeeking and Evans (1990), Cox and Lo (1992) and Bao and McMeeking (1993). Comparisons between the model predictions and experimental measurements at room temperature made by Walls, Bao and Zok (1993) show good agreement.

Without thermal loading, the bridging fibers exert closure forces on the crack surfaces. This increases the fracture and fatigue resistance of the composite. With thermal loading, the bridging fibers can prop open the crack. This will occur if the thermal stresses are large enough and place the fibers in compression. In this case, the effect of the bridging fibers will be to increase the stress intensity at the crack tip. Therefore crack bridging can be detrimental to fatigue crack growth rather than helpful. In addition, the bridge contributions are different in in-phase and in out-of-phase thermomechanical fatigue.

Some previous work is available for thermomechanical behavior of frictionally constrained fiber reinforced composites. The matrix-cracking model of Budiansky, Hutchinson and Evans (1986) included the effect of thermal strain mismatch and showed that thermal strains can promote matrix cracking. In addition, Cox (1990) has analyzed extensively the behavior of a fiber near a free surface due to cyclic thermal strains. However, no analysis has been carried out for bridging fibers in a finite matrix crack during thermomechanical load cycling.

In this paper, matrix fatigue crack growth in fiber reinforced metal matrix composites under combined thermal and mechanical cyclic loading is analyzed and quantified. A crack bridging model is developed first to include the effect of thermal stress. A bridging model is then used to calculate the stress distribution in the bridging zone and the crack tip stress intensity range for both fully bridged and partially bridged cracks. The effect of thermal load on matrix fatigue crack growth and composite fatigue life until fiber failure are predicted using nondimensional loading parameters. Different roles of fiber bridging in in-phase TMF and out-of-phase TMF are revealed. Finally, the implications of the present work for life prediction for metal matrix composites under thermomechanical loading conditions are discussed.

2. CRACK BRIDGING ANALYSIS

2.1 The Crack Bridging Law

Consider a single mode I crack bridged by intact fibers as shown schematically in Fig. 2. The behavior of intact fibers in the bridging zone is represented by a cylindrical model consisting of a single fiber embedded in a matrix cylinder, as shown in Fig. 3. Shear lag analysis following Budiansky et al. (1986), McCartney (1987) and Cox (1990) shows (Appendix A) that under monotonic thermal and mechanical loadings, the crack opening displacement δ is related to the bridging stress t by

$$\delta = \lambda [t + fE_f (\alpha_f - \alpha_m) T]^2 \qquad (1)$$

where T is the temperature defined with T = 0 in the stress free state, and λ is a material parameter given by

$$\lambda = \frac{D(1-f)^2 E_m^2}{4f^2 E^2 E_f \tau} \tag{2}$$

where D is the fiber diameter, f is the volume fraction of fibers, E_m is Young's modulus for the matrix, E_f is the Young's modulus for the fiber, E is the rule of mixtures axial modulus for the composite (see Appendix A) and τ is the shear stress at the sliding interface at temperature T. It should be noted that in certain circumstances the crack will tend to close rather than open during monotonic loading. For example, if T is negative and α_f is greater than α_m, the crack will tend to close when t = 0. This will also be true if t is positive but small. It will be assumed that the crack can remain open and traction free on the matrix surface at all times so that matrix closure effects will not be taken into account. This will generally be true for the common situation in which $\alpha_m > \alpha_f$ and T is negative. Without thermal loading, the crack bridging law (2) becomes $\delta = \lambda t^2$ which has been used in previous fatigue studies (e.g., Bao and McMeeking, 1993).

Following McMeeking and Evans (1990), the crack bridging law under cyclic loading conditions is similar to that in (1) with

$$\Delta\delta = \pm\frac{1}{2}\lambda\left[\Delta t + fE_f(\alpha_f - \alpha_m)\Delta T\right]^2 \tag{3}$$

where $\Delta\delta$ is the change in crack opening displacement, Δt is the change in bridging stress, ΔT is the temperature change as depicted in Fig. 1. The sign preceding λ should be chosen according to whether $\Delta t + fE_f(\alpha_f - \alpha_m)\Delta T$ is positive or negative. The positive sign is used when this term is positive and the negative sign is used when the term is negative (see Appendix A). The parameter λ is that given in eq. (2) except that τ is replaced by $[\tau(T_1) + \tau(T_2)]/2$ where T_1 and T_2 are the temperatures at the extremes

of the cyclic range; i.e. the relevant interface shear stress is the average of the interface shear stresses at the extremes of the cycle. The temperature dependence of τ can be due to a temperature influenced change in material properties or due to the change of the thermal residual compression on the fiber-matrix interface which will affect friction.

The expression in (3) is valid as long as the current slipping zone has increased monotonically in length from the beginning of the increment as given by eq. (A8) & (A10) in Appendix A. Thus, separate increments or half cycles must be defined to account for each stage in which the slip direction reverses, which means every time $\Delta t + f E_f (\alpha_f - \alpha_m) \Delta T$ changes sign. On this basis, arbitrary TMF can be accounted for. For example, if the temperature is rising slowly while the mechanical stress is cycled rapidly, each mechanical stress change would be counted as a half cycle if the magnitude of Δt is sufficiently large to change the sign of $\Delta t + f E_f (\alpha_f - \alpha_m) \Delta T$ even though ΔT is the same for each mechanical stress half cycle. On the other hand, if $\Delta t + f E_f (\alpha_f - \alpha_m) \Delta T$ has the same sign during each mechanical stress half cycle, the TMF half cycle would be the single increment lasting until the temperature rise is completed. Arbitrary TMF can therefore be studied by repeated application of eq. (3) with each half cycle accordingly identified each time $\Delta t + f E_f (\alpha_f - \alpha_m) \Delta T$ changes sign.

2.2 The Bridging Stress Distribution

There are two key quantities pertaining to the thermomechanical fatigue behavior of fiber reinforced metal matrix composites. One is the stress intensity amplitude at the crack tip which governs the matrix cracking and the other is the maximum stress in the bridging fibers which dictates fiber fracture. Both can be obtained from the stress profile in the bridging zone. Typically, the fatigue specimens for matrix cracking fatigue tests are notched panels with finite widths. The calculation of bridging stress distribution in such specimens can be carried out using finite

elements (e.g., Bao and McMeeking, 1993) or by solving integral equations (Cox and Lo, 1992). To gain some insight into the role of crack bridging in thermomechanical fatigue, attention in this paper is focused on a mode I, plane strain crack in a large body, as shown schematically in Fig. 2 and the analysis of finite bodies will be deferred to future work. Specifically, a linear elastic composite infinite body contains a center crack of length 2a and is subjected to remote cyclic loading $\Delta\sigma$. The unbridged center section has the length $2a_o$, while the sections of length $a - a_o$ at both ends of the crack represent the segment bridged by intact fibers. Clearly a fully bridged crack is the special case $a_o = 0$. A partially bridged crack can be created by fiber failure or by the initial presence of a notch. Thus $2a_o$ can be the initial notch size but it can also be the current unbridged length due to fiber failure.

Under cyclic loading conditions, the crack opening displacement change $\Delta\delta$ in the bridging zone is related to the change in bridging stress Δt by the crack bridging traction law eq. (3). The elastic analysis of the body follows a standard approach as used by Marshall et al., (1985) and McCartney (1987). $\Delta\delta$ is related to the amplitude of the applied stress $\Delta\sigma$ and the amplitude of the bridging stress Δt by

$$\Delta\delta = \Delta\delta_A + \Delta\delta_B \tag{4}$$

where

$$\Delta\delta_A = \frac{4}{\bar{E}}\Delta\sigma\sqrt{a^2 - x^2} \tag{5}$$

is the crack opening change induced by the applied stress amplitude $\Delta\sigma$ and

$$\Delta\delta_B = -\frac{4}{\bar{E}}\int_{a_o}^{a} \Delta t(\xi) H(\xi, x, a)\, d\xi \tag{6}$$

is the contribution to $\Delta\delta$ due to the bridging fibers. In eq. (5) & (6), $\bar{E}$ is the effective Young's modulus considering material orthotropy (Bao and McMeeking, 1993) and x is the position in the bridging zone measured from the center of the notch (Fig. 2). The Green's function H in eq. (6) is given by

$$H(\xi,x,a) = \frac{1}{\pi}\log\left|\frac{\sqrt{a^2-x^2}+\sqrt{a^2-\xi^2}}{\sqrt{a^2-x^2}-\sqrt{a^2-\xi^2}}\right| \tag{7}$$

Substitution of eqs. (3), (5) & (6) into eq. (4) and use of suitable normalizations shows that, the governing equation for Δt can be expressed as

$$\pm\left[\Delta\Sigma_b(\bar{x})+\Delta\theta\right]^2/16+\int_{a_o/a}^{1}\Delta\Sigma_b(\xi)H(\xi,\bar{x},1)d\xi = \Delta\Sigma\sqrt{1-\bar{x}^2} \tag{8}$$

where $\bar{x}=x/a$,

$$\Delta\Sigma_b = \frac{D(1-f)^2E_m^2\bar{E}\Delta t}{2f^2E^2E_f\tau a},\ \Delta\Sigma = \frac{D(1-f)^2E_m^2\bar{E}\Delta\sigma}{2f^2E^2E_f\tau a} \tag{9}$$

are the nondimensional bridging stress amplitude and nondimensional applied stress amplitude, respectively, and

$$\Delta\theta = \frac{D(1-f)^2E_m^2\bar{E}(\alpha_f-\alpha_m)\Delta T}{2fE^2\tau a} \tag{10}$$

is the nondimensional thermal stress amplitude. The positive sign preceding the bracketed term should be used if the term in brackets is positive whereas the negative sign should be used if the term in brackets is negative.

2.3 Crack Tip Stress Intensity and Maximum Bridging Stress

The crack tip stress intensity amplitude, ΔK_{tip} is given by

$$\Delta K_{tip} = \Delta K_A + \Delta K_B \tag{11}$$

where $\Delta K_A = \Delta\sigma\sqrt{\pi a}$ is due to the applied stress amplitude and

$$\Delta K_B = -2\sqrt{\frac{a}{\pi}} \int_{a_o}^{a} \frac{\Delta t(x)}{\sqrt{a^2 - x^2}}\, dx \tag{12}$$

is the stress intensity amplitude due to crack bridging. Using the nondimensional parameters defined in eq. (9) & (10), we have

$$\frac{\Delta K_{tip}}{\Delta\sigma\sqrt{\pi a}} = 1 - \frac{2}{\pi\Delta\Sigma} \int_{a_o/a}^{1} \frac{\Delta\Sigma_b(\xi)}{\sqrt{1-\xi^2}}\, d\xi \tag{13}$$

All stress intensity factors given below are computed from eq. (13).

Critical to fiber fracture is the maximum stress in the bridging zone. As demonstrated by McMeeking and Evans (1990), such a stress can be obtained by solving eq. (8), but with the quantities involved redefined. Specifically $\Delta t/2$ in eq. (9) should be replaced by the bridging stress t; $\Delta\sigma/2$ and $\Delta T/2$ in eq. (9) & (10) should be changed to the applied stress σ and the temperature T (measured from the stress-free state), respectively. The solution to eq. (8) will then give the bridging stress t(x) arising due to monotonic loading. Fiber failure models can be applied to the bridging stress to assess the extent of fiber fracture. The values for σ and T used in this calculation should be those occurring simultaneously which produce the largest value for $\phi = \sigma + f E_f (\alpha_f - \alpha_m) T$, during the load cycle. This will produce the highest fiber

stresses in the cycle. In certain circumstances, the largest value of ϕ will be due to the thermal stress alone in the absence of applied load. For example, this will be the case in a material with $\alpha_m > \alpha_f$ which is operated at modest applied stress and below its processing temperature, but above room temperature. The largest value of ϕ will occur at room temperature before warming up and prior to the application of load. However, if fiber failure were to occur due to thermal stresses alone, the material would be impractical. Therefore, the relevant stresses to be used in connection with fiber failure are those occurring when ϕ has its largest value during load cycling.

3. FULLY-BRIDGED MATRIX CRACKS

When the matrix crack depicted in Fig. 2 is fully bridged, with $a_o = 0$, the analysis can be carried out using the equations in Section 2. Upon introduction of an effective bridging stress amplitude $\Delta\phi_b$

$$\Delta\phi_b(x) = \Delta t(x) + f E_f (\alpha_f - \alpha_m) \Delta T \tag{14}$$

and an effective applied stress amplitude $\Delta\phi$

$$\Delta\phi = \Delta\sigma + f E_f (\alpha_f - \alpha_m) \Delta T \tag{15}$$

and with the definitions

$$\Delta\Phi_b = \Delta\Sigma_b + \Delta\theta = \frac{D(1-f)^2 E_m^2 \bar{E} \Delta\phi_b}{2 f^2 E^2 E_f \tau a}, \quad \Delta\Phi = \frac{D(1-f)^2 E_m^2 \bar{E} \Delta\phi}{2 f^2 E^2 E_f \tau a} \tag{16}$$

the governing equation for $\Delta\phi_b$, eq. (8), becomes

$$\left[\Delta\Phi_b(\bar{x})\right]^2/16 + \int_0^1 \Delta\Phi_b(\xi)H(\xi,\bar{x},1)\,d\xi = \Delta\Phi\sqrt{1-\bar{x}^2} \tag{17}$$

The term

$$\int_0^1 \Delta\theta\,H(\xi,\bar{x},1)\,d\xi = \Delta\theta\int_0^1 H(\xi,\bar{x},1)\,d\xi = \Delta\theta\sqrt{1-\bar{x}^2} \tag{18}$$

has been added to both sides of eq. (8) to obtain the final result. The result in eq. (18) arises because $\Delta\theta$ is, of course, independent of ξ.

The negative sign preceding the bracketed term in eq. (17) has been dropped. This can be done because experience has shown that if $\Delta\Phi$ is positive then so is $\Delta\Phi_b(\bar{x})$ for all $\bar{x}$. If $\Delta\Phi$ is negative, the solution for $\Delta\Phi_b(\bar{x})$ can be found by simply reversing the sign of the solution obtained for positive $\Delta\Phi$. The expression eq. (17) is identical to the governing equation used by McMeeking and Evans (1990) for the fully bridged isothermal fatigue case. Consequently, the value for ΔK_{tip} obtained by McMeeking and Evans (1990) for the fully bridged isothermal case is applicable to thermomechanical fatigue of fully bridged cracks by replacement of $\Delta\sigma$ with $\Delta\phi$. The effect of thermal stress in the fully bridged case is as if the applied load amplitude were augmented by $f E_f(\alpha_m - \alpha_m)\Delta T$. This result is analogous to the finding of Budiansky et al. (1986) that steady matrix cracking is driven by the augmented stress $\phi = \sigma + f E_f(\alpha_f - \alpha_m)T$.

Note that the augmentation of the stress amplitude is different in the cyclic case depending on whether in-phase or out-of-phase loading is occurring. In in-phase loading, $\Delta\sigma$ and ΔT have the same sign. If α_m exceeds α_f (usually the case with ceramic fibers in a metal matrix), it follows that in-phase cycling leads to a reduced augmented stress amplitude $\Delta\phi$ compared to isothermal fatigue at the same applied stress level. In general, this will mean that fully bridged fatigue cracks propagate more slowly due to in-phase thermomechanical cycling compared to isothermal fatigue at the

same applied stress. On the other hand, with $\alpha_m > \alpha_f$, out-of-phase cycling ($\Delta\sigma/\Delta T < 0$) will lead to an increased augmented stress amplitude $\Delta\phi$ compared to both isothermal fatigue at the same applied stress and compared to in-phase thermomechanical cycling with the same $\Delta\sigma$ and the same magnitude for ΔT. It follows that when $\alpha_m > \alpha_f$, the fully bridged fatigue crack growth rate for out-of-phase cycling will exceed the rate for isothermal fatigue at the same $\Delta\sigma$ and this latter rate will, in turn, exceed the rate for in-phase thermomechanical cycling at the same $\Delta\sigma$ and with the magnitude of ΔT the same as for the out-of-phase case. An exception to this is in-phase cycling for metal matrix composites with very large temperature changes. If the temperature change is large enough, $\Delta\phi$ can have the opposite sign from $\Delta\sigma$ since $\alpha_f - \alpha_m$ will be negative. If the absolute value of $\Delta\phi$ is then greater than the absolute value of $\Delta\sigma$, the rate of fatigue growth in in-phase TMF will be greater than that for isothermal fatigue. This is therefore an exception to the general rule that for metal matrix composites, out-of-phase TMF fatigue cracking will be faster than isothermal TMF which will in turn out pace in-phase TMF. Another interesting point is that thermal cycling without mechanical stress causes a finite ΔK_{tip}. Thus thermal cycling by itself will cause fatigue crack growth of bridged matrix cracks.

Figure 4 is a plot of the crack tip stress intensity against the thermally augmented applied stress for both the monotonic and cyclic loading cases, as indicated in the figure. These results are valid for arbitrary TMF where each half cycle is defined to occur whenever $\Delta\phi$ changes sign. It should be recalled that in the cyclic case, τ is the average of the interface shear stress at the extreme temperatures of the cycle, whereas τ is the current value in the monotonic case. Notably in Fig. 4, ΔK_{tip} increases monotonically with $\Delta\phi$. This is confirmation that, when $\alpha_m > \alpha_f$, in out-of-phase thermomechanical fatigue the matrix crack growth rate will be larger than that in isothermal mechanical fatigue, and that the opposite is true for in-phase TMF when $\alpha_m > \alpha_f$. Note that Fig. 4 is plotted with absolute values for ϕ or $\Delta\phi$ along the abscissa. This permits the use of the

figure when ϕ or $\Delta\phi$ is negative. Clearly, in the case where ϕ or $\Delta\phi$ is negative, so will $\phi\sqrt{\pi a}$ and $\Delta\phi\sqrt{\pi a}$ and thus K_{tip} and ΔK_{tip} will, in turn, be negative. The meaning of a negative ΔK_{tip} should be understood a follows. In the isothermal case when $\Delta\sigma$ is applied to increase the stress on the body, the crack will tend to open, since ΔK_{tip} will be positive. ΔK_{tip} is negative when $f E_f (\alpha_f - \alpha_m) \Delta T/\Delta\sigma$ is less than -1 and when the mechanical load is increased (i.e. addition of a positive $\Delta\sigma$ to the existing load) the crack will tend to close, this effect being caused by the thermal stresses. The behavior of the crack opening will therefore be out of phase with the applied mechanical load, opening on unloading and closing on reloading.

With less than 2% error in the range $0 \le |\Delta\Phi| \le 8$, the numerical results given in Fig. 4 can be represented by the following fitting formula

$$\Delta K_{tip} / \Delta\phi\sqrt{\pi a} = \sqrt{|\Delta\Phi|/12\pi}\left[1 - 0.03\sqrt{|\Delta\Phi|}\ln\left(2|\Delta\Phi|/3\right)\right] \qquad (19)$$

Eq. (19) is asymptotically exact for small $|\Delta\Phi|$, but not so accurate for larger values of $|\Delta\Phi|$. In typical metal matrix composites (e.g. SiC in Ti alloy), it would be unusual for $|\Delta\Phi|$ to be greater than 4 (Walls et al., 1993). However, for completeness, an approximation for large values of $\Delta\Phi$ will be given. For large values of $|\Delta\Phi|$, McMeeking and Evans (1990) offered the approximation

$$\frac{\Delta K_{tip}}{\Delta\phi\sqrt{\pi a}} = 1 - \frac{3.05}{|\Delta\Phi|}\sqrt{|\Delta\Phi| + 3.3} + \frac{5.5}{|\Delta\Phi|} \qquad (20)$$

which is asymptotically exact for large $|\Delta\Phi|$. The approximations in eq. (19) & (20) differ by less than 3% at $\Delta\Phi = 8$.

To show more clearly how ΔK_{tip} changes with the crack length a, in Fig. 5, a nondimensional stress intensity range, which does not involve crack length,

$$\left(\frac{\Delta K_{tip}}{\Delta\phi}\right)\left[\frac{f^2 E^2 E_f \tau}{D(1-f)^2 E_m^2 \bar{E}|\Delta\phi|}\right]^{1/2}$$

is plotted as a function of the nondimensional crack length

$$\eta = 1/|\Delta\Phi| = \frac{2 f^2 E^2 E_f \tau a}{(1-f)^2 E_m^2 \bar{E}|\Delta\phi| D} \tag{21}$$

The normalized ΔK_{tip} increases rapidly when η is small; at values of $\eta \geq 1$, the normalized ΔK_{tip} essentially reaches a steady-state value of $1/\sqrt{24}$.

Following McMeeking and Evans (1990), the governing equation for matrix fatigue cracking under thermomechanical loading conditions is taken to be the Paris Law

$$da/dN = \beta\left(|\Delta K_{tip}|/\bar{E}_m\right)^n \tag{22}$$

where β and n are material parameters for the matrix material; $\bar{E}_m = \sqrt{(1\text{-}f)\, E_m \bar{E}}$ is an effective modulus accounting for the reduced area of material being cracked as well as the elastic inhomogeneity and anisotropy (Budiansky, Amazigo and Evans, 1988). The steady state ΔK_{tip}, which is a good estimate if η as defined in eq. (21) is greater than 1, is given by

$$\Delta K_{tip}^{ss} = \left[\frac{(1-f)^2 E_m^2 \bar{E} D|\Delta\phi|^3}{24 f^2 E^2 E_f \tau}\right]^{\frac{1}{2}} \tag{23}$$

so that the steady state matrix fatigue crack growth rate for fully bridged cracks is

$$\left(\frac{da}{dN}\right)^{ss} = \beta\left[\frac{(1-f)E_m D|\Delta\phi|^3}{24f^2 E^2 E_f \tau}\right]^{\frac{n}{2}} \tag{24}$$

where $\bar{E}_m = \sqrt{(1\text{-}f)\, E_m \bar{E}}$ has been used and only positive roots should be considered. It follows that during steady state growth of a fully bridged crack, the number of cycles to grow the crack from an initial fully bridged half length of a_i to the current half length a is

$$N^{ss} = \left[\frac{24f^2 E^2 E_f \tau}{(1-f)E_m D|\Delta\phi|^3}\right]^{\frac{n}{2}} \frac{(a-a_i)}{\beta} \tag{25}$$

where only positive roots are used. Relatively few materials will be such that η is less than 1 for fully bridged cracks, so the estimate in eq. (25) will usually be valid. However, if η is less than 1, the numerical results in Figs. 4 & 5 and the estimates given in eq. (19) and (20) can be integrated numerically to predict the fatigue crack growth curves for fully bridged cracks during TMF in which the temperature and mechanical loading are cycled at the same frequency, either in-phase or out-of-phase. The results of such numerical calculations are shown in Fig. 6a & 6b. These integrations were carried out with an initial crack length such that $\eta = 0.025$. Thus, in the plot in each case $\eta = 0.025$ when $N = 0$. However, curves for any case with an initial crack length greater than $\eta = 0.025$ can be obtained simply by translating the origin. In Fig. 6a & 6b, it can be seen that the curves are almost linear at $\eta = 1$ reflecting the near steady state crack propagation occurring there.

4. PARTIALLY-BRIDGED MATRIX CRACKS

Consider a partially-bridged crack in a large body with an unbridged segment $2a_o$, as shown schematically in Fig. 2. The bridging stress distributions are calculated by solving eq. (8) numerically (Marshall et al., 1985; McCartney, 1987) for various values of the crack length ratio a/a_o and the nondimensional mechanical and thermal loading $\Delta\Sigma$ and $\Delta\theta$. Displayed in Fig. 7a are bridging stress profiles for $a_o/a = 0.5$, $\Delta\sigma = 0$ for various $\Delta\theta$. This case is thus subject to thermal loading only without applied stress. It can be seen clearly that a negative $\Delta\theta$ causes a positive $\Delta\Sigma_b$ and vice versa. Since a negative value of $\Delta\Sigma_b$ means that the increment of bridging stress is compressive, such bridging stress increments cause an increase in the stress intensity factor. Since the plot in Fig. 7a can also be used to determine bridging stresses induced by monotonic heating or cooling from a stress free state, the compressive bridging stresses in Fig. 7a show that thermal stress can prop open partially bridged matrix cracks and cause a positive stress intensity factor. This will occur if T is negative and α_m exceeds α_f as is the case typically for metal matrix composites which are cooled down from their processing temperature. In the cyclic case, the thermal bridging stresses will cause a crack tip stress intensity factor amplitude. Thus purely thermal cycling will cause matrix fatigue crack propagation for partially bridged cracks.

Fig. 7b shows the bridging stress distributions for combined mechanical and thermal cycling when $\Delta\Sigma = 0.25$ and $a_o/a = 0.5$. Results for both positive and negative $\Delta\theta$ are shown. Note that for most metal matrix composites with ceramic fibers, $\alpha_f < \alpha_m$. Thus for such typical cases $\Delta\theta < 0$ represents in-phase TMF while $\Delta\theta > 0$ represents out-of-phase TMF. All curves in Fig. 7b have peak stresses at the notch root indicating that fiber fracture is likely to start there. The bridging stress amplitude near the crack tip is compressive when $\Delta\theta$ is positive. This occurs because the crack opening at the tip is zero and eq. (3) shows that the bridging stresses have to be compressive to

sustain this when $\Delta\theta$ is positive. Similarly, when $\Delta\theta$ is negative, the bridging stress at the crack tip has to be tensile. Thus a major portion of the differences in the results shown in Fig. 7b is simply the offset caused by this effect.

It is evident from Fig. 7b that, compared with the purely mechanical fatigue case ($\Delta\theta = 0$), the bridging stress is lower when $\Delta\theta$ is positive and is higher when $\Delta\theta$ is negative. Consequently, the crack tip stress intensity amplitude is expected to be higher when $\Delta\theta$ is positive. However, when $\Delta\theta$ is negative the maximum stress in the bridging zone is higher. Therefore, in the typical case in which positive $\Delta\theta$ represents out-of-phase TMF, the crack tip stress intensity amplitude is greater than in the isothermal case with the same applied stress. Similarly, in the typical case in which negative $\Delta\theta$ represents in-phase TMF, the crack tip stress intensity amplitude is lower than in the isothermal case. This ranking is the same as was found for fully bridged cracks. However, the maximum bridging stress, which will tend to induce fiber failure, is higher in in-phase TMF in the typical case than in the isothermal case and is lower in out-of-phase TMF than in the isothermal case. Thus, in typical cases, in-phase TMF will cause less rapid matrix fatigue crack growth than the isothermal case at the same stress but will be more prone to fiber failure. In contrast, in typical cases, out-of-phase TMF will cause more rapid matrix fatigue crack growth than the isothermal case at the same stress but will be less prone to fiber failure.

Fig. 8 shows the stress intensity factor amplitude due to purely thermal cycling (i.e. no mechanical stress cycling) for partially bridged cracks. The results are shown for several levels of thermal stress amplitude and are shown as a function of bridge length as a fraction of total crack length. The same results apply for positive and negative ΔT, with ΔK_{tip} positive if $(\alpha_f - \alpha_m)\,\Delta T$ is positive and vice versa. These results show, as expected, that there is no stress intensity for unbridged cracks ($a = a_o$) and that the results converge to the fully bridged results when the unbridged segment is a negligible fraction of the matrix crack length. In between, ΔK_{tip} increases monotonically with

crack length for fixed a_o. However, when shown in the form normalized by $f E_f (\alpha_f - \alpha_m) \Delta T \sqrt{\pi a}$, there is a maximum between the results for short and long bridge lengths.

Shown in Fig. 9a & b are normalized crack tip stress intensities $\Delta K_{tip}/\Delta K_A$ plotted against the normalized bridge length $(a - a_o)/a$ for $\Delta\Sigma_o = 0.5$ for several values of $\Delta\theta_o$ where $\Delta K_A = \Delta\sigma \sqrt{\pi a}$, $\Delta\Sigma_o = (a/a_o)\,\Delta\Sigma$ and $\Delta\theta_o = (a/a_o)\,\Delta\theta$. Two features in Fig. 9 are noteworthy. The fatigue driving force ΔK_{tip} increases with increasing $\Delta\theta_o$, as is expected. Further, when $\Delta\theta_o$ is large (say, ≥ 1.0, see Fig. 9b), ΔK_{tip} can exceed ΔK_A, the applied stress intensity amplitude. Due to compressive thermal stresses, the development of a bridge can increase the stress intensity factor amplitude. This indicates that in certain circumstances, the fibers prop open the crack rather than provide shielding. Crack bridging, therefore, can be detrimental to the fatigue behavior of the composite. This is in contrast to the isothermal case in which crack bridging always improves the composite fatigue resistance to matrix cracking. Note also, that if $\Delta\theta_o$ is less than -0.5 (see Fig. 9b), ΔK_{tip} can become negative. Due to tensile thermal stresses, the development of a bridge can provide so much shielding that the sign of the stress intensity factor reverses. This means that when tensile mechanical stress is added to the applied load, the crack opening will diminish rather than open further, and vice versa. Thus, the crack tip cycling will be out of phase with the mechanical stress cycling. Of course, the rate of fatigue crack growth will be unaffected by this phenomenon since it will depend only on the magnitude of ΔK_{tip}. However, it can be seen in Fig. 9b that ΔK_{tip} can pass from positive to negative as a bridge is extended by fatigue crack growth. As a consequence, the rate of fatigue crack growth will diminish as ΔK_{tip} falls to zero and the matrix crack may become non-propagating. However, a change in the mechanical stress amplitude or the thermal stress amplitude will cause ΔK_{tip} to become non-zero and the crack can be caused to recommence growth. Thus, the trapped state of the fatigue crack would be easily destabilized. However, if

$\Delta\theta_o = -\Delta\Sigma_o$ (i.e. if $f E_f (\alpha_f - \alpha_m) \Delta T = -\Delta\sigma$), the net fatigue driving force for extensively bridged cracks (i.e. $\Delta\sigma + f E_f (\alpha_f - E_m) \Delta T$) will be zero. In this case, ΔK_{tip} will approach zero as a bridge is built by fatigue growth and therefore the matrix fatigue crack will become markedly non-propagating.

Fig. 10a & b contains the same results as Fig. 9 but for a higher applied stress amplitude. Comparison with the curves in Fig. 9 indicates that at higher applied stress amplitude, the detrimental effect of the thermal load is less pronounced. This is due to the fact that the larger applied stress induces a stronger beneficial shielding effect in the bridge because of the greater crack opening which occurs. In contrast, the detrimental propping action of the thermal stresses is fixed for a given thermal load.

A feature of all the results in Figs. 8-10 is that $\Delta K_{tip}/\Delta K_A$ approaches zero as $(a - a_o)/a$ goes to unity. The reason is that near $(a - a_o)/a = 1$, there is an extremely long matrix crack with a small unbridged segment in the middle. The effect of the unbridged segment on the value of ΔK_{tip} will be negligible, so the stress intensity factor amplitude should approach the result for the fully bridged crack when $(a - a_o)/a$ is very close to 1. That is, with $\Delta\Sigma_o$ positive, eq. (19) can be rearranged to show that for partially bridged cracks

$$\frac{\Delta K_{tip}}{\Delta K_A} \rightarrow \pm \left| 1 + \frac{\Delta\theta_o}{\Delta\Sigma_o} \right|^{\frac{3}{2}} \sqrt{\frac{\Delta\Sigma_o\, a_o}{12\pi a}} \qquad (26)$$

as $(a - a_o)/a$ approaches 1. The positive root is taken if $1 + \Delta\theta_o/\Delta\Sigma_o$ is positive and the negative root is used if $1 + \Delta\theta_o/\Delta\Sigma_o$ is negative. Thus, if $\Delta\theta_o$ is sufficiently negative, ΔK_{tip} will first pass through zero and become negative ($\Delta K_A = \Delta\sigma \sqrt{\pi a}$ is assumed positive) as $(a - a_o)/a$ gets larger. Then as $(a - a_o)/a$ approaches unity, ΔK_{tip} will approach zero from below. This phenomenon will be a feature of the behavior when $f E_m (\alpha_f - \alpha_m) \Delta T/\Delta\sigma$ is less than -1. The meaning of a negative ΔK_{tip} when $\Delta\sigma$ is

positive has been discussed in the context of the fully bridged crack. When ΔK_{tip} is negative and $\Delta\sigma$ is positive, the crack tip region will tend to close when the mechanical load is increased and will tend to open when the mechanical load is decreased. This out-of-phase effect is caused by the thermal stresses.

There is a further significance to the results in Figs. 7-10. The plots also give the value of $K_{tip}/\sigma\sqrt{\pi a}$ when the load is applied monotonically to a large body containing a partially bridged matrix crack. To interpret the results this way, $\Delta\sigma/2$ in $\Delta\Sigma_o$ should be replaced by σ and $\Delta T/2$ in $\Delta\theta_o$ should be replaced by T. Thus Fig. 9a gives values for $K_{tip}/\sigma\sqrt{\pi a}$ for $D\,(1\text{-}f)^2\,E_m^2\,\bar{E}\,\sigma/f^2\,E^2\,E_f\,\tau\,a_o = 0.5$ for $D\,(1\text{-}f)^2\,E_m^2\,\bar{E}\,(\alpha_f - \alpha_m)\,T/E^2\,f\,\tau\,a_o = -0.5, -0.2, -0.1, 0, 0.2$ and 0.5 and similarly for Figs. 8, 9b, 10a & 10b. This interpretation of the results can be used to confirm that in typical cases, shutting of matrix fatigue cracks is not likely to be an issue. As emphasized previously, the typical case is a metal matrix with ceramic fibers in which $\alpha_m > \alpha_f$. Such materials are processed at high temperature and used in service at temperatures below the processing level. Thus, the operating temperature is negative. Consequently $f\,E_f\,(\alpha_f - \alpha_m)\,T$ will be positive and could readily be a few hundred MPa. For example, when SiC fibers are used in a Ti alloy matrix with $f = 0.35$, each Celsius degree below the stress free temperature induces a value for $f\,E_f\,(\alpha_f - \alpha_m)\,T$ of approximately 1 MPa. Thus the ratio $f\,E_f\,(\alpha_f - \alpha_m)\,T/\sigma$ will be quite large typically (assuming σ to be positive) and so the relevant results are those in Figs. 7-10 for larger values of $\Delta\theta_o$. This makes it clear that as soon as matrix fatigue crack growth occurs and a bridge is developed, a large positive K_{tip} will be induced by that bridge due to the large thermal stress. The fatigue cycling will occur around this mean value of K_{tip} but the cyclic ΔK_{tip} is unlikely to cause the total K_{tip} to go to zero. Thus crack closure is unlikely to occur. This assertion can be considered further in the context of a fully bridged crack which, as discussed, is the state which a matrix fatigue crack propagating without fiber failure in a large body will effectively approach. Fig. 4 shows that a fully

bridged matrix crack with a large positive value of $f E_f (\alpha_f - \alpha_m) T$ will have a large positive value of K_{tip}. It follows that the thermal stresses will prop open a fully bridged matrix crack to a significant extent so that thermomechanical cycling is not likely to cause shutting of the crack.

For investigation of the effect of thermal cycling on the fatigue growth of matrix cracks, the Paris Law Eqn. (22) can be integrated numerically subject to the results in Figs. 8-10 for $\Delta K_{tip}/\Delta K_A$ with ΔK_A always taken to be positive. Fibers are assumed to remain intact during crack growth. Therefore, the unbridged segment length is always the initial notch length. Fig. 11 shows the resulting curves for purely thermal cycling with no mechanical load cycling when the amplitude of the thermal cycles is constant during crack growth. The Paris law exponent is taken to be 2. A small bridge of length $0.001\ a_o$ was assumed to exist at the beginning of the growth process to initiate fatigue cracking. That is, $(a - a_o)/a = 0.001$ initially. In Fig. 11, it can be seen that the rate of growth is initially small. This stage corresponds to the left end of Fig. 8 where ΔK_{tip} is small. The rate of growth increases as the crack lengthens and ΔK_{tip} increases. The rate then evolves to a steady level of growth as large bridge lengths are developed. Displayed in Fig. 12 are the resulting fatigue crack growth curves for $\Delta\Sigma_o = 1$, $n = 2$ for various thermal stress amplitudes. These results are for TMF in which the frequency of temperature cycling is the same as that for mechanical load cycling and the two loads are either exactly in-phase or out-of-phase. Also, the amplitude of the temperature and mechanical stress cycles is constant during crack growth. It is found that when $\Delta\theta_o$ is positive, fatigue crack growth is significantly higher than that due to mechanical load alone, depending on the magnitude of the thermal stress amplitude. When $\Delta\theta_o$ is negative, the amount of fatigue growth is less than in the isothermal case. When $\Delta\theta_o = -1$ which is also exactly the negative of $\Delta\Sigma_o$, the matrix fatigue crack should eventually become non propagating since the fatigue driving force $(\Delta\sigma + f E_f (\alpha_f - \alpha_m) \Delta T)$ for extensively bridged cracks is zero. However, this will occur

beyond $\beta\pi\,[\Delta\sigma/\bar{E}_m]^2\,N = 50$. Similarly, when $\Delta\Sigma_o = -2$, the matrix crack should eventually become non-propagating. It can be seen in Fig. 12 that the case with $\Delta\theta_o = -2$ is propagating very slowly when $\beta\pi\,[\Delta\sigma/\bar{E}_m]^2\,N = 50$.

5. FIBER FRACTURE AND FATIGUE LIFE

Experimental evidence (Walls et al., 1993) shows that when the applied stress is high, fibers fail along the matrix fatigue crack, accelerating the matrix crack growth and leading to a loss of load carrying capacity. Therefore, it can be suggested that the onset of fiber failure is effectively the end of the useful life for a fiber reinforced metal matrix composite material. The onset of fiber failure depends primarily on the fiber strength, which, in practice, has a statistical distribution. However, to gain some insight into the influence of thermal stresses on fiber fracture, we assume that the fibers have a unique strength S. Certain fibers have a narrow strength distribution, so that the assumption of a unique strength is a reasonable approximation to this case. Fibers with a wide strength distribution would fail more gradually than predicted below. In addition, failure of fibers with a wide distribution of strengths can occur inside the matrix rather than at the matrix crack as assumed below.

The governing equation for the bridging stress distribution corresponding to monotonic loading σ and temperature T is essentially identical to Eqn. (8); only the nondimensional parameters need to be redefined. The nondimensional applied load Σ_o is defined as

$$\Sigma_o = \frac{D(1-f)^2\,E_m^2\,\bar{E}\,\sigma}{E^2\,E_f\,f^2\,\tau\,a_o} \tag{27}$$

while the nondimensional thermal load θ_o has the form

$$\theta_o = \frac{D(1-f)^2 E_m^2 \bar{E}(\alpha_f - \alpha_m) T}{E^2 f \tau a_o} \quad (28)$$

For monotonic σ and T, the bridging stress distributions shown in Fig. 7 remain unchanged if $\Delta\Sigma$ is replaced by Σ_o, $\Delta\Sigma_b$ by Σ_b and $\Delta\theta$ by θ_o. Σ_b equals Σ_o with σ replaced by t. As mentioned earlier, the peak stress in the bridging zone usually arises at the notch root. The exception to this is where θ_o is negative with a large magnitude compared to Σ_o. In that case, the largest fiber stress can be at the tip of the matrix crack. The clearest example is where there is no mechanical load as illustrated in Fig. 7a. However, for metal matrix composites, this will be an unusual situation and so we will assume that the critical case is when the largest fiber stress occurs at the root of the unbridged notch. Thus, fibers at the notch root begin to fracture when the bridging stress there rises to fS (f is the fiber volume fraction). Results as shown in Fig. 7b can be used to predict this. The situations giving rise to such fiber failure are summarized in Fig. 13. These are plots of the maximum stress in the bridging zone as a function of bridge length for various temperatures for 2 different applied mechanical stress levels. The maximum stress in the bridging zone has been equated to fS. As a result, the figures show the maximum bridge length possible for a given fiber strength. In Fig. 13, it can be seen that when θ_o is positive, which is typical of metal matrix composites, the maximum stress in the bridge increases monotonically with bridge length. Furthermore, because of compressive thermal stresses, the maximum stress in the bridge is less than that occurring in the isothermal case. When θ_o is negative, the maximum stress in the bridge is higher than in the isothermal case, a situation which occurs because of tensile thermal stresses. It is also apparent that the maximum stress in the bridge diminishes as the bridge length rises beyond a certain level. This means that once fiber failure begins, all fibers will fail since the maximum stress in the bridge

will tend to increase as the bridge disappears due to fiber fracture. However, the typical case for metal matrix composites with θ_o positive will involve gradual fiber failure since the maximum fiber stress will diminish as the bridge length falls due to fiber fracture.

The results such as those shown in Fig. 12 and in 13 can be used to predict the life of a metal matrix composite with a pre-existing notch, subject to TMF with in-phase or out-of-phase cycling at the same frequency with constant amplitude. Crack length versus the number of load cycles is predicted in Fig. 12 while the onset of fiber failure can be determined from Fig. 13. Since the fatigue crack growth rate will rise rapidly after the onset of fiber failure, the end of life can be considered to occur very shortly after fiber failure commences (Walls et al., 1993). In some cases, however, the condition for fiber failure will never be met. That is, if the fiber strength is high, it will always exceed the maximum stress in the fibers in the bridge. In those circumstances, very long bridged matrix cracks will be grown, but the fibers will remain intact. These cases can be considered to give rise to infinitely long life for the metal matrix composite.

For very large panels, the conditions leading to the preservation of fibers can be summarized in the form of a map as used by Bao and McMeeking (1994). Such a map is shown in Fig. 14. The map shows combinations of maximum applied stress, temperature and initial notch length which will lead to fiber failure and to no fiber failure as determined by the deterministic fiber strength. Dividing lines in the map are shown for various temperatures. Below the dividing line, matrix cracks will be grown from the notch, but fibers will never fail and therefore the composite will have infinite life. Above the dividing line, matrix fatigue crack growth will eventually lead to fiber failure, and therefore the composite will have a finite lifetime. It can be seen that if θ_o is negative, fiber failure is more prone to occur. On the other hand, if θ_o is positive, it is more likely that matrix fatigue crack growth will occur without fiber failure. For metal matrix composites, θ_o will generally be positive, since $\alpha_f < \alpha_m$ and T, measured from

the stress free processing temperature, will be negative. Thus, when thermal effects are accounted for, a larger window exists for the preservation of fibers than is apparent from isothermal considerations.

6. CLOSURE

It has been shown that thermal strains can induce bridging stresses in fully and partially bridged matrix cracks. These stresses can, in turn, alter the stress intensity factor at the tip of the matrix crack and therefore affect the fatigue crack growth rate for the crack. For fully bridged cracks, the effect of the thermal stresses is to augment the applied stress amplitude by an amount equal to $f E_f (\alpha_f - \alpha_m) \Delta T$. Therefore, for metal matrix composites, where α_m exceeds α_f, in-phase TMF in which the temperature increases at the same time as the stress will lead to a reduced rate of fatigue crack growth compared to isothermal fatigue. Out-of-phase TMF gives rise to an increased rate of fatigue cracking. On the other hand, in-phase TMF will make it more likely that fibers will fracture and out-of-phase cycling will reduce the likelihood of fiber failure. As in the isothermal case, a low applied stress will avoid fiber failure no matter how long the matrix crack grows while a high applied stress will cause fiber failure and therefore lead to rapid fatigue cracking since the bridging shielding effect will be destroyed. It is notable that thermal cycling by itself without applied load will induce a crack tip stress intensity factor amplitude and therefore will cause matrix fatigue cracking. However, it should be noted that no data exist for matrix fatigue cracking by TMF. The validity of the model presented in this paper can only be confirmed by comparison with data.

ACKNOWLEDGMENT

The research presented in this paper was supported in part by the University Research Initiative at UCSB funded by the Advanced Research Projects Agency through ONR contract N0014-92-J-1808. The work of GB was in addition supported by NSF through a Research Initiative Award MSS-9210250.

REFERENCES

Bao, G. and McMeeking, R.M. (1994), Fatigue crack growth in fiber reinforced metal matrix composites to appear in *Acta Metall. Mater.*.

Budiansky, B., Hutchinson, J.W. and Evans, A.G. (1986), Matrix fracture in fiber-reinforced ceramics, *J. Mech. Phys. Solids*, **34**, 167-189.

Cox, B.N. (1990), Interfacial sliding near a free surface in a fibrous or layered composite during thermal cycling, *Acta Metall. Mater.*, **38**, 2411-2424.

Cox, B.N. (1991), Extrinsic factors in the mechanics of bridged cracks, *Acta Metall. Mater.*, **39**, 1189-1201.

Cox, B.N. and Lo, C.S. (1992), Load ratio, notch and scale effects for bridged cracks in fibrous composites, *Acta Metall. Mater.*, **40**, 69-80.

Cox, B.N. and Marshall, D.B. (1991), Stable and unstable solutions for bridged cracks in various specimens, *Acta Metall. Mater.*, **39**, 579-589.

Evans, A.G. (1991), The mechanical properties of reinforced ceramic, metal and intermetallic matrix composites, *Mater. Sci. Engng.*, **A143**, 63-76.

Hutchinson, J.W. and Jensen, H.M. (1990), Models of fiber debonding and pullout in brittle composites with friction, *Mech. Mater.*, **9**, 139-163.

Marshall, D.B. and Cox, B.N. (1987), Tensile fracture of brittle matrix composites: influence of fiber strength, *Acta Metall. Mater.*, **35**, 2607.

Marshall, D.B., Cox, B.N. and Evans, A.G. (1985), The mechanics of matrix cracking in brittle-matrix fiber composites, *Acta Metall. Mater.*, **33**, 2013-2021.

McCartney, L.N. (1987), Mechanics of matrix cracking in brittle-matrix fiber-reinforced composites, *Proc. Roy Soc. Lond.*, **A409**, 329.

McMeeking, R.M. and Evans, A.G. (1990), Matrix fatigue cracking in fiber composites, *Mech. Mater.*, **9**, 217-227.

Walls, D.P., Bao, G. and Zok, F.W. (1993), Mode I fatigue cracking in a fiber reinforced metal matrix composite, *Acta Metall. Mater.*, **41**, 2061-2071.

APPENDIX A

Consider the cylindrical fiber/matrix model shown in Fig. 3. Shear lag analysis (Budiansky et al., 1986; McCartney, 1987; Cox, 1990) will be used to model the behavior. Both the fibers and the matrix are taken as elastic; creep and plastic deformations in the matrix are neglected. The elastic moduli for the fibers and the matrix are E_f and E_m respectively. The interface between the fibers and the matrix is assumed to be weak and the debond toughness is neglected. Therefore the fibers, with diameter D, behave effectively as frictionally constrained reinforcements. When load is applied to the fiber, or when the temperature changes, a sliding zone of length ℓ develops as shown in Fig. 3. the interface shear stress in the sliding region is τ which is taken to be a function of temperature only. The boundary conditions for the cell are such that an average bridging stress t is applied at the top which is opposed by a stress t/f in the fiber at the matrix crack where f is the volume fraction of fibers. Thus the outer diameter of the cell is taken to be $D/\sqrt{f}$. The stress in the matrix at the matrix crack is zero as is the shear stress everywhere on the outer boundary of the unit cell shown in Fig. 3. The axial mechanical stresses in the fiber t_f and the matrix t_m are related to the bridging stress t by

$$t = f\, t_f + (1-f)\, t_m \tag{A1}$$

In addition, above the sliding region, the axial strain in the fiber equals that in the matrix so that

$$\frac{t_f}{E_f} + \alpha_f T = \frac{t_m}{E_m} + \alpha_m T = \varepsilon \tag{A2}$$

where α_f and α_m are the expansion coefficients for the fiber and matrix respectively and T is the temperature with T = 0 defined to be the state in which the thermal stresses in the composite is zero. It follows that above the sliding region

$$t_m = \frac{E_m}{E}\left[t + fE_f(\alpha_f - \alpha_m)T\right] \tag{A3}$$

Equilibrium of the fiber and the matrix in the sliding zone implies

$$\ell = \frac{(1-f)DE_m\left[t+fE_f(\alpha_f-\alpha_m)T\right]}{4fE\tau(T)} \tag{A4}$$

where $E = fE_f + (1\text{-}f)E_m$ and $\tau(T)$ is the sliding stress at the current temperature. For the analysis of the monotonic case it has been assumed that the term in brackets is positive, which will be discussed below. The opening δ is defined to be the average axial strain in the fiber in the sliding zone minus the axial strain in the composite above the sliding zone multiplied by 2ℓ. The result is such that $t\delta$ is the work done per unit area of matrix crack when the matrix crack is introduced into a previously uncracked system. (Budiansky et al., 1986; McCartney, 1987; Hutchinson and Jensen, 1990) The average strain in the fiber in the sliding zone is

$$\varepsilon_f^{av} = \frac{t}{fE_f} + \alpha_f T - \frac{(1-f)E_m}{2fEE_f}\left[t + fE_f(\alpha_f-\alpha_m)T\right] \tag{A5}$$

whereas the strain in the composite above the sliding zone is

$$\varepsilon = \frac{t}{fE_f} + \alpha_f T - \frac{(1-f)E_m}{fEE_f}\left[t + fE_f(\alpha_f-\alpha_m)T\right] \tag{A6}$$

Multiplying the difference by 2ℓ from (A4) gives

$$\delta = \frac{(1-f)^2 D E_m^2 \left[t + f E_f (\alpha_f - \alpha_m) T\right]^2}{4 f^2 E^2 E_f \tau(T)} \tag{A7}$$

which gives eq. (1) & (2). The reason for assuming that the term in brackets is positive is now clear. If the term in brackets were negative, the proper result (in contrast to eq. (A7)) would predict a negative value for δ. Since the most reasonable assumption is that cracks are closed when $T = 0$ and $\sigma = 0$, negative values for δ are precluded by compressive contact of the crack surfaces.

As noted by Marshall and Oliver (1987), McMeeking and Evans (1990) and Cox (1990), unloading for the fiber causes the initiation of a new sliding zone. In the thermomechanical problem, unloading will be defined as the stage of the cycle during which the applied mechanical tensile stress is being reduced. During unloading, as long as the new sliding zone grows monotonically, its length is given by

$$\ell_u = \pm \frac{(1-f) D E_m \left[t_1 - t + f E_f (\alpha_f - \alpha_m)(T_1 - T)\right]}{4 f E \left[\tau(T_1) + \tau(T)\right]} \tag{A8}$$

where t_1 is the peak applied stress prior to unloading (taken to be tensile), and T_1 is the temperature just prior to unloading as shown in Fig. 1. The stress t is the current applied stress and T is the current temperature. The difference t_1 - t is thus positive. However, the term in the brackets in the numerator can be positive or negative due to the thermal stress. If the term in the brackets in the numerator is positive, the positive sign in eq. (A8) is used, whereas if the bracketed term in the numerator is negative the negative sign should be used to define ℓ_u. The definition of δ and results equivalent to eq. (A5) & (A6) can then be used to predict that

$$\delta_1 - \delta = \pm \frac{(1-f)^2 D E_m^2 \left[t_1 - t + f E_f (\alpha_f - \alpha_m)(T_1 - T)\right]^2}{4 f^2 E^2 E_f \left[\tau(T_1) + \tau(T)\right]} \qquad \text{(A9)}$$

where δ_1 is the value of δ just prior to unloading and δ is the current opening when the applied stress is t and the temperature is T. If the term in the brackets in the numerator is negative, the negative sign in eq. (A9) should be used to give $\delta_1 - \delta$, otherwise the positive sign is used. The negative sign means that during mechanical unloading, the matrix crack actually opens more due to the thermal strains.

Upon reloading from t_2 back up to t with the temperature simultaneously changing from T_2 to T (t_2 and T_2 as shown in Fig. 1), a new slip zone is created once again. The length of this new slip zone is given by

$$\ell_F = \pm \frac{(1-f) D E_m \left[t - t_2 + f E_f (\alpha_f - \alpha_m)(T - T_2)\right]}{4 f E \left[\tau(T) + \tau(T_2)\right]} \qquad \text{(A10)}$$

where, as before, the preceding sign should be chosen to match the sign of the term in brackets in the numerator. Similarly, the current opening on reloading is given by

$$\delta - \delta_2 = \pm \frac{(1-f)^2 D E_m^2 \left[t - t_2 + f E_f (\alpha_f - \alpha_m)(T - T_2)\right]^2}{4 f^2 E^2 E_f \left[\tau(T) + \tau(T_2)\right]} \qquad \text{(A11)}$$

where δ_1 is the value of δ just prior to reloading. If the bracketed term in the numerator in eq. (A11) is negative, the negative sign should be used. This means that during reloading, the crack tends to close due to thermal effects.

Representing $\delta_1 - \delta_2$ by $\Delta\delta$, $t_1 - t_2$ by Δt and $T_1 - T_2$ by ΔT, the magnitude of $\Delta\delta$ for repeated cycling between the same limits is given by

$$\Delta\delta = \pm \frac{(1-f)^2 D E_m^2 \left[\Delta t + f E_f (\alpha_f - \alpha_m) \Delta T\right]^2}{4 f^2 E^2 E_f \left[\tau(T_1) + \tau(T_2)\right]} \qquad \text{(A12)}$$

As above, the preceding sign in eq. (A12) should be chosen to match the sign of the term in the brackets in the numerator. Use of τ to represent $[\tau(T_1) + \tau(T_2)]/2$ then gives eq. (3).

The condition that the length of the slip zone increases monotonically ensures that eq. (A9), (A11) & (3) are valid. When $t_1 - t_2 + f E_f (\alpha_f - \alpha_m)(T_1 - T_2)$ is positive, the length of the slip zone increases monotonically when; (i) for in-phase cycling (a) during unloading

$$\frac{dt}{dT} + f E_f (\alpha_f - \alpha_m) \geq -\frac{t_1 - t + f E_f (\alpha_f - \alpha_m)(T_1 - T)}{\left[\tau(T_1) + \tau(T)\right]} \frac{d\tau}{dT} \qquad \text{(A13)}$$

(b) during reloading

$$\frac{dt}{dT} + f E_f (\alpha_f - \alpha_m) \geq \frac{t - t_2 + f E_f (\alpha_f - \alpha_m)(T - T_2)}{\left[\tau(T) + \tau(T_2)\right]} \frac{d\tau}{dT} \qquad \text{(A14)}$$

and (ii) for out-of-phase cycling (a) during unloading

$$\frac{dt}{dT} + f E_f (\alpha_f - \alpha_m) \leq -\frac{t_1 - t + f E_f (\alpha_f - \alpha_m)(T_1 - T)}{\left[\tau(T_1) + \tau(T)\right]} \frac{d\tau}{dT} \qquad \text{(A15)}$$

and (b) during reloading when

$$\frac{dt}{dT} + f E_f (\alpha_f - \alpha_m) \leq \frac{t - t_2 + f E_\alpha (\alpha_f - \alpha_m)(T - T_2)}{[\tau(T) + \tau(T_2)]} \frac{d\tau}{dT} \qquad \text{(A16)}$$

When $t - t_2 + f E_f (\alpha_f - \alpha_m) (T - T_2)$ is negative, all the inequalities in eq. (A13) to (A16) are reversed.

FIGURES

Figure 13 Maximum fiber stress as a function of bridge length.

Figure 14 Map for fiber failure during crack growth.

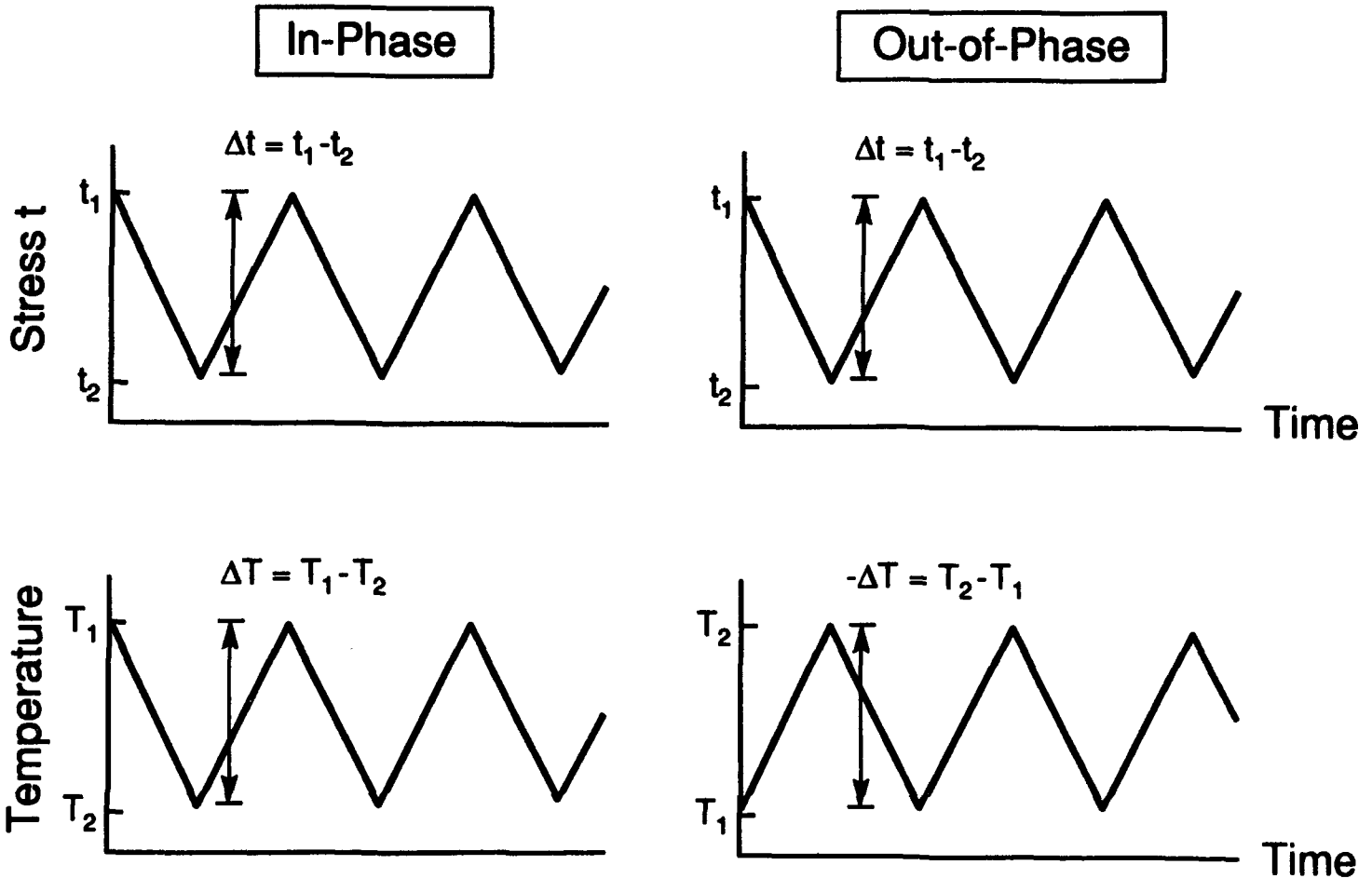
In-Phase
Out-of-Phase
Δt = t1-t2
Δt = t1-t2
Stress t
t1
t2
t1
t2
Time
ΔT = T1-T2
-ΔT = T2-T1
Temperature
T1
T2
T2
T1
Time

Figure 1

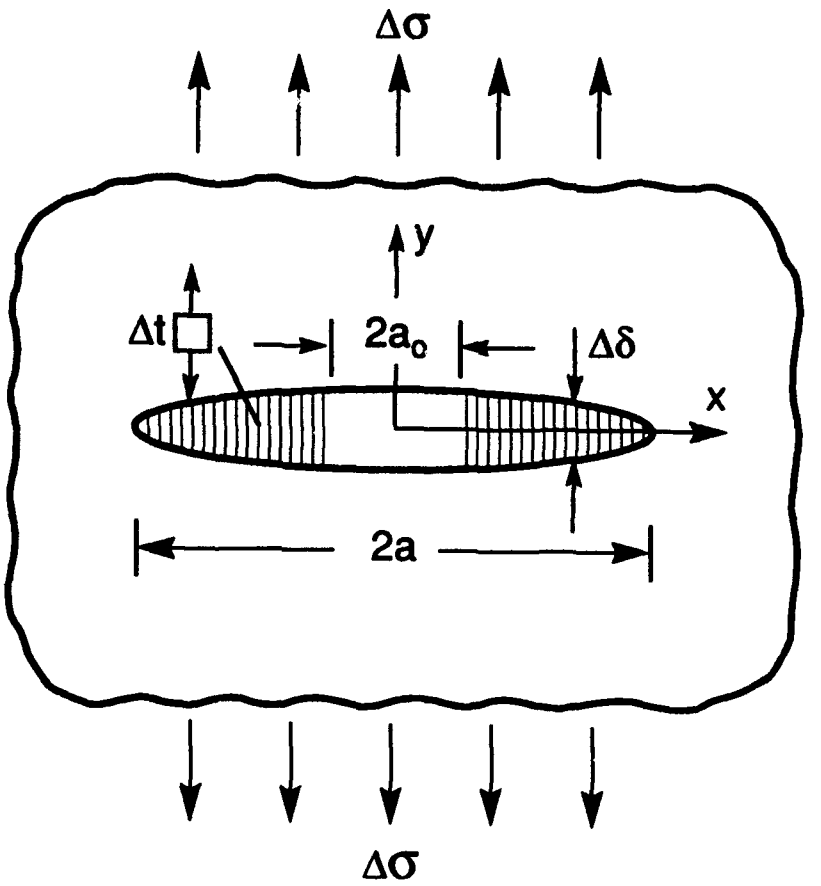

Figure 2

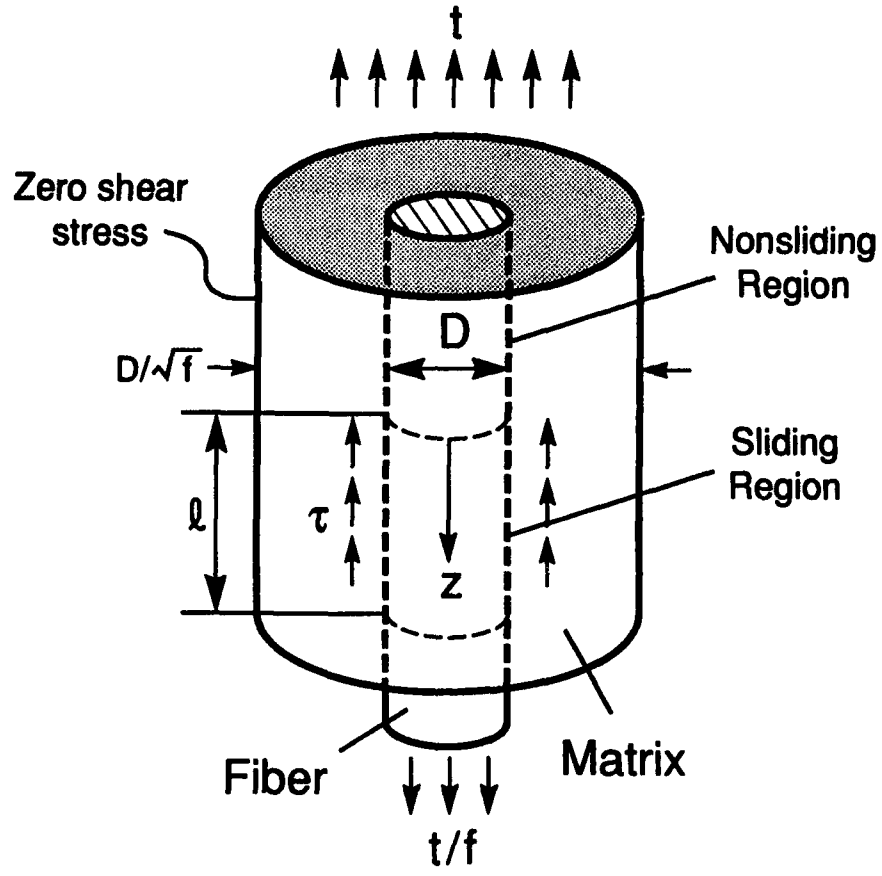
t
Zero shear
stress
Nonsliding
Region
D
D/√f
Sliding
Region
ℓ
τ
z
Fiber
Matrix
t/f

Figure 3

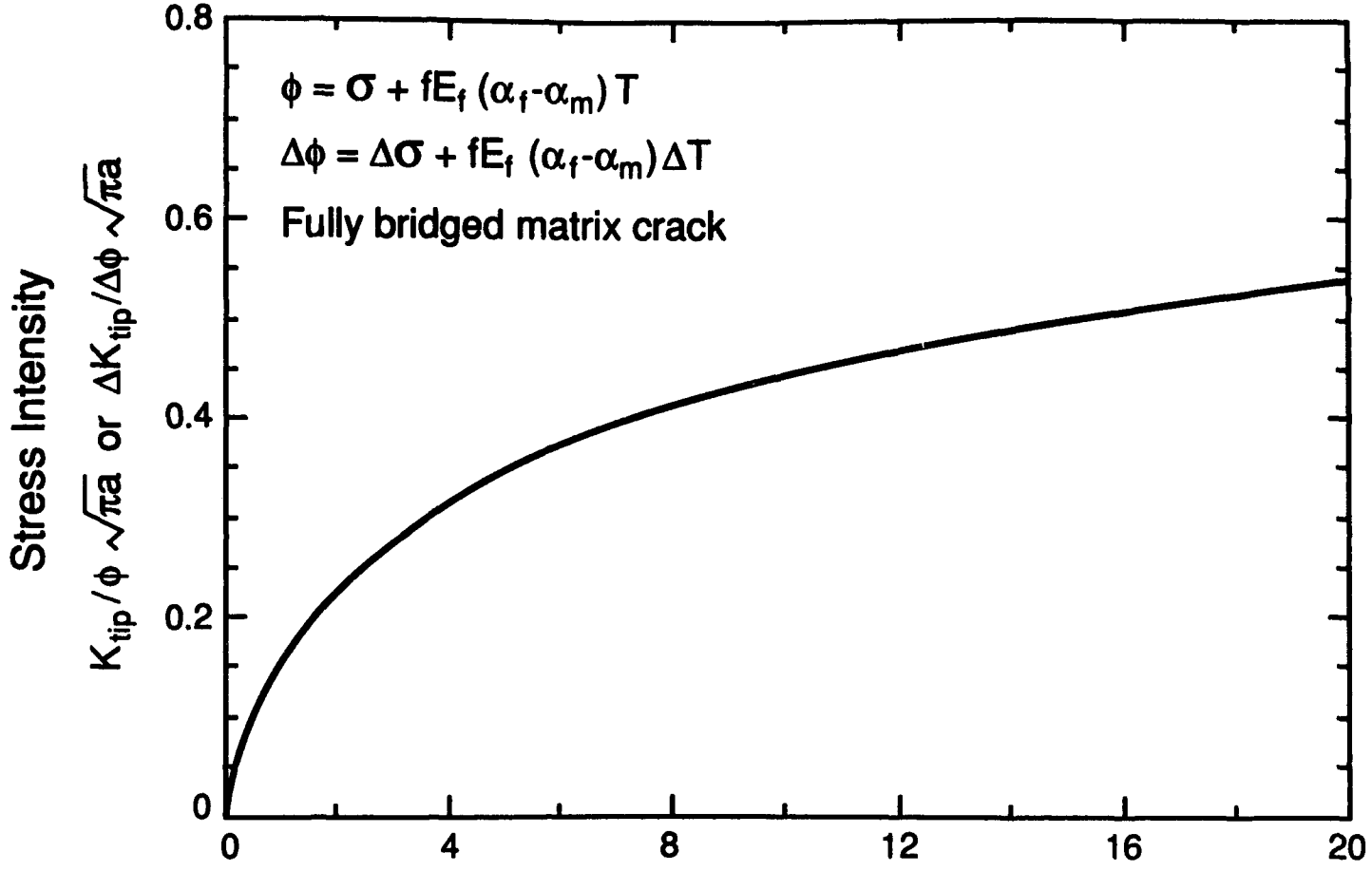
$\phi = \sigma + fE_f(\alpha_f - \alpha_m)T$
$\Delta\phi = \Delta\sigma + fE_f(\alpha_f - \alpha_m)\Delta T$
Fully bridged matrix crack
Stress Intensity
$K_{tip}/\phi\sqrt{\pi a}$ or $\Delta K_{tip}/\Delta\phi\sqrt{\pi a}$
0.8
0.6
0.4
0.2
0
0
4
8
12
16
20
Augmented Stress and Inverse Crack Length
$\frac{D(1-f)^2E_m^2\bar{E}|\phi|}{f^2E^2E_f\tau a}$ or $\frac{D(1-f)^2E_m^2\bar{E}|\Delta\phi|}{2f^2E^2E_f\tau a} = \Delta\Phi$

Figure 4

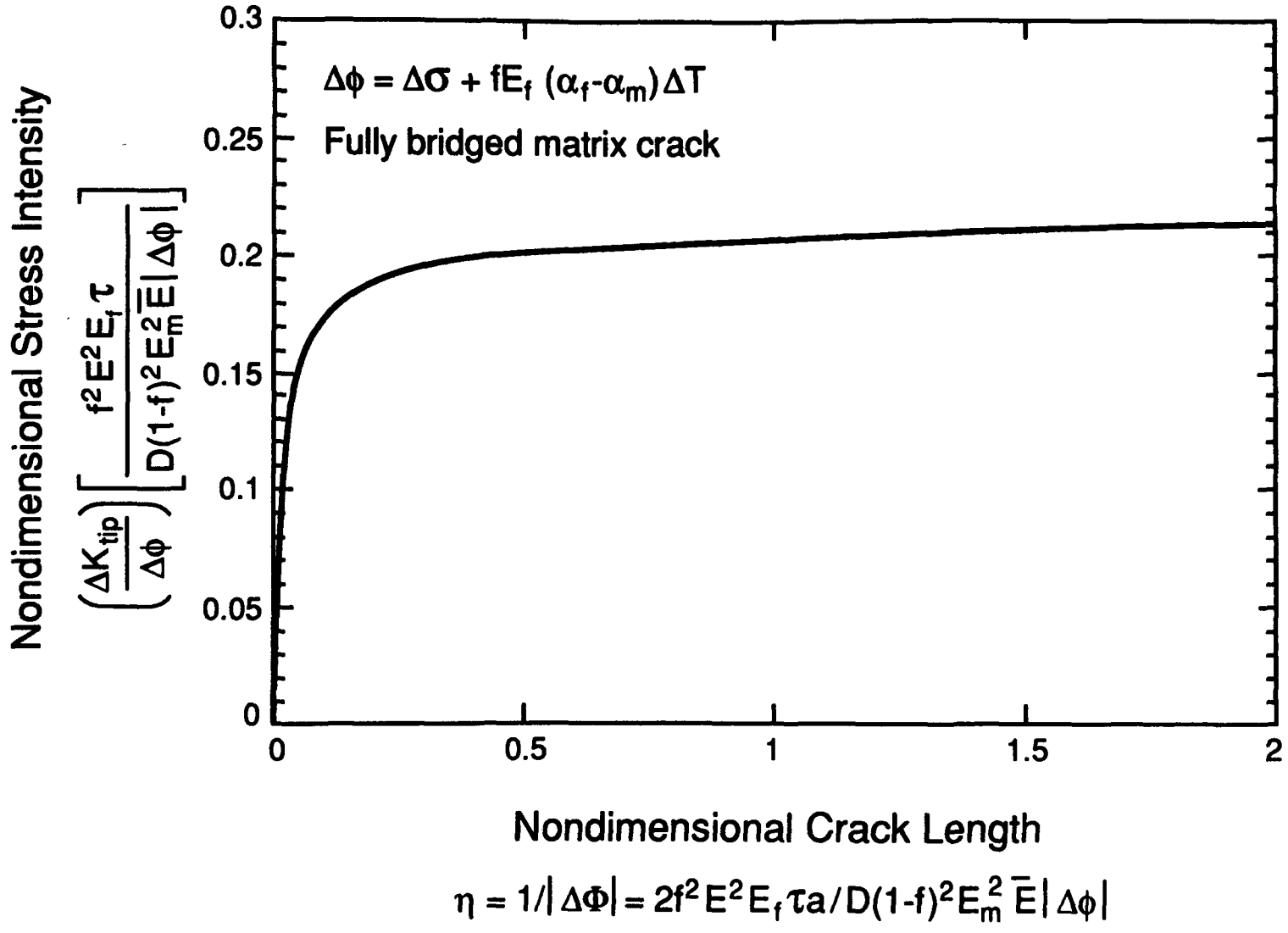
$\Delta\phi = \Delta\sigma + fE_f\,(\alpha_f-\alpha_m)\Delta T$
Fully bridged matrix crack
Nondimensional Stress Intensity
$\left(\frac{\Delta K_{tip}}{\Delta\phi}\right)\left[\frac{f^2E^2E_f\tau}{D(1-f)^2E_m^2\bar{E}|\Delta\phi|}\right]$
0.3
0.25
0.2
0.15
0.1
0.05
0
0
0.5
1
1.5
2
Nondimensional Crack Length
$\eta = 1/|\Delta\Phi| = 2f^2E^2E_f\tau a/D(1-f)^2E_m^2\bar{E}|\Delta\phi|$

Figure 5

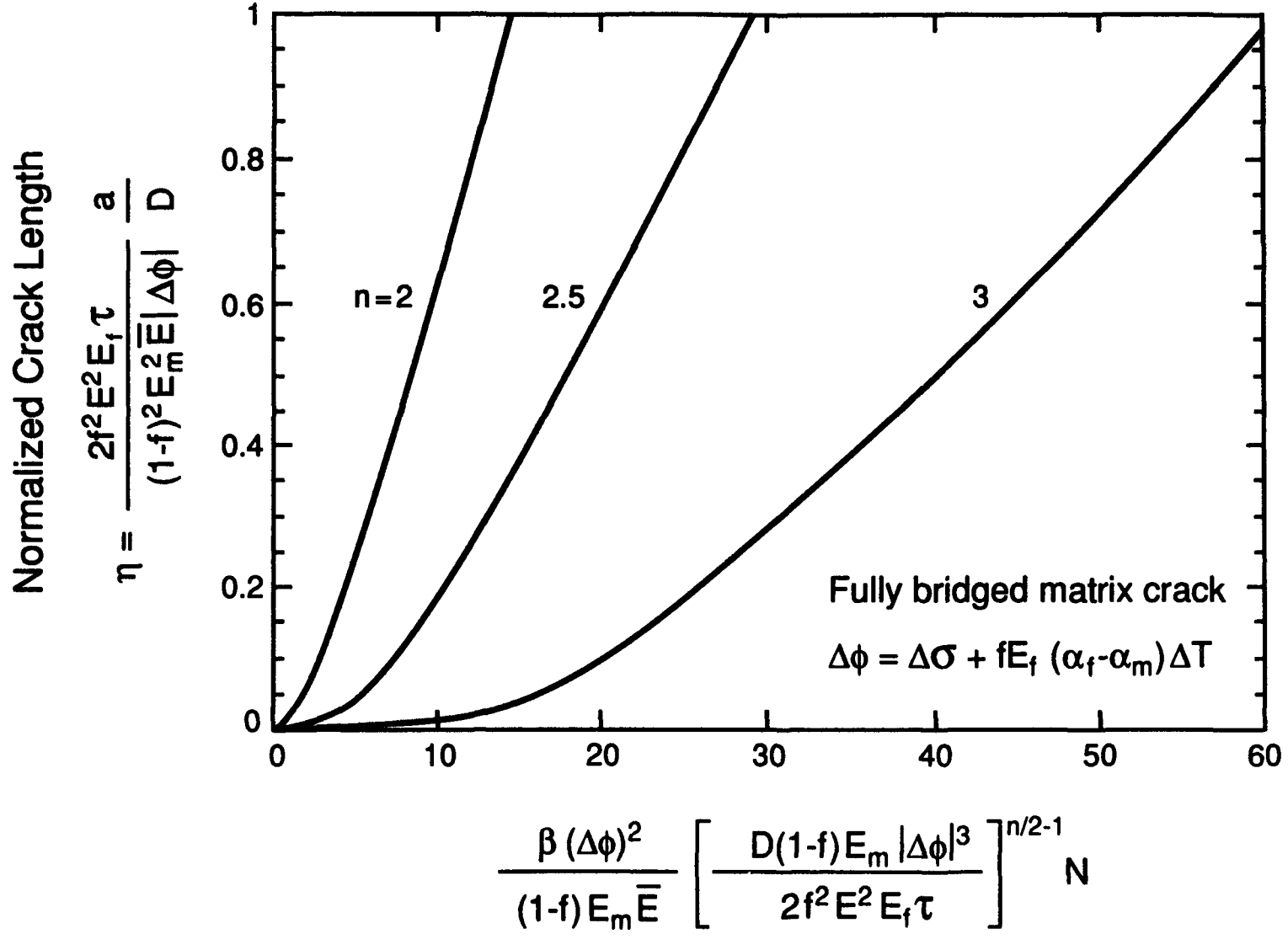
Normalized Crack Length
$\eta = \frac{2f^2E^2E_f\tau}{(1-f)^2E_m^2\bar{E}|\Delta\phi|}\frac{a}{D}$
1
0.8
0.6
0.4
0.2
0
0
10
20
30
40
50
60
n=2
2.5
3
Fully bridged matrix crack
$\Delta\phi = \Delta\sigma + fE_f(\alpha_f-\alpha_m)\Delta T$
$\frac{\beta(\Delta\phi)^2}{(1-f)E_m\bar{E}}\left[\frac{D(1-f)E_m|\Delta\phi|^3}{2f^2E^2E_f\tau}\right]^{n/2-1}N$

Figure 6a

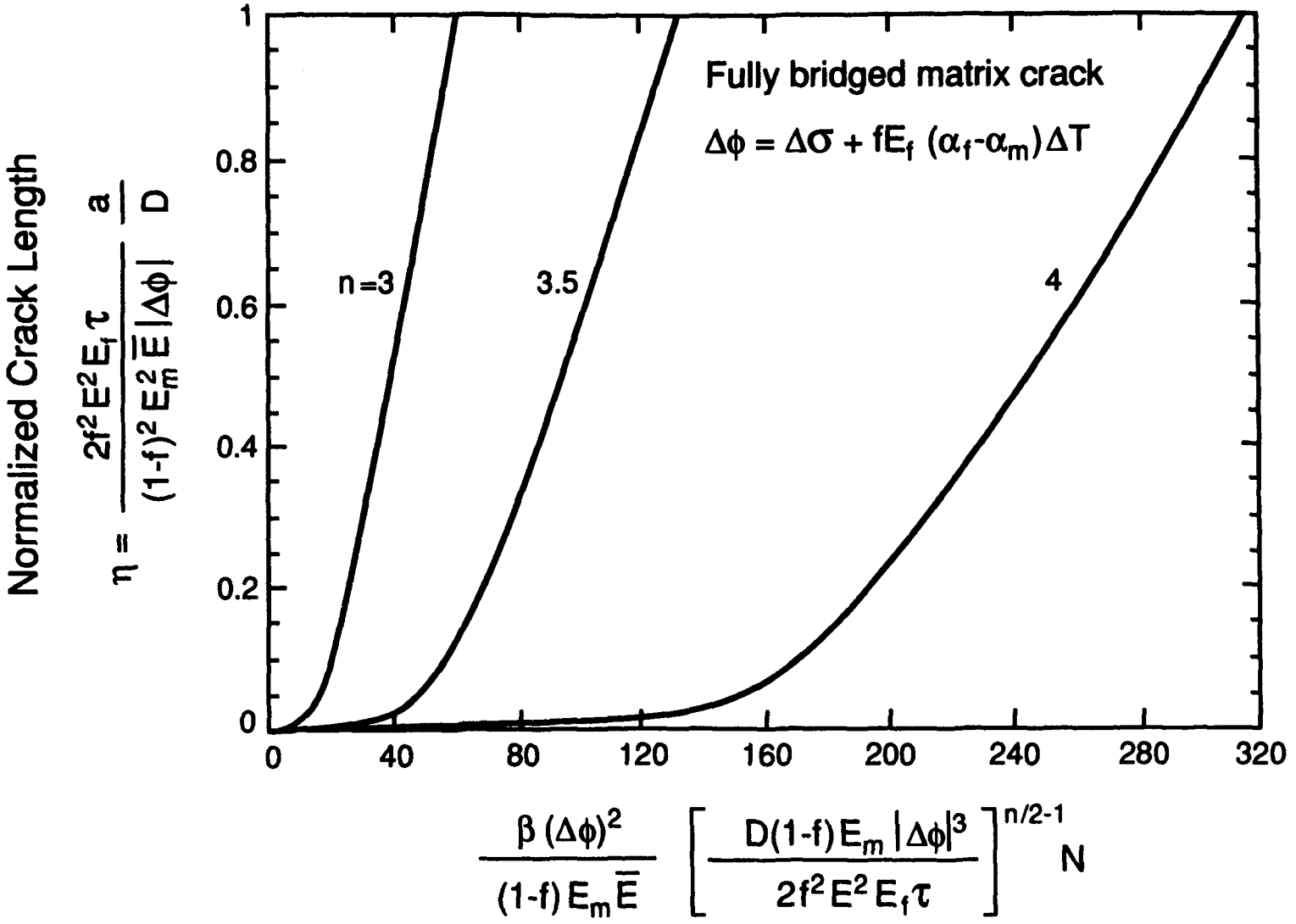
Normalized Crack Length
$\eta = \frac{2f^2E^2E_f\tau}{(1-f)^2E_m^2\bar{E}|\Delta\phi|}\frac{a}{D}$
Fully bridged matrix crack
$\Delta\phi = \Delta\sigma + fE_f(\alpha_f-\alpha_m)\Delta T$
n=3
3.5
4
0
0.2
0.4
0.6
0.8
1
0
40
80
120
160
200
240
280
320
$\frac{\beta(\Delta\phi)^2}{(1-f)E_m\bar{E}}\left[\frac{D(1-f)E_m|\Delta\phi|^3}{2f^2E^2E_f\tau}\right]^{n/2-1}N$

Figure 6b

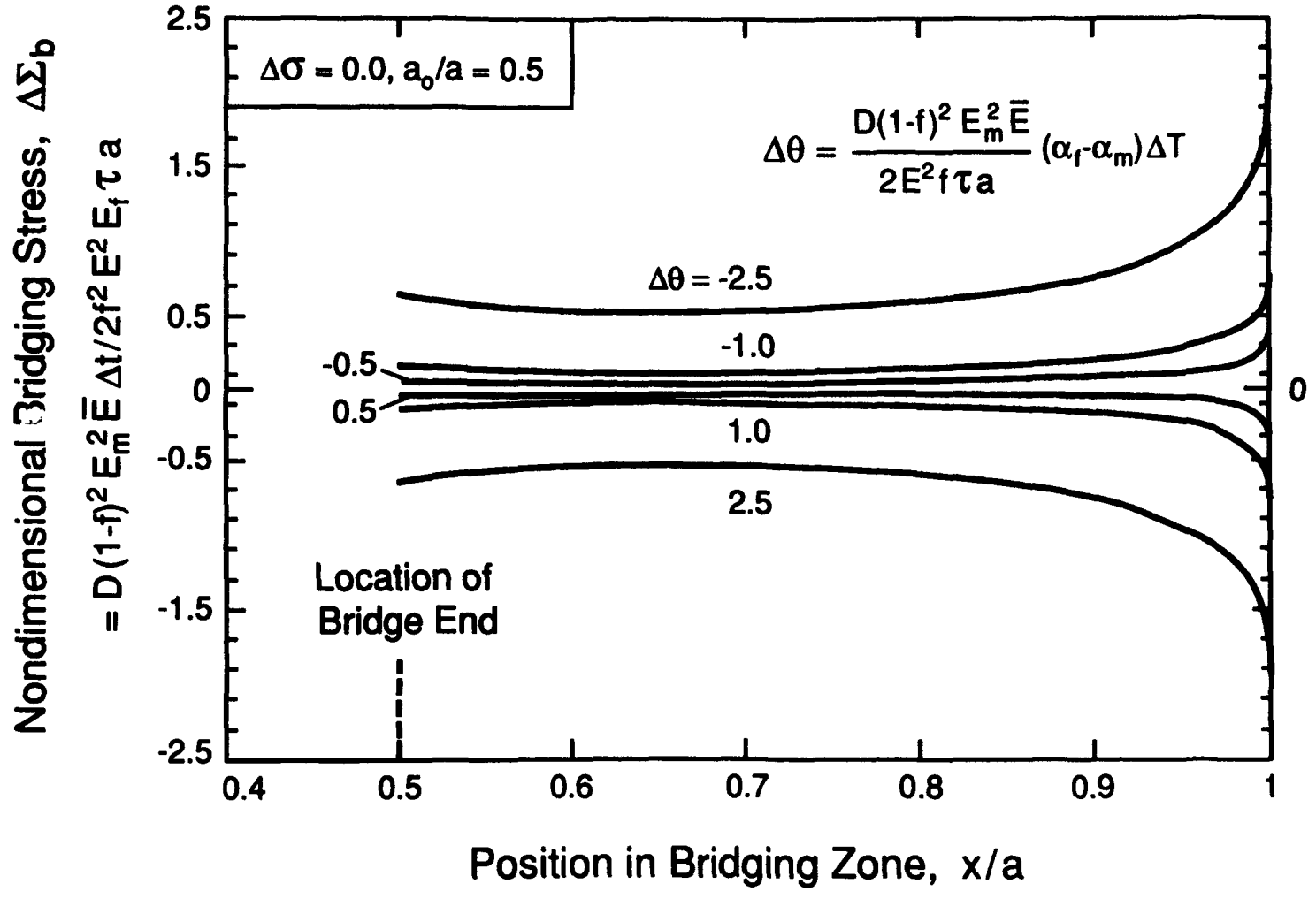
Nondimensional Bridging Stress, $\Delta\Sigma_b$
$= D(1-f)^2 E_m^2 \bar{E}\, \Delta t / 2f^2 E^2 E_f \tau a$
$\Delta\sigma = 0.0, a_o/a = 0.5$
$\Delta\theta = \frac{D(1-f)^2 E_m^2 \bar{E}}{2E^2 f \tau a} (\alpha_f - \alpha_m)\Delta T$
$\Delta\theta = -2.5$
-1.0
-0.5
0.5
1.0
2.5
0
Location of
Bridge End
2.5
1.5
0.5
0
-0.5
-1.5
-2.5
0.4
0.5
0.6
0.7
0.8
0.9
1
Position in Bridging Zone, x/a

Figure 7a

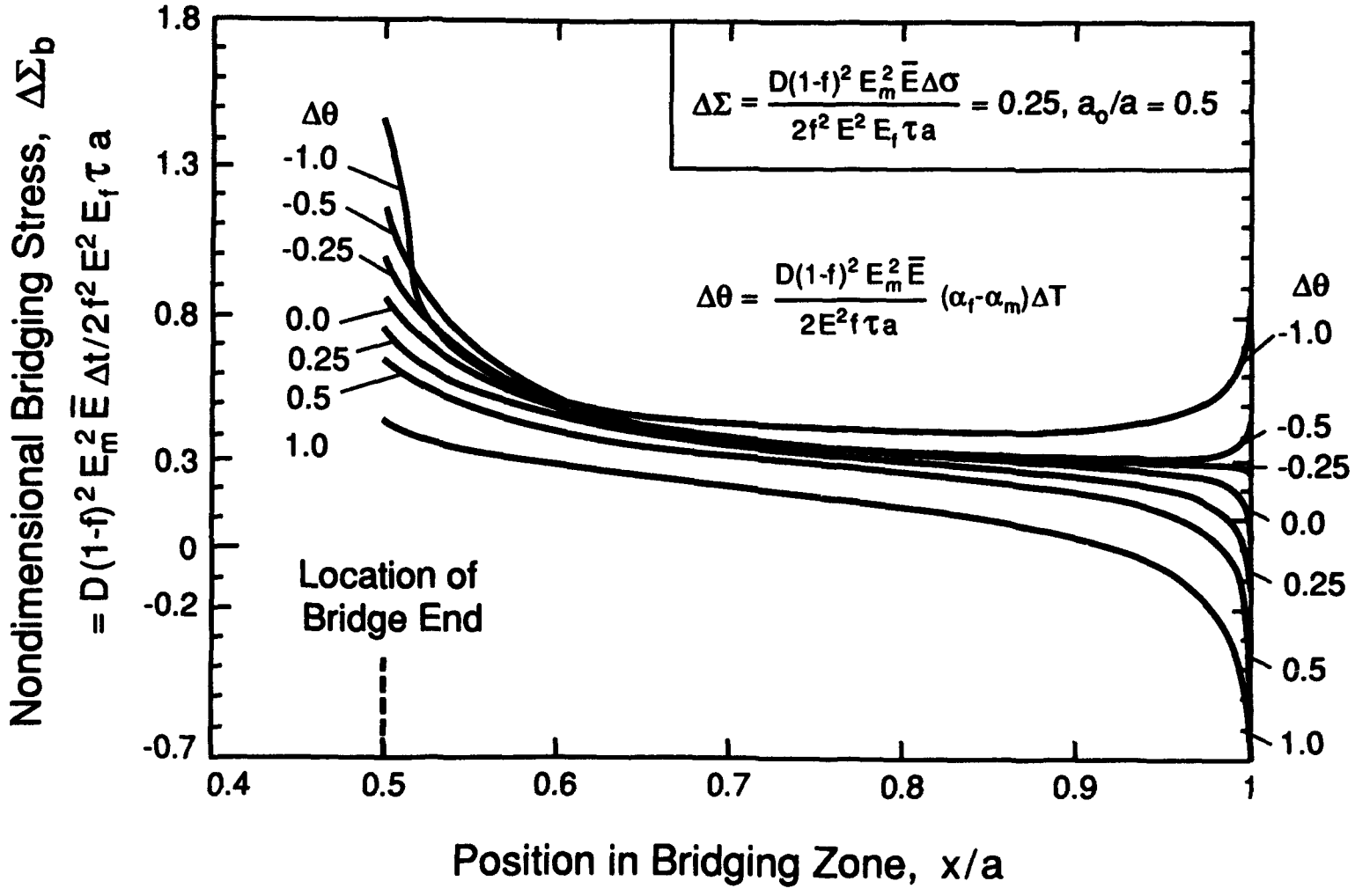
Nondimensional Bridging Stress, $\Delta\Sigma_b$
$= D(1-f)^2 E_m^2 \bar{E}\,\Delta t/2f^2 E^2 E_f \tau a$
$\Delta\Sigma = \frac{D(1-f)^2 E_m^2 \bar{E}\Delta\sigma}{2f^2 E^2 E_f \tau a} = 0.25,\ a_o/a = 0.5$
$\Delta\theta = \frac{D(1-f)^2 E_m^2 \bar{E}}{2E^2 f \tau a}(\alpha_f - \alpha_m)\Delta T$
Δθ
-1.0
-0.5
-0.25
0.0
0.25
0.5
1.0
Location of Bridge End
1.8
1.3
0.8
0.3
0
-0.2
-0.7
0.4
0.5
0.6
0.7
0.8
0.9
1
Position in Bridging Zone, x/a

Figure 7b

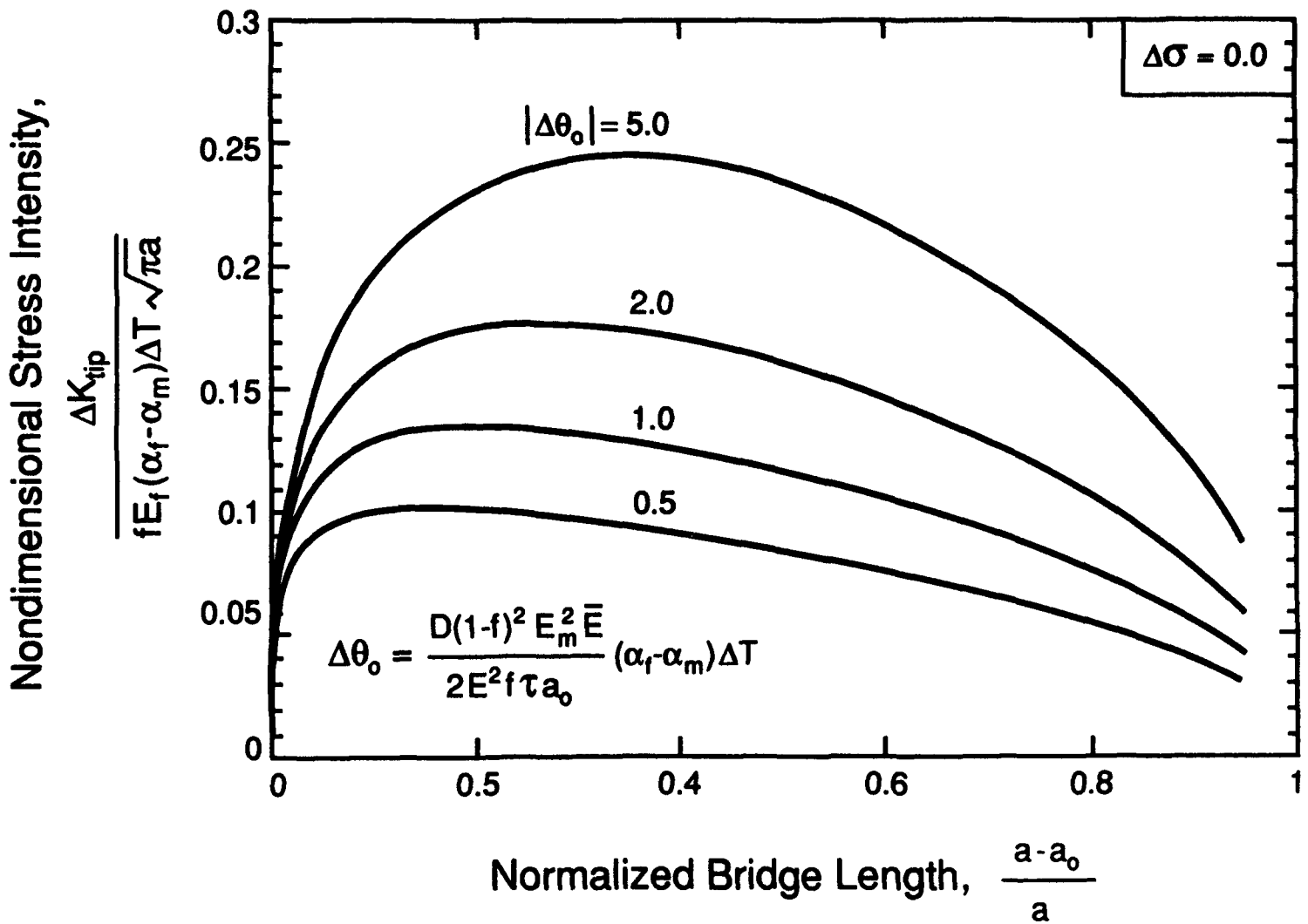
Nondimensional Stress Intensity, $\frac{\Delta K_{tip}}{fE_f(\alpha_f-\alpha_m)\Delta T\sqrt{\pi a}}$
0.3
0.25
0.2
0.15
0.1
0.05
0
0
0.5
0.4
0.6
0.8
1
$\Delta\sigma = 0.0$
$|\Delta\theta_o| = 5.0$
2.0
1.0
0.5
$\Delta\theta_o = \frac{D(1-f)^2 E_m^2 \bar{E}}{2E^2 f \tau a_o}(\alpha_f-\alpha_m)\Delta T$
Normalized Bridge Length, $\frac{a-a_o}{a}$

Figure 8

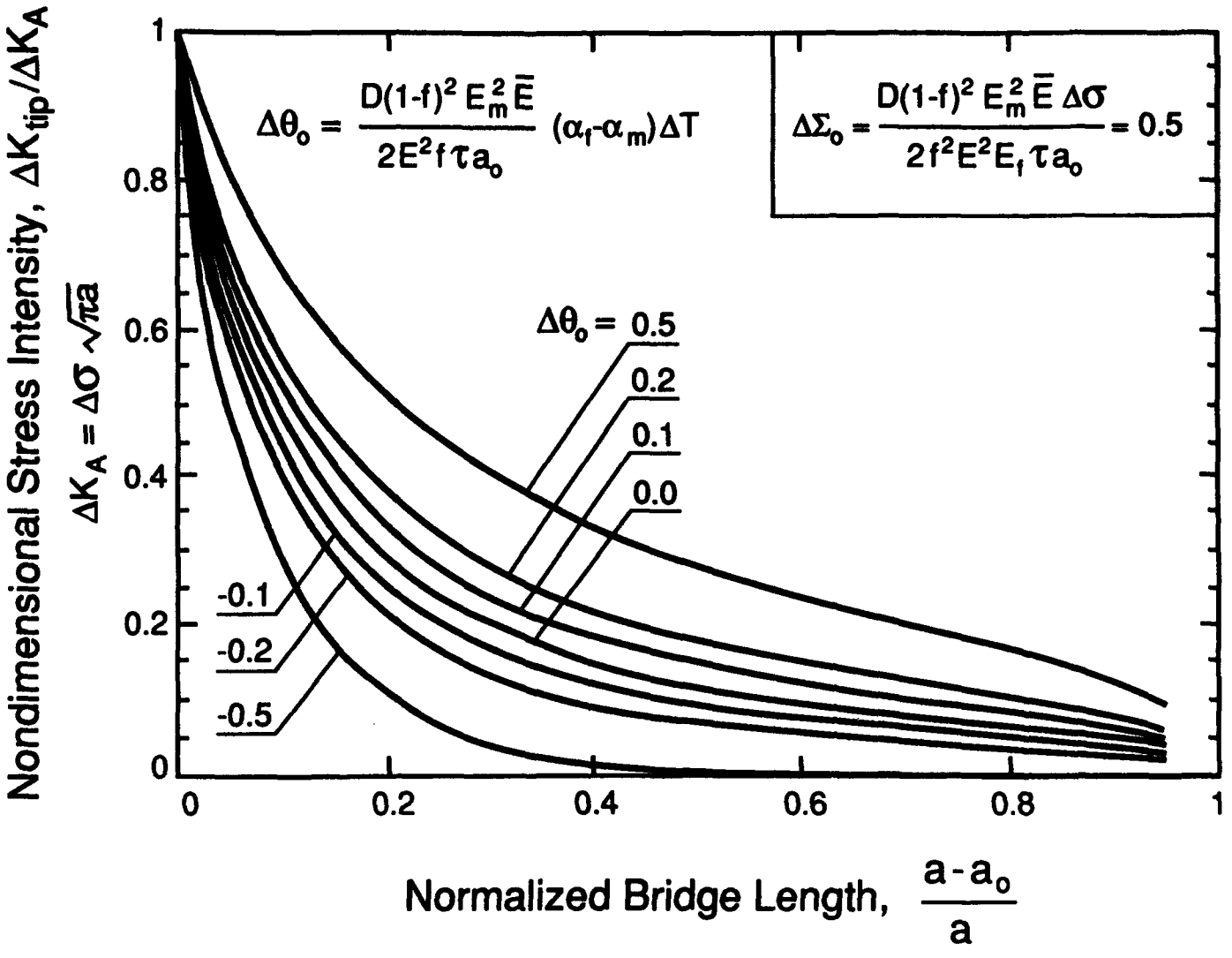
Nondimensional Stress Intensity, $\Delta K_{tip}/\Delta K_A$
$\Delta K_A = \Delta\sigma\sqrt{\pi a}$
$\Delta\theta_o = \frac{D(1-f)^2 E_m^2 \bar{E}}{2E^2 f \tau a_o} (\alpha_f - \alpha_m)\Delta T$
$\Delta\Sigma_o = \frac{D(1-f)^2 E_m^2 \bar{E}\,\Delta\sigma}{2f^2 E^2 E_f \tau a_o} = 0.5$
$\Delta\theta_o$ = 0.5
0.2
0.1
0.0
-0.1
-0.2
-0.5
0
0.2
0.4
0.6
0.8
1
Normalized Bridge Length, $\frac{a-a_o}{a}$

Figure 9a

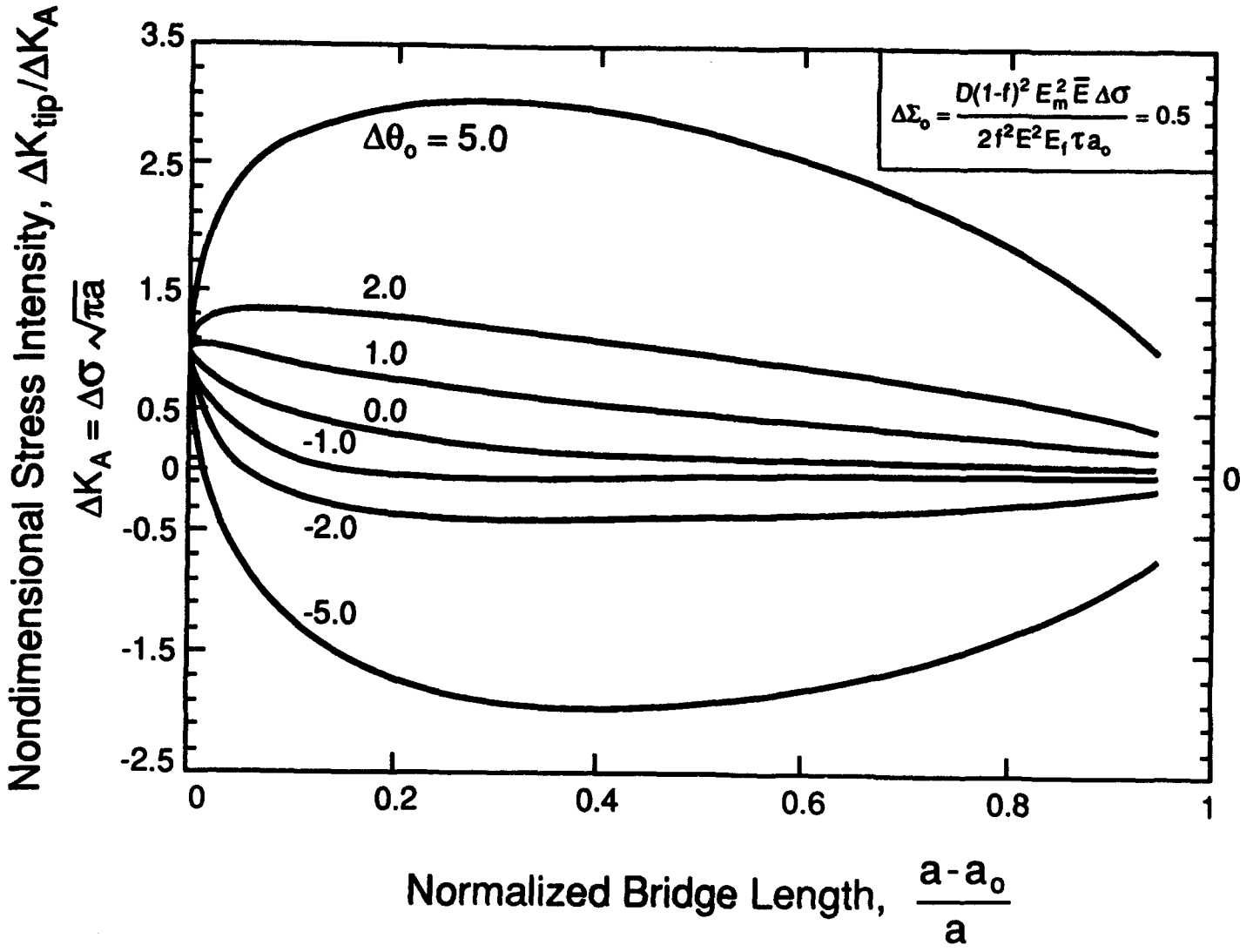
Nondimensional Stress Intensity, $\Delta K_{tip}/\Delta K_A$
$\Delta K_A = \Delta\sigma\sqrt{\pi a}$
$\Delta\Sigma_o = \frac{D(1-f)^2 E_m^2 \bar{E} \Delta\sigma}{2f^2 E^2 E_f \tau a_o} = 0.5$
$\Delta\theta_o = 5.0$
2.0
1.0
0.0
-1.0
-2.0
-5.0
3.5
2.5
1.5
0.5
0
-0.5
-1.5
-2.5
0
0.2
0.4
0.6
0.8
1
Normalized Bridge Length, $\frac{a-a_o}{a}$

Figure 9b

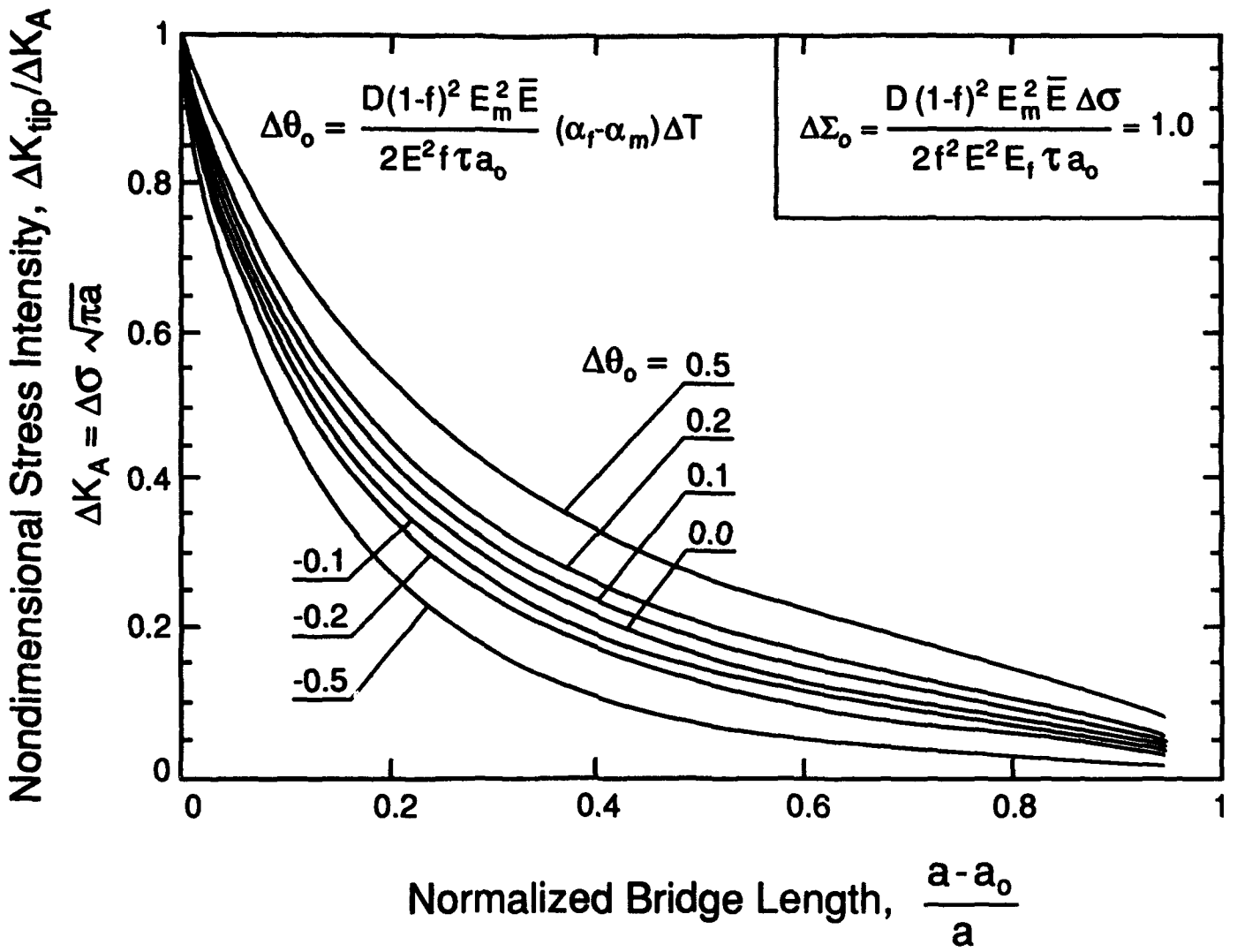
Nondimensional Stress Intensity, $\Delta K_{tip}/\Delta K_A$
$\Delta K_A = \Delta\sigma\sqrt{\pi a}$
$\Delta\theta_o = \frac{D(1-f)^2 E_m^2 \bar{E}}{2E^2 f \tau a_o}(\alpha_f-\alpha_m)\Delta T$
$\Delta\Sigma_o = \frac{D(1-f)^2 E_m^2 \bar{E}\,\Delta\sigma}{2f^2 E^2 E_f \tau a_o} = 1.0$
$\Delta\theta_o$ = 0.5
0.2
0.1
0.0
-0.1
-0.2
-0.5
0
0.2
0.4
0.6
0.8
1
Normalized Bridge Length, $\frac{a-a_o}{a}$

Figure 10a

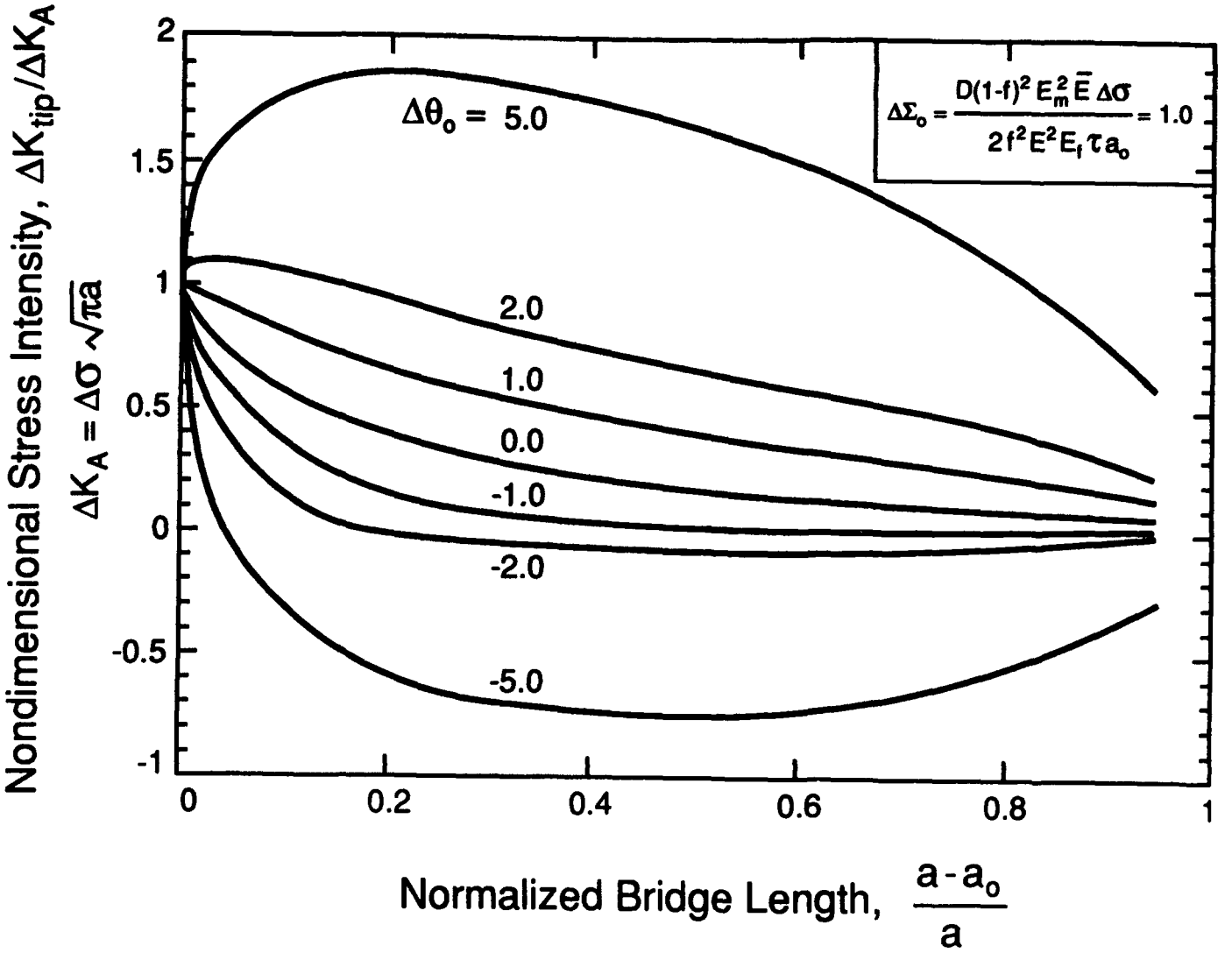
Nondimensional Stress Intensity, $\Delta K_{tip}/\Delta K_A$
$\Delta K_A = \Delta\sigma\sqrt{\pi a}$
$\Delta\Sigma_o = \frac{D(1-f)^2 E_m^2 \bar{E} \Delta\sigma}{2f^2 E^2 E_f \tau a_o} = 1.0$
$\Delta\theta_o$ = 5.0
2.0
1.0
0.0
-1.0
-2.0
-5.0
2
1.5
1
0.5
0
-0.5
-1
0
0.2
0.4
0.6
0.8
1
Normalized Bridge Length, $\frac{a-a_o}{a}$

Figure 10b

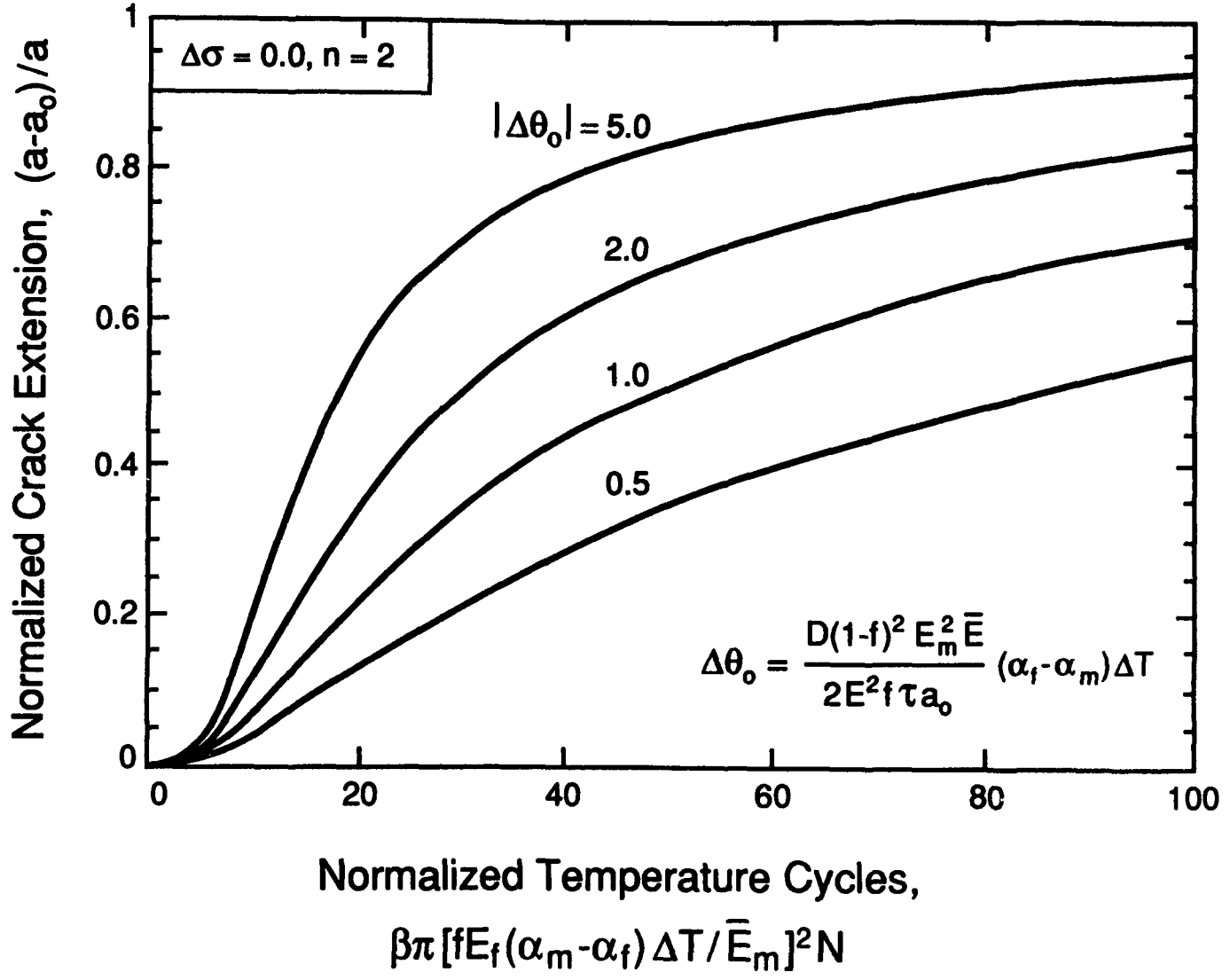
Δσ = 0.0, n = 2
|Δθo| = 5.0
2.0
1.0
0.5
Δθo = D(1-f)² Em² Ē / 2E²fτao (αf-αm)ΔT
Normalized Crack Extension, (a-ao)/a
0
0.2
0.4
0.6
0.8
1
0
20
40
60
80
100
Normalized Temperature Cycles,
βπ[fEf(αm-αf)ΔT/Ēm]²N

Figure 11

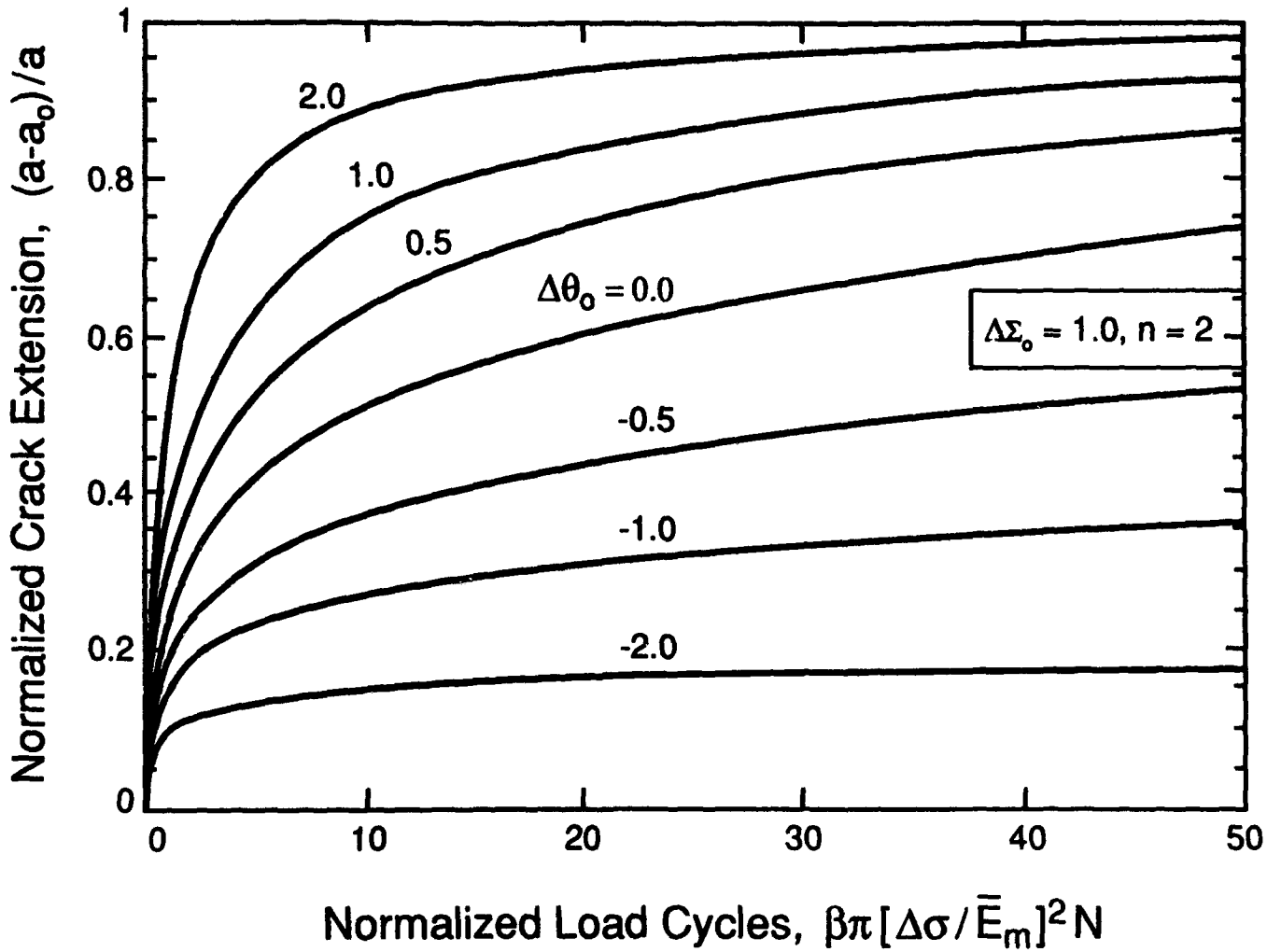
Normalized Crack Extension, $(a-a_o)/a$
Normalized Load Cycles, $\beta\pi[\Delta\sigma/\bar{E}_m]^2 N$
$\Delta\Sigma_o = 1.0$, n = 2
$\Delta\theta_o = 0.0$
2.0
1.0
0.5
-0.5
-1.0
-2.0
0
0.2
0.4
0.6
0.8
1
0
10
20
30
40
50

Figure 12

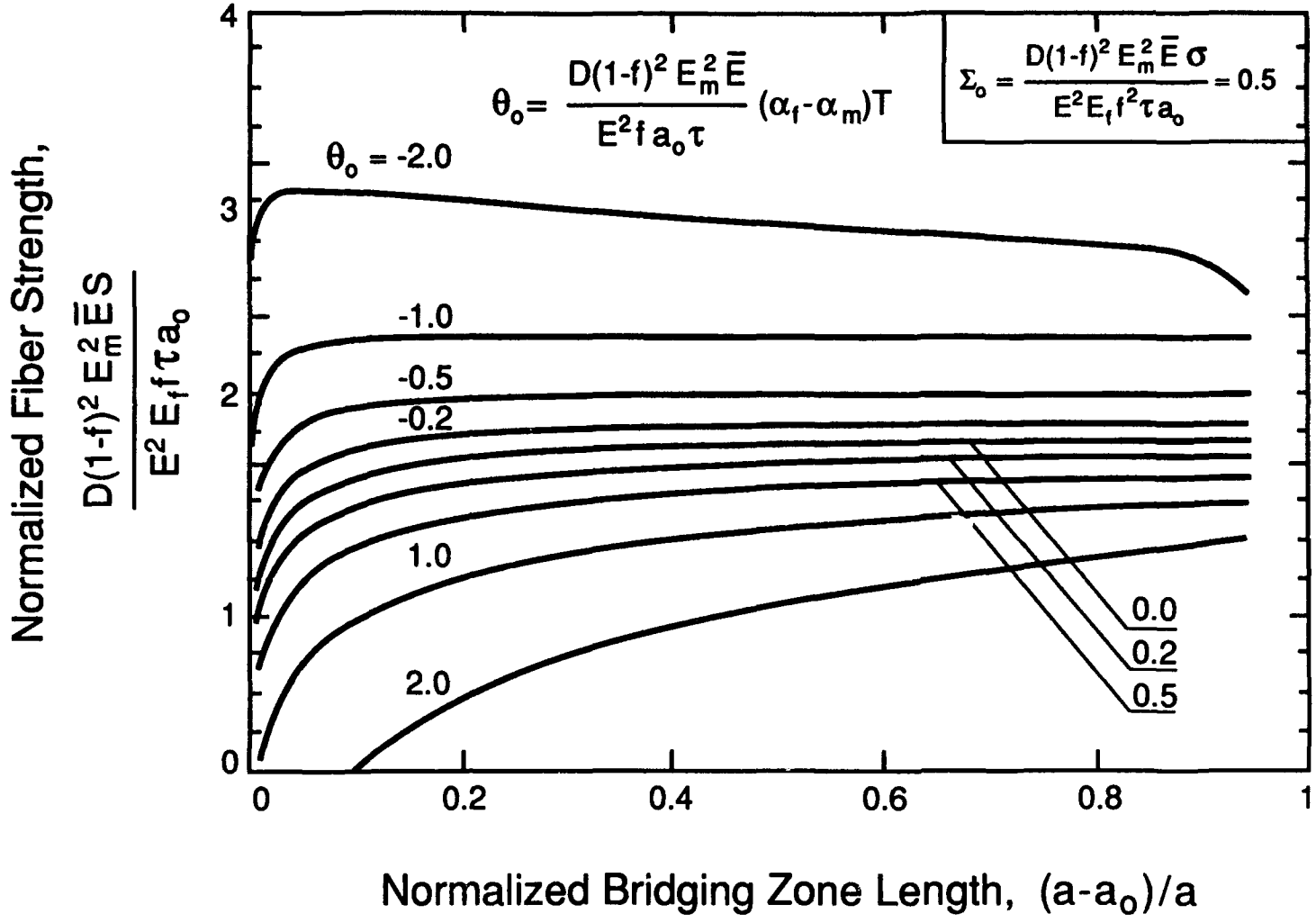
$\theta_o = \frac{D(1-f)^2 E_m^2 \bar{E}}{E^2 f a_o \tau}(\alpha_f - \alpha_m)T$
$\Sigma_o = \frac{D(1-f)^2 E_m^2 \bar{E} \sigma}{E^2 E_f f^2 \tau a_o} = 0.5$
θ_o = -2.0
-1.0
-0.5
-0.2
1.0
2.0
0.0
0.2
0.5
Normalized Fiber Strength, $\frac{D(1-f)^2 E_m^2 \bar{E} S}{E^2 E_f f \tau a_o}$
Normalized Bridging Zone Length, $(a-a_o)/a$
0
1
2
3
4
0
0.2
0.4
0.6
0.8
1

Figure 13a

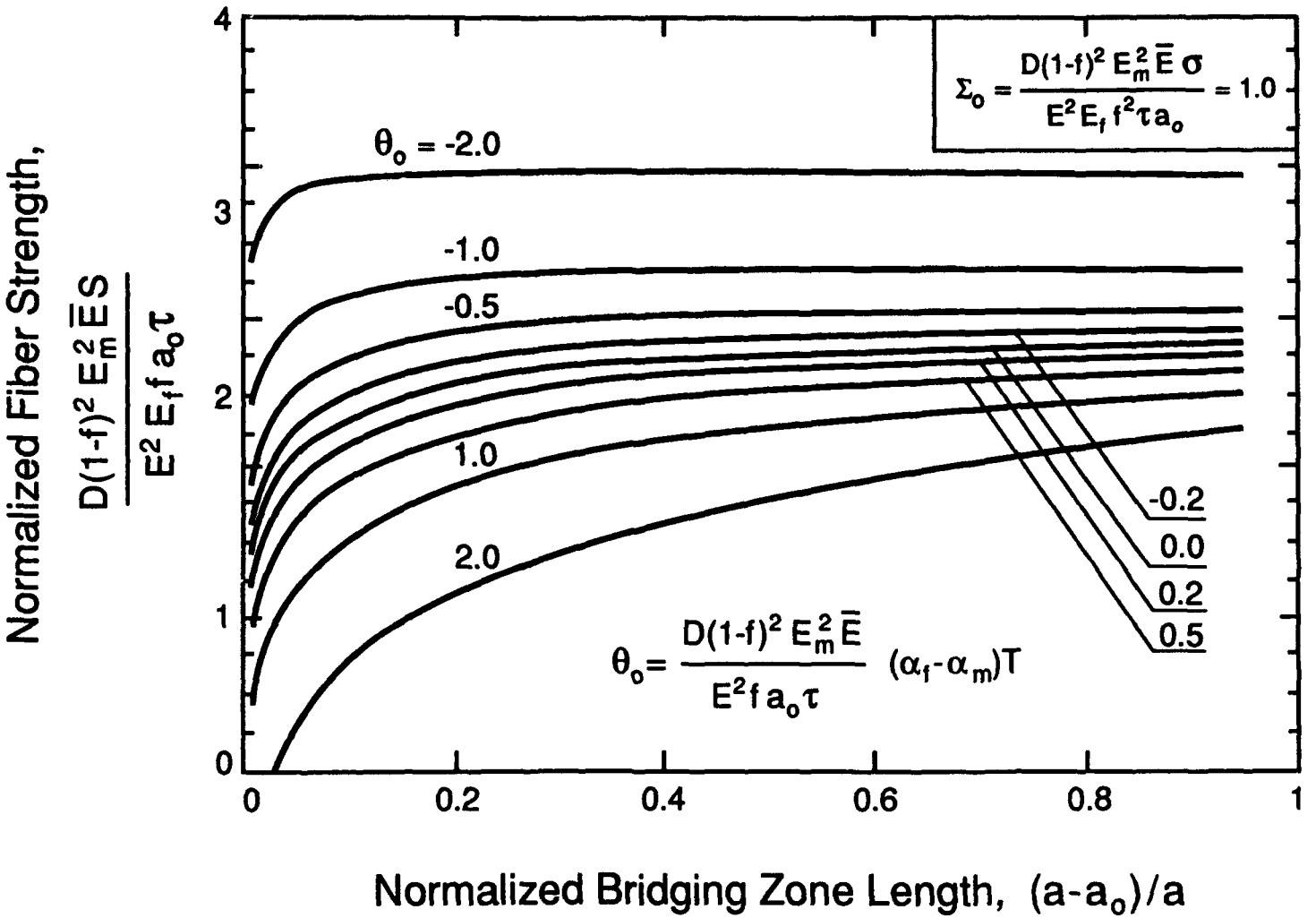
Normalized Fiber Strength, $\frac{D(1-f)^2 E_m^2 \bar{E} S}{E^2 E_f f a_o \tau}$
$\Sigma_o = \frac{D(1-f)^2 E_m^2 \bar{E} \sigma}{E^2 E_f f^2 \tau a_o} = 1.0$
$\theta_o = -2.0$
-1.0
-0.5
1.0
2.0
-0.2
0.0
0.2
0.5
$\theta_o = \frac{D(1-f)^2 E_m^2 \bar{E}}{E^2 f a_o \tau} (\alpha_f - \alpha_m) T$
0
1
2
3
4
0
0.2
0.4
0.6
0.8
1
Normalized Bridging Zone Length, $(a-a_o)/a$

Figure 13b

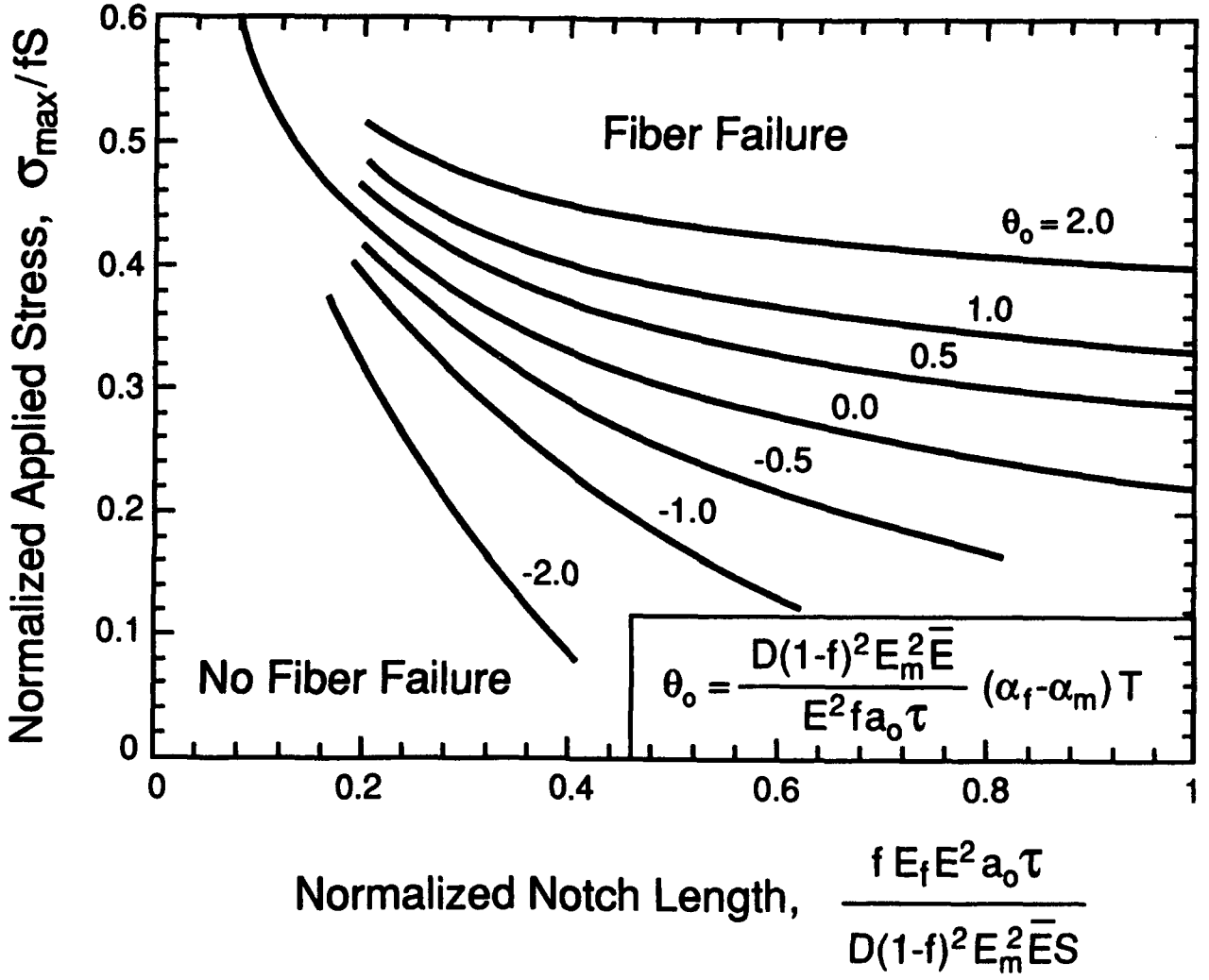
Normalized Applied Stress, σ_{max}/fS
0.6
0.5
0.4
0.3
0.2
0.1
0
Fiber Failure
$\theta_o = 2.0$
1.0
0.5
0.0
-0.5
-1.0
-2.0
No Fiber Failure
$\theta_o = \frac{D(1-f)^2 E_m^2 \bar{E}}{E^2 f a_o \tau} (\alpha_f - \alpha_m) T$
0
0.2
0.4
0.6
0.8
1
Normalized Notch Length, $\frac{f E_f E^2 a_o \tau}{D(1-f)^2 E_m^2 \bar{E} S}$

Figure 14

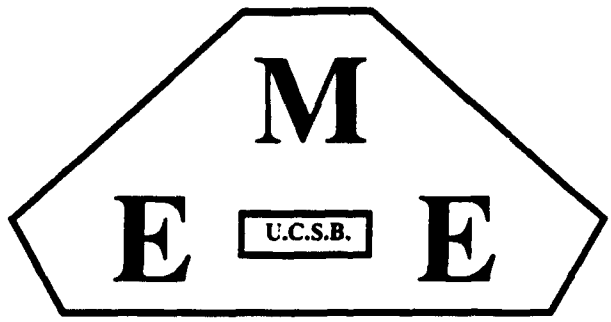

MECHANICAL AND ENVIRONMENTAL
ENGINEERING DEPARTMENT

TRANSVERSE AND CYCLIC THERMAL LOADING OF THE FIBER REINFORCED METAL-MATRIX COMPOSITE SCS6/Ti-15-3

S. Jansson, D.J. Dal Bello and F. A. Leckie

Department of Mechanical & Environmental Engineering

University of California

Santa Barbara, CA 93106-5070

June 1993

ABSTRACT

The transverse properties of a SiC fiber reinforced Ti alloy matrix composite subjected to transverse mechanical and cyclic thermal loading has been investigated. Fibers and matrix have a mismatch in the coefficients of thermal expansion that induces thermal stresses in addition to those caused by mechanical loading. When fluctuations occur in the operating temperature the thermal stresses change and this could cause an incremental accumulation of plastic strain or increase in creep rate. The composite under consideration has a modest mismatch and it was found that the strain accumulation is caused by creep deformation in the matrix at the high temperature portion of the thermal cycles. In the early stages of the deformation for low transverse loading the interface is closed and the creep rate is accelerated by the cyclic thermal stresses. After debond has occurred the cyclic thermal stress component is diminished and the creep rate is given by a matrix with holes.

1. INTRODUCTION

An attractive feature of metal-matrix composites is that excellent longitudinal properties are combined with reasonable transverse and inplane shear strength. This enables the composites to sustain many of the multiaxial stress states which occur in practice when using efficient unidirectional fiber lay-ups. Use of multidirectional reinforcements is less advantageous when weight saving is essential for successful application. In addition to mechanical loading, many components are subjected to cyclic thermal loading, which is expected to influence the matrix dominated transverse and shear properties. Thermal loading causes two components of stress: the first is a stress field resulting from the variation of the temperature field within the

component, the second is the consequence of the mismatch of the coefficients of thermal expansion of fiber and matrix which produces stress fields at the micro-level. In a study of an aluminum metal-matrix composite reinforced with alumina fibers, Jansson and Leckie (1992b) observed that the application of cyclic temperature in combination with constant transverse stress could result in a ratchetting mechanism which produced an increment of transverse strain for each thermal cycle. The source of the ratchetting mechanism is the combination of the stress fields supporting the applied mechanical stress and the cyclic thermal stresses resulting from the thermal mismatch. During each temperature cycle the matrix is subjected to a stress history which results in plastic deformation in the matrix with a bias in the transverse direction. To avoid ratchetting, the combination of the applied transverse stress and the magnitude of the temperature excursion should not exceed a shakedown condition. This system features a significant difference in the coefficients of thermal expansion of fiber and matrix, a low matrix yield strength and a strong interface between fiber and matrix.

In this study a titanium matrix reinforced with silicon carbide fibers is subjected to a similar test program. The present titanium matrix systems feature a weak interface, in contrast to the strong bond which characterizes the alumina-aluminum composite. Furthermore, compared to the Al_2O_3-Al system the mismatch of the coefficients of thermal expansion is substantially lower and the matrix strength substantially higher. The strongly contrasting properties of the SiC-Ti system suggest that the transverse properties differ significantly from the Al_2O_3-Al system, and it is the aim of this investigation to determine these differences.

2. COMPOSITE MATERIAL AND FABRICATION

The composite material SCS6/Ti 15-3 used in this study features many of the properties of titanium matrix composite systems that are currently considered for structural applications. It consists of coated SiC fibers with a diameter of 140 m. The complex C and SiC coating causes the composite to have a weak interface. The fibers are arranged in a uniaxial lay-up with a fiber volume fraction of 35 %. in the β-Ti alloy matrix, Ti-15V-3Cr-3Al-3Sn. The composite is fabricated by Textron using a fiber foil lay-up consolidation technique. The consolidation temperature is approximately 900 C and in the subsequent cool down, the thermal expansion mismatch of fiber and matrix introduces residual stresses.

Ambient tensile properties of the matrix have been obtained from tests on foil extracted from the composite and the fiber modulus from bend tests on extracted fibers [Jansson et al, 1991]. The matrix and fiber stress-strain relationships are shown in Fig. 1, which indicates that the failure strain of the matrix foil is approximately 3%, which is low compared to the values commonly reported for Ti alloys. The remaining fiber and matrix properties have been extracted from the literature and are summarized in Table 1.

A finite element calculation was performed by Gunarwardena et al [1993] to estimate the residual stresses after processing. Due to lack of high temperature data for Ti-15-3 the temperature dependence of elastic modulus and yield strength of the matrix was estimated by using data for the similar alloy Ti-6V-4Al [Nimmer et al, 1991]. The estimated residual stress state in the fiber following a consolidation temperature of 900 C consists of an axial compression

of 720 MPa and a nearly uniform compressive radial stress of 200 MPa. At the interface the radial stress is 200 MPa and compressive while the matrix hoop stress is 500 MPa tensile. In the axial direction the matrix stress is almost uniform and tensile with a value of 400 MPa. No matrix cracking has been observed in the as-received composite [Jansson et al, 1991] which suggests that the matrix toughness is sufficiently high to sustain the residual stresses state induced during fabrication.

3. TRANSVERSE TENSILE RESPONSE

The transverse tensile response measured on a virgin specimen at ambient temperature is shown in Fig. 2. After an initial linear elastic response the behavior becomes nonlinear when the transverse stress exceeds 140 MPa. Thereafter the tangent stiffness gradually decreases and failure occurs at a stress of 420 MPa when the strain is 1.1%. The strength and ductility of the composite are substantially less than the corresponding values for the Ti matrix for which the strength is 950 MPa and failure strain 3%. For weakly bonded composites it was established [Jansson et al 1991] that the limit strength of the composite is obtained by multiplying the matrix area on the weakest plane perpendicular to the loading direction by the ultimate strength of the matrix. The measured matrix area fraction of the failure surface is $A_m = 0.4$, the ultimate strength of the matrix $\sigma_{um} = 950$ MPa so that the theoretical prediction of the composite strength is

$$\overline{\sigma}_L = A_m \frac{2}{\sqrt{3}} \sigma_{um} = 440 \text{ MPa} \qquad (1)$$

This value compares well with the experimental value of 420 MPa. In a more detailed finite element calculation performed by Gunarwardena et al (1993) it was found that the initial

residual stresses ensure contact is maintained at the fiber-matrix interfaces during initial loading. When the applied stress is 140 MPa tensile stresses develop at the interface and debonding is initiated. When the applied stress reaches 200 MPa the debonding is fully developed. The debonding is accompanied by a substantial decrease in the elastic modulus. In the absence of matrix plasticity the calculated elastic response after debond is shown in Fig. 2. When the additional effect of matrix plasticity is included the experimental observations are closely reproduced. The experimental results and the calculations both suggest that the behavior immediately after debond is dominated by a decrease of the elastic modulus and as the applied stress approaches the limit value the deformation is dominated by plastic deformations of the matrix. The debonding prevents build-up of large hydrostatic stresses which can cause loss of matrix ductility [Hancock and Mackenzie, 1976 and Rice and Tracy, 1969]. However the matrix deformation is concentrated in the ligaments between the fibers so that the composite failure strain is 1.1%, which is approximately one third of the matrix failure strain. The results of the detailed computations are consistent with experimental observation indicating that fiber-matrix debonding accounts both for the decrease in the elastic modulus and transverse strength of the composite. The macroscopic failure surface, shown in Fig. 3a, is irregular with visible debonded fibers between the matrix ligaments. A high magnification view of the fracture surface of the matrix ligament, Fig. 3b, indicates the dimpled topology associated with ductile failure.

4. THERMO-MECHANICAL TEST PROGRAM

A schematic of the experimental setup is shown in Fig. 5. The specimens were loaded in a servo-hydraulic machine and heated by means of an induction coil. The strain was measured

by an extensometer with 3/8" gauge length and the temperature was measured by three type K thermocouples mounted at the center and ends of the gauge section. The center thermocouple was used to control the temperature while the top and bottom thermocouples were used to measure the temperature field along the length of the specimen. The recorded temperatures shown in Fig. 6 indicate that a uniform temperature field was achieved in the gauge section of the specimen throughout the cycle. The heating rate was approximately ɔ C/s, resulting in temperature dependent cycle time of order 5 mins for the current tests. It was found that 100 temperature cycles were sufficient to reach a steady state condition. Because of the limited availability of the material each specimen was subjected to one stress level and a number of temperature ranges. The specimens were initially subjected to a low temperature range and the temperature range was subsequently increased in steps of 20 C until failure occurred. The transverse stresses selected were σ = 50, 100, 200 and 350 MPa. The lowest temperature in the cycle T_{min} = 60 C and the upper temperature T_{max} was selected to be in the range 300-550 C. Above this temperature range the material exhibits severe oxidation.

5. EXPERIMENTAL OBSERVATIONS

Representative examples of recorded strain histories are shown in Fig. 7a for a high transverse stress and in Fig. 7b is for a low transverse stress. The measured strain ranges are shown in Fig. 8 as a function of the temperature range $\Delta T = T_{max} - T_{min}$. The steady state strain rates are shown in Fig. 9a as the average rate over a cycle and in Fig. 9b as the strain accumulation per cycle. The test at the highest transverse stress of 350 MPa failed in the first thermal cycle during the temperature decrease. The failure strain was found to be independent

of the loading conditions and was approximately 1%.

The relationship between deformation rate and temperature range, Fig. 9a, indicates that the graphs for the stress extremes have different shapes. For the high applied stress of 300 MPa, the deformation rate increases monotonically with increase in temperature amplitude. For the low stress of 50 MPa the deformation rate at first decreases with increasing temperature amplitude, reaches a minimum value and thereafter increases monotonically with increasing temperature amplitude. For intermediate values of stress the character of the results changes progressively from one extreme behavior to the other. The experimental strain ranges, shown in Fig. 8 as a function of ΔT, also exhibit two extremes of behavior. In the 50 MPa test the measurements indicate a transition from a cyclic strain range corresponding to a coefficient of thermal expansion of 8.5 10^{-6} to a higher value in the range 10.5 - 12 10^{-6} 1/C. The test for the higher loadings exhibits the higher coefficient of thermal expansion from the first loading sequence.

An examination of the sides of the specimens , Fig 10a, shows permanent debond cracks perpendicular to the loading direction. The cracks are distributed rather evenly with the largest crack openings at the pole of the fibers. A higher magnification view, Fig. 10b, indicates that debond occurs both at the fiber matrix interface and in the fiber coating. The photographs also reveal that the fibers are pultruding out of the matrix, indicating that a sliding has occurred in the longitudinal direction between fiber and matrix. An examination of the failure surface, shown in Fig. 4a, indicates that the specimen subjected to thermo-mechanical loading have fewer fibers left on the failure surfaces compared to the ambient tensile test, Fig. 3a. The shape of the

failed ligaments differs from those of the room temperature tests. The failure occurs by the formation of longitudinal necks, typical of a ductile creep fracture. A high magnification view that perpendicular to the failure surface of a matrix ligament, Fig. 4b, shows that the formation of the neck causes small longitudinal cracks to form at the former fiber matrix interface. The portion of the failure surface at the top of the ridge reassembles the texture of the failure surface at ambient temperature.

The above observations would suggest that interface debonding occurs at some stage during all the tests. For stresses 200 MPa or greater the debond occurs on first load while for the lower stress levels the debonding is delayed to some later time in the test. In the 50 MPa test the onset of the debonding process was captured in the strain history for the temperature range 420 C, Fig. 7b. The strain at the beginning of this loading sequence was 0.08%. When the strain reaches 0.15% the deformation rate changes noticeably from 1.1×10^{-3} to 0.33×10^{-3} 1/s. Coinciding with this transition it was observed that coefficient of thermal expansion changed suddenly from 8.5×10^{-6} to 10.5×10^{-6} 1/C.

The test performed at 50 MPa was terminated before the specimen failed. A tensile test was performed at ambient temperature to determine the value of the transverse modulus following thermo-mechanical loading. The result of the test is shown in Fig. 2 together with the tensile curve for a virgin material. The modulus was determined to be 44 GPa, which is only a third of the modulus of the virgin material. Fiber push through tests were also performed on a 0.45 mm thick slice cut from the loaded specimen. Some fibers had such a low sliding resistance that

they fell out during the specimen preparation. The results shown in Fig. 11 are typical of the fibers which exhibited the higher sliding resistance. Even these high values indicate a substantial degradation of the fiber push-through properties after thermal cycling.

6. INTERPRETATION OF THE EXPERIMENTAL RESULTS

From the room temperature transverse tension test, Fig. 2, it was found that the onset of debonding occurs when the transverse stress is 140 MPa, at which point there is discernable change of the gradient of the stress-strain curve until the stress is 200 MPa. Thereafter the change in slope is much more gradual suggesting that the debonding process is complete.

The experimental results and micro-structural observation for the constant load-cyclic temperature also indicate that fiber-matrix debond occurs during the test. When the stress is sufficiently large the deformation rate immediately establishes a steady state value. When the transverse stress is low there is a transient period during which the creep rate is greater than the steady state value. The results of the test in Fig. 7b suggest that the transient period is complete when interface debonding occurs and the coefficient of thermal expansion increases from 8.5 x 10^{-6} to 10.5 x 10^{-6} 1/C. The properties of the composite can be expected to describe the strain range before debond while the post-debond strain range would be dictated by the property of the matrix. Simple calculations, based on the data in Table 1, indicate that the coefficients of thermal expansion for the composite system is 8.5 x 10^{-6} 1/C, which is close to the experimental value before debond. The matrix value of 9.7 x 10^{-6} 1/C is slightly lower than the observed value after debond.

The evidence of the experiments would appear to be consistent with the following interpretation. After processing the stress at the fiber-matrix interface is compressive. When the applied transverse stress is 140 MPa or greater, there is immediate debond at the interface, resulting in a release of the residual stresses and a steady state deformation rate is established after a few cycles. When the transverse stress is lower than 140 MPa there is no initial debond and a compressive residual stress is maintained at the interface. This residual stress field is such that the initial matrix deformation rate is greater than the steady state value. When the plastic strain reaches a value of 0.15% the debond is fully established, the residual stresses are released and steady state deformation rate is established.

Before the experimental results are studied in more detail it is instructive to evaluate the loading conditions in relation to the elastic shakedown conditions. The shakedown boundary when the composite is subjected to constant transverse stress and cyclic temperatures have been determined analytically for this composite system by Jansson and Leckie (1992b). The results are shown in Fig. 12 in a normalized form for three different conditions: the first is for a residual stress field causing a full contact at the interface, the second is for a fully relaxed contact pressure at the interface with longitudinal strain continuity and in the third all the constraints are fully relaxed. For operating conditions within the shakedown condition, the steady state response is purely elastic. However, when the operating condition exceed the shakedown condition ratchetting occurs with an incremental accumulation of plastic strain for each cycle.

An experimental shake down curve has been determined from the data by using $d\varepsilon_p/dN = 10^{-4}$ as the shake down condition. It is plotted on the interaction diagram in Fig. 12 using the most conservative estimate of yield stress. All experimental conditions lie well within the calculated shakedown condition suggesting that time-independent plasticity does not contribute to the incremental deformation observed in the experiments. It is concluded therefore that the source of the deformation must be creep. The average creep rates over a cycle are plotted in Fig. 13 for different operating conditions. Also shown in the graph are the steady state matrix creep data [Tuttle and Rogacki, 1991 and Rosenberg, 1983] and constant stress transverse creep data for the composite after debond [Majumdar and Newaz, 1992]. It is observed that the transverse creep data and the creep rate for cyclic temperature both exhibit the same stress dependency as the matrix data. For the same stress and temperature levels the composite creep rate is much higher than the matrix creep rate. The composite creep rate for cyclic temperature is also higher than the creep rate for the matrix at the highest temperature in the cycle.

Simple estimates are now made to predict creep rates of the composite before and after debond from the matrix creep data.

i. Creep Deformation Rate After Debond

When the transverse stress is greater than 200 MPa there is complete debonding on first loading and the residual stress is released. For no longitudinal constraint the reference stress is

$$\sigma_R = \frac{\overline{\sigma}}{A_m} \tag{2}$$

where $\bar{\sigma}$ is the applied transverse stress and A_m is the matrix area fraction of the weakest ligaments, which is equal to the matrix area fraction of the failure surface. The matrix steady state creep rate given in Fig. 13 can be fitted by the Norton equation with an exponential temperature dependence

$$\frac{\dot{\varepsilon}}{\dot{\varepsilon}_0}=\left[\frac{\sigma}{\sigma_0}\right]^n \exp[\beta(T-T_0)] \tag{3}$$

where $\dot{\varepsilon}_0 = 3.1\ 10^{-12}$, $n = 4.2$, and $\beta = 0.05$ for $\sigma_0 = 100$ MPa and the creep threshold temperature $T_0 = 300$ C. For conditions after debond the reference stress is given by Eqn. (2). Assuming that the temperature variation is triangular and integrating Eqn. (3) over a cycle τ the average creep rate $\bar{\varepsilon}$ per cycle is given by

$$\bar{\varepsilon}=\frac{1}{\tau}\int_0^{\tau}\dot{\varepsilon}dt=\left(\frac{\bar{\sigma}}{\sigma_0}\right)^n \exp[\beta(T_{max}-T_0)]\left(\frac{1}{A_m}\right)^n \frac{1}{\beta\Delta T} \tag{4}$$

from which it can be deduced that the average creep rate is given by the matrix creep at the highest temperature of the cycle multiplied by corrections for the reference stress and the cyclic temperature. The experimental data for the composite normalized using this relation are shown in Fig. 14 together with the matrix data for 100 MPa. It can be concluded that the average creep rate after debond is well represented by this relation.

ii. Creep Rate Before Debond

When the applied transverse is small the deformation rate shown in Fig. 9a first decreases with temperature range, reaches a minimum and then increases monotonically. This

initial decrease in deformation rate can in generally be attributed to stress redistribution and hardening in primary creep. The transition at debond was captured in Fig. 7b when the transverse stress was 50 MPa and temperature range ΔT = 420 C. This loading condition was applied when the accumulated plastic strain following the previous loading history was 0.08% and the strain rate was $1.1x0^{-3}$ 1/s . When the accumulated plastic strain reached 0.15% the strain rate decreased quite rapidly to a constant value of $0.33x10^{-3}$ 1/s.

The effect of the stress redistribution and debonding on the creep rate could be determined from a full numerical analysis. It is more instructive however to calculate the response of the simple representative volume element shown in Fig. 14. The element has a square cross-section for which the matrix area fraction at the weakest plane is $1-\sqrt{f} = 0.41$, which is very close to the measured value of .4 for the composite. The analysis of the elastic stress distribution for the element is outlined in Appendix for an applied transverse stress $\bar{\sigma}$ and temperature change from T_c to T.

From the equations given in the Appendix it is possible to evaluate the history of stress in the matrix during the first thermal cycles before the accumulated creep strain has changed the stress distribution. Since the elastic strain range in the cycle is two orders of magnitude greater than the plastic strain accumulated in the cycle use can be made of the Rapid Cycle Solution developed by Ponter [1976]. In this method the elastic stress distribution over the cycle is used to evaluate the creep rate. The method is simple and valid when the creep strains accumulated over a cycle are small compared to the variation of elastic strains.

Using the stress distribution given in the Appendix and the multiaxial generalization

$$\frac{\dot{\varepsilon}_{ij}}{\dot{\varepsilon}_0}=\frac{3}{2}\left(\frac{\sigma_e}{\sigma_0}\right)^{n-1} s_{ij}\ \exp(\beta(T-T_0)) \tag{5}$$

of the constitutive Eqn. (3) where σ_e is the von Mises equivalent stress and s_{ij} is the stress deviator, the strain rate in the matrix can be calculated to be

$$\frac{\dot{\varepsilon}_{ym}}{\dot{\varepsilon}_0}=\frac{1}{2}\left(\frac{\sigma_T}{D\sigma_0}\right)^{n} R^{\frac{n-1}{2}}\left(2A_1-A_2+(2B_1-B_2)\frac{\bar{\sigma}}{\sigma_T}\right)\exp(\beta(T-T_0)) \tag{6}$$

$$\frac{\dot{\varepsilon}_{zm}}{\dot{\varepsilon}_0}=\frac{1}{2}\left(\frac{\sigma_T}{D\sigma_0}\right)^{n} R^{\frac{n-1}{2}}\left(2A_2-A_1+(2B_2-B_1)\frac{\bar{\sigma}}{\sigma_T}\right)\exp(\beta(T-T_0)) \tag{7}$$

Where

$$R=A_1^2-A_1A_2+A_2^2+[A_1(2B_1-B_2)+A_2(2B_2-B_1)]\frac{\bar{\sigma}}{\sigma_T}+(B_1^2-B_1B_2+B_2^2)\left(\frac{\bar{\sigma}}{\sigma_T}\right)^2$$

$$\sigma_T=E_m(\alpha_m-\alpha_f)(T-T_c)$$

and T_c is the consolidation temperature. The constants B_i , A_i and D are given in the appendix and are functions of the elastic properties of the constituents and fiber volume-fraction. The average creep rate over the cycle for the composite before debond can be calculated by use of Eqn. (A8) that relates the plastic strain increment for the composite to the plastic strain

increments in the matrix. The average creep rate for the cycle is

$$\bar{\dot{\varepsilon}}=\frac{1}{D\Delta t}\int_0^{\Delta t}[B_1(\sqrt{f}-f)\dot{\varepsilon}_{ym}(T(t))+B_2 f\dot{\varepsilon}_{zm}(T(t))]dt \tag{9a}$$

For a triangular temperature variation over the cycle the temperature is linearly dependent on time and a change of integration variable can be performed to give

$$\bar{\dot{\varepsilon}}=\frac{1}{D\Delta T}\int_{T_0}^{T_0+\Delta T}[B_1(\sqrt{f}-f)\dot{\varepsilon}_{ym}(T)+B_2 f\dot{\varepsilon}_{zm}(T)]dT \tag{9b}$$

After debonding has taken place the thermal and residual stresses vanish and the creep deformation is governed by a constant stress in the ligament in Fig. 15. Assuming the same linear temperature variation over the cycle the composite creep rate for the model is found to be

$$\frac{\bar{\dot{\varepsilon}}_{ss}}{\dot{\varepsilon}_0}=\sqrt{f}\left(\frac{\bar{\sigma}}{(1-\sqrt{f})\sigma_0}\right)^n\frac{\exp(\beta(\Delta T+T_0)}{\beta\Delta T} \tag{12}$$

Using the data for the loading condition of Fig. 7b and integrating Eqn. (9b) numerically the ratio of the two rates are found to be $\bar{\dot{\varepsilon}}/\bar{\dot{\varepsilon}}_{ss}$= 4.9 which is in close agreement with the experimental value of 3.3. The experimental rate before debond was measured after a plastic strain accumulation of 0.8 %. The plastic strain cause the residual stress state to relax in the matrix and the experimental value can be expected to be lower that the calculated value because the model does not include this relaxation. It is interesting to note that the model predicts a

matrix creep rate that is approximately 50 times higher than the composite creep rate. However, the interaction between the stiff fiber and matrix limits the strain rate of the composite so it is a tenth of the matrix creep rate.

8. CONCLUSIONS

When the composite SCS6/Ti 15-3 is subjected to a combination of constant transverse and cyclic thermal loading it is observed that the transverse strain ratchets continuously with time for some loading conditions. This has also been observed for the composite FP/Al [Jansson and Leckie, 1992a]. In the case of the FP/Al composite the rachetting strain is caused by time independent plasticity resulting from a large thermal mismatch of the alumina fibers and the aluminum matrix. By contrast the thermal mismatch for the SCS6/Ti 15-3 system is modest and it was established that the source of the ratchetting is time dependent creep deformation, which may be predicted using the simple Norton creep law with a temperature dependence of the Arrhenius type.

Debonding occurs during initial loading when the transverse stress is sufficiently high and after an accumulation of creep strain for lower stress levels. For the lower stress levels the debond is associated with a decrease in creep rate. When debond occurs the residual stress field induced during the fabrication is relaxed. The residual stress state in combination with the stresses due to the mechanical loading give rise to a higher creep rate than for pure mechanical loading.

After debond the creep rate of the composite corresponds to that of a matrix with a void fraction equal to the fiber volume fraction. The effective creep rate of the composite is given by a matrix where the fiber locations are regarded as holes. The transverse elastic modulus is also reduced to a third of the initial value .

The sliding resistance determined from push out tests on fibers is also greatly degraded after thermal cycling. This implies that the sliding resistance cannot be controlled in this composite when subjected to operating conditions which causes inelastic deformations.

9. ACKNOWLEDGEMENT

Funding for this work has been provided by NASA Lewis Research Center (NAG3-834) and the DARPA URI at UCSB (ONR N442-2494-23100). The supply of the composite material by Pratt & Whitney West Palm Beach is greatfully acknowledged. Dr. Tom Makin provided invaluable help in conducting the push-through tests.

10. Appendix

A simple model is developed to provide physical insight and which predicts stress and strain histories. The composite is represented by a square element as shown in Fig. 14. The element is subjected to a constant stress $\overline{\sigma}$ in one of the transverse directions and a temperature change to T from a stress free temperature T_c. It is assumed that the stress component in the unloaded transverse direction is zero throughout the element and that the matrix deformation is dictated by the highly stressed ligaments. Constant stress fields are assumed in each of the section of the element. Equilibrium in the loaded transverse direction then requires

$$\overline{\sigma}=(1-\sqrt{f})\sigma_{ym}+\sqrt{f}\,\sigma_{yf} \qquad \textbf{(A1a)}$$

Assuming that the longitudinal stress is constant in the matrix, equilibrium in the longitudinal direction gives

$$\sigma_{zm}(1-f)+\sigma_{zf}f=0 \qquad \textbf{(A1b)}$$

Compatibility in the transverse and longitudinal directions requires

$$\frac{1}{E_m}[\sigma_{ym}-\nu_m\sigma_{zm}]+(\alpha_m-\alpha_f)(T-T_c)=\frac{1}{E_f}[\sigma_{yf}-\nu_f\sigma_{zf}] \qquad \textbf{(A2a)}$$

$$\frac{1}{E_m}[\sigma_{zm}-\nu_m\sigma_{ym}]+(\alpha_m-\alpha_f)(T-T_c)=\frac{1}{E_f}[\sigma_{zf}-\nu_f\sigma_{yf}] \qquad \textbf{(A2b)}$$

The stresses in the matrix are found to be

$$\sigma_{ym}=\frac{1}{D}[A_1\sigma_T+B_1\overline{\sigma}] \tag{A3a}$$

$$\sigma_{zm}=\frac{1}{D}[A_2\sigma_T+B_2\overline{\sigma}] \tag{A3b}$$

where the elastic constants are

$$A_1=-\left[1+\nu_m+\frac{E_m}{E_f}\left(\frac{1-f}{f}+\nu_f\frac{1-\sqrt{f}}{\sqrt{f}}\right)\right] \tag{A4a}$$

$$A_2=-\left[1+\nu_m+\frac{E_m}{E_f}\left[\nu_f\frac{1-f}{f}+\frac{1-\sqrt{f}}{\sqrt{f}}\right]\right] \tag{A4b}$$

$$B_1=\frac{E_m}{E_f\sqrt{f}}\left[1-\nu_m\nu_f+\frac{E_m}{E_f}\left(\frac{1-f}{f}-\nu_f^2\frac{1-\sqrt{f}}{\sqrt{f}}\right)\right] \tag{A4d}$$

$$B_2=\frac{E_m}{E_f\sqrt{f}}\left[\nu_m-\nu_f+\frac{E_m}{E_f}\nu_f\left(\frac{1-f}{f}-\frac{1-\sqrt{f}}{\sqrt{f}}\right)\right] \tag{A4d}$$

$$D=1-\nu_m^2+\frac{E_m}{E_f}(1-\nu_m\nu_f)\left[\frac{\sqrt{f}+f}{f\sqrt{f}}-2\right]+\left(\frac{E_m}{E_f}\right)^2(1-\nu_f^2)\left[1+\frac{1-f-\sqrt{f}}{f\sqrt{f}}\right] \tag{A4e}$$

and

$$\sigma_T = E_m(\alpha_m - \alpha_f)(T - T_c) \qquad \textbf{(A5)}$$

For a temperature change of $T\text{-}T_C$ = -900 C and use of the data given in Table 1 gives the stresses σ_{ym}= 590 MPa and σ_{zm}= 497 MPa. A detailed finite element analysis (Gunawardena et al, 1993) predicted the residual stresses which occur after processing to be σ_{ym} = 500 MPa and σ_{zm} = 400 MPa .The approximate stress predictions are 20 % higher than those of the more precise finite element analysis but should be capable of predicting creep rates within a factor of 2 which is sufficiently close for the purposes of this investigation.

By use of the reciprocity theorem it can be shown that the plastic strains in the matrix are related to the average strain of the composite as

$$d\overline{\varepsilon^p} = \frac{1}{D}[B_1(1-\sqrt{f})\sqrt{f}\, d\varepsilon^p_{ym} + B_2 f d\varepsilon^p_{zm}] \qquad \textbf{(A6)}$$

REFERENCES

Gunawardena, S.R., Jansson, S. and Leckie, F. A., 1993, "Modeling of anisotropic behavior of weakly bonded fiber reinforced MMC's, to appear in Acta Metallurgica.

Hancock, J.W. and Mackenzie, A.C., 1976, "On the mechanisms of ductile failure in high strength steels subjected to multiaxial stress-states ," Journal of the Mechanics and Physics of Solids, vol. 24, pp. 141-169.

Jansson, S., Deve, H.E. and Evans, A.G., 1991, "The anisotropic mechanical properties of a Ti matrix composite reinforced with SiC fibers," Metallurgical Transactions A, vol.22A, pp. 2975-2984.

Jansson, S. and Leckie, F.A., 1992a, "Mechanical behavior of continuous fiber reinforced aluminum matrix composite subjected to transverse and thermal loading," Journal of the Mechanics and Physics of Solids, vol. 40, pp. 593-612.

Jansson, S. and Leckie, F. A., 1992b, "Transverse tensile and inplane shear strength of weakly bonded fiber reinforced MMC's subjected to cyclic thermal loading," Department of Mechanical Engineering, UC Santa Barbara.

Ponter, A.R.S., 1976, " The analysis of cyclically loaded creeping structures for short cycle times," International Journal of solids and structures, vol. 12 , pp. 809-825.

Rice, J.R. and Tracy, D.M. 1969, "On the ductile enlargement of voids in triaxial stress fields", Journal of the Mechanics and Physics of Solids, vol. 17, pp. 201-217.

Rosenberg, H. W., 1983, "Ti-15-3 Property data," in Beta titanium alloys in the 80's, Boyer R.R and Rosenberg, H.W. Eds., AIME.

Tuttle, M.E. and Rogacki, J., 1991, "Thermoviscoplastic response of Ti-15-3 under various loading conditions," NASA CR-187621.

Majumdar, B.S. and Newaz, G.M., 1992, "Inelastic deformation of metal matrix composites: Part II, plasticity and damage at high temperatures," NASA CR-189096.

Table 1. Elastic constants

	E (GPa)	ν	α (1/C)
Matrix	115	.32	$9.6\ 10^{-6}$
Fiber	360	.17	$4.5\ 10^{-6}$

FIGURE CAPTIONS

Fig. 1 Uniaxial stress strain curves for matrix and fiber.

Fig. 2 Experimental transverse stress strain curves for composite before and after thermo-mechanical loading. In the graph are also shown calculate responses for different residual stress states and interface characteristics.

Fig. 3 a) Fracture surfaces of virgin specimen tested at ambient temperature.

b) A high magnification view of the fracture in the matrix ligament.

Fig. 4 a) Fracture surface of specimen subjected to mechanical and cyclic thermal loading.

b) A high magnification view of the fracture in the matrix ligament.

Fig. 5 Experimental setup.

Fig. 6 Recorded temperature distribution in specimen.

Fig. 7 Accumulation of plastic strain:

a) High transverse loading: σ = 200 MPa and ΔT = 380 C

b) Low transverse loading. σ = 50 MPa and ΔT = 420 C

Fig. 8 Strain range as a function of temperature range and transverse loading.

Fig. 9 a) Average steady state strain rate as a function of temperature and transverse loading.

b) Steady state strain accumulation per cycle as a function of temperature and transverse loading.

Fig. 10 Photographs of side surface of specimen after thermo-mechanical testing;

a) Picture showing debond at fiber-matrix interface.

b) Detailed picture showing debonded pultruding fiber.

Fig. 11 Effect of thermal and mechanical fatigue on interfacial sliding resistance.

Fig. 12 Experimentally determined shakedown conditions and calculated elastic shakedown conditions for different interfaces.

Fig. 13 Steady state creep rate for matrix and composite at constant temperature and composite at cyclic temperature.

Fig. 14 Creep rates normalized with use of Equation (4).

Fig. 15 Simplified unit element for composite.

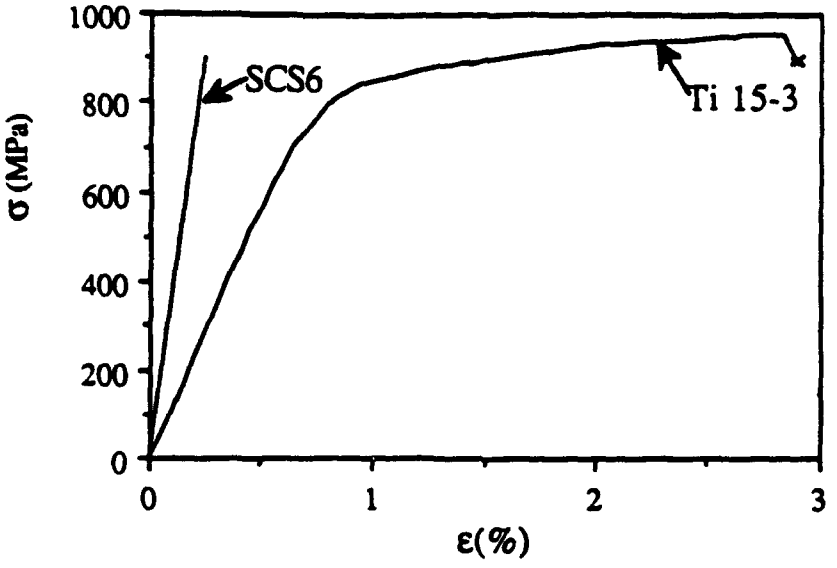

Fig. 1

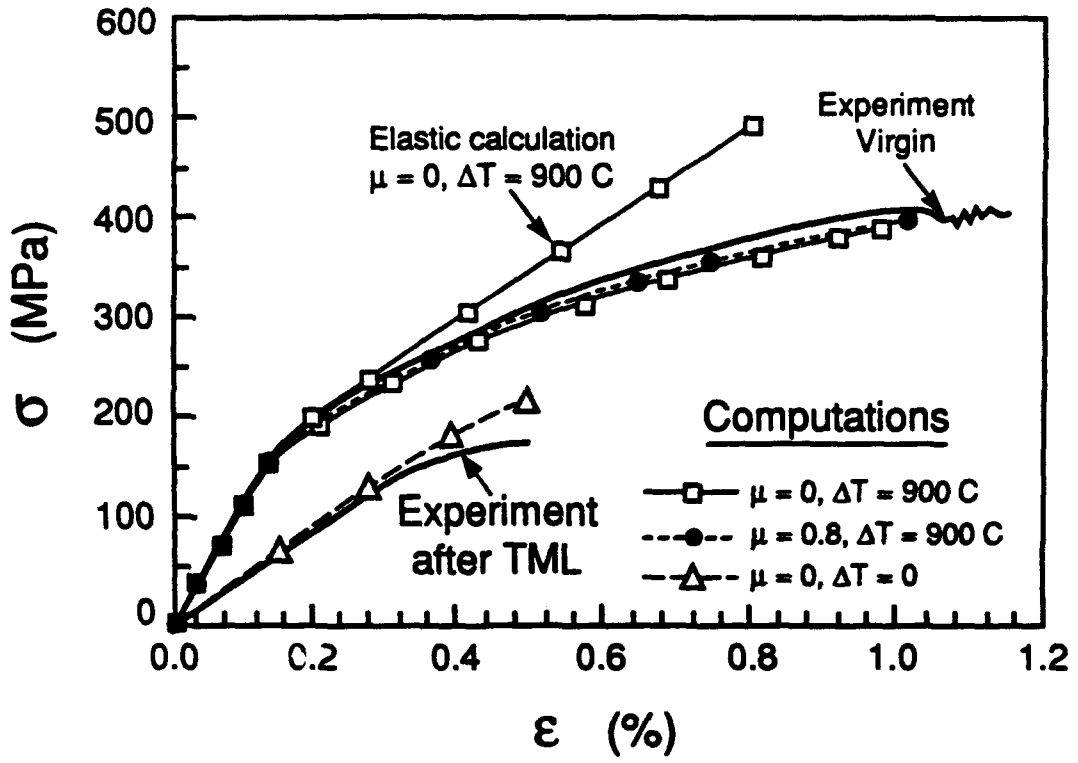
600
500
400
300
200
100
0
σ (MPa)
0.0
0.2
0.4
0.6
0.8
1.0
1.2
ε (%)
Elastic calculation
μ = 0, ΔT = 900 C
Experiment
Virgin
Experiment
after TML
Computations
μ = 0, ΔT = 900 C
μ = 0.8, ΔT = 900 C
μ = 0, ΔT = 0

Fig. 2

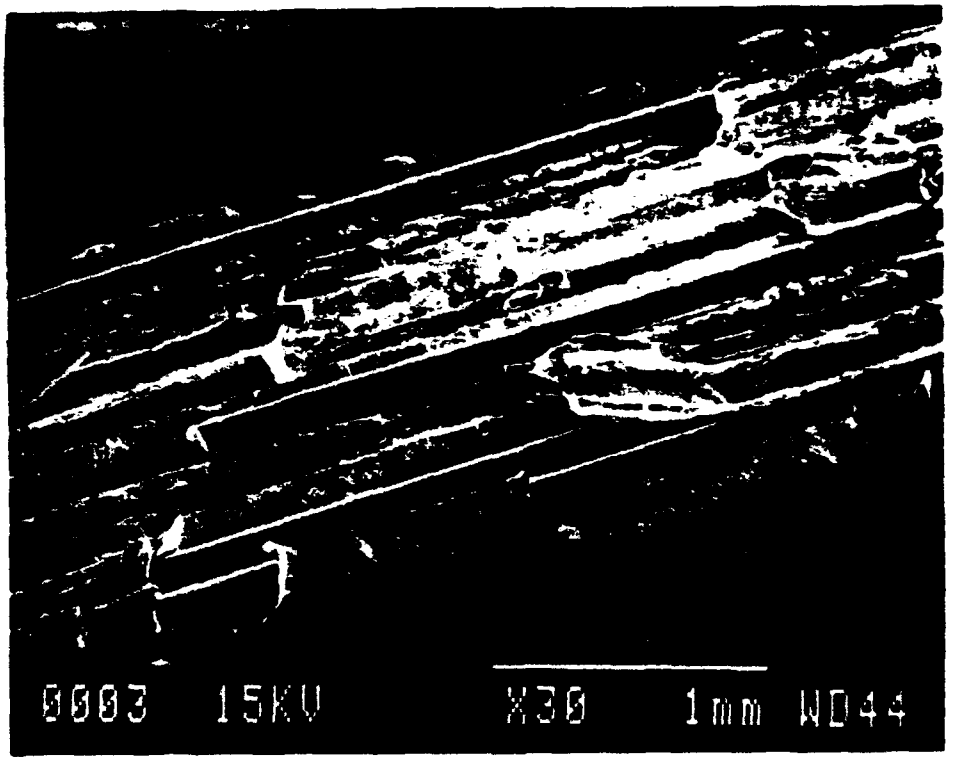

Fig. 3a

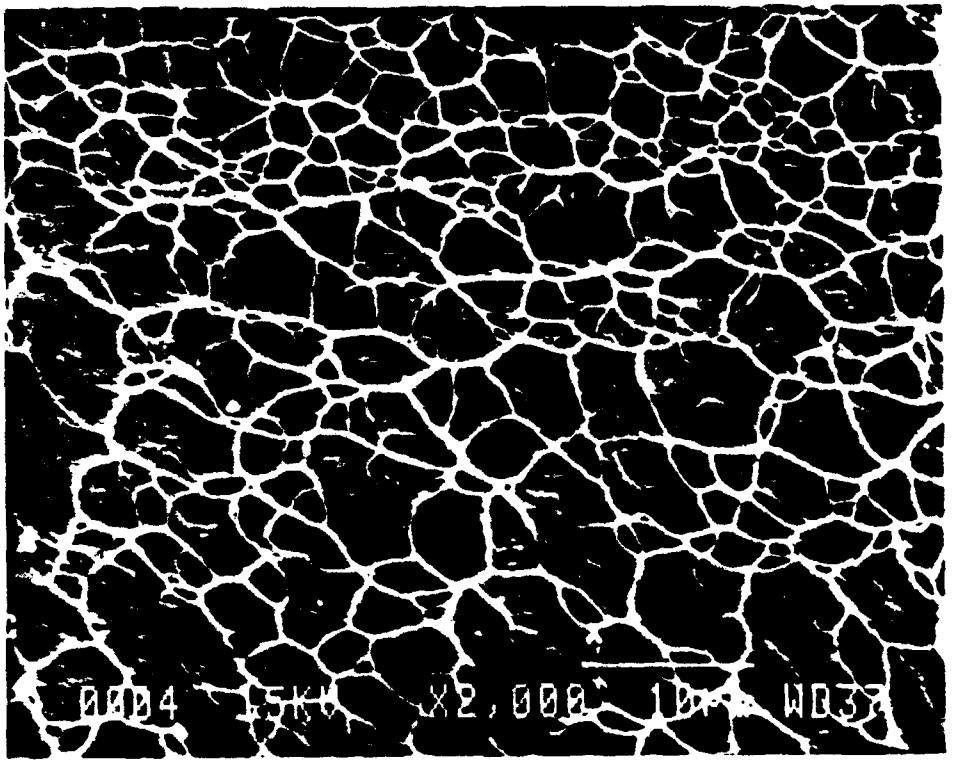

Fig. 3b

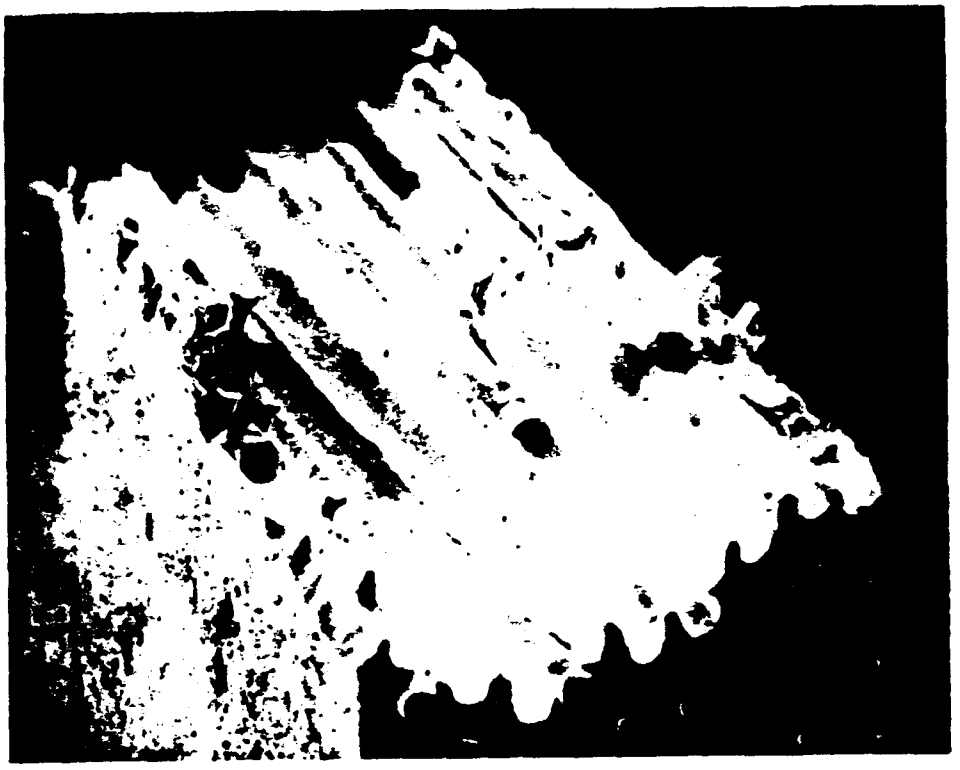

Fig. 4a.

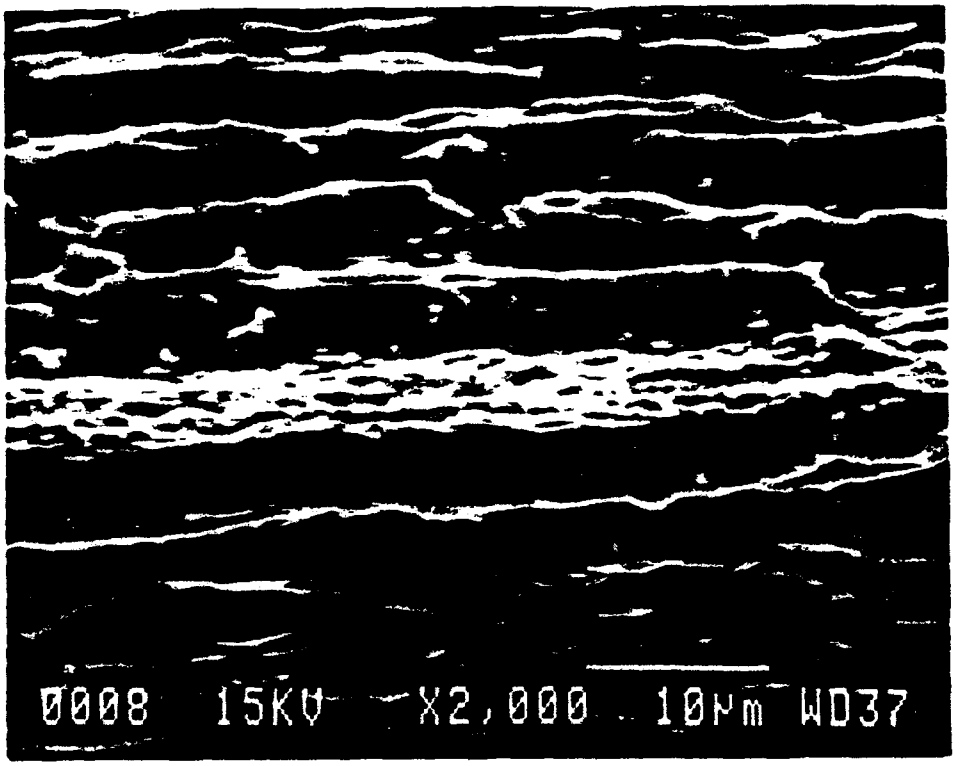

Fig. 4b.

EXPERIMENTAL PROGRAM

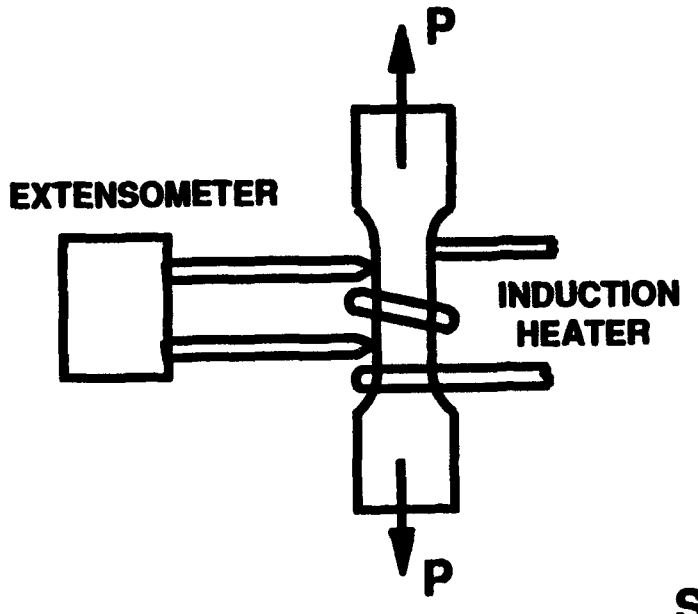

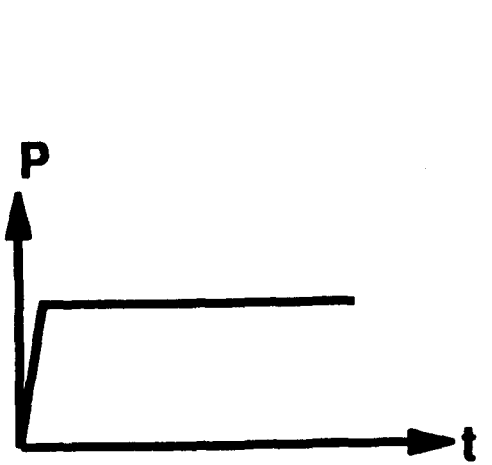

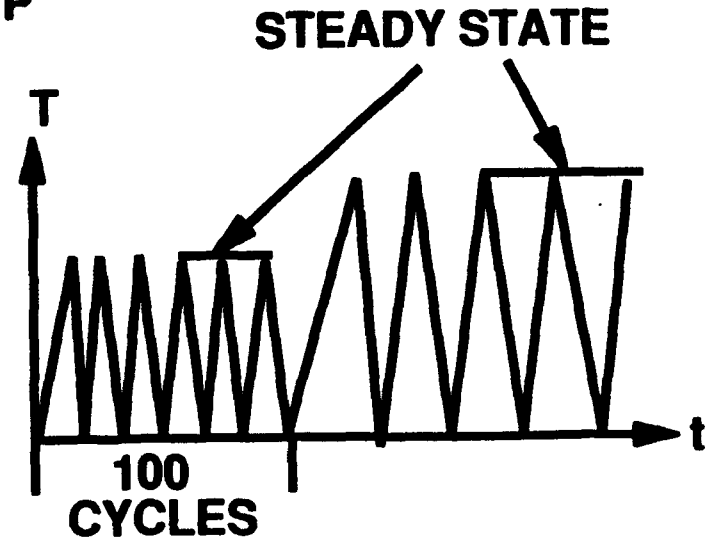

Fig. 5

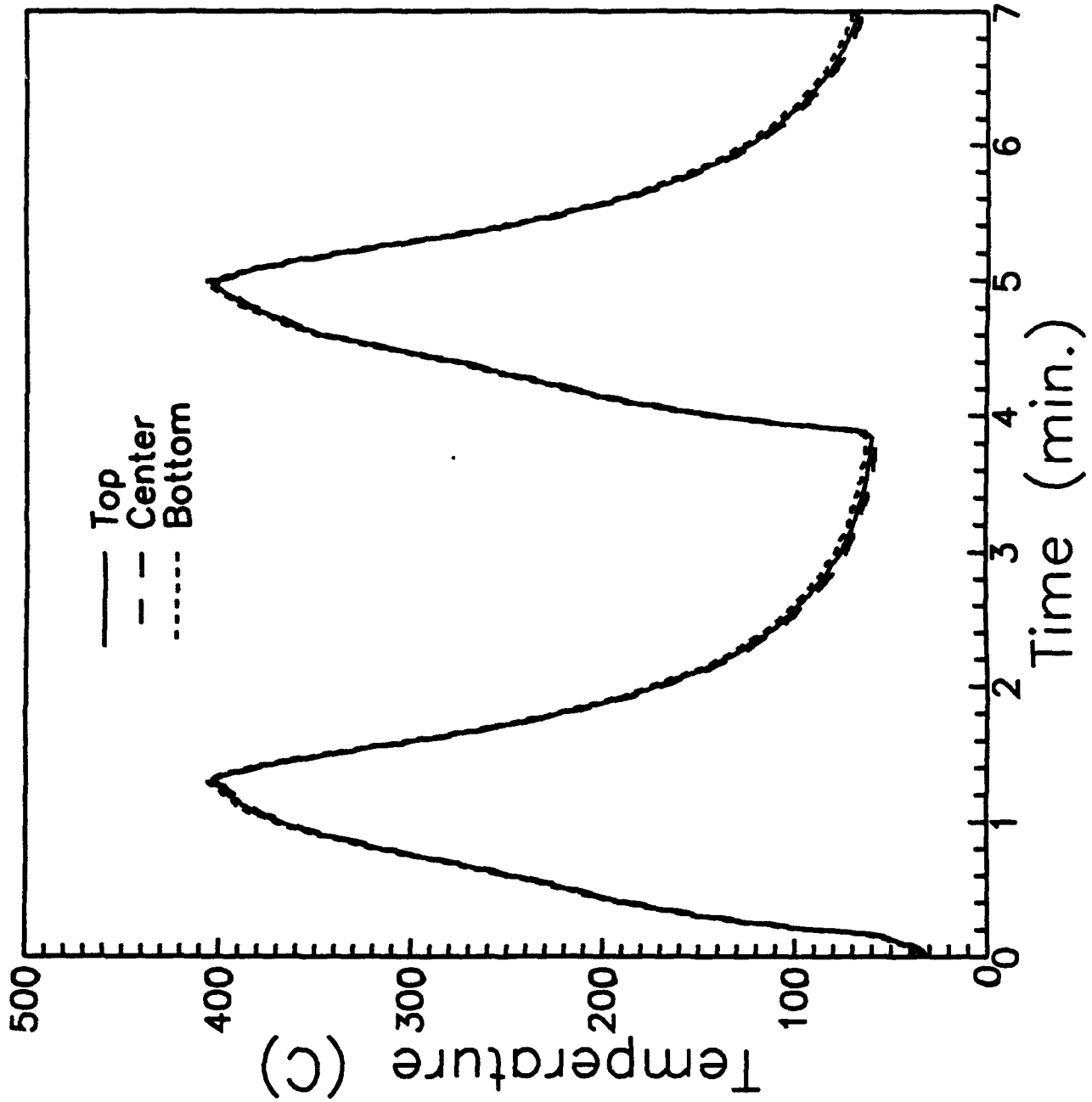
Temperature (C)
500
400
300
200
100
0
0
1
2
3
4
5
6
7
Time (min.)
Top
Center
Bottom

Fig. 6

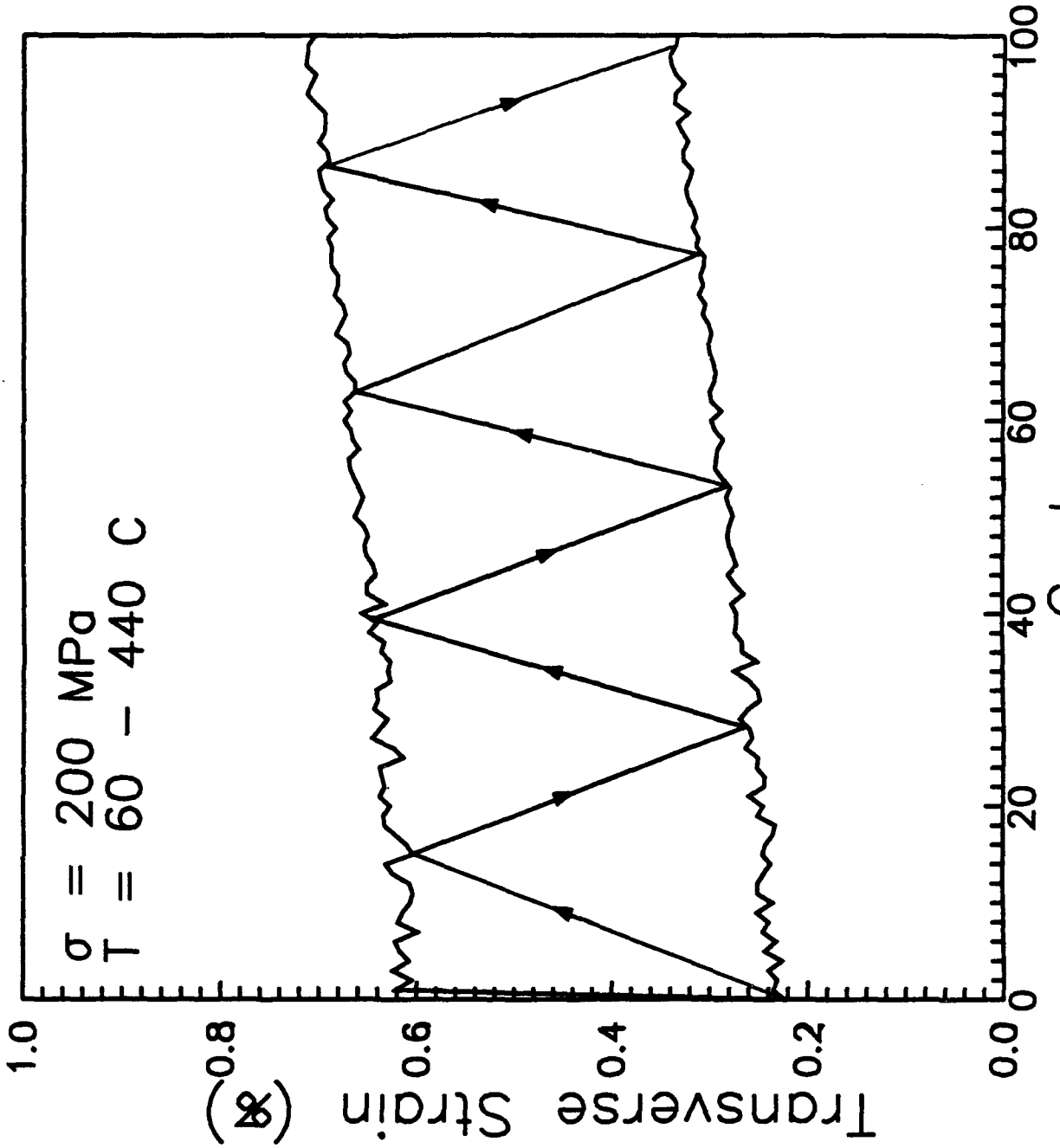
σ = 200 MPa
T = 60 – 440 C
Transverse Strain (%)
Cycles
1.0
0.8
0.6
0.4
0.2
0.0
0
20
40
60
80
100

Fig. 7a

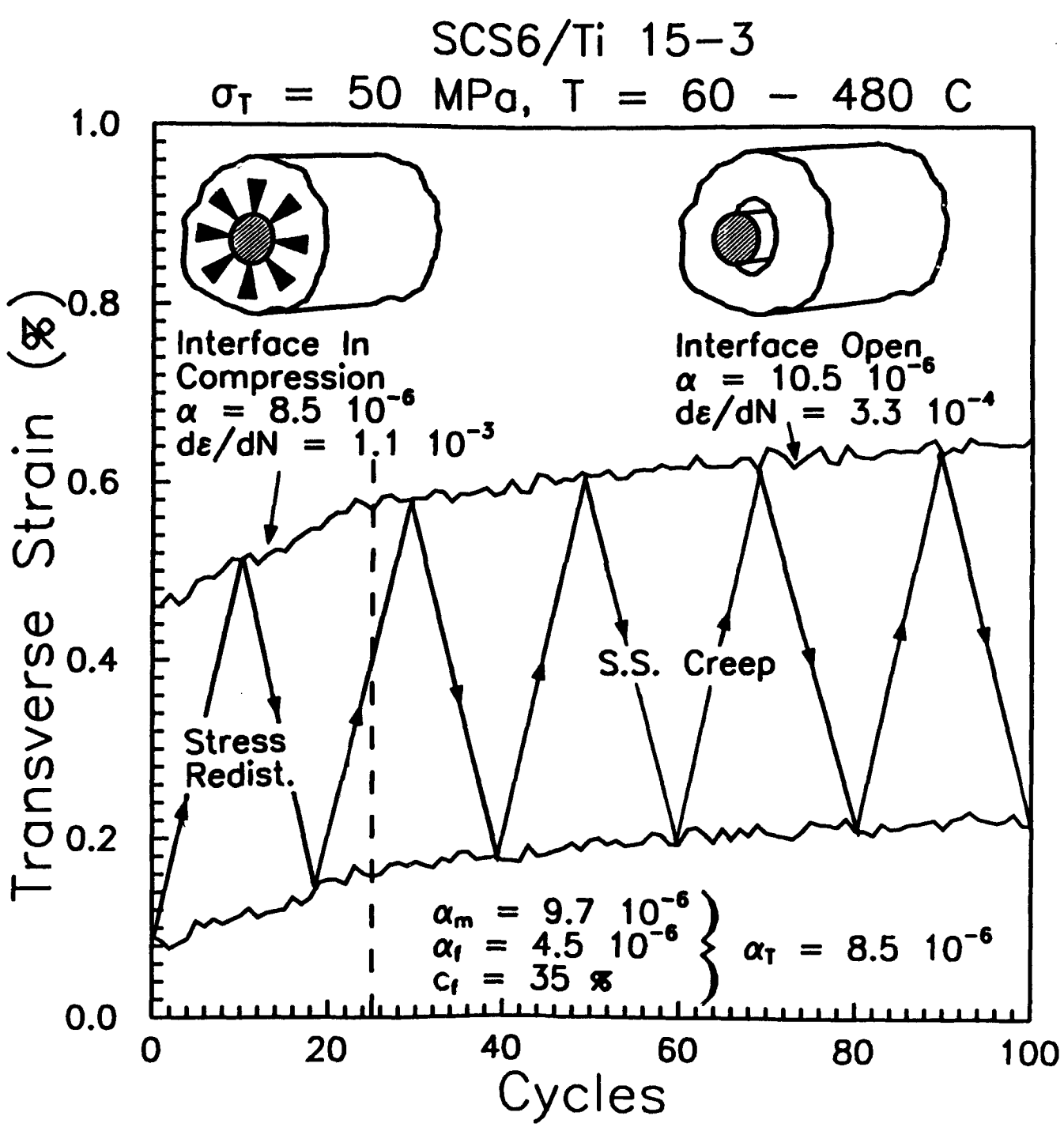
SCS6/Ti 15-3
σ_T = 50 MPa, T = 60 - 480 C
Transverse Strain (%)
1.0
0.8
0.6
0.4
0.2
0.0
0
20
40
60
80
100
Cycles
Interface In Compression
α = 8.5 10^{-6}
$d\varepsilon/dN$ = 1.1 10^{-3}
Interface Open
α = 10.5 10^{-6}
$d\varepsilon/dN$ = 3.3 10^{-4}
S.S. Creep
Stress Redist.
α_m = 9.7 10^{-6}
α_f = 4.5 10^{-6}
c_f = 35 %
α_T = 8.5 10^{-6}

Fig. 7b

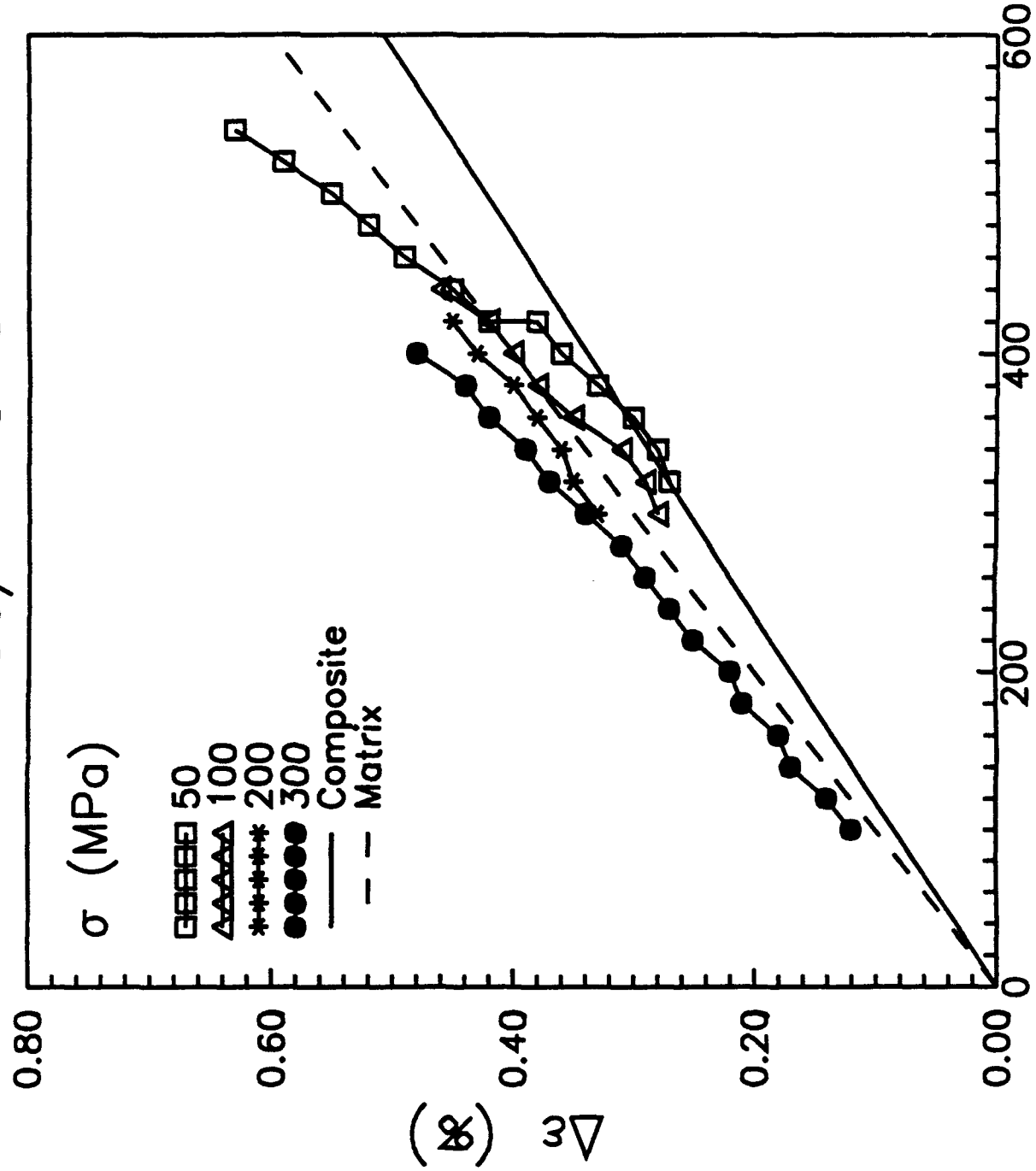
SCS6/Ti 15-3
σ (MPa)
50
100
200
300
Composite
Matrix
0.80
0.60
0.40
0.20
0.00
0
200
400
600
ΔT (C)
Δε3 (%)

Fig. 8

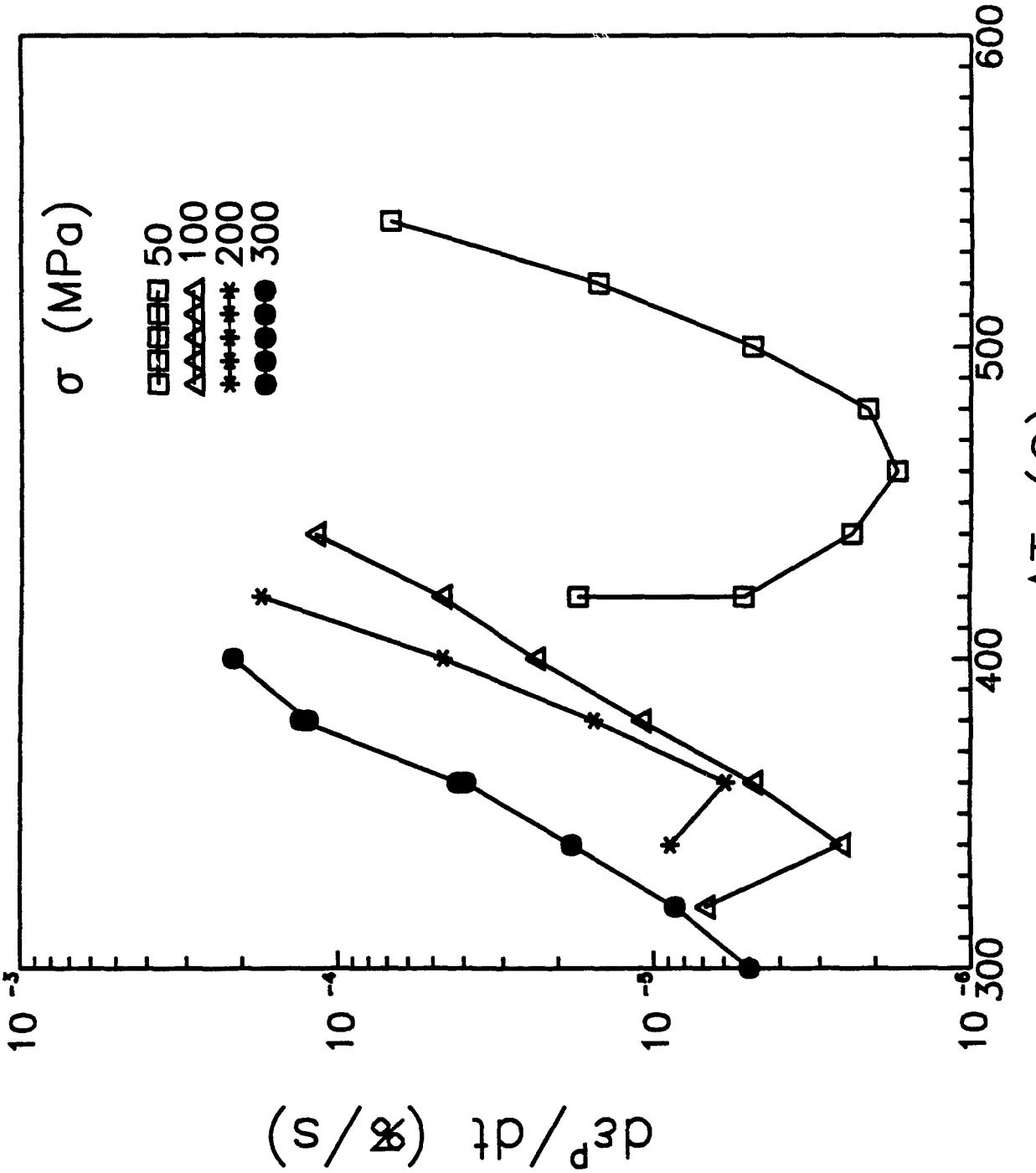
σ (MPa)
50
100
200
300
10^{-3}
10^{-4}
10^{-5}
10^{-6}
300
400
500
600
ΔT (C)
$d\varepsilon^p/dt$ (%/s)

Fig. 9a

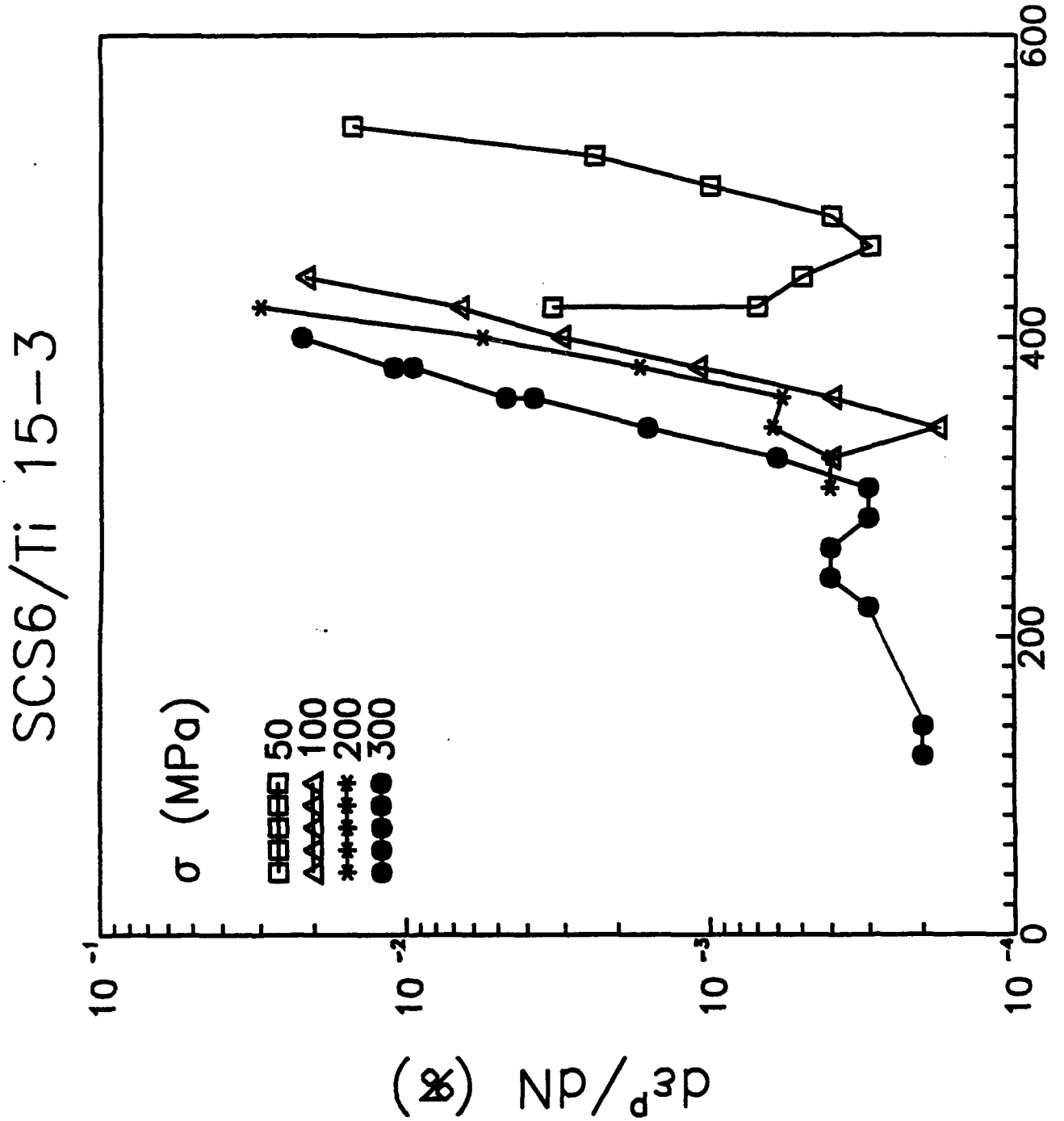
SCS6/Ti 15-3
σ (MPa)
50
100
200
300
ΔT (C)
0
200
400
600
10 -1
10 -2
10 -3
10 -4
(%) NP/d3p

Fig. 9b

Fig. 10a

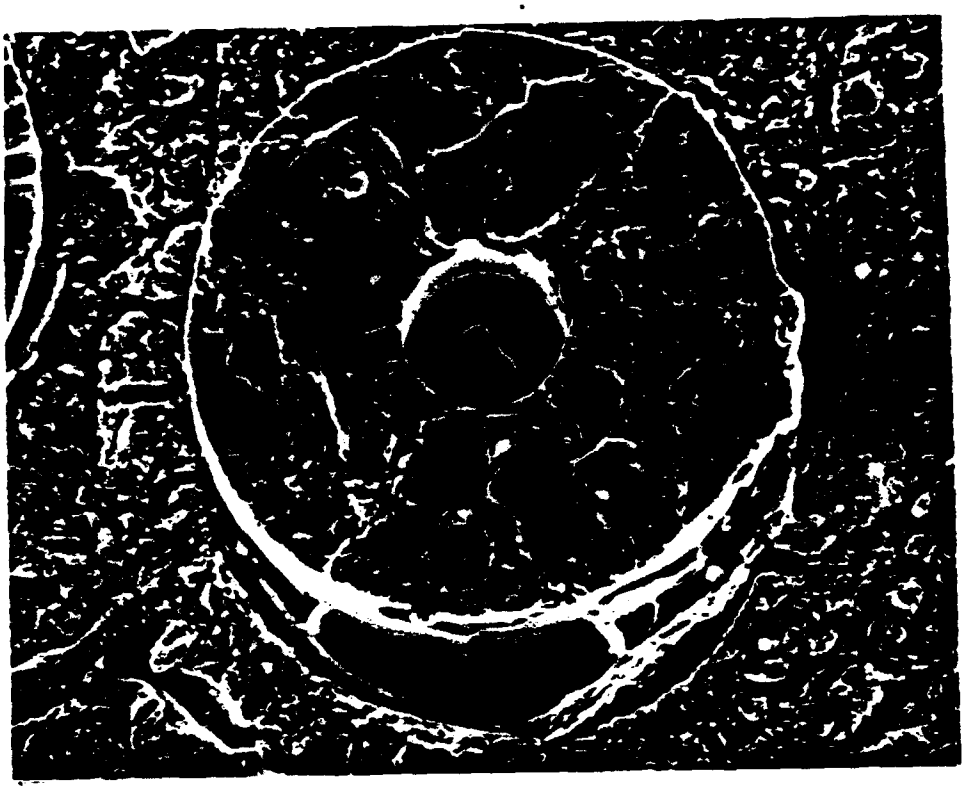

Fig. 10b

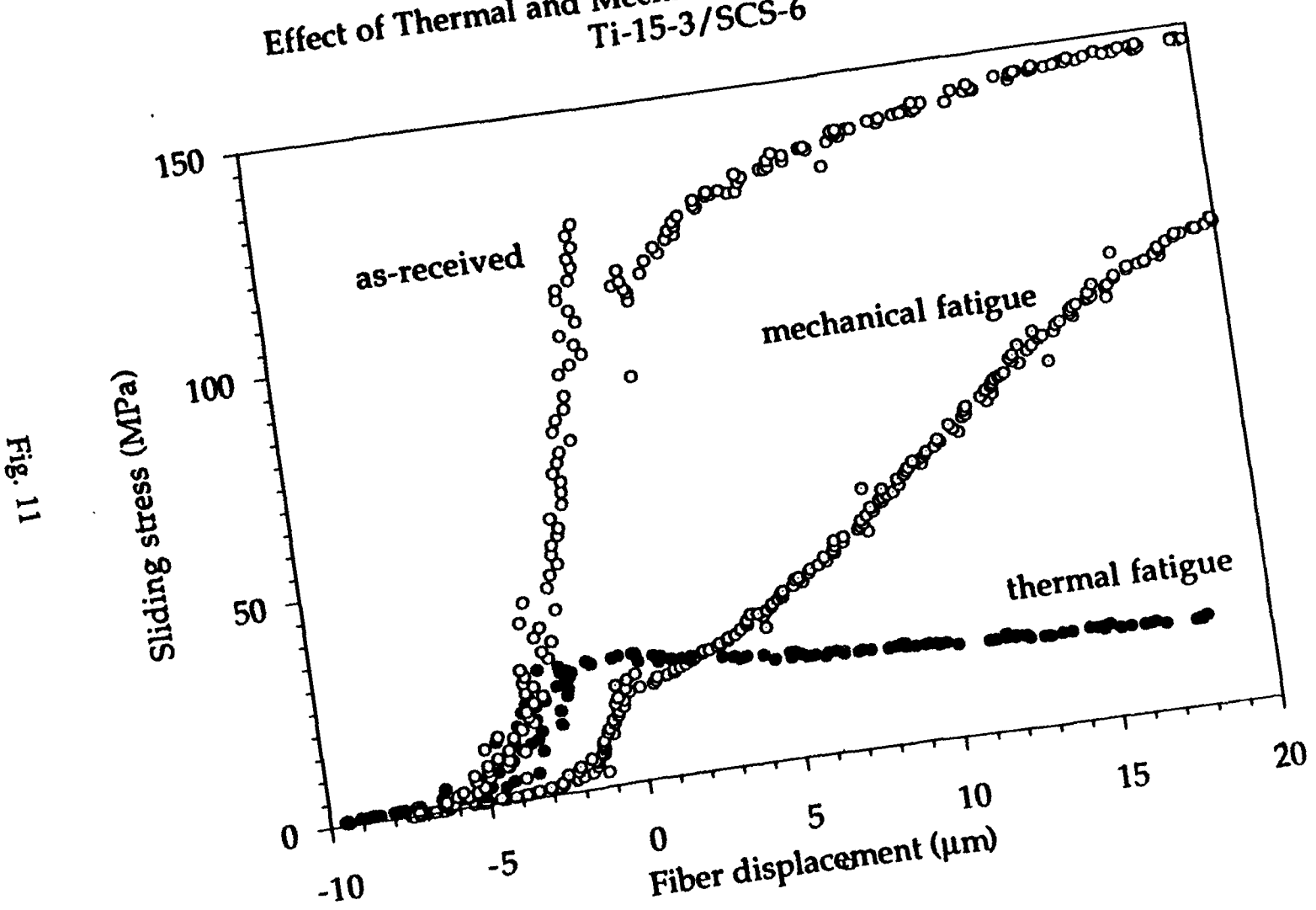
Effect of Thermal and Mechanical Fatigue on Sliding Stress
Ti-15-3/SCS-6
as-received
mechanical fatigue
thermal fatigue
Sliding stress (MPa)
150
100
50
0
-10
-5
0
5
10
15
20
Fiber displacement (μm)

Fig. 11

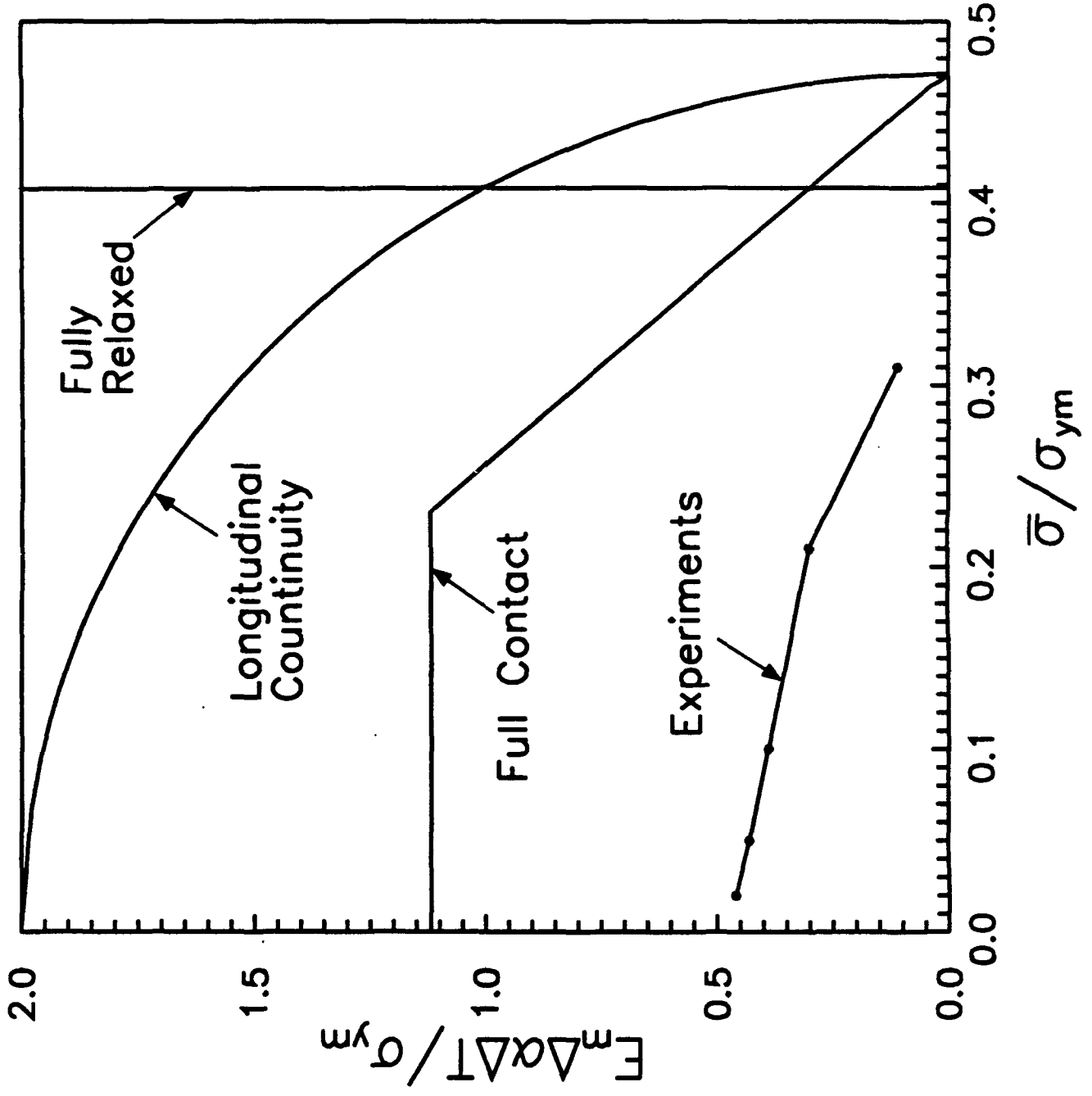
Fully Relaxed
Longitudinal Countinuity
Full Contact
Experiments
$E_m \Delta\alpha\Delta T / \sigma_{ym}$
$\bar{\sigma} / \sigma_{ym}$
2.0
1.5
1.0
0.5
0.0
0.0
0.1
0.2
0.3
0.4
0.5

Fig. 12

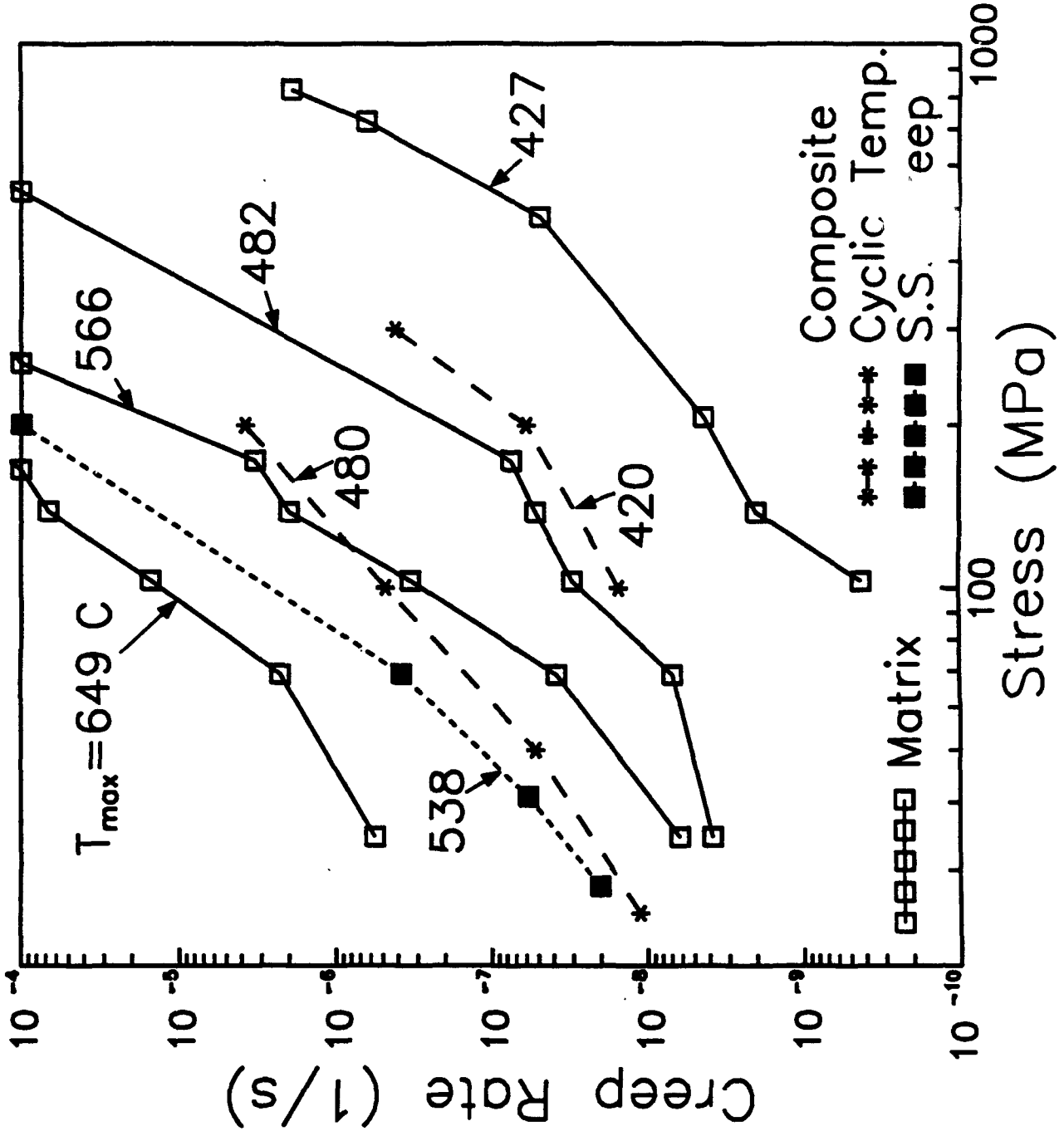
Creep Rate (1/s)
Stress (MPa)
100
1000
Composite
Cyclic Temp.
S.S. Creep
Matrix
T_{max}=649 C
566
482
480
427
420
538

Fig. 13

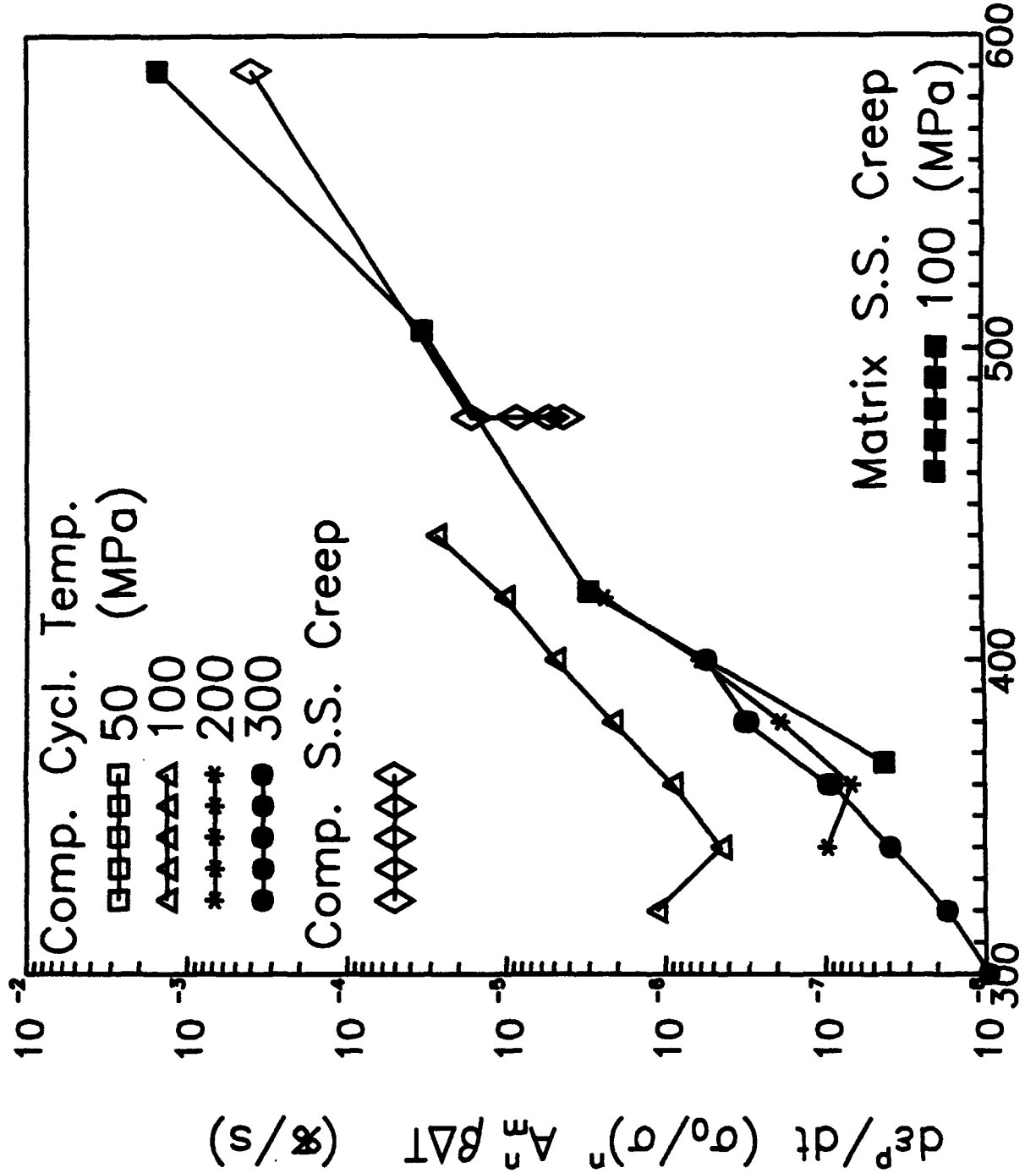
Comp. Cycl. Temp.
50 (MPa)
100
200
300
Comp. S.S. Creep
Matrix S.S. Creep
100 (MPa)
T_{max} (C)
$de^p/dt\ (\sigma_0/\sigma)^n\ A\sigma^n\ \beta\Delta T$ (%/s)

Fig. 14

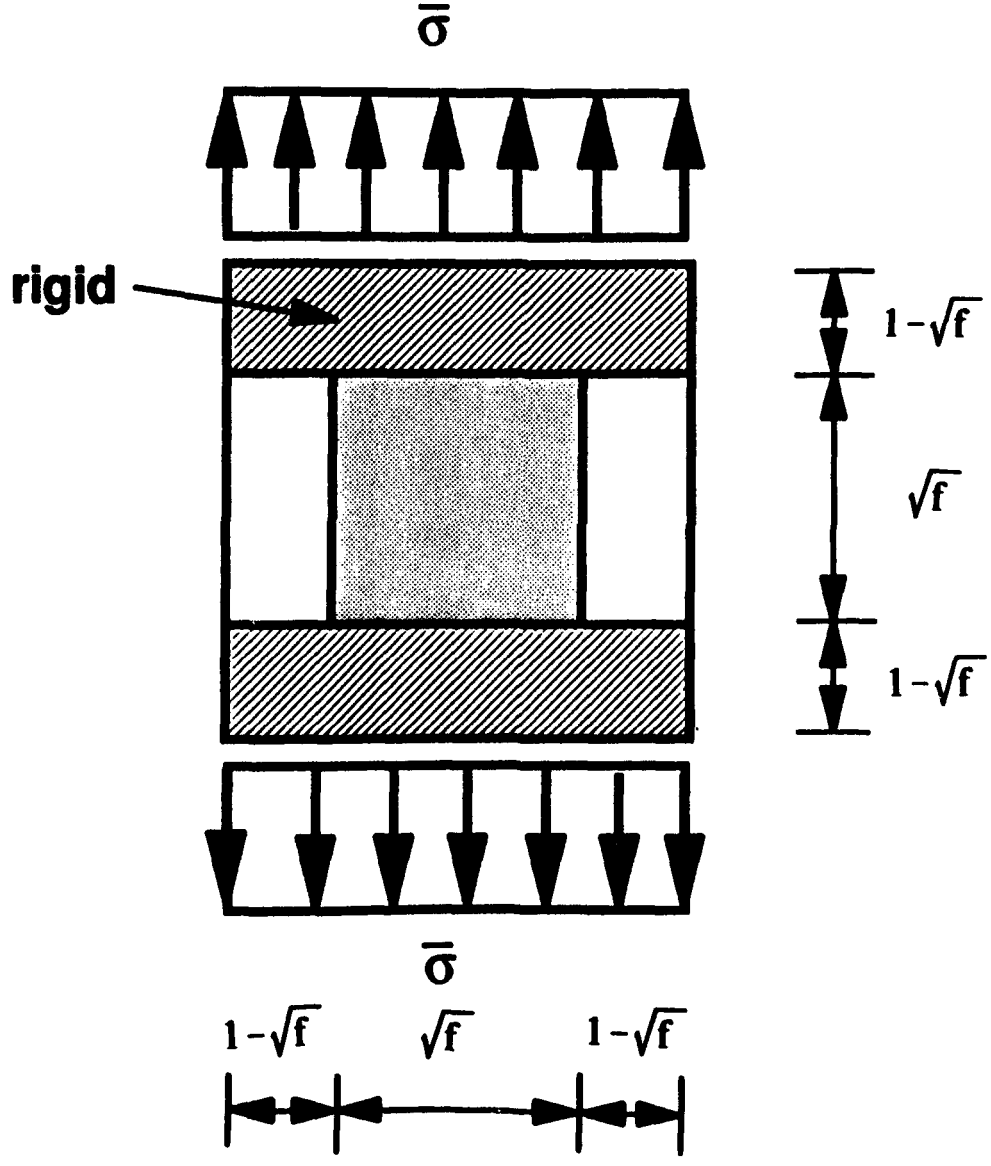
$\bar{\sigma}$
rigid
$1-\sqrt{f}$
$\sqrt{f}$
$1-\sqrt{f}$
$\bar{\sigma}$
$1-\sqrt{f}$
$\sqrt{f}$
$1-\sqrt{f}$

Fig. 15

MATERIALS

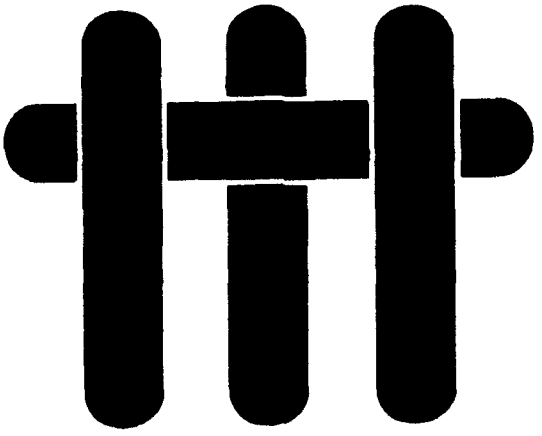

FATIGUE OF CERAMIC MATRIX COMPOSITES

by

A.G. Evans, F.W. Zok and R.M. McMeeking
Materials Department and
Mechanical Engineering Department
College of Engineering
University of California, Santa Barbara
Santa Barbara, California 93106–5050

7H:MS33a(December 29, 1993)4:33 PM/mef

TABLE OF CONTENTS

ABSTRACT

Fatigue in ceramic matrix composites typically occurs when matrix cracks are present by cyclic degradation of the sliding resistance of the interface. The basic mechanisms are discussed and a methodology is developed that enables fatigue life predictions to be made, based on a minimum number of experimental measurements. The methodology relies on analysis of hysteresis loops. Changes in modulus upon cyclic loading as well as the permanent strains are predicted, as well as the fatigue threshold and the S-N curve.

1. INTRODUCTION

Ceramic matrix composites (CMCs) are subject to fatigue upon cyclic mechanical and thermal loading (Holmes, 1993; Zawada and Butkus, 1991; Butkus and Holmes, 1992; Allen *et al.*, 1991; Minford and Prewo, 1987; Rousseau, 1990; Rouby and Reynaud, 1993). Understanding the mechanisms of fatigue represents an important step in the use of these materials. This article provides a review which describes fundamental mechanisms, gives predictions of fatigue damage and relates predictions to experimental measurements.

Various observations and measurements provide the background needed to establish the mechanisms. Three phenomena are consistently present upon cyclic loading of CMCs (Fig. 1.1). Fatigue occurs in accordance with a classical S-N curve subject to a definite threshold σ_{th}. The secant modulus decreases as fatigue proceeds. There are corresponding permanent deformations.

For fatigue to occur, matrix cracks must be present after the first cycle. In consequence, fatigue only arises at stresses that exceed the matrix cracking strength, designated σ_{mc} (Fig. 1.1). Moreover, the fatigue threshold, σ_{th}, is always considerably larger than σ_{mc}. The cyclic opening and closing of these cracks provides the basic fatigue *mechanisms*. The fundamental fatigue model requires that the fiber/matrix interfaces debond and slide as the matrix cracks cycle, manifest as hysteresis loops (Fig. 1.2). An understanding of hysteresis is central to the modelling and prediction of fatigue. There are three possible mechanisms. (i) Changes in the interface sliding resistance may occur upon cycling, with corresponding changes in hysteresis (Fig. 1.3). (ii) The strength of the fibers may be degraded by cyclic sliding along the interface by means of an abrasion mechanism, which introduces flaws in the fibers. (iii) Fatigue crack growth occurs in the matrix itself in accordance with a Paris Law. These three mechanisms are compatible with the fatigue behavior found in high-toughness,

monolithic ceramics, such as Si_3N_4, in which crack face bridging tractions are diminished by cyclic loading (Lathabai et al. 1991; Röedel et al. 1990; Guiu et al. 1992).

For many CMCs, there is no fatigue mechanism operating in the matrix itself, because the matrices have low-toughness. For these composites, either interface or fiber degradation dictate fatigue. When ceramic fibers are used (rather than C), interface degradation is the dominant fatigue mechanism. This mechanism is emphasized in the present article. As the sliding stress τ diminishes upon cycling, the inelastic strain and the ultimate tensile strength (UTS) are affected. The inelastic strain *increases*, because the interface sliding distances increase leading to both a reduction in the secant modulus and a permanent strain. Conversely, the UTS *decreases*, because the effective fiber gauge length operating within the composite increases as τ decreases. This leads to enhanced fiber bundle failures and a classical S-N curve. Matrix cracking and load sharing models are used to predict the fatigue behavior, subject to cyclic interface degradation.

2. THE INTERFACE MODEL

2.1 Basic Model

When matrix cracks are present, large shear stresses are imposed onto the coating between the intact fibers and the matrix. These stresses elicit responses that control the inelastic deformation and the fatigue of CMCs. The first interface event to occur is fracture, or debonding (Hutchinson and Jensen, 1990; Charalambides and Evans, 1989; Gao et al., 1988). Since most CMCs have fibers subject to residual compression, the debond is a mode II (shear) crack that extends either within the coating are at one of the interfaces. Debonding occurs with an energy dissipation per unit area, designated Γ_i. Behind the debond front, the crack faces are in contact, especially at undulations along the fiber (Fig. 2.1). Coulomb friction operates at these contacts, resulting in a sliding

resistance, τ. The thermomechanical properties of interfaces in CMCs are characterized by a combination of Γ_i and τ.

Mode II crack growth within such a thin brittle layer occurs by the formation and coalescence of an array of microcracks, *en echelon* (Fig. 2.2). Generally, the microcracks develop with a spacing that scales within the layer thickness, such that the debond energy is proportional to the intrinsic fracture energy of the coating material itself, Γ_{co}, (Xia and Hutchinson, 1993a),

$$\Gamma_i \approx 4\Gamma_{co} \tag{2.1}$$

Sliding behind the debond front is sensitive to the residual stress, the amplitude of undulations that occur along the fiber, and the friction coefficient. The simplest model is based on a unit cell containing a fiber with circumferential roughness having amplitude, H, and wavelength, L (Fig. 2.1). When the fiber rigidly displaces by L/2, the matrix must displace outward to its maximum extent in order to allow continued sliding of the fiber. The sliding stress may be estimated by analysis of this situation (Liang and Hutchinson, 1993; Kerans et al., 1992; Mackin et al., 1992). The outward elastic displacement of the matrix cylinder, u_m, due to an average interface pressure, p_i, is given by,

$$u_m = p_i \frac{R}{E_m}\left[\frac{1+f}{1-f} + \nu_m\right] \tag{2.2}$$

where R is the fiber radius, E_m the matrix modulus, f the fiber volume fraction and ν_m the matrix Poisson's ratio. The inward elastic displacement of the fiber caused by the same average pressure is

$$u_f = \frac{p_i R}{E_f} \tag{2.3}$$

There is also an elastic contraction of the fiber, caused by the axial fiber strain, ε_f

$$u_v = \nu_f \varepsilon_f \tag{2.4}$$

where ν_f is the Poisson's ratio of the fiber. The total elastic displacement of matrix and fiber must balance the misfit displacement, as modified by *elastic flattening* of the asperities (Liang and Hutchinson, 1993). The misfit displacement is

$$u = R\varepsilon_T + H \tag{2.5}$$

where ε_T is the misfit strain due to differences in the thermal expansion coefficient. Combining Eqns. (2.3) to (2.5) and neglecting the elastic flattening, the average interface pressure becomes,

$$p_i \approx \frac{E_f\left[\varepsilon_T + H/R - \nu_f \varepsilon_f\right]}{1+\left(E_f/E_m\right)\left[(1+f)/(1-f)+\nu_m\right]} \tag{2.6}$$

The sliding stress is related to this average pressure by a Coulomb friction law

$$\tau \sim \mu p_i \tag{2.7}$$

where the proportionality depends on the number of contact points per unit interface area between the fiber and the matrix. The final result is

$$\tau = \mu\left[\varepsilon_T + H/R - \nu_f \varepsilon_f\right]\xi_* \tag{2.8}$$

where ξ_* is a parameter that depends on the elastic properties and the fiber concentration. Interface sliding in CMCs has been understood through these three strain terms, associated with thermal expansion misfit, roughness and Poisson's contraction, respectively.

2.2 Interface Wear

Upon cyclic loading, when matrix cracks are present, the matrix slides past the intact fibers. These sliding displacements change τ and, in consequence, cause further debonding. It has been suggested (McNulty et al., 1993) that the changes in τ be represented by,

$$(\tau - \tau_o)/(\tau_s - \tau_o) = 1 - \exp(-\omega N^{\lambda}) \tag{2.9}$$

where τ_o is the initial value in the first cycle, τ_s is a steady-state value, and ω and λ are numerical coefficients. These reductions in τ are attributed to 'wear' mechanisms operating in the fiber coating (Fig. 2.1), especially at those contacts subject to high pressure. Evidence that a reduction in the height of asperities occurs along the fiber coating has been presented for the analogous problem of fatigue in Ti MMCs (Walls et al., 1992). Related effects probably occur in CMCs, but direct observations have yet to be performed. The 'wear' process is facilitated by the temperature rise that occurs along the interface, as frictional dissipation proceeds. At high frequencies, the increase in temperature can be large enough to oxidize the fiber coating, even though the ambient is at room temperature (Holmes and Cho, 1992). When the fiber coating is C, it reacts to form CO, resulting in a large reduction in τ.

A model that predicts changes in τ with cycling would require a mechanism that reduces the roughness parameters in the sliding model, based on the sliding displacements that occur and the temperature reached. Some simple wear concepts provide insight about the roles of the strain amplitude, $\Delta\sigma$, and temperature amplitude, ΔT.

The basic formula that characterizes adhesive wear, relates the thickness of material removed, Δh, to the sliding displacement ℓ by (Archard, 1953)

$$\Delta h = k\ell \tag{2.10}$$

where k is a coefficient that depends on yield strength. The maximum distance moved is related to the change in crack opening displacement per cycle $\Delta\delta$ by

$$\ell \sim 2N\Delta\delta \tag{2.11}$$

where N is the number of cycles. When the debond energy is small, $\Delta\delta$ is given by (McMeeking and Bao, 1993),

$$\Delta\delta = \left(\Delta\sigma + fE_f\Delta\alpha\Delta T\right)^2 \rho \tag{2.12}$$

where $\Delta\sigma$ is the stress amplitude, ΔT the temperature amplitude and ρ is a coefficient. The extent of the wear thus scales as,

$$\Delta h \sim k\rho N\left(\Delta\sigma + fE_f\Delta\alpha\Delta T\right)^2 \tag{2.13}$$

The effect can be characterized by first establishing the isothermal behavior at a reference stress amplitude $\Delta\sigma_o$,

$$\Delta h_o \sim k \rho N_o \Delta \sigma_o^2 \tag{2.14}$$

Thus, for a general thermomechanical cycle,

$$\frac{\Delta h}{\Delta h_o} = \left[\frac{\Delta\sigma + f E_f \Delta\alpha \Delta T}{\Delta \sigma_o}\right]^2 \frac{N}{N_o} \tag{2.15}$$

This result provides some insight about coupling effects between the stress, the temperature amplitude and the number of cycles. The reduction in the roughness H by Δh would have a direct effect on τ, in accordance with Eqn. (2.8).

3. FIBER PROPERTIES

3.1 Load Sharing

The strength properties of fibers are *statistical* in nature. Consequently, it is necessary to apply principles of weakest link statistics, which define the properties of fibers *within a composite.* The initial decision to be made concerns the potential for interactions between failed fibers and matrix cracks. It has generally been assumed that matrix cracks and fiber failure are non-interacting and that global load sharing (GLS) conditions obtain* (Curtin, 1991; Phoenix and Raj, 1992, Hild *et al.*, 1993). In this case, the stress along a material plane that intersects a failed fiber is equally distributed among all of the intact fibers. Experience has indicated that these assumptions are essentially valid for a variety of CMCs.

---

* However, a criterion for GLS breakdown has yet to be devised.

Subject to the validity of GLS, several key results have been derived. Two characterizing parameters emerge (Henstenburg and Phoenix, 1989): a characteristic length

$$\delta_c^{m+1} = L_o\left[S_o R/\tau\right]^m \tag{3.1}$$

and a characteristic strength

$$S_c^{m+1} = S_o^m\left[L_o \tau/R\right] \tag{3.2}$$

where m is the shape parameter, S_o the scale parameter and L_o the reference length. Various GLS results based on these parameters are described below.

When fibers do not interact, analysis begins by considering a fiber of length 2L divided into 2N elements, each of length δz. The probability that fiber element will fail, when the stress is less than σ, is the area under the probability density curve (Matthews *et al.*, 1976; Freudenthal, 1967)

$$\delta\phi(\sigma) = \frac{\delta z}{L_0}\int_0^{\sigma} g(S)dS \tag{3.3}$$

where $g(S)dS/L_0$ represents the number of flaws per unit length of fiber having a 'strength' between S and S + dS. The local stress, σ, is a function of both the distance along the fiber, z, and the *reference* stress, $\bar{\sigma}_b$. The survival probability P_s for *all elements* in the fiber of length 2L is the product of the survival probabilities of each element (Daniels, 1945),

$$P_s(\bar{\sigma}_b, L) = \prod_{n=-N}^{N}\left[1 - \delta\phi(\bar{\sigma}_b, z)\right] \tag{3.4}$$

where $z = n\delta z$ and $L = N\,\delta z$. Furthermore, the probability Φ_S that the element at z will fail when the peak, reference stress is between $\bar{\sigma}_b$ and $\bar{\sigma}_b + \delta\bar{\sigma}_b$, *but not when the stress is less than* $\bar{\sigma}_b$, is the change in $\delta\phi$ when the stress is increased by $\delta\bar{\sigma}_b$ divided by the survival probability up to σ_b, given by (Matthews *et al.*, 1976; Freudenthal, 1967; Oh and Finnie, 1970)

$$\Phi_s(\bar{\sigma}_b, z) = \left[1-\delta\phi(\bar{\sigma}_b, z)\right]^{-1}\left[\frac{\partial\delta\phi(\bar{\sigma}_b, z)}{\partial\bar{\sigma}_b}\right]d\bar{\sigma}_b. \tag{3.5}$$

Denoting the probability density function for fiber failure by $\Phi(\bar{\sigma}_b, z)$, the probability that fracture occurs at a location z, when the peak stress is $\bar{\sigma}_b$, is governed by the probability that all elements *survive up to a peak stress* $\bar{\sigma}_b$, but that failure occurs, at z, when the stress reaches $\bar{\sigma}_b$ (Thouless and Evans, 1988; Oh and Finnie, 1970). It is given by the product of Eqn. (3.4) with Eqn. (3.5)

$$\Phi_s(\bar{\sigma}_b, z)\delta\bar{\sigma}_b\delta z = \frac{\prod_{-N}^{N}\left[1-\delta\phi(\bar{\sigma}_b, z)\right]}{\left[1-\delta\phi(\bar{\sigma}_b, z)\right]}\left[\frac{\partial\delta\phi(\bar{\sigma}_b, z)}{\partial\bar{\sigma}_b}\right]d\bar{\sigma}_b. \tag{3.6}$$

While the above results are quite general, it is convenient to use a power law to represent g(S),

$$\int_0^{\sigma} g(S)dS = (\sigma/S_0)^m. \tag{3.7}$$

Alternative representations of g(S) are not warranted at the present level of development. Using this assumption, Eqn. (3.6) becomes (Thouless and Evans, 1988)

$$\Phi(\bar{\sigma}_b, z) = \exp\left\{-2\int_0^L \left[\frac{\sigma(\bar{\sigma}_b, z)}{S_0}\right]^m \frac{dz}{L_0}\right\} \left(\frac{2}{L_0}\right) \frac{\partial}{\partial \bar{\sigma}_b} \left[\frac{\sigma(\bar{\sigma}_b, z)}{S_0}\right]^m . \quad (3.8)$$

This basic result has been used to obtain solutions for several problems (Thouless and Evans, 1988; Sutcu, 1989; Curtin, 1991).

3.2 The Ultimate Tensile Strength

When multiple matrix cracking precedes failure of the fibers in the 0° bundles, the load along each matrix crack plane is borne entirely by the fibers. *Nevertheless, the matrix has a crucial role,* because stress transfer between the fibers and the matrix still occurs through the sliding resistance, τ. Consequently, some stress can be sustained by the failed fibers. This stress transfer process occurs over a distance related to the characteristic length, δ_c. As a result, the stresses on the intact fibers along any plane through the material are less than those experienced within a 'dry' fiber bundle (in the absence of matrix). The transfer process also allows the stress in a failed fiber to be unaffected at distance $\tilde{>} \delta_c$ from the fiber fracture site (Fig. 3.1). Consequently, composite failure requires that fiber *bundle failure occurs within* δ_c (Curtin, 1991). In essence, δ_c becomes a measure of the gauge lengths operating within the composite. This leads to an ultimate tensile strength (UTS) *independent of gauge length,* L_g, provided that $L_g > \delta_c$.‡ The magnitude of the UTS can be computed by first evaluating the average stress on *all* fibers, failed plus intact, along an arbitrary plane through the material. Then, by differentiating with respect to the stress on the *intact* fibers, in order to obtain the maximum, the UTS becomes,

$$S_g = f_\ell S_c F(m) \quad (3.9a)$$

‡ At small gauge lengths ($L_g < \delta_c$), the UTS becomes gauge length dependent and exceeds S_u (Hild *et al.*, 1993).

with

$$F(m) = \left[2/(m+1)\right]^{1/(m+1)}\left[(m+1)/(m+2)\right]$$

It is of interest to compare this result to that found for a 'dry' bundle. Then, the 'fiber bundle' strength S_b, depends on the gauge length in accordance with (Corten, 1967),

$$S_b = f S_o \left(L_o/L_g\right)^{1/m} e^{-1/m} \tag{3.9b}$$

In all cases, $S_g > S_b$. The effect of the interface on the UTS is apparent when Eqn. (3.2) is inserted into Eqn. (3.9a) to give

$$S_g = f_t\, F(m)\, S_o \left[\frac{L_o\, \tau}{R\, S_o}\right]^{1/(m+1)} \tag{3.10}$$

Specifically, if τ *decreases* because of cyclic degradation, the UTS also *decreases*. This arises because the stress transfer length δ_c increases leading to a larger effective gauge length within the composite. This phenomenon is considered to be the fundamental origin of S-N behavior in CMCs.

3.3 Inelastic Strains

As the load increases, the fibers fail systematically, resulting in a characteristic fiber fragment length. At composite failure, there can be multiple cracks within some

fibers.‡ Fiber failure results in inelastic strains. The stress/strain relationship for a monomodal fiber strength distribution is (Hild et al., 1993),

$$\sigma = f E_f \varepsilon \left\{ 1 + \sum_{n \geq 1} \frac{(-1)^n}{2n!} \left[\frac{2 + n(m+1)}{1 + n(m+1)} \right] \left(E_f \varepsilon / S_c \right)^{n(m+1)} \right\} \tag{3.11}$$

Bimodal flaw populations in fibers can produce different behaviors, as found in SiC/CAS (He et al., 1993, Curtin, 1993)

4. MATRIX CRACKING IN UNIDIRECTIONAL MATERIAL

4.1 The Matrix Cracking Stress

The development of damage in the form of matrix cracks within 1-D CMCs subject to tensile loading has been traced by direct optical observations on specimens with carefully polished surfaces and by acoustic emission detection (Kim and Pagano, 1991; Beyerle *et al.*, 1992; Pryce and Smith, 1992; Kim, 1992, Cho *et al.*, 1992; Kim and Katz, 1988), as well as by ultrasonic velocity measurements (Baste *et al.*, 1992). Interrupted tests, in conjunction with sectioning and SEM observations, have also be used. Analyses of the matrix damage found in 1-D CMCs provides the basis upon which the behavior of 2-D CMCs may be addressed. The *matrix cracks* are found to interact with predominantly intact fibers, subject to interfaces that debond and slide. This process is established at a stress, designated σ_{mc} (Fig. 1.2). The crack spacing $\bar{d}$ decreases with increase in stress above σ_{mc} and may eventually attain a saturation spacing, d_s, at stress σ_s (Fig. 4.1). The details of crack evolution are governed by the distribution of matrix flaws. The matrix cracks reduce the unloading $\bar{E}$ and secant E_s moduli, and also induce

‡ The existence of many fiber fragments is still compatible with a high ultimate tensile strength. A good analogy being the strength of a wire rope.

a permanent strain, ε_0 (Fig. 1.2). Relationships between E_s, ε_0 and constituent properties provide the key connections between processing and macroscopic performance, via the properties of the constituents. The basic cell model is shown in Fig. 4.2.

The deformations caused by matrix cracking, in conjunction with interface debonding and sliding, exhibit three regimes. These depend on the magnitude of the debond stress, σ_i, as governed by the debond energy, through the relationship (Hutchinson and Jensen, 1990),

$$\begin{aligned} \sigma_i &= (1/c_1)\sqrt{E_m \Gamma_i / R} - E_m \varepsilon_T (c_2/c_1) \\ &\equiv \sigma_D - \sigma^T \end{aligned} \tag{4.1a}$$

which has a useful non-dimensional form

$$\Sigma_i = \sigma_i/\sigma \tag{4.1b}$$

Here c_i are coefficients defined by Hutchinson and Jensen (1990) and σ^T is designated the misfit stress. A mechanism map that identifies the three regimes is shown in Fig. 4.3 (Vagaggini and Evans, 1993). When $\Sigma_i > 1$, debonding does not occur, whereupon matrix crack growth is an entirely elastic phenomenon. When $\Sigma_i < 1/2$, small debond energy (SDE) behavior arises. The characteristic of this regime is that the reverse slip length at the interface, upon complete unloading, exceeds the debond length. In SDE, Γ_i is typically small and does not affect certain properties, such as the hysteresis loop width. Hereafter, the term SDE is used, loosely, to represent the behavior expected when $\Gamma_i \rightarrow 0$. A large debond energy (LDE) regime also exists, when $1/2 < \Sigma_i \leq 1$. In this situation, reverse slip is impeded by the debond.

The approach used to simulate mode I cracking under monotonic loading is to define tractions σ_b acting on the crack faces, induced by the fibers (Fig. 4.4) and to determine their effect on the crack tip by using the J-integral (Marshall *et al.*, 1985; Budiansky *et al.*, 1986),

$$\mathcal{G}_{tip} = \mathcal{G} - \int_0^u \sigma_b du \tag{4.2}$$

where $\mathcal{G}$ is the energy release rate and u is the crack opening displacement. Cracking is considered to proceed when $\mathcal{G}_{tip}$ attains the pertinent fracture energy. Since the fibers are not failing, the crack growth criterion involves matrix cracking only. A lower bound is given by (Budiansky *et al.*, 1986; McCartney, 1987)

$$\mathcal{G}_{tip} = \Gamma_m(1-f) \tag{4.3}$$

with Γ_m being the matrix toughness. Upon crack extension, $\mathcal{G}$ becomes the crack growth resistance, Γ_R, whereupon

$$\Gamma_R = \Gamma_m(1-f) + \int_0^u \sigma_b du. \tag{4.4}$$

The sliding distance ℓ, in the absence of fiber failure, is related to the crack surface tractions, $\sigma_{r,y}$, by (Hutchinson and Jensen, 1990),

$$\ell = \left[RE_m(1-f)/2\tau_0 E_L f\right](\sigma_b - \bar{\sigma}_i) \tag{4.5}$$

where E_L is the initial longitudinal composite modulus. The sliding length is, in turn, related to the crack opening displacement, u_s. The corresponding traction law is,

$$\sigma_b - \overline{\sigma}_i = \left[2\xi\tau_o E_L f u_s/R\right]^{1/2} \tag{4.6}$$

where

$$\xi \equiv f E_f/(1-f)E_m$$

The preceding basic results can be used to obtain solutions for matrix cracking (Aveston, Cooper and Kelly (ACK), 1971; Marshall *et al.*, 1985; Budiansky *et al.*, 1986; McCartney, 1987; Zok and Spearing, 1992; Singh, 1989). Present understanding involves the following factors. Because the fibers are intact, a steady-state condition exists wherein the tractions on the fibers in the crack wake balance the applied stress. This special case may be addressed by integrating Eqn. (4.2) up to a limit $u = u_0$. This limit is obtained from Eqn. (4.6) by equating σ_b to σ. For SDE, this procedure gives (Budiansky *et al.*, 1986)

$$\mathcal{G}_{tip}^0 = \frac{\left(\sigma+\sigma^T\right)^3 E_m^2 (1-f)^2 R}{6\tau_0 f^2 E_f E_L^2} \tag{4.7}$$

A *lower bound to the matrix cracking stress*, σ_{mc}, is then obtained by invoking Eqn. (4.3), such that (Budiansky *et al.*, 1986)

$$\begin{aligned} \sigma_{mc} &= E_L\left[\frac{6\tau_o \Gamma_m f^2 E_f}{(1-f)E_m^2 R E_L}\right]^{1/3} - \sigma^T \\ &\equiv \sigma_{mc}^o - \sigma^T \end{aligned} \tag{4.8}$$

The non-linear composite properties are usually dominated by fully-developed matrix cracks that form at stresses above σ_{mc}. However, in some cases, *small* matrix cracks can form at stresses below σ_{mc} (Kim and Pagano, 1991). These occur either within matrix-rich regions or around processing flaws. These small flaws may provide access of the atmosphere to the interfaces and cause degradation.

A corresponding result for LDE is (Fig. 4.3) (Budiansky et al., 1993),

$$\left(\frac{\sigma_{mc}+\sigma^T}{\sigma^o_{mc}}\right)^3 - 3\left(\frac{\sigma_{mc}+\sigma^T}{\sigma^o_{mc}}\right)\left(\frac{\sigma_D}{\sigma^o_{mc}}\right)^2 + 2\left(\frac{\sigma_D}{\sigma^o_{mc}}\right)^3 = 1 \qquad (4.9)$$

4.2 Crack Evolution

The evolution of additional cracks at stresses above σ_{mc} (Fig. 4.1) involves two factors: *screening* and *statistics* (Zok and Spearing, 1992; Cho *et al.*, 1992). When the sliding zones between neighboring cracks overlap, *screening* occurs and $\mathcal{G}_{tip}$ differs from $\mathcal{G}^0_{tip}$. The relationship is dictated by the location of the neighboring cracks. When a crack forms midway between two existing cracks with a separation 2d, subject to SDE, $\mathcal{G}_{tip}$ is related to $\mathcal{G}^0_{tip}$ by (Zok and Spearing, 1992)

$$\mathcal{G}_{tip}/\mathcal{G}^0_{tip} = 4(d/2\ell)^3 \qquad (\text{for } 0 \le d/\ell \le 1) \qquad (4.10a)$$

and

$$\mathcal{G}_{tip}/\mathcal{G}^0_{tip} = 1-4(1-d/2\ell)^3 \qquad (\text{for } 1 \le d/\ell \le 2) \qquad (4.10b)$$

When d is sufficiently small, Eqn. (4.10a) applies and $\mathcal{G}_{tip}$ is independent of the stress. Once this occurs, $\mathcal{G}_{tip}$ cannot increase and is unable to again satisfy the matrix crack

growth criterion (Eqn. 4.3). This occurs with spacing, $\bar{d}_s$, at an associated stress σ_s (Fig. 4.1). This saturation spacing is given by,

$$\bar{d}_s/R = \chi\left[\Gamma_m(1-f)^2 E_f E_m / f\tau_o^2 E_L R\right]^{1/3} \tag{4.11a}$$

where χ is a coefficient that depends on the spatial aspects of crack evolution: periodic, random, etc. Combining Eqn. (4.11a) with Eqn. (4.8), $\bar{d}_s$ becomes

$$\bar{d}_s \tau_o/R = \left(\chi/6^{1/3}\right)\sigma_{mc}^{o}\left[(1-f)E_m/fE_L\right] \tag{4.11b}$$

Note that this result is *independent* of the residual stress, because the terms containing $(\sigma_b + \sigma^T)$ in Eqns. (4.5) and (4.7) cancel when inserted into Eqn. (4.10a). Simulations for spatial randomness indicate that, $\chi \approx 1.5$ (Spearing and Zok, 1993). Moreover, these same simulations indicate that the saturation stress should vary as

$$\sigma_s = 1.26\sigma_{mc}^{o} - \sigma^T \tag{4.12}$$

In addition to these screening effects, the actual *evolution of matrix cracks* at stresses above σ_{mc} is governed by *statistics* that relate to the size and spatial distribution of matrix flaws. Various simulations have been performed (Spearing and Zok, 1993; Curtin, 1993). In these, a condition $\lambda_s \lesssim 1$ corresponds to a high density of matrix flaws already large enough to be at steady-state, and vice versa. The simulated crack densities (Fig. 4.5) indicate a sudden burst of cracking *at* $\sigma = \sigma_{mc}$, when $\lambda_s < 1$, followed by a gradual increase with continued elevation of the stress. The saturation stress is similar to that given by Eqn. (4.12). In contrast, when $\lambda_s >> 1$, the cracks evolve more gradually

with stress, reaching saturation at substantially higher levels of stress.‡ These simulated behaviors are qualitatively similar to those measured by experiment (Fig. 4.1). It has been found that a simple formula can be used to approximate crack evolution in most CMCs (Evans *et al.*, 1993), given by (Fig. 4.1),

$$\bar{d} \approx \bar{d}_s \frac{[\sigma_s/\sigma_{mc} - 1]}{[\sigma/\sigma_{mc} - 1]} \tag{4.13}$$

At stresses, $\sigma > \sigma_s$, the crack density remains essentially constant. There is no additional stress transfer between the fibers and the matrix. In this case, the tangent modulus is of order (Aveston *et al.*, 1971):

$$E_t \equiv d\sigma/d\varepsilon = fE_f \tag{4.14}$$

In practice, the tangent modulus is usually found to be smaller because of fiber failure (Eqn. 3.10) as well as fiber straightening effects allowed by matrix cracking (He et al., 1993).

5. MATRIX CRACKING IN 2-D MATERIALS

General comparisen between the tensile stress/strain curves [$\sigma(\varepsilon)$], for 1-D and 2-D materials (Fig. 5.1) provides important perspective. It is found that $\sigma(\varepsilon)$ for 2-D materials is quite closely matched by simply scaling down the stress for the 1-D curves by 1/2. The behavior of 2-D materials must, therefore, be *dominated* by the 0° plies,‡

‡ Nevertheless, the saturation spacing remains insensitive to λ_s (Spearing and Zok, 1993).
‡ Furthermore, since some of the 2-D materials are woven, the 1/2 scaling infers that the curvatures introduced by weaving have minimal effect on the stress/strain behaviors.

because these plies provide a fiber volume fraction in the loading direction about half that present in 1-D material (Evans *et al.*, 1993).

The typical matrix crack evolution found in 2-D CMCs is depicted in Fig. 5.2. Cracks first form in the 90° plies at a stress, σ_τ, and multiply over a small stress range above σ_τ. Subsequently, these cracks extend laterally into the 0° plies. This occurs stably subject to increasing stress. Finally, the matrix cracking may saturate and the fibers then carry the load prior to composite failure. The most significant 2-D effects occur at the *initial deviation from linearity*. At this stage, matrix cracks that form in 90° plies evolve at lower stresses than cracks in 1-D materials. The associated non-linearities are usually slight and do not normally contribute substantially to the overall non-linear response of the material. However, these cracks have important implications for oxidation embrittlement and creep rupture and require analysis. Matrix cracking in the 90° plies often proceeds by a tunneling mechanism (Fig. 5.2). Tunnel cracking evolves at a stress σ_τ (Xia *et al.*, 1993; Hutchinson and Suo, 1992), given by

$$\sigma_\tau = \sigma_\tau^\circ - \sigma^R\left(E_L + E_T\right)/2E_T \tag{5.1}$$

with

$$\sigma_\tau^\circ = \left[E\Gamma_R/h\right]^{1/2} g\left(f, E_f/E_m\right)$$

where

$$E_\circ = E_L\left(1 + E_L/E_T\right)/2\left[E_L/E_T - \nu_L^2\right]$$

E_T is the initial transverse modulus of the 1-D material, h is the ply thickness, σ^R is the residual stress at the ply level and ν_L is defined by

$$\nu_L = (\nu/2)(1+E_L/E_T).$$

Γ_R is the fracture energy of the 90° ply given approximately by

$$\Gamma_R \approx (1\text{-}f)\,\Gamma_m$$

The function g depends quite strongly on whether the transverse fibers either remain in contact with the matrix upon loading or separate (Fig. 5.3).

The unloading modulus associated with tunnel cracks, $\bar{E}/E_o$, depends primarily on the crack density, $h/\bar{L}$, with $\bar{L}$ being the mean crack spacing in the 90° plies (Xia *et al.*, 1993; Laws and Dvorak, 1990), as illustrated for contacting fibers on Fig. 5.4. The ratio $\bar{E}/E_o$ is larger when the fibers separate. Note that, at large crack densities, a limiting value E_ℓ is reached, given by,

$$E_\ell/E_o = E_L/(E_L+E_T) \tag{5.2}$$

The corresponding permanent strain is

$$\varepsilon_o = \left(1/\bar{E} - 1/E_o\right)\sigma^R(E_L+E_T)/2E_L \tag{5.3}$$

Examples of the overall stress/strain response are summarized in Fig. 5.5.

Lateral extension of these tunnel cracks into the matrix of the 0° plies results in behavior similar to that found in 1-D material. In most cases, the cracks extend stably into the 0° plies, resulting in inelastic strain. The overall behavior can be expressed through groups of non-dimensional parameters. The evolution of crack length a with stress σ has the form (Xia and Hutchinson, 1993b),

$$\sigma/\sigma_o = F_1\left[a/h, h/\bar{L}, \Sigma_{mc}\right] \tag{5.4}$$

where

$$\Sigma_{mc} \equiv \beta\sigma^o_{mc}/\sigma_o = \left[\frac{6\pi^{1/2}E_f E_L^{1/2} f^2 \tau_o h^{1/2}}{R\Gamma_m^{1/2}(1-f)^{1/2}E_m^2 A^{1/2}E_o}\right]^{1/3}$$

$$\beta = (AE_L/E_o)^{1/3}$$

$$\sigma_o = \sqrt{AE_L(1-f)\Gamma_m/\pi h(1-\nu^2)}$$

and A is an orthotropy factor (Budiansky and Cui, 1993). The function F_1 is plotted on Fig. 5.6 for a typical crack spacing, $h/\bar{L} = 1$. Extension of the cracks occurs at stresses below that at which matrix cracking would develop if the material were unidirectional. Moreover, when the cracks emerge from the 0° plies, σ/σ^o_{mc} is in the range, 0.7 – 0.9.

The corresponding inelastic strain $\varepsilon_{p\ell}$ as the cracks extend is given by,

$$E_o\varepsilon_{p\ell}/\beta\sigma^o_{mc} = F_2\left(a/h, \bar{L}/h, \Sigma_{mc}\right) \tag{5.5}$$

where F_2 is plotted on Fig. 5.7, for $h/\bar{L} = 1$. These results may be used to predict stress/strain curves, illustrated on Fig. 5.8, up to the stress at which the cracks extend through the 0° plies.

A simplified form of the above results is preferred for subsequent analysis of fatigue. Inspection reveals that the extension of the matrix cracks across the 0° plies occurs in approximate accordance with the following formula,

$$(\sigma/\sigma_o) - 1 \approx (a/h)(\Sigma_{mc} - 1) \tag{5.6}$$

Moreover, the cracks penetrate the 0° plies (a = 3h) at a stress σ^*, given by

$$\sigma_* = 3\beta\sigma_{mc} - 2\sigma_o \tag{5.7}$$

At stresses above σ_*, the subsequent behavior depends on the interface properties. When τ and Γ_i are relatively *small*, the debond zones overlap at matrix cracks emanating from tunneling cracks in the 90° plies. Crack saturation is achieved at $\sigma \approx \sigma_*$. The subsequent load is then borne by the fibers, resulting in an essentially constant tangent modulus given by Eqn. (3.10). Such behavior is exemplified by SiC/CAS. Conversely, when either τ or Γ_i are large, the slip zones from these cracks do no overlap at $\sigma = \sigma_*$. Then, upon further loading, *additional cracks* form in the 0° plies. The subsequent behavior is precisely analogous to that found in unidirectional material‡,as exemplified by SiC/SiC composites made by CVI (Guillaumat, 1993).

6. HYSTERESIS

6.1 Unidirectional Material

Analyses of the plastic strains caused by matrix cracks, combined with calculations of the compliance change, provide a constitutive law for the material (He et al., 1993). The important parameters are the permanent strain ε_o and the secant modulus, E_s. These quantities, in turn, depend on several constituent properties; the sliding stress, τ, the debond energy, Γ_i, and the misfit stress σ^T. The plastic strains also govern the *hysteresis* that arises when the material is unloaded and reloaded (Vagaggini et al.,

‡ Subject to knowledge of the stresses borne by the 0° plies.

1993). This hysteresis relates in a fundamental way to the fatigue process. For this reason, the most important hysteresis results are summarized below.

Matrix cracks *increase* the elastic compliance. Numerical calculations indicate that the *unloading elastic modulus*, E^*, is given by (He *et al.*, 1993),

$$E_L/E^* - 1 = \left(R/\bar{d}\right)\mathcal{B}\left[f, E_f/E_m\right] \tag{6.1}$$

where $\mathcal{B}$ is a function. Finite element calculations give the values for $\mathcal{B}$ plotted on Fig. 6.1. In practice, $\mathcal{B}$ is often larger because of fiber straightening effects (He et al., 1993). An example for SiC/CAS is shown on Fig. 6.2. The matrix cracks also cause a permanent strain associated with relief of the residual stress. This strain, ε^*, is related to the modulus and the misfit stress by (He *et al.*, 1993),

$$\varepsilon^* \equiv \sigma^T\left[1/E^* - 1/E_L\right] \tag{6.2}$$

The preceding effects occur *without* interface sliding. The incidence of *sliding* leads to *plastic strains* that superpose onto ε^*. The strains can be calculated from the crack opening displacement (Eqn. 4.6) by using

$$\varepsilon_s = \frac{b_2}{(b_2 + b_3)}\,\frac{u_s}{\bar{d}} \tag{6.3}$$

There are two basic behaviors depending on the stress relative to the saturation stress, σ_S. When $\sigma < \sigma_S$, $\bar{d}$ decreases with increase in stress and the inelastic strains are relatively large. When $\sigma > \sigma_S$, the inelastic strain arises primarily because of fiber failures (Eqn. 3.10).

When $\sigma < \sigma_s$, there are two different results. These obtain for SDE and LDE, respectively, as differentiated by the magnitude of Σ_i (Fig. 4.3). For SDE ($\Sigma_i = 1/2$), the permanent strain is (Vagaggini and Evans, 1993)

$$\left(\varepsilon_o - \varepsilon^*\right)\Sigma_H^2 = 4\left(1-\Sigma_i\right)\Sigma_T + 1 - 2\Sigma_i^2 \tag{6.4}$$

where Σ_H is a hysteresis index given by

$$\Sigma_H \equiv \sigma_H/\sigma$$

with

$$\sigma_H = 2\left[E_f/E_m\left(1-f\right)\right]\sqrt{\bar{d}\,\tau_o E_m/b_2 R}$$

and

$$\Sigma_T \equiv \sigma^T/\sigma. \tag{6.5}$$

The secant modulus is

$$1/E_s = 1/E_\cdot + \varepsilon_o/\sigma \tag{6.6}$$

Upon unloading and reloading, the curves have mirror symmetry (Fig. 1.2). In practice, only one (unloading or reloading) need be analyzed. For example, the unload strain ε_u at stress, σ_u, is

$$\varepsilon_u = \left[4\left(1-\Sigma_i\right)\Sigma^T + 1 - 2\Sigma_i^2 + 2\Sigma_u - \Sigma_u^2\right]\Sigma_H^{-2} + \sigma_u/E^* + \varepsilon^* \tag{6.7}$$

where $\Sigma_u = \sigma_u/\sigma$. It is convenient to define a strain difference

$$\Delta\varepsilon_u = \varepsilon_u^o - \varepsilon_u$$

$$= \left(\sigma - \sigma_u^2\right)/\sigma_H^2 + \left(\sigma - \sigma_u\right)/E. \tag{6.8}$$

where ε_u^o is the strain at the peak stress. There is a corresponding result for reloading. This strain difference can be used to evaluate τ_o and E_* from experimental measurements, as discussed in the following section.

For LDE, the permanent strain is (Vagaggini and Evans, 1993),

$$\left(\varepsilon_o - \varepsilon^*\right)\Sigma_H^2 = 2\left(1-\Sigma_i\right)\left(1-\Sigma_i+2\Sigma_T\right) \tag{6.9}$$

There is a corresponding change in the secant modulus (Eqn. 6.6). The unloading strain is initially parabolic and given by Eqn. (6.7), such that $\Delta\varepsilon_u$ is still given by Eqn. (6.8). Then, when

$$\Sigma_u \leq 2\Sigma_i - 1 \tag{6.10}$$

linearity resumes, such that

$$\varepsilon_u = 2\Sigma_H^{-2}\left(1-\Sigma_i\right)\left[2\Sigma^T + \left(1-\Sigma_i\right) + 2\Sigma_u\right] + \sigma_u/E^* + \varepsilon^* \tag{6.11}$$

giving

$$\Delta\varepsilon_u = 4\left(1-\Sigma_i\right)\left(\sigma-\sigma_u\right)/\sigma_H^2 + \left(\sigma-\sigma_u\right)/E^* \tag{6.12}$$

Beyond saturation, ($\bar{d} \geq \bar{d}_s$), the extra inelastic strains are given by Eqn. (3.10). The permanent strain and the secant modulus change accordingly. There is also a change in the hysteresis. Upon unloading, the initial behavior is still parabolic with $\Delta\varepsilon_u$ given by Eqn. (6.8). A *transition* then takes place when the stress σ_u reaches the reverse slip zone overlap stress, σ_ℓ. This overlap stress is given by Eqn. (4.5), with $\ell = \bar{d}$,

$$\sigma_\ell - \sigma_i = 2\tau_o \bar{d} E_L f / R E_m (1-f) \tag{6.13}$$

When $\sigma_u < \sigma_\ell$, the unloading strain difference becomes

$$\Delta\varepsilon_u = \frac{\sigma_u (1-f) E_m}{E_f E f} + \frac{\sigma_u}{E^*} - \frac{\tau \bar{d}}{E_f R} \tag{6.14}$$

In composites with relatively large values of τ_o and/or Γ_i, matrix crack *closure* effects often arise upon unloading as $\sigma \to 0$ (Fig. 1.2b). The closure stress, $\sigma_{c\ell}$, then becomes the effective minimum, σ_{min}. When this behavior arises, analysis of the unloading strain is the preferred method for obtaining the constituent properties. The analysis must be restricted to $\sigma_u > \sigma_{c\ell}$ in order to avoid spurious interpretations.

6.2 2-D Material

As cracking proceeds in the 90° plies, the fraction of the load borne by the 0° plies increases. The nominal stress on these plies σ_L (σ) is related to the moduli by,

$$\sigma_L / \sigma = E_L / \bar{E} \tag{6.15}$$

with $\bar{E}$ given by Fig. 5.4 . This result applies before the matrix cracks penetrate the 0° plies. The changes that occur once 0° ply cracking commences have yet to be analyzed. An approximate procedure has been used, which appears to provide useful predictions. The stress ratio σ_L/σ is computed from Fig. 5.4, at the appropriate crack spacing in the 90° plies. Typically, this is in the range 1.8–2, with 2 being the maximum possible value. This ratio is then assumed to remain constant as cracking proceeds in the 0° plies. With this modification, the unidirectional results described above give direct predictions of the permanent strain, the reload strain and the secant modulus.

7. CYCLIC CRACK GROWTH

7.1 Mechanisms

For many CMCs, there is no fatigue mechanism operating in the matrix itself, because the matrices are low-toughness materials. For these materials, the *criterion* for crack extension is that energy release rate at the tip, $\mathcal{G}_{tip}$, reaches the matrix fracture energy Γ_m. In this case, fatigue relies on cyclic degradation mechanisms operating at the interfaces. The important fatigue phenomena may be elucidated by equating $\mathcal{G}_{tip}$ and Γ_m, but allowing τ to vary with cycles, N.

In composites involving a tough ceramic matrix, there is an additional contribution to matrix crack growth given by the Paris law criterion‡,

$$da/dN = \beta_f \left(\Delta K_{tip}/E\right)^p \tag{7.1}$$

where a is the matrix crack length, N the number of cycles, β_f is a fatigue coefficient for the matrix and p the fatigue exponent. Moreover, when oxide matrices are used, *stress*

‡ For fatigue, stress intensity factors K are used more commonly than the energy release rate, $\mathcal{G}$. Hence K's are emphasized in this section.

corrosion is also possible. Then, the matrix cracks extend by static fatigue at a growth rate governed by (Wiederhorn, 1967)

$$da/dt = v_o\left(K_{tip}/K_o\right)^n \tag{7.2}$$

where t is time, K_o and v_o are reference values of the energy release rate and velocity, respectively, and n is the exponent.

A simple transformation converts the monotonic crack growth parameters into cyclic parameters that can be used to interpret and simulate fatigue growth of matrix cracks. The key transformation is based on the relationship between interface sliding during loading and unloading, which relates the monotonic result to the cyclic equivalent (McMeeking and Evans, 1990):

$$(\tfrac{1}{2})\Delta\sigma_b(x/a, \Delta\sigma) = \sigma_b(x/a, \Delta\sigma/2) \tag{7.3}$$

where $\Delta\sigma$ is the range in the applied stress. Notably, the amplitude of the *change* in fiber traction $\Delta\sigma_b$ caused by a change in applied stress, $\Delta\sigma$, is twice the fiber traction σ_b which would arise in the monotonic loading of a previously unopened crack, caused by an applied stress equal to half the stress change. There is a similar relationship for the stress intensity range experienced by the crack tip,

$$\Delta K_{tip} = 2K_{tip}(\Delta\sigma/2). \tag{7.4}$$

When the fibers remain intact, a cyclic *steady-state* can be obtained with the above transformations (McMeeking and Evans, 1990),

$$\Delta K_{tip} = (R/12)^{1/2}\ (\Delta\sigma/\Delta\mathcal{T}) \tag{7.5}$$

where $\Delta\mathcal{T}$ is a cyclic sliding parameter, given by

$$\Delta\mathcal{T} = \xi\left(\tau_o E/\Delta\sigma E_f\right)^{1/2}$$

The corresponding matrix crack growth rate is determined from the Paris law, as,

$$\frac{da}{dN} = \beta_f\left[\frac{\Delta\sigma\sqrt{R}}{\sqrt{12}\,\Delta\mathcal{T}E_m}\right]^p. \tag{7.6}$$

The effects of fiber breaking can be introduced by using the fiber strength, S_g. Once the fibers begin to fail, the unbridged crack length is continuously adjusted to maintain a stress at the unbridged crack tip equal to the fiber strength (Bao and McMeeking, 1993). If the fibers are relatively weak and break close to the crack front, the bridging zone is always a small fraction of the crack length, and there is minimal shielding by the fibers. Conversely, when the fiber strength exceeds a critical value, they never break before the crack extends across the plate and the fatigue crack growth rate always diminishes as the crack grows. This is the case found in most CMCs. The sensitivity of these behaviors to fiber strength is quite marked (Fig. 7.1).

This basic matrix crack growth model can be extended to include thermomechanical fatigue (TMF). This can be achieved by means of another transformation wherein all of the range terms in Eqns. (7.3) to (7.6) are replaced, as follows (McMeeking, 1993),

$$\begin{aligned}\Delta\sigma &\Rightarrow \Delta\sigma + fE_f\left(\alpha_f - \alpha_m\right)\Delta T \\ \Delta\sigma_b &\Rightarrow \Delta\sigma_b + fE_f\left(\alpha_f - \alpha_m\right)\Delta T\end{aligned} \tag{7.7}$$

where ΔT represents the temperature cycle and $\Delta\sigma$ the stress cycle. It is immediately apparent that matrix crack growth rates are expected to be quite different for out-of-phase and in-phase TMF. A key result is that, whereas $\Delta\mathcal{G}_{tip}$ always reduces upon initial crack extension, either for stress cycling alone or for in-phase TMF, it can *increase* for out-of-phase TMF.

7.2 Composite Behavior

Composite behavior is addressed here for materials in which matrix fatigue is minimal. The consequence is that, for unidirectional material, all of the matrix cracking occurs in the first cycle. The crack density and the elastic modulus, E_*, remain constant upon further cycling, provided that σ_{max} does not increase in subsequent cycles. However, the interface sliding resistance diminishes, causing both a permanent deformation and a diminished secant modulus, as cycling proceeds. The reduction in τ also diminishes the ultimate tensile strength, because the effective gauge length is increased, leading to S-N behavior. The preceding analysis of the inelastic strain and of the UTS may be used directly to predict the fatigue behavior. This is described in section 8. When stress corrosion occurs in the matrix, matrix cracks continue to form as cycling proceeds. This effect can be included in the fatigue model.

Fatigue in a 0/90 cross ply system, has some different aspects, which depend on the maximum stress reached on the first cycle, designated σ_{max} (1). The behavior may be understood with reference to the results presented on Fig. 5.6. There are three regimes. (i) When σ_{max} (1) $\lesssim \sigma_0$, there are no matrix cracks and cyclic loading does not lead to any property changes. (ii) Between σ_0 and σ_*, cracks form in the 90° plies during the first cycle and these cracks partially penetrate the 0° plies. In this case, the cracks in the 0° plies extend during cycling, leading to reductions in elastic modulus, E_* and secant modulus, E_s, as well as an increase in the permanent strain, ε_0. (iii) At stresses

above σ_*, most cracks penetrate the 0° plies on the first cycle. Upon subsequent cycling, the behavior is essentially the same as that found for unidirectional materials. The changes in elastic modulus are minimal, but there is a decrease in secant modulus and an increase in permanent strain.

In the range $\sigma_0 < \sigma_{max}\,(1) < \sigma_c$, an approximate solution for crack growth through the 0° plies can be obtained by using Eqn. (5.6). At the simplest level, it may be assumed that all interfaces degrade uniformly in accordance with Eqn. (2.9). In practice, the interface must progressively degrade as the cracks extend and interact with the fibers. The uniform degradation approximation thus represents an upper limit for the crack growth rate. This solution is given by,

$$a/h = (\sigma_{max} - \sigma_o)/\left[\beta\,\sigma_{mc}^{o}\,N^{-\lambda/3} - \sigma_o\right] \tag{7.8}$$

The number of cycles needed to extend the crack across the 0° plies, N_*, is then

$$N_* \approx \left[3\beta\,\sigma_{mc}^{o}/(\sigma_{max} + 2\sigma_o)\right]^{3/\lambda} \tag{7.9}$$

When $N < N_*$, because the matrix cracks are extending, there will be a decrease in the elastic modulus, as well as the usual changes in E_s and ε_o, which can be estimated from the crack length using Fig. 5.7.

At $N > N_*$, the material behaves in the same manner as unidirectional material. However, the stress acting in the 0° plies needs to be known before the fatigue properties can be predicted.

8. FATIGUE METHODOLOGY

8.1 Philosophy

A practical methodology should be able to predict the overall fatigue response from a small number of critical experiments. The present concept is to use a few tensile and fatigue tests to evaluate the constituent properties (Fig. 8.1). These are then used to predict the S-N curve, the changes in elastic modulus, the permanent strain and the thermomechanical fatigue response. Two general observations facilitate the analysis.
(i) Measurements of the crack density $\bar{d}$ are non-trivial. A procedure that does not require such measurements is preferred. This has been found possible, because all of the relevant formulae contain the non-dimensional quantity,

$$\mathcal{L} = \tau\bar{d}/E_m R \equiv \frac{\sigma_H^2(1-f)^2 b_2}{4E_f^2} \tag{8.1}$$

(ii) There are three types of constituent property which affect fatigue. The first type is *stress independent*. These are initial modulus, E, and the misfit stress σ^T. The second type is dependent on the *maximum stress* reached during the first cycle, σ_{peak}. These properties are elastic modulus, E^*, and the misfit relief strain, ε^*. The third is *cycle dependent*. These are the sliding parameter $\mathcal{L}$, and the UTS, S_g.

8.2 Tensile Tests

Tension tests with periodic unloading are used to evaluate the constituent properties. Parameters given immediately by the stress/strain curve (Fig. 8.1) are E and $S_g(1)$. Here the designation (1) is used to refer to the first cycle. At each unload or reload, corresponding to a particular peak stress, σ_{peak}, the permanent strain ε_o (1) is

recorded and the unload strain differential, $\Delta\varepsilon_u$, is determined. The latter is obtained from the data and fitted with a polynominal. Differentiation then gives the hysteresis modulus,

$$E_H^{-1} = d(\Delta\varepsilon_u)/d\sigma_u \tag{8.2}$$

This modulus is related to the interface parameter, $\mathcal{L}$, (1) and the elastic modulus, E_*, when $\sigma_u < \sigma_\ell$ by (Eqn. 6.8),

$$E_H^{-1} = E_*^{-1} + \left[(1-f)^2 b_2 / 2E^2 f^2\right]\sigma_u/\mathcal{L}(1) \tag{8.3}$$

A least squares linear fit of $E_H^{-1}(\sigma_u)$ to Eqn. (8.3) gives $\mathcal{L}(1)$ and E_*. The analysis is repeated at several values of σ_{peak}, to give, $E_*(\sigma_{peak})$ and $\mathcal{L}(1, \sigma_{peak})$.

In order to further enhance the fidelity of the data, the linearities between both $\mathcal{L}(1)$ and E_* with σ_{peak} are noted. Specifically since τ_o is essentially independent of σ_{peak}, Eqn. (4.13) indicates that $\mathcal{L}(1)$ usually varies as:

$$\mathcal{L}(1) = \mathcal{L}_s\left[\frac{\sigma_s/\sigma_{mc} - 1}{\sigma_{peak}/\sigma_{mc} - 1}\right] \tag{8.4}$$

where $\mathcal{L}_s$ represents the magnitude of the sliding parameter at $\sigma_{peak} = \sigma_s$. It is also evident from Eqn. (6.1) that $\mathcal{L}(\sigma_{peak})$ and $E_*(\sigma_{peak})$ are related by

$$[E/E_* - 1]/\mathcal{L} = \mathcal{B} \tag{8.5}$$

where $\mathcal{B}$ is a constant. The linearity expected from Eqns. (8.4) and (8.5) facilitates a least squares fit to obtain the following parameters: σ_{mc}, σ_s, $\mathcal{L}_s$. At stresses above σ_s, both $\mathcal{L} = \mathcal{L}_s$ and $E^* = E^*_s$ remain constant.

Various approaches can be used to obtain the misfit stress, σ^T, subject to the material being either SDE or LDE. For example, with SDE materials, the permanent strain $\varepsilon_o(1, \sigma_{peak})$ can be used. For this purpose, the product, $\varepsilon_o \mathcal{L}(1, \sigma_{peak})$ has an explicit dependence on the peak stress (Eqn. 5.4), given by,

$$\mathcal{L}\varepsilon_o\left(1, \sigma_{peak}\right) = x\sigma^2_{peak} + 4x\sigma_{peak}\sigma^T + \mathcal{L}\sigma^T\left[1/E^* - 1/E\right] \tag{8.6}$$

where

$$x = (4/b_2)(c_2/a_2c_1)^2.$$

A least squares fit to Eqn. (8.6) with x known allows σ^T to be obtained from the second term on the RHS. At this stage, the following parameters are known:

$$E, E^*\left(\sigma_{peak}\right), \sigma^T, S_g(1), \mathcal{L}_s, \mathcal{L}\left(1, \sigma_{peak}\right), \sigma_{mc}, \sigma_s$$

8.3 Cyclic Tests

Cyclic loading experiments are conducted at fixed stress amplitude $\Delta\sigma$ and fixed ratio of maximum to minimum stress, $\mathcal{R}$. Hysteresis measurements are made periodically during the test (Figs. 1.3 and 8.1). A convenient test condition is: $\sigma_{max} = 0.7\, S_g$, $\mathcal{R} = 0.05$. The hysteresis unload behavior is analyzed, using Eqn. (8.3) to obtain E^* and $\mathcal{L}(N)$. There are two basic behaviors. (i) When both stress corrosion and

matrix fatigue are absent, the crack spacing and E^* remain constant and the cyclic degradation of the interface is obtained directly

$$\mathcal{L}(N)/\mathcal{L}(1) \Rightarrow \tau/\tau_o \tag{8.7a}$$

This is expressed in the form

$$\tau/\tau_o = F(N) \tag{8.7b}$$

When E^* is found to change upon cycling, the crack spacing $\bar{d}$ diminishes because of either stress corrosion or matrix fatigue. Then, τ/τ_o is not given by changes in $\mathcal{L}(N)$. However, since $\bar{d}$ and E^* are related by Eqn. (6.1), it is still possible to obtain τ/τ_o using

$$\frac{\mathcal{L}(N)}{\mathcal{L}(1)}\left[\frac{E/E^*(1)-1}{E/E^*(N)-1}\right] \Rightarrow \tau/\tau_o \tag{8.8}$$

One complication arises because the slip overlap stress decreases during cycling. This causes the hysteresis loop shape to change. When this occurs, the hysteresis loop width *diminishes* upon further cycling and there is a change in $\Delta\varepsilon_u$ from parabolic to linear when the unloading stress $\sigma_u \rightarrow \sigma_\ell$. Analysis of the hysteresis loops to obtain τ/τ_o is *confined to the parabolic range,* in which Eqn. (8.3) is still applicable. However, to check for consistency, it is noted that slip overlap occurs at σ_{max} after N_ℓ cycles, where N_ℓ is obtained from Eqn. 6.13, by equating σ_ℓ to σ_{max}, as

$$\mathcal{L}(N_\ell) = \frac{(1-f)}{Ef}\,\frac{(\sigma_{max}-\sigma_i)}{2} \tag{8.9}$$

8.4 S-N Curves

When matrix crack growth does not occur during cycling, it is straightforward to predict the S(N) curve from the above measurements. The failure criterion specifies that failure occurs when the UTS decreases to $\sigma_{max} \Rightarrow \sigma_{max} = S_g(N)$. This criterion is combined with the measurement of $\tau/\tau_o(N, \Delta\sigma_o)$ to give the cycles to failure, N_f. The simple result is

$$N_f = (\sigma_{max}/S_g)\, F^{-1}. \tag{8.10}$$

For the case in which $\tau(N)$ is given by Eqn. (2.9), with S_g given by Eqn. (3.10), the cycles to failure are,

$$N_f = (S_g/\sigma_{max})^{(m+1)/\lambda}$$

provided that $\sigma_{max} > \sigma_{th}$, given by

$$\sigma_{th} = S_g\,(\tau_s/\tau_o)^{1/(m+1)}$$

A typical example is plotted on Fig. 8.2.

8.5 The Secant Modulus

The permanent strains prior to slip zone overlap can be predicted by a formula obtained upon rearranging Eqn. (6.4)

$$\varepsilon_o(N,\sigma_{max},\Delta\sigma) = \varepsilon^*(\sigma_{max}) + \frac{\mathcal{L}(1)}{\mathcal{L}(N)}\left[\varepsilon_o(1,\sigma_{max}) - \varepsilon^*(\sigma_{max})\right] \tag{8.11}$$

when overlap occurs, there are no further changes in ε_o. When $\bar{d}$ remains constant during fatigue, since ε_o (1, σ_{max}) is known from the tensile data, it is straightforward to predict ε_o (N, σ_{max}, $\Delta\sigma$) from Eqn. (8.11), by inserting $\mathcal{L}$(N) from Eqn. (8.7). Changes in $\bar{d}$ upon cycling, manifest as changes in E^*, can be included by using E^* (N) to re-evaluate ε^* (N).

With ε_o now known, the secant modulus can be predicted from Eqn. (6.11), by using

$$1/E_s = 1/E^* + \varepsilon_o/\sigma_{max} \tag{8.12}$$

One limitation is that a model for predicting changes in crack spacing $\bar{d}$ with $\Delta\sigma$ and $\mathcal{R}$-ratio does not yet exist for matrices susceptible to either stress corrosion or fatigue. This is not a serious limitation for many technologically important non-oxide CMCs. For certain oxide matrix CMCs, and high toughness Si_3N_4 matrix CMCs, further analysis is needed to address this problem. In the interim, experimental measurements of crack spacing are required.

9. PRELIMINARY FATIGUE EXPERIMENTS

Some preliminary fatigue results are presented to illustrate the methodology described in Sections 8.3 and 8.4. For this purpose, cyclic loading experiments have been conduced on a unidirectional CAS/SiC composite and the hysteresis measurements used to predict the fatigue life. This composite exhibits an unusually rapid degradation in the interface sliding stress with cyclic loading. Moreover, the

matrix is susceptible to stress corrosion, making it necessary to measure crack spacing in order to predict cyclic behavior. Nevertheless, it will be demonstrated that the fatigue life can be predicted with good accuracy. The fatigue threshold is particularly well defined.

The results to be described refer to tension fatigue tests conducted on straight specimens, with dimensions 150 x 3 x 4 mm and with axial strains measured using a 10 mm extensometer. Tests conducted at several stress ranges $\Delta\sigma$, with a fixed stress ratio R=0.05, have the typical hysteresis loops shown in Fig 9.1. Initially, the width of the hysteresis loops increases with cycles, a result of the degradation in τ. However, upon further cycling, the loop width decreases. Moreover, the loops exhibit a linear portion following loading to large stresses, $\sigma - \sigma_{min}$. The tangent modulus E_H in the linear region is essentially $E_H = f\,E_f = 74$ GPa. These two latter effects are associated with the overlap of the slipped regions between adjacent matrix cracks, caused by the degradation in τ.

The evolution of matrix cracking with loading cycles is shown in Fig 9.2. The crack spacing decreases rapidly in the first few cycles and subsequently reaches a saturation value of ~140 μm. During the period in which the matrix cracks develop by stress corrosion ($N \leq 10$), the hysteresis loops exhibit a consequent asymmetry, and do not close upon reloading.

The sliding stress was evaluated by analyzing the parabolic regions of the loading stress-strain curves. The results are plotted in Fig. 9.3. The initial sliding stress τ_o = MPa, is consistent with previous measurements obtained by pushout tests (Mackin and Zok, 1993). The sliding stress drops rapidly with N, reaching a saturation level of ~5 MPa following ~30 cycles.

The degradation function τ/τ_0 has been obtained by fitting the data in Fig. 9.3 with Eqn. 2.9. This function was then combined with Eqn 8.10 to obtain the fatigue life prediction, shown in Fig. 9.4. Evidently the predictions are in good agreement with the

experimental measurements. In particular, the fatigue threshold, σ_{th}, appears to be given with good fidelity.

10. CONCLUDING REMARKS

A methodology has been described which may be used to predict the fatigue response of CMCs when the dominant mechanism is the cyclic degradation of the interface sliding stress. It predicts the S-N curve, the permanent strain and the modulus reduction, based on a relatively few hysteresis loop measurements. An illustration of S-N behavior has been given for a SiC/CAS material.

In some cases, it would be expected that fiber strength degradation occurs during fatigue. Such behavior arises when C fibers are used. It may also occur at high temperatures, particularly upon thermomechanical fatigue. A procedure for including fiber strength degradation is a priority for further research.

REFERENCES

Allen, R.F., Beevers, C.J. and Bowen, P. (1993) *Composites*, **24 [2]**.

Archard, J.F. (1953) *J. Appl. Phys.*, **24**, 981.

Aveston, J., Cooper, G.A. and Kelly, A. (1971) in *The Properties of Fiber Composites*, NPL Conf. Proc., pp. 15–26.

Bao, G. and McMeeking, R.M. (1993) *Acta Metall. Mater.*, in press.

Baste, S., El Guerjouma, R. and Andoin, B. (1992) *Mech. of Mtls.*, **14**, 15–32.

Beyerle, D., Spearing, S.M. and Evans, A.G. (1992a) *J. Am. Ceram. Soc.*, **75[12]** 3321–30.

Beyerle, D., Spearing, S.M., Zok, F. and Evans, A.G. (1992b) *J. Am. Ceram. Soc.*, **75[10]** 2719–25.

Budiansky, B. and Cui, L. (1993) to be published.

Budiansky, B., Hutchinson, J.W. and Evans, A.G. (1986) *J. Mech. Phys. Solids*, **34**, 167–89.

Budiansky, B., Hutchinson, J.W. and Evans, A.G. (1993) to be published.

Butkus, L.M. and Holmes, J.W. (1992) *Ceram. Eng. Sci. Proc.*

Charalambides, P.G. and Evans, A.G. (1989) *J. Am. Ceram. Soc.*, **72**, 746-53

Cho, C., Holmes, J.W. and Barber, J.R. (1992) *J. Am. Ceram. Soc.*, **75[2]** 316–24.

Corten, H.T. (1967) *Modern Composite Materials* (eds. Broutman, L.J. and Krock, R.H.) Addison, p. 27.

Curtin, W.A. (1991a) *J. Mater. Sci.*, **26**, 5239-53

Curtin, W.A. (1991b) *J. Am. Ceram. Soc.*, **74**, 2837.

Daniels, H.E. (1945) *Proc. Roy. Soc.*, **A183**, 405.

Evans, A.G., Domergue, J.M. and Vagaggini, E. (1993) *J. Am. Ceram. Soc.*, to be published.

Freudenthal, A., *Fracture* (1967) (ed. Liebowitz, H.) Academic Press.

Gao, Y.C., Mai, Y-W. and Cotterell, B. (1988) *J. App. Math. Phys.* (ZAMP), **39**, 550-72.

Guiu, M., Li, M. and Reece, M.J. (1992) *J. Am. Ceram. Soc.*, **75**, 2976.

He, M.Y., Wu, B.X., Evans, A.G. and Hutchinson, J.W. (1993) *Mech. of Mtls.*, in press.

Henstenburg, R.B. and Phoenix, S.L. (1989) *Polym. Comp.* **10[5]**, 389–406.

Hild, F., Domergue, J.M., Leckie, F.A. and Evans, A.G. (1993) *Intl. Jnl. Solids Structures*, to be published.

Holmes, J.W. (1993) "Elevated Temperature Creep and Fatigue Behavior of Fiber Reinforced Ceramics," to be published in *Elevated Temperature Mechanical Behavior*

of Ceramic Matrix Composites, Nair, S.V and Jakus, K., Eds., Butterworth-Heinemann, Stoneham, MA.

Holmes, J.W. and Cho, C. (1992) *J. Am. Ceram. Soc.*, **75**, 929.

Hutchinson, J.W. and Jensen, H. (1990) *Mech. of Mtls.*, **9**, 139.

Hutchinson, J.W. and Suo, Z. (1991) *Appl. Mech. Rev.*, **28**.

Kim, R.Y. (1992) *Ceram. Eng. Sci. Proc.*, **13**, 281–300.

Kim, R.Y. and Katz, A.P. (1988) *Ceram. Eng. Sci. Proc.*, **9**, 853–60.

Kim, R.Y. and Pagano, N. (1991) *J. Am. Ceram. Soc.*, **74**, 1082–90.

Lathabai, S., Rödel, J. and Lawn, B.R. (1991) *J. Am. Ceram. Soc.*, **74**, 1340.

Laws, N. and Dvorak, G. (1980) *Jnl. Composite Mtls.*, **22**, 900.

Liang, C and Hutchinson, J.W. (1993) to be published.

Mackin, T.J., Warren, P. and Evans, A.G. (1992) *Acta Metall. Mater.*, **40**, 1251-57.

Mackin, T.J. and Zok, F.W. (1993) *J. Am. Ceram. Soc.*, **75**, 3169-71.

Marshall, D.B., Cox, B.N. and Evans, A.G. (1985) *Acta Metall.*, **33**, 2013–21.

Matthews, J.R., Shack, W.J. and McClintock, F.A. (1976) *J. Am. Ceram. Soc.*, **59**, 304.

McCartney, L.N. (1987) *Proc. Roy. Soc.*, **A409**, 329–50.

McMeeking, R.M. (1993) *International Journal of Solids and Structures*, in press.

McMeeking, R.M. and Bao, G. (1993) to be published.

McMeeking, R.M. and Evans, A.G. (1990) *Mech. of Mtls.*, **9**, 217–27.

McNulty,J., Zok, F.W. and Evans, A.G. (1993) to be published.

Minford, E. and Prewo, K.M. (1987) in, *Tailoring Multiphase and Composite Ceramics*, Tressler, R.E., Messing, G.L., Pantano, C.G. and Newnham, R.E., Eds., Plenum Press, New York and London, pp. 561-70.

Oh, H.L. and Finnie, I. (1970) *Intl. J. Frac.*, **6**, 287.

Phoenix, L. and Raj, R. (1992) *Acta Metall. Mater.*, **40**, 2813–28.

Pryce, A.W. and Smith, P. (1992) *J. Mater. Sci.*, **27**, 2695–2704.

Rödel, J., Kelly, J.F. and Lawn, B.R. (1990) *J. Am. Ceram. Soc.*, **73**, 3313.

Rousseau, C.Q. (1990) *Thermal and Mechanical Behavior of Metal Matrix and Ceramic Matrix Composites, ASTM STP 1080*, eds. Kennedy, J.M., Moeller, H.H. and Johnson, W.S., American Society for Testing and Materials, Philadelphia, PA.

Spearing, S.M. and Zok, F.W. (1993) *Jnl. Eng. Mtls. Tech.*, in press.

Suresh, S. (1991) "Fatigue of Materials," Cambridge Solid State Science Series, Cambridge University Press, Cambridge, UK.

Sutcu, M. (1989) *Acta Metall.*, **37[2]** 651–61.

Thouless, M.D. and Evans, A.G. (1988) *Acta Metall.*, **36**, 517.

Vagaggini, E. and Evans, A.G. (1993) *J. Am. Ceram. Soc.*, in press.

Wiederhorn, S.M. (1972) *J. Am. Ceram. Soc.*, **55**, 81.

Xia, C., Carr, R.R. and Hutchinson, J.W. (1993) *Harvard Univ. Report Mech-202, Acta Metall. Mater.*, in press.

Xia, C. and Hutchinson, J.W. (1993a) Harvard Univ. Report Mech-208, *Intl. Jnl. Solids Structures*, to be published.

Xia, C. and Hutchinson, J.W. (1993b) Harvard Univ. Report.

Zawada, L.P. and Butkus, L.M. (1991) *J. Am. Ceram. Soc.*, **74 [11]** 2851–58.

Zok, F.W. and Spearing, S.M. (1992) *Acta Metall. Mater.*, **40**, 2033.

FIGURE CAPTIONS

Fig. 1.1 Fatigue effects in ceramic matrix composites: a) S-N curve, and b) decrease in elastic modulus.

Fig. 1.2 Typical tensile stress-strain curves for CMCs. Also shown are typical hysteresis loops, a) without and b) with crack closure.

Fig. 1.3 Effects of cycling on the hysteresis loop.

Fig. 2.1 A schematic of the interface model.

Fig. 2.2 A mode II crack in a thin brittle layer.

Fig. 3.1 A schematic of stress redistribution around a failed fiber.

Fig. 4.1 The change in crack density with stress for a unidirectional CAS/SiC composite (Beyerle *et al.*, 1992).

Fig. 4.2 The cell model used to relate macroscopic strains to constituent properties.

Fig. 4.3 The mechanism map distinguishing the regimes of interface response (Vagaggini and Evans, 1993).

Fig. 4.4 A schematic of a growing matrix crack with bridging fibers.

Fig. 4.5 Simulations of crack density evolution as a function of the matrix flaw size variable, designated λ_s (Spearing and Zok, 1993).

Fig. 5.1 Comparison between stress-strain curves for 2-D and 1-D materials. (a) Data for SiC/SiC and SiC/CAS, (b) schematic.

Fig. 5.2 Matrix crack formation in 2-D materials.

Fig. 5.3 Effect of interface bonding on the stress for tunnel cracking (Xia *et al.*, 1993).

Fig. 5.4 Change in modulus caused by tunnel cracking (Xia *et al.*, 1993).

Fig. 5.5 Predicted stress/strain curves for tunnel cracking (Xia *et al.*, 1993).

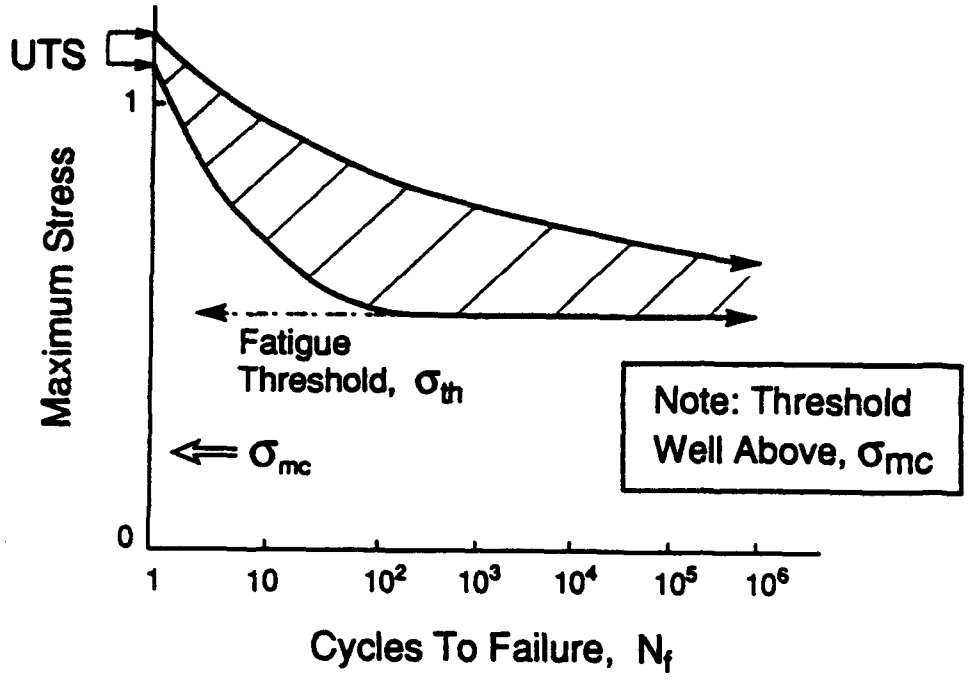

Figure 1.1 (a)

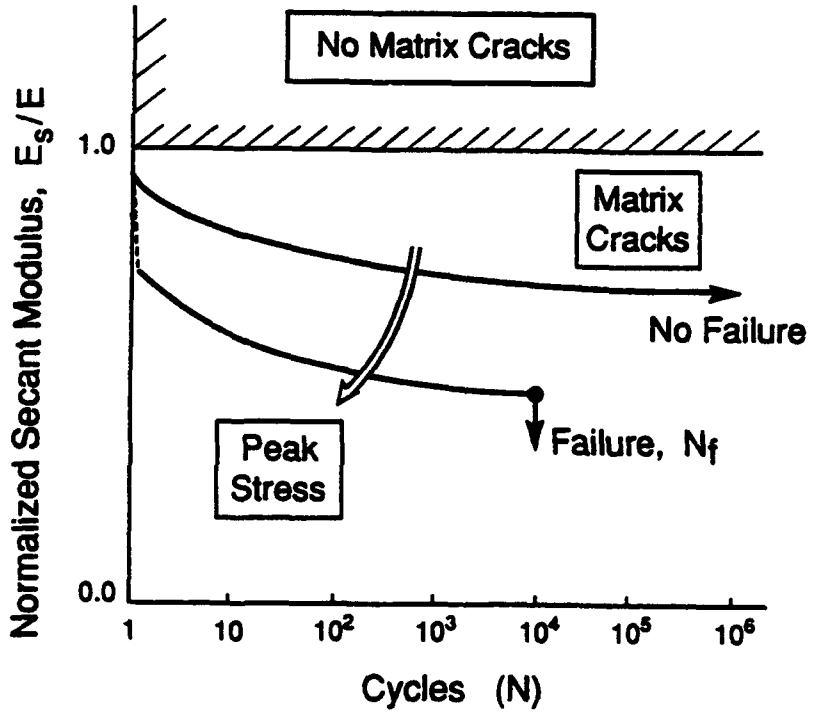

Figure 1.1 (b)

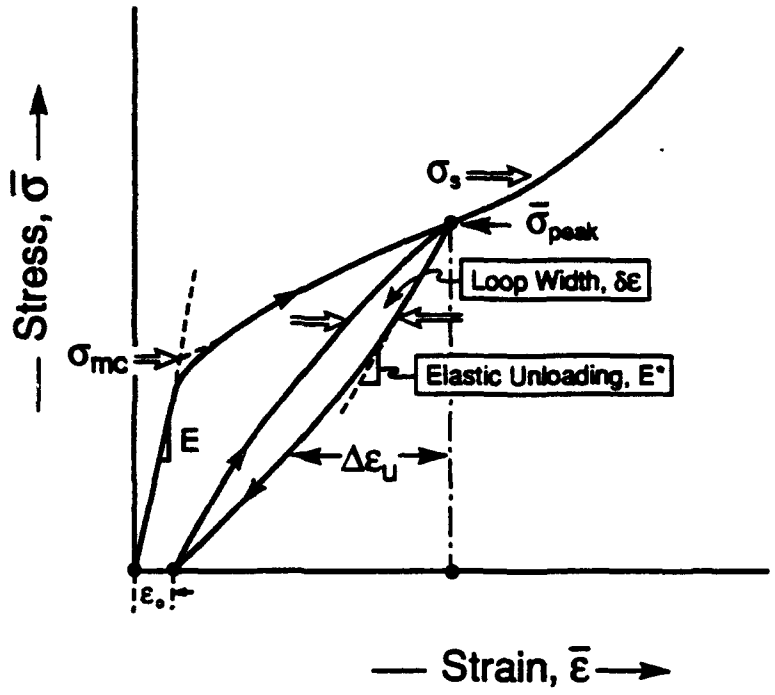

Fig. 1.2(a)

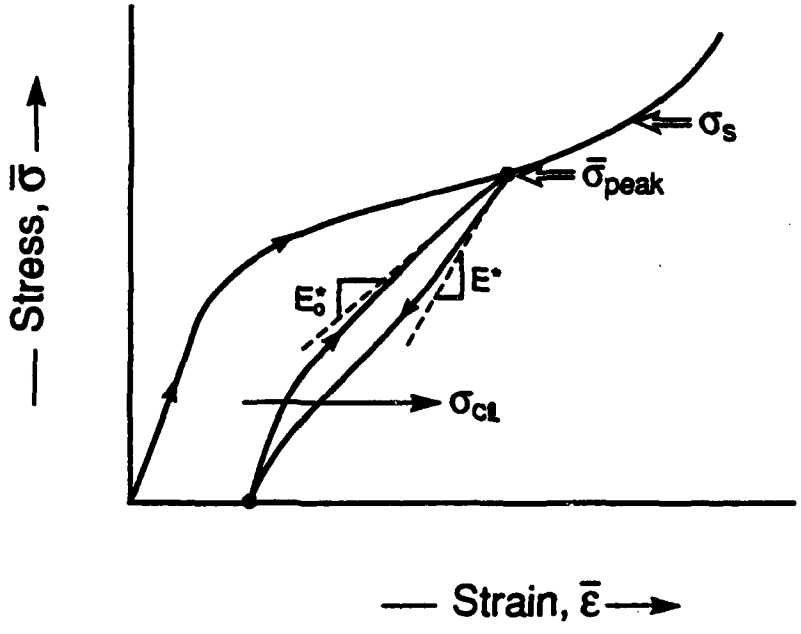

Fig. 1.2(b)

Interface Degradation Probe

Measurement of $\tau(N)$

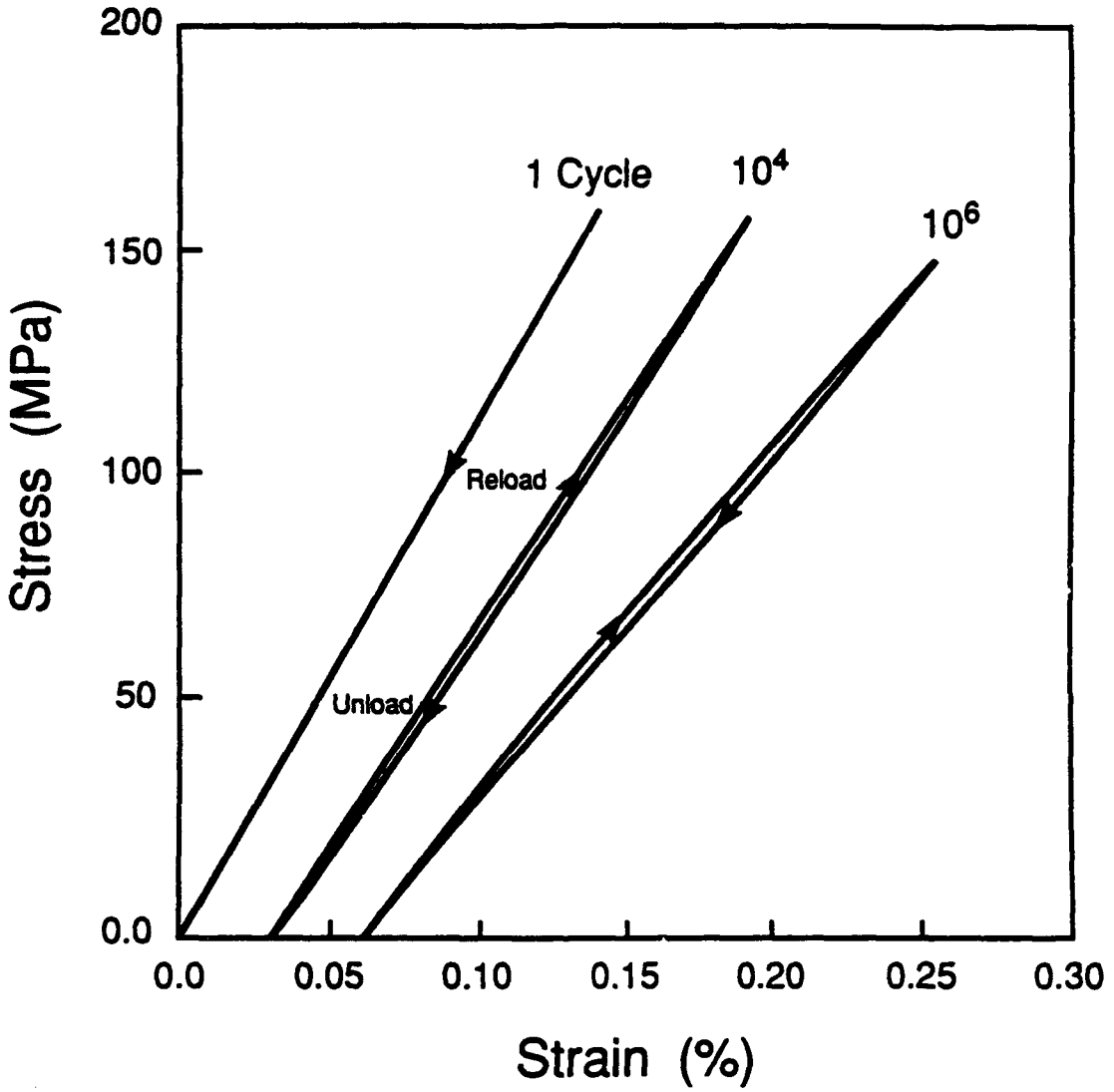

As τ changes Upon Fatigue

- Inelastic Strain Increases
- Elastic Modulus Decreases

Model

Figure 1.3

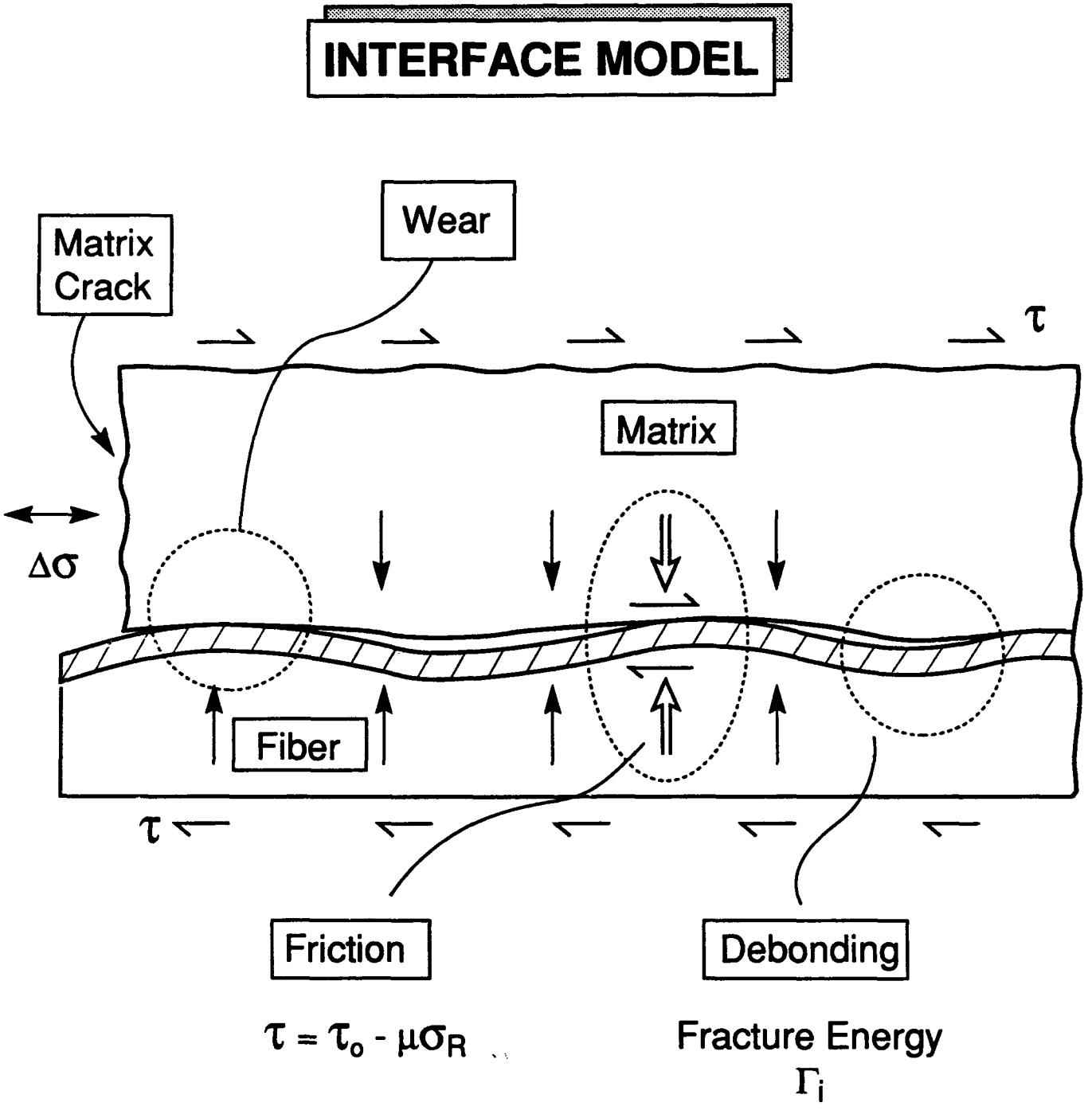
INTERFACE MODEL
Matrix Crack
Wear
τ
Matrix
Δσ
Fiber
τ
Friction
Debonding
τ = τo - μσR
Fracture Energy
Γi

Fig. 2.1

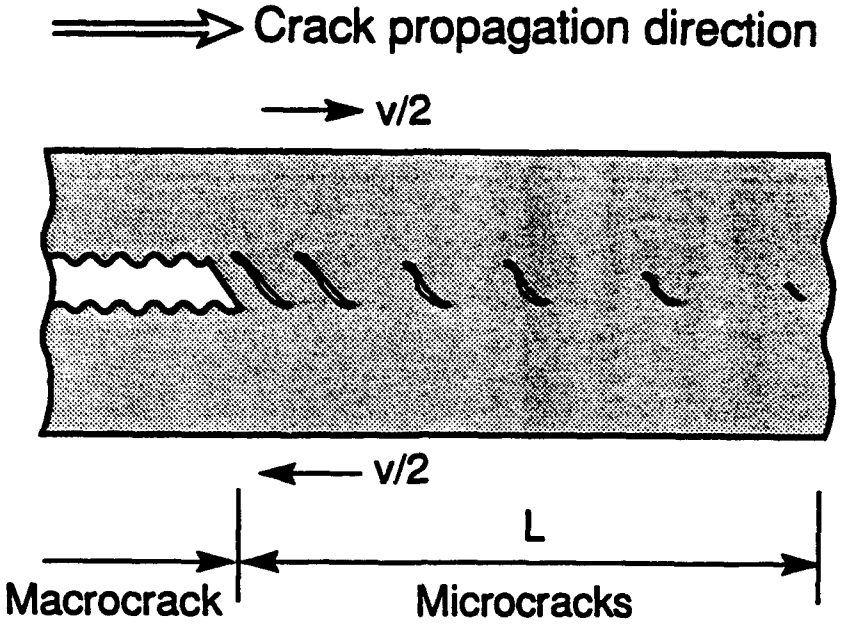
Crack propagation direction
v/2
v/2
L
Macrocrack
Microcracks

Fig. 2.2

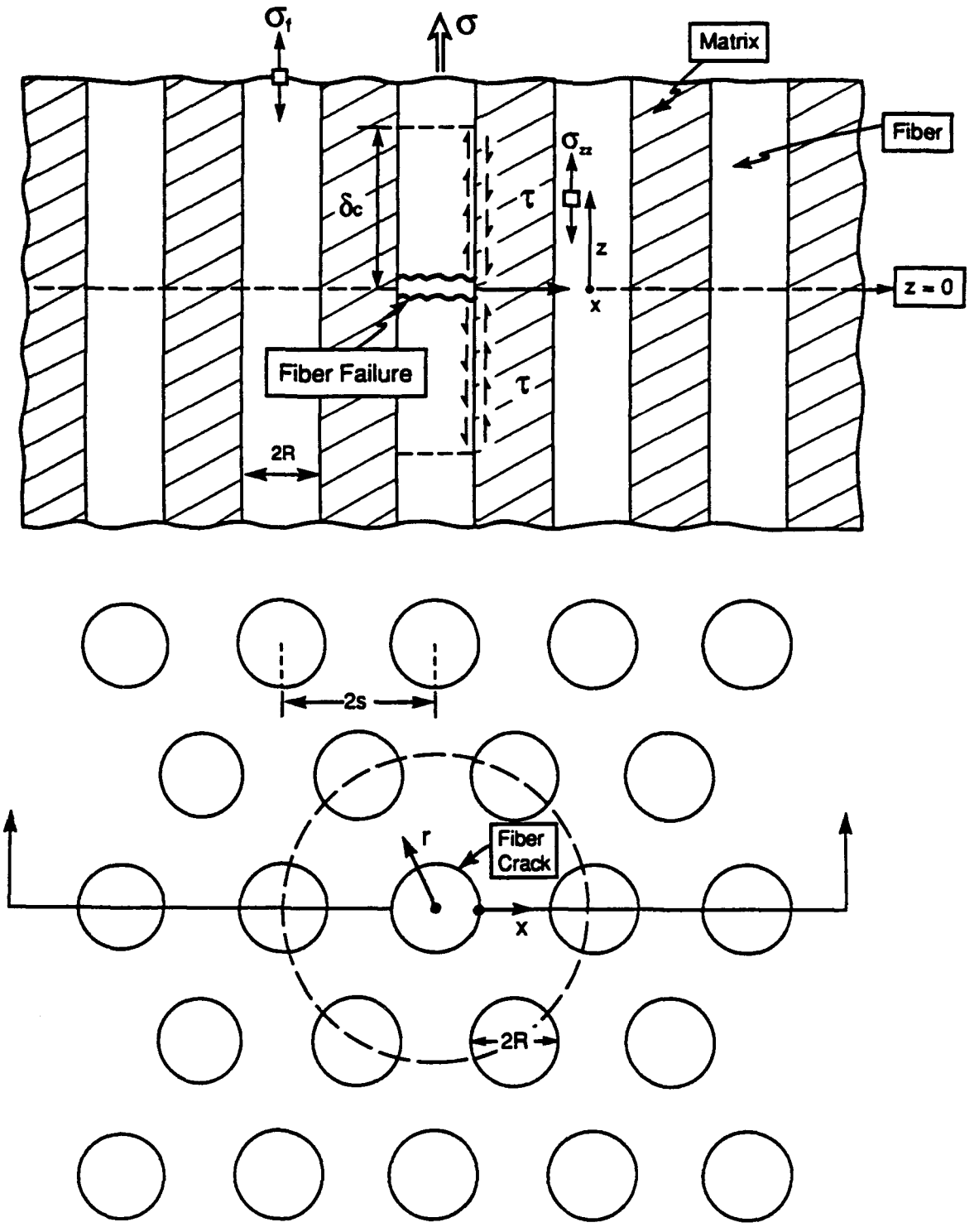
σf
σ
Matrix
Fiber
σzz
δc
τ
z
z = 0
x
Fiber Failure
τ
2R
2s
r
Fiber
Crack
x
2R

Figure 3.1

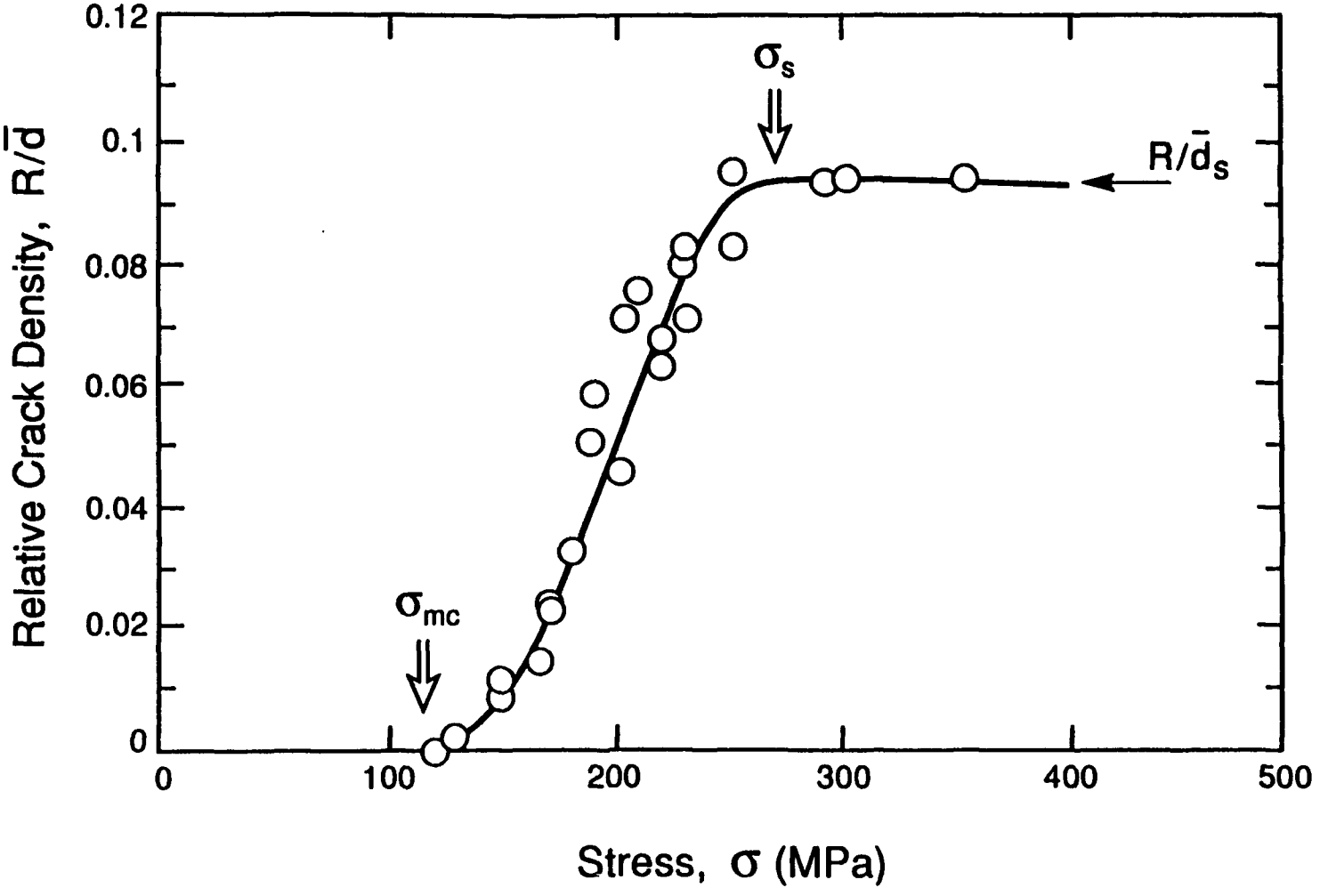
0.12
0.1
0.08
0.06
0.04
0.02
0
0
100
200
300
400
500
Relative Crack Density, R/d̄
Stress, σ (MPa)
σs
σmc
R/d̄s

Fig. 4.1

Measurement of Sliding

Matrix Crack Model

Hysteresis Loops

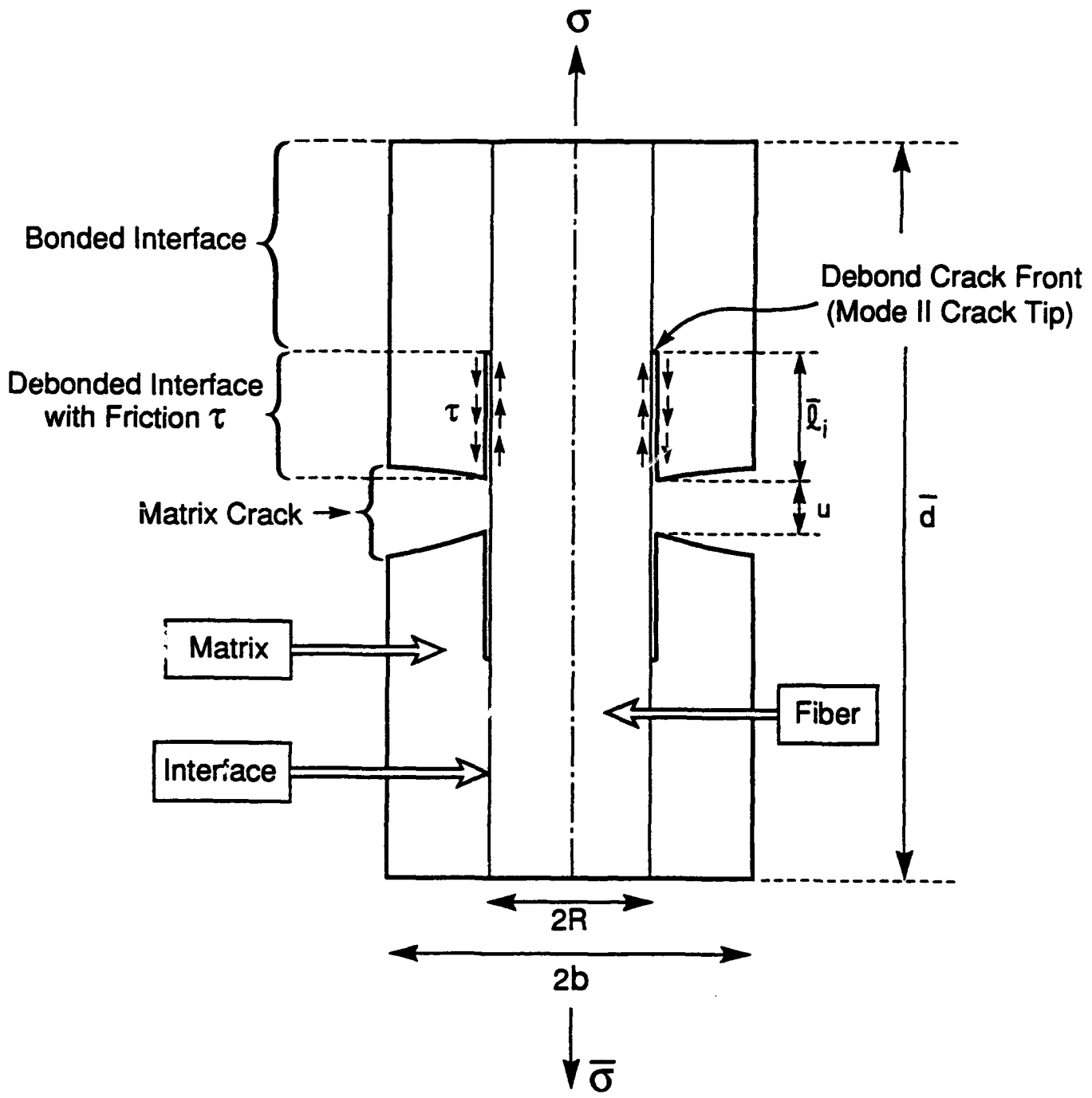

Figure 4.2

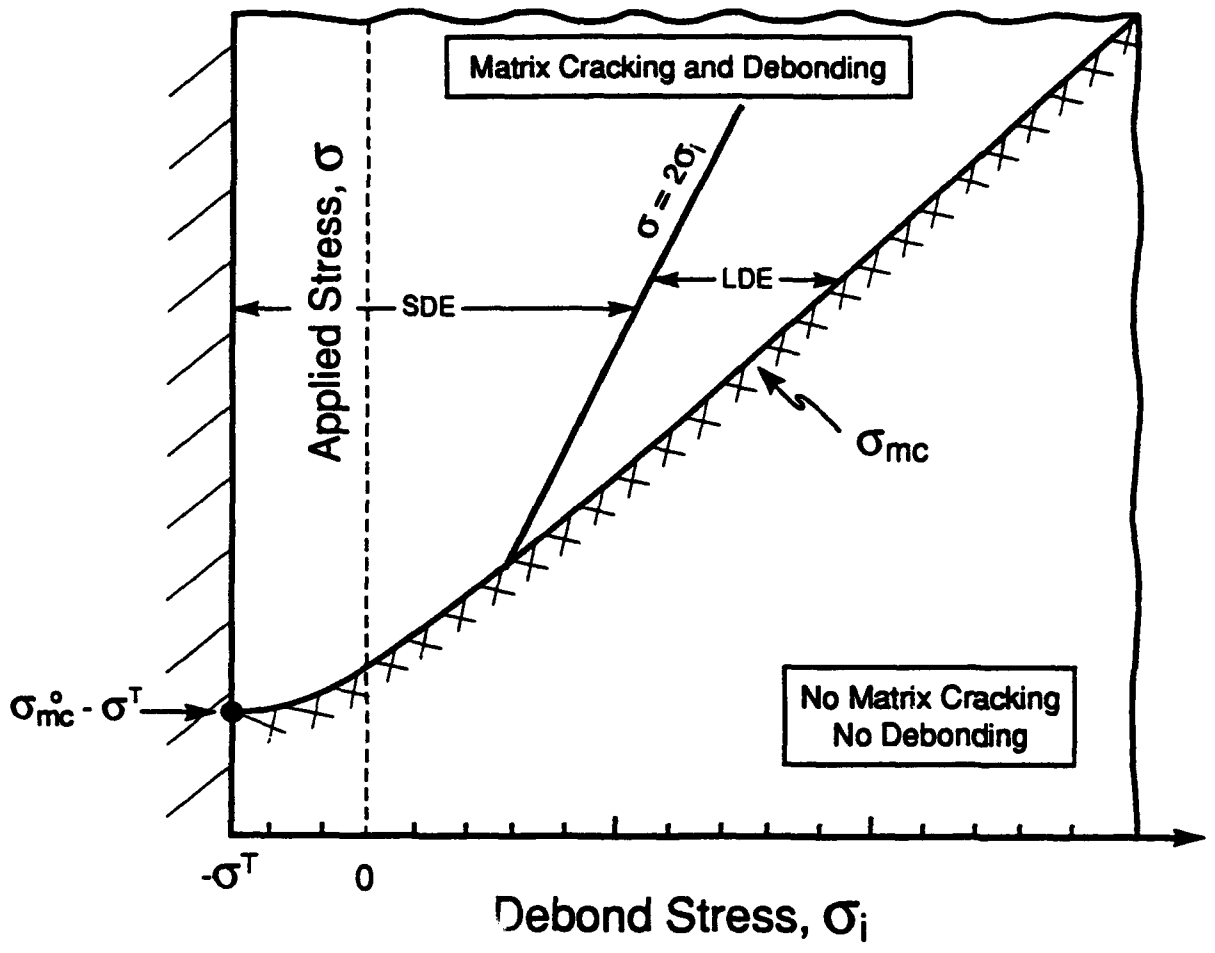
Matrix Cracking and Debonding
Applied Stress, σ
σ = 2σi
SDE
LDE
σmc
No Matrix Cracking
No Debonding
σmc° - σT
-σT
0
Debond Stress, σi

Figure 4.3

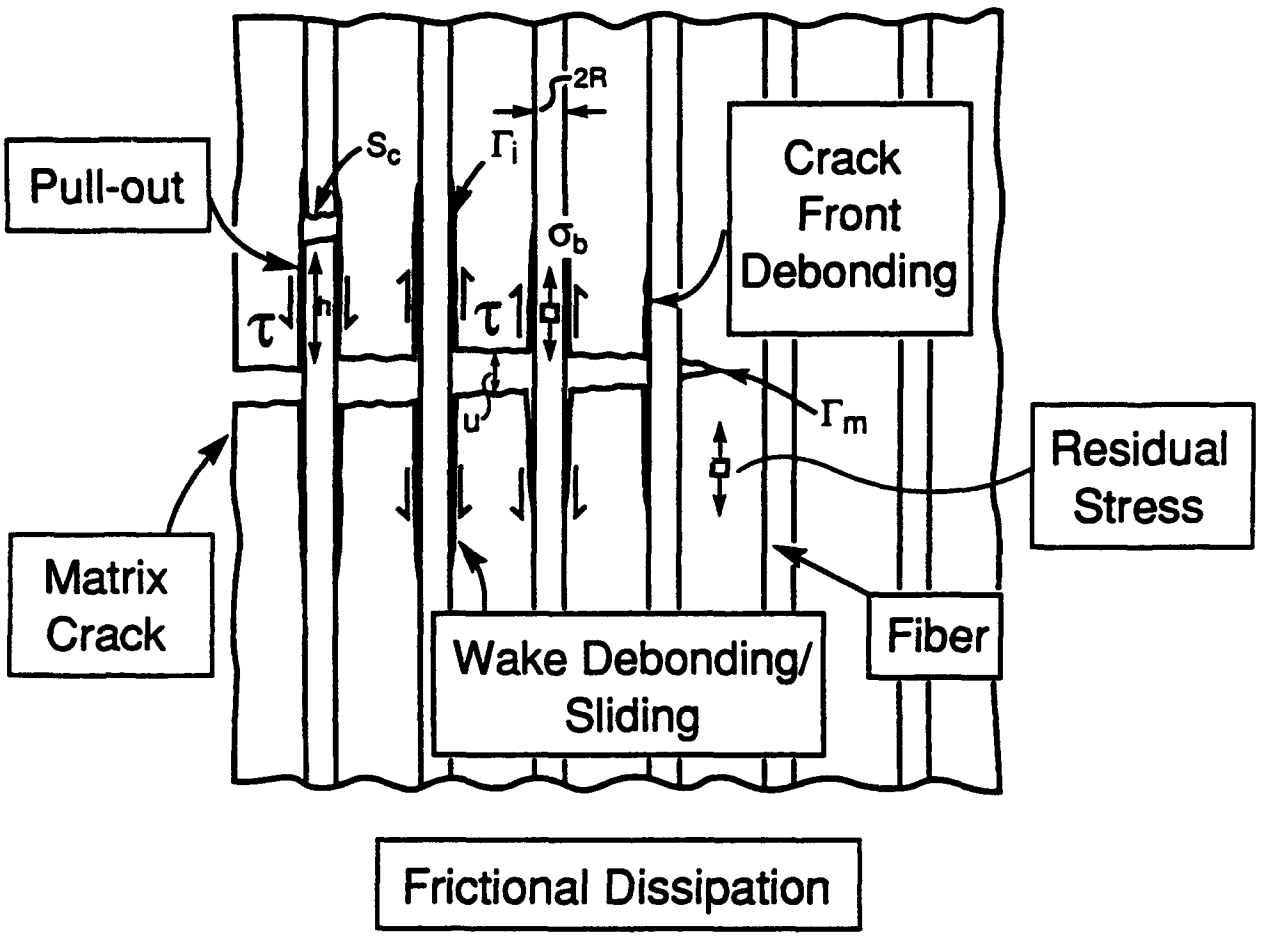
2R
s_c
Γ_i
σ_b
Pull-out
Crack
Front
Debonding
τ
h
τ
u
Γ_m
Residual
Stress
Matrix
Crack
Wake Debonding/
Sliding
Fiber
Frictional Dissipation

Fig. 4.4

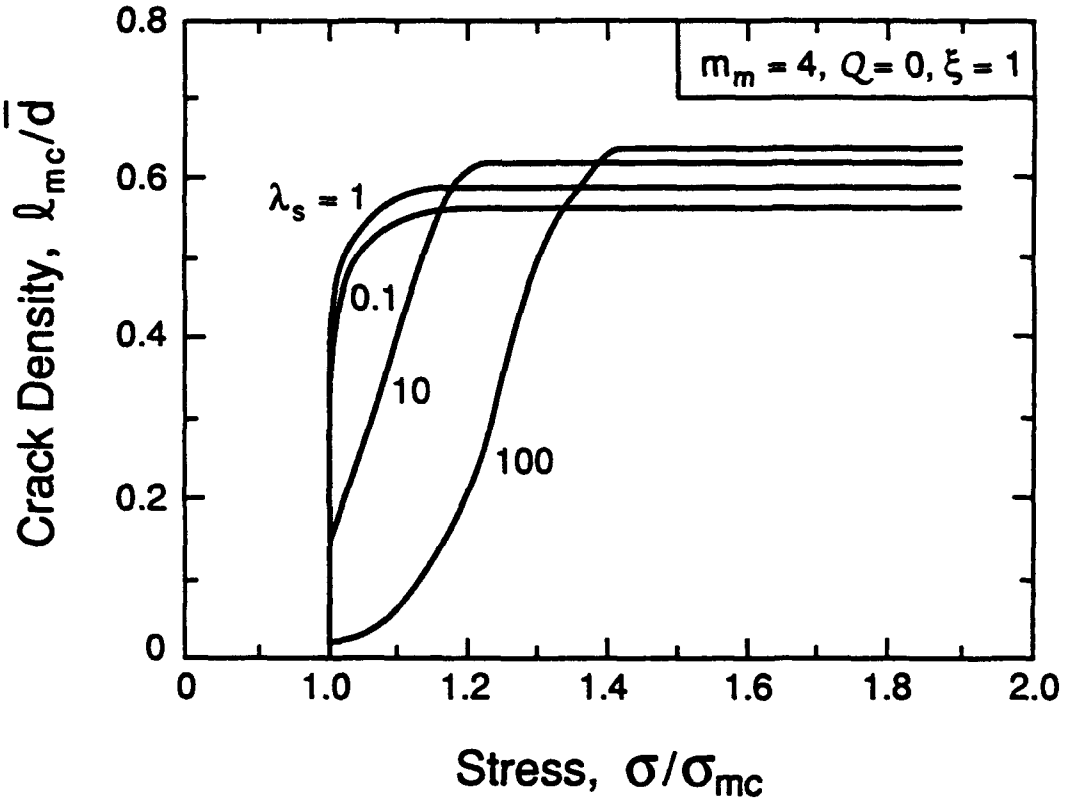
0.8
0.6
0.4
0.2
0
0
1.0
1.2
1.4
1.6
1.8
2.0
$m_m = 4, Q = 0, \xi = 1$
$\lambda_s = 1$
0.1
10
100
Crack Density, $\ell_{mc}/\bar{d}$
Stress, σ/σ_{mc}

Fig. 4.5

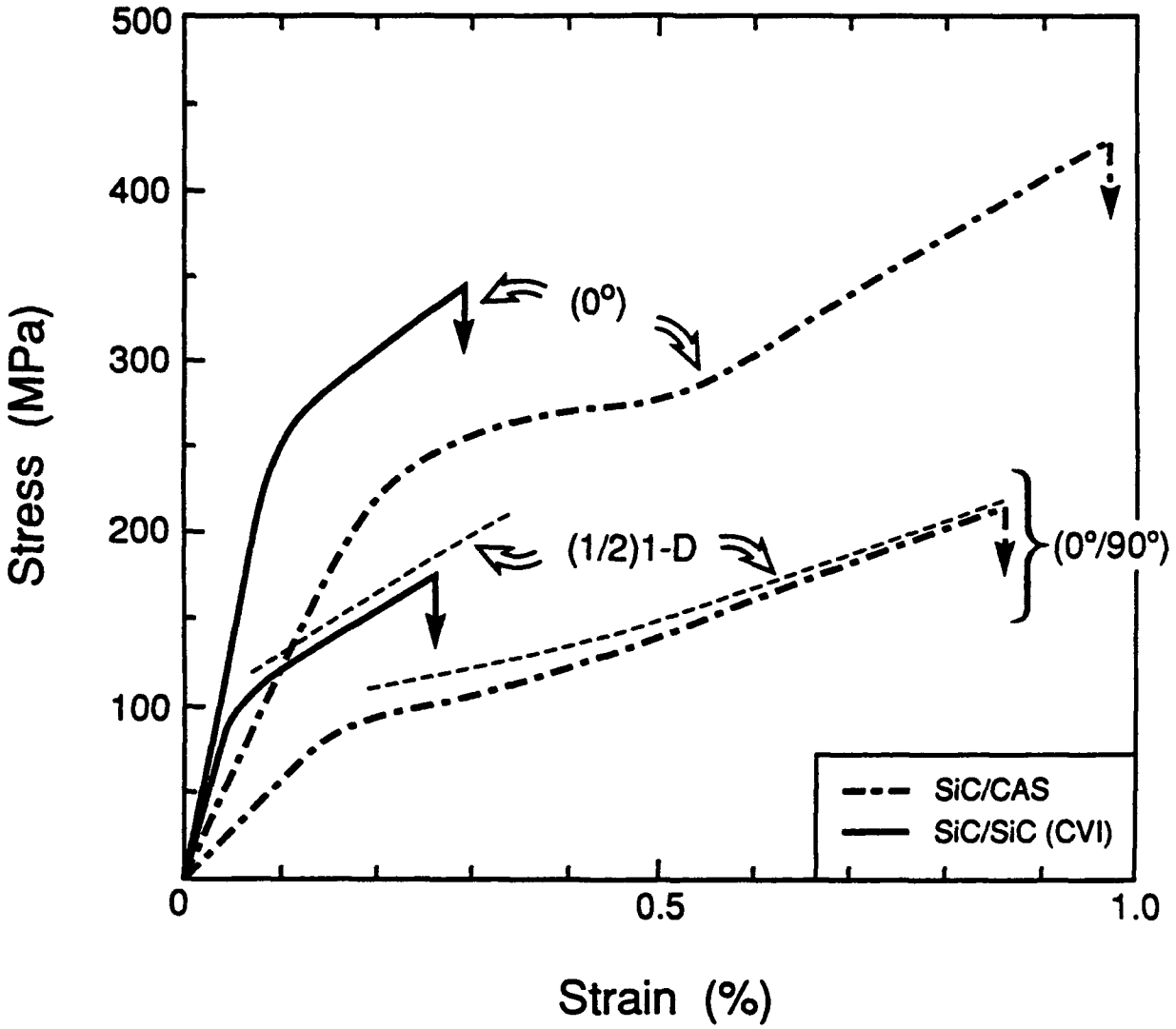
500
400
300
200
100
Stress (MPa)
0
0.5
1.0
Strain (%)
(0°)
(1/2)1-D
(0°/90°)
SiC/CAS
SiC/SiC (CVI)

Fig. 5.1a

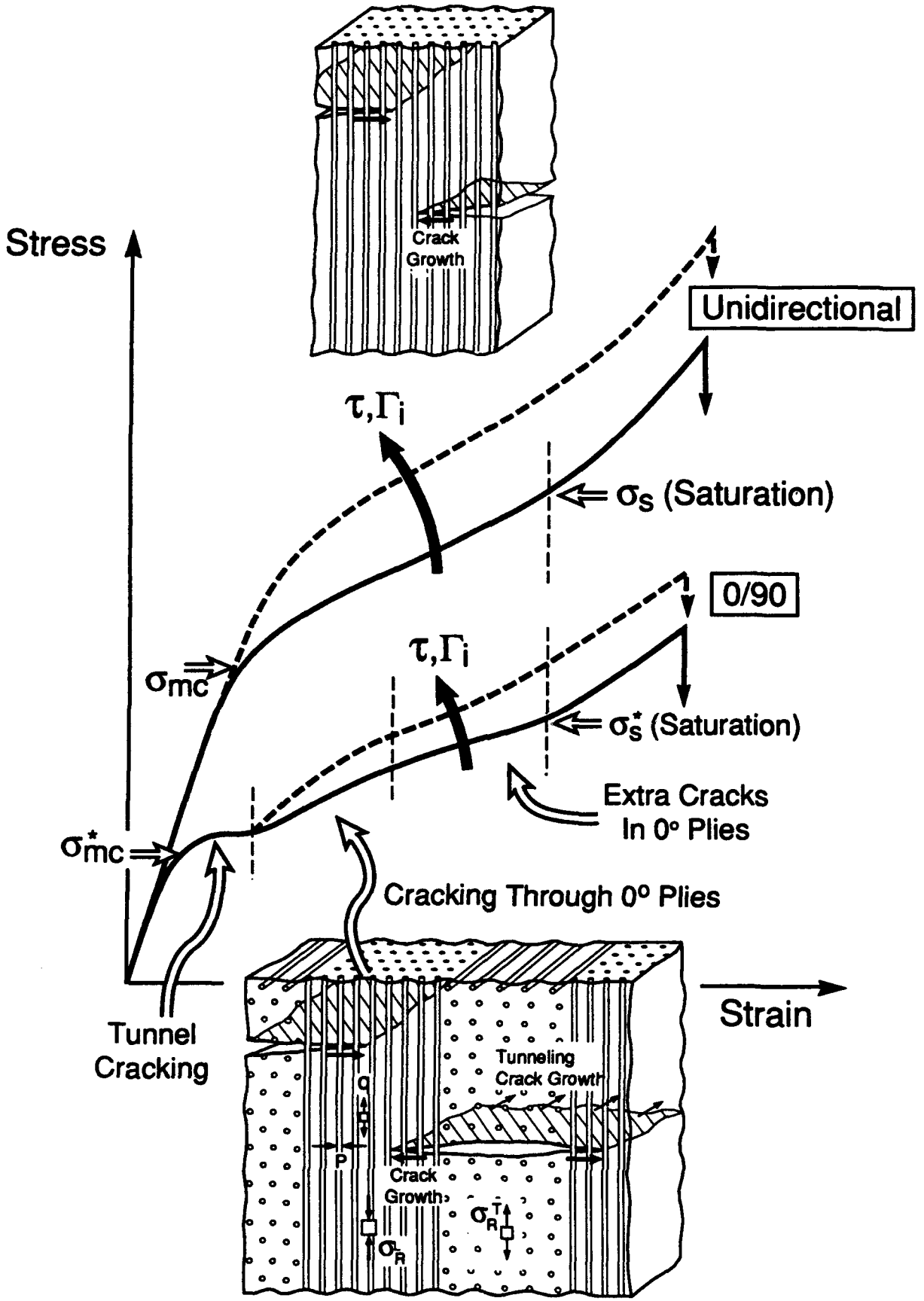

Evans.URI-11/93-amk-D48s1249-4

Fig. 5.1b

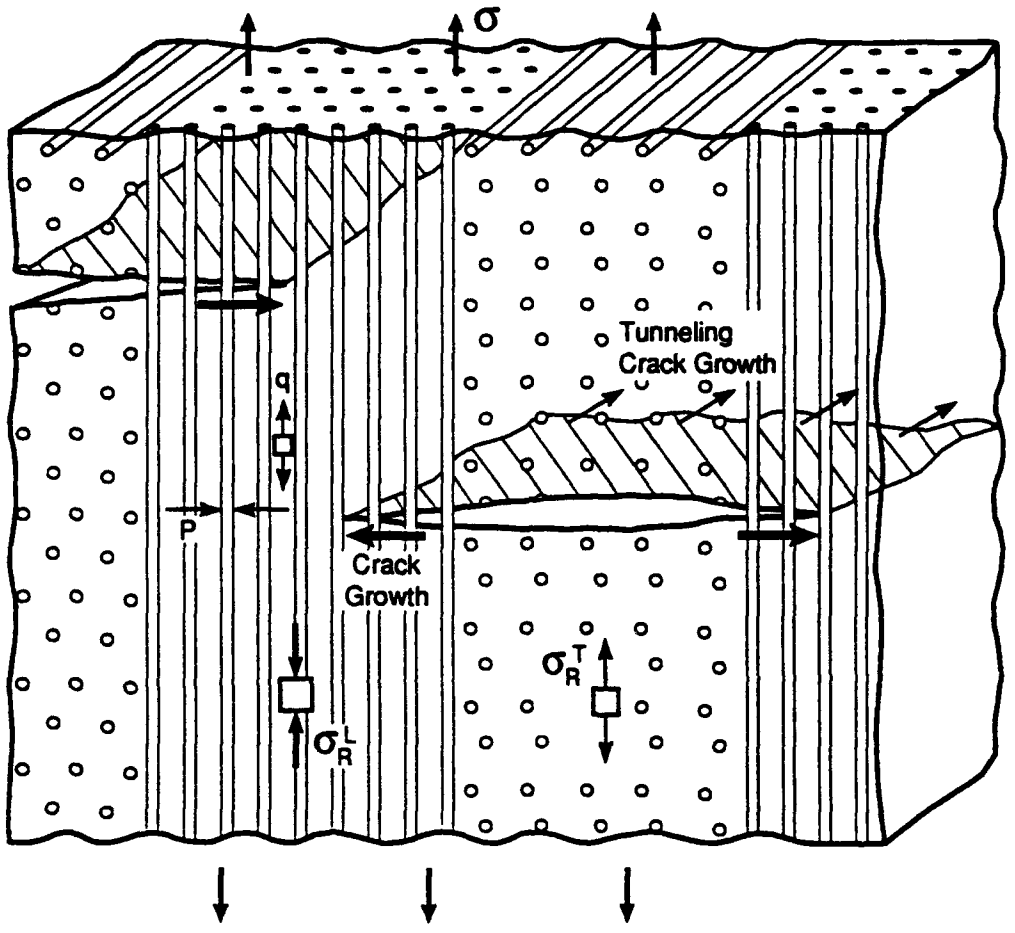

Fig. 5.2

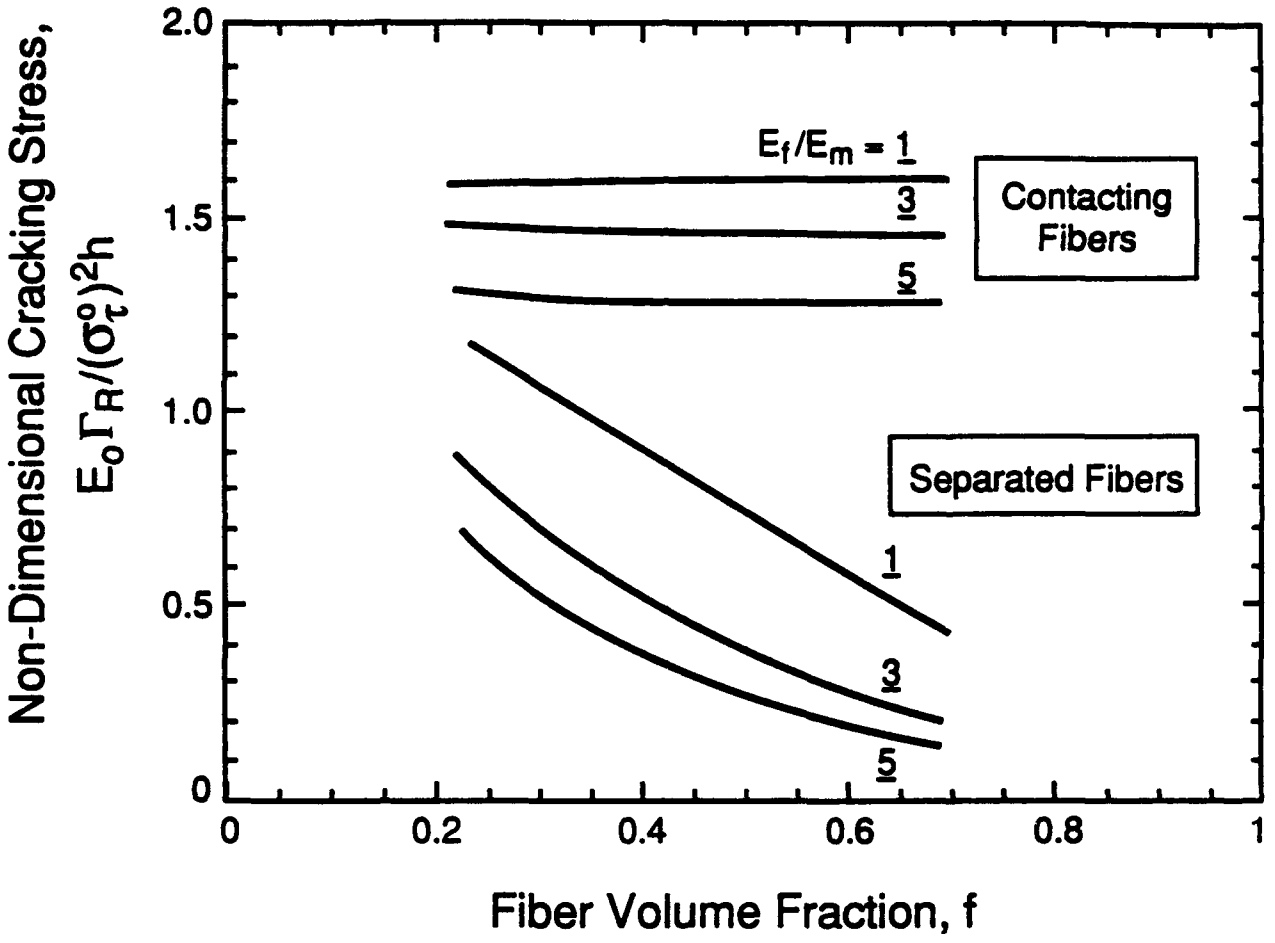
Non-Dimensional Cracking Stress,
$E_o\Gamma_R/(\sigma_\tau^o)^2h$
2.0
1.5
1.0
0.5
0
0
0.2
0.4
0.6
0.8
1
E_f/E_m = 1
3
5
Contacting Fibers
Separated Fibers
1
3
5
Fiber Volume Fraction, f

Fig. 5.3

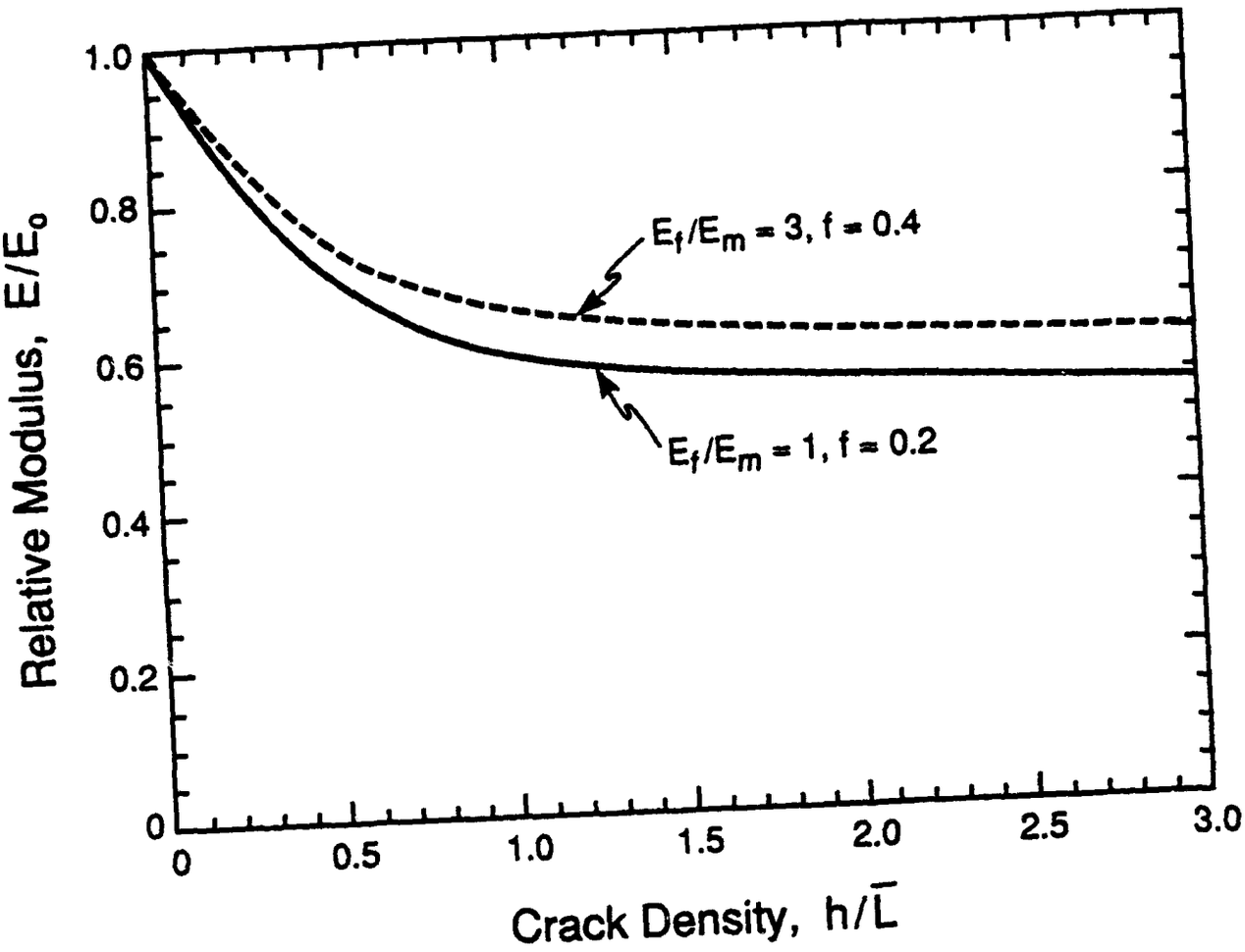
1.0
0.8
0.6
0.4
0.2
0
Relative Modulus, $\bar{E}/E_o$
$E_f/E_m = 3, f = 0.4$
$E_f/E_m = 1, f = 0.2$
0
0.5
1.0
1.5
2.0
2.5
3.0
Crack Density, $h/\bar{L}$

Fig. 5.4

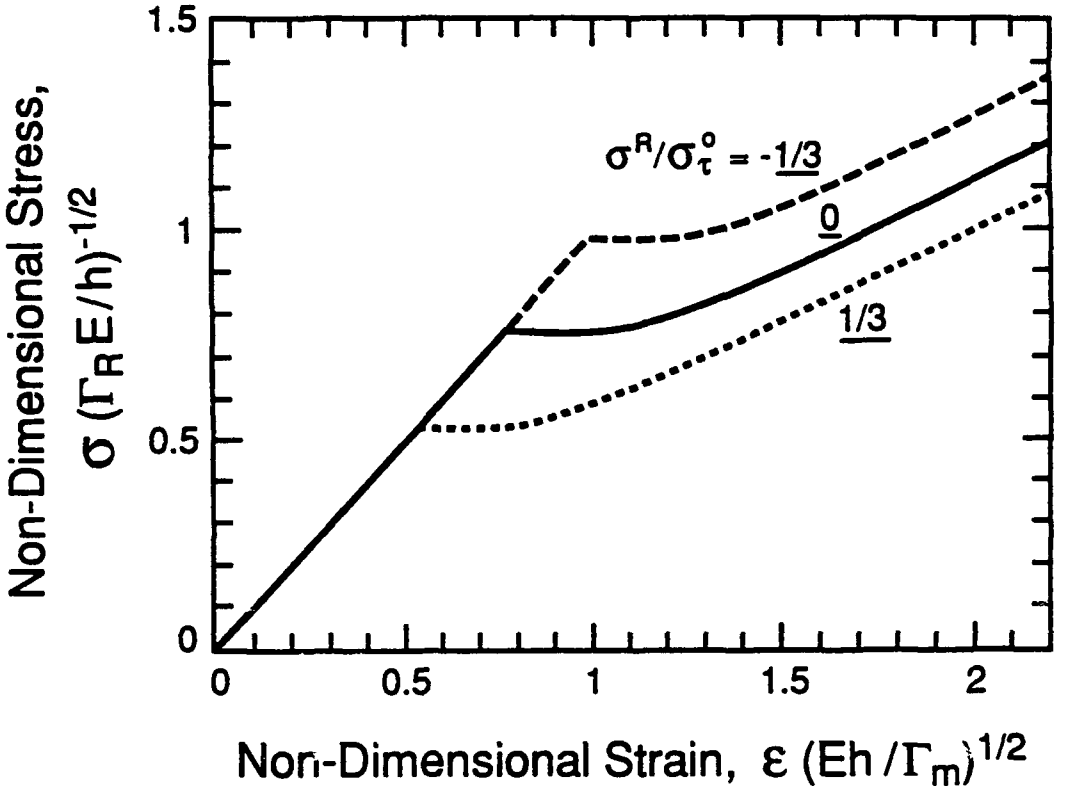
1.5
1
0.5
0
0
0.5
1
1.5
2
σ^R/σ^o_τ = -1/3
0
1/3
Non-Dimensional Stress, $\sigma\,(\Gamma_R E/h)^{-1/2}$
Non-Dimensional Strain, $\varepsilon\,(Eh/\Gamma_m)^{1/2}$

Fig. 5.5

Fig. 5.6

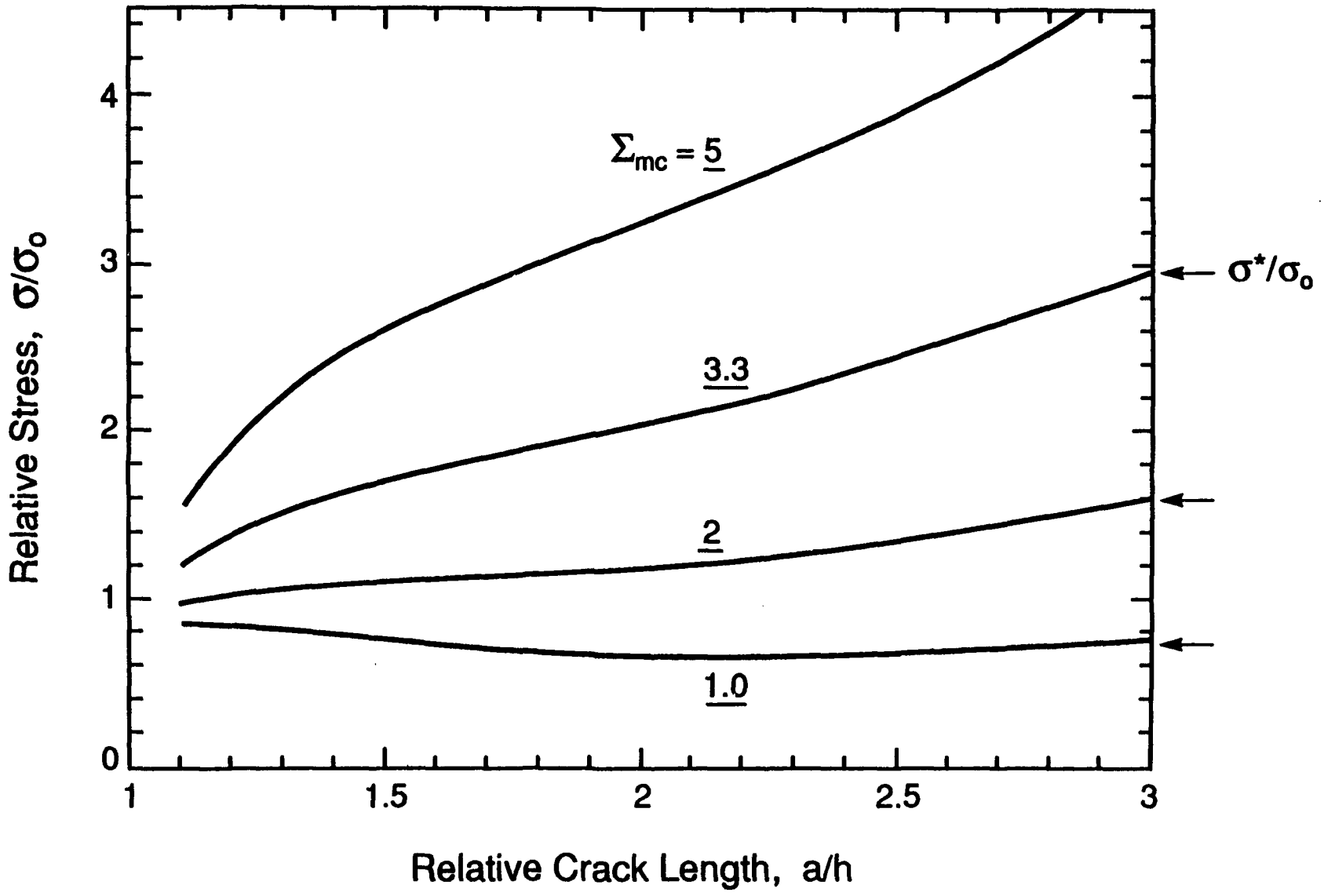

Evans.URI-12/93-amk-D4681175-2

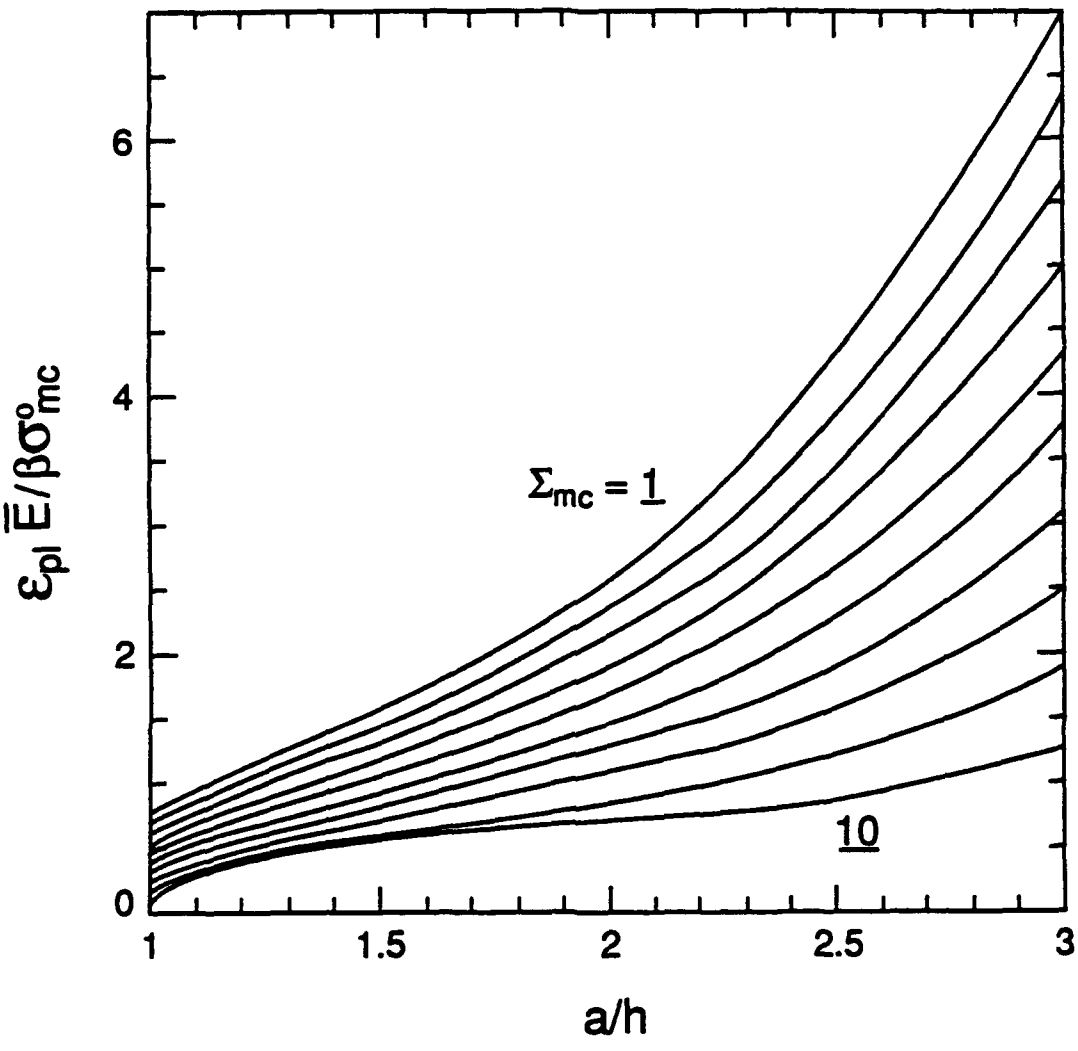
$\varepsilon_{pl}\,\bar{E}/\beta\sigma^{o}_{mc}$
6
4
2
0
1
1.5
2
2.5
3
a/h
$\Sigma_{mc} = 1$
10

Figure 5.7

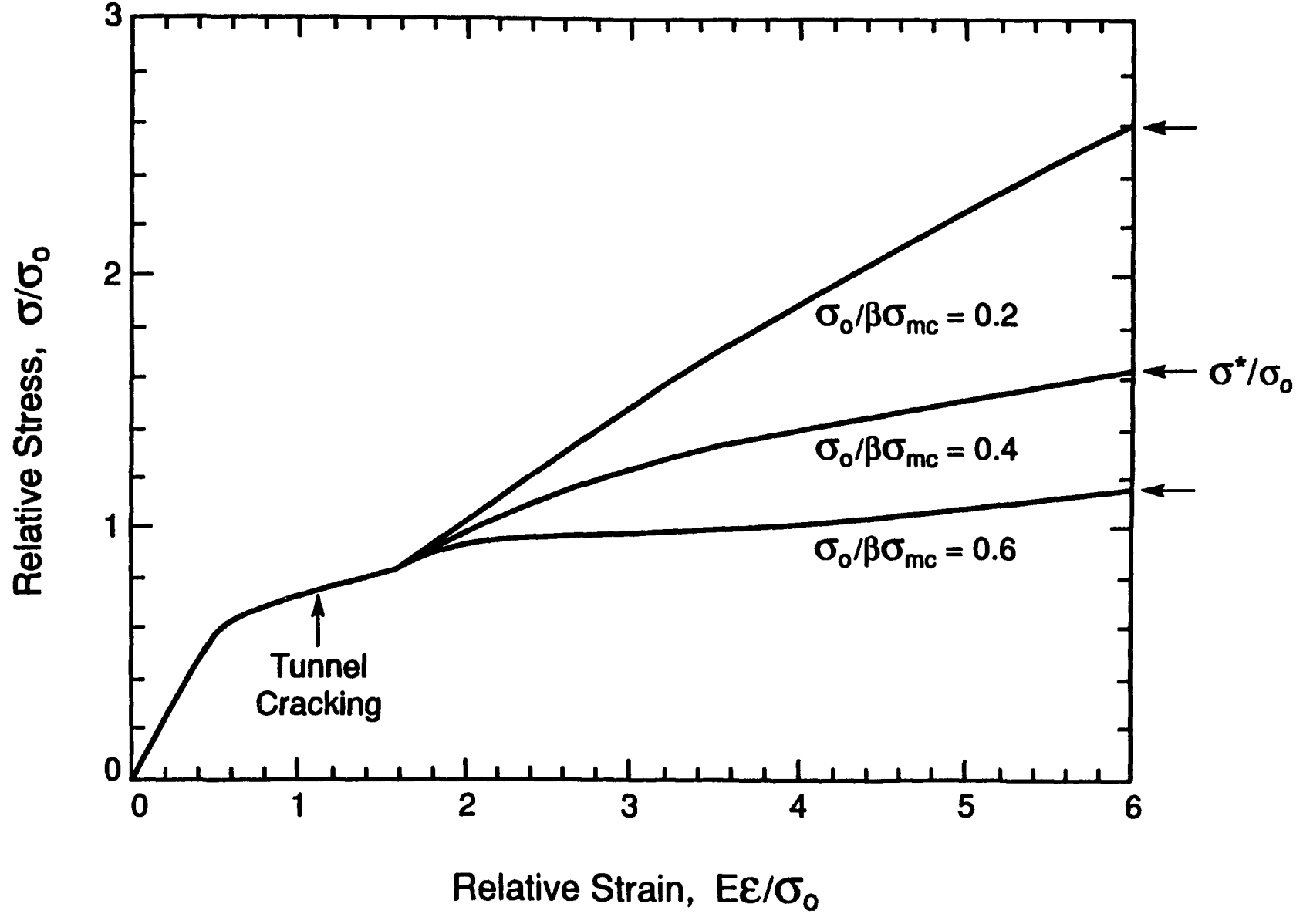

Fig. 5.8

Evans.URI-12/93-amk-D4681175-4

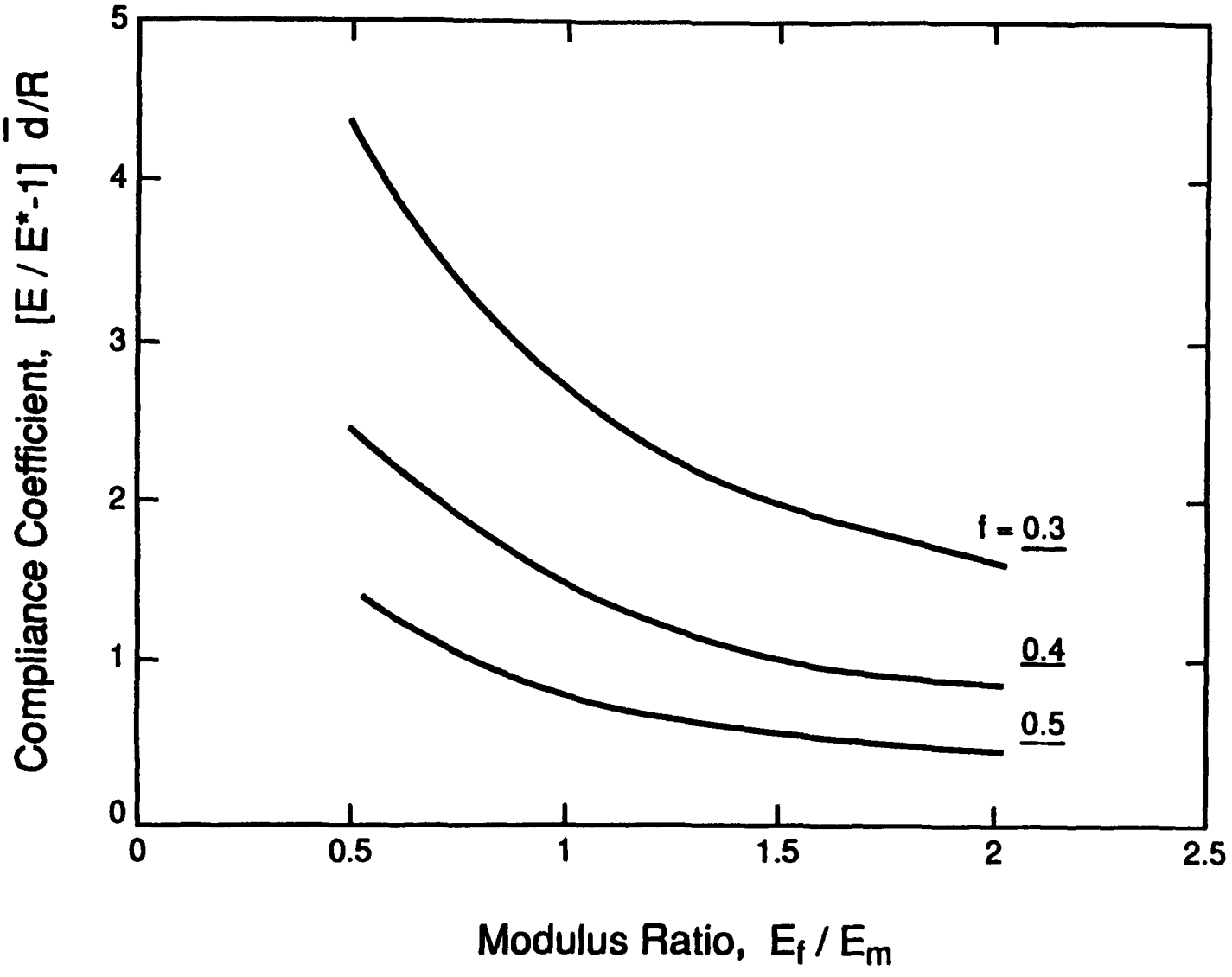
Compliance Coefficient, [E / E*-1] d̄/R
Modulus Ratio, E_f / E_m
f = 0.3
0.4
0.5
0
1
2
3
4
5
0
0.5
1
1.5
2
2.5

Fig. 6.1

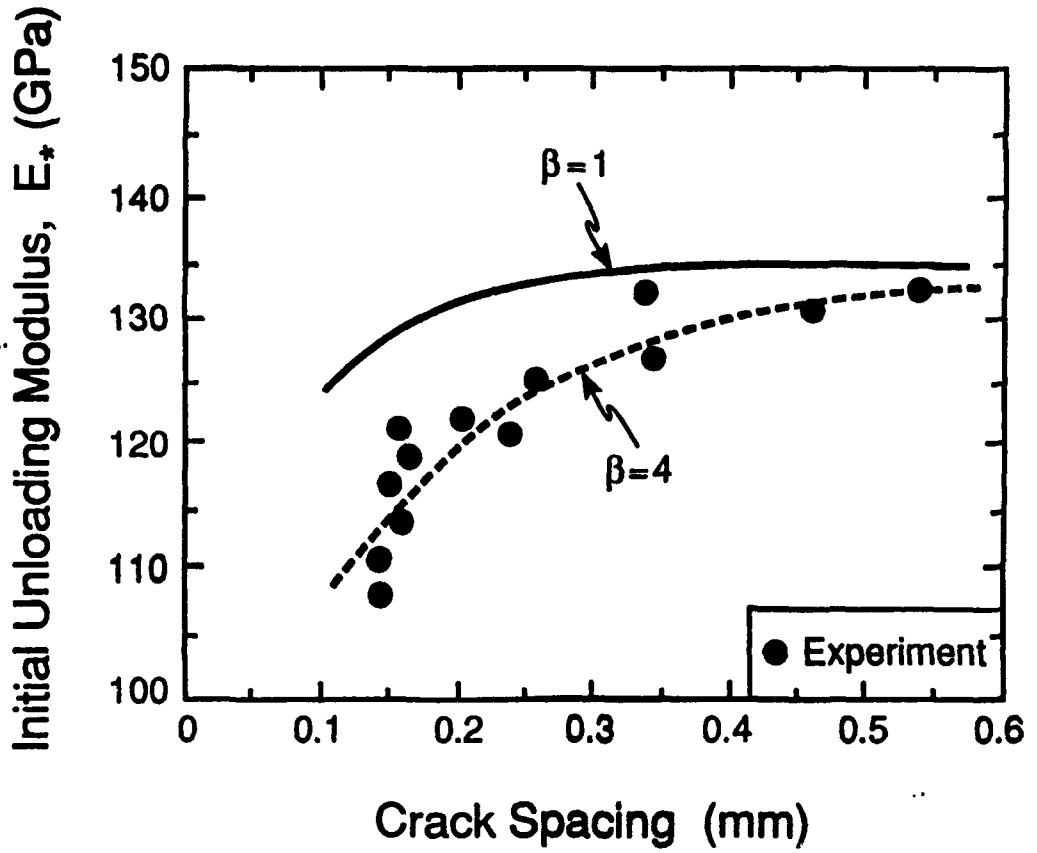
Initial Unloading Modulus, E* (GPa)
150
140
130
120
110
100
0
0.1
0.2
0.3
0.4
0.5
0.6
Crack Spacing (mm)
β=1
β=4
Experiment

Fig. 6.2

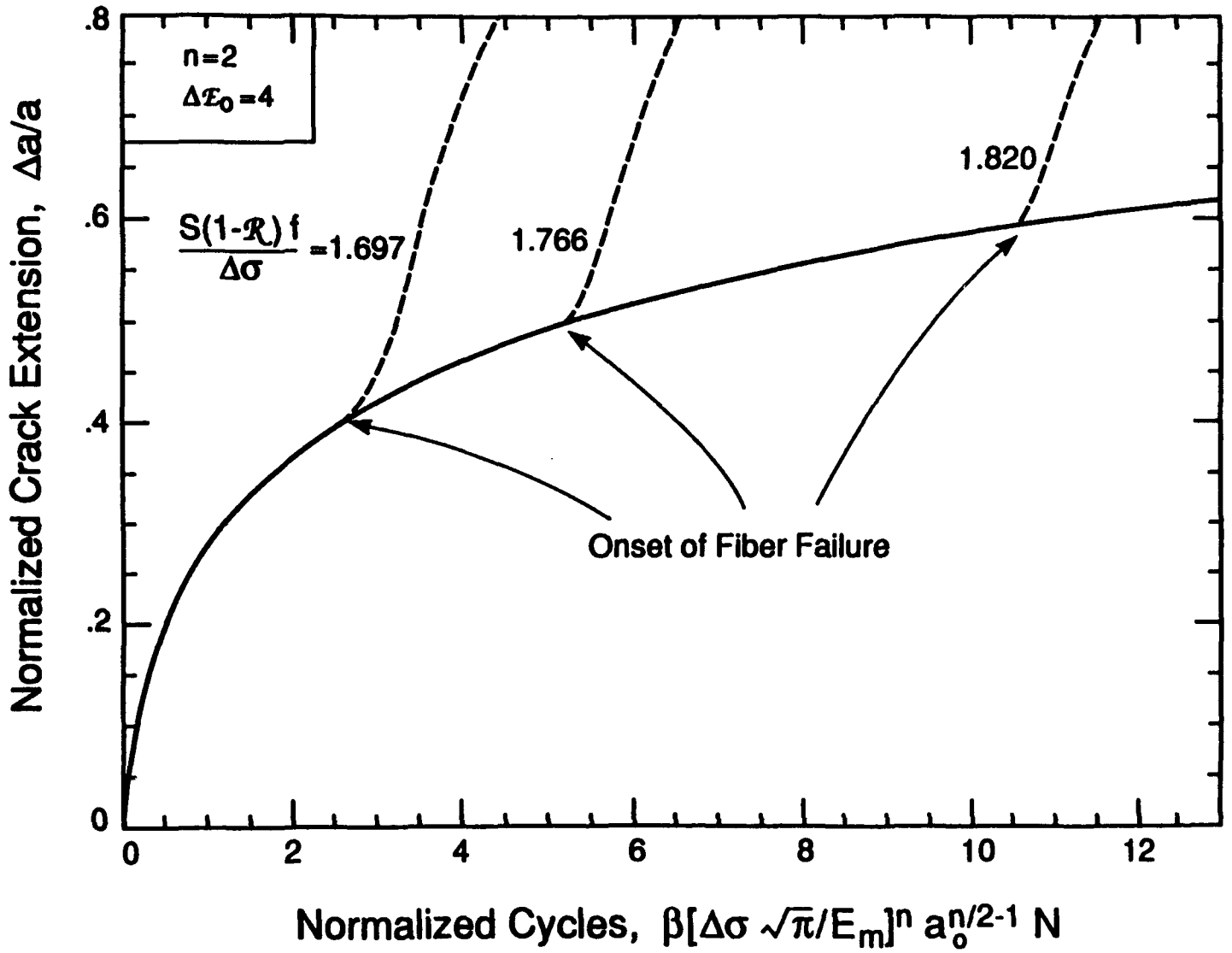
n=2
$\Delta\mathcal{E}_0$=4
$\frac{S(1-\mathcal{R})f}{\Delta\sigma}$ =1.697
1.766
1.820
Onset of Fiber Failure
Normalized Crack Extension, Δa/a
Normalized Cycles, $\beta[\Delta\sigma\sqrt{\pi}/E_m]^n a_o^{n/2-1} N$
0
.2
.4
.6
.8
0
2
4
6
8
10
12

Fig. 7.1

Fatigue Methodology

CMC Life Program

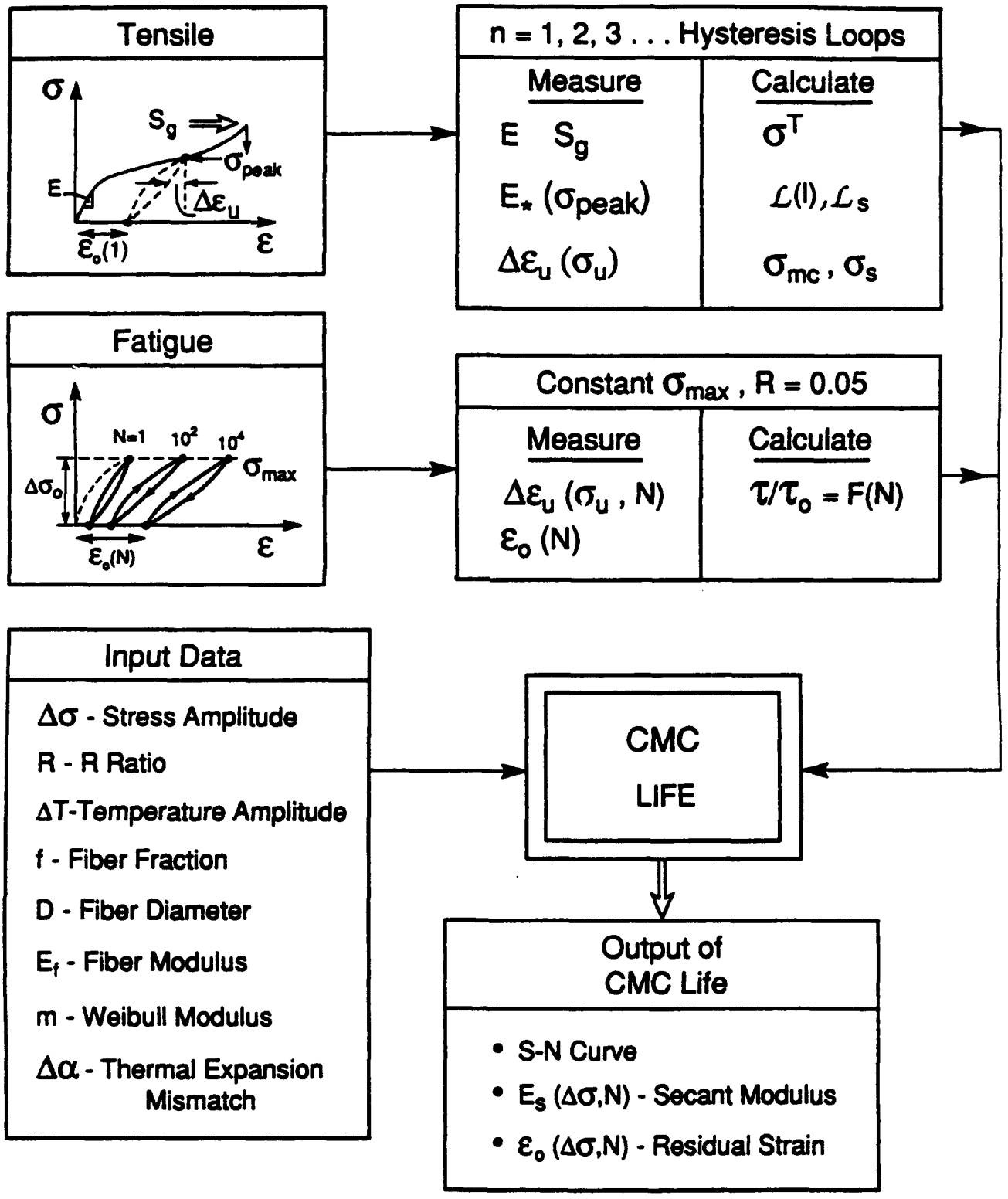

Figure 8.1

FATIGUE DEGRADATION OF INTERFACE

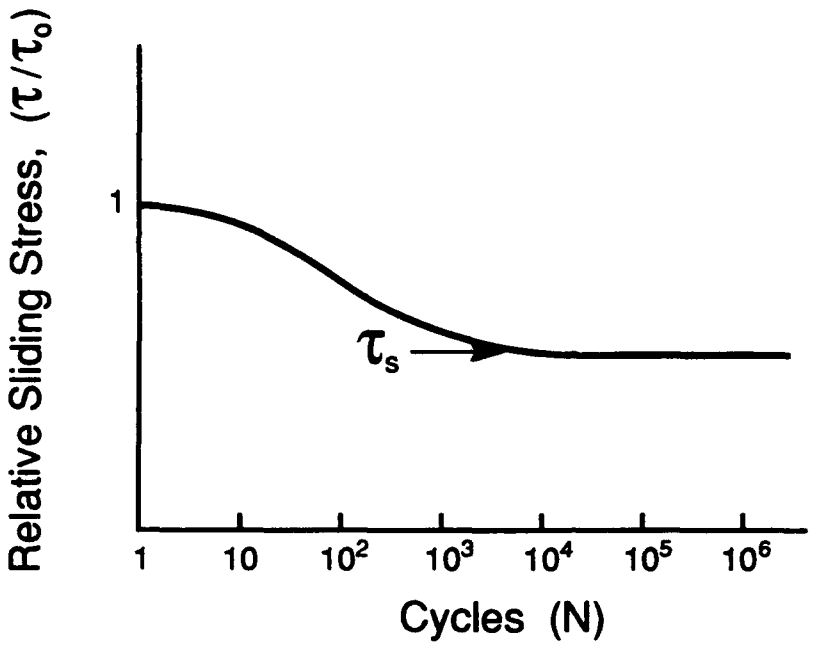

Reduction In Interface Sliding Resistance During Fatigue

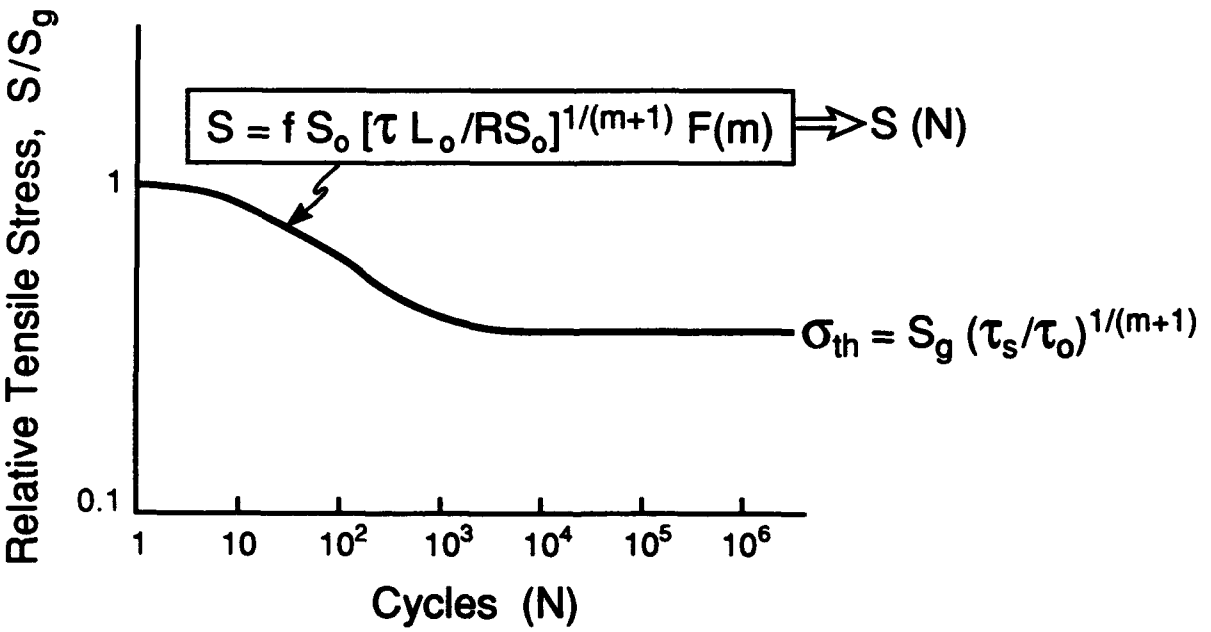

Reduction in UTS Caused By Interface Degradation

Fig. 8.2

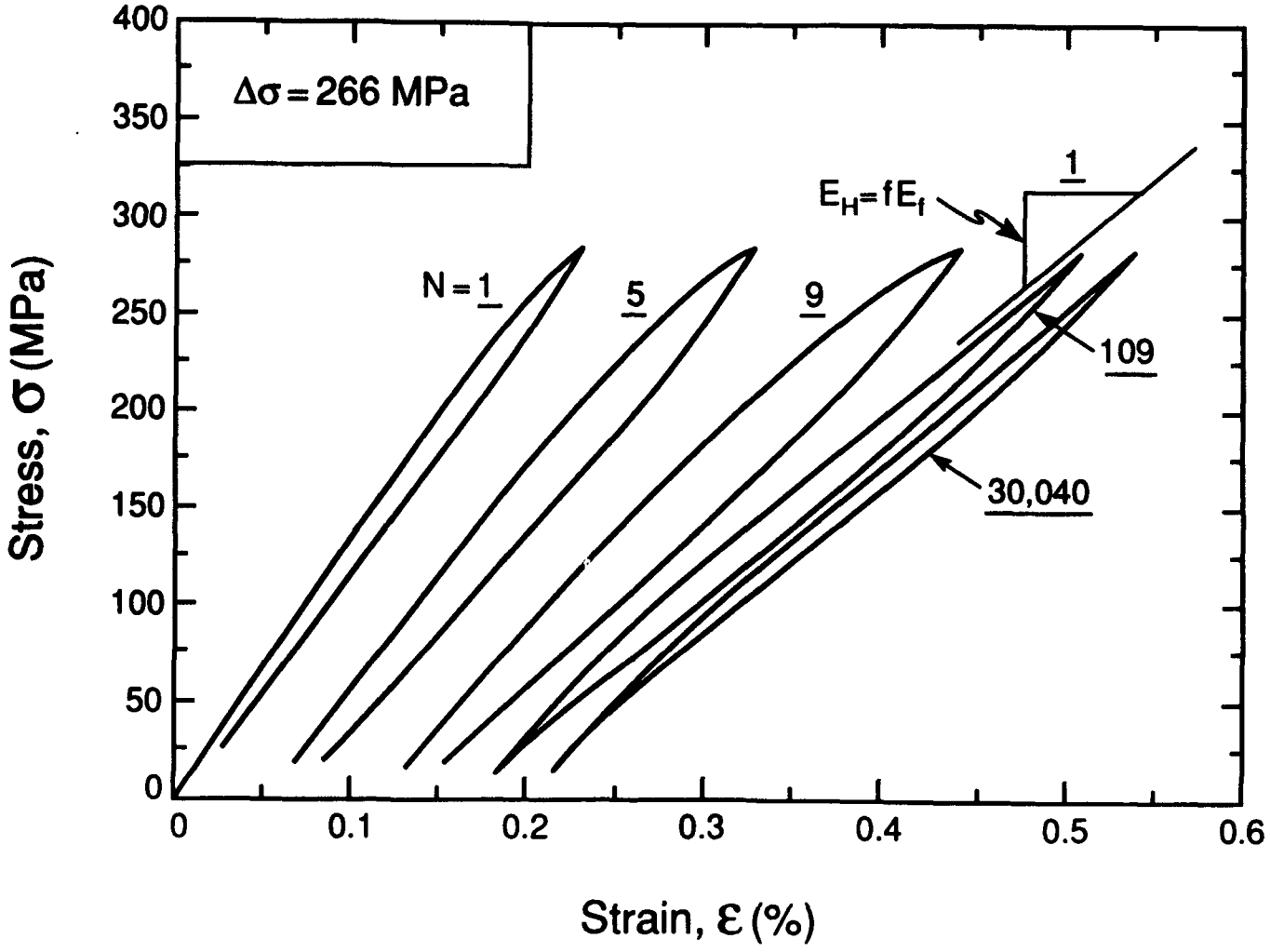
Δσ = 266 MPa
N = 1
5
9
109
30,040
1
$E_H = fE_f$
Stress, σ (MPa)
Strain, ε (%)
400
350
300
250
200
150
100
50
0
0
0.1
0.2
0.3
0.4
0.5
0.6

Figure 9.1

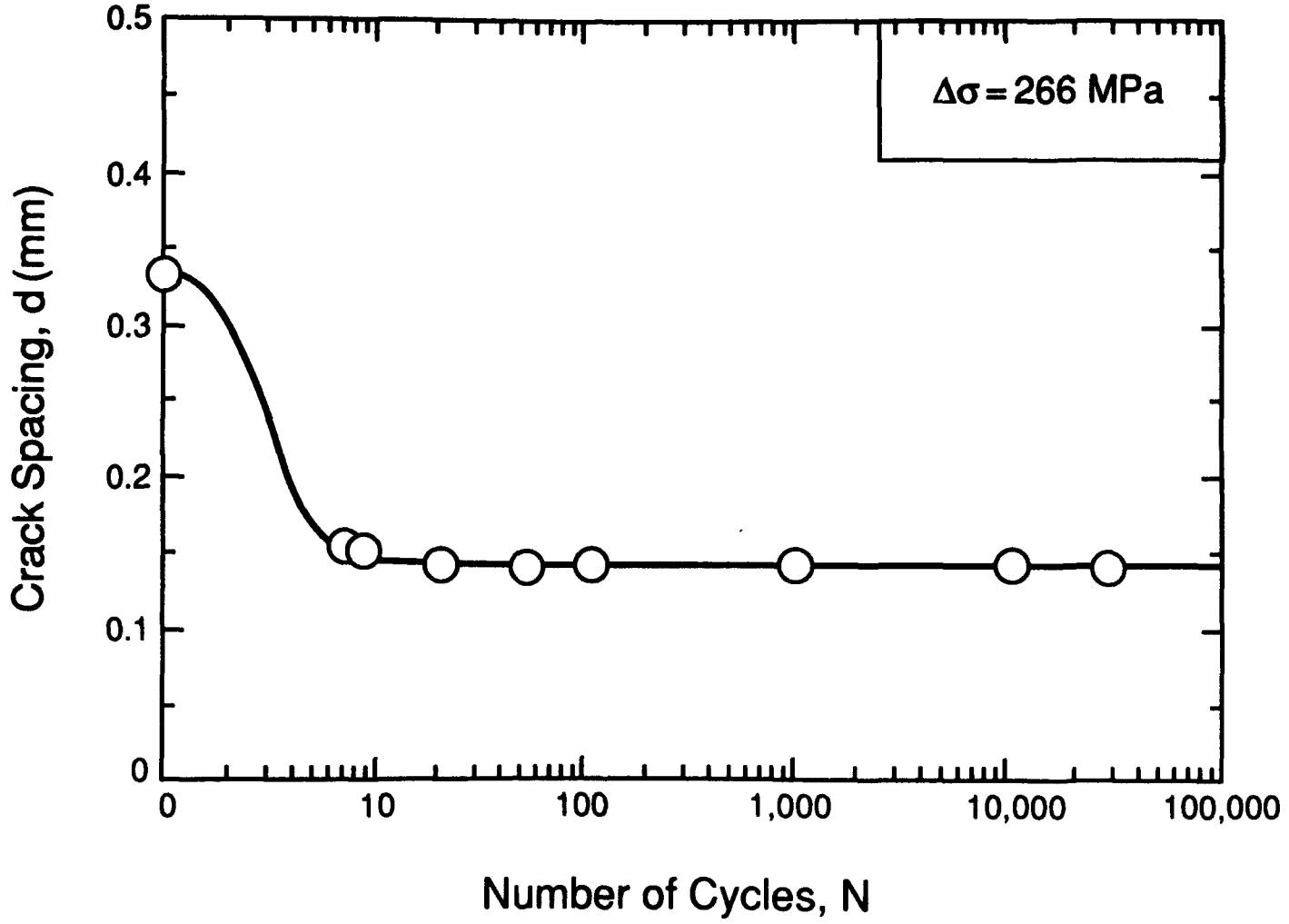
Δσ = 266 MPa
Crack Spacing, d (mm)
0.5
0.4
0.3
0.2
0.1
0
0
10
100
1,000
10,000
100,000
Number of Cycles, N

Figure 9.2

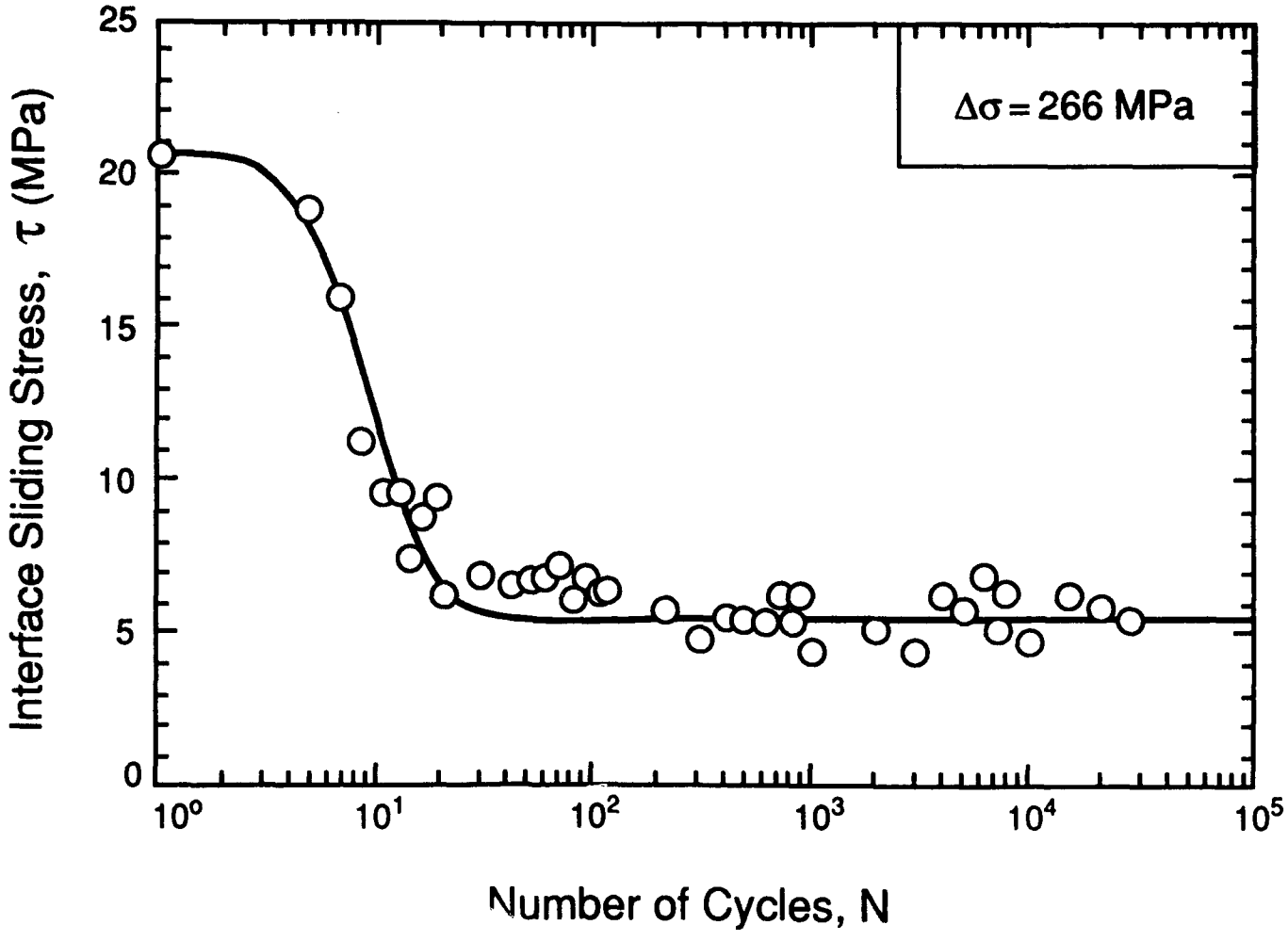
Interface Sliding Stress, τ (MPa)
25
20
15
10
5
0
Δσ = 266 MPa
10⁰
10¹
10²
10³
10⁴
10⁵
Number of Cycles, N

Figure 9.3

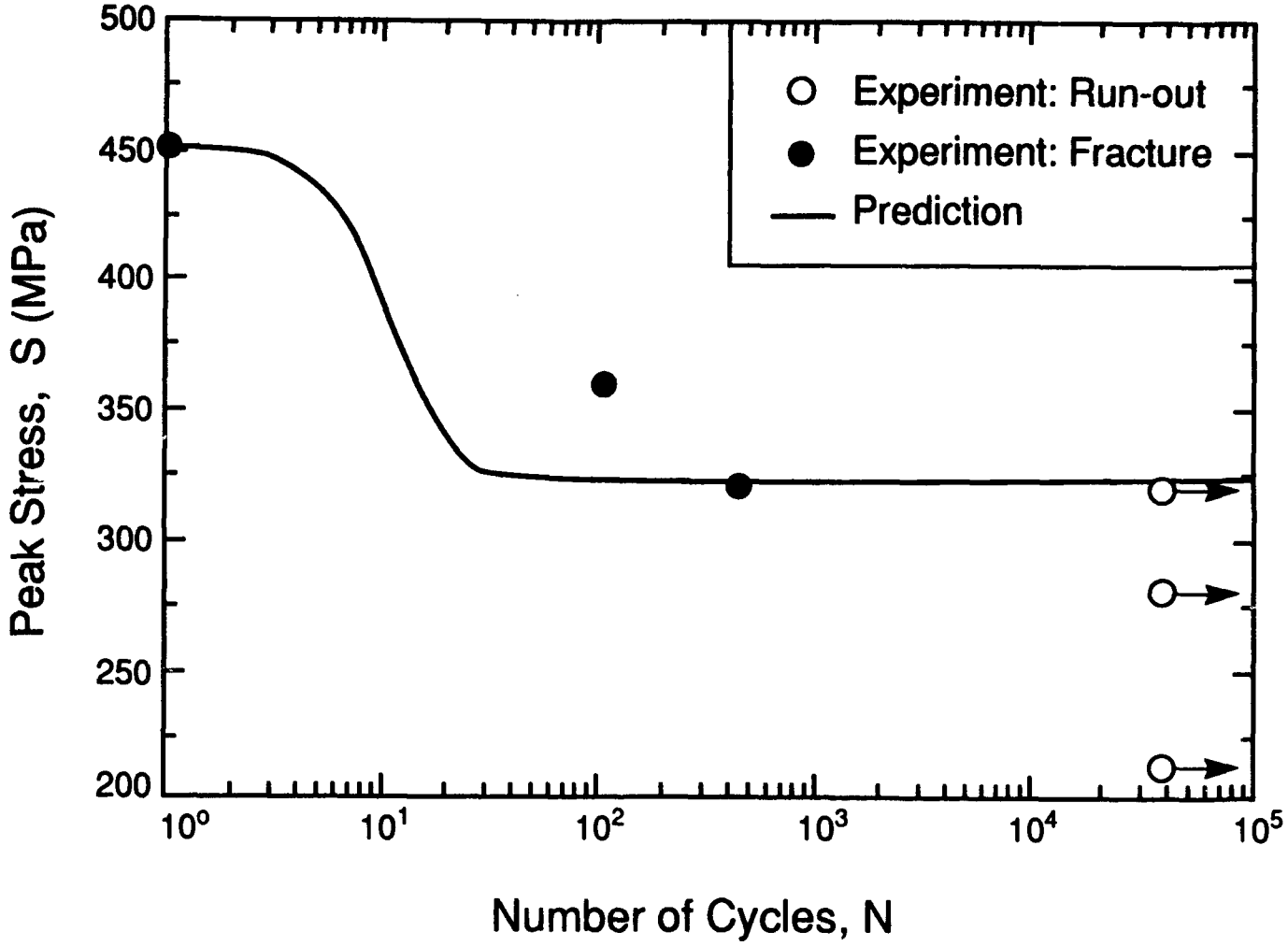
Peak Stress, S (MPa)
500
450
400
350
300
250
200
10^0
10^1
10^2
10^3
10^4
10^5
Number of Cycles, N
Experiment: Run-out
Experiment: Fracture
Prediction

Figure 9.4

Pergamon

Acta metall. mater. Vol. 42, No. 3, pp. 893–911, 1994

0956-7151/94 $6.00 + 0.00

DUCTILE-REINFORCEMENT TOUGHENING IN γ-TiAl INTERMETALLIC-MATRIX COMPOSITES: EFFECTS ON FRACTURE TOUGHNESS AND FATIGUE-CRACK PROPAGATION RESISTANCE

K. T. VENKATESWARA RAO[1], G. R. ODETTE[2] and R. O. RITCHIE[1]

[1]Department of Materials Science and Mineral Engineering, University of California, Berkeley, CA 94720 and [2]Materials Department, College of Engineering, University of California, Santa Barbara, CA 93106, U.S.A.

(Received 30 June 1993)

Abstract—The influence of the type, volume fraction, thickness and orientation of ductile phase reinforcements on the room temperature fatigue and fracture resistance of γ-TiAl intermetallic alloys is investigated. Large improvements in toughness compared to monolithic γ-TiAl are observed in both the TiNb- and Nb-reinforced composites under monotonic loading. Toughness increases with increasing ductile phase content, reinforcement thickness and strength; orientation effects are minimal. Crack-growth behavior is characterized by steep resistance curves primarily due to crack trapping/renucleation and extensive crack bridging by the ductile-phase particles. In contrast, under cyclic loading the influence of ductile phases on fatigue resistance is strongly dependent upon reinforcement orientation. Compared to monolithic γ-TiAl, improvements in fatigue-crack growth resistance are observed in TiNb-reinforced composites only in the face (C–L) orientation; crack-growth rates for the edge (C–R) orientation are actually faster in the composite. In comparison, Nb-particle reinforcements offer less toughening under monotonic loading but enhance the fatigue properties compared to TiNb reinforcements under cyclic loading.

1. INTRODUCTION

Titanium aluminide alloys based on the ordered intermetallic compound γ-TiAl ($L1_0$ structure) are currently of considerable interest as advanced high-temperature structural materials, owing primarily to their higher specific modulus, greater elevated-temperature strength and better oxidation resistance compared to conventional titanium alloys, superalloys and α_2-Ti_3Al based intermetallic alloys [1–7]. The alloys are currently being developed as potential materials for use in the cooler compressor sections of high-performance turbine engines and for skin structures of hypersonic and high-speed civil transport vehicles. However, the application of monolithic γ-TiAl is severely limited by its relatively low tensile ductility (<2%) and fracture toughness (~8 MPa$\sqrt{m}$) at ambient temperatures. Accordingly, much work in recent years has focused on obtaining an understanding of the structure–property relationships in these alloys and in improving their ductility and fracture resistance.

Both alloy modification (intrinsic) and compositing (extrinsic) approaches to toughening γ-TiAl have been explored [3–11]. Microalloying with elements such as V, Cr, Mn, Mo and Nb and optimized thermomechanical processing treatments have led to toughened dual-phase microstructures composed of alternating microlaminae of γ (TiAl) and α_2 (Ti_3Al). In this case, toughening contributions arise from an intrinsic change in the deformation mechanism, i.e. mechanical twinning of the γ-phase [7], as well as crack deflection and blunting at γ/α_2 or γ/γ interfaces, and shear-ligament bridging by the more ductile α_2 phase [4–7].

Composite approaches to toughening have centered around reinforcing TiAl with small volume fractions of ductile Nb, TiNb or Ti–6Al–4V particles [8–11]. The primary objective is to enhance toughness by crack-tip shielding arising from tractions provided by unbroken ductile ligaments bridging the crack wake, akin to approaches first proposed for brittle ceramics [12–14]. When the length of the bridging zone is *very* small compared to the specimen and crack length dimensions, the toughness increases with crack extension up to a maximum steady-state level, K_{SSB}, associated with the development of a steady-state bridging zone length, L_{SSB}. At this small-scale bridging limit, K_{SSB}, is given as [11]

$$K_{SSB} = \sqrt{K_i^2 + E' f t \sigma_0 \chi} \qquad (1)$$

where K_i is the critical crack-tip stress intensity factor required for crack initiation, E' is the plane-strain elastic modulus of the composite [$\approx E/(1-\nu^2)$, ν being the Poisson's ratio], σ_0, f, and t refer to the yield strength, volume fraction and characteristic dimension of the reinforcement, respectively. The non-dimensional work of rupture, χ, is the area under the

normalized-reinforcement stress $[\sigma(u)]$-displacement (u) function, defined as [13]

$$\chi = \int_0^{u^*/t} \left[\frac{\sigma(u)}{\sigma_0}\right] d\left(\frac{u}{t}\right) \quad (2)$$

where u^* is the critical crack-opening displacement at the point of reinforcement rupture. The characteristic dimension, t, is appropriately defined based on the reinforcement geometry, i.e. the diameter of a fiber, the average diameter of circle inscribing a sphere, and the thickness of a foil (lamina) or a pan-cake shaped reinforcement. Typical values of χ for γ-TiAl reinforced with Nb or Nb-alloys range between 0.9 to 1.5. Much larger values of χ, up to 4 or more, can be obtained using strain-hardening reinforcements that undergo extensive debonding from the matrix [9]. For nominal values of $\chi = 1.2$, $\sigma_0 = 400$ MPa and $t = 100\,\mu$m, the addition of a mere 20 vol.% of ductile particles ($f = 0.2$) yields K_{SSB} values of about 44 MPa$\sqrt{}$m, over five times the nominal TiAl toughness of 8 MPa$\sqrt{}$m. Additional toughening mechanisms include crack trapping, crack renucleation, crack deflection and branching, and process-zone phenomena such as microcracking and twinning. Many of these latter contributions are incorporated into K_i, which is larger than the intrinsic K_{Ic} toughness of the brittle γ-TiAl matrix.

Despite the success in toughening γ-TiAl with ductile-phase reinforcements, the composites may have lower crack-growth resistance under cyclic fatigue conditions [15, 16] than monolithic γ-TiAl, as illustrated in Fig. 1. Under monotonic loads, the γ-TiAl + 10 vol.% TiNb composite exhibits an initiation toughness of about 16 MPa$\sqrt{}$m, nearly twice that of pure γ-TiAl [Fig. 1(a)]; the fracture resistance increases with further crack extension (referred to as resistance-curve or R-curve behavior) primarily due to bridging by unbroken TiNb ligaments in the crack wake [Fig. 1(b)]. In contrast, the diminished role of crack bridging under cyclic loads due to subcritical fatigue failure of the ductile TiNb phase [Fig. 1(d)], can lead to marginally faster crack velocities in

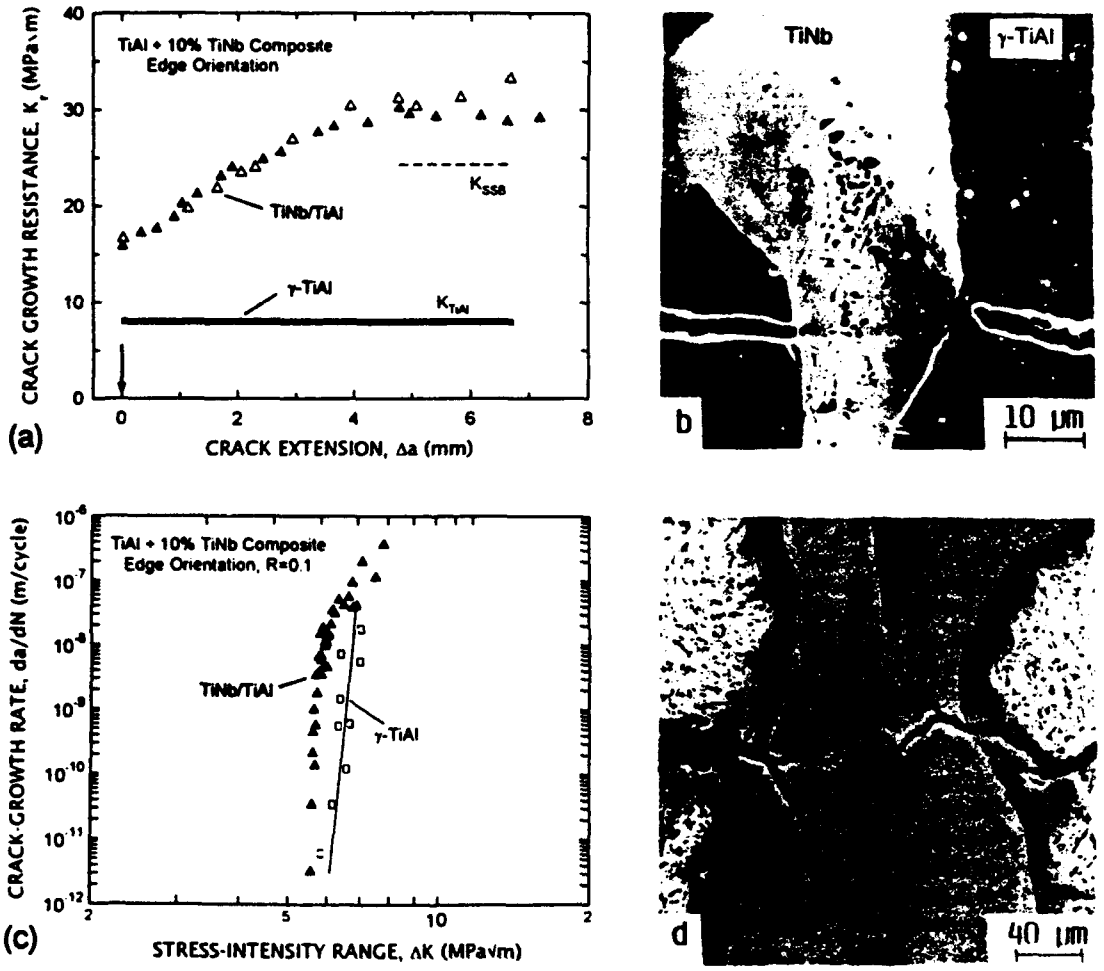

Fig. 1. Illustration of the contrasting role of ductile reinforcements on crack-growth behavior in a β-TiNb/γ-TiAl composite, showing (a) improved toughness compared to γ-TiAl under monotonic loading, due to (b) crack bridging by uncracked TiNb ligaments, and (c) faster growth rates in the composite under cyclic loading, (d) due to premature failure of the TiNb particles [after Ref. 15].

the composite compared to unreinforced TiAl [Fig. 1(c)].

Accordingly, it is the objective of the present paper to provide an extensive evaluation of ductile-phase toughening in γ-TiAl intermetallic-matrix composites by systematic measurements of the influence of volume fraction, thickness, orientation and type of reinforcement on their fatigue and fracture toughness properties. Specifically, a comparison of Nb and TiNb ductile phases provides the opportunity to evaluate the effects of widely different interface and reinforcement constitutive properties on the monotonic and cyclic crack-growth resistance of ductile-phase toughened composites.

2. MATERIALS AND EXPERIMENTAL PROCEDURES

2.1. Materials and fabrication

The ductile-phase toughened composites under study, listed in Table 1, were fabricated by phase blending -80 mesh γ-TiAl (Ti-55 at.% Al, with small additions of Nb, Ta, C and O) with various amounts of single-phase β-TiNb (Ti–33 at.% Nb) or pure Nb powders of $-35+50$ mesh (nominal size $\sim$300–500 μm) or $-50+140$ mesh (nominal size $\sim$100–300 μm). The blends were hot pressed and forged to upset ratios of 10:1 at 1025 ± 15°C, producing a pancake-shaped ductile particle morphology. Assuming a uniform thickness of $\sim$10% of the particle diameter, the nominal aspect ratio of the pancaked reinforcements is about 5:1 and the nominal particle thicknesses are $\sim$40 and $\sim$20 μm for $-35+50$ and $-50+140$ mesh powders, respectively.

The actual microstructures, however, were much more heterogeneous, as illustrated in Figs 2 and 3, and consisted of a distribution of irregularly shaped, lenticular-crenulated particles. Volume fractions and characteristic dimensions of the ductile particles varied, both between specimens and locally within a specimen. Measurements along the cracked edge and on the fracture surface of representative specimens (Fig. 3) showed a rather wide range of particle thicknesses (between 50 and 150% of nominal values) and aspect ratios in part due to the particle-size distribution and irregularities in particle shape. Furthermore, unusually thick reinforcements resulted when two particles were welded during processing, more frequently so at the higher volume fractions. Local fracture-surface area fractions of the ductile phase, taken along 500 μm slices, were found to vary by up to a factor of 2; however, specimen averages were generally within a few percent of the nominal values. Henceforth, the discussions will reference nominal reinforcement parameters, recognizing that these are surrogate measures for more complex distributions.

Table 1. Details of ductile-phase toughened γ-TiAl composites

Reinforcement	Mesh size	Nominal reinforcement volume fraction	Nominal reinforcement thickness (μm)
TiNb	$-35+50$	0.05	40
TiNb	$-35+50$	0.10	40
TiNb	$-35+50$	0.20	40
TiNb	$-50+140$	0.20	20
Nb	$-35+50$	0.20	40

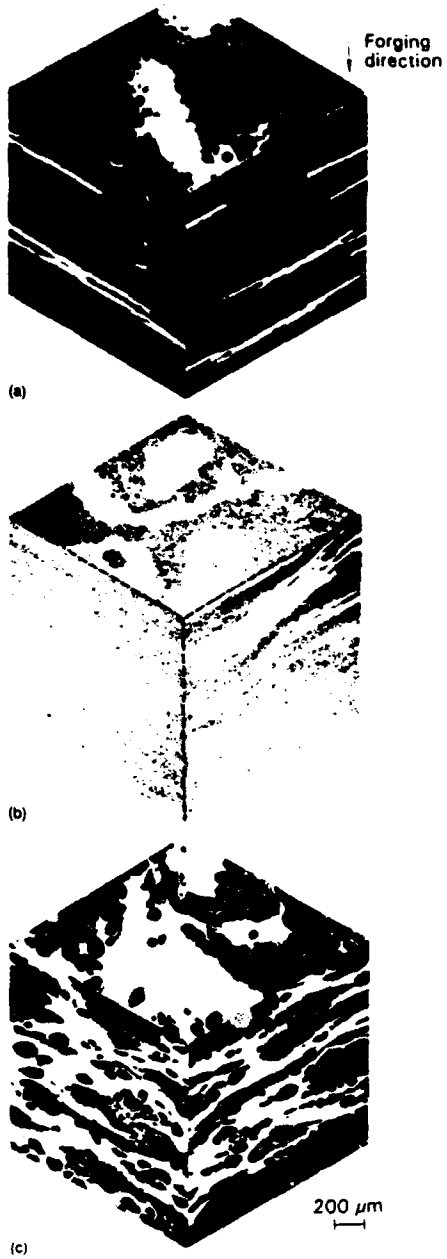

Fig. 2. Three-dimensional optical micrographs of typical γ-TiAl intermetallic–matrix composite microstructures reinforced with (a) 5 vol.%, (b) 10 vol.%, and (c) 15 vol.% of TiNb phase; the TiNb particle thickness is $\sim$40 μm.

The matrix consisted primarily of $\sim$2–10 μm-sized grains of γ-TiAl (ordered $L1_0$ tetragonal structure) with small regions of α_2-Ti_3Al (ordered hexagonal

Fig. 3. Montage of SEM micrographs of the fractured surfaces of TiAl + 20 vol.% TiNb composite showing the distribution of ruptured ductile TiNb particles. Note the variations in particle thickness and the non-uniformity of their distribution.

DO_{19} structure). Yield and ultimate strengths for unreinforced γ-TiAl range between 400 and 500 MPa at room temperature with a tensile elongation of $\sim$1.8% [3, 4]. While the yield strength (σ_0) of the TiNb phase is about 430 MPa, this solid-solution hardened Ti–Nb alloy does not post-yield harden (strain-hardening exponent, $n \sim 0$). Thus, deformation in the TiNb phase is highly localized and the measured fracture strains strongly depend on specimen geometry and gauge length. Niobium, on the other hand, has a lower yield strength of about 140 MPa, but strain hardens extensively with an initial exponent of $n \sim 0.3$, reaching an ultimate strength (σ_u) of 250 MPa before failing at a nominal fracture strain of $\sim$0.45 [9].

2.2. Interface characteristics

Thermomechanical processing at high temperatures caused interfacial reactions between the γ-TiAl matrix and TiNb and Nb reinforcements (Fig. 4) [10, 17]. The $\sim$5–10 μm thick reaction product layer between TiNb and TiAl was composed of α_2 ($\sim$3–5 μm) separated by a sharp boundary from a mixed region ($\sim$2–5 μm) of α_2 and B_2 (ordered), and possibly some ω ($B8_2$) phase. Transmission-electron microscope (TEM) observations in Fig. 4(e) also indicated the presence of dislocations in ductile α_2 grains within the TiNb/TiAl reaction layer interface. The corresponding Nb/TiAl interface consisted of a $\sim$1–2 μm brittle σ (D_8) region and thinner layers of T_2 (Ti–44Al–11Nb at.%) and δ (Nb_3Al–A15 structure) adjacent to TiAl and Nb phases, respectively. In addition, microcracks were observed in the relatively brittle (dislocation- and twin-free) σ grains [Fig. 4(b)]. The reaction-layer phases are critical in mediating the interface toughness, debonding characteristics and resultant constrained-deformation behavior of the reinforcing phase; results are summarized in Table 2.

In the case of Nb/TiAl, the brittle σ reaction-layer phases result in a significant amount of debonding;

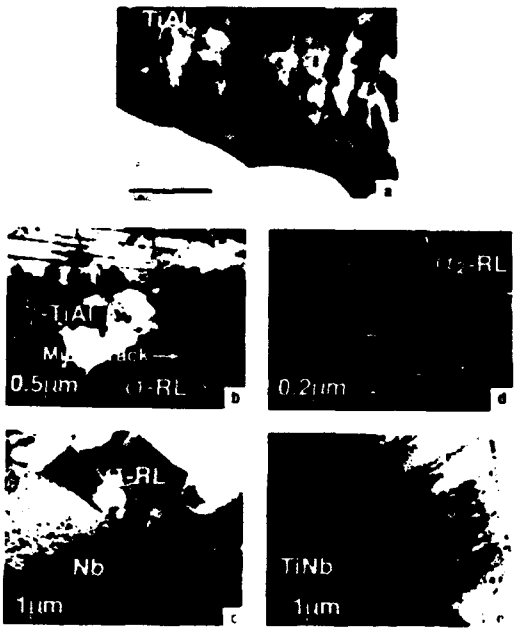

Fig. 4. Transmission electron microscope images of the reaction-layer (RL) interface characteristics between (a–c) Nb and γ-TiAl, and (d,e) β-TiNb and γ-TiAl.

Table 2. Summary of interfacial properties between TiNb TiAl and Nb TiAl

Interface	Interface phase	Maximum stress σ_{max}/σ_0	Critical displacement u^*/t	Debond length l_d/t	Work of rupture χ	Interfacial fracture energy Γ_i(J/m^2)
TiNb/γ-TiAl	α_2	2.2 ± 0.3	0.7 ± 0.2	<0.2	1.1 ± 0.2	>330
Nb/γ-TiAl	σ	1.8 ± 0.2	1.1 ± 0.3	1.0 ± 0.3	1.3 ± 0.3	~ 45

the interfacial toughness is estimated to be about 45 J/m^2 [9]. Typical debond length to particle thickness ratios (l_d/t) were roughly unity compared to values of about 4 reported for laminate foils [9]. This difference is probably due to the irregular shape and smaller thickness of the particles in the composite. However, in either case, the effect of matrix constraint on $\sigma(u)$ is minimal and the peak stress (σ_{max}) and normalized failure displacement (u^*/t) are approximately equivalent to the corresponding ultimate tensile strength and total elongation strains measured in geometrically-similar tensile tests; values of σ_{max}/σ_0 and u^*/t for the Nb particles are ~ 1.8 and 2.2, respectively.

In contrast, only minimal particle debonding ($l_d/t < 0.2$) was observed for the TiNb/TiAl composites compared to values of 0.75 ± 0.25 observed in sandwich tests [9], again the variation being attributable to the particle thickness and shape. Debond cracking occurred in the γ-TiAl matrix or γ/α_2 interface, suggesting a reaction-layer toughness in excess of ~ 330 J/m^2. Particle constraint factors cannot be measured directly but are expected to be at least comparable to values between 2 and 2.5 measured in sandwich tests; in fact, the constraint may be even higher due to the minimal debonding. The critical crack-opening displacements, u^*/t, were ~ 0.7.

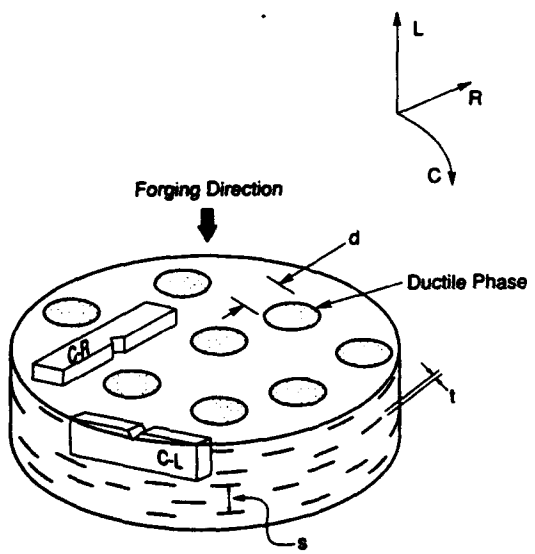

Fig. 5. Nomenclature for specimen and reinforcement orientations in the composite forging, namely C–R and C–L; L, C and R refer to the forging, circumferential and radial directions, respectively. C–R and C–L are also referred to as the *Edge* and *Face* orientations, respectively.

2.3. *Fracture toughness testing*

The fracture toughness behavior of TiNb/TiAl and Nb/TiAl composites was characterized in terms of $K_r(\Delta a)$ resistance curves, i.e. toughness as a function of crack extension. Specimens were fabricated by electro-discharge machining in two different orientations relative to the forging direction, namely, C–R and C–L (Fig. 5). The crack intersects the *edges* of the pancake-shaped particles in the C–R orientation; in the C–L configuration the crack intersects the *faces* of the pancakes [11]. Hence, C–R and C–L are subsequently referred to as the edge and face orientations, respectively. Tests were conducted using ~ 5 mm thick and 12.7 to 15.2 mm wide, pre-cracked, single-edge notch bend SE(B), TiNb/TiAl composite specimens, with a span-to-width ratio of about 3:1, loaded in three-point bending; the Nb/TiAl samples were 2.5 mm thick and 7.5 mm wide. To facilitate a direct comparison of the extrinsic toughening behavior in the various composites, a set of 7.5 mm wide TiNb/TiAl specimens were also tested.

Pre-cracking was achieved by initiating stable crack growth from the electro-discharge machined chevron notch by slow monotonic loading, under displacement control, using a servo-hydraulic testing machine. Subsequently, a major portion of the pre-crack bridging zone was removed by grinding the crack wake to within $\sim 50\ \mu$m behind the crack front. The final pre-crack depth to specimen width ratio (a_0/W) varied from about 0.3–0.5 for the various test samples.

R-curve tests were carried out by monotonically loading the pre-cracked samples under displacement control in laboratory air (~ 22°C, $\sim 45\%$ relative humidity) until crack extension was initiated. Crack lengths and crack/particle interactions were monitored using a high-resolution optical video camera system. In general, crack initiation was followed by a load drop and crack arrest after a small yet rapid uncontrolled jump. Automated detection of these load drops or direct observation of crack extension was used to trigger additional unloading, by about 15%, to further stabilize cracking. After measuring the new crack length (and recording other relevant observations), loads were again increased until the next initiation event. Applied load and crack-length measurements were used to calculate the initiation/re-initiation stress intensities (K_r) according to ASTM Standard E-399 [18]. The complete resistance curve was evaluated up to a/W ratios >0.8 by carrying out a large number of interrupted initiation/arrest (loading/unloading) cycles.

It is important to emphasize that small-scale bridging conditions, stipulated by the model in equation (1), are seldom met in practice under monotonic loading. For the TiNb/TiAl and Nb/TiAl composites studied in this work, monotonic bridging-zone lengths are often comparable to specimen and crack size dimensions, i.e. large-scale bridging conditions are prevalent; specimen widths in excess of 500 mm would be needed in some cases to fulfill small-scale bridging requirements. Crack-growth behavior under large-scale bridging is a function of the entire $\sigma(u)$ function as well as K_i and E' [11]; moreover, the extrinsic, large-scale bridging toughness can be significantly greater than K_{ssb} and is sensitive to test specimen size and geometry. Accordingly, R-curve measurements in this study must be considered as *extrinsic* and explicitly depend both on specimen width and initial a_0/W. While repeated tests demonstrated that results were reproducible, reinforcement heterogeneity and specimen-to-specimen differences in W and a_0/W can complicate direct comparison of $K_r(\Delta a)$ curves for the various composite architectures. Effects of these variations were mitigated, whenever possible, by comparing results for the most similar and representative test specimens and excluding data for a/W values greater than 0.8. In addition, corrections to experimental crack-growth data were made, where necessary, to account for large-scale bridging. Small-scale bridging conditions may, however, be common under cyclic loading because of the short bridging zones.

2.4. Fatigue-crack propagation testing

Cyclic crack-growth behavior in TiNb/TiAl composites under tension-tension loading was examined primarily with 25 mm-wide, 2.5 mm-thick, compact tension C(T) specimens in the edge (C–R) orientation; approximately 1-mm thick C(T) samples were used to characterize behavior in pure TiNb. Due to limitations in the available material, corresponding properties in the face (C-L) orientation of TiNb/TiAl composites and unreinforced γ-TiAl were determined using 15 mm-wide, 2.5 mm thick SE(B) samples (span ~60 mm) loaded in four-point bending. Behavior in Nb/TiAl (face orientation) was examined using 2.5 mm-thick and 7.5 mm-wide samples under identical loading conditions. All specimens were fabricated with a wedge-shaped (semi-chevron) starter notch to facilitate fatigue pre-cracking, which was performed under alternating tensile loads prior to testing.

Experiments were performed in laboratory air (~22°C, ~45% relative humidity) on computer-controlled servo-hydraulic testing machines operating under stress-intensity control. This was achieved by continuously monitoring the crack length, to a resolution better than $\pm 5\,\mu$m, using thin metallic foils bonded to the specimen surface, similar to techniques used for fatigue testing of ceramics [19, 20]. Unless otherwise stated, cyclic loads were applied at a constant nominal load ratio, $R\,(=K_{min}/K_{max})$, of 0.1 and a frequency of 50 Hz (sine wave); however, additional tests at R ratios of 0.5 and 0.7 were carried out on selected composites. To characterize the crack-growth rate behavior at different stress intensities, the applied stress-intensity range, $\Delta K\,(=K_{max}-K_{min})$, was gradually increased and/or decreased using exponential load-shedding schemes (variable ΔK at constant R), with the K-gradient set to $\pm 0.1\ \text{mm}^{-1}$ [21]. Using such procedures, crack-growth rates per cycle (da/dN) ranging between 10^{-6} and 10^{-12} m/cycle were obtained; the stress-intensity range corresponding to the slowest growth rate, $da/dN \leqslant 10^{-12}$ m/cycle, is operationally defined as the fatigue threshold, ΔK_{TH}, below which no appreciable crack extension is observed for specific cyclic loading conditions. Tests on Nb- and TiNb-reinforced TiAl composites were terminated under increasing-ΔK conditions, at ΔK levels marking the acceleration in crack-growth rates to very high values; for monolithic γ-TiAl, the tests ended when the specimen fractured. Cyclic crack-growth data are presented in terms of the crack-growth rate per cycle, da/dN, as a function of the applied stress-intensity range, ΔK.

Premature contact between the cracked surfaces above the minimum load (crack closure) was monitored using strain gauges mounted on the back face of the specimens; the closure stress intensity, K_{cl}, was specified by the load at the first deviation from linearity on the unloading compliance curve, reflecting initial contact between the two surfaces. Where K_{cl} exceeds K_{min}, the *local* (near-tip) stress-intensity range can be computed as $\Delta K_{eff} = K_{max} - K_{cl}$. The extent of bridging by ductile particles under cyclic loading was estimated by comparing the crack length (of a bridged crack) estimated from back-face strain compliance with equivalent values (for an unbridged crack) measured using bonded metal-foil gauges; procedures are described in Ref. [22]. These global estimates were supplemented by *in situ* observations of crack/particle interactions on the specimen surface, using a high-resolution optical telescope.

2.5. Fractography

Profiles of crack paths in the plane of loading and crack fronts across the specimen thickness were examined by taking metallographic sections parallel and normal to the crack growth direction, respectively. These sections and all fracture surfaces were imaged using optical and scanning electron microscopy (SEM). In addition, crack-reinforcement interactions and specific fracture mechanisms were examined by SEM by periodically interrupting tests (cyclic loading) or by using an *in situ* loading stage in the microscope (monotonic loading).

3. RESULTS AND DISCUSSION

3.1. Fracture toughness properties

The basic processes leading to toughening under monotonic loading in the TiAl composites examined

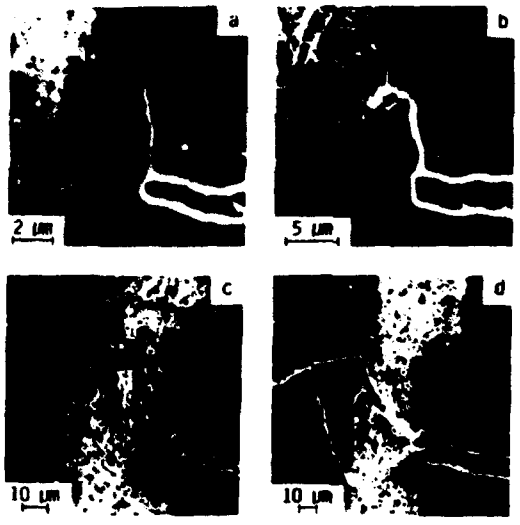

Fig. 6. Summary of crack/reinforcement interactions in TiNb/TiAl composites under monotonic loading, showing (a) crack arrest at the interface with minimal debonding between TiAl and the reaction layer, (b) crack-tip blunting at the TiNb particle, (c) renucleation of the crack in front of the particle leading to crack bridging, and (d) large-scale plastic deformation in the TiNb particle leading to final rupture. Images were obtained using a SEM with an *in situ* loading stage; arrow indicates the general direction of crack growth.

are illustrated in Figs 6 and 7. Specifically, Fig. 6 shows a typical sequence of events as the crack intersects a ductile TiNb particle in the composite: (a) crack arrest at the ductile α_2 layer; (b) penetration of the reaction layer and initiation of plastic deformation in the particle; (c) renucleation in the matrix ahead of the particle; and (d) large-scale deformation along intense slip bands prior to particle rupture. Note that the TiNb particles do not decohere from the matrix during crack extension but exhibit limited debond cracking along the γ/α_2 interface, as seen in Fig. 6(a) and 6(b), similar to observations made on sandwiched-composite tests [9]. The bridging zones, i.e. the length scales over which TiNb reinforcements remain intact in the crack wake, are on the order of several millimeters (Table 3).

The resulting composite fracture surfaces in Fig. 7 show minimal secondary cracking at the interface. The constituent phases exhibit similar fractographic

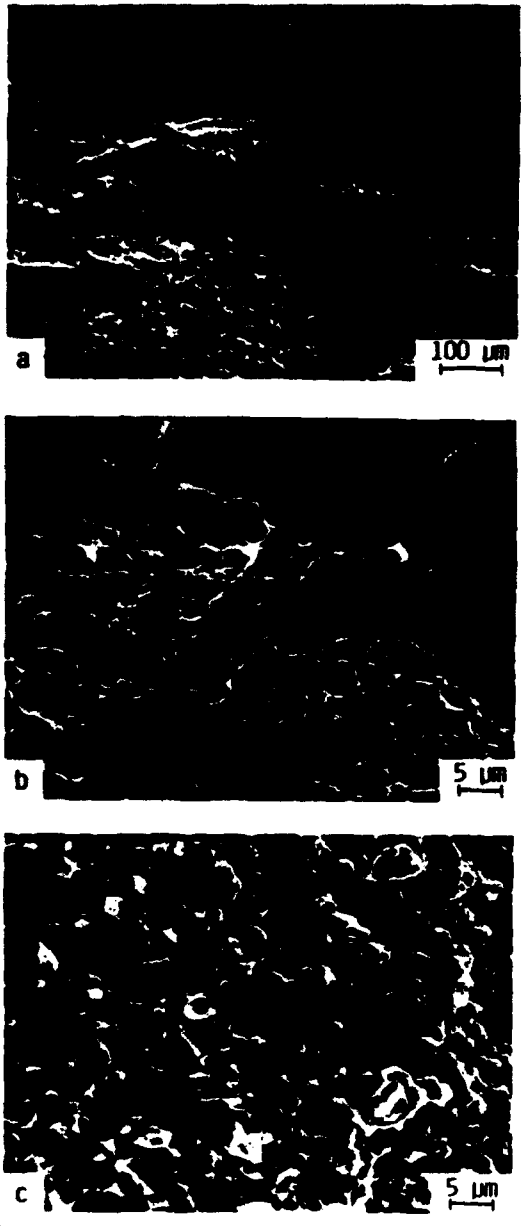

Fig. 7. Fractography of fracture surfaces in TiNb/TiAl composites under monotonic loading, (a–c) at various magnifications, showing (b) transgranular cleavage failures in γ-TiAl, and (c) dimpled rupture in the ductile TiNb phase. Arrow indicates the general direction of crack growth.

Table 3. Summary of monotonic crack-growth data in γ-TiAl composites

Reinforcement	Volume fraction f	Particle thickness t (μm)	Initiation toughness K_i (MPa$\sqrt{}$m) Edge	Face	R-Curve slope dK_r/da (MPa$\sqrt{}$m/mm) Edge	Face	Steady-state toughness K_{ssb} (MPa$\sqrt{}$m)	Steady-state bridge length L_{ssb} (mm)
TiNb	0.05	40	11.3	12.7	2.1	2.5 (1.9)[a]	18.3	38.8
TiNb	0.1	40	18.6	15.7	2.5	3.3 (2.9)[a]	24.7	22.3
TiNb	0.2	40	17.3	19.0	4.2	5.0	32.6	13.7
TiNb	0.2	20	18.9	18.4	2.3	2.4 (2.2)[a]	26.6	5.3
TiNb[b]	0.2	40	17.5	19.1	12.4	9.6	32.6	13.7
Nb[b]	0.2	40	12.2	13.8	6.9	5.5	21.2	57.5

[a]Values in parenthesis are corrected to 15.2 mm width.
[b]7.5 mm-wide specimens.

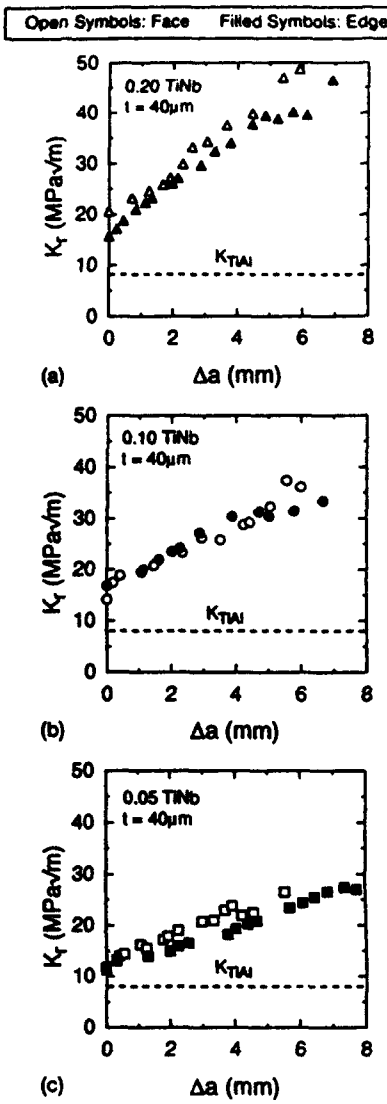

Fig. 8. Resistance curves characterizing the crack-growth behavior in TiNb/TiAl composites under monotonic loading, as a function of the volume fraction, (a) 20, (b) 10 and (c) 5 vol.% of TiNb phase (thickness, $t = 40\,\mu m$), in the edge (or C–R, denoted by open symbols) and face (or C–L, denoted by filled symbols) orientations. Dashed line K_{TiAl} represents the toughness of pure γ-TiAl.

features in composite and monolithic form; the ductile TiNb particles fail by a transgranular, microvoid nucleation and coalescence mechanism, as evidenced by the dimpled surfaces in Fig. 7(b). Fractures in γ-TiAl are predictably brittle, characterized by transgranular cleavage with small regions showing intergranular failure [Fig. 7(c)]. The distribution of ruptured ductile TiNb particles dispersed over the brittle TiAl fracture surface is illustrated in Fig. 3.

Effects of these crack-extension processes on resistance-curve behavior as a function of the ductile-reinforcement characteristics are summarized in Figs 8 and 9; estimates of the crack-initiation toughness, K_i, and R-curve slope, dK_r/da, values based on linear

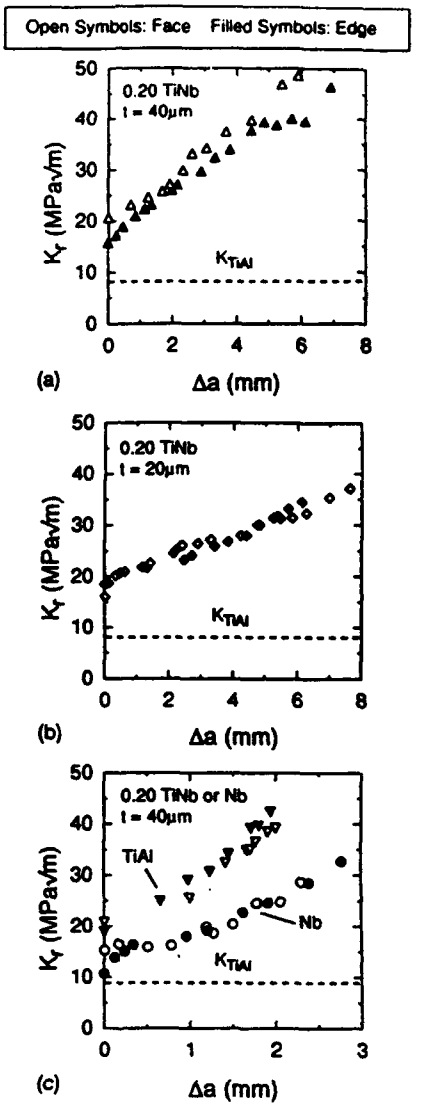

Fig. 9. Influence of (a,b) reinforcement thickness, t, of 20 μm vs 40 μm, and (c) reinforcement type, TiNb vs Nb, on the monotonic crack-growth resistance of γ-TiAl composites, for a volume fraction, $f = 0.2$, in the edge (open symbols) and face (filled symbols) orientations. Note that results presented in Fig. 9(c) were obtained using 7.5 mm-wide specimens (under large-scale bridging), both for TiNb/TiAl and Nb/TiAl composites, to enable a direct comparison; all other data presented are for 15 mm-wide samples. Dashed line represents the toughness of pure γ-TiAl, K_{TiAl}.

†Note that specimens in the face orientation with TiNb volume fractions of 0.05 and 0.10 were 12.7 mm-wide compared to the typical width of 15.2 mm. While the crack-initiation toughness would not be influenced by such size differences, K_r increases more rapidly with crack advance in smaller test specimens. For example, large-scale bridging calculations indicate that at crack extensions of 7 mm, the smaller specimen size increases the extrinsic toughness by ~25% and ~13% for the 5 and 10 vol.% TiNb-reinforced γ-TiAl composites, respectively.

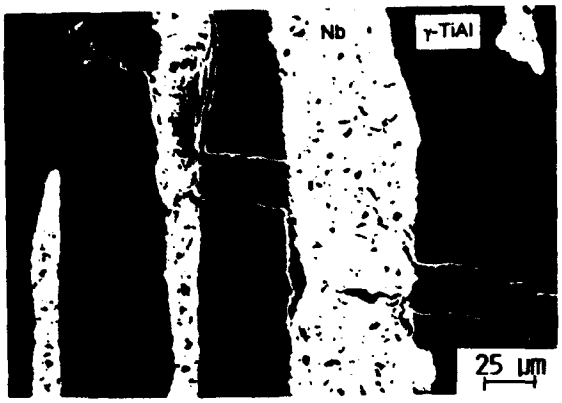

Fig. 10. SEM micrograph of fracture path morphologies in Nb/TiAl composites under monotonic loading. Note the extensive debonding at the interface compared to TiNb/TiAl composites.

least-square fits to the experimental data are listed in Table 3. Despite the influence of specimen size on the measured fracture properties†, it is clear that both crack-initiation toughness and crack-growth toughness, i.e. the slope of the resistance curve, increase with ductile-phase content for the 40 μm-thick TiNb reinforcements [Fig. 8(a–c)]. In comparison, reinforcement orientation has a minimal effect on ductile-phase toughening at lower volume fractions, particularly after specimen-size variations are considered. The toughness is marginally superior in the face orientation, compared to the edge, but only for TiAl composites reinforced with 20 vol.% TiNb.

The reduction in reinforcement thickness from ~40 to 20 μm at a volume fraction of 0.2 decreases the slope of the resistance curve, but does not appear to have a large effect on the initiation toughness [Fig. 9(a, b)]. The effectiveness of Nb vs TiNb ductile reinforcements in enhancing the monotonic fracture resistance of γ-TiAl composites, compared in Fig. 9(c), illustrates the significance of *effective* particle strength on toughness as mediated by the combination of yield stress, constraint (for TiNb) and strain hardening (for Nb). Specifically, the Nb particles in Nb/TiAl composites readily delaminate from the matrix during crack advance (Fig. 10) and relax constraint (or reduce the degree of triaxiality) during fracture compared to the highly constrained failure of TiNb ligaments in TiNb/TiAl composites (Fig. 6). Consequently, the higher (constrained) maximum effective strength of the TiNb reinforcements (~950 MPa) yield a significantly higher crack-initiation toughness and a steeper resistance curve compared to Nb additions (unconstrained, effective strength of Nb ~250 MPa). The larger critical opening displacement in Nb ($u^* \sim 1.1t$) vs TiNb ($u^* \sim 0.7t$) appears to have no effect on the initiation toughness and relatively little effect on crack-growth toughness in these small samples. Furthermore, little effect of orientation on toughness is noted for either reinforcement.

The effects of reinforcement volume fraction (f) and thickness (t) on the apparent crack-initiation and crack-growth toughness values are more clearly shown in Fig. 11(a–c) [the small symbols in Fig. 11(a)

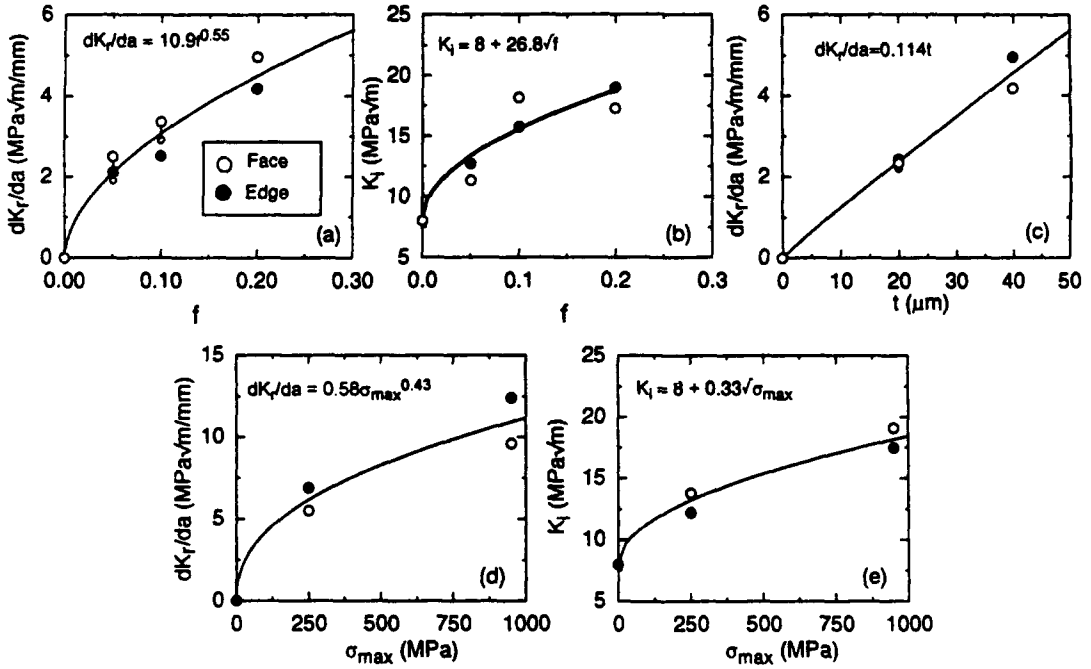

Fig. 11. Variations in crack-initiation toughness, K_i, and crack-growth toughness, dK_r/da, with (a,b) volume fraction f, of reinforcement phase, (c) particle thickness, t, and (d,e) reinforcement strength, σ_{max}, for both Nb/TiAl and TiNb/TiAl composites.

represent the estimated size corrections to a common specimen width of 15.2 mm]. With respect to volume fraction of TiNb, f_{TiNb}, [Fig. 11(a, b)] power-law fits yield

$$\frac{dK_r}{da} = 10.9(f_{TiNb})^{0.55}$$

$$K_i = 8 + 26.8(f_{TiNb})^{0.5}. \quad (3)$$

The corresponding fit of dK_r/da to the TiNb particle thickness, t_{TiNb}, yields a linear dependence [Fig. 11(c)]. Particle thickness has little effect on crack-initiation toughness; hence, a plot of these data is not shown. Figure 11(d) and (e) plot the apparent crack-initiation toughness values and resistance-curve slopes vs the effective maximum reinforcement strength, yielding power-law fits

$$\frac{dK_r}{da} = 0.58(\sigma_{max})^{0.43} \quad (4)$$

$$K_i = 8 + 0.33(\sigma_{max})^{0.5}. \quad (5)$$

The extrinsic toughening behavior measured in this study cannot be analyzed using the intrinsic, steady-state, small-scale bridging model represented by equation (1). Nevertheless, the experimental trends are *qualitatively* consistent with predictions that toughness increases with the square root of the reinforcement volume fraction and strength. The linear dependence of toughness on particle thickness is not predicted by equation (1). The particle thickness effect on crack-growth toughness (dK_r/da) is probably a consequence of the combination of a higher effective strength (particularly in the initial portion of the R-curve) and longer extrinsic bridge length (particularly at large a/W) for the large-scale bridging conditions experienced in these tests.

One puzzling result, however, is the absence of an effect of particle thickness on the apparent initiation toughness. Recall that the elevation of K_i above the K_{ic} value for γ-TiAl matrix is attributed to a combination of crack trapping, deflection, and renucleation mechanisms along with the presence of a small ($\sim 50\,\mu m$) residual crack-bridging zone. While crack deflection contributions are not believed to be significant, the toughening increment associated with renucleation and residual bridging effects would be expected to scale roughly with the square root of the reinforcement thickness [11, 23]. This suggests that crack trapping (pinning by ductile phases, as in the case of a tunnel crack) effects in the edge orientation may be comparable to toughening contributions from crack-renucleation mechanisms in the face orientation. More research is needed to resolve the effect of particle thickness and orientation on the apparent crack-initiation toughness.

A more rigorous analysis of these data must take into account the effects of large-scale bridging, by calculating self-consistent solutions to the crack-opening profile, $u(x)$, the distribution of tractions in the crack wake, $\sigma(x)$, and the stress-displacement function of the composite, $\sigma(u)$, where x is the distance behind from the crack tip; details are presented elsewhere [11]. Using this model, the intrinsic steady-state toughness, K_{SSB}, and steady-state bridging length, L_{SSB}, were estimated by computing the $K_r(\Delta a)$ curves up to steady-state in a very large specimen. The calculations assumed nominal reinforcement parameters given in Table 2; K_i and E' are approximated by the initiation toughness, K_i, and the nominal plane-strain elastic modulus of TiAl (193 GPa). The stress-displacement function for the composite is of the form

$$\sigma(u) = \sigma_{max}(u/u_p) \text{ for } u \leqslant u_p \quad (6a)$$

$$\sigma(u) = \sigma_{max}[1 - (u/u'^*)^{0.5}] \text{ for } u > u_p \quad (6b)$$

where, u_p is the displacement at peak stress (taken as $2\,\mu m$), and u'^* is taken as twice the *average* critical particle displacement or the corresponding value measured in sandwich tests. This formulation of $\sigma(u)$ is a modification to the nearly saw-toothed stress-displacement functions measured in the sandwich tests in order to account approximately for the *distribution* of particle thicknesses in the actual composite. Results from these calculations, summarized in Table 3, also indicate that significant intrinsic toughening can be achieved in γ-TiAl composites even under small-scale bridging conditions. Also note the remarkably long steady-state bridging lengths under small-scale bridging conditions.

Results on crack-growth resistance curves measured under monotonic loading can be summarized as follows. Even small volume fractions of ductile reinforcements produce marked toughening due (i) the formation of large bridging zones and (ii) crack trapping and renucleation mechanisms which mediate the critical crack-tip stress intensity. The slope of the R-curve increases with reinforcement volume fraction, strength and thickness; with the exception of particle thickness, similar trends are observed for crack-initiation toughness. Reinforcement orientation appears to have relatively little effect on the degree of toughening on these composites. Overall, the experimentally measured extrinsic toughening behavior is consistent with predictions of large-scale bridging models.

3.2. *Fatigue-crack propagation behavior*

Cyclic fatigue-crack growth results in the ductile-particle reinforced γ-TiAl composites, along with data for unreinforced γ-TiAl and β-TiNb constituent phases, are plotted in Figs 12–14; fatigue-threshold data and other crack-growth parameters are summarized in Table 4. As noted in previous studies on the TiNb/TiAl system [15, 16], under cyclic loading, cracks propagate subcritically at stress intensities of 4–12 MPa$\sqrt{m}$ for all γ-TiAl composite microstructures and specimen orientations, below the K_i values necessary to initiate and sustain cracking under monotonic loading (Table 3). Subcritical crack

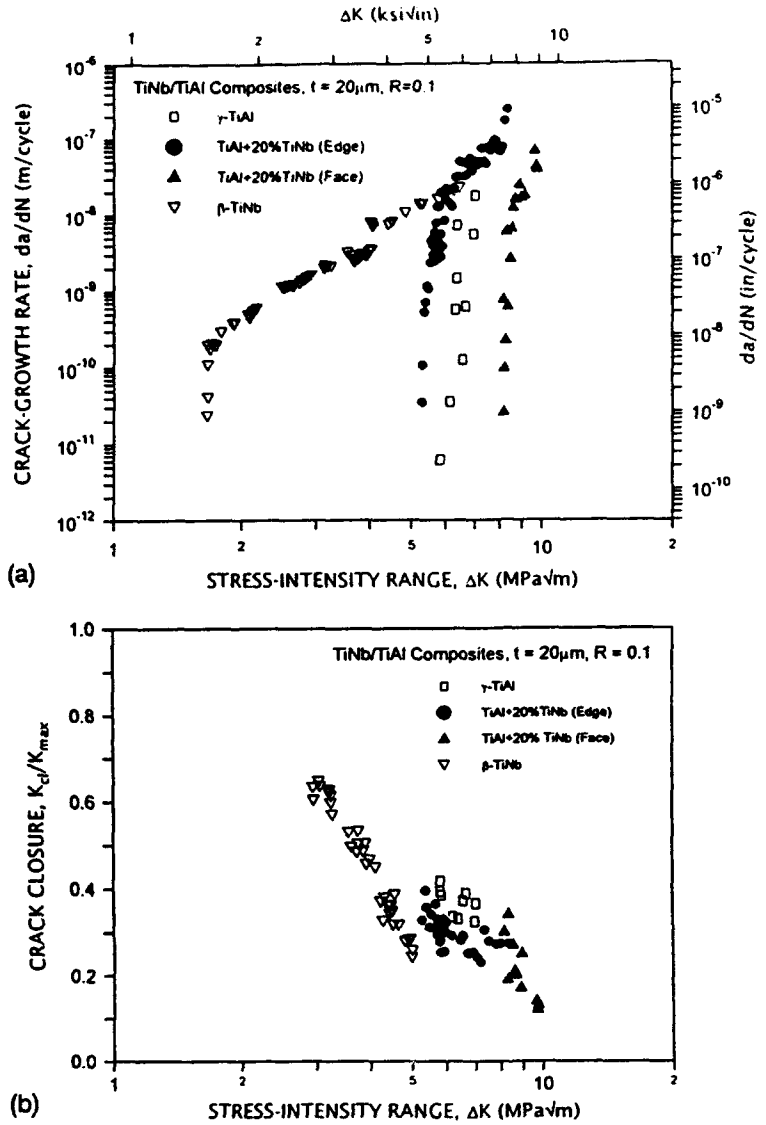

Fig. 12. (a) Cyclic crack propagation and (b) crack-closure behavior in a γ-TiAl + 20 vol.% β-TiNb ($t \sim 20\,\mu$m) composite, in the edge (C–R) and face (C–L) orientations, at $R = 0.1$, compared with the crack-growth properties of the constituent phases, monolithic γ-TiAl and β-TiNb.

propagation under cyclic loads must therefore be considered an important damage mode in the structural design and use of ductile-phase toughened brittle-matrix composites.

The general features of da/dN–ΔK curves for the composites resemble those seen for most metallic materials with a low-growth rate region (region I) at ΔK levels close to the fatigue threshold, where the rate of crack advance strongly depends on applied ΔK, followed by an intermediate or mid-growth rate region (region II) where this dependence is moderate. However, unlike behavior in metals, crack-growth behavior for the γ-TiAl composites in this mid-growth rate regime† is still very sensitive to the applied ΔK, especially at low volume fractions. In fact, when expressed in terms of the empirical Paris power-law relationship that is often used to describe fatigue crack-growth rate behavior in this region.

$$da/dN = C\Delta K^m \tag{7}$$

the exponent m ranges between 10 and 20 for the various composites, compared to values of ~2–4 that are typically reported for monolithic metallic materials; $m \sim 4.6$ for pure β-TiNb [Table 4, Fig. 12(a)]. In other words, the mid-growth rate (power-law) regime of cyclic crack growth is relatively small for ductile-phase toughened TiAl composites and virtually non-existent for unreinforced γ-TiAl ($m \sim 30$). At high ΔK levels approaching the

†Behavior in this region is characterized by curve fitting the da/dN data between 10^{-9} and 10^{-6} m/cycle.

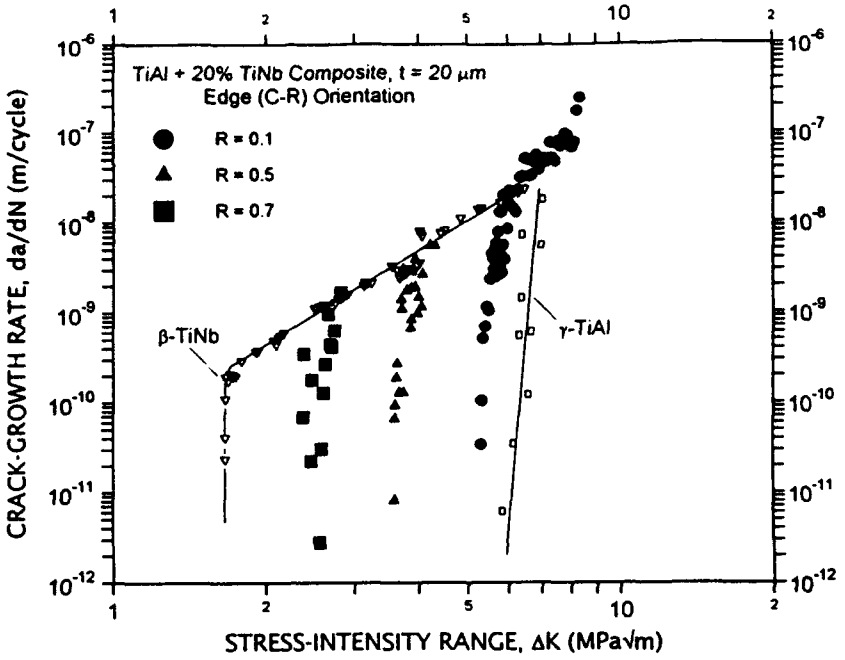

Fig. 13. Influence of load ratio, $R = 0.1$, 0.5 and 0.7, on the cyclic fatigue-crack growth behavior in a γ-TiAl composite reinforced with 20 vol.% ($t \sim 20\,\mu$m) TiNb particles in the edge (C–R) orientation.

initiation toughness, K_i (high-growth rate regime, region III), a rapid increase in crack-extension rates is seen for small changes in ΔK, similar to behavior near the fatigue threshold.†

3.2.1. Orientation effects for TiNb/TiAl composites. Figure 12(a) depicts the cyclic fatigue-crack growth data for the edge and face orientations in the γ-TiAl composite reinforced with 20 vol.% of $\sim 20\,\mu$m-thick TiNb particles. Specifically, in the edge orientation, region I fatigue-crack growth rates in the composite are faster than in unreinforced γ-TiAl and much slower than in pure β-TiNb. The near-threshold cyclic crack-growth behavior ($da/dN < 10^{-9}$ m/cycle) of the composite is essentially bounded by properties of the individual phases. In region II, growth rates in the edge-orientation of the composite are comparable to those measured in monolithic β-TiNb.

However, Fig. 12(a) also reveals that the crack velocities in the TiNb/TiAl composite for the face (C-L) orientation are slower than in γ-TiAl; in fact, the composite fatigue properties are superior to both unreinforced TiAl and TiNb. Thus, unlike the response under monotonic loading, the reinforcement orientation has a marked effect on cyclic crack-growth behavior. More importantly, these results clearly demonstrate that the incorporation of ductile reinforcements *can* also enhance the cyclic fatigue-crack propagation resistance of brittle γ-TiAl intermetallic alloys, in addition to improving their fracture toughness. However, the magnitude of improvement is relatively small, indicated by ~ 2 MPa$\sqrt{\text{m}}$ shift in the entire da/dN–ΔK curve compared to the nearly five-fold increase in toughness seen under monotonic loads, and is seen only specific orientations i.e., where the crack periodically encounters the pancake faces of ductile particles. Similar reinforcement-orientation effects are also observed in other TiNb/TiAl composite microstructures [Fig. 14(b)].

Corresponding measurements of the extent of crack closure in the TiNb/γ-TiAl composites and their two unreinforced constituents are shown in Fig. 12(b) in terms of the closure stress intensity, K_{cl}, normalized by K_{max}, as a function of ΔK. The K_{cl}/K_{max} values in the edge orientation of composite are slightly lower compared to TiAl in the edge orientation suggesting faster growth rates due to increased ΔK_{eff} values locally at the crack tip; no such distinction is apparent in the face orientation. Although such variations are partly consistent with observed reinforcement-orientation effects on cyclic crack growth, closure effects do not appear to completely account for the differences in crack-growth rates between the composite and monolithic alloys. Specifically, at high ΔK levels where the influence of closure is reduced, cracks propagate faster in the edge-oriented composite than in pure γ-TiAl or β-TiNb [Fig. 14(a)]. As such, it seems more likely that cyclic crack-growth rate variations are principally

†It should be noted that fatigue-crack growth behavior in the high-ΔK regime (region III) has not been fully characterized in this study due to the rapid crack velocities inherent with test frequencies of 50 Hz used for cyclic loading, especially for brittle-matrix composites.

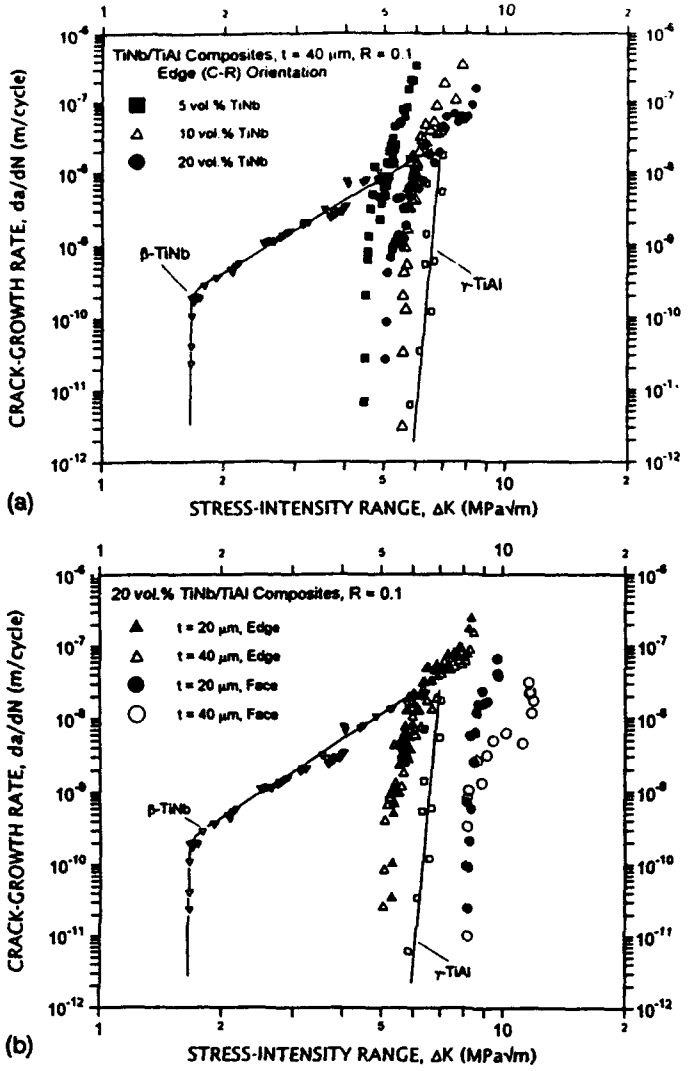

Fig. 14. Microstructural effects of (a) volume fraction ($t \sim 40\ \mu m$) and (b) particle thickness ($f \sim 0.2$) on the cyclic fatigue-crack propagation resistance of TiNb/TiAl composites in the edge (C–R) orientation, at $R = 0.1$.

attributable to differences in intrinsic mechanisms of cyclic crack advance in these microstructures.

3.2.2. Load ratio effects. The effect of load ratio ($R = K_{min}/K_{max}$) on cyclic crack-growth rates, in the 20 vol.% TiNb/γ-TiAl composite in the edge (C–R) orientation, is shown in Fig. 13. Compared to a baseline of $R = 0.1$, load ratios of 0.5 and 0.7 reduce the fatigue threshold stress-intensity values by about 27 and 51%, respectively. This phenomenon is consistent with behavior observed in many metallic materials [24], where increasing R accelerates crack-growth rates for a given ΔK, especially in the near-threshold and high-ΔK regions. Although the marked sensitivity to applied ΔK in the threshold regime is essentially unchanged, higher load ratios suppress the intermediate growth-rate regime (region II) separating the behavior at near-threshold and high stress intensities. The latter occurs at K_{max} of ~ 8.5–$9.3\ MPa\sqrt{m}$, slightly in excess of the matrix fracture toughness of $\sim 8\ MPa\sqrt{m}$, and is independent of the load ratio.

As noted above, premature crack closure is observed to occur in the composites at stress intensities above K_{min}, presumably from the wedging of fracture-surface asperities including any intrinsic bridging ligaments or broken remnants, e.g. at threshold, K_{cl} is $\sim 0.4\ K_{max}$. As a result, for load ratios below 0.4, such closure causes a net increase in K_{min} or a reduction in the driving force from the nominal (applied) value of ΔK to a local "near-tip" value ΔK_{eff}, thereby resulting in slower crack-growth rates. At high R, closure effects are minimal ($K_{min} > K_{cl}$) and the crack remains open during the entire loading cycle; accelerated crack-growth rates are thus to be expected. From these considerations, load ratio effects on cyclic crack growth in the composite are

Table 4. Summary of cyclic crack growth data in γ-TiAl composites

Material	Load ratio R	Threshold ΔK_{TH} (MPa$\sqrt{}$ m)	Exponent[a] m	Constant[b] C
γ-TiAl	0.1	5.8	29.4	9.7×10^{-31}
β-TiNb	0.1	1.7	4.6	3.0×10^{-11}
Edge orientation				
γ-TiAl + 5% TiNb (40 μm)	0.1	4.5	17.6	5.3×10^{-18}
+ 10% TiNb (40 μm)	0.1	5.6	14.1	1.1×10^{-16}
+ 20% TiNb (40 μm)	0.1	5.0	9.6	2.0×10^{-13}
+ 20% TiNb (20 μm)	0.1	5.3	9.7	2.5×10^{-13}
	0.5	3.6	—	—
	0.7	2.6	—	—
Face orientation				
γ-TiAl + 20% TiNb (40 μm)	0.1	8.2	6.7	1.0×10^{-15}
+ 20% TiNb (20 μm)	0.1	8.2	14.8	1.1×10^{-22}
+ 20% Nb (40 μm)	0.1	10.1	8.7	1.0×10^{-18}

[a]For crack-growth rates between 10^{-9} and 10^{-6} m/cycle.
[b]Units: m/cycle (MPa$\sqrt{}$m)$^{-m}$

expected to be small for $R > 0.4$, since K_{cl} is at least $\sim 0.4\,K_{max}$. However, other factors are clearly relevant in view of the marked differences in behavior between $R = 0.5$ and 0.7, e.g. the rapid crack growth at K_{max} levels approaching the matrix K_{Ic} due to cleavage fracture of γ-TiAl [Fig. 7(c)], akin to the high-ΔK behavior controlled by static-mode fracture mechanisms seen in metallic alloys [24].

3.2.3. Crack–particle interactions. In contrast to behavior under monotonic loads (Fig. 6), crack-path morphologies in TiNb/γ-TiAl microstructures under cyclic loads reveal that there is minimal ductile-ligament bridging in the crack wake (Fig. 15). Crack paths in the plane of loading and crack fronts across the specimen thickness ($\sim 150\,\mu$m behind the crack tip) clearly indicate that the TiNb particles rapidly fail under cyclic loading without any sign of plastic deformation. In the edge (C–R) orientation, fatigue cracks traverse the ductile particles apparently without significant interaction [Fig. 15(a)]; crack blunting, crack renucleation and resultant in-plane bridging effects, which are so dominant under monotonic

Fig. 15. SEM micrographs of crack-path morphologies in TiNb/γ-TiAl composites under cyclic loading in the (a) edge (C–R) and (b) face (C–L) orientations, taken at specimen mid-thickness location in the loading plane. Horizontal arrow indicates the crack-growth direction.

loads, are simply not observed. This conclusion was verified by *in situ* telescopic observations on the specimen surface, and also by quantitative estimates of the extent of crack bridging at various ΔK levels. Crack lengths, estimated from elastic-compliance measurements using strain gauges, were within $\pm 200\,\mu m$ (<2%) of those measured using indirect d.c. potential methods, indicating that crack-bridging effects in fatigue are relatively insignificant. No discernible differences in crack paths were noted at the various load ratios.

Although cracking is still continuous through the matrix and ductile phases in the face (C–L) orientation, as shown in Fig. 15(b), there is indication of crack branching, deflection, multiple cracking in the matrix and coplanar bridging (associated with a non-planar and discontinuous crack front across the specimen thickness because of overlapping cracks on different planes), consistent with the improved crack-growth resistance in this orientation. Crack renucleation in the matrix ahead of the TiNb particle under cyclic loading is observed at ΔK levels of $\sim$9–10 MPa$\sqrt{m}$; however, due to the rapid fatigue fracture of the TiNb particle, the effective range of crack/particle interactions is limited to a few hundred microns or less (cyclic bridging zone ~ particle thickness); equivalent dimensions under monotonic loading are on the order of several millimeters (Table 3). In fact, even in the face orientation, the TiNb particles show minimal evidence of plastic stretching.

Corresponding fracture-surface morphologies are shown in Fig. 16. Unlike the microvoid coalescence seen under monotonic loading (Fig. 7), the TiNb phase fails by transgranular shear under cyclic loading in both the composite and monolithic form [Fig. 16(b)]; features resemble fatigue failures in coherent-particle hardened alloys that deform by planar slip [25]. Likewise, the γ-TiAl matrix also shows intrinsic fatigue damage, evidenced by the parallel slip markings in Fig. 16(c), in addition to the transgranular and intergranular cleavage modes of failure [Fig. 16(c)].

From these observations and other studies [15, 16] it may be inferred that the lack of toughening from crack-bridging mechanisms under cyclic loads is the principal reason for subcritical crack-growth effects in TiNb/TiAl composites at ΔK levels below their crack-initiation toughness values. Such enhanced crack growth results from fatigue-induced failure of the ductile particles before the crack can establish a bridging zone, which is already limited under cyclic loading because of the relatively small crack-opening displacements associated with the lower stress intensities.

The sources for reinforcement-orientation effects on cyclic crack growth are not altogether clear. Potential explanations include: (i) fatigue failure of the reinforcements in the edge orientation in fewer cycles, since the opening along the crack flanks and resultant plastic displacements would be larger than corresponding crack-tip opening displacements in the face orientation; (ii) restriction of crack deflection, branching and coplanar bridging effects in the edge orientation by the reinforcement; and (iii) differences in the phase angle of any local debond cracks.

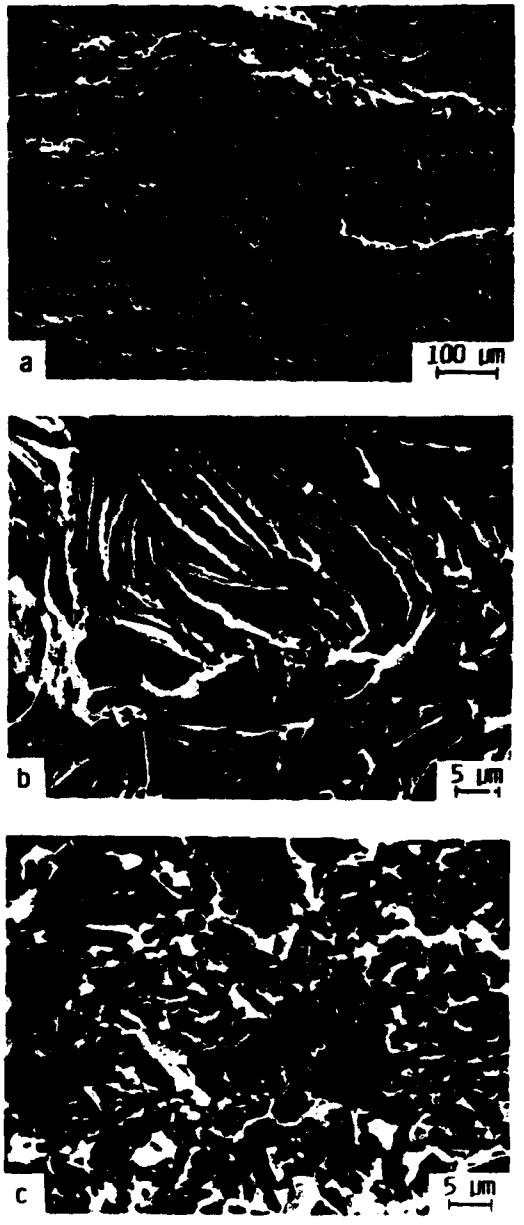

Fig. 16. (a–c) SEM images of fracture surfaces in TiNb/γ-TiAl composites under cyclic loading at various magnification levels. Micrographs (b) and (c) illustrate the cracking features in β-TiNb and γ-TiAl regions of the composite. Horizontal arrow indicates the general direction of crack growth.

3.2.4. Reinforcement size and volume fraction effects. The influence of TiNb reinforcement volume fractions, ranging between 0.05–0.2 ($\sim 40\,\mu m$-thick), on fatigue-crack growth behavior of TiNb/TiAl composites in the edge orientation, is illustrated in

Fig. 14(a). While fatigue thresholds for all composites fall below the value for monolithic γ-TiAl, there appears to be no consistent effect of f_{TiNb} on the fatigue threshold; ΔK_{TH} values range between $\sim 4.5\ MPa\sqrt{m}$ ($f_{TiNb} \sim 0.05$) and $\sim 5.6\ MPa\sqrt{m}$ ($f_{TiNb} \sim 0.1$).

However, the slope of da/dN-ΔK curves (measured as the exponent, m) in the intermediate growth-rate region is found to decrease consistently with increasing ductile-phase content (Table 4); the ΔK interval for region II and the maximum ΔK marking the onset of region III show a corresponding decrease. In effect, intermediate crack-growth rates in the composites, at a given ΔK, are lowered by increasing the reinforcement volume fraction. More notably, crack-growth rates in the composites with 10 vol.% TiNb, and particularly 5 vol.% TiNb, are significantly *higher* than those found in either unreinforced TiNb or TiAl. These interesting, albeit puzzling, effects could be associated with the competing role of residual stresses or crack-closure effects (which increase ΔK_{tip}) vs limited crack bridging/trapping (which reduces ΔK_{tip}); with increasing f_{TiNb}, crack bridging/trapping effects may become dominant.

Reinforcement thickness has a minimal effect on cyclic crack-growth behavior in the edge (C–R) orientation, for samples containing 20 vol.% TiNb [Fig. 14(b)]. However, increasing TiNb particle thickness from ~ 20 to 40 μm is found to retard crack advance in the face (C–L) orientation, especially for ΔK levels in the mid-growth rate regime, above $\sim 9\ MPa\sqrt{m}$. Toughening mechanisms associated with crack renucleation in the matrix ahead of the ductile particle, which scale with particle thickness [11, 23], are believed to account for the improved fatigue resistance of coarse microstructures. Once again, note that reinforcement-orientation effects are prominent under cyclic loading, with face-oriented composites exhibiting better crack-growth resistance over γ-TiAl and β-TiNb.

3.2.5. TiNb vs Nb reinforcements. Figure 17 compares the fatigue-crack growth properties of γ-TiAl reinforced with 20 vol.% ($\sim 40\ \mu$m thick) Nb particles in face (C–L) orientation to corresponding behavior in the TiNb/TiAl, both in the edge and face orientations. While both reinforcements in the face orientation improve the fatigue resistance of γ-TiAl, the cyclic toughening increment is clearly greater for the Nb phase than for TiNb. The fatigue threshold for the Nb/TiAl composite, $\Delta K_{TH} \sim 10\ MPa\sqrt{m}$, is about 75 and 40% larger than the pure γ-TiAl ($\sim 6\ MPa\sqrt{m}$) and the TiNb/TiAl composite ($\sim 8\ MPa\sqrt{m}$), respectively. This is in contrast to fracture toughness behavior under monotonic loading, where the high-strength TiNb reinforcements are significantly more effective in impeding crack advance. When compared at a fixed ΔK of $10\ MPa\sqrt{m}$, growth rates are nearly five orders of magnitude

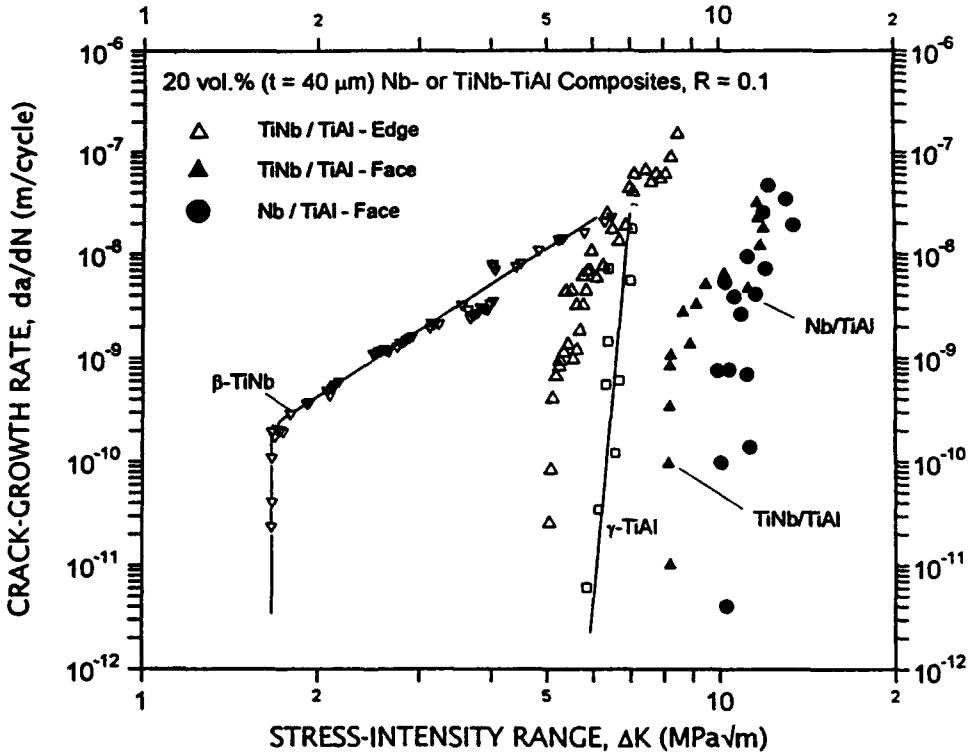

Fig. 17. Effect of Nb vs TiNb ductile reinforcements on the cyclic crack-growth resistance of γ-TiAl in the face (C–L) orientation ($R = 0.1$). Note the superiority of Nb/γ-TiAl composites due to their relatively weak interfacial bonding compared to TiNb/γ-TiAl.

Fig. 18. Summary of cyclic crack-path morphologies (in the plane of loading) observed for the Nb/γ-TiAl composite in the face (C–L) orientation, showing significant interfacial debonding, cracking ahead of the Nb particles and evidence of crack bridging. Horizontal arrow represents the crack-growth direction.

slower in Nb/TiAl than in TiNb/TiAl. However, the enhancement in fatigue resistance of γ-TiAl from Nb additions is far less compared to that equivalent increase in fracture toughness [Fig. 9(c)].

Such improved fatigue-crack growth properties using Nb reinforcements can be traced to significant secondary-cracking effects locally near the Nb/TiAl interface. As illustrated in Fig. 18, these are characterized by (i) crack arrest at the interface, (ii) decohesion along the interface and (iii) crack renucleation in the brittle matrix ahead of the particle, prior to particle failure. Analogous to behavior under monotonic loads, the brittle σ-layer interface surrounding Nb particles is expected to be less fatigue resistant and susceptible to debonding compared to the ductile α_2 layer around TiNb particles. Nevertheless, such debonding at the Nb/TiAl interface relaxes constraint, diffuses plastic strains, and prevents continuous crack penetration into the ductile Nb phase; these mechanisms, in addition to crack renucleation which preserves *local* crack-tip bridging, extend the fatigue life of the Nb reinforcements. However, the extent of debonding during fatigue is less than that seen under monotonic loading (Fig. 10) and is much more evident in Nb/TiAl. Conversely, debonding is not evident for TiNb/TiAl composites under fatigue, as under monotonic loading, and consequently the cracks advanced continuously through the α_2 layer

into the TiNb particle without significant interfacial interactions, thereby leading to rapid failure of the TiNb phase. Moreover, the TiNb phase is inherently more susceptible to fatigue failure in fewer cycles (due to localized planar-slip deformation) than the strain-hardening Nb phase, consistent with previous results. (Note that fatigue-crack growth rates in Nb are also strongly dependent on interstitial H_2, C, N_2, O_2, and Si impurity contents [26].)

Finally, it is useful to estimate the magnitude of toughening associated with various mechanisms under cyclic loading to provide some insight into their relative contributions. The effects of local crack bridging in fatigue (Fig. 18), specifically in the face orientation, on the reduction in near-tip stress intensity, ΔK_b, may be assessed using the Dugdale approximation [27]

$$\Delta K_b = \frac{2}{\sqrt{\pi}} f\sigma_e \sqrt{2L_b} \tag{8}$$

where, L_b is the bridging-zone length and σ_e the effective value for uniform bridging tractions in that zone. Taking $L_b \sim 40\,\mu$m (bridging zone ~ reinforcement thickness) and the average bridging tractions under cyclic loading to be roughly one half the flow stress ($\sigma_e \sim 0.5[\sigma_0 + \sigma_u]/2$, or ~215 and ~100 MPa for TiNb and Nb, respectively), the in-plane bridging contributions, ΔK_b, for a composite reinforced with 20 vol.% ductile particles are a mere ~0.4 and ~0.2 MPa$\sqrt{m}$ for TiNb and Nb phases, respectively. Measured shifts in the da/dN–ΔK curves (Fig. 17) are, respectively, ~2 and ~4 MPa$\sqrt{m}$ for the TiNb/TiAl and Nb/TiAl composites, implying that other mechanisms are relevant. Crack trapping and renucleation of the fatigue crack in the ductile phase associated with blunting (via interfacial decohesion for Nb), and coplanar bridging from multiple and discontinuous crack fronts (for TiNb and Nb) are expected to provide the additional contributions to the fatigue-crack growth resistance.

4. CONCLUDING REMARKS

The present results extend previous studies [15, 16] in illustrating the contrasting role of ductile reinforcements on monotonic (fracture toughness) and cyclic (fatigue) crack-growth resistance of intermetallic–matrix composites. With respect to R-curve toughness, the principal factors are effective reinforcement strength and ductility as mediated by constraint imposed by debonding characteristics of the interface and resultant constrained deformation properties of the reinforcement; local crack/particle interactions contribute to intrinsic crack-initiation toughness. Reinforcement thickness (initiation toughness) and orientation (edge vs face) effects on toughness, previously seen in coarse laminated composites, appear to be modest for the pancake-shaped ductile-phase toughened composites, suggesting competing effects of various local crack/particle interactions on monotonic crack-growth resistance.

Very different mechanisms and microstructural factors are associated with fatigue-crack propagation resistance. This is perhaps best illustrated by the degradation in fatigue thresholds compared to γ-TiAl and accelerated crack-growth rates relative to either monolithic constituent in the edge-oriented TiNb/TiAl composites, particularly at low volume fractions. The premature cracking or low-cycle fatigue failure of ductile particles at small crack-opening displacements under cyclic loading result in very limited bridging zones and therefore minimal toughening. Improved fatigue resistance is seen only in the face-oriented composites, the increase being attributed to local crack-particle interaction mechanisms that are similar to those under monotonic loading, yet are far less potent under cyclic loading. The fatigue resistance of the composites is further enhanced by weak (debonding) particle–mat[illegible]ter-faces and ductile particles with optimal fat[illegible]o-erties, e.g. strain-hardening phases with high[illegible]us and strength. Debonding can be induced at inherently strong reaction-layer interfaces by applying thin oxide coatings between constituents, although this can reduce the toughness. These observations suggest that ductile phases are associated with multiple and competing mechanisms, with the net effect under fatigue loading being sensitive to reinforcement architecture, volume fraction and particle thickness.

Such differing, and in some cases contradictory, requirements for superior toughness and fatigue resistance suggest that optimized composite microstructures may require a variety of reinforcements and architectures based on alternative shielding mechanisms. For example, a semi-continuous network of the ductile phase offering a preferred crack path may provide improved fatigue resistance by promoting crack meandering. This in turn promotes crack-tip shielding from roughness-induced crack closure by wedging of enlarged fracture-surface asperities, and has proved to be very effective in improving the fatigue-crack growth resistance of duplex ferritic/martensitic steels and α/β titanium alloys [28, 29]. Such an approach should also provide adequate toughness under monotonic loads due to the formation of extensive bridging zones.

5. CONCLUSIONS

Based on an experimental study of the monotonic and cyclic crack-growth properties of ductile-phase toughened γ-TiAl intermetallic composites, reinforced with either β-TiNb or Nb, the following conclusions can be made:

1. Brittle γ-TiAl intermetallic alloys can be significantly toughened under monotonic loading by dispersing ductile Nb or TiNb reinforcements; compared to a fracture toughness of 8 MPa$\sqrt{m}$ for pure γ-TiAl, both type of composites show increased

crack-initiation toughness (K_i) and marked resistance-curve behavior with $K_r(\Delta a)$ values in excess of $\sim 40\ MPa\sqrt{m}$. Under monotonic loading, the stronger β-TiNb particles impart greater toughening than Nb reinforcements.

2. Improvement in crack-growth toughness (as reflected by the resistance-curve slope, dK_r/da) under monotonic loading is primarily attributed to shielding effects, associated with extensive bridging by intact TiNb or Nb ligaments, over dimensions of several millimeters, in the crack wake. A number of local crack-particle interactions enhance the crack-initiation toughness, and provide secondary contributions to crack-growth toughness. Depending on the measure, toughness increases with thickness (K_i) and volume fraction (K_i, dK_r/da) of the ductile-phase particles; however, reinforcement orientation appears to have a relatively minor effect.

3. Ductile TiNb and Nb reinforcements also lead to enhanced cyclic fatigue-crack growth resistance of γ-TiAl, although the effect is specific *only* to the face (C–L) orientation and is seen as a modest increase in the fatigue threshold, ΔK_{TH}. The increase appears to be associated with local crack–particle interaction mechanisms, including crack renucleation (in the matrix and/or particle), crack branching, limited interface debonding and discontinuous (out-of-plane) crack bridging.

4. Conversely in the edge (C–R) orientation, TiNb particles actually *degrade* the ΔK_{TH} relative to γ-TiAl, and at low volume fractions accelerate the intermediate crack-growth rates relative to *either* monolithic constituents. Behavior is primarily due to the premature fatigue fracture of ductile phases under cyclic loads, which severely limits bridging in the crack wake, and the absence of any other microstructural interactions.

5. In direct contrast to their effect on toughness under monotonic loading, in the face (C–L) orientation, Nb particles yield better fatigue-crack growth resistance compared to TiNb particles. This results from extensive debonding of Nb particles from the γ-TiAl matrix, due to the weak Nb/TiAl interface, and their inherently better fatigue properties compared to TiNb reinforcements.

Acknowledgements—This work was supported by the U.S. Air Force Office of Scientific Research under Grant No. AFOSR-90-0167 (KTVR and ROR), and by the Defense Advanced Research Projects Agency under Contract No. URI-N00014-86-K-0753 (GRO). Thanks are due to Dr Alan H. Rosenstein for his continued support, Pratt and Whitney for provision of materials, Professor G. E. Lucas, Dr R. H. Dauskardt for helpful discussions, and J. W. Sheckherd, C. Liu, C. Muhlstein and D. Nath for experimental assistance.

REFERENCES

1. C. T. Liu, J. O. Stiegler and F. H. Froes, *Metals Handbook* **2**, 913 (1991).
2. R. L. Fleischer, D. M. Dimiduk and H. A. Lipsitt, *Ann. Rev. Mater. Sci.* **19**, 231 (1989).
3. Y. W. Kim, *Acta metall. mater.* **40**, 1121 (1992).
4. Y. W. Kim and D. M. Dimiduk, *J. Metals* **43(8)**, 40 (1991).
5. K. S. Chan and Y. W. Kim, *Metall. Trans. A* **23A**, 1663 (1992).
6. K. S. Chan, *J. Metals* **44(5)**, 30 (1992).
7. H. E. Dève, A. G. Evans and D. S. Shih, *Acta metall. mater.* **40**, 1259 (1992).
8. C. K. Elliott, G. R. Odette, G. E. Lucas and J. W. Sheckherd, in *High-Temperature/High-Performance Composites* (edited by F. D. Lemkey, A. G. Evans, S. G. Fishman and J. R. Strife), MRS Symp. Proc., Vol. 120, p. 95. MRS, Pittsburgh, Pa (1988).
9. H. E. Dève, A. G. Evans, G. R. Odette, R. Mehrabian, M. L. Emiliani and R. J. Hecht, *Acta metall. mater.* **38**, 1491 (1990).
10. G. R. Odette, H. E. Dève, C. K. Elliott, A. Hasegowa and G. E. Lucas, in *Interfaces in Ceramic Metal Interfaces* (edited by R. Y. Lin, R. J. Arsenault, G. P. Martins and S. G. Fishman), p. 443. TMS-AIME, Warrendale, Pa (1990).
11. G. R. Odette, B. L. Chao, J. W. Sheckherd and G. E. Lucas, *Acta metall. mater.* **40**, 2381 (1992).
12. V. D. Krstic, P. S. Nicholson and R. G. Hoagland, *J. Am. Ceram. Soc.* **64**, 499 (1981).
13. M. F. Ashby, F. J. Blunt and M. Bannister, *Acta metall.* **37**, 1847 (1989).
14. B. D. Flinn, M. Rühle and A. G. Evans, *Acta metall.* **37**, 3001 (1989).
15. K. T. Venkateswara Rao, G. R. Odette and R. O. Ritchie, *Acta metall. mater.* **40**, 353 (1992).
16. K. T. Venkateswara Rao and R. O. Ritchie, in *Intermetallic Matrix Composites II* (edited by D. Miracle, J. Graves and D. Anton), MRS Symp. Proc., Vol. 273, p. 127. MRS, Pittsburgh, Pa (1992).
17. A. Hasegowa, G. E. Lucas and G. R. Odette, unpublished results, Univ. of California, Santa Barbara (1992).
18. American Society for Testing and Materials Standard E399-90, 3.01, 506 (1992).
19. R. O. Ritchie and R. H. Dauskardt, *J. Ceram. Soc. Japan* **99**, 1047 (1991).
20. R. H. Dauskardt and R. O. Ritchie, *Closed Loop* **27**, 7 (1989).
21. American Society for Testing and Materials Standard E647-91, 3.01, 674 (1992).
22. R. O. Ritchie, W. Yu and R. J. Bucci, *Engng Fract. Mech.* **32**, 361 (1989).
23. M. Y. He, F. E. Heredia, D. J. Wissuchek, M. C. Shaw and A. G. Evans, *Acta metall. mater.* **41**, 1223 (1993).
24. R. O. Ritchie, *Int. Metall. Rev.* **20**, 205 (1979)
25. K. T. Venkateswara Rao and R. O. Ritchie, *Int. Mater. Rev.* **37**, 153 (1992).
26. S. Fariabi, A. L. W. Collins and K. Salama, *Metall. Trans. A* **14A**, 701 (1983).
27. H. Tada, P. C. Paris and G. R. Irwin, *The Stress Analysis of Cracks Handbook*, Paris Prod. Inc./Del Corp., St Louis, Mo. (1985).
28. J.-K. Shang, J. L. Tzou and R. O. Ritchie, *Metall. Trans. A* **18A**, 1613 (1987).
29. J. M. Larsen, T. Nicholas, A. W. Thompson and J. C. Williams, in *Small Fatigue Cracks* (edited by R. O. Ritchie and J. Lankford), pp. 499–512. T.M.S.-A.I.M.E., Warrendale, Pa (1986).

Creep Models for Metal Matrix Composites with Long Brittle Fibers

*Z. – Z. Du and R. M. McMeeking**

*Materials Department and Mechanical Engineering Department**

University of California

Santa Barbara, California 93106

April, 1994

Abstract

Creep models for metal matrix composites reinforced by long brittle fibers with weak interfaces are presented. These models extend the work of McLean(1) to include effects of fiber breaks and the consequential stress relaxation in the broken fibers on the creep strain and the creep rupture time when global load sharing occurs. Systematic analyses are conducted for composites with a wide range of fiber volume fractions, Young's modulus of the fibers and the matrix, interfacial sliding stress and Weibull properties for the strength of the fibers. The results derived from this study are compared with those predicted by McLean's model(1) and another model accounting for part of the effects of broken fibers. The creep life is found to be sensitive to the extent of fiber stress relaxation in the broken fibers. Models, which ignore this effect overestimate the creep rupture time especially when the composite is subjected to a low or moderate level of stress.

1 Introduction.

The use of advanced continuous fiber reinforced metal matrix composites (SiC/Ti, Al_2O_3/Al) as engineering materials requires that the materials have sound mechanical behavior at both elevated and room temperatures. The mechanical behavior of metal matrix composites in terms of strength, plasticity and fatigue at room temperature is relatively well understood (2-6). Moreover, a comprehensive constitutive model which takes into account the material anisotropic behavior for the situation where the composite is subjected to a multi-axial loading has been developed(4). In contrast, relatively little work has been done on modeling the response of metal matrix composites at elevated temperatures. In order that comprehensive predictive models similar to those used in low temperature environments can be assembled for high temperature applications, the mechanical behavior associated with time dependent creep deformation of metal matrix composites has to be addressed.

In the range of operational temperatures, fibers usually do not creep but the matrix can creep. For example, in the case of a SiC/Ti composite at 600^0C, which normally is the peak value of the operational temperature, the homologous temperature for the matrix material is 0.45, which will lead to deformation by power law creep. The reinforcement, in contrast, operates at a homologous temperature of 0.2 and therefore should exhibit little time-dependent creep deformation.

A number of models have been developed to address creep problems in this regime for composites reinforced either by continuous or discontinuous fibers. Cell models are widely used for this purpose(7-11). Dragone and Nix(7) and Bao et al.(8) undertook

detailed numerical analyses on discontinuous fiber reinforced composites, while Kelly and Street(9), McLean(1), Goto and McLean(10) and most recently, McMeeking(11) adopted approximate models without recourse to complete numerical treatment. Of these models, McLean's (1), which is concerned with a composite with a power-law creeping matrix reinforced by elastic fibers, is particularly of interest. In his model, it is assumed that the fibers do not either creep or fracture and deform elastically at a rate governed by the surrounding creeping matrix. The governing equations for stress σ and strain ϵ in the model are given by

$$\sigma_f = E_f \varepsilon \tag{1}$$

$$\dot{\varepsilon} = \frac{\dot{\sigma}_m}{E_m} + B\sigma_m^n \tag{2}$$

and

$$\sigma = f\sigma_f + (1-f)\sigma_m \tag{3}$$

where f is the fiber volume fraction, E_f and E_m are the Young's modulus of the fibers and the matrix respectively, σ_f and σ_m are the fiber and the matrix stresses respectively, and n and B are the creep exponent and creep constant of the matrix respectively.

In McLean's (1) model, the strain rate decreases as the stress in the matrix decreases due to the matrix creep. As time progresses, the fibers therefore sustain more load formerly carried by the creeping matrix. Eventually, when the matrix stress is completely relaxed, all of the load is carried by the intact fibers and the strain approaches a steady state. This type of behavior is associated with matrix stress

relaxation which is usually completed in a relatively short time. For the situation where the composite is subjected to a low level of stress, this model predicts creep strain with reasonable success. However, when a relatively large load is applied to the composite, damage initiates in the form of isolated or localized fiber breaks(12,13). In addition, crack like defects can also be introduced in the fibers during manufacture. In either situation, in order for the creeping matrix to deform at a rate that is compatible with the more compliant broken fibers, creep strains must increase. Furthermore, the more fibers fail, the larger is the increase in creep strain. The composite therefore may never exhibit a steady-state creep rate and instead may progress directly from a primary to a tertiary stage(12). In this regime McLean's original model(1), which ignores such effects, underestimates the creep strain and fails to predict creep ruptures resulting from the failure of fibers. However, McLean(14) has also developed a model which includes the effect of statistical fiber failure and has predicted creep curves with a tertiary stage.

Recently, theoretical studies on fiber failure stochastics within the framework of global load sharing, whereby the load shed from a broken fiber is shared nearly equally among all intact fibers, have been carried out by Curtin (15) for composites with weak interfaces. This has led to a statistical strength prediction procedure for uniaxial composites. However, in his study, the effect of a creeping matrix on the stress distribution in the composite has not been addressed. The methodology used by Curtin (15), however, provides insight for including such an effect. McLean relaxation will cause the fiber stress to increase which increases fiber fracture and effective fiber compliance. If the fiber stress rises above the effective strength of the fibrous system,

failure of the composite will occur rapidly, leading to rupture after creep.

Another phenomenon associated with the failure of the fibers, which has received little attention, is the stress relaxation in the broken fibers. Previous work has addressed the evolution of the stress concentration around a broken fiber in a viscoelastic or power-law creeping matrix(16, 17). Other modeling has involved the finite element analysis of the matrix and fiber behavior with broken fibers(18, 19). When a fiber is broken, the stress in the fiber is gradually relaxed due to matrix shear stress leading to creep. This reduces the load carrying capacity of the broken fiber. The more the stress relaxes in the broken fiber, the higher is the load carried by the intact fibers. As a result, the strain in the intact fibers increases and more fibers fail. This effect influences the creep strain to rupture and the rupture life. Such behavior is important when a considerable amount of fibers fail, resulting from a high applied stress in the composite or a low to moderate Weibull modulus of the fibers. It is demonstrated in this paper that fiber stress relaxation is a relatively slow process in comparison with matrix stress relaxation. The fiber stress relaxation therefore leads to a significant reduction of the strength of the fibrous system in the long term, giving rise to a limited creep life for the composite even when the composite is subjected to a relatively low stress.

The remainder of the paper is organized in the following way. Section 2 describes three creep models. The first two consider the situation where there are broken fibers in the composite, but the consequential fiber stress relaxation due to creep is omitted. These models are established by extending Curtin's work(15) on fiber failure stochastics within the framework of global load sharing to include the effect of a creeping

matrix. In one model, McLean relaxation is assumed to occur uninfluenced by fiber failure. In the other, the additional compliance due to fiber failure is permitted to influence the McLean relaxation and is similar to McLean's damage model(14). The third model is much more comprehensive. It is concerned with the effects of both fiber breaks and the consequential fiber stress relaxation due to matrix creep in shear. Section 3 presents the results obtained from various models for composites with a wide range of fiber volume fractions, Young's modulus of the fibers and the matrix, ratios of the interface sliding or yield stress to the fiber strength and the Weibull modulus of the fibers. Analyses of the results and comparisons in terms of creep strain and creep rupture time among these models are also presented. The results are discussed in Section 4.

2 Creep Rupture Models

In this section, detailed derivations for the three models are described. When the models are developed, a number of assumptions are made. The major one is that the composite is in the global load sharing regime(2, 15). Stress concentrations due to broken fibers do not cause localized damage in the material. Instead, damage in the fibers develops in an uncoordinated manner. In addition, fibers are elastic and brittle and deform at a rate compatible with the surrounding creeping matrix. The interface between the fibers and the matrix is weak and will slide or yield in shear when the shear stress on the interface equals a critical value τ_o. This will occur adjacent to fiber breaks controlling load transfer between the broken fiber and the matrix.

2.1 Curtin's Model for Stochastic Fiber Failure

Curtin's (15) analysis of stochastic fiber failure with global load sharing is outlined first. Consider a representative volume for the composite subjected to a uniaxial stress σ as illustrated in Fig.1(a). The stress at a cross section of AB in accordance with the rule of mixtures is such that

$$\sigma = (1 - f)\sigma_m + f\overline{\sigma}_f \tag{4}$$

where f is the fiber volume fraction, σ_m is the uniform matrix stress and $\overline{\sigma}_f$ is the average stress in fibers at AB.

For a broken fiber, as illustrated in Fig.1(b), the shear stress is set equal to τ_0 near the end of fiber break, and by equilibrium, the stress recovery distance L_f is

$$L_f = \frac{DE_f\varepsilon}{4\tau_0} \tag{5}$$

where D is the fiber diameter, E_f is the Young's modulus of the fiber and ϵ is the axial strain in the composite. The probability that a fiber breaks within the distance L_f from AB is q. The stress in a fiber which is unbroken up to a distance L_f from AB is $E_f\epsilon$. Random position of breaks in fibers broken within a distance L_f from AB (as illustrated in Fig.1(b)) implies that the average stress at AB in such fibers is $\frac{1}{2}E_f\epsilon$. Therefore, the average stress in fibers at AB is given by

$$\overline{\sigma}_f = (1 - q)E_f\epsilon + q\frac{1}{2}E_f\epsilon \tag{6}$$

If fibers broken twice within the distance L_f from AB are negligible and the fiber length L is much larger than the stress recovery length L_f, the number of fracture

nuclei in the fibers with strength up to $E_f\varepsilon$ predicts q. Weibull statistics then gives

$$q = \frac{2L_f}{L_0}\left(\frac{E_f\varepsilon}{S_0}\right)^m \tag{7}$$

where L_0 and S_0 are length and strength parameters of the Weibull distribution and m is the Weibull modulus. Substituting L_f of eqn(5) into eqn(7) then provides the expression for the fiber failure probability

$$q = \left(\frac{E_f\varepsilon}{S_c}\right)^{m+1} \tag{8}$$

where S_c is a characteristic stress for the fibrous system such that (15, 20, 21)

$$S_c = \left(\frac{2S_0^m\tau_o L_0}{D}\right)^{\frac{1}{m+1}} \tag{9}$$

Substitution of q of eqn(8) into eqn(6) then gives the average stress in the fibers at AB

$$\overline{\sigma}_f = E_f\varepsilon\left[1 - \frac{1}{2}\left(\frac{E_f\varepsilon}{S_c}\right)^{m+1}\right] \tag{10}$$

It can be seen that the average stress in the fibers depends not only on the strain in the composite and Young's modulus of the fibers but also on the Weibull strength properties of the fibers.

The maximum value for $\overline{\sigma}_f$ occurs when

$$\varepsilon = \frac{S_c}{E_f}\left(\frac{2}{m+2}\right)^{\frac{1}{m+1}} \tag{11}$$

and is

$$S = S_c\left(\frac{2}{m+2}\right)^{\frac{1}{m+1}}\left(\frac{m+1}{m+2}\right) \tag{12}$$

It follows that S is the effective strength of the fibrous system.

2.2 Rupture Based on McLean Relaxation

Consider a unidirectionally reinforced material subject to a fixed axial stress beginning at time t=0. The solution to eqns(1)-(3) given by McLean(1) is

$$\varepsilon(t) = \frac{\sigma}{fE_f} - \frac{(1-f)}{fE_f}[(\frac{E}{E_m\sigma})^{n-1} + \frac{f(n-1)E_fE_mBt}{E}]^{-\frac{1}{n-1}} \tag{13}$$

where E is the rule of mixtures modulus

$$E = fE_f + (1-f)E_m \tag{14}$$

The stress in a fiber is the strain multiplied by E_f. Two rupture models can be postulated. In one model, rupture is considered to occur when the strain in the fibers equals the value from eqn(11), which is the strain at maximum load for the Curtin fiber strength model. Creep of the matrix is considered to accelerate rapidly thereafter, leading to rupture after negligible additional time. This is termed the strain based McLean rupture model and gives

$$BE_fS_c^{n-1}t_r = \frac{E}{f(n-1)E_m}\{[\frac{\sigma}{(1-f)S_c} - \frac{f}{1-f}(\frac{2}{m+2})^{\frac{1}{m+1}}]^{1-n} - (\frac{E_m\sigma}{ES_c})^{1-n}\} \tag{15}$$

where t_r is the time to rupture. The second McLean based model assumes that rupture occurs when the stress in the fibers reaches the effective strength S from the Curtin model. This gives

$$BE_fS_c^{n-1}t_r = \frac{E}{f(n-1)E_m}\{[\frac{\sigma}{(1-f)S_c} - \frac{f}{1-f}(\frac{2}{m+2})^{\frac{1}{m+1}}(\frac{m+1}{m+2})]^{1-n} - (\frac{E_m\sigma}{ES_c})^{1-n}\} \tag{16}$$

which is termed the stress based McLean rupture model. It predicts shorter rupture times than the strain based model.

2.3 Curtin Rupture Model

The creep response of the global load sharing composite can be predicted with eqn(10) used as the effective stress-strain relationship for the fibers. The matrix response is given by eqn.(2) and the fibers and matrix are coupled together through eqn(4). By substitution of the average fiber stress $\overline{\sigma}_f$ of eqn(10) into eqn(4) and rearrangement, an expression for the matrix stress is obtained as

$$\frac{\sigma_m}{S_c} = \frac{1}{1-f}\{\frac{\sigma}{S_c} - f(\frac{E_f\varepsilon}{S_c})[1 - \frac{1}{2}(\frac{E_f\varepsilon}{S_c})^{m+1}]\} \tag{17}$$

Differentiation of eqn(17) with respect to time then gives the matrix stress rate for constant stress σ

$$\frac{\dot{\sigma}_m}{S_c} = -\frac{f}{1-f}(\frac{E_f}{S_c})[1 - (1+\frac{m}{2})(\frac{E_f\varepsilon}{S_c})^{m+1}]\dot{\varepsilon} \tag{18}$$

Consequently, combination of eqns(17) and (18) with eqn(2) provides the evolution law for the creep strain

$$\frac{1 + \frac{f}{1-f}\frac{E_f}{E_m}[1 - (1+\frac{m}{2})(\frac{E_f\varepsilon}{S_c})^{m+1}]}{\{\frac{\sigma}{S_c} - f(\frac{E_f\varepsilon}{S_c})[1 - \frac{1}{2}(\frac{E_f\varepsilon}{S_c})^{m+1}]\}^n}\frac{E_f\dot{\varepsilon}}{S_c} = \frac{BS_c^{n-1}E_f}{(1-f)^n} \tag{19}$$

Integration of eqn(19) hence gives the strain as a function of time. However, this cannot be achieved analytically and a numerical scheme is required to perform the task. When eqn(19) is solved, it proves convenient to present the equation in terms of normalized parameters. If the stress, strain, time and the Young's modulus of the fibers and the matrix in eqn(19) are non-dimenisionalized such that $\hat{\sigma} = \sigma/S_c$, $\hat{\varepsilon} = E_f\varepsilon/S_c$, $\hat{t} = tBE_fS_c^{n-1}$ and $\hat{E} = E_f/E_m$, eqn(19) then reduces to

$$\frac{1 + \frac{f}{1-f}\hat{E}[1 - (1+\frac{m}{2})\hat{\varepsilon}^{m+1}]}{[\hat{\sigma} - f\hat{\varepsilon}(1 - \frac{\hat{\varepsilon}^{m+1}}{2})]^n}\frac{d\hat{\varepsilon}}{dt} = \frac{1}{(1-f)^n} \tag{20}$$

This can be rearranged to give

$$\hat{t} = (1-f)^n \int_{\hat{\varepsilon}_0}^{\hat{\varepsilon}} \frac{1 + \frac{f}{1-f}\hat{E}[1-(1+\frac{m}{2})\hat{\varepsilon}^{m+1}]}{[\hat{\sigma} - f\hat{\varepsilon}(1-\frac{\hat{\varepsilon}^{m+1}}{2})]^n} d\hat{\varepsilon} \qquad (21)$$

where $\hat{\varepsilon}_0$ is the initial strain which can be obtained from eqn(10) by use of $\sigma_m = E_m\varepsilon$ and $\hat{\varepsilon} = E_f\varepsilon/S_c$ in eqn(4). Integration of the above expression with the trapezoidal rule provides a value of $\hat{t}$. A tertiary creep behavior is often predicted, terminated by divergence of the strain. This is caused by widespread fiber failure and is considered to be creep rupture.

2.4 Fiber Relaxation Model

When this model is developed, two steps are taken. First, a cell model which is concerned with the stress relaxation in a single broken fiber surrounded by intact neighbors is described. From the analysis of the cell model, the governing partial differential equation for the evolution of the fiber stress is derived. Then, in order to account for the fibers broken randomly during creep, an approximate binary model averaging the effect of initially broken, progressively broken and intact fibers is developed. The analysis of the binary model allows the creep strain of the composite to be evaluated.

2.4.1 Governing Equations for Stress Relaxation in a Broken Fiber

Consider a cell model as illustrated in Fig.2. It consists of a long broken elastic fiber of length L and diameter D embedded in a creeping matrix. A uniaxial tensile stress σ is applied parallel to the axis of this cell. Within the unit cell it is assumed that

there is only one pre-existing fiber break and the break occurs in the middle of the fiber, i.e. at $z = \frac{L}{2}$. The neighboring fibers are intact.

The displacement on the lateral surface of the unit cell is $u_c(z,t)$ such that $u_c(z,t) = \varepsilon(t)z$, where $\varepsilon(t)$ is the strain of the composite. The displacement in the lower segment of the broken fiber is $u_f(z,t)$ and the shear strain in the matrix γ_m is then given by

$$\gamma_m = \frac{u_c(z,t) - u_f(z,t)}{w} \tag{22}$$

where w is

$$w = \frac{D}{2}(f^{-\frac{1}{2}} - 1) \tag{23}$$

to represent a material with volume fraction of fibers f.

The shear strain rate in the matrix can be expressed by

$$\dot{\gamma}_m = \frac{\dot{\tau}}{G_m} + 3B{\sigma_e}^{n-1}\tau \tag{24}$$

where G_m is the shear modulus of the matrix, τ is the shear stress in the matrix and σ_e is the effective stress such that

$$\sigma_e = \sqrt{\frac{3}{2}S_{ij}S_{ij}} \tag{25}$$

where S_{ij} is the deviatoric stress. For the problem analyzed, the effective stress is found to be

$$\sigma_e = \sqrt{\sigma_m^2 + 3\tau^2} \tag{26}$$

where σ_m is the longitudinal matrix stress. The longitudinal matrix stress is assumed to be independent of the z and r whereas the matrix shear stress τ is taken to be dependent on z but independent of r. The longitudinal matrix stress σ_m is computed

from the composite response as if the fiber in the unit cell were intact and therefore is controlled by eqn(2).

Additional equations are provided by equilibrium and the elastic behavior of the lower segment of the broken fiber. These are

$$\frac{\partial \sigma_f^b}{\partial z} = -\frac{4\tau}{D} \tag{27}$$

and

$$\sigma_f^b = E_f \frac{\partial u_f(z,t)}{\partial z} \tag{28}$$

where σ_f^b is the stress in the broken fiber. Except where $\tau = 0$, eqn(27) implies that there will be a gradient of stress in the fiber. The load shed from the fiber cannot be taken up by the matrix since σ_m is assumed to be uniform. Thus, the stress is transmitted by shear to other fibers. Combination of eqn(27) with eqn(28) then gives an expression for the shear stress in terms of fiber displacement

$$\tau = -\frac{1}{4} D E_f \frac{\partial^2 u_f(z,t)}{\partial z^2} \tag{29}$$

The value of τ is limited by the interfacial sliding stress τ_0, i.e. $|\tau| \leq \tau_0$.

By substitution of γ_m from eqn(22) and τ of eqn.(29) into eqn(24), a governing partial differential equation for the evolution of the displacement in the broken fiber is derived

$$\frac{1}{w}\left[\frac{\partial u_c(z,t)}{\partial t} - \frac{\partial u_f(z,t)}{\partial t}\right] = -\frac{D E_f}{4 G_m} \frac{\partial^3 u_f(z,t)}{\partial z^2 \partial t} - \frac{3}{4} B D \sigma_e{}^{n-1} E_f \frac{\partial^2 u_f(z,t)}{\partial z^2} \tag{30}$$

where σ_e is given by eqn.(26). The boundary conditions are

$$\frac{\partial u_f(L/2,t)}{\partial z} = 0 \tag{31}$$

to represent the free end of the broken fiber and $u_f(0,t) = 0$ as noted in Fig.2. Initial conditions represent the stress in the elastic state for a broken fiber. Thus

$$u_f(z,0) = \epsilon(0)z \qquad 0 \leq z \leq \frac{L}{2} - L_f \tag{32}$$

where L_f is computed from eqn(5) with $\epsilon = \epsilon(0)$. The remaining portion of the fiber has

$$u_f(z,0) = \frac{L^2\epsilon(0)}{2L_f}[\frac{z}{L} - \frac{z^2}{L^2} - (\frac{1}{2} - \frac{L_f}{L})^2] \qquad \frac{L}{2} - L_f \leq z \leq \frac{L}{2} \tag{33}$$

to ensure compatibility and agreement with stress recovery from the load free end.

The partial differential equation (30), along with initial and boundary conditions, is solved numerically with a finite difference scheme. Details are given in the appendix. Results for the stress in the fiber are shown in Fig.3 when the unit cell shown in Fig.2 is subjected to a constant overall strain $\epsilon = 0.5S_c/E_f$. Therefore, these results represent the stress in a broken fiber in a relaxation test when there are not too many broken fibers. An important point is that in a relaxation test of a fresh composite, fibers would break on initial loading and not thereafter. The longitudinal stress σ_f^b in the broken fiber is presented in Fig.3 as a function of a distance along the fiber at various times for a composite with a fiber volume fraction of 0.35, a ratio of the fiber to matrix Young's moduli of 3, a ratio of the interfacial shear stress to the characteristic fiber stress τ_o/S_c of 0.01 and a creep exponent for the matrix of 3. The stress recovery segment can be seen in Fig.3 in the vicinity of the break. The stress recovery length, L_f, which is defined as the distance measured from the fiber break along the fiber direction to a point at which the tensile stress just attains the level of the remote fiber stress, increases as time increases. Within the stress recovery length, the stress decays

with the increasing time, showing that the fiber is relaxing as the matrix creeps in shear. Examination of Fig.3 reveals that stress relaxation of this type takes a long time. This behavior is in contrast to that associated with the matrix stress which relaxes in a short time. For example, it is found from eqns.(1)-(3) that the matrix stress reduces by 50% at $tBE_fS_c^2 = 160$ and by 90% at $tBE_fS_c^2 = 5.3 \times 10^3$.

Another interesting feature of the results presented in Fig.3 is that although it decreases with increasing time, the gradient within the stress recovery length at any given instant is found to be weakly dependent on position. Since the stress gradient is proportional to the shear stress in the matrix, an approximation can be made that at a given instant, the shear stress evaluated at any position along the fiber within the stress recovery length is identical. As a result, this uniform reduction of the stress gradient in the recovery zone can be used to characterize the degree of fiber stress relaxation.

Similarly, beyond the stress recovery segment, the stress in the fiber is almost uniform and almost constant at its original value. This indicates that the solution is insensitive to the fiber length, a situation which will prevail until the stress recovery segment reaches the specimen end which is at z=0.

2.4.2 Model for Randomly breaking fibers

In a creep test at constant applied stress, fibers will break randomly as the strain increases. At any stage, the fibers can be divided among those that are intact and those which are broken. The survival probability of the fiber in accordance with a

two parameter Weibull distribution is given by

$$P_s(\varepsilon) = exp[-\frac{L}{L_0}(\frac{E_f\varepsilon}{S_0})^m] \tag{34}$$

Let $\overline{\sigma}_f^b$ be the average stress in the broken fibers. The overall average fiber stress is then given by

$$\overline{\sigma}_f = P_s(\varepsilon)E_f\varepsilon + [1 - P_s(\varepsilon)]\overline{\sigma}_f^b \tag{35}$$

Composite response can now be predicted from integration of eqn(2) subject to eqns(4) and (35).

As an example, consider the case with no matrix creep, In this situation, the average stress in a broken fiber segment of length L/2 with only one break is given by

$$\overline{\sigma}_f^b = \frac{2}{L}\int_0^{\frac{L}{2}} \sigma_f^b(z)dz \tag{36}$$

The stress $\sigma_f^b(z)$ is equal to $E_f\varepsilon$ over most of the fiber length and falls linearly to zero in the stress recovery segment of length L_f (given by eqn(5)) near the break. Thus, the average stress in the broken fibers is

$$\overline{\sigma}_f^b = (1 - \frac{L_f}{L})E_f\varepsilon \tag{37}$$

leading to

$$\overline{\sigma}_f = \{1 - [1 - P_s(\varepsilon)]\frac{L_f}{L}\}E_f\varepsilon \tag{38}$$

When the absolute value of the argument for the exponential in eqn(34) is small compared to unity, eqn(38) then gives

$$\overline{\sigma}_f = [1 - \frac{L_f}{L_o}(\frac{E_f\varepsilon}{S_o})^m]E_f\varepsilon \tag{39}$$

which is identical with eqn(6) combined with eqn(7). Thus, under the same assumption, the present model is identical to that of Curtin for the average stress in the fibers as fiber breakage takes place.

In a similar fashion, the model can be applied directly to a relaxation test with a creeping matrix. For example, Fig.3 gives the stress in a broken fiber during a test at constant strain and eqn(36) can be used as before to obtain the average stress in the broken fiber. As discussed above, an approximate representation of the stress in the fiber is a uniform value $E_f\varepsilon$ joined to a linear fall off within the distance L_f from the break, where L_f is a function of time. (This approximation must be abandoned before L_f grows to L/2.) Under similar assumptions as used in deriving them, eqn(37) through (39) can be used once more to give the average stress in all fibers with L_f taken to be a function of time. The stress relaxation so implied for the fibers can be combined in volume fraction weighted terms with the stress relaxation in the matrix to give the overall stress for the composite material. In a relaxation test with the strain ϵ imposed rapidly at t=0, the matrix stress is

$$\sigma_m = [(E_m\varepsilon)^{1-n} + (n-1)BE_m t]^{-\frac{1}{n-1}} \tag{40}$$

In a creep test at constant applied stress, a problem arises that fibers will break randomly as the strain in the composite increases. A model for this would include identification of the fibers newly broken at each stage and a calculation of the stress in them thereafter according to eqn(30). However, this would involve the numerical solution of the p.d.e. for dozens if not hundreds of fibers. Given the approximations involved in the derivation of eqn(30) in the first place, such an approach is probably out of place. Instead, progressively breaking fibers can be allowed for in a rudimentary

fashion for each increment of strain by averaging the stress in fibers newly broken during the increment of strain with the current stress in the existing broken fibers. The current stress in the broken fibers is computed by incrementing the solution of eqn(30). The fraction of fibers which break during an increment of time is given by differencing eqn(34) to provide

$$\Delta P_s(\varepsilon) = -\frac{mLE_f}{L_0 S_0}\left(\frac{E_f\varepsilon}{S_0}\right)^{m-1} exp[-\frac{L}{L_0}\left(\frac{E_f\varepsilon}{S_0}\right)^{m}]\frac{d\varepsilon}{dt}\Delta t \tag{41}$$

and $-\Delta P_s(\varepsilon)$ is the fraction newly broken. It follows that the fraction broken at the end of the increment is $1 - P_s(\varepsilon) - \Delta P_s(\varepsilon)$ where ε is the strain at the beginning of the increment. The stress in the newly broken fibers is $(\varepsilon + \Delta\varepsilon)E_f$ except near the break where it decays linearly to zero at the break over the distance $L_f(\varepsilon + \Delta\varepsilon)$. The results for the averaged stresses are

$$\begin{aligned}\sigma^b_{f(new)}(z) = Min[\frac{4\tau_0(0.5L - z)}{D}; \sigma^b_f(z)]\frac{1 - P_s(\varepsilon)}{1 - P_s(\varepsilon) - \Delta P_s(\varepsilon)} \\ + Min[\frac{4\tau_0(0.5L - z)}{D}; E_f(\varepsilon + \Delta\varepsilon)]\frac{-\Delta P_s(\varepsilon)}{1 - P_s(\varepsilon) - \Delta P_s(\varepsilon)}\end{aligned} \tag{42}$$

where σ^b_f is the stress in the existing broken fibers at the end of the increment as computed from eqn(30). Note that the first term on the right hand side of eqn.(42) represents the contribution from the existing broken fibers and the second term is due to the addi'ional fibers broken during the increment. The Min function is required to ensure that the new value for τ does not exceed τ_o. Finally, the variable u_f needed in eqn(30) is found from numerical integration of eqn(28) with $\sigma^b_{f(new)}$ used on the left hand side. The resulting values of u_f are then used as the starting point for a new

time incrementation of eqn(30). At all stages eqn(2) is used to compute the increment of strain for the composite and eqns(4), (35) and (36) used to couple the solution to eqn(30) for the broken fibers with the longitudinal creep of the matrix.

When a composite with f=0.35, $E_f/E_m = 3$, $\tau_o/S_c = 0.01$, m=5 and n=3 is subjected to a constant uniaxial tensile stress such that $\sigma = 0.2S_c$, the stress in a broken fiber normalized by the fiber stress far away from the break, is presented in Fig.4 as a function of a distance along the fiber at various times. It is found that the extent of stress relaxation in the broken fiber is more significant in comparison with that obtained with a constant displacement loading. This seems to be a result of the increase of fiber failure due to the increase of the strain which replenishes the stress level driving the creeping matrix shear.

As with the broken fiber stress calculated during a relaxation test, the stress relaxation significantly affects only the stress recovery segment of the fiber near the break. The stress in the portion of the fiber away from the break is almost uniform and is at the stress level in the intact fibers. This result indicates that the length of the fiber does not influence the relaxation of the fiber stress to any significant extent. As a result, lumping all broken fibers together and doing a single calculation for stress relaxation can be partially justified. Only those fibers which break very near the end of the specimen are wrongly represented since the stress recovery segment will quickly reach the specimen end from those breaks. However, it is obvious that lumping of all the fibers into one broken fiber stress relaxation calculation cannot be fully justified.

Results obtained for the stress in a broken fiber with different values of fiber volume fraction, f, modulus ratio E_f/E_m, creep exponent n and ratio of interfacial

sliding stress to characteristic fiber stress τ_o/S_c show similar trends to those shown in Fig.4 except that a low fiber volume fraction f, a high modulus ratio E_f/E_m, a low creep exponent n and a high ratio of interfacial sliding stress to characteristic fiber stress τ_o/S_c all cause the broken fiber stress to relax faster.

3 Creep Strain and Creep Rupture

The results for the creep strains at constant applied stress $\sigma/S_c = 0.2$ predicted by the various models are illustrated in Fig.5 as a function of time for materials with a matrix creep exponent n=3, a ratio of the fiber to the matrix Young's modulus $E_f/E_m = 3$, a Weibull modulus of the fiber m=5, fiber volume fractions f=0.5 and 0.25 and ratios of the interfacial sliding stress to the characteristic stress of the fibers $\tau_o/S_c = 0.005$ and 0.01. When the fiber volume fraction is high, e.g. f=0.5, all models predict an identical result in terms of the creep strain. This occurs because at this stress, the fibers allow only a low strain in the composite. As a result, the strain is so low that fiber failure in the composite is negligible.

For the composite with a relatively low fiber volume fraction, e.g. f=0.25, the effect of the fibers on the overall deformation of the composite is less stringent. At this stress, the composite experiences a higher strain. As a result, more fiber failure and the consequential fiber stress relaxation occurs during creep, giving rise to an even higher strain in the composite. This is clear in Fig.5 where there are obvious differences for the results predicted by different models when f=0.25. The results predicted using the fiber relaxation model and the Curtin model are higher than

those predicted by McLean's model. Note that with the Curtin model the results for $\tau_o/S_c = 0.005$ and 0.01 are exactly identical. The Curtin model accounts for the additional creep permitted when fibers break and their end regions unload. The fiber relaxation model accounts for the additional creep which occurs when broken fibers gradually unload completely.

The composite eventually fails if the fiber relaxation or the Curtin model are used. Failure occurs when the creep strain increments diverge numerically. This behavior is clearly illustrated in Fig.5 where failure of the composite is marked by the arrows. The failure point marked for the McLean model is where the stress in the fibers reaches S as given in eqn(12). The fiber relaxation model gives shorter creep rupture times than the Curtin model due to the reduction of the effective fiber strength associated with the fiber stress relaxation. In addition, a longer creep rupture time is observed for a composite with $\tau_o/S_c = 0.005$ than for that with $\tau_o/S_c = 0.01$. This is attributed to the fact that the matrix shear stress in a composite with a higher value of τ_o can be higher which drives matrix shearing creep and fiber stress relaxation faster.

Although the predictions for the strain differ in detail among the various models when the fiber volume fraction is low, examination of the results reveals that the differences of the strain predicted by each model are relatively small at any given time until near the end of life. For example, at $tBE_fS_c^2 = 1600$, just before the creep rupture occurs, the strains predicted by the fiber relaxation model for the composite with $\tau_o/S_c = 0.01$ and with the Curtin model are only 13% and 7% higher respectively than the strain predicted using McLean's model. These results indicate that McLean's model, which is the simplest one, is reasonably appropriate to predict the creep strain

even when the composite experiences fiber fractures. However, McLean's model does not directly predict creep rupture of the composite.

For the case with a composite having an intermediate value of the fiber volume fraction, e.g. f=0.35, and subjected to the same level of stress, i.e. $\sigma/S_c = 0.2$, the strains obtained from different models are plotted in Fig.6 as a function of time for different values of fiber Weibull modulus, m. It can be seen that for the composite with a fiber Weibull modulus m=5, the differences among various models remain small indicating that fiber failure is negligible. However, for the case with a smaller Weibull modulus, e.g. m=2, fibers are more likely to break and as a result, differences in the strain are observed among all the models. The fiber relaxation model predicts a failure of the composite with $\tau_0/S_c = 0.01$ but when $\tau_0/S_c = 0.005$, rupture does not occur within the time plotted. The strains predicted by the fiber relaxation model for the composite with a ratio $\tau_0/S_c = 0.005$ are nearly identical with those predicted with the Curtin model. These values at $tBE_fS_c^2 = 4 \times 10^4$ are about 11% higher than predicted by McLean's model, which is, of course, unaffected by the Weibull modulus.

At a relatively high level of stress such that $\sigma/S_c = 0.25$, all the models predict similar results for the composite with a fiber Weibull modulus m=10, as shown in Fig.7. However, for the case with m=5, both the fiber relaxation model and the Curtin model predict higher strains than McLean's model at any given time. These higher strains prompt failure of the composite for m=5 within the time plotted in Fig.7. The failure point marked for m=10 is when the stress in the fibers for the McLean calculation equals S as given by eqn(12).

At an even higher level of stress such that $\sigma/S_c = 0.3$, even the composite with fiber Weibull modulus m=10 experiences creep rupture within the time plotted in Fig.9 and is predicted by both the fiber relaxation model and the Curtin model. The failure point marked for McLean's model is when the fiber stress equals S as given by eqn(12). All these results suggest that at the same level of applied stress and mean fiber strength, the lower the fiber Weibull modulus, the higher is the creep strain and the more likely is the composite to exhibit creep rupture.

The effect of the ratio of the fiber to the matrix Young's modulus on the creep strain and the creep rupture time is illustrated in Fig.9(a) and 9(b) for the composite with a fiber volume fraction of 0.35. Not surprisingly, the composite with a low ratio E_f/E_m would experience a higher strain due to the more compliant fibers, leading to the earlier creep rupture predicted by the fiber relaxation model.

Fig.10 shows the applied stress as functions of creep rupture times predicted by different models for the material with n=3, m=5, $E_f/E_m = 3$, $\tau_o/S_c = 0.01$ and f=0.35. Fig.11 is similar but for f=0.25. Strain based rupture for McLean's model occurs when the composite strain equals the level predicted in eqn(11). Stress based rupture for McLean's model occurs when the fiber stress equals S given by eqn(12). In general, it can be seen from Fig.10 that at a given level of stress, the creep rupture time predicted using the Curtin model is higher than that predicted by the fiber relaxation model. The former however, is lower than that predicted by the strain based rupture criterion with McLean's model. Stress based rupture with McLean's model occurs intermediate to the prediction of the fiber relaxation model and the Curtin model. Examination of Fig.10 also reveals that the results predicted by both

the Curtin model and the McLean model exhibit a creep rupture threshold below which a non-creeping state is reached. These threshold stresses are predicted by eqn(12) for the Curtin model and by eqn(11) (as $E_f\varepsilon$) for the strain based rupture criterion with McLean's model. For the case shown in Fig.10, the thresholds for the two models are $\sigma/S_c = 0.244$ and 0.284 respectively. In contrast, the results predicted using the fiber relaxation model have a creep rupture threshold at the fiber bundle strength for dry fibers. This is so because fiber relaxation will eventually unload all the broken fibers. Thus only the intact fibers support load after a sufficiently long time has passed. This is identical to what happens in a bundle of fibers without matrix or friction between them. If the applied stress is above the bundle strength for the dry fibers, creep of the matrix must continue and eventually will accelerate rather than slow down. It is this acceleration of the creep which causes tertiary behavior and eventual rupture. The stress strain curve for a dry bundle of fibers obeying the two parameter Weibull distribution is given by $E_f\varepsilon$ multiplied by $P_s(\varepsilon)$ given by eqn(34). As a result, the dry fiber bundle strength is

$$S_b = S_o(\frac{L_o}{mL})^{\frac{1}{m}} exp(-\frac{1}{m}) \tag{43}$$

This, therefore, represents the creep rupture threshold for long fiber composites. If the applied stress is below this, the composite will eventually reach a non-creeping state. It is notable that this threshold is dependent on L, where L is the length of the specimen or component. For the case illustrated in Fig.10, the threshold is such that $S_b/S_c = 0.151$.

It is useful to consider the differences in the results predicted by various models in more detail. It is found that at a high level of stress, e.g. $\sigma/S_c = 0.3$, the fiber stress

relaxation model and the Curtin model predict creep rupture times which are 20 times and 9 times lower respectively than that predicted by the strain based criterion for McLean's model. Compared to each other, these values differ only by a factor of 2. This occurs because at such a high stress, the failure of fibers happen so fast that the stress in the broken fibers has not had time to relax.

At a relatively low stress, e.g. $\sigma/S_c = 0.25$, the impact of the fiber stress relaxation becomes more significant. This is clearly illustrated in Fig.10, where the fiber relaxation model predicts a creep rupture time which is 13 times lower than that predicted using the Curtin model. At an even lower applied stress, e.g. $\sigma/S_c = 0.21$, the influence of the fiber stress relaxation on the creep rupture time is even more pronounced. This stress is below the threshold for the Curtin model and so an infinite creep life is predicted by both the Curtin model and the strain and stress based criteria for McLean's model. This is in contrast to a finite creep rupture time predicted by the fiber relaxation model.

4 Discussions

In this paper, McLean's model for creep deformation of metal matrix composites reinforced by continuous fibers has been extended to include the effects of fiber failure and the consequential fiber stress relaxation. Two models have been developed. The first one considers fiber breaks but ignores the effect of the following fiber stress relaxation. The evolution law for the creep strain is established by extending Curtin's work(15) on fiber failure stochastics within the framework of global load sharing to

include the effect of a creeping matrix. Relatively simple numerical calculations are required to solve the governing equation (21) derived from this model. The second model is more comprehensive with emphasis on the aspect of fiber stress relaxation in the broken fibers due to matrix/fiber shear stress interaction. It involves solving a partial differential equation derived from a cell model for the fiber stress relaxation to determine the fiber stresses, Then a non-linear equation obtained from the analysis of the composite as a whole is solved to evaluate the strain numerically for each iteration. This model requires significant numerical calculations and computer time.

From the set of problems analyzed, the major features associated with the fiber stress relaxation have been identified. These have been compared with phenomena associated with the matrix stress relaxation as discussed by McLean(1). It is found that the fiber stress relaxation tends to influence the creep strain and the rupture behavior more significantly at long times than at shorter times. This is in contrast to the impact of the matrix stress relaxation which is known to increase the composite strain quickly due to creep, perhaps ultimately leading to a non-creeping state. The results presented in this paper show that even when there are fiber breaks in the composite, the models, including McLean's model, all provide a reasonable prediction for the creep strain. This suggest that McLean's model, which is the simplest one, can be used to make an approximate prediction for the creep strain. However, when examining the creep rupture times predicted by different models(e.g. as in Figs.10-11), we find that the creep life is very sensitive to the extent of fiber stress relaxation in the broken fibers. The other models, which ignore such effects, severely overestimate the creep rupture times especially when the composite is subjected to a low level of

stress. This suggests that the development of a comprehensive model including fiber stress relaxation is essential for predicting the creep life at low stress.

In this paper, certain material parameters have been varied to assess the sensitivity of the predicted creep strain and the creep rupture time to the variation of the individual parameter. It is found that a low fiber volume fraction f, a low modulus ratio E_f/E_m, a high interfacial sliding stress, a low characteristic fiber stress and a low Weibull modulus of the fiber all make the composite creep faster, perhaps giving rise to quicker rupture of the composite. Although all material parameters influence the creep strain and the creep rupture time, most interest centers on the interfacial sliding stress since this quantity can be tailored for a given composite in which the fiber and matrix properties and the fiber volume fraction are set. From the results presented, it appears that a low value of the interfacial sliding stress is desirable to minimize the strain and provide a longer creep life.

Finally, There has been some success in comparing the models presented in the current paper with experimental data for creep and rupture. This will be reported in separate publications.

5 Acknowledgments

The work was sponsored by the Advanced Research Projects Agency through the University Research Initiative at the University of California, Santa Barbara (ONR Contract N-0014-92-J-1808)

6 References

1. M. McLean, (1985) Creep deformation of metal matrix composite, Composite Science and Technology, **23**, 37

2. M.Y. He, A.G. Evans and W. A. Curtin, (1993) The ultimate tensile strength of metal and ceramic-matrix composites, Acta. Metall. Mater. **41**, 871

3. S. Jansson, H.E. Deve and A.G. Evans, (1991) The anisotropic mechanical properties of a Ti matrix composite reinforced with SiC fibers, Metal Tran. **22a**, 2975

4. S. R. Gunawardena, S. Jansson and F.A. Leckie, (1993), Modeling of anisotropic behavior of weakly bonded fiber reinforced MMCs, Acta. Metall. Mater. **41**, 3147

5. G. Bao and R.M. McMeeking, (1994) Fatigue crack growth in fiber-reinforced metal-matrix composites, Acta. Metall. Mater. (to appear)

6. Z-Z. Du and R.M. McMeeking, (1994) Control of strength anisotropy of metal matrix fiber composites (to be published)

7. T.L. Dragone and W.D. Nix (1990), Geometric factors affecting the internal stress distribution and high temperature creep rate of discontinuous fiber reinforced metals, Acta. Metall. Mater. **38**, 1941

8. G. Bao, J.W. Hutchinson and R. M. McMeeking (1991), Particle reinforcement of ductile matrices against plastic flow and creep, Acta Metall.

Mater. **39**, 1871

9. A. Kelly and K.N. Street (1972), Creep of discontinuous fiber composite II, Theory for the steady-state, Proc. R. Soc. London, **A328**, 283

10. S. Goto and M. McLean (1991), Role of interfaces in creep of fiber- reinforced metal matrix composite II short fibers, Acta Metall. Mater. **39**, 165

11. R. M. McMeeking (1993), Power law creep of a composite material containing discontinuous rigid aligned fibers Int, J. Solids and Structures, **30**, 1807

12. C. Weber et al. (1994), to be published.

13. N. Ohno, K. Toyoda, N. Okamoto, T. Miyake and S. Nishide (1993), Creep behavior of a unidirectional SCS-6/Ti-15-3 metal matrix composite at 450^0C, Trans. ASME (Series H, J. Engr. Mater. Tech.)

14. M. McLean, (1989), Creep of metal matrix composites, in Materials and Engineering Design: The Next Decade (Eds. B.F. Dyson and D.R. Hayhust), Institute of Metals, London, 287

15. W.A. Curtin, (1991), Theory of mechanical properties of ceramic matrix composites, J. Am. Ceramic Sol. **74**, 2837

16. D.C. Lagoudas, C.-Y. Hui and S. L. Phoenix, (1989), Time evolution of overstress profiles near broken fibers in a composite with a viscoelastic matrix, Int. J. Solids Structures, **25**, 45

17. D.D. Mason, C.-Y. Hui and S. L. Phoenix, (1992), Stress profiles around a fiber break in a composite with a nonlinear power law creeping matrix, Int. J. Solids and Structures, **29**, 2829

18. E. Barbero and K.W. Kelly (1992), Predicting longitudinal creep of a continuous fiber metal matrix composite, to be published.

19. Y. Song, G. Bao and C.-Y. Hui, (1994), On creep of unidirectional fiber composites with fiber damage, to be published.

20. M. Sutcu (1989), Weibull statistics applied to fiber failure in ceramic composites and work of fracture, Acta Metall. **37**, 651

21. M. D. Thouless and A.G. Evans (1988) Effects of pullout on the mechanical properties of ceramic matrix composites, Acta Metall. **36**, 517

Appendix: Finite difference scheme

In this appendix the finite difference scheme that was employed to solve eqn(30) of the main text is described. Attention is centered on the situation where the unit cell is subjected to a constant displacement loading. Similar procedure can be applied to the case with a constant uniaxial stress. If the stress, strain, displacement, length, time and the Young's modulus of the fiber and the matrix in eqn(30) are non-dimenisionalized, respectively, in the following manners such that $\hat{\sigma} = \sigma/S_c$, $\hat{\epsilon} = E_f\epsilon/S_c$, $\hat{t} = tBE_fS_c^{n-1}$, $\hat{E} = E_f/E_m$, $\hat{u}(\hat{z},\hat{t}) = u(z,t)E_f/LS_c$, $\hat{\tau} = \tau/S_c$, $\hat{\sigma}_e = \sigma_e/S_c$, $\hat{\sigma}_f^b = \sigma_f^b/S_c$, $\hat{D} = D/L$, $\hat{L}_f = L_f/L$ and $\hat{z} = z/L$, eqn.(30) becomes

$$\frac{\partial\hat{u}_f(\hat{z},\hat{t})}{\partial\hat{t}} = \frac{1+\nu}{4}\hat{D}^2\hat{E}(f^{-1/2}-1)\frac{\partial^3\hat{u}_f(\hat{z},\hat{t})}{\partial\hat{z}^2\partial\hat{t}} + \frac{3}{8}\hat{D}^2\hat{\sigma}_e^{n-1}(f^{-1/2}-1)\frac{\partial^2\hat{u}_f(\hat{z},\hat{t})}{\partial\hat{z}^2} \tag{A1}$$

Let

$$\hat{u}_f(\hat{z},\hat{t}+\Delta\hat{t}) = \hat{u}_f(\hat{z},\hat{t}) + \Delta\hat{t}\frac{\partial\hat{u}_f(\hat{z},\hat{t})}{\partial\hat{t}} \tag{A2}$$

eqn(A1) can then be written as

$$\hat{u}_f(\hat{z},\hat{t}+\Delta\hat{t}) - \hat{u}_f(\hat{z},\hat{t}) = \alpha[\frac{\partial^2\hat{u}_f(\hat{z},\hat{t}+\Delta\hat{t})}{\partial\hat{z}^2} - \frac{\partial^2\hat{u}_f(\hat{z},\hat{t})}{\partial\hat{z}^2}] + \beta\Delta\hat{t}\hat{\sigma}_e^{n-1}\frac{\partial^2\hat{u}_f(\hat{z},\hat{t})}{\partial\hat{z}^2} \tag{A3}$$

where α and β are given by

$$\alpha = \frac{1+\nu}{4}\hat{D}^2\hat{E}(f^{-\frac{1}{2}}-1) \tag{A4}$$

$$\beta = \frac{3}{8}\hat{D}^2(f^{-\frac{1}{2}}-1) \tag{A5}$$

At $\hat{t} = 0^+$ when the fiber just breaks, by noting that $\frac{\partial^2 \hat{u}_f(\hat{z},0)}{\partial \hat{z}^2} = 0$ and $\hat{u}_f(\hat{z},0) = \hat{\varepsilon}_0 \hat{z}$, eqn(A3) reduces to

$$\alpha \frac{\partial^2 \hat{u}_f(\hat{z},0^+)}{\partial \hat{z}^2} - \hat{u}_f(\hat{z},0^+) = -\hat{\varepsilon}_0 \hat{z} \tag{A6}$$

An approximate solution is given by

$$\hat{u}_f(\hat{z},0^+) = \hat{z}\hat{\varepsilon}_0 \qquad 0 \le \hat{z} \le 0.5 - \hat{L}_f \tag{A7}$$

$$\hat{u}_f(\hat{z},0^+) = \frac{\hat{\varepsilon}_0}{2\hat{L}_f}[\hat{z} - \hat{z}^2 - (0.5 - \hat{L}_f)^2] \qquad 0.5 - \hat{L}_f \le \hat{z} \le 0.5 \tag{A8}$$

The corresponding tensile and shear stresses can also be obtained by

$$\hat{\sigma}_f^b(\hat{z},0^+) = Min[\frac{4\hat{\tau}_0(\frac{1}{2} - \hat{z})}{\hat{D}}, \frac{\partial \hat{u}_f(\hat{z},0^+)}{\partial \hat{z}}] \tag{A9}$$

and

$$\hat{\tau}(\hat{z},0^+) = Min[\hat{\tau}_0, -\frac{\hat{D}}{4}\frac{\partial^2 \hat{u}_f(\hat{z},0^+)}{\partial \hat{z}^2}] \tag{A10}$$

Consequently, the initial values for the problem are obtained.

Let

$$\frac{\partial \hat{u}_f(\hat{z},\hat{t})}{\partial \hat{z}} = \frac{\hat{u}_f(\hat{z}+\Delta\hat{z},\hat{t}) - \hat{u}_f(\hat{z},\hat{t})}{\Delta \hat{z}} \tag{A11}$$

and

$$\frac{\partial^2 \hat{u}_f(\hat{z},\hat{t})}{\partial \hat{z}^2} = \frac{\hat{u}_f(\hat{z}+\Delta\hat{z},\hat{t}) - 2\hat{u}_f(\hat{z},\hat{t}) + \hat{u}_f(\hat{z}+\Delta\hat{z},\hat{t})}{\Delta \hat{z}^2} \tag{A12}$$

eqn(A3) becomes

$$\begin{aligned}(\alpha + \beta\hat{\sigma}_e\Delta\hat{t})\hat{u}_f(\hat{z}-\Delta\hat{z},\hat{t}+\Delta\hat{t}) - (\Delta\hat{z}^2 + 2\alpha + 2\beta\hat{\sigma}_e\Delta\hat{t})\hat{u}_f(\hat{z},\hat{t}+\Delta\hat{t}) \\ +(\alpha + \beta\hat{\sigma}_e\Delta\hat{t})\hat{u}_f(\hat{z}+\Delta\hat{z},\hat{t}+\Delta\hat{t}) = -\Delta\hat{z}^2\hat{u}_f(\hat{z},\hat{t}) \\ +\alpha[\hat{u}_f(\hat{z}-\Delta\hat{z},\hat{t}) - 2\hat{u}_f(\hat{z},\hat{t}) + \hat{u}_f(\hat{z}+\Delta\hat{z},\hat{t})]\end{aligned} \tag{A13}$$

The above equation can also be written in the following general form

$$(\alpha + \beta\hat{\sigma}_e\Delta\hat{t})\hat{u}_f(i-1,j+1) - (\Delta\hat{z}^2 + 2\alpha + 2\beta\hat{\sigma}_e\Delta\hat{t})\hat{u}_f(i,j+1)$$
$$+(\alpha + \beta\hat{\sigma}_e\Delta\hat{t})\hat{u}_f(i+1,j+1) = \alpha[\hat{u}_f(i-1,j) - 2\hat{u}_f(i,j) + \hat{u}_f(i+1,j)]$$
$$-\Delta\hat{z}^2\hat{u}_f(i,j) \quad \text{(A14)}$$

where i and j indicate the distance and the time increments respectively. It can be seen that the problem on solving a partial differential equation effectively becomes one for finding the roots for a series of linear equations with a tridiagonal matrix. When j=0, i.e. $\hat{t} = 0^+$ the quantities in the right hand side of the above equation are known. The unknown quantities in the left hand side of the equation can be solved combined with boundary conditions such that $\hat{u}_f(k+1/2,j+1) - \hat{u}(k/2,j+1) = 0$ and $\hat{u}_f(0,j+1) = 0$, where k is the total number of divisions made for the fiber. Using the results obtained as initial values for the next time increment and repeating the above analysis then give new values of the displacement. It is noted that $\hat{\sigma}_e$ is calculated from the values at the start of the increments for each step.

List of Figures

loading such that $\frac{\sigma}{S_c} = 0.2$.

Fig.6 The creep strains predicted by different models as a function of time for materials with a fiber volume fraction f=0.35, a ratio of fiber to matrix Young's modulus $\frac{E_f}{E_m} = 3$, a creep exponent of the matrix n=3, two different Weibull moduli of the fibers m and two different ratios of interfacial sliding stress to characteristic fiber stress $\frac{\tau_o}{S_c}$ when the composite is subjected to a constant uniaxial loading such that $\frac{\sigma}{S_c} = 0.2$.

Fig.7 The creep strains predicted by different models as a function of time for materials with a fiber volume fraction f=0.35, a ratio of fiber to matrix Young's modulus $\frac{E_f}{E_m} = 3$, a creep exponent of the matrix n=3, two different Weibull moduli of the fiber m and two different ratios of interfacial sliding stress to characteristic fiber stress $\frac{\tau_o}{S_c}$ when the composite is subjected to a constant uniaxial loading such that $\frac{\sigma}{S_c} = 0.25$.

Fig.8 The creep strains predicted by different models as a function of time for materials with a fiber volume fraction f=0.35, a ratio of fiber to matrix Young's modulus $\frac{E_f}{E_m} = 3$, a creep exponent of the matrix n=3, two different Weibull moduli of the fiber m and two different ratios of interfacial sliding stress to characteristic fiber stress $\frac{\tau_o}{S_c}$ when the composite is subjected to a constant uniaxial loading such that $\frac{\sigma}{S_c} = 0.3$.

Fig.9 The creep strains predicted by different models as a function of time for materials with a fiber volume fraction f=0.35, a creep exponent of the matrix n=3, a Weibull modulus of the fiber m=5, two different ratios of interfacial sliding

stress to characteristic fiber stress $\frac{\tau_o}{S_c}$ and two different ratios of fiber to matrix Young's modulus: (a) $\frac{E_f}{E_m} = 1$ and (b) $\frac{E_f}{E_m} = 5$ when the composite is subjected to a constant uniaxial loading such that $\frac{\sigma}{S_c} = 0.2$

Fig.10 The applied stress as a function of creep rupture time predicted by different models for a material with a ratio of fiber to matrix Young's modulus $\frac{E_f}{E_m} = 3$, a creep exponent of the matrix n=3, a Weibull modulus of the fiber m=5, a ratio of interfacial sliding stress to the characteristic fiber stress $\frac{\tau_o}{S_c} = 0.01$ and a fiber volume fraction f=0.35

Fig.11 The applied stress as a function of creep rupture time predicted by different models for a material with a ratio of fiber to matrix Young's modulus $\frac{E_f}{E_m} = 3$, a creep exponent of the matrix n=3, a Weibull modulus of the fiber m=5, a ratio of interfacial sliding stress to the characteristic fiber stress $\frac{\tau_o}{S_c} = 0.01$ and a fiber volume fraction f=0.25

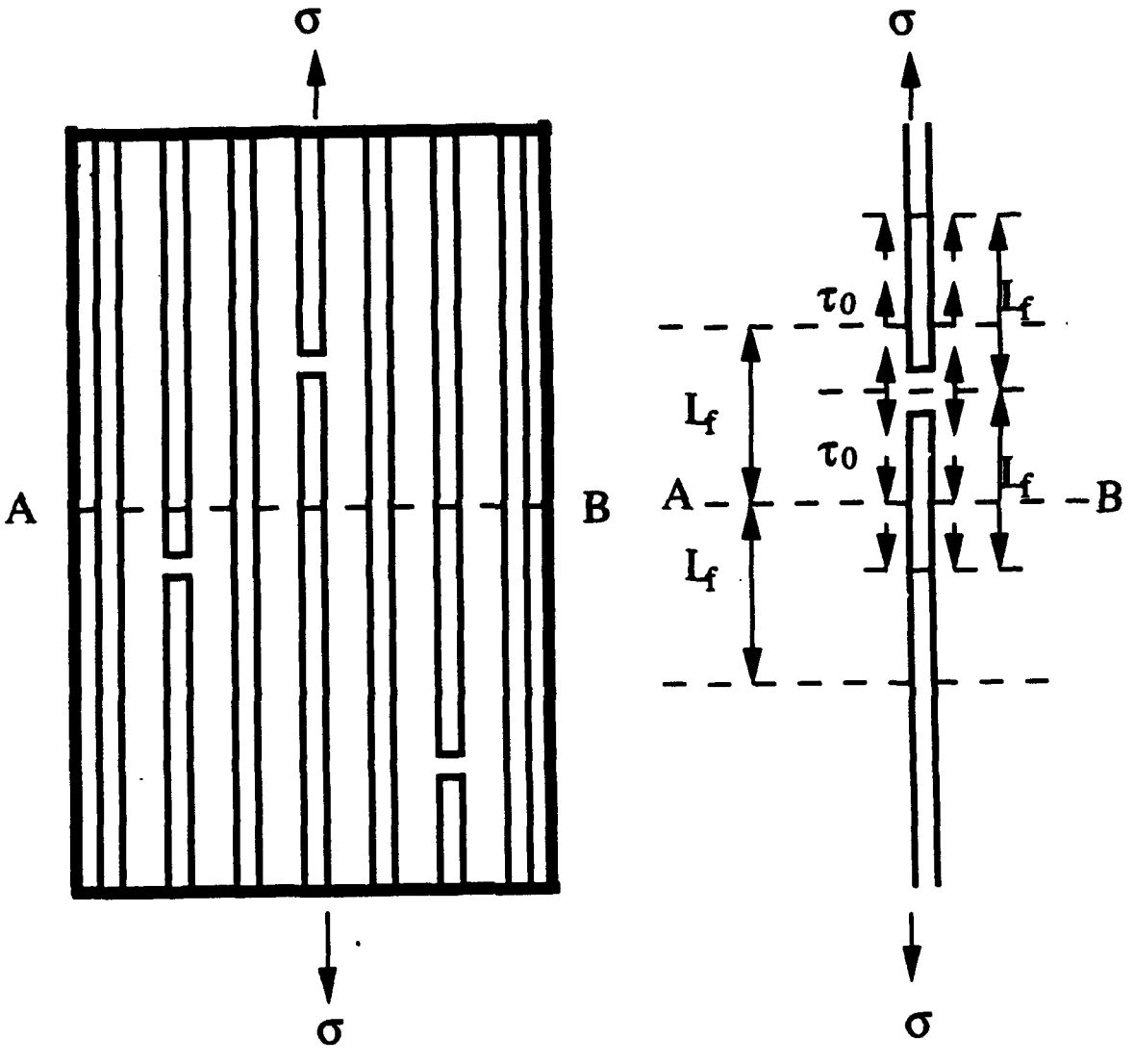

Fig.1

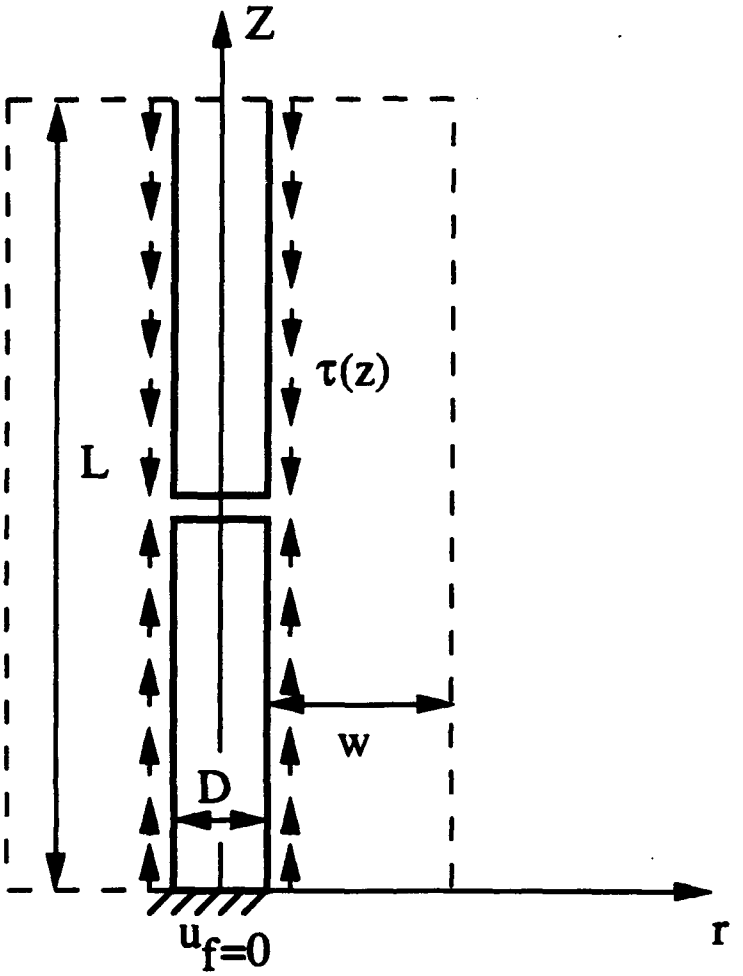

Fig.2

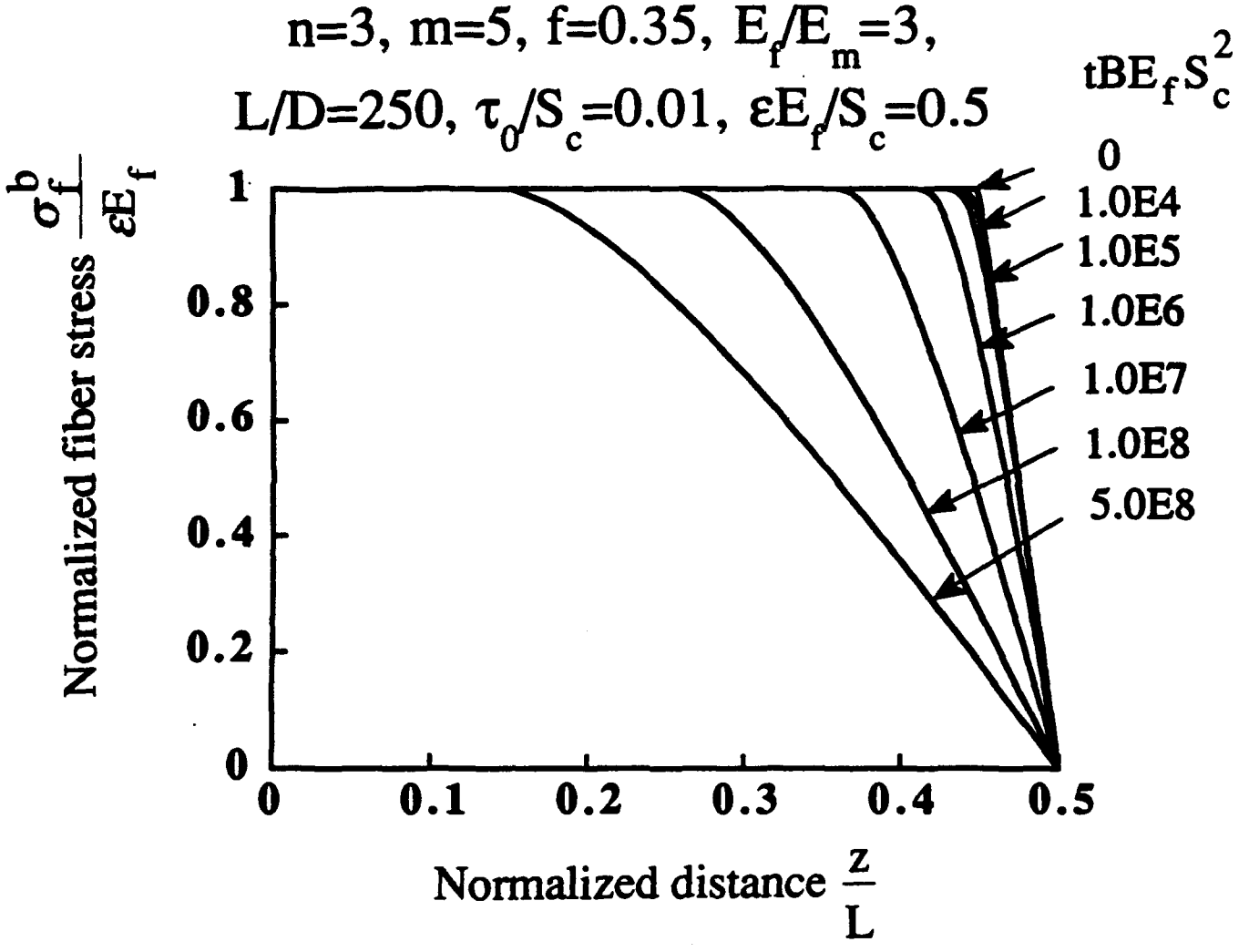
n=3, m=5, f=0.35, E_f/E_m=3,
L/D=250, τ_0/S_c=0.01, $\varepsilon E_f/S_c$=0.5
$tBE_fS_c^2$
0
1.0E4
1.0E5
1.0E6
1.0E7
1.0E8
5.0E8
Normalized fiber stress $\frac{\sigma_f^b}{\varepsilon E_f}$
1
0.8
0.6
0.4
0.2
0
0
0.1
0.2
0.3
0.4
0.5
Normalized distance $\frac{z}{L}$

Fig.3

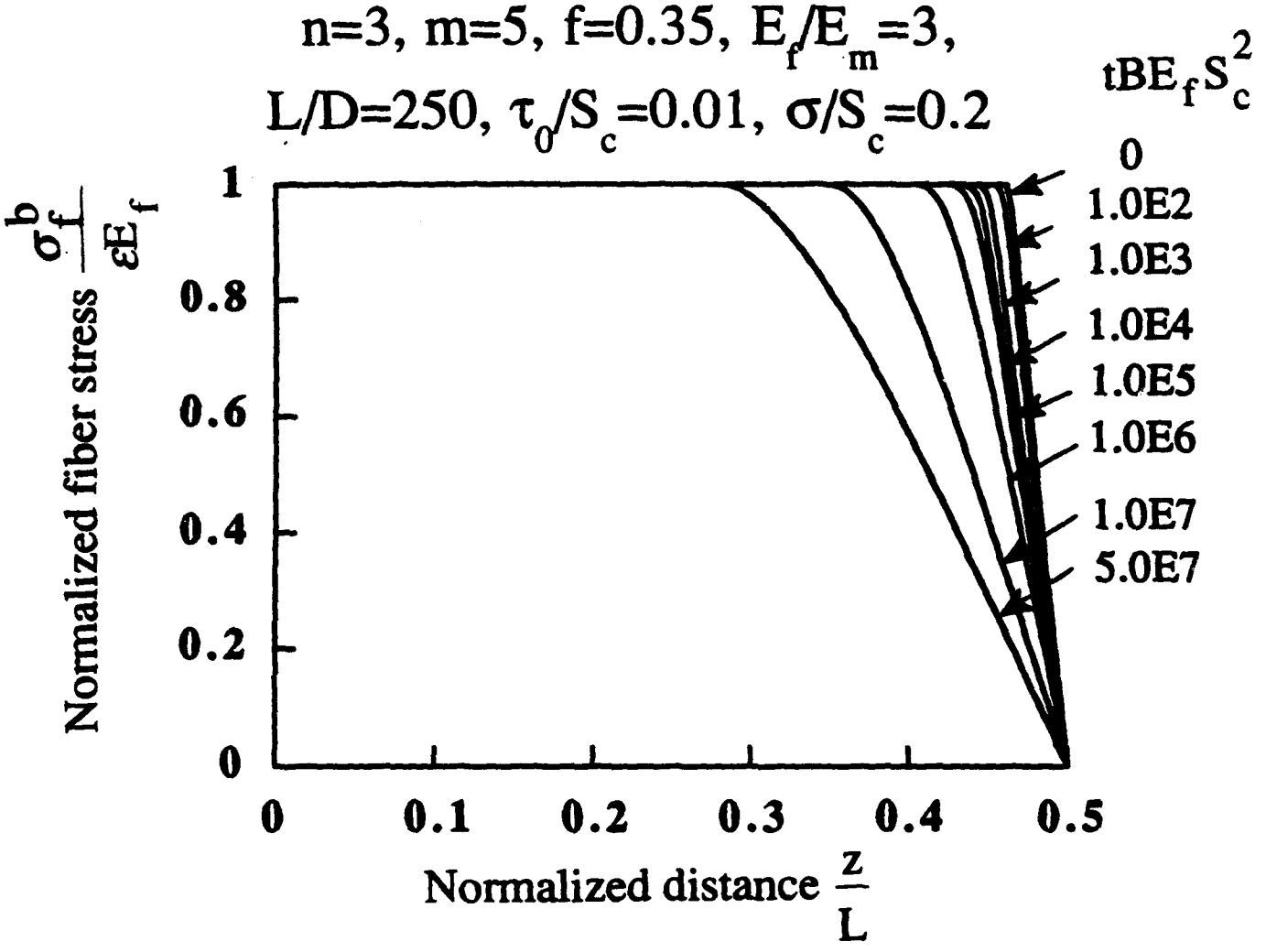
n=3, m=5, f=0.35, E_f/E_m=3,
L/D=250, τ_0/S_c=0.01, σ/S_c=0.2
tBE_fS_c^2
0
1.0E2
1.0E3
1.0E4
1.0E5
1.0E6
1.0E7
5.0E7
Normalized fiber stress σ_f^b/εE_f
1
0.8
0.6
0.4
0.2
0
0
0.1
0.2
0.3
0.4
0.5
Normalized distance z/L

Fig.4

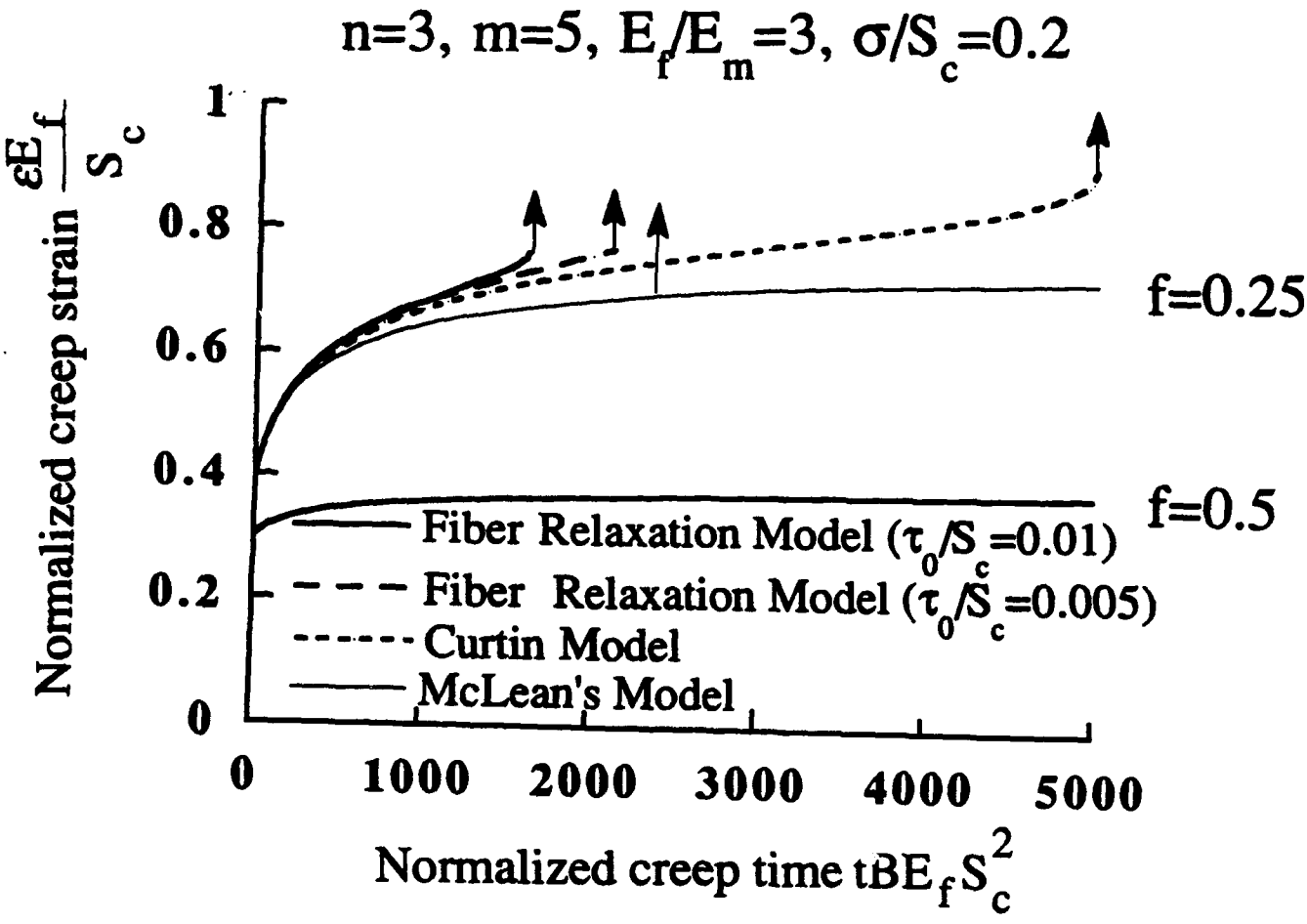
n=3, m=5, E_f/E_m=3, σ/S_c=0.2
Normalized creep strain $\frac{\varepsilon E_f}{S_c}$
1
0.8
0.6
0.4
0.2
0
f=0.25
f=0.5
Fiber Relaxation Model (τ_0/S_c=0.01)
Fiber Relaxation Model (τ_0/S_c=0.005)
Curtin Model
McLean's Model
0
1000
2000
3000
4000
5000
Normalized creep time $tBE_fS_c^2$

Fig.5

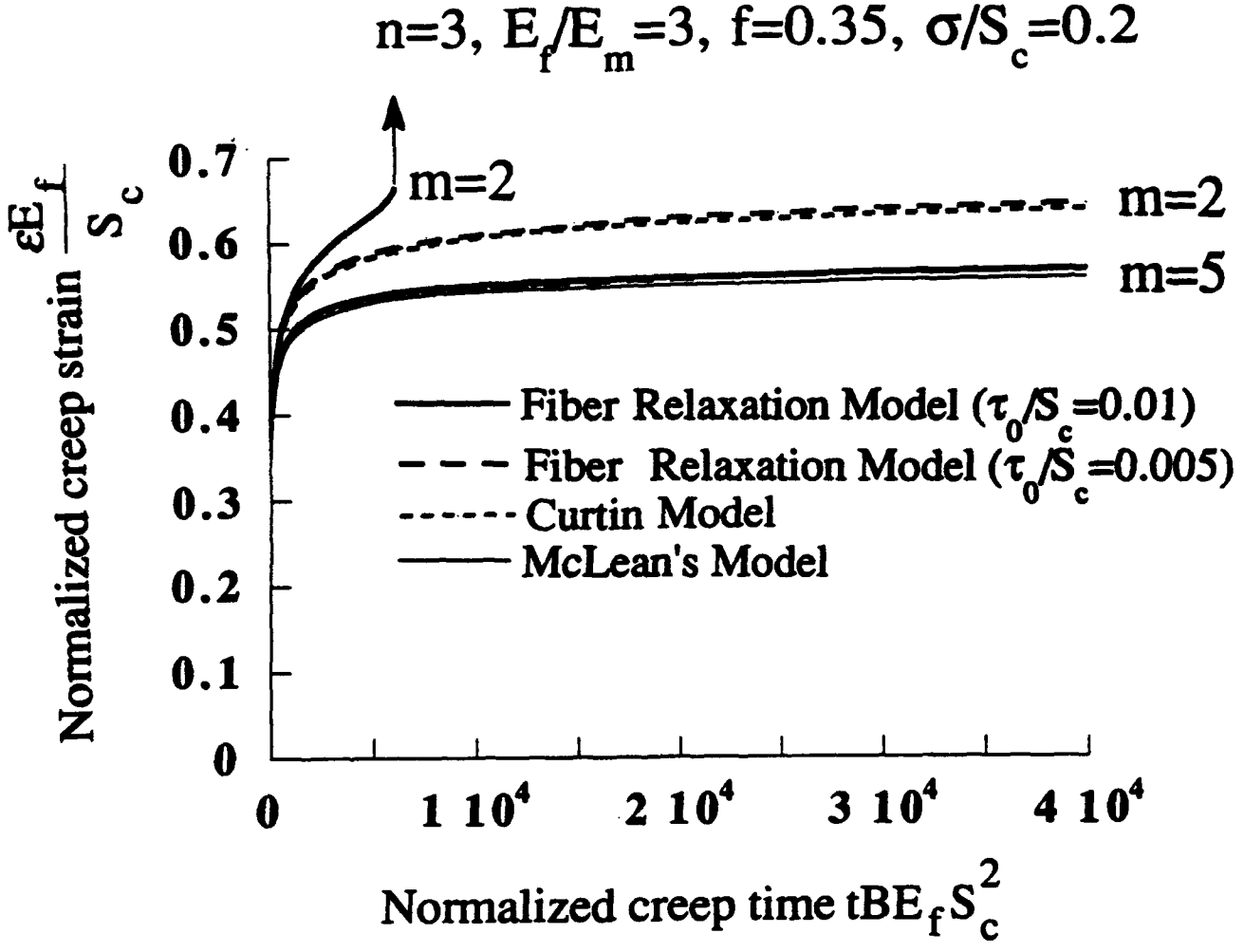
n=3, E_f/E_m=3, f=0.35, σ/S_c=0.2
m=2
m=2
m=5
Fiber Relaxation Model (τ_0/S_c=0.01)
Fiber Relaxation Model (τ_0/S_c=0.005)
Curtin Model
McLean's Model
Normalized creep strain $\frac{\varepsilon E_f}{S_c}$
0.7
0.6
0.5
0.4
0.3
0.2
0.1
0
0
1 10^4
2 10^4
3 10^4
4 10^4
Normalized creep time $tBE_fS_c^2$

Fig.6

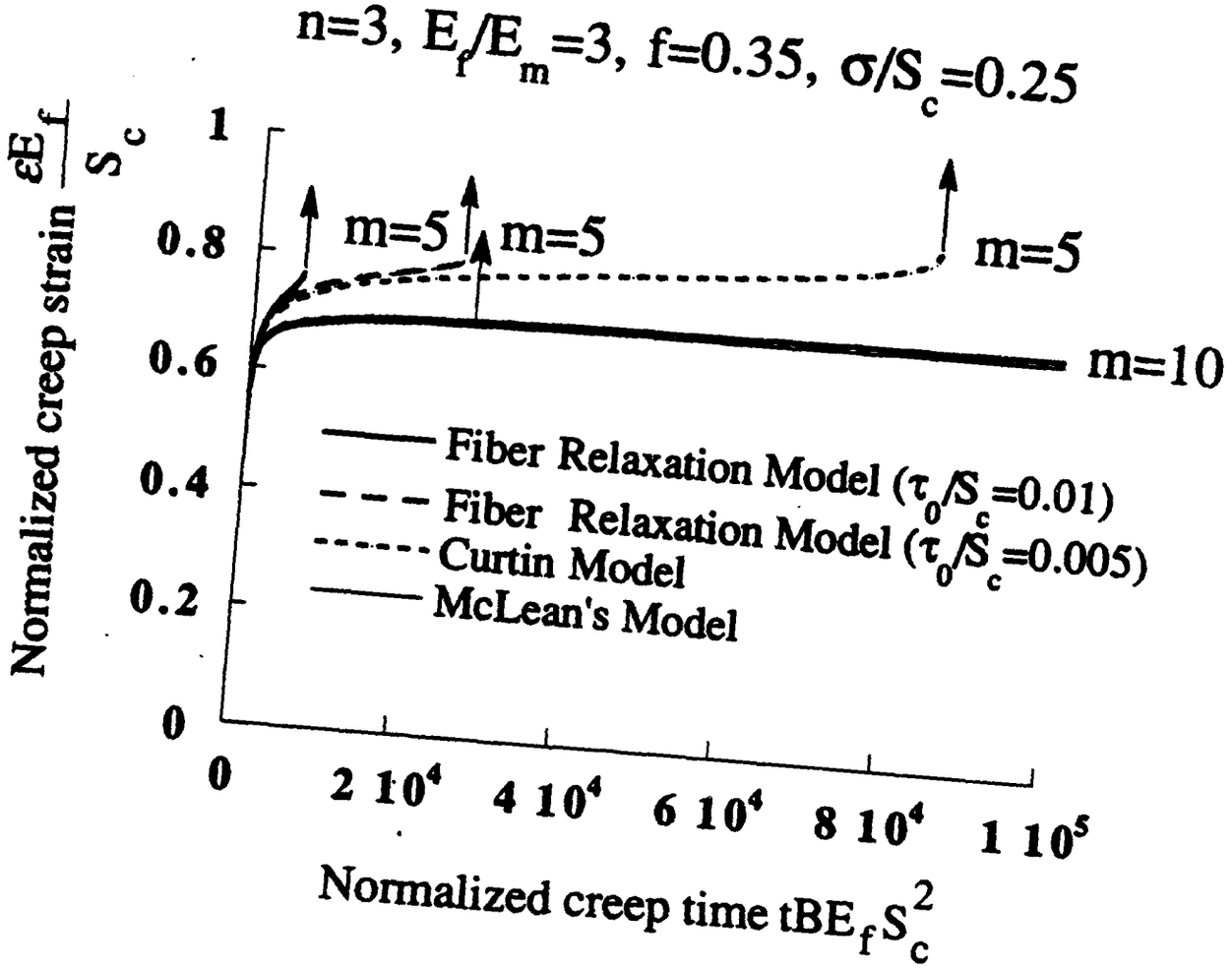
n=3, E_f/E_m=3, f=0.35, σ/S_c=0.25
Normalized creep strain $\frac{\varepsilon E_f}{S_c}$
1
0.8
0.6
0.4
0.2
0
m=5
m=5
m=5
m=10
Fiber Relaxation Model (τ_0/S_c=0.01)
Fiber Relaxation Model (τ_0/S_c=0.005)
Curtin Model
McLean's Model
0
2 10⁴
4 10⁴
6 10⁴
8 10⁴
1 10⁵
Normalized creep time $tBE_fS_c^2$

Fig.7

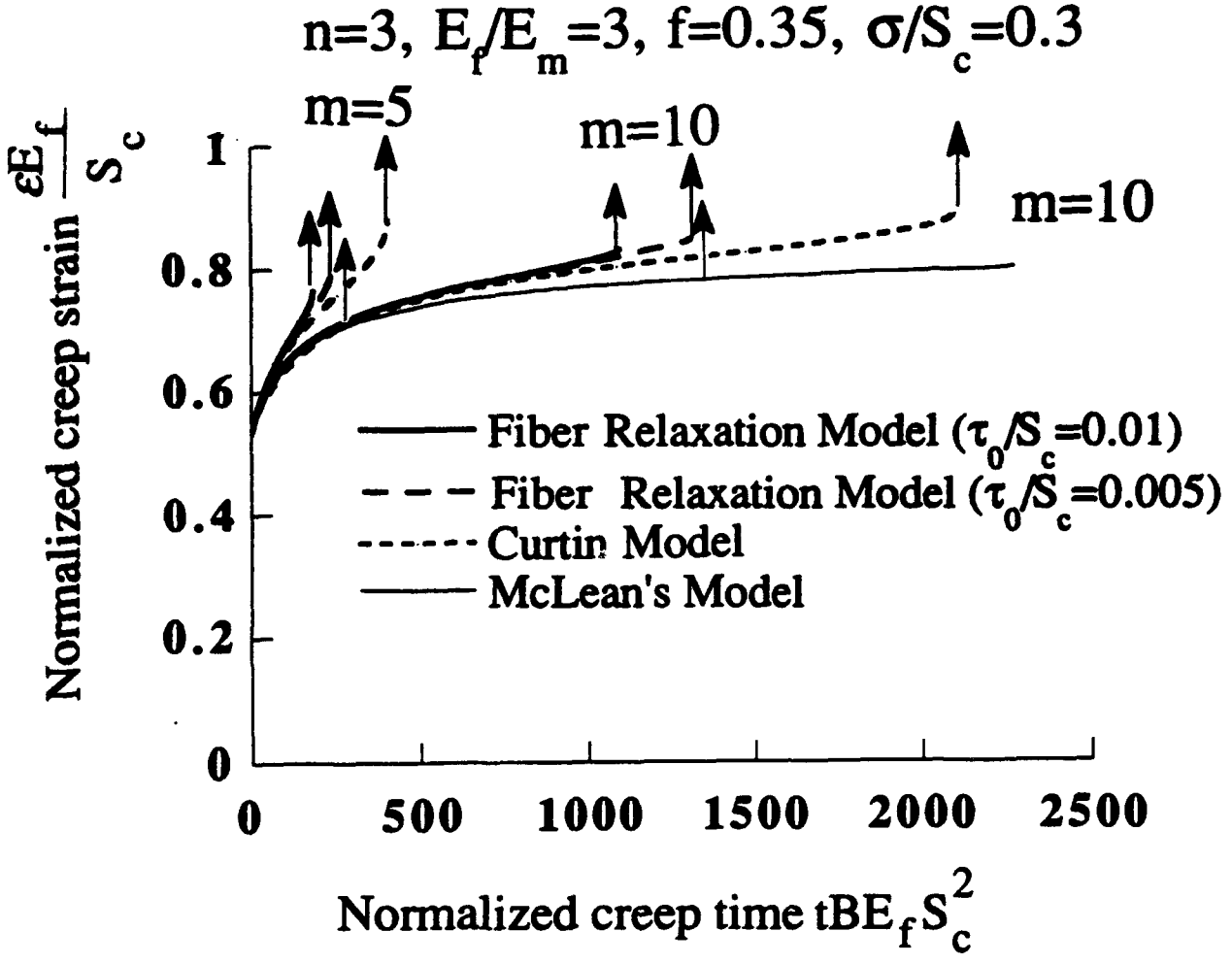
n=3, E_f/E_m=3, f=0.35, σ/S_c=0.3
m=5
m=10
m=10
Normalized creep strain $\frac{\varepsilon E_f}{S_c}$
1
0.8
0.6
0.4
0.2
0
0
500
1000
1500
2000
2500
Fiber Relaxation Model (τ_0/S_c=0.01)
Fiber Relaxation Model (τ_0/S_c=0.005)
Curtin Model
McLean's Model
Normalized creep time $tBE_fS_c^2$

Fig.8

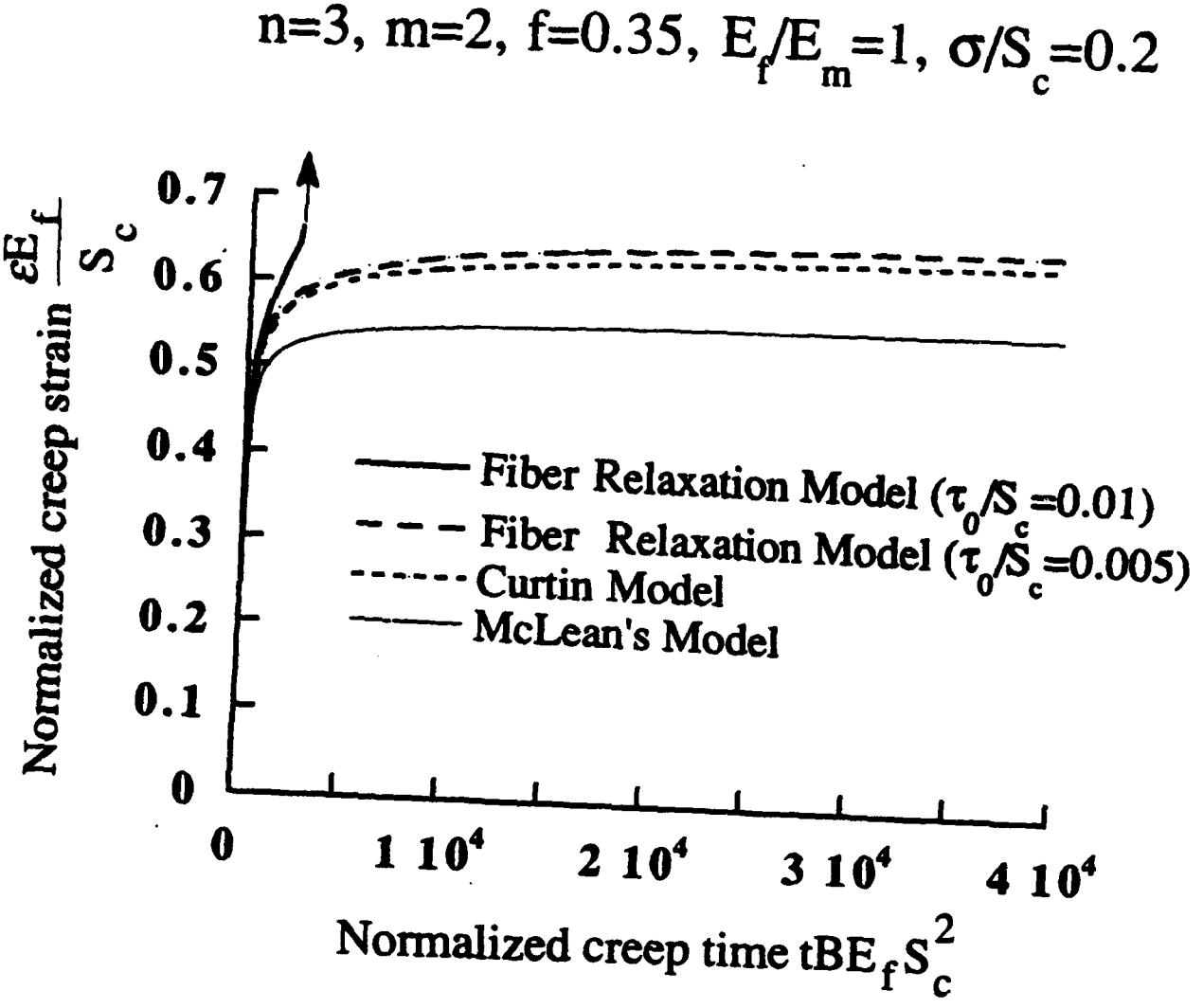
n=3, m=2, f=0.35, E_f/E_m=1, σ/S_c=0.2
Normalized creep strain $\frac{\varepsilon E_f}{S_c}$
0.7
0.6
0.5
0.4
0.3
0.2
0.1
0
0
1 10^4
2 10^4
3 10^4
4 10^4
Normalized creep time $tBE_fS_c^2$
Fiber Relaxation Model (τ_0/S_c=0.01)
Fiber Relaxation Model (τ_0/S_c=0.005)
Curtin Model
McLean's Model

Fig.9(a)

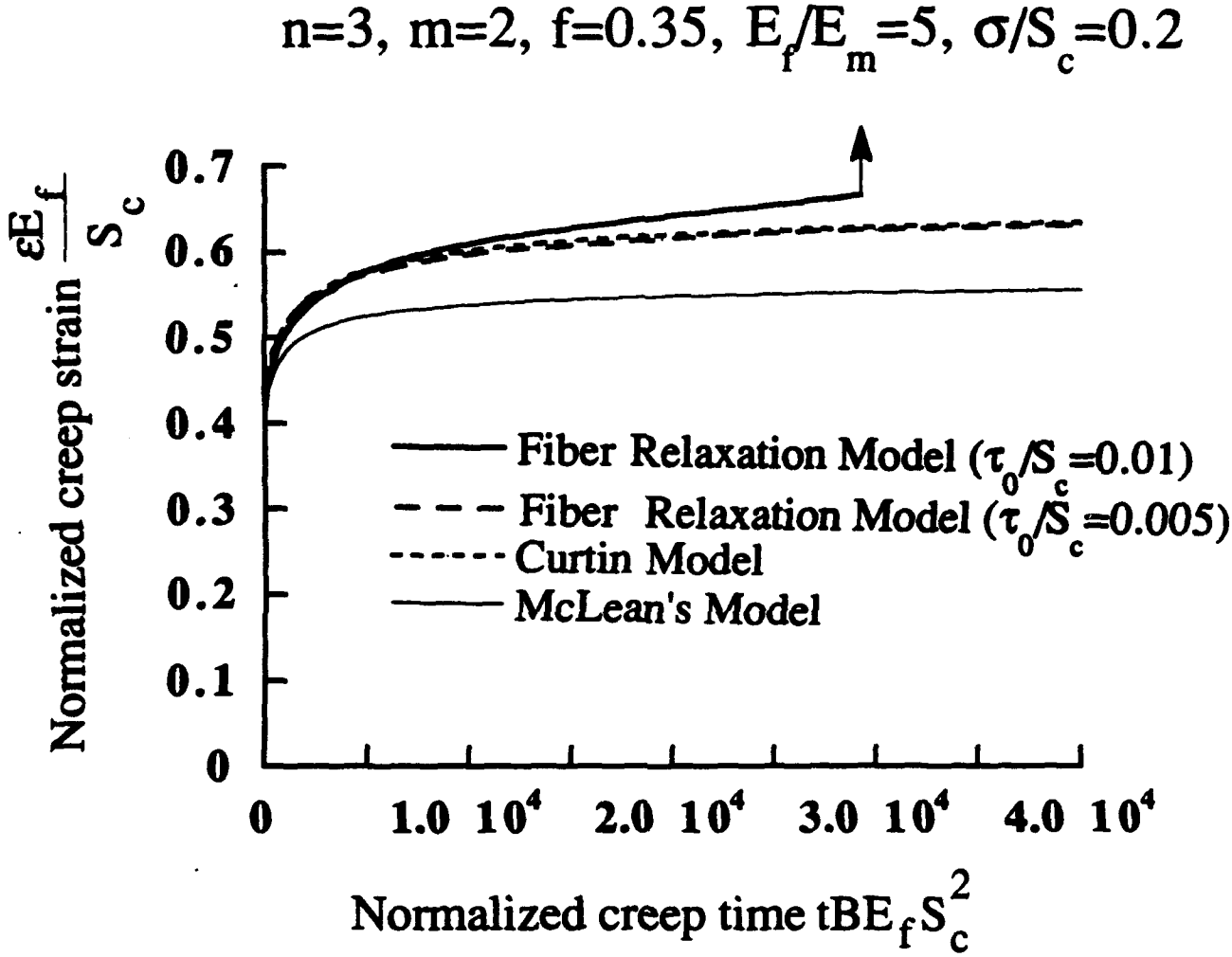
n=3, m=2, f=0.35, E_f/E_m=5, σ/S_c=0.2
Normalized creep strain $\frac{\varepsilon E_f}{S_c}$
0.7
0.6
0.5
0.4
0.3
0.2
0.1
0
Fiber Relaxation Model (τ_0/S_c=0.01)
Fiber Relaxation Model (τ_0/S_c=0.005)
Curtin Model
McLean's Model
0
1.0 10^4
2.0 10^4
3.0 10^4
4.0 10^4
Normalized creep time $tBE_fS_c^2$

Fig.9(b)

$n=3,\ m=5,\ E_f/E_m=3,\ f=0.35,\ L/D=250$

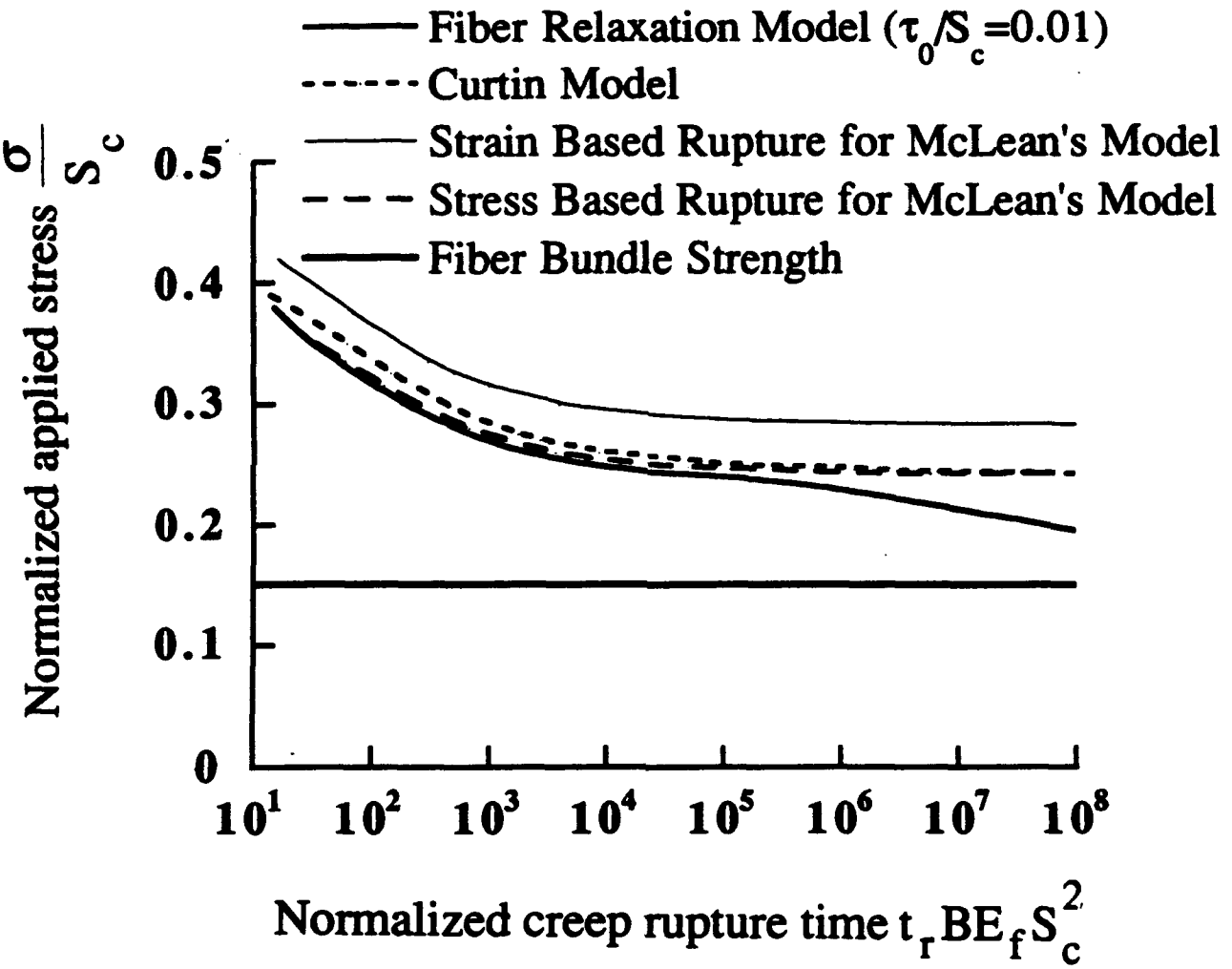

Fig.10

n=3, m=5, E_f/E_m=3, f=0.25, L/D=250

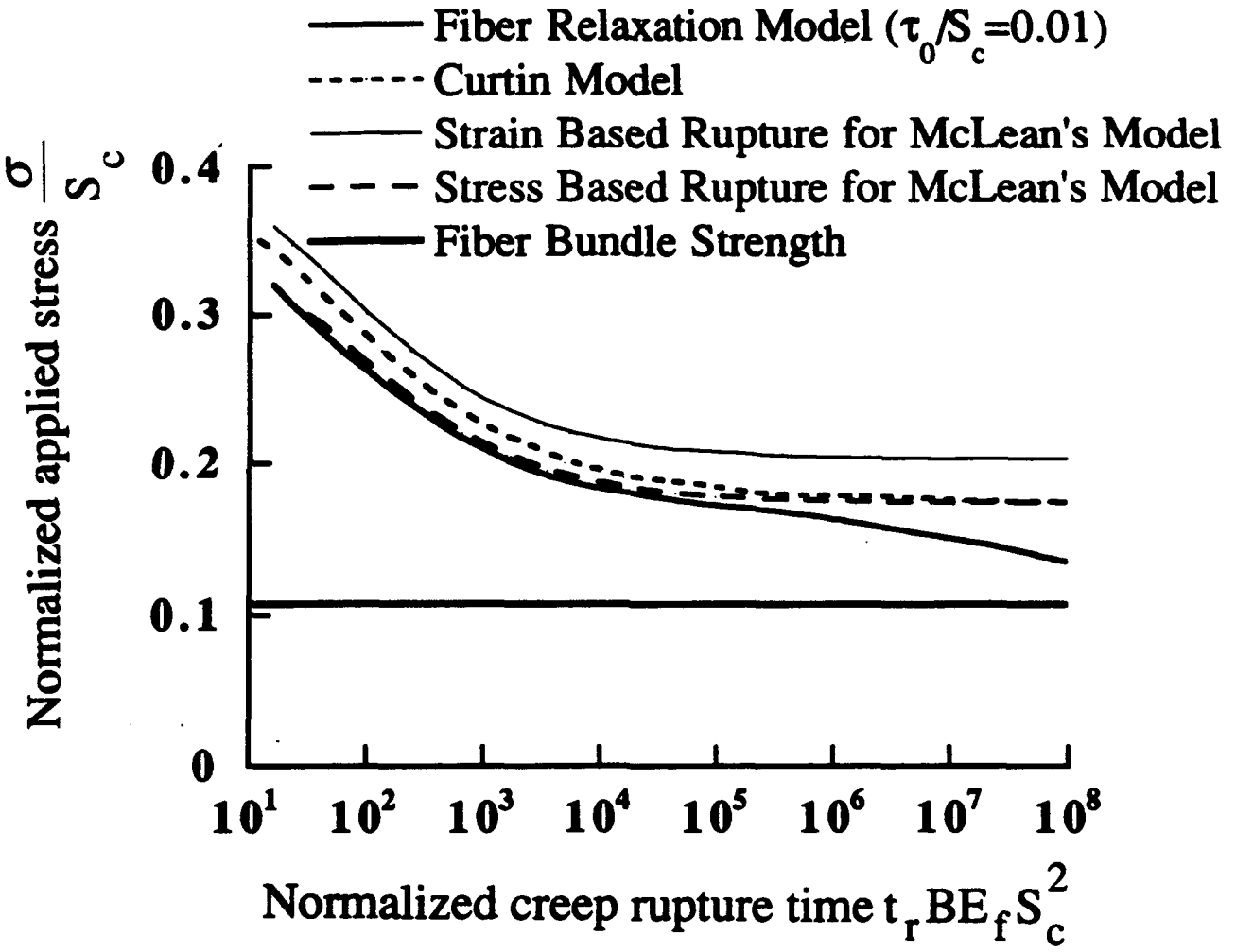

Fig.11

MATERIALS

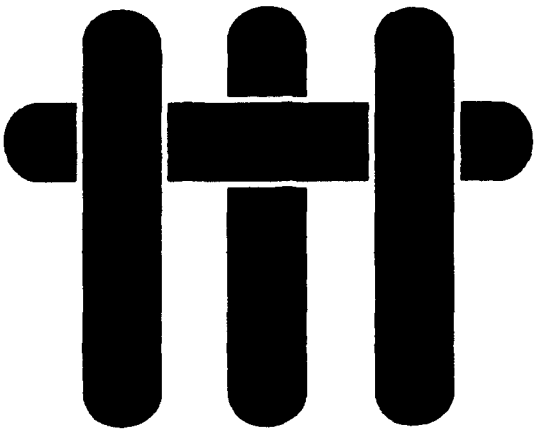

MODELS FOR THE CREEP OF CERAMIC MATRIX COMPOSITE MATERIALS

Robert M. McMeeking

Department of Mechanical and Environmental Engineering
University of California
Santa Barbara, California 93106

September 1992

4H:MS26(September 1, 1992)10:25 AM/mef

Introduction

This review is intended to focus on ceramic matrix composite materials. However, the creep models which exist and which will be discussed are generic in the sense that they can apply to materials with polymer, metal or ceramic matrices. Only a case by case distinction between linear and nonlinear behavior separates the materials into classes of response. The temperature dependent issue of whether the fibers creep or do not creep permits further classification. Therefore, in the review of the models, it is more attractive to use a classification scheme which accords with the nature of the material response rather than one which identifies the materials per se. Thus, this review could apply to polymer, metal or ceramic matrix materials equally well.

Only fiber and whisker reinforced materials will be considered. The fibers and whiskers will be identified as ceramics but with different characteristics from the matrix. As noted above, at certain temperatures, the reinforcement phase will not be creeping and then it will be treated as elastic or rigid as appropriate to the model. At higher temperatures, the reinforcement phase will creep, and that must be allowed for in the appropriate model. On the other hand, the case of creeping fibers in an elastic matrix will not be considered, although certain of the models have a symmetry between fiber and matrix which permits such an interpretation. The models reviewed will be for materials with long fibers, broken long fibers and short fibers or whiskers. Aligned fibers and two and three dimensional reinforcement by long fibers will be discussed. However, general laminate behavior will not be a subject of this review.

The material behaviors considered will include linear elasticity plus linear or nonlinear creep behavior. The nonlinear case will be restricted to power law rheologies. In some cases the elasticity will be idealized as rigid. In ceramics, it is commonly the case that creep occurs by mass transport on the grain boundaries[1]. This usually leads to a linear rheology. In the models considered, this behavior will be represented by a continuum creep model with a fixed viscosity. That is, the viscosity is strain rate

independent, although it will in general be temperature dependent. Thus, the mass transport per se will not be explicit in the models. In some situations, even though the mechanism is mass transport, the creep behavior involves a power law response with a low exponent. Such a case is polycrystalline alumina at certain temperatures[1]. This explains the inclusion of power law models in this review. An additional constitutive feature considered in this review is mass transport on the interface between the fiber and the matrix. This path can be a faster route for diffusion than the grain boundaries within the matrix. Therefore it merits a separate treatment as a mechanism for creep. A rudimentary model for the progressive breaking of reinforcements will be discussed. Creep void growth and other types of rupture damage in the matrix and the fiber will, however, be excluded from consideration.

Because the creep behavior of a ceramic composite often has a linear rheology, the behavior of the composite usually can be represented by an anisotropic viscoelastic constitutive law. Thus, a rather general model for such composites involves hereditary integrals with time dependent creep or relaxation moduli[2,3] with a general anisotropy. the parameters for the law can be determined through creep and relaxation tests, but a multiplicity of experiments are required to evaluate all the functions appearing in a general anisotropic law. As a consequence, some guidance from micromechanics is essential for the generalization of the results. In this review, the focus will be on the micromechanics based models and the hereditary integral methods will not be considered. However, the micromechanics models can, if desired, be recast in the classical viscoelastic form. It should be noted that there exists a vast literature on the linear elastic properties of reinforced materials. These elasticity models can be converted into creep models by use of standard methods of linear viscoelasticity[2]. This approach will be avoided in this review even though it can provide effective creep models for ceramic matrix composites. Instead, the focus in this chapter will be on models which involve nonlinearities or have features such as interface diffusion which

are not accounted for when linear elastic models are converted to linear viscoelastic constitutive laws.

Material Models

All phases of the composite material will be assumed to be isotropic. The creep behavior of a ceramic will be represented by the law

$$\dot{\varepsilon}_{ij} = \frac{1}{2G}\dot{S}_{ij} + \frac{1}{9K}\delta_{ij}\,\dot{\sigma}_{kk} + \frac{3}{2}B\,\bar{\sigma}^{n-1}\,S_{ij} + \alpha\,\delta_{ij}\,\dot{T} \qquad (1)$$

where $\dot{\underline{\varepsilon}}$ is the strain rate, $\underline{\sigma}$ is the stress, $\dot{\underline{\sigma}}$ is the stress rate, G is the elastic shear modulus, K is the elastic bulk modulus, δ_{ij} is the Kronecker delta, B is the creep rheology parameter, n is the creep index, $\underline{S}$ is the deviatoric stress and the effective stress $\bar{\sigma}$ is defined by

$$\bar{\sigma} = \sqrt{\tfrac{3}{2}\,S_{ij}\,S_{ij}}, \qquad (2)$$

α is the coefficient of thermal expansion and $\dot{T}$ is the rate of change of temperature. In all expressions the Einstein repeated index summation convention is used. x_1, x_2 and x_3 will be taken to be synonymous with x, y and z so that $\sigma_{11} = \sigma_{xx}$ etc.. The parameter B will be temperature dependent through an activation energy expression and can be related to microstructural parameters such as grain size, diffusion coefficients etc. on a case by case basis depending on the mechanism of creep involved[1]. In addition, the index will depend on the mechanism which is active. In the linear case, n = 1 and B is equal to $1/3\eta$ where η is the linear shear viscosity of the material. Stresses, strains and material parameters for the fibers will be denoted with a subscript or superscript f and for the matrix with a subscript or superscript m.

Various models will be used for the interface between the fiber and the matrix. For bonded interfaces, complete continuity of all components of the velocity will be invoked. The simplest model for a weak interface is that a shear drag equal to τ opposes the relative shear velocity jump across the interface. The direction of the shear drag is determined by the direction of the relative velocity. However, the magnitude of τ is independent of the velocities. This model is assumed to represent friction occurring mainly because of roughness of the surfaces or due to a superposed large normal pressure on the interface. Creep can, of course, relax the superposed normal stress over time, but on a short time scale the parameter τ can be assumed to be relatively invariant. No attempt will be made to account for Coulomb friction associated with local normal pressures on the interface.

On the other hand, a model for the viscous flow of creeping material along a fiber surface is exploited in some of the cases covered. This model is thought to represent the movement of material in steady state along a rough fiber surface and is given by (McMeeking, to be published)

$$v_i^{Rel} = \bar{B}\ \bar{\sigma}^{n-1}\ n_j\ \sigma_{jk}\left(\delta_{ki} - n_k\ n_i\right) \tag{3}$$

where $\underline{v}^{Rel}$ is the relative velocity of the matrix material with respect to the fiber, $\bar{B}$ is a rheology parameter proportional to B but dependent also on roughness parameters for the fiber, $\underline{n}$ is the unit outward normal to the fiber surface and the stress is that prevailing in the creeping matrix material. The law simply says that the velocity is in the direction of the shear stress on the interface but is controlled by power law creep.

When there is mass transport by diffusion taking place in the interface between the fiber and the matrix, the relative velocity is given by[1]

$$\underline{v}^{Rel} = -\underline{n}\left(\underline{\nabla}.\underline{j}\right) \tag{4}$$

where $\underline{j}$ is the mass flux of material in the plane of the interface and $\underline{\nabla}$ is the divergence operator in 2-dimensions also in the plane of the interface. The mass flux in the interface is measured as the mass per unit time passing across a line element of unit length in the interface. The flux is proportional to the stress gradient so that

$$\underline{j} = \mathcal{D}\,\underline{\nabla}\,\sigma_{nn} \tag{5}$$

where $\mathcal{D}$ is an effective diffusion coefficient and

$$\sigma_{nn} = \underline{n}.\underline{\sigma}.\underline{n} \tag{6}$$

is the normal stress at the interface. Combination of eq. (4 & 5) for a homogeneous interface gives

$$\underline{v}^{Rel} = -\underline{n}\;\mathcal{D}\;\nabla^2\,\sigma_{nn}. \tag{7}$$

The diffusion parameter $\mathcal{D}$ controls mass transport in a thin layer at the interface and so its relation to other parameters can be stated as[1]

$$\mathcal{D} = \frac{\delta D_b \Omega}{kT} \tag{8}$$

where δ is the thickness of the thin layer in which diffusion is occurring, D_b is the diffusion coefficient in the material near or at the interface, Ω is the atomic volume, k is Boltzmann's constant and T is the absolute temperature. The diffusion could occur in the matrix material, in the fiber or in both. The relevant diffusion parameters for the matrix, the fiber or some weighted average would be used respectively.

It is worth noting that the "rule of mixtures" for stress, stress rate, strain and strain rate is always an exact result in terms of the averages over the phases[4]. That is

$$\sigma_{ij} = f\,\sigma_{ij}^{f} + (1-f)\,\sigma_{ij}^{m} \tag{9}$$

$$\varepsilon_{ij} = f\,\varepsilon_{ij}^{f} + (1-f)\,\varepsilon_{ij}^{m} \tag{10}$$

etc. where the unsuperscripted tensor variables are the averages over the composite material and the superscripted variables are the averages over the fibers (f) and the matrix (m) respectively. The volume fraction of the fibrous phase is f. The result applies irrespective of the configuration of the composite material, e.g. unidirectional or multidirectional reinforcement. However, an allowance must be made for the contribution arising from gaps which can appear such as at the ends of fibers. The difficulty in the use of the rule of mixtures is the requirement that the average values in the fibers and in the matrix must be known somehow.

Materials with Long Intact Fibers

Creep laws for materials with long intact fibers are relevant to cases where the fibers are unbroken at the outset, and never fracture during life. As a model, it also applies to cases where some but not all of the fibers are broken so that some fibers remain intact during service. Obviously these situations would occur only when the manufacturing procedure can produce composites with many or all of the fibers intact.

In the problem of the creep of materials with intact unidirectional fibers, as shown in Fig. 1, most of the insights arise from the compatibility of the strain rates in the fibers and in the matrix. When a stress σ_{zz} is applied to the composite parallel to

the fibers, the strains and strain rates of the fibers and the matrix in the z-direction must be all the same[5]. This gives rise to a creep law of the form

$$\dot{\varepsilon}_{zz} = \frac{\dot{\sigma}_{zz}}{E_L} + \dot{\varepsilon}^c_{zz} + \alpha_L \dot{T} \tag{11}$$

and

$$\dot{\varepsilon}_{xx} = \dot{\varepsilon}_{yy} = -\frac{\nu_L \dot{\sigma}_{zz}}{E_L} + \dot{\varepsilon}^c_{xx} + \alpha_T \dot{T} \tag{12}$$

where E_L is the longitudinal composite modulus, $\dot{\varepsilon}^c_{zz}$ is the longitudinal creep strain rate, α_L is the longitudinal coefficient of thermal expansion, ν_L is the Poisson's ratio for the composite relating transverse elastic strain to longitudinal stress, $\dot{\varepsilon}^c_{xx}$ is the transverse creep strain rate and α_T is the transverse coefficient of thermal expansion. The temperature is taken to be uniform throughout the composite material. Evolution laws for the creep rates are required and these laws involve the stress levels in the matrix and fibers. Thus, in turn, evolution laws are required for the matrix and fiber stresses.

The exact laws, based on continuum analysis of the fibers and the matrix would be very complicated. The analysis would involve equilibrium of stresses around and in the fibers and compatibility of matrix deformation with the fiber strains. Furthermore, end and edge effects near the free surfaces of the composite material would introduce complications. However, a simplified model can be developed for the interior of the composite material based on the notion that the fibers and the matrix interact only by having to experience the same longitudinal strain. Otherwise, the phases behave as two uniaxially stressed materials. McLean[5] introduced such a model for materials with elastic fibers and he notes that McDanels, Signorelli and Weeton[6] developed the model

for the case where both the fibrous and the matrix phase are creeping. In both cases, the longitudinal parameters are the same, namely

$$E_L = f\ E_f + (1-f)\ E_m \tag{13}$$

$$\alpha_L = [f\ E_f\ \alpha_f + (1-f)\ E_m\ \alpha_m]/E_L \tag{14}$$

$$\dot{\varepsilon}^c_{zz} = [f\ E_f\ B_f\ \sigma_f^{n_f} + (1-f)\ E_m\ B_m\ \sigma_m^{n_m}]/E_L. \tag{15}$$

When the fibers do not creep, B_f is simply set to zero. The longitudinal stress σ_{zz} in the fibers and the matrix are denoted σ_f and σ_m respectively. To accompany eq. (13-15), evolution laws for the fiber and the matrix stresses are required. These are

$$\dot{\sigma}_f = E_f\ (\dot{\varepsilon}_{zz} - B_f\ \sigma_f^{n_f} - \alpha_f\ \dot{T}) \tag{16}$$

and

$$\dot{\sigma}_m = E_m\ (\dot{\varepsilon}_{zz} - B_m\ \sigma_m^{n_m} - \alpha_m\ \dot{T}). \tag{17}$$

Indeed, combining these by the rule of mixtures, eq. (9), leads to eq. (13) to (15).

Since the fibers and the matrix do not interact transversely, the model implies that no transverse stresses develop in the matrix or the fibers. The rule of mixtures, eq. (10), then leads to

$$\nu_L = f\ \nu_f + (1-f)\ \nu_m \tag{18}$$

$$\alpha_T = f\ \alpha_f + (1-f)\ \alpha_m + f\ (1-f)\ (\alpha_f - \alpha_m)\ (\nu_f\ E_m - \nu_m\ E_f)/E_L \tag{19}$$

and

$$\dot{\varepsilon}^c_{xx} = -\frac{1}{2}(1-f)\,B_m\,\sigma_m^{n_m} - \frac{1}{2}\,f\,B_f\,\sigma_f^{n_f} + f(1-f)\,(B_m\,\sigma_m^{n_m} - B_f\,\sigma_f^{n_f})\,(\nu_f\,E_m - \nu_m\,E_f)/E_L. \tag{20}$$

The data suggest that the elastic parameters in this model are reasonably good to first order[7] and experience with plasticity calculations[8,9,10] indicates that there is little plastic constraint between fibers and matrices at low volume fractions. Thus, the model should work reasonably well for any creep exponents at low volume fractions of fibers. Indeed, McLean[5] has used the isothermal version of the model successfully to explain longitudinal creep data for materials with non-creeping fibers.

Of interest, is the prediction of the uniaxial stress model when the applied stress and the temperature are held constant. The governing equations (19), (16) & (17) then have the feature that as time passes the solution always tends towards asymptotic values for stress in the fibers and the matrix. The evolution of the matrix stress occurs according to

$$\left[\frac{1}{E_m} + \frac{1-f}{fE_f}\right]\dot{\sigma}_m = B_m\,\sigma_m^{n_m} - B_f\left[\frac{\sigma-(1-f)\sigma_m}{f}\right]^{n_f} \tag{21}$$

and it can be shown that for any initial value of matrix stress, the matrix stress rate tends to zero. Therefore, the matrix stress tends toward the value which makes the right hand side of eq. (21) equal to zero. This can be solved easily for four common ceramic cases. One is when both matrix and fibers creep with a linear rheology so that both creep indices are equal to one. In that case the stresses tend towards the state in which

$$\sigma_m = \frac{B_f \sigma}{f B_m + (1-f) B_f} \tag{22}$$

and

$$\sigma_f = \frac{B_m \sigma}{f B_m + (1-f) B_f}. \tag{23}$$

Another case is when the fibers creep linearly and the matrix creeps with an index of 2. Then the matrix tends towards a stress

$$\sigma_m = \left(\frac{B_f}{B_m}\right)\left[\sqrt{\left(\frac{B_m}{B_f}\right)\frac{\sigma}{f} + \frac{(1-f)^2}{4f^2}} - \frac{1-f}{2f}\right] \tag{24}$$

and of course $\sigma_m = [\sigma - (1-f)\,\sigma_m]/f$. The opposite case of a linear matrix and quadratic fibers is such that the fibers tend towards the stress

$$\sigma_f = \left(\frac{B_m}{B_f}\right)\left[\sqrt{\left(\frac{B_f}{B_m}\right)\frac{\sigma}{1-f} + \frac{f^2}{4(1-f)^2}} - \frac{f}{2(1-f)}\right] \tag{25}$$

and $\sigma_m = [\sigma - f\,\sigma_f]/(1-f)$. Finally, when the fibers do not creep, the matrix stress tends towards zero and the fiber stresses approach $\sigma/(1-f)$.

In the latter case, the transient stress can be stated as well. The isothermal result for constant σ is[5]

$$\sigma_m(t) = \left\{\frac{(n-1) f E_f E_m B t}{E_L} + \frac{1}{[\sigma_m(0)]^{n-1}}\right\}^{1-n} \tag{26}$$

when $n \neq 1$ and

$$\sigma_m(t) = \sigma_m(0) \exp(-f\ E_f\ E_m\ B\ t/E_L) \tag{27}$$

when $n = 1$. The subscript on the creep rheology parameter for the matrix has been dropped and the unsubscripted B refers to the matrix henceforth. In both cases $\sigma_f = [\sigma - (1-f)\sigma_m]/f$ and the composite strain is σ_f/E_f. The stress at time zero would be computed from the prior history with $t = 0$ being the time when both the temperature and the applied stress become constant. For example if the temperature is held constant at creep levels until equilibrium is achieved and then the load is suddenly applied, $\sigma_m(0) = \sigma E_m/E_L$. To the extent that there are any thermal residual stresses at $t = 0$, they will contribute to $\sigma_m(0)$. However, eq. (26) & (27) make it clear that thermal residual stresses will be relaxed away be creep.

Steady Transverse Creep with Well-Bonded Elastic Fibers The previous paragraph has made it clear that if there are elastic fibers and a constant macroscopic stress is applied, the longitudinal creep rate will eventually fall to zero. With constant transverse stresses applied as well, the process of transient creep will be much more complicated than that associated with eq. (27) and (28). However, it can be deduced that the longitudinal creep rate will still fall to zero eventually. Furthermore, any transverse steady creep rate must occur in a plane strain mode. During such steady creep, the fiber does not deform further because the stress in the fiber is constant. In addition, any debonding which might tend to occur would have achieved a steady level because the stresses are fixed.

For materials with a strong bond between the matrix and the fiber, models for steady transverse creep are available. The case of a linear matrix is represented exactly

by the effect of rigid fibers in an incompressible linear elastic matrix and is covered in texts on elastic materials[7,11,12]. For example, the transverse shear modulus, and therefore the shear viscosity, of a material containing up to about 60% rigid fibers in a square array is approximated well by[11]

$$G_T = \frac{1+2f}{1-f} G_m . \tag{28}$$

It follows that in the coordinates of Fig. 1, steady transverse creep with well bonded fibers obeys

$$\dot{\varepsilon}_{yy} = -\dot{\varepsilon}_{xx} = \frac{3B}{4}\left(\frac{1-f}{1+2f}\right)\left(\sigma_{yy} - \sigma_{xx}\right) \tag{29}$$

and

$$\dot{\varepsilon}_{xy} = \frac{3B}{2}\left(\frac{1-f}{1+2f}\right)\sigma_{xy} \tag{30}$$

with $\dot{\varepsilon}_{zz} = 0$. A material with fibers in a hexagonal array will creep slightly faster than this. Similarly, creep in longitudinal shear with fibers in a square array can be approximated well by

$$\dot{\varepsilon}_{xz} = \frac{3B}{2}\left(\frac{1-f}{1+f}\right)\sigma_{xz} \tag{31}$$

and

$$\dot{\varepsilon}_{yz} = \frac{3B}{2}\left(\frac{1-f}{1+f}\right)\sigma_{yz} . \tag{32}$$

There are few comprehensive results for power law matrices. Results given by Schmauder and McMeeking[11] for up to 60% by volume of fibers in a square array with a creep index of 5 can be represented approximately by

$$\dot{\varepsilon}_{xx} = -\dot{\varepsilon}_{yy} = 0.42\, B\, |\sigma_{xx} - \sigma_{yy}|^4\, (\sigma_{xx} - \sigma_{yy})/S^5 \tag{33}$$

where $\dot{\varepsilon}_{zz} = \dot{\varepsilon}_{xy} = \sigma_{xy} = 0$

$$S = (1 + f^2)/(1 - f) \tag{34}$$

is the creep strength, defined to be the stress required for the composite at a given strain rate divided by the stress required for the matrix alone at the same strain rate. The expression in eq. (34) is only suitable for n = 5. The result in eq. (33) when f = 0 is the plane strain creep rate for the matrix alone. Results for $\sigma_{xy} \neq 0$ are not given because of the relative anisotropy of the composite with a square array of fibers. Relevant results for other power law indices and other fiber arrangements are not available in sufficient quantity to allow representative expressions to be developed for them.

Three-Dimensional Continuous Reinforcement This configuration of reinforcement can be achieved by the use of a woven fiber reinforcement or interpenetrating networks of the two phases. Another possibility is that random orientation of whiskers produces a percolating network and even if the whiskers are not bonded together, this network effectively forms a mechanically continuous phase. In the case of woven reinforcements, there may be some freedom for the woven network to reconfigure itself by the straightening of fibers in the weave or because of void space in the matrix. Such effects will be ignored and it will be assumed that the fibers are relatively straight and that there is little or no void space in the matrix. A straightforward model for these

materials is that the strain rate is homogeneous throughout the composite. The response is then given by

$$\dot{\sigma}_{ij} = 2\bar{G}\,\dot{\varepsilon}_{ij} + (\bar{K} - \tfrac{2}{3}\bar{G})\,\delta_{ij}\,\dot{\varepsilon}_{kk} - 3\bar{K}\,\bar{\alpha}\,\dot{T}\,\delta_{ij} - 3\,f\,G_f\,B_f\,\bar{\sigma}_f^{n_f-1})\,S_{ij}^f - 3\,(1-f)\,G_m\,B_m\,\bar{\sigma}_m^{n_m-1}\,S_{ij}^m \tag{35}$$

where

$$\bar{G} = f\,G_f + (1-f)\,G_m \tag{36}$$

$$\bar{K} = f\,K_f + (1-f)\,K_m \tag{37}$$

and

$$\bar{\alpha} = f\,\alpha_f\,K_f + (1-f)\,\alpha_m\,K_m. \tag{38}$$

The evolution of the fiber and matrix average stresses appearing in the last two terms in eq. (35) is given by eq. (35) with f = 1 and f = 0 respectively. It is of interest that the constitutive law in eq. (35) is independent of the configuration of the reinforcements and the matrix. As a consequence, the law is fully isotropic and therefore may be unsuitable for woven reinforcements with unequal numbers of fibers in the principal directions. In addition, the fully isotropic law may not truly represent materials in which the fibers are woven in 3 orthogonal directions. Perhaps these deficiencies could be remedied by replacing the thermoelastic part of the law with an appropriate anisotropic model. A similar alteration to the creep part may be necessary but no micromechanical guidance is available at this stage.

If the composite strain rate is known, the composite stress during steady state isothermal creep can be computed from the rule of mixtures for the stress, eq. (9). This gives

$$S_{ij} = \frac{2}{3}\left[\frac{f}{B_f}\left(\frac{\dot{\bar{\varepsilon}}}{B_f}\right)^{\frac{1-n_f}{n_f}} + \frac{1-f}{B_m}\left(\frac{\dot{\bar{\varepsilon}}}{B_m}\right)^{\frac{1-n_m}{n_m}}\right]\dot{\varepsilon}_{ij} \tag{39}$$

where $\dot{\underline{\varepsilon}}$ must be deviatoric (i.e. $\dot{\varepsilon}_{kk} = 0$) and

$$\dot{\bar{\varepsilon}} = \sqrt{\frac{2}{3}\dot{\varepsilon}_{ij}\,\dot{\varepsilon}_{ij}}. \tag{40}$$

A hydrostatic stress can be superposed, but it is caused only by elastic volumetric strain of the composite. The result in eq. (39) is, perhaps, not very useful since it is rare that a steady strain rate will be kinematically imposed. When both fiber and matrix creep, the steady solutions for a fixed stress in isothermal states are quite complex but can be computed by numerical inversion of eq. (39). The solution can however be given for the isothermal case where the fibers do not creep. (For non-fiber composites, this should be interpreted to mean that one of the network phases creeps while the other does not.) The matrix deviatoric stress is then given by

$$S^m_{ij}(t) = \frac{S^m_{ij}(0)}{\bar{\sigma}_m(0)}\left[3(n-1)f\,G_f\,G_m\,B\,t/\bar{G} + \left(\bar{\sigma}_m(0)\right)^{1-n}\right]^{\frac{1}{1-n}} \tag{41}$$

when $n \neq 1$ and for $n = 1$

$$S^m_{ij}(t) = S^m_{ij}(0)\,\exp(-3\,f\,G_f\,G_m\,B\,t/\bar{G}). \tag{42}$$

The subscripts on B and n have been dropped since only the matrix creeps. The interpretation of time and the initial conditions for eq. (41) & (42) are the same as for eq. (26) & (27). The fiber deviatoric stresses are given by

$$S_{ij}^{f} = [S_{ij} - (1-f)\, S_{ij}^{m}]/f \tag{43}$$

and the composite deviatoric strain e_{ij} is therefore

$$e_{ij} = S_{ij}^{f}/2\, G_f. \tag{44}$$

The volumetric strains are invariant and given by

$$\varepsilon_{kk} = \sigma_{kk}/3\, \bar{K}. \tag{45}$$

As expected, the matrix deviatoric stresses will be relaxed away completely. Thereafter, the "fiber" phase sustains the entire deviatoric stress. As a consequence, in the asymptotic state

$$S_{ij}^{f} = S_{ij}/f \tag{46}$$

and the composite strain will be given by (44) to (46) as

$$\varepsilon_{ij} = \frac{\sigma_{ij}}{2fG_f} + \left(\frac{1}{3\bar{K}} - \frac{1}{2fG_f}\right)\frac{1}{3}\sigma\, \delta_{ij}. \tag{47}$$

It follows that in uniaxial stress, with $\sigma_{zz} = \sigma$ and $\varepsilon_{zz} = \varepsilon$, the asymptotic result will be

$$\varepsilon = \left[\frac{1}{3fG_f} + \frac{1}{9\overline{K}}\right]\sigma. \tag{48}$$

This result indicates that the composite will have an asymptotic modulus slightly stiffer than $f E_f$ because the matrix phase is capable of sustaining a hydrostatic stress.

Two-Dimensional Continuous Reinforcement This configuration of reinforcement occurs when fibers are woven into a mat. It could also represent whisker reinforced materials in which the whiskers are randomly oriented in the plane, especially if uniaxial pressing has been used to consolidate the composite material. In the case of the whisker reinforced material, it is to be assumed that their volume fraction is so high that they touch each other. The whiskers have either been bonded together, say by diffusion, or the contact between the whiskers acts, as is likely, as a bond even if there is no interdiffusion.

In a simple model for this case, which as in the 3-d case ignores fiber straightening and anisotropy of the fibrous network, a plane stress version of eq. (35) can be developed. As such, it can only be used for plane stress states. Consider the x-y plane to be that in which the fibers are woven or the whiskers are lying. The strain rates in this plane are taken to be homogeneous throughout the composite material and σ_{zz}, σ_{xz} and σ_{yz} are taken to be zero. The resulting law is

$$\begin{aligned}\dot{\sigma}_{\alpha\beta} = {} & 2\overline{G}\left[\dot{\varepsilon}_{\alpha\beta} + \frac{\overline{\nu}}{1-\overline{\nu}}\delta_{\alpha\beta}\dot{\varepsilon}_{\gamma\gamma} - \frac{1+\overline{\nu}}{1-\overline{\nu}}\hat{\alpha}\dot{T}\delta_{\alpha\beta}\right] \\ & -3fG_f B_f \overline{\sigma}_f^{n_f-1}\left[S^f_{\alpha\beta} + \frac{\nu_f}{(1-\nu_f)}\delta_{\alpha\beta}S^f_{\gamma\gamma}\right] \\ & -3(1-f)G_m B_m \overline{\sigma}_m^{n_m-1}\left[S^m_{\alpha\beta} + \frac{\nu_m}{(1-\nu_m)}\delta_{\alpha\beta}S^m_{\gamma\gamma}\right]\end{aligned} \tag{49}$$

where Greek subscripts range over 1 & 2 and where

$$\frac{\bar{\nu}}{1-\bar{\nu}} = \left[f G_f \frac{\nu_f}{1-\nu_f} + (1-f) G_m \frac{\nu_m}{1-\nu_m} \right] / \bar{G} \tag{50}$$

and

$$\hat{\alpha} = \left[f \alpha_f G_f \frac{1+\nu_f}{1-\nu_f} + (1-f) \alpha_m G_m \frac{1+\nu_m}{1-\nu_m} \right] / \left(\frac{1+\bar{\nu}}{1-\bar{\nu}} \bar{G} \right). \tag{51}$$

The fiber and matrix evolution laws for stress are identical to eq. (49) with $f = 0$ and $f = 1$ respectively. Being isotropic in the plane, this law suffers from the same deficiencies as the 3-d version regarding the orthotropy of the woven mat and any inequality between the warp and the woof. As before, this could be remedied with an anisotropic version of the law.

In steady state isothermal creep, the relationship between in plane components of stress and in plane components of strain rate are given by

$$\sigma_{\alpha\beta} = \frac{2}{3} \left[\frac{f}{B_f} \left(\frac{\dot{\bar{\varepsilon}}}{B_f} \right)^{\frac{1-n_f}{n_f}} + \frac{1-f}{B_m} \left(\frac{\dot{\bar{\varepsilon}}}{B_m} \right)^{\frac{1-n_m}{n_m}} \right] \left(\dot{\varepsilon}_{\alpha\beta} + \dot{\varepsilon}_{\gamma\gamma} \delta_{\alpha\beta} \right) \tag{52}$$

with $\sigma_{xz} = \sigma_{yz} = \sigma_{zz} = 0$ and with $\dot{\bar{\varepsilon}}$ given by eq. (40) but with $\dot{\varepsilon}_{xz} = \dot{\varepsilon}_{yz} = 0$. As in the 3-d case, this must be inverted numerically to establish a steady state isothermal creep rate for a given imposed stress.

When the fibers are elastic and non-creeping, the isothermal behavior at fixed applied plane stress is given in terms of the deviatoric stress by eq. (41) or (42) and

eq. (43). The expression for the deviatoric composite strain, eq. (44), still applies. However, the composite strain obeys

$$\dot{\varepsilon}_{\gamma\gamma} = \frac{3}{2}(1-f)\frac{G_m}{\bar{G}} B \bar{\sigma}_m^{n-1} \frac{(1+\nu_m)(1-\bar{\nu})}{(1+\bar{\nu})(1-\nu_m)} S_{\gamma\gamma}^m \tag{53}$$

and

$$\dot{\varepsilon}_{zz} = -\left[f\frac{\nu_f}{1-\nu_f} + (1-f)\frac{\nu_m}{1-\nu_m}\right]\dot{\varepsilon}_{\gamma\gamma} - \frac{3}{2}(1-f)\frac{(1-2\nu_m)}{(1-\nu_m)} B \bar{\sigma}_m^{n-1} S_{\gamma\gamma}^m . \tag{54}$$

The latter result indicates that the volumetric strains can be relaxed to some extent by matrix creep. This contrasts with the 3-d case where complete compatibility of strains precludes such relaxation. The extent to which the relaxation occurs has not yet been calculated. However, if it is assumed that the relaxation can be complete so that the matrix volumetric strain is zero, then the fiber stress tends towards $\sigma_{\alpha\beta}/f$ and therefore the composite strain approaches

$$\varepsilon_{ij} = \frac{1+\nu_f}{f E_f}\sigma_{ij} - \frac{\nu_f}{f E_f}\delta_{ij}\sigma_{\gamma\gamma} \tag{55}$$

which, of course, is restricted to plane stress. It can be seen that in uniaxial stress, the effective asymptotic modulus would now equal $f E_f$. A properly calculated solution for $\varepsilon_{kk}(t)$ is required to investigate whether this result holds true.

Uniaxial Reinforcement with Long Brittle Fibers

The reinforcement configuration of interest now is once more that depicted in Fig. 1 and the loading will be restricted to a longitudinal steady stress σ_{zz}. The possibility will be taken into account that the fibers might be overstressed and therefore could fail. Only elastic fibers which break in a brittle manner will be considered, although ceramic fibers are also known to creep and possibly rupture due to grain boundary damage. Frictionally constrained fibers only will be considered since well bonded fibers will fail upon matrix cracking and vice versa. The case where the fibers have a deterministic strength S can be considered. In that situation, the fibers will remain intact when the fiber stress is below the deterministic strength level and they will break when the fiber stress exceeds the strength. The fracturing of the fibers could occur during the initial application of the load, in which case elastic analysis is appropriate. If the fibers survive the initial application of the load, then subsequent failure can occur as the matrix relaxes according to eq. (26) or (27) and the fiber stress increases. Thus the time elapsed before first fiber failure can be estimated based on eq. (26) or (27) by setting the fiber stress equal to the deterministic strength. This predicts that failure of a fiber will occur when

$$\sigma_m = [\sigma - f S]/(1 - f) \tag{56}$$

from which the time to failure can be computed through eq. (26) or (27). The failure of one fiber in a homogeneous stress state will cause a neighboring fiber to fail nearby because of the fiber/matrix shear stress interaction and the resulting localized load sharing around the broken fiber. Thus a single fiber failure will tend to cause a spreading of damage in the form of fiber breaks near a single plane across the section. This will lead to localized rapid creep and elastic strains in the matrix near the breaks perhaps giving rise to matrix failure. It follows therefore that tertiary failure of the

composite will tend to occur soon after the occurrence of one fiber failure when the fiber strength is deterministic.

Tertiary failure processes akin to this have been modelled by Phoenix and coworkers[13-15] in the context of epoxy matrix composites. Indeed, they show that such tertiary failures can occur even when the fiber strength is statistical in nature. This mechanism will not be pursued further in this paper but some other basic results considered on the assumption that when there is a sufficient spread in fiber strengths such tertiary failures can be postponed well beyond the occurrence of first fiber failure or indeed eliminated completely. Thus, attention will be focused on fibers which obey the classical Weibull model that the probability of survival of a fiber of length L stressed to a level σ_f is given by

$$P_s = \exp\left[-\frac{L}{L_g}\left(\frac{\sigma_f}{S}\right)^m\right] \tag{57}$$

where L_g is a datum gauge length, S is a datum strength and m is the Weibull modulus. Clearly the results given below can be generalized to account for variations on the statistical form which differ from eq. (57). However, the basic ideas will remain the same.

Long Term Creep Threshold Consider a specimen of length L_s containing a very large number of wholly intact fibers. A stress σ is suddenly applied to the specimen parallel to the fibers. The temperature has been raised to the creep level already and is now held fixed. Upon first application of the load, some of the fibers will break. The sudden application of the load means that the initial response is elastic. This elastic behavior has been modelled by Curtin[16] among others but details will not be given here. If the applied stress exceeds the ultimate strength of the composite in this elastic mode of

response, then the composite will fail and long term creep is obviously not an issue. However, it will be assumed that the applied stress is below the elastic ultimate strength and therefore creep can commence. It should be noted, however, that matrix cracking can occur in the ceramic matrix and the characteristics of creep relaxation would depend on the degree of matrix cracking. However, this aspect of the problem will not be considered in detail. For cases where there is matrix cracking and for which the specimen length L_s is sufficiently long, Curtin[16] has given the theoretical prediction that the ultimate elastic strength is

$$S_u = f\,[4\,L_g\,S^m\,\tau/D\,(m\,+\,2)]^{1/(m+1)}\;\;(m+1)/(m+2) \tag{58}$$

where τ is the interface shear strength between the fiber and the matrix and D is the diameter of the fibers. The interface shear strength is usually controlled by friction. For specimens shorter than δ_c, the ultimate brittle strength exceeds S_u where δ_c is given by[16]

$$\delta_c = [S\;L_g^{1/m}\;D/2\,\tau]^{m/(m+1)}. \tag{59}$$

This critical length is usually somewhat less than the datum gauge length.

When the applied stress σ is less than S_u, creep of the matrix will commence after application of the load. During this creep, the matrix will relax and the stress on the fibers will increase. Therefore, further fiber failure will occur. In addition, the process of matrix creep will depend on the extent of prior fiber failure and, as mentioned previously, on the amount of matrix cracking. The details will be rather complicated. However, the question of whether steady state creep or, perhaps, rupture will occur or whether sufficient fibers will survive to provide an intact elastic specimen can be answered by consideration of the stress in the fibers after the matrix has been assumed

to relax completely. Clearly, when the matrix carries no stress, the fibers will at least fail to the extent they do in a dry bundle. It is possible that a greater degree of fiber failure will be caused by the transient stresses during creep relaxation, but this effect has not yet been modelled. Instead, the dry bundle behavior will be used to provide an initial estimate of fiber failure in these circumstances.

Given eq. (57), the elastic stress strain curve for a fiber bundle is

$$\sigma = f E_f \varepsilon \exp\left[-\frac{L_s}{L_g}\left(\frac{E_f \varepsilon}{S}\right)^m\right]. \tag{60}$$

Thus when a stress σ is applied to the composite, creep will occur until the strain has the value consistent with eq. (60). Numerical inversion of eq. (60) can be used to establish this strain. The stress-strain curve in eq. (60) has a stress maximum when

$$\varepsilon = \frac{S}{E_f}\left(\frac{L_g}{m L_s}\right)^{\frac{1}{m}} \tag{61}$$

with a corresponding stress level given by

$$\sigma_c = f S\left(\frac{L_g}{m L_s}\right)^{\frac{1}{m}} \exp(-1/m). \tag{62}$$

This result is plotted as a function of m in Fig. 2. If $\sigma < \sigma_c$, the composite will creep until the strain is consistent with eq. (60) and thereafter no further creep strain will occur. Of course, the non creeping state will be approached asymptotically. (It should be noted that due to possible fiber failure during the creep transient, the true value for σ_c may lie below the result given in eq. (62).) For an applied composite stress equal to

or exceeding σ_c, creep will not disappear with time because all of the fibers will eventually fail and the strain will continue to accumulate.

The critical threshold stress for ongoing creep given by eq. (62) is specimen length dependent. For very long specimens, the threshold stress is low whereas short specimens will require a high stress for ongoing creep to continue without limit. On the other hand, the ultimate brittle strength as given by eq. (58) for a composite specimen longer than δ_c is specimen length independent. Thus there are always specimens long enough so that σ_c is less than S_u. This means that the specimen can be loaded without failure initially and if σ exceeds σ_c, the specimen will go into a process of long term creep. (It should be remembered, however, that this model is based on the assumption that tertiary failure is delayed and does not occur until a substantial amount of matrix creep has occurred.) For shorter specimens, the relationship between σ_c and S_u depends on the material parameters appearing in eq. (58) and (62). However, for typical values of the parameters, σ_c is less than S_u so that there is usually a window of stress capable of giving rise to long term creep without specimen failure when the specimen length exceeds δ_c. Typical values for the parameters are given by, among others, Hild et al.[17]. From these parameters, predictions for σ_c can be made. For example, a LAS matrix composite containing 46% of SiC (Nicalon) fibers (m equals 3 or 4) is predicted to have a value for σ_c between 400 MPa and 440 MPa for a specimen length of 25 mm whereas its measured ultimate brittle strength is between 660 MPa and 760 MPa. At 250 mm specimen length, the long term creep threshold σ_c is predicted to fall to the range 185 MPa to 250 MPa. Similarly, a CAS matrix composite with 37% SiC (Nicalon) fibers (m equals 3.6) in a specimen length of 25 mm is predicted to suffer long term creep if the stress exceeds 160 MPa whereas the measured ultimate brittle strength is 430 MPa. For a 250 mm specimen length, this creep threshold is predicted to fall to 85 MPa. Thus it is clear that in some practical cases, applied stresses which are modest fractions of the elastic ultimate strength will cause long term creep.

Steady State Creep For specimens which have (i) previously experienced an applied stress exceeding the long term creep threshold or (ii) which had every fiber broken prior to testing or service (e.g. during processing) or (iii) which had few fibers intact to begin with so that initially the long term creep threshold is much lower than σ_c as predicted by eq. (62), a prediction of the long term creep behavior can be made. Prior to this state, there will, of course, be a transient which involves matrix creep and, perhaps, the fragmentation of fibers. This transient has not been fully modelled. Only a rudimentary assessment of the creep behavior has been made revealing the following features.

For those composites initially having some of the fibers intact, there will always be some which must be stretched elastically. This will require a stress which will tend towards the value given by eq. (60) with f replaced by f_i, the volume fraction of fibers initially intact. If a relaxation test were carried out, the stress would asymptote to the level predicted by eq. (60). The remaining broken fibers will interact with the matrix in a complex way, but at a given strain and strain rate, a characteristic stress contribution can be identified in principle. Details have not been worked out. However, the total stress would be the sum of the contribution from the broken and unbroken fibers. If the transient behavior is ignored (i.e. assumed to die away relatively fast compared to the strain rate) a basic model can be constructed.

Steady State Creep with Broken Fibers First, consider a composite with a volume fraction f of fibers, all of which are broken. There are two possible models for the steady state creep behavior of such a material. In one, favored by Mileiko[18] and Lilholt[19] among others, the matrix serves simply to transmit shear stress from one fiber to another and the longitudinal stress in the matrix is negligible. The kinematics of this model requires void space to increase in volume at the ends of the fibers. However,

with broken fibers there is no inherent constraint on this occurring. Furthermore, if matrix cracking has occurred, the matrix will not be able to sustain large amounts of longitudinal tension and its main role will be to transmit shear from fiber to fiber. Indeed, matrix cracking will probably promote this mode of matrix flow since there will be no driving stress for other mechanisms of straining. The other model, favored by McLean[20] and developed by Kelly and Street[21] involves a stretching flow of the matrix between fibers at a rate equal to the macroscopic strain rate of the composite material. This requires substantial axial stress in the matrix. In addition, volume is preserved by the flow and there is no need for space to develop at the end of the fiber. The model requires a considerable matrix flow to occur transporting material from the side of a given fiber to its end and the injection of matrix in between adjacent ends of the broken fibers. There is good reason to believe that the Mileiko[18] pattern of flow prevails when there are broken fibers.

In a version of the Mileiko[18] model in which it is assumed that each of six neighboring fibers has a break somewhere within the span of the length of a given fiber but that the location of those breaks is random within the span, the relationship between the steady state creep rate and the composite stress is (McMeeking, unpublished work)

$$\dot{\varepsilon} = g(n, f)\,(D/L)^{n+1}\; B\,\sigma^{n} \tag{63}$$

where L is the average length of the broken fiber segments and

$$g(n,f) = 2\sqrt{3}\left[\frac{\sqrt{3}\,(2n+1)}{2n\,f}\right]^{n}\left(\frac{\left(1-f^{\frac{n-1}{2}}\right)}{(n-1)}\right) \tag{64}$$

when $n \neq 1$ and

$$g(1, f) = (9/f)\ ln(1/\sqrt{f}). \tag{65}$$

These functions have been computed for uniform fiber length and based on a hexagonal shape for the fiber even though interpreted to be circular. That explains why creep strength goes to infinity at f = 0 rather than at f less than 1. In this creep model, the influence of both volume fraction and the aspect ratio L/D on the strain rate is clear with both having a strong effect. As noted, this model could serve as a constitutive law for the creep of a material in which all of the fibers are broken to fragments of average length L. In addition, it could be used for short fiber composites which have weak bonds between the fiber end and the matrix so that debonding can readily occur and void space can develop as a result. However, the aspect ratio L/D should be large so that the Mileiko[18] flow pattern will occur and end effects can be neglected when the composite creep law is computed.

The shear stress transmitted to a fiber is limited to the shear strength τ. As a result, the formula given in eq. (63) is valid only up to a composite macroscopic stress of

$$\sigma = \frac{2nf}{2n+1}\left(\frac{L}{D}\right)\tau \tag{66}$$

for both the linear and nonlinear cases. According to the model, at this level of applied stress, the shear stress on the fiber interface will start to exceed τ. Therefore, at stresses higher than the value given in eq. (66), the strain rate will exceed the level predicted in eq. (63). This situation will persist in the presence of matrix cracks up to a composite macroscopic stress of

$$\sigma_{LIM} = f \tau L/D \tag{67}$$

at which stress the entire fiber surface is subject to a shear stress equal in magnitude to τ. Then, the mechanism represented by eq. (63) provides an indeterminate strain rate as in rate independent plasticity. Thus σ_{LIM} can be thought of as a yield stress. This concept is probably satisfactory for materials with many matrix cracks so that there is no constraint on stretching the matrix. However, when there are no matrix cracks, the strain rate is probably controlled by the mechanism which generates void space at the fiber ends. This has been considered to require negligible stress in the version of the model leading to eq. (63). For a proper consideration of the limit behavior, the contribution to the stress arising from void development at the fiber ends should be taken into account.

The Effect of Fiber Fracture If the stress applied to the composite is increased, the stress sustained by fibers will increase also. When the probability of survival of fibers obeys the statistical relationship given by eq. (57), the effect of a raised stress will be to fracture more fibers, with a preference for breaking long fibers. This will have the effect of reducing the average fiber length L and therefore raising the strain rate at a given applied stress as can be deduced from eq. (63). Therefore, the composite will no longer have a simple power law behavior in steady state creep since the fiber fragment length will depend on the largest stress which the composite material has previously experienced. In this regard, the elastic transients will play an important role in determining the fiber fragment length. However, the average fragment length in steady state creep will generally be smaller than the average fragment length arising during initial elastic response. Therefore, some guidance can be obtained from a model designed to predict the steady state creep response only.

For the Mileiko[18] model of composite creep leading to the steady state creep rate for fixed fiber length given in eq. (63), a rudimentary fiber fragment length model gives (McMeeking, unpublished work)

$$L = (m+1)\left[\frac{(n+1)\,f\,S}{(2n+1)\,\sigma}\right]^{m} L_g \tag{68}$$

subject to L being less than the specimen length. When a stress σ is applied to the composite material and steady state is allowed to develop, the average length for the fiber fragments is predicted by eq. (68). This model is by no means precise, based as it is on some approximations in the calculations as well as the notion that all fibers can be treated as if they had the same length. However, the model conveys the important notion that the fiber fragment length will fall as the applied stress is increased.

The fiber fragment average length during steady state creep can be substituted into eq. (63) from which results

$$\dot{\varepsilon} = h\,(n, f, D/L_g, m, S)\;B\;\sigma^{n+m+nm} \tag{69}$$

where h is a rather complicated function of its arguments and can readily be calculated. A significant conclusion is that the creep index for the composite is no longer just n but is n+m+nm. Thus a ceramic matrix material with a creep index for the matrix of 1 will have composite creep index of 2m + 1. In the case of a fiber with a Weibull modulus of m = 4, the composite creep index will be 9. Similar effects will be apparent in composites with a nonlinearly creeping ceramic matrix, say with n = 2. It has been observed that *metal* matrix composites with noncreeping reinforcements often have a creep index which differs from that of the matrix[5,22] and the effect is usually attributed

to damage of the fibers or of the interface. It can be expected that ceramic matrix composites will exhibit a similar behavior.

It should be noted that the model leading to eq. (69) is incomplete since the stress required to cause the enlargement of void space at the fiber breaks is omitted from consideration. At high strain rates this contribution to stress can be expected to dominate other contributions. Therefore at high stress or strain, the creep behavior will diverge from eq. (69) and perhaps exhibit the nth power dependence on stress as controlled by the matrix. The creep rate at these high stresses can be expected to *exceed* the creep rate of the matrix at the same applied stress since the void space at the fiber ends is a form of damage.

Creep of an Initially Undamaged Composite The issue to be addressed in this section is the long term behavior of a composite stressed above the threshold σ_c given by eq. (62) which means that the specimen will creep continuously. As in the immediately preceding sections, elastic transient effects will be omitted from the model of long term creep of the initially undamaged composite. No model exists as yet for the transient behavior, but there is little doubt that the transient behavior is important. Many composite materials in service at creep temperatures will probably always respond in the transient stage since the time for that to die away will typically be rather long. However, a quasi-steady state model, as before, will give some insight into the state towards which the transients will be taking the material. However, the model presented below is rather selective, since it includes some elastic effects and ignores others. It is not known how deficient this feature of the model is. Perhaps the material state will evolve rather rapidly towards the state predicted below and therefore the model may have some merit.

The specimen is composed of a mixture of matrix, unbroken fibers and broken fibers. The volume fraction of intact fibers is given by eq. (57) with $L = L_s$, the specimen length. To the neglect of transients, the macroscopic stress supported by these intact fibers is given by eq. (60). The strain will now exceed the level of eq. (61) associated with the ultimate strength of the fiber bundle. Therefore the stress supported by the intact fibers will be less than σ_c which is the ultimate strength of the fiber bundle without matrix. The applied stress exceeds σ_c and the balance in excess of the amount borne by the intact fibers will cause the composite material to creep.

The steady state result given in eq. (69) will be taken to express the creep behavior controlled by the broken fibers. The volume fraction of broken fibers is

$$f_b = 1 - \exp\left[-\frac{L_s}{L_g}\left(\frac{E_f\,\varepsilon}{S}\right)^m\right] \tag{70}$$

and a material with this volume fraction of broken fibers creeping at a rate $\dot{\varepsilon}$ will support a stress

$$\sigma_b = [\dot{\varepsilon}/B\ h\,(n, f_b, D/L_g, m, S)]^{1/p} \tag{71}$$

where

$$p = n + m + nm \tag{72}$$

which comes directly from eq. (69). The total stress sustained by the composite material is therefore

$$\sigma = f_b\,\sigma_b + \sigma_u \tag{73}$$

where σ_u is the contribution due to unbroken fibers. This leads to

$$\sigma = f_b \left[\dot{\varepsilon} / B\, h(f_b)\right]^{1/p} + f E_f \varepsilon \exp\left[-\frac{L_s}{L_g}\left(\frac{E_f \varepsilon}{S}\right)^m\right] \tag{74}$$

which can be seen to be a rather nonlinear Kelvin-Voigt material in which the stress is the sum of a viscous element and an elastic element both of which are nonlinear. As the strain increases, the second term on the right hand side of eq. (74) (i.e. the term due to the intact fibers) will diminish and become rather small when only a few unbroken fibers are left. At the same time, f_b will approach f and so the strain rate will approach the steady state rate for a material in which all of the fibers are broken. However, as long as a few fibers remain intact, the creep behavior will not precisely duplicate that for the fully broken material. This transient effect will be compounded by the redistribution of stress from the matrix to the fibers which will occur both after the first application of load to the composite material and after each fracture of a fiber, both effects having been omitted from this version of the model.

Creep of Materials with Strong Interfaces

It seems unlikely that long fiber ceramic matrix composites with strong bonds will find application because of their low temperature brittleness. However, for completeness, a model which applies to the creep of such materials can be stated. It is that due to Kelly and Street[21]. It is possible also that the model applies to aligned whisker reinforced composites since they may have strong bonds. In addition, the model has a wide currency since it is believed to apply to weakly bonded composites as

well. However, the Mileiko[18] model predicts a lower creep strength for weakly bonded or unbonded composites and therefore is considered to apply in that case.

The Kelly and Street[21] model uses the notion that creep of the composite material can be modelled by the behavior of a unit cell. Each unit cell contains one fiber plus matrix around it so that the volume of the fiber divided by the volume of the unit cell equals the fiber volume fraction of the composite material. The perimeter of the unit cell is assumed to be deforming at a rate consistent with the macroscopic strain rate of the composite material. (It can be observed at this stage that this notion is inconsistent with the presence of transverse matrix cracks which would make it impossible to sustain the longitudinal stress necessary to stretch the matrix. This is an additional reason why the Kelly and Street[21] model is not likely to be applicable to unbonded ceramic matrix materials which are likely to have matrix cracks.) Only steady state creep of materials with aligned reinforcements which are shorter than the specimen is considered. The unit cell is assumed to conserve volume. This means that material originally adjacent to the reinforcement must flow around the fiber and finish up at its end. This phenomenon has to occur when the end of the fiber or whisker is strongly bonded to the matrix. For this reason, the Kelly and Street[21] model is considered to be relevant to materials with strong bonds.

Kelly and Street[21] analyzed this model but their deductions were not consistent with the mechanics. McMeeking[23] has remedied this deficiency for nonlinear materials. His results for n = 2 are relevant to composite materials with nonlinearly creeping ceramic matrices which tend to have low creep indices. In that case, the steady state creep rate is given by eq. (63) with n = 2 and

$$g(2,f) = \frac{75\sqrt{3}}{8f^2}\left(\frac{1}{2} - \frac{8}{5}\sqrt{f} + \frac{3}{2}f - \frac{1}{2}f^2 + \frac{1}{10}f^3\right) \tag{75}$$

which is invalid for $f = 0$. When f is close to zero a different form should be used which accounts for the matrix stress so that the matrix creep law is recovered smoothly as the volume fraction of fiber disappears. This result is developed below and is given in eq. (77). Comparison of eq. (75) with eq. (64) for $n = 2$ will show that the model of Kelly and Street[21] creeps more slowly than the Mileiko[18] law confirming that the Mileiko model is the preferred one when it is kinematically admissible.

It is thought that at higher temperatures, the interface between the fiber and the matrix becomes weak and sliding occurs according to the constitutive law given in eq. (3). In that case, creep of a composite with a well bonded interface obeys eq. (63) with $n = 2$ and[23]

$$g(2,f) = \frac{25\sqrt{3}}{8f^2}\left[3\left(\frac{1}{2} - \frac{8}{5}\sqrt{f} + \frac{3}{2}f - \frac{1}{2}f^2 + \frac{1}{10}f^3\right) + \frac{(1-f)^3\,\bar{B}}{2D\,B}\right]. \qquad (76)$$

This form for g is identical with that in eq. (75) when $\bar{B} = 0$. Thus, sliding at the interface increases the creep rate at a given stress. If $\bar{B}/B\,D$ is very large, signifying a very weak interface, then the interface term will dominate the matrix term in eq. (76). It should be noted that there is a relative size effect, with large diameter fibers making sliding less important.

At large strain rates, stretching of the matrix as it slides past the matrix will contribute to the creep strength. Under those circumstances, the term g(2, f) in eq. (63) should be replaced by[23]

$$\bar{g}(2,f) = \left[1/\sqrt{g(2,f)} + (1-f)\left(\frac{D}{L}\right)^{1.5}\right]^{-2} \qquad (77)$$

where, in eq. (77), g(2, f) is to be calculated according to eq. (76). Note that as g(2, f) becomes large (i.e., the composite strain rate is large because either f is small or $\bar{B}$ is large), the composite strain rate will approach

$$\dot{\varepsilon} = B\,[\sigma/(1-f)]^2 \tag{78}$$

which is the rate that would prevail if the fibers were replaced by long cylindrical holes.

Creep of Materials with a Linear Rheology The equivalent correction to the Kelly and Street[21] model for cases where the matrix creep obeys a linear rheology (n = 1) was not given by McMeeking[23]. However, consideration of this case can be included in a model with accounts for the ability of a well bonded interface between the fiber and the matrix to sustain sliding according to eq. (3) and in which mass transport may cause the effect described by eq. (4). In unpublished work, McMeeking has given the steady state creep law for the composite material in these circumstances to be

$$\sigma = \frac{\dot{\varepsilon}}{B}\left[h(f)\left(\frac{L}{D}\right)^2 + 1 - f\right] \tag{79}$$

where

$$1/h(f) = \frac{9}{8f}\left[4\ln\left(1/\sqrt{f}\right) - 3 + 4f - f^2\right] + \frac{3\bar{B}(1-f)^2}{fBD} + \frac{48f\mathcal{D}}{BD^3} \tag{80}$$

Recall that if sliding between the fiber and the matrix occurs readily, $\bar{B}$ will be large and also rapid mass transport is associated with a large value of $\mathcal{D}$.

It is thought that as the temperature is increased, the relative importance of sliding and mass transport is enhanced. Thus at low creep temperatures, $\bar{B}/B\ D$ and $\mathcal{D}/B\ D^3$ would be small. Then only the first term on the right hand side of eq. (80) will be important and when L/D is large, as required by this asymptotic model, the creep strength will be high. As the temperature is increased, either $\bar{B}/B\ D$ or $\mathcal{D}/B\ D^3$ or both will increase in magnitude. When they become large, h(f) will become small and the creep strength of the composite will fall, as can be seen in eq. (79). However, if h(f) becomes negligible, the steady state creep law for the composite will be approximately

$$\dot{\varepsilon} = B\,\sigma/(1-f). \tag{81}$$

As in the case of the quadratic matrix rheology, the creep behavior when sliding dominates (or as in this new case mass transport is significant) is the same as for a material containing cylindrical holes instead of fibers even if the interface is nominally well bonded. This behavior will occur when h(f) is much smaller than $(D/L)^2$ so that the relevant term containing h(f) in eq. (79) is negligible.

It should be noted that the creep behavior is affected in the way predicted by eq. (79) and (80) whether interface sliding occurs readily or mass transport occurs rapidly at the interface between the fiber and the matrix. It follows that rapid sliding by itself is sufficient to diminish the creep strength of the composite material and long range mass transport at the interface is not necessary. Note also that if the matrix does not creep (i.e. B = 0) neither sliding nor mass transport will have any effect on creep and the composite will be rigid. This feature arises because the matrix must deform when any sliding or mass transport occurs at the interface.

An additional feature is a size effect in the creep law when sliding or mass transport at the interface are significant enough to affect the composite behavior. A small diameter fiber (i.e. small D) will tend to enhance the effect of sliding or mass

transport on the creep rate of the composite and the composite will creep faster. Similarly, a large diameter fiber will tend to suppress the effect of sliding or mass transport and the creep strength of the composite will correspondingly be increased. Similar effects tied to grain size are known to occur in the creep of ceramics and metals controlled by mass transport on the grain boundaries[1]. Note that the mass transport term in eq. (80) is much more sensitive to fiber diameter than the sliding term. The cubic dependence on fiber diameter in the mass transport controlled term will cause it to disappear rapidly as D is increased. However, if both $\mathcal{D}$ and $\bar{B}$ are substantial, the creep strength of a composite will not be improved substantially by increase of fiber diameter until both the effects of sliding and mass transport are suppressed. It seems likely that in practice this will mean that mass transport will be relatively easy to eliminate as a contributor to rapid creep strain of the composite by increase of the fiber diameter, whereas the effect of sliding at a given temperature will be more persistent. Furthermore, there is also an interplay with volume fraction, with the importance of interface sliding being greater at low volume fractions of fibers and mass transport being more significant at higher volume fractions.

Discussion

As previously noted, this chapter has been concerned mainly with those models for the creep of ceramic matrix composite materials which feature some novelty which cannot be represented simply by taking models for the linear elastic properties of a composite and, through transformation, turning the model into a linear viscoelastic one. If this were done, the coverage of models would be much more comprehensive since elastic models for composites abound. Instead, it was decided to concentrate mainly on phenomena which cannot be treated in this manner. However, it was necessary to introduce a few models for materials with linear matrices which could have been

developed by the transformation route. Otherwise, the discussion of some novel aspects such as fiber brittle failure or the comparison of nonlinear materials with linear ones would have been incomprehensible. To summarize those models which could have been introduced by the transformation route, it can be stated that the inverse of the composite linear elastic modulus can be used to represent a linear steady state creep coefficient when the kinematics are switched from strain to strain rate in the relevant model.

No attempt has been made to discuss in a comprehensive manner models which are based on finite element calculations or other numerical analyses. Only some results of Schmauder and McMeeking[10] for transverse creep of power law materials were discussed. The main reason that such analyses were in general omitted is that they tend to be in the literature for a small number of specific problems and little has been done to provide comprehensive results for the range of parameters which would be technologically interesting - i.e. volume fractions of reinforcements from zero to 60%, reinforcement aspect ratios from 1 to 10^6, etc.. Attention was restricted in this chapter to cases where comprehensive results could be stated. In almost all cases, this means that only approximate models were available for use. Furthermore, numerical analyses for creep in the literature tend to be for metal matrix composites and so use creep indices which are rather high for ceramic matrices. Indeed, this latter fault applies to the finite element calculations so far performed by Schmauder and McMeeking[10] even though there was an attempt to be comprehensive. Those finite element results which are available in the literature such as the work by Dragone and Nix[24] are very valuable and provide accurate results for a number of specific cases against which the more approximate models discussed in this chapter can be checked. A limited amount of this checking for a single model has been done by McMeeking[23] in comparison with the Dragone and Nix[24] calculations. The results show that the approximate model is reasonably accurate. However, more extensive checking of the approximate models is

required and to do this in many cases it will be necessary to create the finite element analyses.

Also omitted from this chapter was any attempt to compare the models with experiments. This would require a lengthy chapter by itself and some comparisons are given elsewhere in this book. In addition, limited data are available for such comparisons in general. For metals, there are some successful comparisons[5] and some unsuccessful ones[22]. It seems that when there is good knowledge of the material properties and the operating mechanisms, the right model can be chosen, but lack of such knowledge makes it virtually impossible to identify which features must be present in the model. Thus, multidisciplinary work is necessary to understand the microstructure, to identify the mechanisms and to select and develop the appropriate model. An example of such an effort, although for the closely related subject of the plastic yielding of a metal matrix composite, is the work of Evans, Hutchinson and McMeeking[25], where careful control of the metallurgy and the experiments was used to confirm the validity of the models.

Acknowledgment

This research was performed while the author was supported by the DARPA University Research Initiative at the University of California, Santa Barbara contract ONR N00014-86-K0753.

References

1 M. F. Ashby and H. Frost, Deformation Maps, Pergamon Press, Oxford (1982).

2 R. M. Christensen, Theory of Viscoelasticity: An Introduction, Academic Press, New York (1982).

3 R. A. Schapery, "On the Characterization of Nonlinear Viscoelastic Materials," Polymer Engineering and Science, **9**, 295-310 (1969).

4 R. Hill, "Elastic Properties of Reinforced Solids: Some Theoretical Principles," J. Mech. Phys. Solids, **11**, 357-72 (1963).

5 M. McLean, "Creep Deformation of Metal-Matrix Composites," Composites Science and Technology, **23**, 37-52 (1985).

6 D. McDanels, R. A. Signorelli and J. W. Weeton, NASA Report No. TND-4173, NASA Lewis Research Center, Cleveland, Ohio (1967).

7 R. M. Christensen, Mechanics of Composite Materials, Wiley-Interscience, New York (1979).

8 S. Jannson and F. A. Leckie, "Mechanical Behavior of a Continuous Fiber-Reinforced Aluminum Matrix Composite Subjected to Transverse and Thermal Loading," Journal of the Mechanics and Physics of Solids, **40**, 593-612 (1992).

9 G. Bao, J. W. Hutchinson and R. M. McMeeking, "Particle Reinforcement of Ductile Matrices against Plastic Flow and Creep," Acta Metallurgica et Materialia, **39**, 1871-1882 (1991).

10 S. Schmauder and R. M. McMeeking, unpublished work (1992).

11 J. E. Ashton, J. C. Halpin and P. H. Petit, Primer on Composite Materials Analysis, Technomic Publishing, Stanford, CT (1969).

12 J. M. Whitney and R. L. McCullough, Micromechanical Materials Modeling, (Delaware Composites Design Encyclopedia, Vol. 2), Technomic Publishing, Lancaster, PA (1989).

[13] S. L. Phoenix, P. Schwartz and H. H. Robinson IV, "Statistics for the Strength and Lifetime in Creep-Rupture of Model Carbon/Epoxy Composites," Composites Science and Technology, **32**, 81-120 (1988).

[14] D. C. Lagoudas, C.-Y. Hui and S. L. Phoenix, "Time Evolution of Overstress Profiles Near Broken Fibers in a Composite with a Viscoelastic Matrix," International Journal of Solids and Structures, **25** 45-66 (1989).

[15] H. Otani, S. L. Phoenix and P. Petrina, "Matrix Effects on Lifetime Statistics for Carbon Fibre-Epoxy Microcomposites in Creep Rupture," Journal of Materials Science, **26**, 1955-1970 (1991).

[16] W. A. Curtin, "Theory of Mechanical Properties of Ceramic Matrix Composites," Journal of the American Ceramic Society, **74**, 2837-2845 (1991).

[17] F. Hild, J.-M. Domergue, F. A. Leckie and A. G. Evans, "Tensile and Flexural Ultimate Strength of Fiber-Reinforced Ceramic-Matrix Composites," to be published (1992).

[18] S. T. Mileiko, "Steady State Creep of a Composite Material with Short Fibres," Journal of Materials Science, **5**, 254-261 (1970).

[19] H. Lilholt, "Creep of Fibrous Composite Materials," Composites Science and Technology, **22**, 277-294 (1985).

[20] D. McLean, "Viscous Flow of Aligned Composites," Journal of Materials Science, **7**, 98-104 (1972).

[21] A. Kelly and K. N. Street, "Creep of Discontinuous Fibre Composites II, Theory for the Steady State," Proceedings of the Royal Society, London, **A328**, 283-293 (1972).

[22] T. G. Nieh, "Creep Rupture of a Silicon Carbide Reinforced Aluminum Composite," Metallurgical Transactions A, **15A**, 139-146 (1984).

[23] R. M. McMeeking, "Power Law Creep of a Composite Material Containing Discontinuous Rigid Aligned Fibers," to appear in International Journal of Solids and Structures (1992).

[24] T. L. Dragone and W. D. Nix, "Geometric Factors Affecting the Internal Stress Distribution and High Temperature Creep Rate of Discontinuous Fiber Reinforced Metals," Acta Metallurgica et Materialia, **38**, 1941-1953 (1990).

[25] A. G. Evans, J. W. Hutchinson and R. M. McMeeking, "Stress-Strain Behavior of Metal Matrix Composites with Discontinuous Reinforcements," Scripta Metallurgica et Materialia, **25**, 3-8 (1991).

Figure Captions

Fig. 1 A uniaxially reinforced fiber composite.

Fig. 2 Threshold for long term creep of a uniaxially reinforced composite as a function of Weibull modulus for the fiber strength distribution.

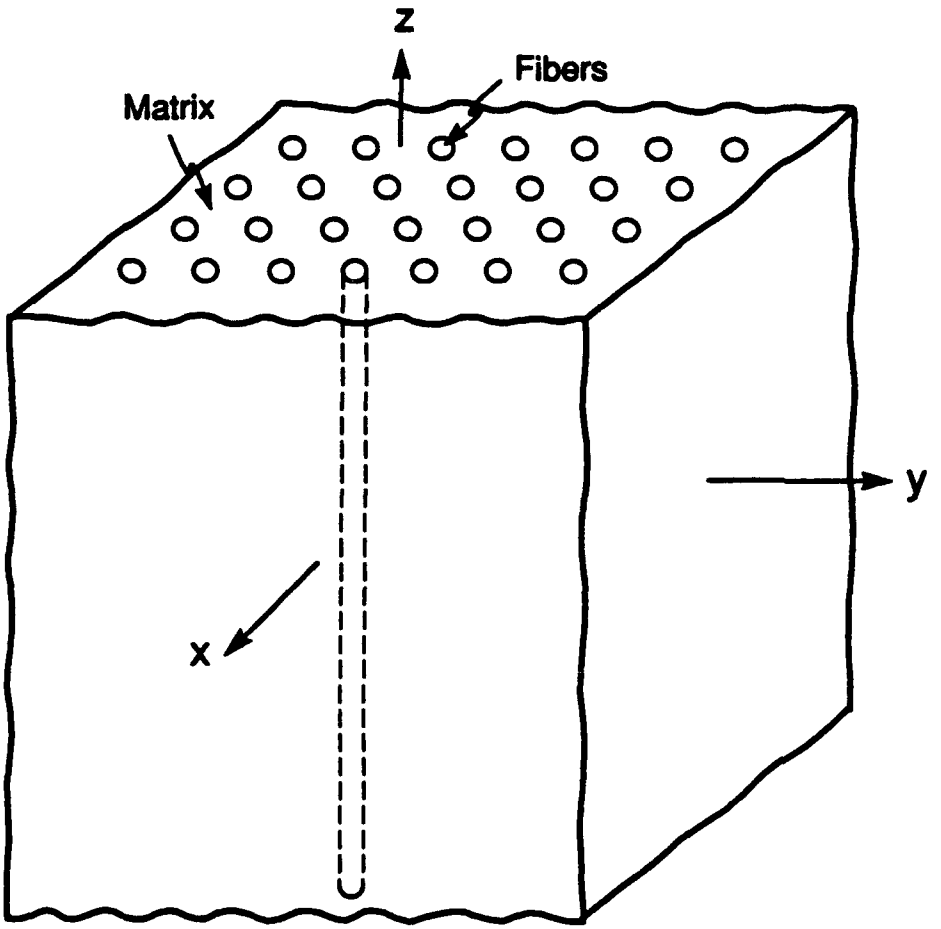

Fig. 1

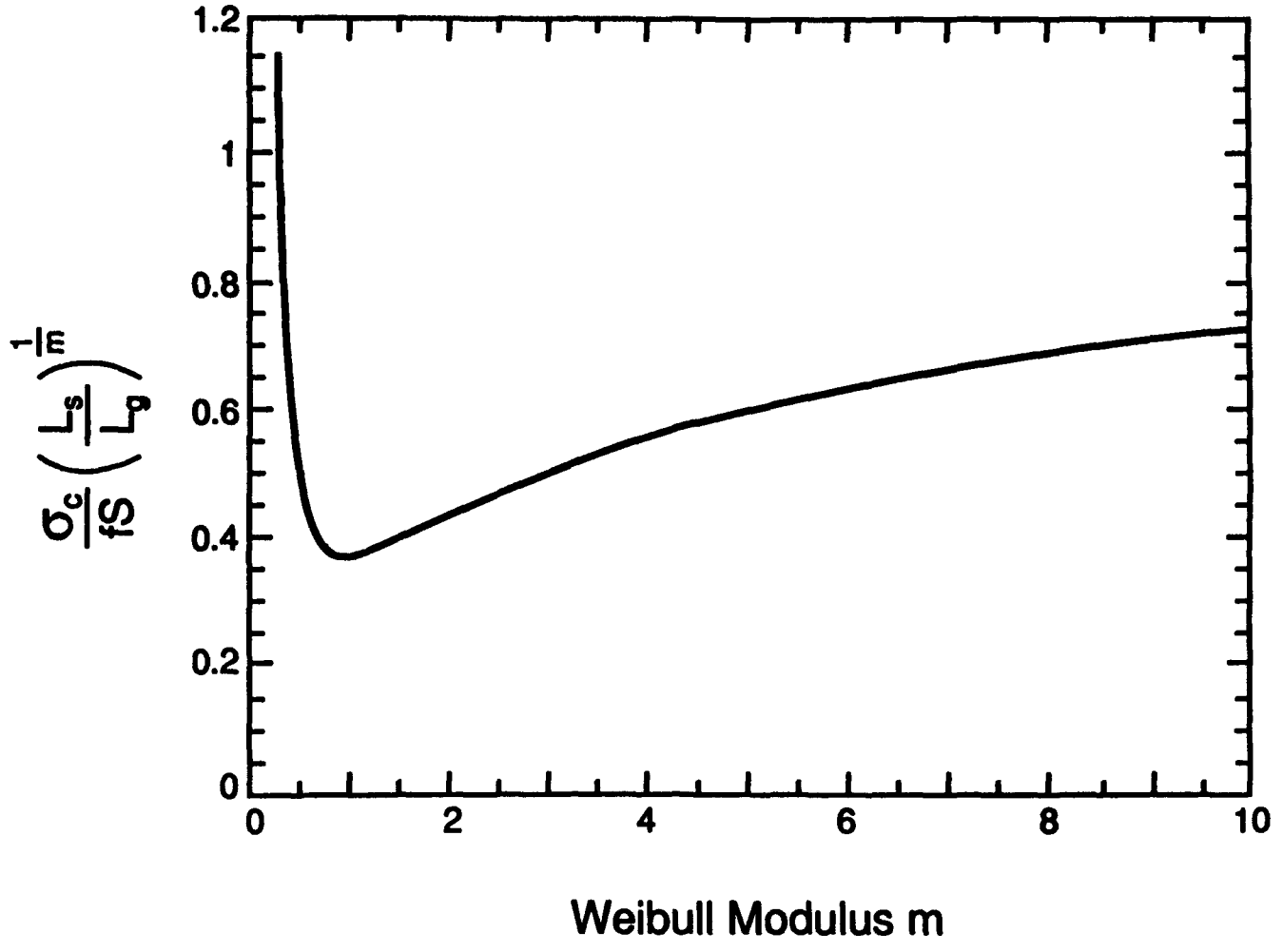

Fig. 2

POWER LAW CREEP WITH INTERFACE SLIP AND DIFFUSION IN A COMPOSITE MATERIAL

Kitae T. Kim* and Robert M. McMeeking**

*Department of Mechanical Engineering, Pohang Institute of Science and Technology, Pohang 790-600, Korea

**Department of Mechanical and Environmental Engineering University of California, Santa Barbara, CA 93106, USA

Submitted to Mechanics of Materials

September, 1993

Summary The leading order solution for the power law creep of a matrix around a rigid finite fiber is developed. The matrix is well bonded to the fiber but the interface is assumed to be capable of slip with a drag which is linearly proportional to the slip velocity. In addition, mass transport by stress driven diffusion is assumed also to be possible at the interface between the fiber and the matrix. It is found that when there is no slip or interface mass transport, the composite has a high creep strength compared to the matrix. However, both slip and mass transport acting individually or together are capable of reducing the creep strength of the composite material. If slip occurs very readily or mass transport is very rapid or both, the creep strength of the composite can fall below that of the pure matrix material. It is notable that mass transport and interface slip with a linear rheology have an identical effect on the creep strength of the composite material.

Introduction

Cell models have been used extensively to represent the mechanical properties of fiber or whisker reinforced materials [1-5]. Kelly and Street [1] presented a model for the power law creep of a material with aligned fibers. McMeeking [2] improved this model by analyzing the matrix flow field more accurately. In both of these treatments, the interface between the matrix and the fiber was taken to be well bonded with no slip or to slip in a manner controlled by the rheology of the matrix. Another possibility allowed for in these treatments was an interphase between the matrix and the fiber but with the same power law exponent as the matrix. On the other hand, it is desirable to have models in which slip and diffusion is allowed for at the fiber-matrix interface. In addition, many composite materials have an interphase between the matrix and the

fiber with very different creep properties. The purpose of this paper is to provide an enhancement of McMeeking's [2] model to feature interface slip and diffusion and the influence of a distinct interphase. A previous treatment of these features by Goto and McLean [3] was based on the original Kelly and Street [1] model without the benefit of the improved flow fields analyzed by McMeeking [2].

Debonding is not allowed for in the model presented here. The main reason is that debonding occurs primarily on the fiber end. Mileiko [6] and Lilholt [7] have developed models in which the end of the fiber is debonded and gaping occurs between the fiber end and the matrix during creep deformation. The degree of freedom permitted by this allows matrix deformation to occur in simple shear between adjacent reinforcements. As a result, the flow field in the matrix is quite different from that computed by McMeeking [2]. The latter work involves a flow field in which material is squeezed out from between reinforcements, extruded around the fiber end and deposited there. This eliminates gaping at the fiber end and preserves incompressibility. Since the results in this paper represent an extension of McMeeking's [2] work, it is necessary to invoke the hypothesis of a strong bond between the fiber and the matrix. Thus, the situation for which the model in this paper is most relevant is a fiber with a strong interphase strongly bonded to the fiber and matrix but with creep properties distinct from the matrix.

The analysis follows closely the method of McMeeking [2] and generates the leading order solution in an asymptotic analysis. Background to this can be found in the squeeze film solution of Johnson [8]. The small parameter in the analysis is b/L as shown in Fig. 1. Since $2b$ represents the center to center spacing of neighboring parallel fibers, the ratio b/L is approximately equal to $1/(\sqrt{f}\,\lambda)$ where f is the volume fraction of fibers and $\lambda = L/a$ is the aspect ratio of the fibers. Thus for the solution to be

asymptotically valid, the aspect ratio of the fibers should be large and the volume fraction of the fibers must be finite and such that $\sqrt{f}\,\lambda$ is large.

An additional feature of the approach is that in the estimation of the creep strength of the composite material, contributions due to flow around the fiber ends are neglected. This can be justified as follows. The most significant effect of the fiber ends is taken into account, namely the way that the well bonded fiber end requires material to be squeezed out from the region adjacent to the side of the fiber and extruded around the fiber end to flow into the region beyond the reinforcement. The pattern of flow in the fiber end region is not very important to the results obtained because the fiber end regions typically represent a small fraction of the total volume of the composite material, especially since λ must be large for the analysis to be valid. Thus the creep dissipation of the composite material will be dominated by the dissipation which takes place in the regions adjacent to the side of the fiber and the dissipation in the fiber end region can be neglected. Thus it is sufficient to analyze in detail only the flow in the region adjacent to the side of the fiber. This is the axisymmetric volume with section ABCD shown in Fig. 1.

Formulation

The geometry of the problem is shown in Fig. 1. The fiber is rigid with length 2L and diameter 2a and it is assumed that all fibers have the same aspect ratio. The matrix creeps with a power law rheology and is incompressible. Only steady state creep is considered. The unit cell with diameter 2b and a length somewhat longer than 2L is chosen so that the ratio of the volume of the fiber to the volume of the unit cell equals the volume fraction of fibers in the composite material. The exact relationship of a/b to

the composite volume fraction depends on how the fibers are packed into the matrix and on the end to end and side to side spacing of the fibers [2].

The unit cell deforms in such a way that its cylindrical shape is preserved. The axial strain rate is $\dot{\varepsilon}$ and by incompressibility the transverse strain rate is $-\dot{\varepsilon}/2$. Therefore the radial velocity at $r = b$ on the side of the unit cell is $-\dot{\varepsilon}\, b/2$ as indicated in Fig. 1. The shear stress on the side of the unit cell is zero. However, the radial stress is not uniformly zero there, but is zero on average. This ensures that the net transverse stress is zero so that the only applied load is the axial stress σ_a, as shown in Fig. 1.

The boundary conditions on the fiber surface involve slip of the matrix relative to the fiber, so that the axial velocity on the fiber surface can be nonzero. A linear rheology for the resulting drag will be assumed. This can be justified in terms of an interphase which is creeping in the linear regime controlled by Nabarro-Herring or Coble creep [9]. The creep behavior of the interphase can be expressed then as $\tau = \eta\, \dot{\gamma}$ where τ is the shear stress, η is the viscosity and $\dot{\gamma}$ is the shear strain rate. The thickness of the thin interphase is t and therefore the shear strain rate in the interphase is $v_z(a)/t$ where $v_z(a)$ is the axial velocity of the matrix material immediately adjacent to the interphase. It follows that the slip boundary condition at the fiber surface can be stated as

$$\sigma_{rz} = \mu\, v_z \tag{1}$$

where σ_{rz} is the shear stress at the fiber surface and $\mu = \eta/t$. If a no slip condition prevails (i.e. no interphase), the boundary condition becomes $v_z = 0$ on the fiber surface.

Mass transport by diffusion is assumed to be possible at the interface between the fiber and the matrix. The process is driven by stress differences with material

traveling from compressive or low tensile stress regions to high tensile stress locations. The process is assumed to occur fastest on the interface between different materials or in the interphase between the fiber and the matrix. Consequently, diffusion processes in the matrix and in the fiber are neglected.

The end of the fiber will be under the greatest tension. However, the flow of the matrix around the fiber end is neglected in the model and it follows that diffusion to the end of the fiber should be neglected as well. Consequently, diffusion processes only on the side of the fiber will be included in the model. The mass transport rate in the z direction at the interface is given by

$$j_z(z) = \mathcal{D}\frac{\partial \sigma_{rr}(a,z)}{\partial z} \tag{2}$$

where j_z is the volume of transported material passing through a unit length of the fiber surface in unit time, σ_{rr} (a, z) is the radial stress on the surface of the fiber, $\mathcal{D}$ is a diffusion coefficient for the interface given by

$$\mathcal{D} = \frac{D_b \delta_b \Omega}{kT} \tag{3}$$

where D_b is the interface or interphase diffusion coefficient, δ_b is an effective interface thickness or is the interphase thickness, k is Boltzmann's constant and T is the absolute temperature. Volume conservation requires

$$v_r(a,z) + \frac{dj_z(z)}{dz} = 0 \tag{4}$$

where v_r (a, z) is the velocity at which the matrix moves away from the fiber surface. It follows that

$$v_r(a,z) = -\mathcal{D}\frac{d^2\sigma_{rr}(a,z)}{dz^2} \tag{5}$$

which is the remaining boundary condition on the fiber surface. If mass transport is inactive, the boundary condition is v_r (a, z) = 0.

Analysis

The domain of the problem is the axisymmetric region with section ABCD in Fig. 1 ($a \le r \le b$; $0 \le z \le L$). Considering the boundary conditions in Fig. 1, we assume [2]

$$\sigma_{rr} \approx \sigma_{\theta\theta} \approx \sigma_{zz} \approx \sigma,\ \sigma_{rz} << \sigma \tag{6}$$

which can be justified by asymptotic analysis when b/L is small. It follows that the term $\partial\sigma_{rz}/\partial z$ can be neglected and, the governing equilibrium equation in a cylindrical coordinate system reduces to

$$\frac{\partial\sigma_{rz}}{\partial r} + \frac{\sigma_{rz}}{r} + \sigma'(z) = 0 \tag{7}$$

where σ is the hydrostatic part of the stress and σ' (z) denotes $d\sigma/dz$. Note that $\sigma = \sigma$ (z) in (7) results from the radial equilibrium equation upon use of (6).

The matrix obeys power law creep with an incompressible rheology given by

$$\dot{\varepsilon}_{ij} = \frac{3}{2}\dot{\varepsilon}_o\left(\frac{\bar{\sigma}}{\sigma_o}\right)^{n-1}\frac{s_{ij}}{\sigma_o} \tag{8}$$

where $\dot{\varepsilon}_{ij}$ is the strain rate, s_{ij} is the deviatoric stress given by

$$s_{ij} = \sigma_{ij} - \sigma\,\delta_{ij} \tag{9}$$

$\bar{\sigma}$ is the effective stress such that

$$\bar{\sigma} = \sqrt{\frac{3}{2}s_{ij}\,s_{ij}} \tag{10}$$

and σ_o and $\dot{\varepsilon}_o$ are material constants. Note that to leading order the effective stress in this problem reduces to

$$\bar{\sigma} = \sqrt{3}\,\sigma_{rz} \tag{11}$$

given that σ_{rz} is positive. Thus, the creep law can be written as

$$\frac{\partial v_z}{\partial r} = \sqrt{3}\,\dot{\varepsilon}_o\left(\frac{\sqrt{3}\,\sigma_{rz}}{\sigma_o}\right)^n \tag{12}$$

where the term $\partial v_r/\partial z$ is ignored due to smallness [2]. Incompressibility provides

$$\frac{\partial v_r}{\partial r} + \frac{v_r}{r} + \frac{\partial v_z}{\partial z} = 0 \tag{13}$$

The boundary conditions on AB ($z = 0$) are

$$v_z(r, 0) = 0 \tag{14}$$

$$\sigma_{rz}(r, 0) = 0. \tag{15}$$

On AD ($r = a$) one boundary condition is eq. (5) repeated here for completeness

$$v_r(a,z) = -\mathcal{D}\frac{\partial^2 \sigma_{rr}(a,z)}{\partial z^2} \tag{16}$$

if the interface diffusion is considered, otherwise $v_r(a, z) = 0$, while the slip condition from eq. (1) becomes

$$v_z(a, z) = \sigma_{rz}(a, z)/\mu \tag{17}$$

where $\mathcal{D}$ is the interface diffusion parameter and μ is the interface drag parameter.

On BC ($r = b$) the boundary conditions are

$$\sigma_{rz}(b, z) = 0 \tag{18}$$

and

$$v_r(b,z) = -\frac{b\dot{\epsilon}}{2}. \tag{19}$$

An additional condition on r = b is that

$$\int_0^L \sigma(z)\,dz = 0 \tag{20}$$

to ensure that the transverse stress is approximately zero. The approximation arises because the cell extends a small distance above CD, but that portion is neglected.

Note that no explicit boundary conditions are posed for CD. This is consistent with the neglect of the details of flow around the fiber end. The average axial stress at CD will be of interest and determines σ_a. The creep strength S of the composite material is defined as the average axial stress in the composite at a given axial strain rate divided by the stress in the matrix alone at the same axial strain rate. Thus,

$$S = \frac{\sigma_a(\dot{\epsilon})}{\left[\dot{\epsilon}/\left(\dot{\epsilon}_o/\sigma_o^n\right)\right]^{1/n}} = \frac{\sigma_a(\dot{\epsilon})/\sigma_o}{\left(\dot{\epsilon}/\dot{\epsilon}_o\right)^{1/n}}. \tag{21}$$

Solution

Integration of (7) subject to eq. (18) gives

$$\sigma_{rz} = \frac{b}{2}\,\sigma'(z)\left(\frac{b}{r} - \frac{r}{b}\right). \tag{22}$$

Note that $\sigma'(z)$ is positive for $z > 0$ and thus so is σ_{rz}. Consequently, eq. (12) shows that

$$\frac{\partial v_z}{\partial r} = \sqrt{3}\,\dot{\varepsilon}_o\left(\frac{\sqrt{3}\,b\sigma'(z)}{2\sigma_o}\right)^n\left(\frac{b}{r}-\frac{r}{b}\right)^n. \tag{23}$$

Integration of eq. (23) with (17) provides

$$v_z(r,z) = \frac{b}{2\mu}\left(\frac{b}{a}-\frac{a}{b}\right)\sigma'(z) + \sqrt{3}\,\dot{\varepsilon}_o\left(\frac{\sqrt{3}\,b\sigma'(z)}{2\sigma_o}\right)^n\int_a^r\left(\frac{b}{\rho}-\frac{\rho}{b}\right)^n d\rho. \tag{24}$$

Differentiation of eq. (24) with respect to z provides the axial strain rate which is inserted into the incompressibility condition (13). Integration of eq. (13) with respect to r and use of eq. (19) gives

$$\begin{aligned} v_r(r,z) = {} & \frac{3^{\frac{n+1}{2}}\,\dot{\varepsilon}_o\,nb}{2\sigma_o^n\,r}\left(\frac{b\sigma'(z)}{2}\right)^{n-1}\sigma''(z)\int_r^b\rho\int_a^\rho\left(\frac{b}{\xi}-\frac{\xi}{b}\right)^n d\xi\,d\rho \\ & + \frac{b\sigma''(z)}{4\mu r}\left(b^2-r^2\right)\left(\frac{b}{a}-\frac{a}{b}\right) - \frac{b^2\dot{\varepsilon}}{2r} \end{aligned} \tag{25}$$

The boundary condition specifying the interface diffusion, eq. (16), i.e.,

$$v_r(a,z) = -\mathcal{D}\frac{\partial^2\sigma_{rr}(a,z)}{\partial z^2} \approx -\mathcal{D}\frac{\partial^2\sigma(z)}{\partial z^2} = -\mathcal{D}\sigma''(z), \tag{26}$$

then provides the nonlinear differential equation

$$H\left(\frac{a}{b},n\right)\frac{b^{n+3}\,\dot{\varepsilon}_o}{2a}\frac{d}{dz}\left[\frac{\sigma'(z)}{\sigma_o}\right]^n + \left\{\mathcal{D}+\frac{\left(1-a^2/b^2\right)^2b^2}{4\mu\left(a^2/b^2\right)}\right\}\sigma''(z) = \frac{b^2\dot{\varepsilon}}{2a} \tag{27}$$

where

$$H\left(\frac{a}{b},n\right) = \frac{3^{\frac{n+1}{2}}}{2^n}\int_{a/b}^{1}\eta\int_{a/b}^{\eta}\left(\frac{1}{\xi}-\xi\right)^n d\xi\, d\eta \tag{28}$$

The differential equation can be restated as

$$\frac{d}{d\hat{z}}\left[\frac{d\hat{\sigma}(\hat{z})}{d\hat{z}}\right]^n + C\frac{d^2\hat{\sigma}(\hat{z})}{d\hat{z}^2} = 1 \tag{29}$$

where $$\hat{z} = \frac{z}{L} \tag{30}$$

$$\hat{\sigma} = \left[2H\left(\frac{a}{b},n\right)\frac{\dot{\varepsilon}_o b}{\dot{\varepsilon} L}\right]^{\frac{1}{n}}\frac{b\sigma}{L\sigma_o} \tag{31}$$

and

$$C = 2\left[\frac{\mathcal{D}}{b^2} + \frac{\left(1-a^2/b^2\right)^2}{4\mu a^2/b^2}\right]\frac{\sigma_o}{\dot{\varepsilon} L}\frac{a}{b}\left[\frac{\dot{\varepsilon} L}{2H\left(\frac{a}{b},n\right)\dot{\varepsilon}_o b}\right]^{\frac{1}{n}} \tag{32}$$

which is inherently positive. It can be seen that in the normalized variables, all solutions are controlled by a single parameter, C, which accounts for geometry, size, matrix creep properties, interface properties and the axial strain rate.

Eq. (29) can be integrated once and symmetry with respect to $\hat{z}$ invoked to give

$$\left[\frac{d\hat{\sigma}(z)}{d\hat{z}}\right]^n + C\frac{d\hat{\sigma}(z)}{d\hat{z}} = \hat{z}. \tag{33}$$

Linear case: When the matrix flows with a linear rheology (i.e. Nabarro-Herring or Coble creep) the creep exponent n = 1. The solution to eq. (33) is then

$$\hat{\sigma}(\hat{z}) = \frac{3\hat{z}^2 - 1}{6(1+C)} \tag{34}$$

where (20) has been used to determine the constant of integration. Thus, the axial and radial stress vary quadratically parallel to the fiber axis and are compressive near the center of the fiber at $\hat{z} = 0$.

The applied stress will be taken to be approximately equal to the matrix stress at $\hat{z} = 1$ (i.e. at z = L). This neglects the relatively small increment of stress induced by flow of the matrix around the fiber end. The normalized stress at $\hat{z} = 1$ is evaluated to be

$$\hat{\sigma}(1) = \frac{1}{3(1+C)}. \tag{35}$$

The result for $3\hat{\sigma}(1)$ is plotted against C in Fig. 2. By a balance of axial forces, the normalized fiber stress is

$$\hat{\sigma}_f(\hat{z}) = \frac{b^2/a^2}{6(1+C)}\left[2 - \left(1 - \frac{a^2}{b^2}\right)\left(3\hat{z}^2 - 1\right)\right] \tag{36}$$

where

$$\hat{\sigma}_f = 2H\left(\frac{a}{b},1\right)\frac{\dot{\varepsilon}_o b^2 \sigma_f}{\dot{\varepsilon} L^2 \sigma_o} \tag{37}$$

with $\sigma_f(z)$ the axial fiber stress. That is, $\hat{\sigma}_f$ is normalized in the same way that $\hat{\sigma}$ is (see eq. (31)). The fiber stress therefore rises quadratically from the applied level at the fiber end to a maximum value of

$$\hat{\sigma}_f^{max} = \frac{3b^2/a^2 - 1}{6(1+C)} \tag{38}$$

at the center of the fiber at $\hat{z} = 0$. It follows that the maximum fiber stress is always $(3\,b^2/a^2 - 1)/2$ times the applied stress irrespective of the state of the interface. Note that a^2/b^2 can be interpreted in terms of the fiber volume fraction. If the fibers are very long with little space between them end to end then a^2/b^2 is approximately equal to the volume fraction. Other estimates can be made for a^2/b^2 depending on the geometry of packing [1,2].

The applied stress is given by eq. (35), restated as

$$\sigma_a = \frac{\frac{1}{6}(L/b)^2\,\dot{\varepsilon}}{\frac{\dot{\varepsilon}_o}{\sigma_o}H\left(\frac{a}{b},1\right) + \left[\frac{\mathcal{D}}{b^2} + \frac{\left(1-a^2/b^2\right)^2}{4\mu\,a^2/b^2}\right]\frac{a}{b^2}} \tag{39}$$

with $$H\left(\frac{a}{b},1\right) = \frac{3}{2}\left[\frac{a^2}{2b^2} - \frac{1}{2}\ln\frac{a}{b} - \frac{3}{8} - \frac{a^4}{8b^4}\right]. \quad (40)$$

It should be noted that this estimate is only valid for large values of L/b and therefore should not be used when L is comparable to b. It is also not suitable for a = 0 since the matrix behavior is not recovered in that limit. Correction terms have been suggested by McMeeking [2] for the case with the perfect interface to allow for recovery of the pure matrix limit.

A correction term is desirable to cover the situation in which the interface drag disappears (i.e. $\mu \rightarrow 0$) or the interface diffusion becomes very fast ($\mathcal{D} \rightarrow \infty$) or both. The results of McMeeking [2] and a simple model for axial straining of the matrix indicate that when the right hand side of eq. (39) goes to zero, σ_a should be given approximately by

$$\sigma_a = \frac{\sigma_o \dot{\varepsilon}}{\dot{\varepsilon}_o}\left(1 - \frac{a^2}{b^2}\right) \quad (41)$$

(Note: the formula in eq. (41) neglects constraint when there is no mass transport or drag in which case σ_a would be somewhat higher.) The model of eq. (41) means that the composite material is weaker than the matrix by itself which would sustain a stress equal to $\sigma_o \dot{\varepsilon}/\dot{\varepsilon}_o$. With no drag at the fiber-matrix interface or with infinitely fast mass transport, the fibers simply serve to eliminate matrix material and therefore weaken the composite. For a model which behaves sensibly when μ goes to zero, the right hand sides of eq. (39) and (41) can simply be added.

Inspection of eq. (39) reveals that the creep strength of the material is always quadratic in L/b so that long fibers promote creep resistance no matter the state of the interface. When there is no interface diffusion and no interface slip, the creep strength is

$$S_o = L^2/6\, b^2\, H\,(a/b,1) \tag{42}$$

which is the ratio of the applied stress for the composite material to the applied stress in the pure matrix at the same strain rate. When either interface diffusion or interface slip or both are active, the creep strength is degraded. A similar effect was identified by Sofronis and McMeeking [10] in particulate composites. The extent of the effect depends on the magnitudes of $\mathcal{D}$ and μ. It is expected that these parameters will be temperature dependent as will be the effective matrix viscosity $\sigma_o/\dot{\varepsilon}_o$. However, the activation energies for $\sigma_o/\dot{\varepsilon}_o$, $\mathcal{D}$ and μ can be expected to be different in general and so their relative magnitudes will depend on temperature. Therefore, temperature is expected to be an important consideration in the extent of degradation of the creep strength by interface diffusion and slip.

An important conclusion to be drawn from eq. (39) is that the effect on creep strength of interface diffusion and interface slip is the same. Furthermore, only one mechanism need be active for the creep strength to be degraded. Thus, one cannot automatically say that interface diffusion is responsible for loss of creep strength in fiber reinforced materials at high temperatures as is sometimes stated [11,12] because it could equally well be due to interface slip. An experiment identifying slip or diffusion would be required to distinguish the mechanisms.

If either mass transport is very rapid so that $\mathcal{D}$ is very large or the drag generated by slip is very low so that μ is very small, the denominator in eq. (39) will be very large. As a result, the creep strength of the composite material will be low, with the effect of the fiber length nullified by interface slip and mass transport. This makes it clear that the creep strength of the composite material is critically dependent on the integrity of the interface between the matrix and the fiber.

Quadratic case: When n = 2, the differential eq. (33) can be solved quite straight-forwardly. The solution is

$$\hat{\sigma}(\hat{z}) = \frac{C}{4}(1-2\hat{z}) + \frac{1}{12}\left(C^2+4\hat{z}\right)^{\frac{3}{2}} - \frac{1}{120}\left(C^2+4\right)^{\frac{5}{2}} + \frac{C^5}{120}. \tag{43}$$

It follows that the applied stress is given by

$$\sigma_a = \frac{\sqrt{2}\,\sigma_o\left(\frac{\dot{\varepsilon}}{\dot{\varepsilon}_o}\right)^{\frac{1}{2}}\left(\frac{L}{b}\right)^{\frac{3}{2}}}{5\left[H\left(\frac{a}{b},2\right)\right]^{\frac{1}{2}}}\left\{-\frac{5C}{8}+\frac{1}{48}\left(C^2+4\right)^{\frac{3}{2}}\left(6-C^2\right)+\frac{1}{48}\,C^5\right\} \tag{44}$$

where $$H\left(\frac{a}{b},2\right) = \frac{3\sqrt{3}}{4}\left[-\frac{8}{5}+\frac{1}{10}\left(\frac{a}{b}\right)^5-\frac{1}{2}\left(\frac{a}{b}\right)^3+\frac{3}{2}\frac{a}{b}+\frac{1}{2}\frac{b}{a}\right]. \tag{45}$$

Since the matrix alone would sustain a stress of $\sigma_o(\dot{\varepsilon}/\dot{\varepsilon}_o)^{1/2}$, the creep strength of the composite can be easily ascertained. It can be seen that the creep strength of the

composite material is proportional to $(L/b)^{3/2}$ irrespective of the state of the interface. This creep strength, in normalized form, is plotted against C in Fig. 2. The result presented in eq. (44) and plotted in Fig. 2 is valid only if L/b is sufficiently large to ensure that the asymptotic limit is relevant. It is suggested, but not proved, that $L/b \geq 10$ would guarantee the validity of eq. (44) and Fig. 2.

From eq. (2), it can be seen that when there is no interface diffusion and no slip, $C = 0$. The term in eq. (44) in the curly brackets is then unity, so that the term outside the curly brackets in eq. (44) is the creep strength of the composite with a perfect interface. When interface diffusion is active or slip is possible or both, C is finite and increases in magnitude as the mass transport rate goes up (i.e. $\mathcal{D}$ increases) and as slip becomes easier to induce (i.e. μ decreases). Thus, the plot in Fig. 2 shows the creep strength of the composite material versus the degree of interface activity as measured by C. However, the form of C as stated in eq. (32) shows clearly that interface diffusion and interface slip are indistinguishable as far as their effect on the creep strength of the composite material are concerned, since $\mathcal{D}$ and $1/\mu$ both cause a proportional increase in C.

It should be borne in mind that C is dependent on the strain rate $\dot{\varepsilon}$ of the composite material as well as the interface diffusion and slip parameters. In the quadratic case, C is inversely proportional to the square root of the strain rate. Consequently, when the stress is high, so that the strain rate is also high, the strength of the composite material will be more like that of the case where the interface is free of diffusion and is not slipping. At low stress, the strain rate will be low and so C will be high leading to a reduction in the creep strength of the material. It is apparent that when the strain rate is high, the nonlinearity of the matrix creep response causes the matrix contribution to dominate the creep strength. Over a narrow range of stress, the

transition from interface dominated response to matrix dominated response can be interpreted as changing the creep index of the composite material to less than that of the matrix material. It is sometimes observed in experiments that the creep index of a composite material with large rigid reinforcements differs from that of the matrix [13] although typically the index for the composite is higher than that of the matrix rather than lower. McMeeking [14] has rationalized the higher index of composite materials in terms of fiber failure (although other damage mechanisms would have a similar effect) and interface diffusion and slip with a linear rheology is now seen to have a contrary effect.

When C is very large, stretching of the matrix in the axial direction will dominate shearing. As a consequence, the creep strength of the composite will no longer be given by eq. (44) which will be negligibly small. Instead, an estimate of the creep strength when $C \to \infty$ can be given by

$$\sigma_a = \sigma_o \left(\dot{\varepsilon}/\dot{\varepsilon}_o\right)^{\frac{1}{2}} \left(1 - a^2/b^2\right) \tag{46}$$

which is based on uniform axial straining of the matrix material. As before, this estimate neglects constraint when there is no interface drag but also no diffusion. An estimate of the creep strength over the whole range of C can therefore be made by adding eq. (44) to eq. (46).

Nonlinear Cases For several integer values of n, we obtained numerical solutions for eq. (33). A shooting method was used to find a solution satisfying eq. (20) with integration of the equation carried out by a 4th-order Runge-Kutta method with an

interval halving technique. The numerical solutions for n = 2 were compared with the analytical solution of eq. (43). In addition, for all values of n, the solution with C = 0 was compared with the analytical result of McMeeking [2]. The agreement between numerical and analytical solutions was very good.

The strength of the composite material in each case was taken to be given by $\sigma(z)$ at z = L. The results are plotted in Fig. 2 as a function of C for several values of n. All of the comments previously made in the context of n = 2 apply to the results for other values of n plotted in Fig. 2. Allowance must be made for the different values of n involved; e.g. C is proportional to $\dot{\varepsilon}^{\frac{1}{n}-1}$, but that still means that C varies inversely with the strain rate (except when n = 1). In addition, when $C \to \infty$ the creep strength can be estimated by

$$\sigma_a = \sigma_o (\dot{\varepsilon}/\dot{\varepsilon}_o)^{1/n} \quad (1 - a^2/b^2) \tag{47}$$

instead of through eq. (46). Therefore, the discussion of the results for n = 2 in the previous section serves also as a discussion of the results for the other values of n.

Creep Strength of Composites

The results plotted in Fig. 2, although concise, are difficult to interpret since both the parameters of the ordinate and the abscissa are complicated. To aid in interpretation of the results, some specific cases are illustrated in Figs. 3-5. The creep strength is

$$S = \frac{\sigma_a}{\sigma_o}\left(\frac{\dot{\varepsilon}_o}{\dot{\varepsilon}}\right)^{\frac{1}{n}} \tag{48}$$

and is the ratio of the stress in the composite material divided by the stress in the pure matrix at the same strain rate. For simplicity, it has been assumed that $S \rightarrow 1$ when diffusion is very rapid or interface slip occurs with very little drag. That is, without drag or with extremely rapid mass transport, the composite material behaves like the matrix rather than the weakened material having the strength given by eq. (47). In any case, the models are considered to be quite approximate in this extreme case and the main reason for using a limiting value for S is to avoid giving the impression in the figures that the creep strength goes to zero completely.

Fig. 3 shows the creep strength as a function of the interface drag for a material in which $a^2/b^2 = 0.2$ (which can be interpreted as a 20% volume fraction of fibers) and a fiber aspect ratio $L/a = 5$. There is no interface diffusion. It is of interest that the creep strength of the composite tends to decay if

$$\hat{\mu} = \frac{\mu L \dot{\varepsilon}}{\sigma_o}\left(\frac{\dot{\varepsilon}_o\, b}{\dot{\varepsilon}\, L}\right)^{\frac{1}{n}} \tag{49}$$

falls below 10 and is effectively lost if $\hat{\mu}$ is below 10^{-1}. Therefore, generalizing to other cases, $\hat{\mu}$ is a figure of merit for the composite with values above unity necessary for creep strength and above 10 for good creep strength. Fig. 4 shows that this concept is general with the transition from high creep strength to low creep strength occurring at around $\hat{\mu} = 1$ for materials with different volume fractions of fibers.

Fig. 5 shows the creep strength as a function of the interface diffusion coefficient when $a^2/b^2 = 0.2$ and $L/a = 5$. The interface drag coefficient $\hat{\mu} = 10$ so that in the absence of interface mass transport the composite has good creep strength. The plot shows that the creep strength tends to diminish if

$$\hat{\mathcal{D}} = \frac{\mathcal{D}\sigma_o}{b^2 L \dot{\varepsilon}}\left(\frac{\dot{\varepsilon} L}{\dot{\varepsilon}_o b}\right)^{\frac{1}{n}} \tag{50}$$

rise above 10^{-1}. If $\hat{\mathcal{D}}$ is greater than 10, the creep strength of the composite is gone. Thus $\hat{\mathcal{D}}$ plays a similar role as $\hat{\mu}$ as a figure of merit for the composite, with the transition from high creep strength to low creep strength occurring at around $\hat{\mathcal{D}} = 1$.

Approximate Creep Strength

The plots in Fig. 2 suggest that all of the results in that figure can be approximated by $1/(1+C)$ which is the exact result for the linear case with $n = 1$. This approximation has deficiencies when C is less than 2 but in an absolute sense, the error will be small if C exceeds 2. In addition, the use of this result permits some insight into the behavior of the solution not afforded by the figures alone although these features are present in a particular way in Figs. 3-5. The approximation can be expressed as

$$S = \frac{\sigma_a}{\sigma_o}\left(\frac{\dot{\varepsilon}_o}{\dot{\varepsilon}}\right)^{\frac{1}{n}} = \frac{\dfrac{n}{1+2n}\left(\dfrac{L}{b}\right)^{1+\frac{1}{n}}}{\left[2H\left(\dfrac{a}{b},n\right)\right]^{\frac{1}{n}} + 2\left[\dfrac{\mathcal{D}}{b^2} + \dfrac{\left(1-a^2/b^2\right)^2}{4\mu a^2/b^2}\right]\dfrac{\sigma_o a}{\dot{\varepsilon}_o b^2}\left(\dfrac{\dot{\varepsilon} L}{\dot{\varepsilon}_o b}\right)^{\frac{1}{n}-1} + \left(1-\dfrac{a^2}{b^2}\right)} \tag{51}$$

In this expression, the term $1 - a^2/b^2$ has been included on the right hand side in addition to the approximation devised from Fig. 2. The expression shows the interplay between strain rate and the condition of the interface. If $\mathcal{D}$ is zero and μ is infinite so that there is a well bonded interface without interface slip or mass transport, the creep strength is dominated by the first term on the right hand side of eq. (51) and, since L/b is large, the creep strength will be high. If $\mathcal{D}$ or μ are nonzero and finite, the creep strength depends on the strain rate. If the strain rate is high, diffusion and slip will be rendered unimportant and the creep strength will be like that of a well bonded composite without slip or mass transport at the interface. This means that the creep strength is matrix dominated at high strain rates and the creep index of the composite will be that of the matrix, i.e. n.

At lower strain rates, the term containing $\mathcal{D}$ and μ in eq. (51) will become relevant if $\mathcal{D}$ and μ are finite and nonzero. This will reduce the creep strength below that of the well bonded composite without interface slip or diffusion. If the strain rate is plotted against the stress for strain rates at which $\mathcal{D}$ and μ affect the creep strength, the creep index will be inferred to be less than n, the matrix creep index.

At very low strain rates, the term containing $\mathcal{D}$ and μ in eq. (51) will dominate if $\mathcal{D}$ and μ are finite and nonzero. The first term on the right hand side of eq. (51) will be

small and possibly will be negligible compared to $1 - a^2/b^2$. Thus the interface slip or the interface mass transport has destroyed the creep strength of the composite and the creep strength will be entirely due to the volume fraction of the composite which is matrix material. At these strain rates, the creep index of the composite will be that of the matrix, n, and the creep strength will be lower than that of the matrix by itself.

The transition from high to low creep strength for the composite material will take place around $\xi = 1$ where

$$\xi = \left[2H\left(\frac{a}{b},n\right)\right]^{\frac{1}{n}}\left(\frac{b^2\dot{\varepsilon}_o}{a\sigma_o}\right)\left(\frac{L\dot{\varepsilon}}{b\dot{\varepsilon}_o}\right)^{1-\frac{1}{n}} \Big/ 2\left[\frac{D}{b^2} + \frac{\left(1-a^2/b^2\right)^2}{4\mu a^2/b^2}\right] \tag{52}$$

That is, for values of ξ substantially higher than 1, the composite material will have high creep strength. On the other hand, if ξ is substantially less than 1, the creep strength of the composite will be comparable to or worse than that of the matrix material alone. The combined figure of merit ξ as expressed in eq. (52) indicates the importance of various parameters which can affect the composite creep strength such as strain rate, fiber volume fraction, fiber aspect ratio and the interface properties $\mathcal{D}$ and μ. These latter parameters will generally depend on temperature and the temperature dependence will often differ from the temperature dependence of the matrix creep. Thus the figure of merit ξ will generally be temperature dependent. Such behavior has been observed in experiments [11,12] and the loss of creep strength at high temperature in composites has been attributed to the dominance of interfacial mass transport. However, the model presented in this paper suggests that the loss of creep strength can occur due to slip at high temperature without any need for long range mass transport at the interface.

Acknowledgment

This research was supported by the DARPA University Research Initiative at the University of California, Santa Barbara (ONR Prime Contract N00014-92-J-1808).

References

1. A. Kelly and K.N. Street, "Creep of Discontinuous Fibre Composites II, Theory for the Steady-State," *Proc. Roy. Soc. Lond.*, **A328**, 1972, pp. 283-293.

2. R.M. McMeeking, "Power Law Creep of a Composite Material Containing Discontinuous Rigid Aligned Fibers," to appear in *International Journal of Solids and Structures* (1993).

3. S. Goto and M. McLean, "Role of Interfaces in Creep of Fibre-Reinforced Metal-Matrix Composites-II Short Fibres," *Acta Metall. Mater.*, **39**, 1991, pp. 165-177.

4. G. Bao, J.W. Hutchinson and R.M. McMeeking, "Particle Reinforcement of Ductile Matrices Against Plastic Flow and Creep," *Acta Metall Mater.*, **39**, 1991, pp. 1871-1882.

5. G. Bao, F. Genna, J.W. Hutchinson and R.M. McMeeking, "Models for the Strength of Ductile Matrix Composites," in Intermetallic Matrix Composites, MRS Symposium Proceedings, Vol. **194**, (Eds. D.L. Anton, P.L. Martin, D.B. Miracle and R.M. McMeeking) MRS, Pittsburgh, 1990, pp. 3-15.

6. S.T. Mileiko, "Steady State Creep of a Composite Material with Short Fibres," *J. Mater. Sci.*, **5**, 1970, pp. 254-261.

7. H. Lilholt, "Creep of Fibrous Composite Materials," *Composite Sci. Tech.*, **22**, 1985, pp. 277-294.

8. R.E. Johnson, "Power-Law Creep of a Material Being Compressed Between Parallel Plates: A Singular Perturbation Problem," *J. Engg. Math*, **18**, 1984, pp. 105-117.

9. M.F. Ashby and H. Frost, "Deformation Maps, Pergamon Press, Oxford, 1982.

10. P. Sofronis and R.M. McMeeking, "The Effect of Interface Diffusion ad Slip on the Creep Resistance of Particulate Composite Materials," to appear in *Mech. Mater.*, 1993.

11. J. Rosler, J.J. Valencia, C.G. Levi, A.G. Evans and R. Mehrabian, "The High Temperature Behavior of TiAl Containing Carbide Reinforcements," *Mat. Res. Soc. Proc.*, 194, 1990, 241-248.

12. J. Rosler, G. Bao and A.G. Evans, "The Effects of Diffusional Relaxation on the Creep Strength of Composites," *Acta Metall.*, **39**, 1991, 2733-2738.

13. T.G. Nieh, "Creep Rupture of a Silicon Carbide Reinforced Aluminum Composite," *Metall. Trans. A.*, **15A**, 1984, pp. 139-146.

14. R.M. McMeeking, "Models for the Creep of Ceramic Matrix Composite Materials," to appear in Elevated Temperature Mechanical Behavior of Ceramic Matrix Composites (S.V. Nair and K. Jakus, eds.) Butterworth-Heinemann, Stoneham, Mass, 1993.

List of Figure Captions

Fig. 1 Unit cell for creep analysis.

Fig. 2 Applied stress for the composite material as a function of strain rate, matrix creep properties, interface slip, interface mass transport and unit cell geometry.

Fig. 3 Creep strength of a composite material as a function of the interface drag coefficient when there is no interface mass transport.

Fig. 4 Creep strength of a composite material as a function of the interface drag coefficient when there is no interface mass transport.

Fig. 5 Creep strength of a composite material as a function of the interface diffusion coefficient.

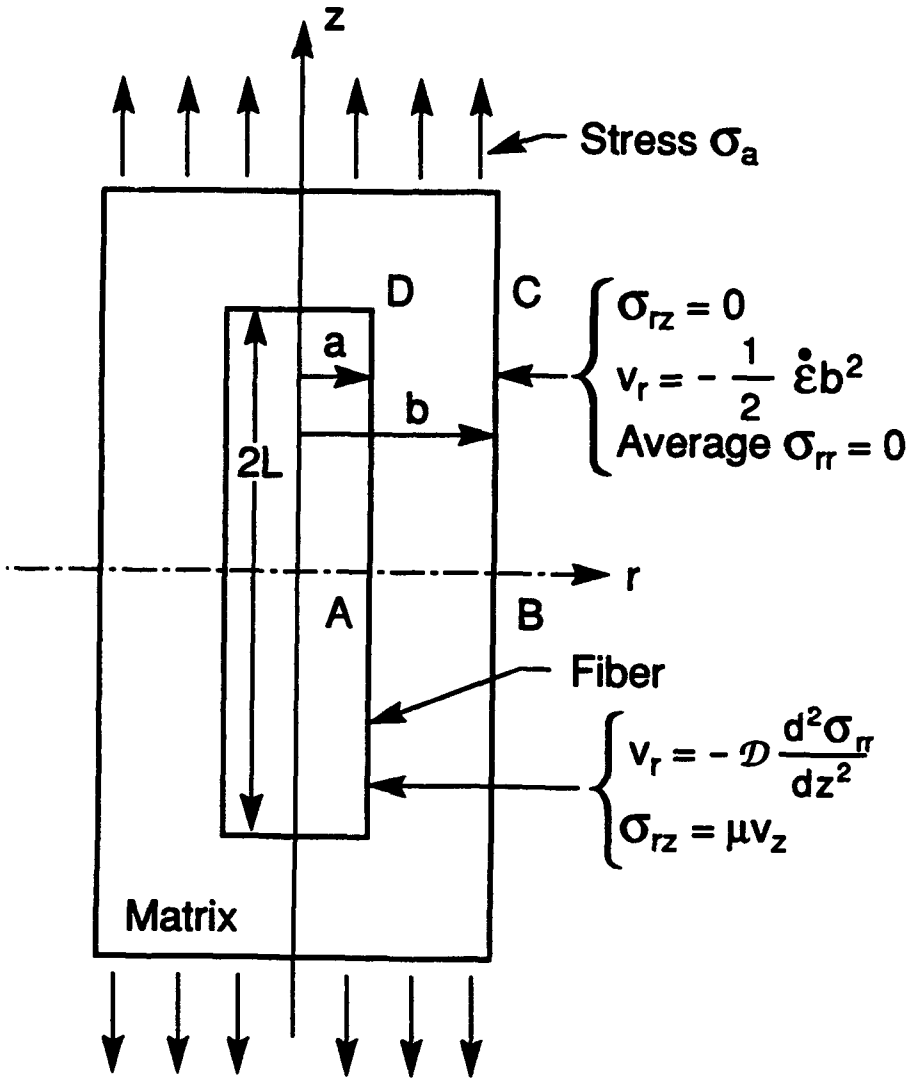
z
Stress σ_a
D
C
a
b
2L
$\sigma_{rz} = 0$
$v_r = -\frac{1}{2}\dot{\varepsilon}b^2$
Average $\sigma_{rr} = 0$
r
A
B
Fiber
$v_r = -\mathcal{D}\frac{d^2\sigma_{rr}}{dz^2}$
$\sigma_{rz} = \mu v_z$
Matrix

Figure 1

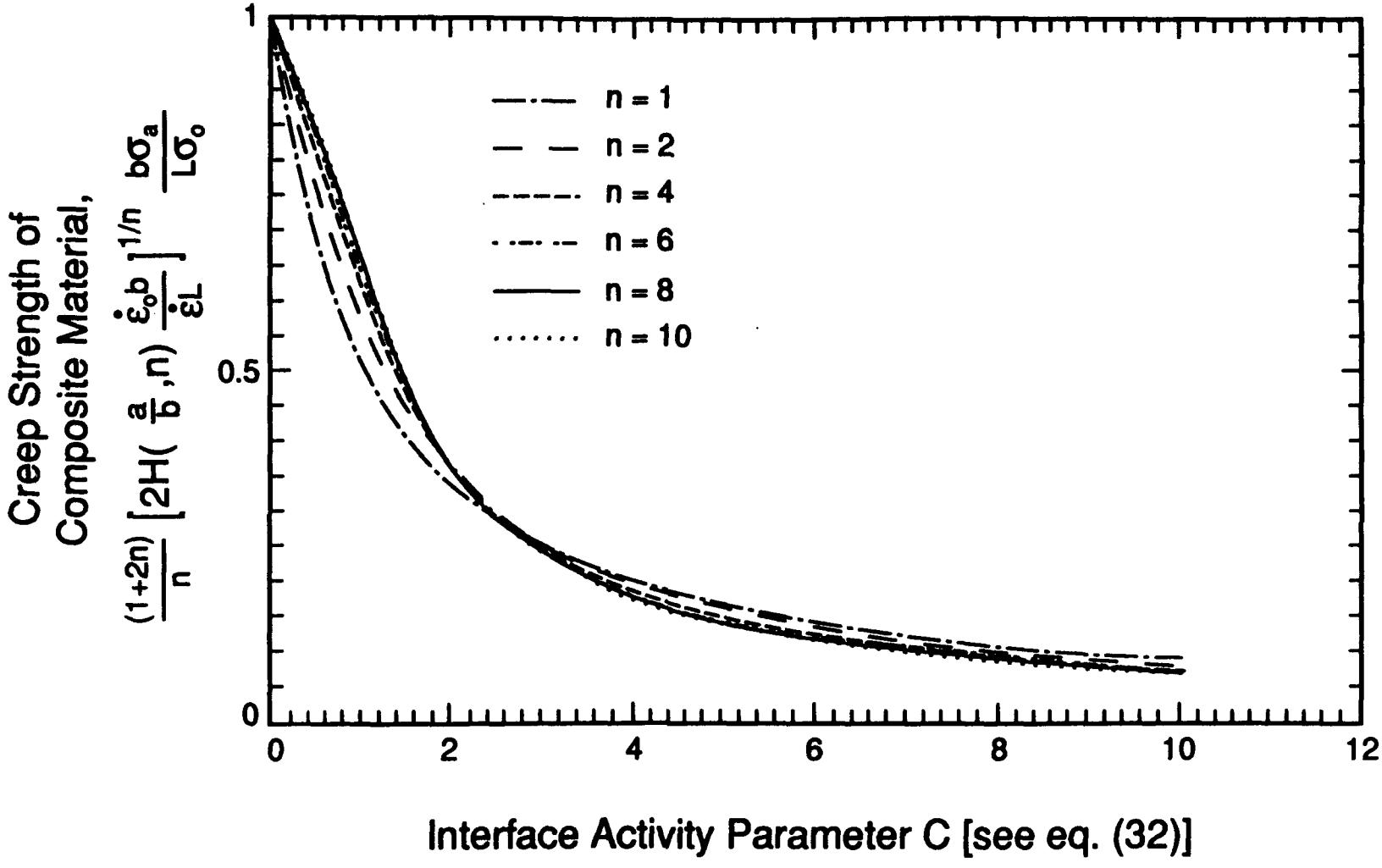
Creep Strength of Composite Material, $\frac{(1+2n)}{n}\left[2H\left(\frac{a}{b},n\right)\frac{\dot{\varepsilon}_o b}{\dot{\varepsilon}L}\right]^{1/n}\frac{b\sigma_a}{L\sigma_o}$
n = 1
n = 2
n = 4
n = 6
n = 8
n = 10
1
0.5
0
0
2
4
6
8
10
12
Interface Activity Parameter C [see eq. (32)]

Figure 2

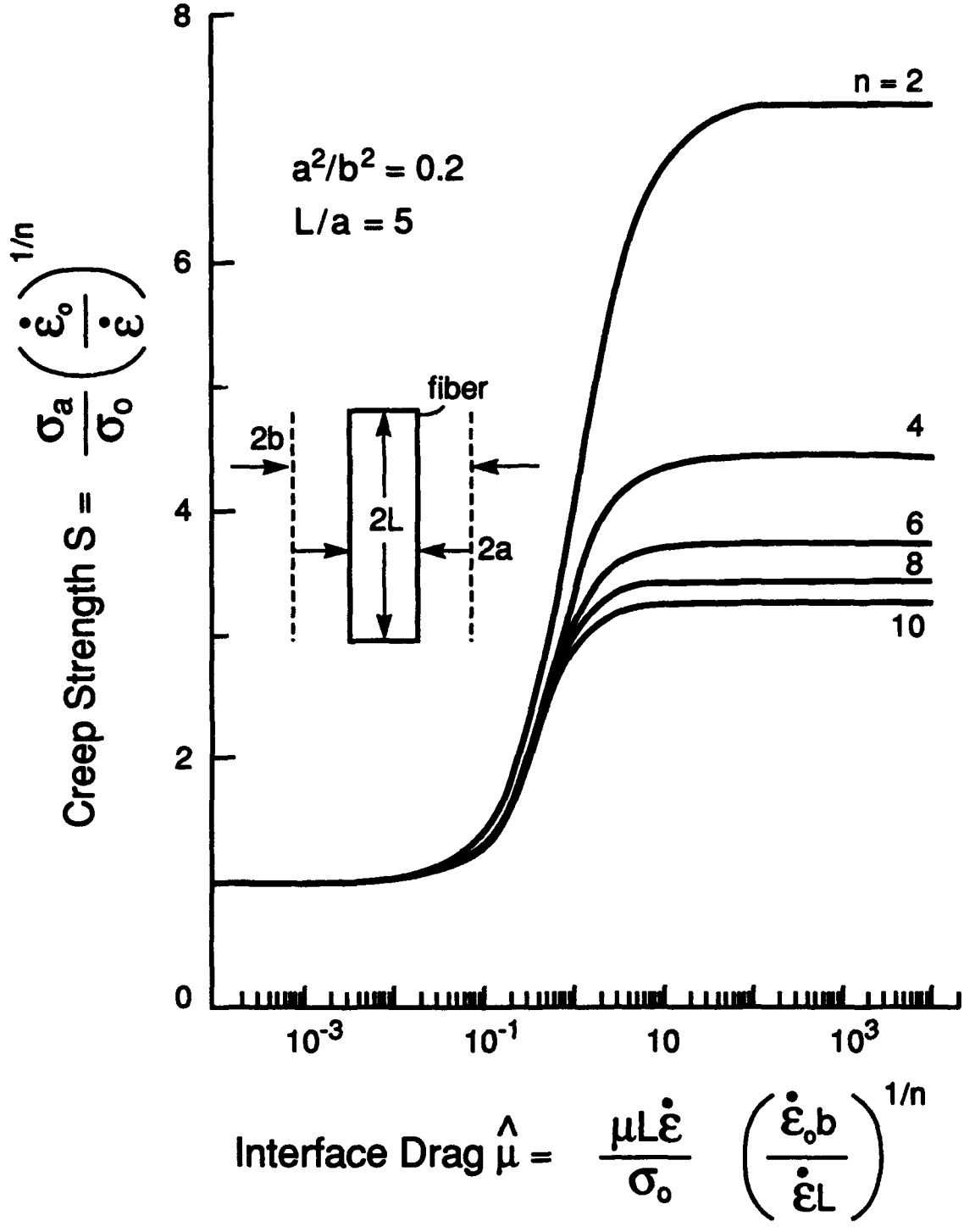
8
6
4
2
0
n = 2
4
6
8
10
$a^2/b^2 = 0.2$
L/a = 5
fiber
2b
2L
2a
Creep Strength $S = \frac{\sigma_a}{\sigma_o}\left(\frac{\dot{\varepsilon}_o}{\dot{\varepsilon}}\right)^{1/n}$
10^{-3}
10^{-1}
10
10^3
Interface Drag $\hat{\mu} = \frac{\mu L \dot{\varepsilon}}{\sigma_o}\left(\frac{\dot{\varepsilon}_o b}{\dot{\varepsilon} L}\right)^{1/n}$

Figure 3

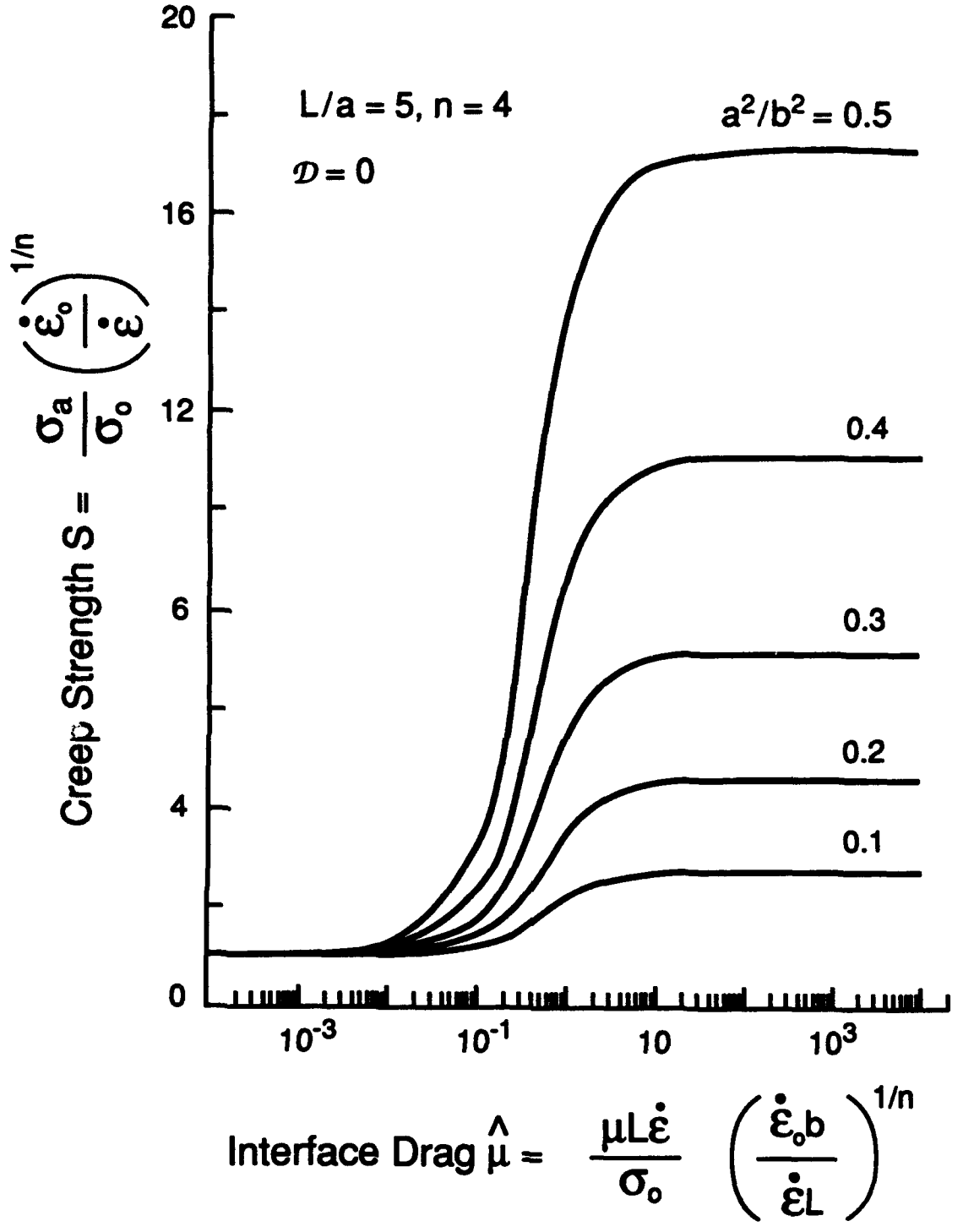
L/a = 5, n = 4
$\mathcal{D} = 0$
$a^2/b^2 = 0.5$
0.4
0.3
0.2
0.1
Creep Strength $S = \frac{\sigma_a}{\sigma_o}\left(\frac{\dot{\varepsilon}_o}{\dot{\varepsilon}}\right)^{1/n}$
Interface Drag $\hat{\mu} = \frac{\mu L \dot{\varepsilon}}{\sigma_o}\left(\frac{\dot{\varepsilon}_o b}{\dot{\varepsilon} L}\right)^{1/n}$
0
4
6
12
16
20
10^{-3}
10^{-1}
10
10^{3}

Figure 4

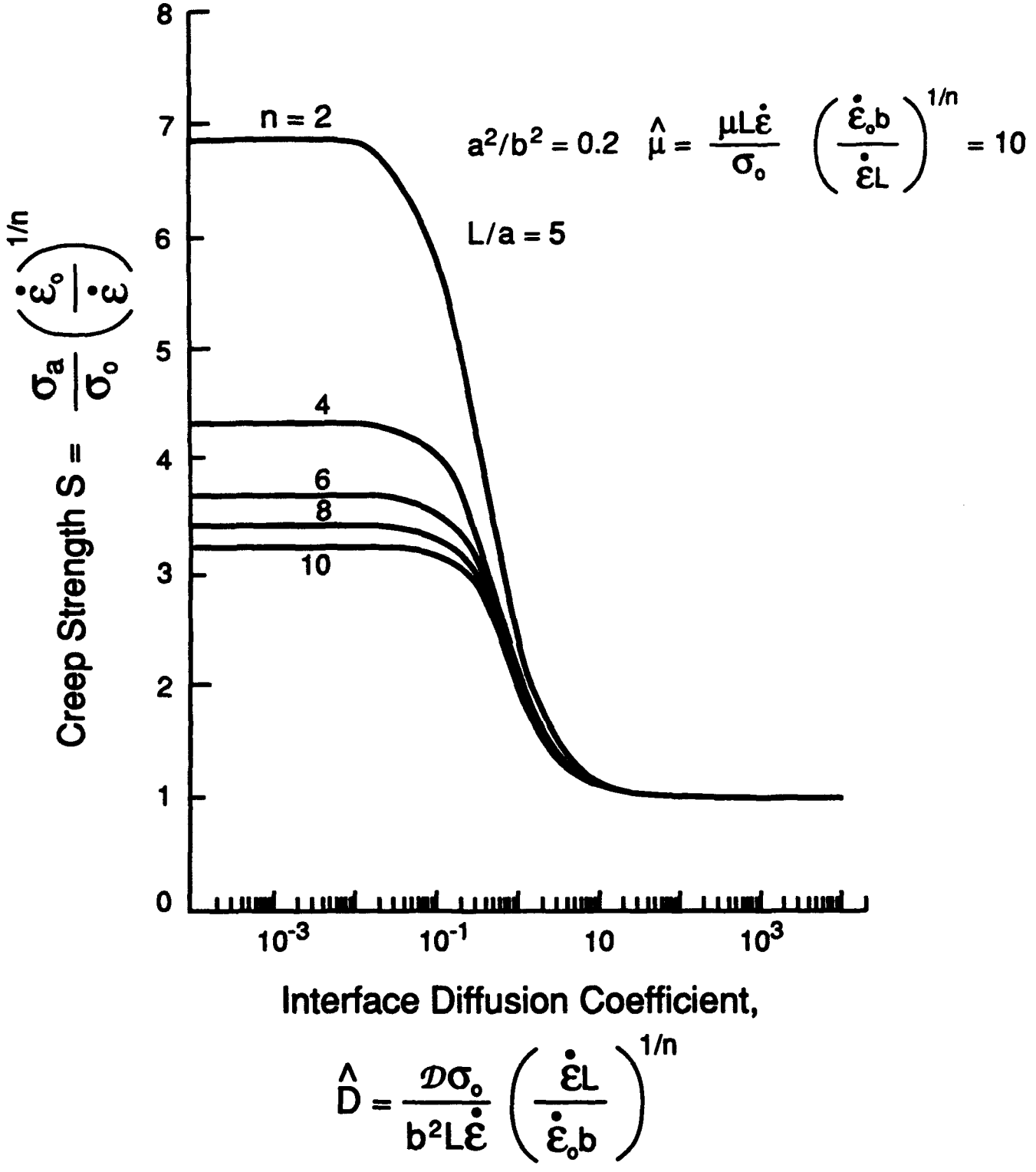
n = 2
4
6
8
10
$a^2/b^2 = 0.2$
$\hat{\mu} = \frac{\mu L \dot{\varepsilon}}{\sigma_o} \left(\frac{\dot{\varepsilon}_o b}{\dot{\varepsilon} L}\right)^{1/n} = 10$
L/a = 5
Creep Strength $S = \frac{\sigma_a}{\sigma_o} \left(\frac{\dot{\varepsilon}_o}{\dot{\varepsilon}}\right)^{1/n}$
0
1
2
3
4
5
6
7
8
10^{-3}
10^{-1}
10
10^3
Interface Diffusion Coefficient,
$\hat{D} = \frac{\mathcal{D}\sigma_o}{b^2 L \dot{\varepsilon}} \left(\frac{\dot{\varepsilon} L}{\dot{\varepsilon}_o b}\right)^{1/n}$

Figure 5

STEADY STATE CREEP OF FIBER-REINFORCED COMPOSITES: CONSTITUTIVE EQUATIONS AND COMPUTATIONAL ISSUES

N. Aravas, Cao Cheng and P. Ponte Castañeda
Department of Mechanical Engineering
and Applied Mechanics
University of Pennsylvania
Philadelphia, PA 19104
USA

Abstract

The general form of the constitutive equations that describe steady-state creep of fiber-reinforced metal-matrix composites with transversely isotropic overall symmetry is developed. The physical meaning of the constitutive functions involved is discussed in detail. A method for the numerical integration of the constitutive equations is developed. The 'linearization moduli' associated with the integration algorithm are computed, and the constitutive model is implemented in a general purpose finite element program. A constitutive model for steady-state creep of fiber-reinforced composite that has been developed recently by deBotton and Ponte Castañeda (1993) is also considered. A number of 'unit cell' problems with periodic boundary conditions, consistent with the requirements of homogenization theory, are solved using the finite element method, and the results are compared with the predictions of the analytical model of deBotton and Ponte Castañeda.

Submitted to the *International Journal of Solids and Structures*

1 Introduction

Fiber-reinforced metal-matrix composites are expected to play a key role in achieving the performance goals of the next generation of aircraft engines. Compared to traditional metal alloys, these materials have superior creep resistance at elevated temperatures, as well as high strength to stiffness ratio.

In view of their potential as high-temperature structural materials, metal-matrix composites have attracted increasing attention recently, and several attempts to develop constitutive models for the mechanical behavior of such materials have been made. Several *one-dimensional* models that can be used to predict the creep behavior of fiber-reinforced composites under simple types of loading are already available in the literature; we mention amongst these the work of Mileiko (1970), Kelly and Street (1972), McLean (1985, 1988), Goto and McLean (1991a,b), and McMeeking (1993a,b). Johnson (1977) appears to be the first to propose a set of *three-dimensional* constitutive equations for creeping transversely isotropic materials; he based his model for steady-state creep in directionally-solidified eutectic alloys on a generalization of the Bailey-Norton law, which connects the creep strain rate and applied stress by a power-law relation. More recently, deBotton and Ponte Castañeda (1993) have developed estimates as well as rigorous bounds for the dissipation functions of multiple-phase fiber composites, in which the constituent phases are non-linear isotropic materials. The work of deBotton and Ponte Castañeda was presented in the context of nonlinear elastic materials, but it can be also used to describe the *steady-state* creep of fiber-reinforced transversely isotropic composites. A review of several models for the effect of fibers on the creep characteristics of unidirectional composites has been presented by McMeeking (1993a). It appears that, whereas some progress has been made in developing constitutive equations for creeping anisotropic composites, there have been only few experimental studies on fiber-reinforced composite systems having practical utility at elevated temperatures. The creep behavior of metal-matrix composites reinforced with continuous fibers was studied recently by Weber et al. (1992). Their results show that, when both the matrix and the fibers creep, the composite exhibits steady-state behavior, following an initial transient; however, when the fibers do not creep, transient creep of the composite is observed, with a creep strain limited by the elastic deformation of the fibers.

In this paper, we develop the general three-dimensional form of the constitutive equations that describe steady-state creep of fiber-reinforced metal-matrix composites with transversely

isotropic overall symmetry. The constitutive equations for the creep strain rate involve four scalar functions that depend on the five transversely isotropic invariants of the stress tensor; the physical meaning of these constitutive functions is discussed in detail. The numerical implementation of the general form of the transversely isotropic constitutive equations in a finite element program is discussed, and a method for the numerical integration of such equations is presented. A specific constitutive model for steady-state creep of fiber-reinforced composites that has been developed recently by deBotton and Ponte Castañeda (1993) is examined. The predictions of the model are compared with the solutions of a number of 'unit cell' problems; periodic boundary conditions, consistent with the requirements of homogenization theory, are imposed on the unit cell problems, and the solutions are obtained using the finite element method. Finally, the model of deBotton and Ponte Castañeda (1993) is implemented in a general purpose finite element program, and the problem of a composite plate with a hole is solved.

Standard notation is used throughout. Boldface symbols denote tensors the order of which is indicated by the context. All tensor components are written with respect to a fixed Cartesian coordinate system, and the summation convention is used for repeated indices, unless otherwise indicated. The prefices tr and det indicate the trace and the determinant respectively, a superscript T the transpose of a second order tensor, a superposed dot the material time derivative, and the subscripts s and a the symmetric and anti-symmetric parts of a second order tensor. Let $\mathbf{a}$ and $\mathbf{b}$ be vectors, $\mathbf{A}$ and $\mathbf{B}$ second order tensors, and $\mathbf{C}$ and $\mathbf{D}$ fourth order tensors; the following products are used in the text $(\mathbf{ab})_{ij} = a_i b_j$, $(\mathbf{A}\cdot\mathbf{a})_i = A_{ij}a_j$, $(\mathbf{a}\cdot\mathbf{A})_i = a_j A_{ji}$, $(\mathbf{A}\cdot\mathbf{B})_{ij} = A_{ik}B_{kj}$, $\mathbf{A}:\mathbf{B} = A_{ij}B_{ij}$, $(\partial\mathbf{A}/\partial\mathbf{B})_{ijkl} = \partial A_{ij}/\partial B_{kl}$, $(\mathbf{AB})_{ijkl} = A_{ij}B_{kl}$, $(\mathbf{C}:\mathbf{A})_{ij} = C_{ijkl}A_{kl}$, and $(\mathbf{C}:\mathbf{D})_{ijkl} = C_{ijmn}D_{mnkl}$.

2 Constitutive equations

We consider infinitesimal deformations and write the infinitesimal strain tensor $\boldsymbol{\epsilon}$ as the sum of the elastic and the creep strains, i.e.

$$\boldsymbol{\epsilon} = \boldsymbol{\epsilon}^{e} + \boldsymbol{\epsilon}^{cr}. \tag{1}$$

The focus of this paper is the steady state creep behavior of fiber-reinforced composites. However, for comparison purposes, we start with a brief discussion of some commonly used constitutive equations for creeping *isotropic* materials.

2.1 Creep of isotropic materials

The constitutive equation for the steady state creep strain rate is of the form

$$\dot{\epsilon}^{cr} = \mathbf{g}(\boldsymbol{\sigma}, s) \tag{2}$$

where $\mathbf{g}$ is an isotropic function of its arguments, $\boldsymbol{\sigma}$ is the stress tensor, and s is a set of material constants. Using the representation theorems for isotropic functions, we can readily show that the most general form of the last equation is (Wang, 1970a,b; Smith, 1971)

$$\dot{\epsilon}^{cr} = c_1 \mathbf{I} + 2\, c_2\, \boldsymbol{\sigma} + 3\, c_3\, \boldsymbol{\sigma}^2 \tag{3}$$

where the c_i's are functions of s and the three isotropic stress invariants $I_1 = \mathrm{tr}(\boldsymbol{\sigma})$, $I_2 = \mathrm{tr}(\boldsymbol{\sigma}^2)$ and $I_3 = \mathrm{tr}(\boldsymbol{\sigma}^3)$.

We assume next that the creep strain rate $\dot{\epsilon}^{cr}$ is derived from a creep potential $\Psi = \Psi(\boldsymbol{\sigma}, s)$, i.e.

$$\dot{\epsilon}^{cr} = \frac{\partial \Psi}{\partial \boldsymbol{\sigma}}. \tag{4}$$

The creep potential must be an isotropic function, i.e. a function of the form

$$\Psi = \Psi(I_1, I_2, I_3, s). \tag{5}$$

Using the chain rule, we can readily show that

$$\dot{\epsilon}^{cr} = \frac{\partial \Psi}{\partial \boldsymbol{\sigma}} = \sum_{i=1}^{3} \frac{\partial \Psi}{\partial I_i} \frac{\partial I_i}{\partial \boldsymbol{\sigma}} = c_1 \mathbf{I} + 2\, c_2\, \boldsymbol{\sigma} + 3\, c_3\, \boldsymbol{\sigma}^2, \tag{6}$$

where now

$$c_i = \frac{\partial \Psi}{\partial I_i}. \tag{7}$$

The three-dimensional form of the standard steady-state 'power-law' creep constitutive equations is

$$\dot{\epsilon}^{cr} = \frac{\partial \Psi}{\partial \boldsymbol{\sigma}} = \frac{3}{2}\, \dot{\epsilon}_0 \left(\frac{\sigma_e}{\sigma_0}\right)^{n-1} \frac{\boldsymbol{\sigma}'}{\sigma_0} \qquad \text{where} \qquad \Psi = \Psi(I_1, I_2) = \frac{\sigma_0\, \dot{\epsilon}_0}{n+1} \left(\frac{\sigma_e}{\sigma_0}\right)^{n+1}, \tag{8}$$

$\boldsymbol{\sigma}'$ is the stress deviator, $\sigma_e = (1.5\, \sigma'_{ij} \sigma'_{ij})^{1/2} = [0.5\, (3\, I_2 - I_1^2)]^{1/2}$ is the von Mises equivalent stress, n is the creep exponent, and $(\sigma_0, \dot{\epsilon}_0)$ are material constants. Equation (8) is a special case of (3) with

$$c_1 = -\frac{2}{3}\, I_1\, c_2, \qquad c_2 = \frac{3}{4}\, \frac{\dot{\epsilon}_0}{\sigma_0} \left(\frac{\sigma_e}{\sigma_0}\right)^{n-1}, \qquad c_3 = 0. \tag{9}$$

Note that the power-law creep equation (8) does not involve a quadratic stress generator term $\boldsymbol{\sigma}^2$ (i.e. $c_3 = 0$).

2.2 Fiber-reinforced composites

Consider next a material reinforced by aligned fibers. The macroscopic response of the composite is assumed to be transversely isotropic, and the unit vector $\mathbf{n}$ in the direction of the fibers is used to define the axis rotational symmetry.

2.2.1 Elasticity

The elastic strain is written in terms of the stress tensor $\boldsymbol{\sigma}$ as

$$\boldsymbol{\epsilon}^e = \mathbf{C}^{-1} : \boldsymbol{\sigma} \tag{10}$$

where $\mathbf{C}$ is the fourth-order elasticity tensor for a linear transversely isotropic material. The elasticity tensor is of the form (Aravas, 1992)

$$\mathbf{C} = 2a\mathbf{II} + 2b\mathbf{J} + 2c\mathbf{aa} + d\mathbf{P} + e(\mathbf{Ia} + \mathbf{aI}), \tag{11}$$

where $\mathbf{I}$ is the second order identity tensor, $\mathbf{J}$ is the fourth-order identity tensor with cartesian components $J_{ijkl} = (\delta_{ik}\delta_{jl} + \delta_{il}\delta_{jk})/2$, $\mathbf{a}$ is the orientation tensor $\mathbf{a} = \mathbf{nn}$, (a, b, c, d, e) are elastic constants, and

$$P_{ijkl} = \frac{1}{2}(a_{ik}\,\delta_{jl} + a_{il}\,\delta_{jk} + \delta_{ik}\,a_{jl} + \delta_{il}\,a_{jk}). \tag{12}$$

The constants (a, b, c, d, e) are related to the standard elastic moduli $(E_{11}, \mu_{12}, \mu_{23}, K_{23}, \nu_{12})$, as defined for example in Christensen's (1979) book, by

$$a = \frac{1}{2}(K_{23} - \mu_{23}), \qquad b = \mu_{23}, \qquad c = \frac{1}{2}E_{11} + \frac{1}{2}\mu_{23} - 2\mu_{12} + \frac{1}{2}(1 - 2\nu_{12})^2 K_{23}, \tag{13}$$

$$d = 2(\mu_{12} - \mu_{23}), \qquad e = \mu_{23} - (1 - 2\nu_{12})K_{23}, \tag{14}$$

where the x_1-axis is in the direction of transverse isotropy.

2.2.2 Creep

The constitutive equation for the steady state creep strain rate is of the form

$$\dot{\boldsymbol{\epsilon}}^{cr} = \mathbf{f}(\boldsymbol{\sigma}, s) \tag{15}$$

where $\mathbf{f}$ is a transversely isotropic function, and s is collection of material parameters such as the volume fraction of the fibers, the material constants that enter the constitutive equations of the matrix and the fibers, etc. Using the results of Liu (1982) together with the

representation theorems for isotropic functions (Wang, 1970a,b; Smith, 1971), we can readily show that the most general form of the above constitutive equations is

$$\dot{\boldsymbol{\epsilon}}^{cr} = a_1\,\mathbf{I} + 2\,a_2\,\boldsymbol{\sigma} + 3\,a_3\,\boldsymbol{\sigma}^2 + a_4\,\mathbf{a} + a_5\,(\boldsymbol{\sigma}\cdot\mathbf{a} + \mathbf{a}\cdot\boldsymbol{\sigma}) + a_6(\boldsymbol{\sigma}^2\cdot\mathbf{a} + \mathbf{a}\cdot\boldsymbol{\sigma}^2) \equiv \mathbf{f}(\boldsymbol{\sigma}, s), \quad (16)$$

where the a_i's are functions of s, and the following five transversely isotropic invariants:

$$I_1 = \mathrm{tr}(\boldsymbol{\sigma}),\quad I_2 = \mathrm{tr}(\boldsymbol{\sigma}^2),\quad I_3 = \mathrm{tr}(\boldsymbol{\sigma}^3),\quad I_4 = \mathrm{tr}(\boldsymbol{\sigma}\cdot\mathbf{a}) = \mathbf{n}\cdot\boldsymbol{\sigma}\cdot\mathbf{n},\quad I_5 = \mathrm{tr}(\boldsymbol{\sigma}^2\cdot\mathbf{a}) = \mathbf{n}\cdot\boldsymbol{\sigma}^2\cdot\mathbf{n}. \quad (17)$$

An alternative set of commonly used transversely isotropic invariants is given in Appendix A.

If the creep response of the material is incompressible, then the following equation must be satisfied for all values of $\boldsymbol{\sigma}$:

$$3\,a_1 + 2\,a_2\,I_1 + 3\,a_3\,I_2 + a_4 + 2\,a_5\,I_4 + 2\,a_6\,I_5 = 0. \quad (18)$$

We consider composite materials in which both the fibers and the matrix are isotropic with constitutive equations such that $\dot{\boldsymbol{\epsilon}}^{cr}(-\boldsymbol{\sigma}) = -\dot{\boldsymbol{\epsilon}}^{cr}(\boldsymbol{\sigma})$. We assume that the same is true for the composite, and require that the constitutive equation of the composite (16) satisfies the condition $\dot{\boldsymbol{\epsilon}}^{cr}(-\boldsymbol{\sigma}) = -\dot{\boldsymbol{\epsilon}}^{cr}(\boldsymbol{\sigma})$ as well. Then, one can readily show that $\dot{\boldsymbol{\epsilon}}^{cr}(\mathbf{0}) = \mathbf{0}$, and that the functions a_i are such that

$$a_i(-I_1, I_2, -I_3, -I_4, I_5) = -a_i(I_1, I_2, I_3, I_4, I_5) \qquad \text{for} \qquad i = 1,3,4,6, \quad (19)$$

and

$$a_i(-I_1, I_2, -I_3, -I_4, I_5) = a_i(I_1, I_2, I_3, I_4, I_5) \qquad \text{for} \qquad i = 2,5, \quad (20)$$

which imply that

$$a_1 = a_3 = a_4 = a_6 = 0 \qquad \text{when} \qquad I_1 = I_3 = I_4 = 0. \quad (21)$$

We assume next that the creep strain rate $\dot{\boldsymbol{\epsilon}}^{cr}$ is derived from a creep potential $\Psi = \Psi(\boldsymbol{\sigma}, s)$. In view of the assumed transverse isotropy, Ψ must be of the form

$$\Psi = \Psi(I_1, I_2, I_3, I_4, I_5, s). \quad (22)$$

Using the chain rule, we can readily show that

$$\dot{\boldsymbol{\epsilon}}^{cr} = \frac{\partial\Psi}{\partial\boldsymbol{\sigma}} = \sum_{i=1}^{5}\frac{\partial\Psi}{\partial I_i}\frac{\partial I_i}{\partial\boldsymbol{\sigma}} = a_1\,\mathbf{I} + 2\,a_2\,\boldsymbol{\sigma} + 3\,a_3\,\boldsymbol{\sigma}^2 + a_4\,\mathbf{a} + a_5\,(\boldsymbol{\sigma}\cdot\mathbf{a} + \mathbf{a}\cdot\boldsymbol{\sigma}), \quad (23)$$

where now

$$a_i = \frac{\partial \Psi}{\partial I_i}. \tag{24}$$

Note that equation (23) is a special case of the more general form (16) with $a_6 = 0$.

Consider now the case in which both the matrix- and fiber-material creep according to the power-law equation (8). Since quadratic stress generators are absent in (8), we introduce the assumption that the corresponding creep equation for the composite does not involve quadratic stress generators either, i.e. $a_3 = \partial \Psi / \partial I_3 \equiv 0$. We emphasize, however, that this is meant to be only a reasonable *approximation*; in general, such quadratic generators may appear in (23) even though they are absent in (8).

Summarizing, we mention that the assumed constitutive equation for the creep strain rate of the fiber-reinforced material is

$$\dot{\boldsymbol{\epsilon}}^{cr} = a_1 \mathbf{I} + 2\, a_2\, \boldsymbol{\sigma} + a_4\, \mathbf{a} + a_5\, (\boldsymbol{\sigma} \cdot \mathbf{a} + \mathbf{a} \cdot \boldsymbol{\sigma}) \equiv \mathbf{f}(\boldsymbol{\sigma}, s). \tag{25}$$

3 Identification of material functions a_i

Let the coordinate axis x_3 be along the direction of the fibers, so that $\mathbf{n} = \mathbf{e}_3$, where $\mathbf{e}_3$ is the unit base vector along the x_3-axis. Then the constitutive equation (25) can be written as

$$\dot{\epsilon}^{cr}_{ij} = a_1\, \delta_{ij} + 2\, a_2\, \sigma_{ij} + a_4\, \delta_{i3}\, \delta_{j3} + a_5\, (\sigma_{i3}\, \delta_{j3} + \delta_{i3}\, \sigma_{j3}), \tag{26}$$

or, equivalently,

$$\dot{\epsilon}^{cr}_{11} = a_1 + 2\, a_2\, \sigma_{11}, \tag{27}$$

$$\dot{\epsilon}^{cr}_{22} = a_1 + 2\, a_2\, \sigma_{22}, \tag{28}$$

$$\dot{\epsilon}^{cr}_{33} = a_1 + a_4 + 2\, (a_2 + a_5)\, \sigma_{33}, \tag{29}$$

$$\dot{\epsilon}^{cr}_{12} = 2\, a_2\, \sigma_{12}, \tag{30}$$

$$\dot{\epsilon}^{cr}_{23} = (2\, a_2 + a_5)\, \sigma_{23}, \tag{31}$$

$$\dot{\epsilon}^{cr}_{31} = (2\, a_2 + a_5)\, \sigma_{31}. \tag{32}$$

The relevant invariants I_i now take the form

$$I_1 = \mathrm{tr}(\boldsymbol{\sigma}), \quad I_2 = \mathrm{tr}(\boldsymbol{\sigma}^2), \quad I_4 = \sigma_{33}, \quad I_5 = \sigma_{31}^2 + \sigma_{32}^2 + \sigma_{33}^2. \tag{33}$$

Equations (27)-(32) show that:

- a_2 and a_5 relate to the response of the composite under shear, whereas a_1 and a_4 refer to longitudinal and transverse tension,

- if $a_5 = \partial W/\partial I_5 \equiv 0$, then the response of the material is identical under longitudinal $(\sigma_{23}, \sigma_{31})$ or transverse shear (σ_{12}),

- in view of (21), longitudinal shear loading (i.e. $\sigma_{13} \neq 0$ and/or $\sigma_{23} \neq 0$, other $\sigma_{ij} = 0$) causes longitudinal shear strain rates only, i.e. $\dot{\epsilon}^{cr}_{11} = \dot{\epsilon}^{cr}_{22} = \dot{\epsilon}^{cr}_{33} = \dot{\epsilon}^{cr}_{12} = 0$,

- in view of (21), transverse shear loading (i.e. $\sigma_{12} \neq 0$, other $\sigma_{ij} = 0$) causes transverse shear strain rates only, i.e. $\dot{\epsilon}^{cr}_{11} = \dot{\epsilon}^{cr}_{22} = \dot{\epsilon}^{cr}_{33} = \dot{\epsilon}^{cr}_{13} = \dot{\epsilon}^{cr}_{23} = 0$.

The last two conclusions are true even when the quadratic stress generator is included in the constitutive equation for $\dot{\epsilon}^{cr}$, because the function a_3 vanishes under longitudinal or transverse shear, in view of equation (21).

4 Finite element implementation of the constitutive model

In this section, we discuss the implementation of the general form of the constitutive model described in section 2 in a finite element program. In a finite element environment, the solution of the creep problem is developed incrementally and the constitutive equations are integrated at the element Gauss points. In a displacement based finite element formulation the solution is deformation driven. At a material point, the solution $(\boldsymbol{\sigma}_n, \boldsymbol{\epsilon}_n)$ at time t_n as well as the strain $\boldsymbol{\epsilon}_{n+1}$ at time $t_{n+1} = t_n + \Delta t$ are supposed to be known and one has to determine the solution $\boldsymbol{\sigma}_{n+1}$.

4.1 Numerical integration of the constitutive equations

We start with the elasticity equation (10)

$$\boldsymbol{\sigma}_{n+1} = \mathbf{C} : \boldsymbol{\epsilon}^e_{n+1} = \mathbf{C} : (\boldsymbol{\epsilon}^e_n + \Delta\boldsymbol{\epsilon} - \Delta\boldsymbol{\epsilon}^{cr}) = \boldsymbol{\sigma}^e - \mathbf{C} : \Delta\boldsymbol{\epsilon}^{cr}, \tag{34}$$

where $\Delta\boldsymbol{\epsilon} = \boldsymbol{\epsilon}_{n+1} - \boldsymbol{\epsilon}_n$ and $\Delta\boldsymbol{\epsilon}^{cr} = \boldsymbol{\epsilon}^{cr}_{n+1} - \boldsymbol{\epsilon}^{cr}_n$ are the total- and creep-strain increments, and $\boldsymbol{\sigma}^e = \boldsymbol{\sigma}_n + \mathbf{C} : \Delta\boldsymbol{\epsilon}$ is the (known) elastic predictor.

The creep constitutive equation (25) is integrated using a generalized trapezoidal method:

$$\Delta\boldsymbol{\epsilon}^{cr} = [\alpha\,\mathbf{f}(\boldsymbol{\sigma}_{n+1}, s) + (1-\alpha)\,\mathbf{f}(\boldsymbol{\sigma}_n, s)]\,\Delta t \qquad (0 \le \alpha \le 1). \tag{35}$$

When α=0,1 or 1/2 the integration scheme reduces to the forward Euler, backward Euler or the trapezoidal method respectively.

Summarizing, we write

$$\mathbf{F}(\Delta\boldsymbol{\epsilon}^{cr}) \equiv \Delta\boldsymbol{\epsilon}^{cr} - [\alpha\,\mathbf{f}(\boldsymbol{\sigma}_{n+1}(\Delta\boldsymbol{\epsilon}^{cr}), s) + (1-\alpha)\,\mathbf{f}(\boldsymbol{\sigma}_n, s)]\,\Delta t = \mathbf{0}, \tag{36}$$

where

$$\boldsymbol{\sigma}_{n+1}(\Delta\boldsymbol{\epsilon}^{cr}) = \boldsymbol{\sigma}^e - \mathbf{C} : \Delta\boldsymbol{\epsilon}^{cr}. \tag{37}$$

We choose $\Delta\boldsymbol{\epsilon}^{cr}$ as the primary unknown and treat (36) as the basic equation in which $\boldsymbol{\sigma}_{n+1}$ is defined by (37). The solution is obtained using Newton's method. The first estimate for $\Delta\boldsymbol{\epsilon}^{cr}$ used to start the Newton loop is obtained using a forward Euler scheme, i.e. $(\Delta\boldsymbol{\epsilon}^{cr})_{\text{est}} = \mathbf{f}(\boldsymbol{\sigma}_n, t_n, s)\,\Delta t$. An alternative and more accurate estimate for $\Delta\boldsymbol{\epsilon}^{cr}$ can be obtained by using the so-called 'forward gradient' technique as described in the following. The function $\mathbf{f}(\boldsymbol{\sigma}_{n+1})$ is approximated by

$$\mathbf{f}(\boldsymbol{\sigma}_{n+1}) \simeq \mathbf{f}(\boldsymbol{\sigma}_n) + \left(\frac{\partial \mathbf{f}}{\partial \boldsymbol{\sigma}}\right)_n : \Delta\boldsymbol{\sigma} = \mathbf{f}(\boldsymbol{\sigma}_n) + \left(\frac{\partial \mathbf{f}}{\partial \boldsymbol{\sigma}}\right)_n : \mathbf{C} : (\Delta\boldsymbol{\epsilon} - \Delta\boldsymbol{\epsilon}^{cr}) \tag{38}$$

and substituted into (36), which then yields the following estimate for $\Delta\boldsymbol{\epsilon}^{cr}$:

$$(\Delta\boldsymbol{\epsilon}^{cr})_{\text{est}} = \left[\mathbf{J} + \alpha\left(\frac{\partial \mathbf{f}}{\partial \boldsymbol{\sigma}}\right)_n : \mathbf{C}\,\Delta t\right]^{-1} : \left[\mathbf{f}(\boldsymbol{\sigma}_n) + \alpha\left(\frac{\partial \mathbf{f}}{\partial \boldsymbol{\sigma}}\right)_n : \mathbf{C} : \Delta\boldsymbol{\epsilon}\right]\Delta t. \tag{39}$$

The Jacobian associated with the Newton loop in equation (36) is given by

$$\frac{\partial \mathbf{F}}{\partial \Delta\boldsymbol{\epsilon}^{cr}} = \mathbf{J} - \alpha\,\Delta t\left(\frac{\partial \mathbf{f}}{\partial \boldsymbol{\sigma}}\right)_{n+1} : \frac{\partial \boldsymbol{\sigma}_{n+1}}{\partial \Delta\boldsymbol{\epsilon}^{cr}} = \mathbf{J} + \alpha\,\Delta t\left(\frac{\partial \mathbf{f}}{\partial \boldsymbol{\sigma}}\right)_{n+1} : \mathbf{C}. \tag{40}$$

Once $\Delta\boldsymbol{\epsilon}^{cr}$ is found, equation (37) defines the stress $\boldsymbol{\sigma}_{n+1}$, and this completes the integration procedure.

In the following, we derive the general form of $\partial \mathbf{f}/\partial \boldsymbol{\sigma}$. Recalling the creep constitutive equation

$$\dot{\boldsymbol{\epsilon}}^{cr} = \frac{\partial \Psi}{\partial \boldsymbol{\sigma}} = \sum_{i=1}^{5} \frac{\partial \Psi}{\partial I_i}\frac{\partial I_i}{\partial \boldsymbol{\sigma}} = \mathbf{f}(\boldsymbol{\sigma}), \tag{41}$$

we readily conclude that

$$\frac{\partial \mathbf{f}}{\partial \boldsymbol{\sigma}} = \frac{\partial^2 \Psi}{\partial \boldsymbol{\sigma} \partial \boldsymbol{\sigma}} = \sum_{i=1}^{5} \sum_{j=1}^{5} \frac{\partial^2 \Psi}{\partial I_i \partial I_j} \frac{\partial I_i}{\partial \boldsymbol{\sigma}} \frac{\partial I_j}{\partial \boldsymbol{\sigma}} + \sum_{i=1}^{5} \frac{\partial \Psi}{\partial I_i} \frac{\partial^2 I_i}{\partial \boldsymbol{\sigma} \partial \boldsymbol{\sigma}}, \tag{42}$$

where

$$\frac{\partial I_1}{\partial \boldsymbol{\sigma}} = \mathbf{I}, \qquad \frac{\partial^2 I_1}{\partial \boldsymbol{\sigma} \partial \boldsymbol{\sigma}} = \mathbf{0}, \tag{43}$$

$$\frac{\partial I_2}{\partial \boldsymbol{\sigma}} = 2\boldsymbol{\sigma}, \qquad \frac{\partial^2 I_2}{\partial \boldsymbol{\sigma} \partial \boldsymbol{\sigma}} = 2\mathbf{J}, \tag{44}$$

$$\frac{\partial I_3}{\partial \boldsymbol{\sigma}} = 3\boldsymbol{\sigma}^2, \qquad \frac{\partial^2 I_3}{\partial \sigma_{ij} \partial \sigma_{kl}} = 3\left(\delta_{ik}\,\sigma_{lj} + \sigma_{ik}\,\delta_{lj}\right), \tag{45}$$

$$\frac{\partial I_4}{\partial \boldsymbol{\sigma}} = \mathbf{a}, \qquad \frac{\partial^2 I_4}{\partial \boldsymbol{\sigma} \partial \boldsymbol{\sigma}} = \mathbf{0}, \tag{46}$$

$$\frac{\partial I_5}{\partial \boldsymbol{\sigma}} = \boldsymbol{\sigma} \cdot \mathbf{a} + \mathbf{a} \cdot \boldsymbol{\sigma}, \qquad \frac{\partial^2 I_5}{\partial \sigma_{ij} \partial \sigma_{kl}} = a_{ik}\,\sigma_{lj} + \sigma_{ik}\,a_{lj}. \tag{47}$$

We conclude this section with a brief discussion of the appropriate time increment used in the integration procedure. Let $\sigma_{\max}$ be the maximum of the absolute values of the stress components (i.e., $\sigma_{\max} = \max|\sigma_{ij}|$) and define

$$\text{CETOL} = 0.1\,\frac{\sigma_{\max}}{E_{11}}, \tag{48}$$

where E_{11} is the elastic modulus defined in section 2.3. The time increment Δt is chosen so that the maximum difference in the creep strain increment calculated from the creep strain rate based on the conditions at the beginning and at the end of the increment is always less than CETOL, i.e.

$$|f_{ij}(\boldsymbol{\sigma}_{n+1}) - f_{ij}(\boldsymbol{\sigma}_n)|\,\Delta t < \text{CETOL} \qquad \text{for all} \quad i,j. \tag{49}$$

4.2 Linearization moduli

In an implicit finite element code, the overall discretized equilibrium equations are written at the end of the increment, resulting in a set of non-linear equations for the nodal unknowns. If a full Newton scheme is used to solve the global non-linear equations, one needs to calculate the so-called 'linearization moduli' $\mathcal{J}$

$$\mathcal{J} = \frac{\partial \boldsymbol{\sigma}_{n+1}}{\partial \boldsymbol{\epsilon}_{n+1}}. \tag{50}$$

For simplicity, we drop the subscript $(n+1)$ with the understanding that all quantities are evaluated at the end of the increment, unless otherwise indicated. Starting with the elasticity equation (34), we find

$$\partial\boldsymbol{\sigma} = \mathbf{C} : \partial\boldsymbol{\epsilon} - \mathbf{C} : \partial\Delta\boldsymbol{\epsilon}^{cr}. \tag{51}$$

The differential $\partial\Delta\boldsymbol{\epsilon}^{cr}$ is evaluated from equation (35) as follows

$$\partial\Delta\boldsymbol{\epsilon}^{cr} = \frac{\partial\Delta\boldsymbol{\epsilon}^{cr}}{\partial\boldsymbol{\sigma}} : \partial\boldsymbol{\sigma} = \alpha\,\Delta t\,\frac{\partial \mathbf{f}}{\partial\boldsymbol{\sigma}} : \partial\boldsymbol{\sigma}. \tag{52}$$

Substituting the last equation into (51) and solving for $\partial\boldsymbol{\sigma}/\partial\boldsymbol{\epsilon}$, we find

$$\mathcal{J} = \frac{\partial\boldsymbol{\sigma}}{\partial\boldsymbol{\epsilon}} = \left(\mathbf{J} + \alpha\,\Delta t\,\mathbf{C} : \frac{\partial \mathbf{f}}{\partial\boldsymbol{\sigma}}\right)^{-1} : \mathbf{C} = \left(\mathbf{C}^{-1} + \alpha\,\Delta t\,\frac{\partial \mathbf{f}}{\partial\boldsymbol{\sigma}}\right)^{-1}. \tag{53}$$

Note that $\partial f_{ij}/\partial\sigma_{kl}$ is symmetric with respect to the pair of indices (i,j) and (k,l). Therefore, in view of (53) and the usual symmetries of the elasticity tensor $\mathbf{C}$, the Jacobian $\mathcal{J}_{ijkl}$ is also symmetric with respect to (i,j) and (k,l), which leads to a symmetric 'stiffness matrix' in the finite element computations.

4.3 The case of plane stress

In this section, we consider the case in which the fibers are all parallel to the $x_3 = 0$ plane (i.e. $\mathbf{n} = n_1\mathbf{e}_1 + n_2\mathbf{e}_2$) and the applied loads are such that $\sigma_{33} = \sigma_{31} = \sigma_{32} = 0$. The stress and strain tensors are now of the form

$$\boldsymbol{\sigma} = \sigma_{\alpha\beta}\mathbf{e}_\alpha\mathbf{e}_\beta \qquad \text{and} \qquad \boldsymbol{\epsilon} = \epsilon_{\alpha\beta}\mathbf{e}_\alpha\mathbf{e}_\beta + \epsilon_{33}\mathbf{e}_3\mathbf{e}_3, \tag{54}$$

where Greek subscripts range over the integers (1,2).

In such problems, the the strain increments $\Delta\epsilon_{11}$, $\Delta\epsilon_{22}$ and $\Delta\epsilon_{12}$ are known, but the out-of-plane component of the strain increment $\Delta\epsilon_{33}$ is not defined kinematically; therefore, some modifications to the method described in section 4.1 are needed.

The total- and creep-strain increments are written as

$$\Delta\boldsymbol{\epsilon} = \Delta\epsilon_{\alpha\beta}\mathbf{e}_\alpha\mathbf{e}_\beta + \Delta\epsilon_{33}\mathbf{e}_3\mathbf{e}_3 \qquad \text{and} \qquad \Delta\boldsymbol{\epsilon}^{cr} = \Delta\epsilon^{cr}_{\alpha\beta}\mathbf{e}_\alpha\mathbf{e}_\beta + \Delta\epsilon^{cr}_{33}\mathbf{e}_3\mathbf{e}_3. \tag{55}$$

The plane stress condition $\sigma_{33} = 0$ requires that

$$C_{33ij}(\Delta\epsilon_{ij} - \Delta\epsilon^{cr}_{ij}) = 0 \qquad \text{or} \qquad \Delta\epsilon_{33} = (C_{33ij}\,\Delta\epsilon^{cr}_{ij} - C_{33\alpha\beta}\,\Delta\epsilon_{\alpha\beta})/C_{3333}. \tag{56}$$

Summarizing, we write

$$\mathbf{F}(\Delta\boldsymbol{\epsilon}^{cr}) \equiv \Delta\boldsymbol{\epsilon}^{cr} - [\alpha\,\mathbf{f}(\boldsymbol{\sigma}(\Delta\boldsymbol{\epsilon}^{cr}),t,s) + (1-\alpha)\,\mathbf{f}(\boldsymbol{\sigma}_n,t_n,s)]\,\Delta t = \mathbf{0}, \tag{57}$$

$$\sigma_{ij}(\Delta\boldsymbol{\epsilon}^{cr}) = \hat{\sigma}^e_{ij} + C_{ij33}\,\Delta\epsilon_{33}(\Delta\boldsymbol{\epsilon}^{cr}) - C_{ijkl}\,\Delta\epsilon^{cr}_{kl}, \tag{58}$$

$$\Delta\epsilon_{33}(\Delta\boldsymbol{\epsilon}^{cr}) = (C_{33ij}\,\Delta\epsilon^{cr}_{ij} - C_{33\alpha\beta}\,\Delta\epsilon_{\alpha\beta})/C_{3333}, \tag{59}$$

where

$$\hat{\sigma}^e_{ij} = (\boldsymbol{\sigma}_n)_{ij} + C_{ij\alpha\beta}\,\Delta\epsilon_{\alpha\beta}. \tag{60}$$

We choose $\Delta\boldsymbol{\epsilon}^{cr}$ as the primary unknown and treat (57) as the basic equation in which $\boldsymbol{\sigma}(\Delta\boldsymbol{\epsilon}^{cr})$ is defined by (58)-(60). The solution is obtained using Newton's method. The corresponding Jacobian is

$$\frac{\partial\mathbf{F}}{\partial\Delta\boldsymbol{\epsilon}^{cr}} = \mathbf{J} - \alpha\,\Delta t\,\frac{\partial\mathbf{f}}{\partial\boldsymbol{\sigma}} : \frac{\partial\boldsymbol{\sigma}}{\partial\Delta\boldsymbol{\epsilon}^{cr}} = \mathbf{J} + \alpha\,\Delta t\,\frac{\partial\mathbf{f}}{\partial\boldsymbol{\sigma}} : (\mathbf{C}-\mathbf{A}), \tag{61}$$

where

$$A_{ijlk} = C_{ij33}\,C_{33kl}/C_{3333}. \tag{62}$$

5 An analytical model for creeping fiber-reinforced materials

deBotton and Ponte Castañeda (1993) have presented recently a constitutive model for non-linear composite materials reinforced by continuous fibers. They developed their model in the context of infinitesimal non-linear elasticity, but their results can be used to describe *steady-state* creep as well.

For the special case of incompressible behavior in which the creep potential for both the matrix and the fibers is a function of the von Mises equivalent stress σ_e, their model can be summarized as follows. Let the creep potentials for the matrix and the fibers be of the form

$$\Psi^{(k)} = \Psi^{(k)}(\sigma_e), \qquad k = 1,2, \tag{63}$$

where $k = 1$ refers to the matrix and $k = 2$ to the fibers. If the matrix is the 'weaker' material, then the creep potential of the composite is estimated to be (deBotton and Ponte Castañeda, 1993)

$$\Psi(I_1,I_2,I_4) = \hat{\Psi}(\sigma_s^2,\sigma_d^2) = \min_{\omega,\eta}\left[c_1\,\Psi^{(1)}\left(\sigma_e^{(1)}\right) + c_2\,\Psi^{(2)}\left(\sigma_e^{(2)}\right)\right], \tag{64}$$

where c_1 and c_2 are the volume fractions of the matrix and the fibers respectively ($c_1+c_2=1$), and

$$\sigma_e^{(1)}(\boldsymbol{\sigma},\omega,\eta) = \left\{\left[(1+c_2\,\omega)^2+c_2\,\omega^2\right]\,\sigma_s^2(\boldsymbol{\sigma})+(1+c_2\,\eta)^2\,\sigma_d^2(\boldsymbol{\sigma})\right\}^{1/2}, \tag{65}$$

$$\sigma_e^{(2)}(\boldsymbol{\sigma},\omega,\eta) = \left[(1-c_1\,\omega)^2\,\sigma_s^2(\boldsymbol{\sigma})+(1-c_1\,\eta)^2\,\sigma_d^2(\boldsymbol{\sigma})\right]^{1/2}, \tag{66}$$

$$\sigma_s^2(\boldsymbol{\sigma}) = 3\,(\tau_n^2+\tau_p^2)=\frac{1}{2}\,(3\,I_2-I_1^2)-\frac{1}{4}\,(I_1-3\,I_4)^2, \tag{67}$$

$$\sigma_d^2(\boldsymbol{\sigma}) = (\sigma_n-\sigma_p)^2=\frac{1}{4}\,(3\,I_4-I_1)^2, \tag{68}$$

$$\sigma_n = \mathbf{n}\cdot\boldsymbol{\sigma}\cdot\mathbf{n}, \tag{69}$$

$$\sigma_p = \frac{1}{2}\,\boldsymbol{\sigma}:(\mathbf{I}-\mathbf{nn}). \tag{70}$$

The quantities $\sigma_n, \sigma_p, \tau_n$ and τ_p are the alternative set of transversely isotropic invariants discussed in Appendix A.

Note that in (64) the creep potential Ψ is independent of I_5, which implies that the predicted response of the composite will be the same under longitudinal and transverse shear.

Let $\hat{\eta}$ and $\hat{\omega}$ be the values of η and ω that minimize the right hand side of (64) for a given stress state $\boldsymbol{\sigma}$, i.e.

$$\Psi = c_1\,\Psi^{(1)}(\boldsymbol{\sigma},\hat{\omega},\hat{\eta})+c_2\,\Psi^{(2)}(\boldsymbol{\sigma},\hat{\omega},\hat{\eta}). \tag{71}$$

In general, $\hat{\eta}$ and $\hat{\omega}$ are functions of $\boldsymbol{\sigma}$, and the corresponding equation for the creep strain rate is

$$\dot{\boldsymbol{\epsilon}}^{cr} = c_1\frac{\partial\Psi^{(1)}}{\partial\boldsymbol{\sigma}}+c_2\frac{\partial\Psi^{(2)}}{\partial\boldsymbol{\sigma}}+\left(c_1\frac{\partial\Psi^{(1)}}{\partial\hat{\omega}}+c_2\frac{\partial\Psi^{(2)}}{\partial\hat{\omega}}\right)\frac{\partial\hat{\omega}}{\partial\boldsymbol{\sigma}}+\left(c_1\frac{\partial\Psi^{(1)}}{\partial\hat{\eta}}+c_2\frac{\partial\Psi^{(2)}}{\partial\hat{\eta}}\right)\frac{\partial\hat{\eta}}{\partial\boldsymbol{\sigma}}. \tag{72}$$

However, in view of the minimization in (64), each of the terms in parentheses on the right hand side of the above equation vanishes identically. Therefore, in computing $\dot{\boldsymbol{\epsilon}}^{cr}$, one may regard $\hat{\omega}$ and $\hat{\eta}$ as constants (deBotton and Castañeda, 1993). The corresponding constitutive equation for the creep strain rate can be now written as

$$\begin{aligned}\dot{\epsilon}_{ij}^{cr} &= c_1\frac{\Psi^{(1)\prime}}{\sigma_e^{(1)}}\left\{\left[(1+c_2\,\hat{\omega})^2+c_2\,\hat{\omega}^2\right]\sigma_s\frac{\partial\sigma_s}{\partial\sigma_{ij}}+(1+c_2\,\hat{\eta})^2\,\sigma_d\frac{\partial\sigma_d}{\partial\sigma_{ij}}\right\}\\ &+ c_2\frac{\Psi^{(2)\prime}}{\sigma_e^{(2)}}\left[(1-c_1\,\hat{\omega})^2\,\sigma_s\frac{\partial\sigma_s}{\partial\sigma_{ij}}+(1-c_1\,\hat{\eta})^2\,\sigma_d\frac{\partial\sigma_d}{\partial\sigma_{ij}}\right],\end{aligned} \tag{73}$$

where

$$\Psi^{(k)\prime} = \left[\frac{d\Psi^{(k)}(\sigma_e)}{d\sigma_e}\right]_{\sigma_e=\sigma_e^{(k)}} \qquad k=1,2, \tag{74}$$

and

$$\sigma_s \frac{\partial \sigma_s}{\partial \sigma_{ij}} = \frac{3}{2}\sigma'_{ij} - \frac{1}{2}(\sigma_n - \sigma_p)(3\,n_i\,n_j - \delta_{ij}), \tag{75}$$

$$\sigma_d \frac{\partial \sigma_d}{\partial \sigma_{ij}} = \frac{1}{2}(\sigma_n - \sigma_p)(3\,n_i\,n_j - \delta_{ij}). \tag{76}$$

It should be noted that the above model is independent of the hydrostatic stress $p = \sigma_{kk}/3$ and that the predicted creep response is volume preserving, i.e. $\dot{\epsilon}^{cr}_{kk} = 0$.

If the fibers are *rigid*, then one can formally set $\Psi^{(2)} = 0$. The minimization in (64) then yields

$$\hat{\omega} = -\frac{1}{1+c_2} \qquad \text{and} \qquad \hat{\eta} = -\frac{1}{c_2}. \tag{77}$$

Then $\sigma_e^{(1)} = \sigma_s/\sqrt{1+c_2}$ and the estimated creep potential and the corresponding constitutive equations of the composite become

$$\Psi(I_1, I_2, I_4) = c_1\,\Psi^{(1)}(\sigma_e^{(1)}), \tag{78}$$

$$\dot{\epsilon}^{cr}_{ij} = \frac{c_1\Psi^{(1)\prime}}{\sqrt{1+c_2}}\frac{\partial \sigma_s}{\partial \sigma_{ij}} = \frac{c_1}{2\sqrt{1+c_2}}\frac{\Psi^{(1)\prime}}{\sigma_s}\left[3\,\sigma'_{ij} - (\sigma_n - \sigma_p)(3\,n_i\,n_j - \delta_{ij})\right]. \tag{79}$$

Using the last equation, one can readily show that

$$\mathbf{n}\cdot\dot{\boldsymbol{\epsilon}}^{cr}\cdot\mathbf{n} = \mathbf{0}, \tag{80}$$

i.e., the composite is inextensible in the direction of the rigid fibers. If $\mathbf{n} = \mathbf{e}_3$, then the constitutive equations (79) become

$$\dot{\epsilon}^{cr}_{11} = -\dot{\epsilon}^{cr}_{22} = \frac{A}{2}(\sigma'_{11} - \sigma'_{22}), \quad \dot{\epsilon}^{cr}_{33} = 0, \quad \text{and} \quad \dot{\epsilon}^{cr}_{ij} = A\,\sigma_{ij} \quad \text{for} \quad i \neq j, \tag{81}$$

where

$$A = \frac{3}{2}\frac{c_1}{\sqrt{1+c_2}}\frac{\Psi^{(1)\prime}}{\sigma_s}. \tag{82}$$

6 Comparison with results of homogenization theory

The predictions of the constitutive model described in the previous section are compared here with the results of periodic homogenization theory (Sanchez-Palencia, 1980; Bakhvalov and Panasenko, 1989). The homogenization techniques were originally developed in the context of linear elasticity, but they have been extended to infinitesimal non-linear elasticity (Suquet,

1982; Jansson, 1992). The comparisons are carried out for non-linear elastic materials, for which the model of deBotton and Ponte Castañeda (1993) has been developed.

The non-linear composite is assumed to be *macroscopically homogeneous* and we seek to determine an *effective* constitutive equation of the form $\mathbf{\Sigma} = \mathbf{g}(\mathbf{E})$, where $\mathbf{\Sigma}$ and $\mathbf{E}$ are the macroscopic stress and strain respectively, and $\mathbf{g}$ is a tensor-valued constitutive function to be determined. The *macroscopic* field equations for a certain elasticity problem involving the composite are

$$\frac{\partial \Sigma_{ji}}{\partial x_j} + b_i = 0, \tag{83}$$

$$\mathbf{\Sigma} = \mathbf{g}(\mathbf{E}), \tag{84}$$

$$E_{ij} = \frac{1}{2}\left(\frac{\partial u_i}{\partial x_j} + \frac{\partial u_j}{\partial x_i}\right), \tag{85}$$

where $\mathbf{u}$ is the displacement field, and $\mathbf{b} = \mathbf{b}(\mathbf{x})$ is the body force.

In the following, we summarize some of the results of homogenization theory as developed by Sanchez Palencia (1980) (see also Lene and Leguillon, 1982; Suquet, 1982, 1987; Lene, 1986; Jansson, 1992).

6.1 Homogenization theory

The composite is now modeled as an *inhomogeneous* continuum made of two different homogeneous non-linear elastic constituents. The microstructure is assumed to be *periodic*, i.e. the constituents of the composite are arranged in such a way that it can be constructed by the periodic repetition of self-similar elements. We define the 'unit cell' as the smallest such repeatable element. The characteristic length l of the unit cell is assumed to be small compared to any characteristic dimension L of the body, i.e.

$$\delta = \frac{l}{L} << 1. \tag{86}$$

Let $\mathbf{x}$ denote the position vector with respect to a fixed global cartesian coordinate system. A local variable $\mathbf{y}$ is introduced for the unit cell by

$$\mathbf{y} = \frac{\mathbf{x}}{\delta} \qquad \text{or} \qquad \mathbf{x} = \delta\,\mathbf{y}, \tag{87}$$

so that a change of $O(1)$ in $\mathbf{y}$ corresponds to a $O(\delta)$ change in $\mathbf{x}$. Note that the coordinate $\mathbf{x}$ is *constant* at the unit cell level, where positions are described in terms of $\mathbf{y}$.

In view of the periodicity of the microstructure, the constitutive equations at any point of the heterogeneous medium can be written as

$$\boldsymbol{\sigma} = \mathbf{f}(\epsilon, \frac{\mathbf{x}}{\delta}) = \mathbf{f}(\epsilon, \mathbf{y}), \tag{88}$$

$\mathbf{f}$ being a periodic function consistent with the periodicity of the microstructure, i.e. such that

$$\mathbf{f}(\epsilon, \frac{\mathbf{x}}{\delta} + l_i \mathbf{e}_i) = \mathbf{f}(\epsilon, \frac{\mathbf{x}}{\delta}), \qquad i = 1,2,3 \qquad \text{(no sum over } i\text{)} \tag{89}$$

where l_i is the characteristic length of the unit cell in the i-th coordinate direction, and $\mathbf{e}_i$ is the unit vector in that direction. Functions of the type of equation (89) will be referred to in the following as Y-periodic.

Next, we search for an asymptotic expansion of the displacement field $\mathbf{u}$ as $\delta \to 0$. A two-scale expansion of the form (Sanchez Palencia, 1980)

$$\mathbf{u}(\mathbf{x},\mathbf{y}) = \mathbf{u}^{(0)}(\mathbf{x}) + \delta\, \mathbf{u}^{(1)}(\mathbf{x},\mathbf{y}) + \delta^2\, \mathbf{u}^{(2)}(\mathbf{x},\mathbf{y}) + O(\delta^3) \tag{90}$$

is attempted, where the functions $\mathbf{u}^{(1)}$, $\mathbf{u}^{(2)}$, etc. are Y-periodic. In the above equation $\mathbf{u}^{(0)}(\mathbf{x})$ corresponds to the macroscopic deformation field $\mathbf{E}(\mathbf{x})$, whereas the subsequent Y-periodic terms $\mathbf{u}^{(1)}$, $\mathbf{u}^{(2)}$, etc. are local perturbations due to the presence of the fibers in the continuum.

The corresponding strain expansion is

$$\begin{aligned} \boldsymbol{\epsilon}(\mathbf{x},\mathbf{y}) &= \left[\mathbf{E}(\mathbf{x}) + \boldsymbol{\epsilon}^{y(1)}(\mathbf{x},\mathbf{y})\right] + \delta\, \left[\boldsymbol{\epsilon}^{x(1)}(\mathbf{x},\mathbf{y}) + \boldsymbol{\epsilon}^{y(2)}(\mathbf{x},\mathbf{y})\right] + O(\delta^2) && (91) \\ &\equiv \boldsymbol{\epsilon}^{(0)}(\mathbf{x},\mathbf{y}) + \delta\, \boldsymbol{\epsilon}^{(1)}(\mathbf{x},\mathbf{y}) + O(\delta^2), && (92) \end{aligned}$$

where

$$\epsilon_{ij}^{x(k)} = \frac{1}{2}\left(\frac{\partial u_i^{(k)}}{\partial x_j} + \frac{\partial u_j^{(k)}}{\partial x_i}\right) \qquad \text{and} \qquad \epsilon_{ij}^{y(k)} = \frac{1}{2}\left(\frac{\partial u_i^{(k)}}{\partial y_j} + \frac{\partial u_j^{(k)}}{\partial y_i}\right). \tag{93}$$

Note that $\boldsymbol{\epsilon}^{x(0)}(\mathbf{x}) = \mathbf{E}(\mathbf{x})$. The stress field can be written as

$$\boldsymbol{\sigma}(\mathbf{x},\mathbf{y}) = \mathbf{f}(\boldsymbol{\epsilon}^{(0)},\mathbf{y}) + \delta\, \mathbf{c}(\boldsymbol{\epsilon}^{(0)},\mathbf{y}) : \boldsymbol{\epsilon}^{(1)} + O(\delta^2) \equiv \boldsymbol{\sigma}^{(0)}(\mathbf{x},\mathbf{y}) + \delta\, \boldsymbol{\sigma}^{(1)}(\mathbf{x},\mathbf{y}) + O(\delta^2), \tag{94}$$

where

$$\mathbf{c}(\boldsymbol{\epsilon}^{(0)},\mathbf{y}) = \left[\frac{\partial \mathbf{f}(\epsilon,\mathbf{y})}{\partial \epsilon}\right]_{\epsilon=\epsilon^{(0)}}. \tag{95}$$

The equilibrium equations become

$$\frac{1}{\delta}\frac{\partial \sigma_{ji}^{(0)}}{\partial y_j} + \left(\frac{\partial \sigma_{ji}^{(0)}}{\partial x_j} + \frac{\partial \sigma_{ji}^{(1)}}{\partial y_j} + b_i\right) + O(\delta) = 0. \tag{96}$$

In view of the Y-periodicity of $\mathbf{u}^{(1)}$ and $\mathbf{f}$, the fields $\epsilon^{(0)}$, $\epsilon^{(1)}$, $\boldsymbol{\sigma}^{(0)}$ and $\boldsymbol{\sigma}^{(1)}$ are Y-periodic as well. Also, since the outward unit normal $\mathbf{N}$ to the boundary ∂Y of the unit cell takes opposite values on opposite sides of ∂Y, the traction vector $\mathbf{t}^{(0)} = \mathbf{N} \cdot \boldsymbol{\sigma}^{(0)}$ is Y-anti-periodic.

Collecting terms having like powers of δ, we obtain the following hierarchy of problems.

6.1.1 Leading order problem (the unit cell problem)

We can recast the leading order terms of the above equations in the following form.

$$\hat{\mathbf{u}}(\mathbf{y}) \equiv \mathbf{E}(\mathbf{x}) \cdot \mathbf{y} + \mathbf{u}^{(1)}(\mathbf{x}, \mathbf{y}), \tag{97}$$

$$\hat{\epsilon}_{ij}(\mathbf{y}) \equiv \epsilon_{ij}^{(0)}(\mathbf{x}, \mathbf{y}) = \frac{1}{2}\left(\frac{\partial \hat{u}_i}{\partial y_j} + \frac{\partial \hat{u}_j}{\partial y_i}\right), \tag{98}$$

$$\hat{\boldsymbol{\sigma}}(\mathbf{y}) \equiv \boldsymbol{\sigma}^{(0)}(\mathbf{x}, \mathbf{y}) = \mathbf{f}(\hat{\epsilon}, \mathbf{y}), \tag{99}$$

$$\frac{\partial \hat{\sigma}_{ji}}{\partial y_j} = 0, \tag{100}$$

with

$$\mathbf{u}^{(1)} \quad \text{Y-periodic}, \qquad \hat{\mathbf{t}} = \mathbf{N} \cdot \hat{\boldsymbol{\sigma}} \quad \text{Y-anti-periodic}, \tag{101}$$

where $\hat{\mathbf{u}}(\mathbf{y})$, $\hat{\epsilon}(\mathbf{y})$ and $\hat{\boldsymbol{\sigma}}(\mathbf{y})$ be the displacements, strains and stresses of the unit cell. Recall that $\mathbf{x}$ is constant at the unit cell level; therefore, the macroscopic strain field $\mathbf{E}(\mathbf{x})$ is also constant in (97) and can be viewed as the macroscopic 'applied load' to the unit cell. The field equations (97)-(100) over the unit cell together with the conditions (101) define a well-posed boundary value problem that can be solved for $(\hat{\mathbf{u}}, \hat{\epsilon}, \hat{\boldsymbol{\sigma}})$ or, equivalently, for $(\mathbf{u}^{(1)}, \epsilon^{(0)}, \boldsymbol{\sigma}^{(0)})$ (e.g., see Suquet, 1987). One can readily show that, if the constitutive function $\mathbf{f}$ in (88) is convex, then the unit cell problem has a unique solution.

For any function $\phi(\mathbf{x}, \mathbf{y})$, we define

$$< \phi >= \frac{1}{|Y|} \int_Y \phi(\mathbf{x}, \mathbf{y})\, dV_y, \tag{102}$$

where Y denotes the unit cell. Using equations (98) and (99) and taking into account the Y-periodicity of $\mathbf{u}^{(1)}$, we find

$$< \hat{\epsilon} >=< \epsilon^{(0)} >= \epsilon^{x(0)} = \mathbf{E} \qquad \text{and} \qquad < \hat{\boldsymbol{\sigma}} >=< \boldsymbol{\sigma}^{(0)} > . \tag{103}$$

The solution of the unit cell problem can be used to determine the functional relationship between $< \hat{\boldsymbol{\sigma}} >$ and $< \hat{\epsilon} >$, i.e. to find a tensor-valued function $\mathbf{h}$ such that

$$< \hat{\boldsymbol{\sigma}} >= \mathbf{h}(< \hat{\epsilon} >). \tag{104}$$

Note that, in view of (103), the last equation can be also written as

$$< \boldsymbol{\sigma}^{(0)} >= \mathbf{h}(< \boldsymbol{\epsilon}^{(0)} >). \tag{105}$$

We conclude this section by stating the well known result

$$< \hat{\sigma}_{ij} >= \frac{1}{2Y} \int_{\partial Y} (\hat{t}_i \, y_j + \hat{t}_j \, y_i) \, dS_y. \tag{106}$$

6.1.2 Second order equations

The equilibrium equation yields, to second order,

$$\frac{\partial \sigma_{ji}^{(0)}(\mathbf{x},\mathbf{y})}{\partial x_j} + \frac{\partial \sigma_{ji}^{(1)}(\mathbf{x},\mathbf{y})}{\partial y_j} + b_i(\mathbf{x}) = 0. \tag{107}$$

Taking the Y-average of the above equation and using the fact that $\boldsymbol{\sigma}^{(1)}$ is Y-periodic, we find

$$\frac{\partial < \sigma_{ji}^{(0)} >}{\partial x_j} + b_i = 0. \tag{108}$$

We summarize our findings by restating equations (108), (105), (103a) and (93a) as follows

$$\frac{\partial < \sigma_{ji}^{(0)} >}{\partial x_j} + b_i = 0, \tag{109}$$

$$< \boldsymbol{\sigma}^{(0)} > = \mathbf{h}(< \boldsymbol{\epsilon}^{(0)} >), \tag{110}$$

$$< \epsilon_{ij}^{(0)} > = \frac{1}{2} \left(\frac{\partial u_i^{(0)}}{\partial x_j} + \frac{\partial u_j^{(0)}}{\partial x_i} \right). \tag{111}$$

Equations (109)-(111) define the *homogenized problem* for $\mathbf{u}^{(0)}(\mathbf{x})$. Comparing equations (109)-(111) to the macroscopic field equations (83)-(85), we conclude that the function $\mathbf{h}$, determined from the solution of the unit cell problem, provides the leading-order *homogenized* constitutive equation for the composite.

In the following, we use the finite element method to obtain numerical solutions of the unit cell problem for various types of loading. The solutions are then used to calculate numerically the function $\mathbf{h}$, which is the leading-order constitutive function of the homogenized composite.

6.2 Numerical solution of the unit cell problem

We consider a composite material made of a non-linear elastic matrix reinforced by continuous aligned fibers, which are assumed to be non-linear elastic as well. The constitutive equations for the matrix and the fibers are of the form

$$\epsilon = \frac{\partial \Psi^{(k)}}{\partial \boldsymbol{\sigma}} = \frac{3}{2}\,\epsilon_{0k}\left(\frac{\sigma_e}{\sigma_{0k}}\right)^{n_k-1}\frac{\boldsymbol{\sigma}'}{\sigma_{0k}}, \qquad \Psi^{(k)}(\sigma_e) = \frac{\sigma_{0k}\,\epsilon_{0k}}{n_k+1}\left(\frac{\sigma_e}{\sigma_{0k}}\right)^{n_k+1}, \qquad k = 1,2. \quad (112)$$

The distribution of the fibers is assumed to be periodic, with the fibers arranged in a hexagonal array. The linear and quadratic stress invariants of the hexagonal arrangement are the same as those of a transversely isotropic system; therefore, a hexagonal array of fibers can be used to study *linear* transversely isotropic elastic materials, since the elastic potential is a function of the linear and quadratic stress invariants only (Green and Adkins, 1960; Jansson, 1992). In the general case, however, where terms of higher degree are involved, the hexagonal system will provide only an *approximation* for a *non-linear* transversely isotropic material.

The fibers are assumed to be aligned with the y_3 coordinate direction, and the unit cell is infinitely long in that direction. Figure 1 shows the cross section of the unit cell on the y_1-y_2 plane.

The macroscopic applied loads are taken to coincide with the principal material directions. In particular, the following four types of loading are considered:

1. Longitudinal tension: $\sigma_{33} \neq 0$, all other $\sigma_{ij} = 0$,

2. Transverse tension: $\sigma_{11} \neq 0$, all other $\sigma_{ij} = 0$,

3. Transverse shear: $\sigma_{12} = \sigma_{21} \neq 0$, all other $\sigma_{ij} = 0$,

4. Longitudinal shear: $\sigma_{31} = \sigma_{13} \neq 0$, all other $\sigma_{ij} = 0$,

where the σ_{ij}'s are understood to represent the components of the *macroscopic* stress $\boldsymbol{\Sigma}$, which is consistent with the macroscopic strain $\mathbf{E}$.

In view of the geometric symmetries of the unit cell and the applied loads, the periodic boundary conditions (101) of the unit cell problem can be transformed to 'classical' traction and displacement boundary conditions. A detailed discussion of this transformation is given in the Appendix B. It should be emphasized, however, that the periodic boundary conditions

cannot be reduced to classical boundary conditions when more general types of loading are considered.

The unit cell problem is solved using the ABAQUS general purpose finite element program (Hibbitt, 1984). The calculations are carried out for $n_1 = 10$, $n_2 = 3$, $\sigma_{01} = \sigma_{02} = \sigma_0$ and $\epsilon_{01} = \epsilon_{02} = \epsilon_0 = 10^{-5}$. The 'deformation plasticity' model in ABAQUS has an additional 'linear-elastic' term on the right hand side of equation (112a); the elastic moduli used in the finite element computations are four orders of magnitude larger than σ_0, so that the contribution of the additional elastic terms becomes negligible. The volume fraction of the fibers is 39.5%, i.e. $c_2 = 0.395$, $c_1 = 0.605$. Figure 2 shows the finite element mesh used for problems 1, 2 and 3; the dark and white regions in Fig. 2 represent the fibers and the matrix respectively. The layout shown in Fig. 2 is repeated in the third direction to produce the layer of three-dimensional elements used for the solution of problem 4. The type of elements and the exact boundary conditions used in the calculation can be found in the Appendix B.

Figure 3 shows the calculated longitudinal stress-strain curve. In Figure 3, and in all subsequent figures, the solid line is the prediction of the model of deBotton and Ponte Castañeda, whereas the circles indicate the results of the finite element calculations. The predictions of the analytical model agree well with the solution of the unit cell problem.

Figure 4 shows the calculated transverse stress-strain curve. At a transverse strain $\epsilon_{11} = 0.01$, there is a 7% difference between the prediction of the analytical model and the finite element solution.

Figure 5 shows the transverse shear stress-strain response. At a transverse shear strain $\epsilon_{12} = \gamma_{12}/2 = 0.01$, there is a 13% difference between the prediction of the analytical model and the unit cell solution.

The finite element solution of problem 4 (longitudinal shear) produces a shear stress-strain curve identical to that shown in Fig. 5 for the transverse shear. This is consistent with the structure of the analytical model which also predicts identical response to longitudinal and transverse shear.

Figures 3–5 show that, at a given strain level, the stress predicted by the analytical model is always higher than that of the finite element solution. This is consistent with the fact that the complementary elastic energy function Ψ developed by deBotton and Ponte Castañeda is an upper bound to the actual complementary energy of the composite. It should be also noted that the model of deBotton and Ponte Castañeda is developed for a transversely isotropic composite with a *random* distribution of fibers, whereas the unit cell calculations

refer to a composite with a given *periodic* microstructure (hexagonal array).

7 An example: a plate with a hole

The model of deBotton and Ponte Castañeda is implemented in the ABAQUS general purpose finite element program. This code provides a general interface so that a specific constitutive model can be introduced as a 'user subroutine.' The constitutive equations are integrated using the method presented in section 4 with $\alpha = 1/2$ (trapezoidal method).

Figure 6 shows a schematic representation of a plate with a hole; the plate is reinforced by continuous aligned fibers as shown in the figure, and the ratio $w/2a$ equals 6. Elasticity and creep are assumed to be the only possible mechanisms of deformation. The diameter of a typical fiber is assumed to be small compared to the size of the hole and the thickness of the plate, so that the continuum model described in section 5 can be used in the calculations. As a model material, we consider a γ-TiAl matrix reinforced by polycrystalline Al_2O_3 continuous fibers. The fiber volume fraction is assumed to be 20%, i.e. $c_2 = 0.20$. Typical values of the elastic constants are $E = 200$ GPa and $\nu = 0.3$ for γ-TiAl, and $E = 385$ GPa and $\nu = 0.33$ for Al_2O_3, where E and ν are Young's modulus and Poisson's ratio respectively. Using the estimation procedure described in Christensen (1979), we find the following values for the elastic constants of the composite: $E_{11} = 235$ GPa, $\mu_{12} = 85$ GPa, $\mu_{23} = 85$ GPa, $K_{23} = 220$ GPa, and $\nu_{12} = 0.31$. The matrix and the fibers are assumed to creep according to a power-law equation of the form

$$\dot{\epsilon}^{cr} = \frac{\partial \Psi^{(k)}}{\partial \sigma} = \frac{3}{2}\,\dot{\epsilon}_{0k}\left(\frac{\sigma_e}{\sigma_{0k}}\right)^{n_k-1}\frac{\sigma'}{\sigma_{0k}}, \qquad \Psi^{(k)}(\sigma_e) = \frac{\sigma_{0k}\,\dot{\epsilon}_{0k}}{n_k+1}\left(\frac{\sigma_e}{\sigma_{0k}}\right)^{n_k+1}, \qquad k = 1,2. \quad (113)$$

The model of deBotton and Ponte Castañeda is used to describe the creep behavior of the composite. The following creep constants are used in the computations: $n_1 = 2.6$ and $\dot{\epsilon}_{01}/\sigma_{01}^{n_1} = 1.304 \times 10^{-9}$ MPa$^{-n_1} \cdot s^{-1}$ for the matrix, and $n_2 = 1$ and $\dot{\epsilon}_{02}/\sigma_{02}^{n_2} = 10^{-9}$ MPa$^{-n_2} \cdot s^{-1}$ for the fibers.

Plane stress conditions are assumed, and two types of loading are considered, in which a constant tensile stress of 70 MPa is applied a) in the direction of the fibers, and b) in the transverse direction. In both cases, the load is applied suddenly to the plate at the time $t = 0$. The instantaneous response of the material is elastic and the elastic stress distribution provides the initial condition for the creep problem.

Four-node isoparametric elements with 2×2 Gauss integrations are used in the calculations. The analysis is carried out incrementally and the maximum size of the time increment is controlled by the formula in equation (49). At every element integration point, the values of $\hat{\omega}$ and $\hat{\eta}$ that minimize the right hand side of (64) are found using the values of the stress tensor $\boldsymbol{\sigma}_n$ at the beginning of each increment.

Figures 7–10 show contour plots of several transversely isotropic invariants of the creep strain $\boldsymbol{\epsilon}^{cr}$ at a time t =1 hr for both cases analyzed. The invariants plotted in these figures are (deBotton and Ponte Castañeda, 1993):

$$\epsilon_p^{cr} = \frac{1}{2}\boldsymbol{\epsilon}^{cr} : \boldsymbol{\beta} = \frac{1}{2}(\epsilon_{11}^{cr} + \epsilon_{33}^{cr}), \tag{114}$$

$$\epsilon_n^{cr} = \boldsymbol{\epsilon}^{cr} : \mathbf{a} = \epsilon_{22}^{cr}, \tag{115}$$

$$(\gamma_p^{cr})^2 = \frac{1}{2}(\boldsymbol{\epsilon}^{cr} \cdot \boldsymbol{\beta}) : (\boldsymbol{\epsilon}^{cr} \cdot \boldsymbol{\beta}) - \frac{1}{4}(\boldsymbol{\epsilon}^{cr} : \boldsymbol{\beta})^2 = (\epsilon_{13}^{cr})^2 + \frac{1}{4}(\epsilon_{11}^{cr} - \epsilon_{33}^{cr})^2, \tag{116}$$

$$(\gamma_n^{cr})^2 = (\boldsymbol{\epsilon}^{cr})^2 : \mathbf{a} - (\boldsymbol{\epsilon}^{cr} : \mathbf{a})^2 = (\epsilon_{12}^{cr})^2 + (\epsilon_{23}^{cr})^2, \tag{117}$$

where $\mathbf{n} = \mathbf{e}_2$, $\boldsymbol{\beta} = \mathbf{I} - \mathbf{nn} = \mathbf{e}_1\mathbf{e}_1 + \mathbf{e}_3\mathbf{e}_3$, and the cartesian components refer to the coordinate system shown in Fig. 6. The strain in the direction of the fibers ϵ_n and the in-plane 'volumetric' strain ϵ_p attain their maximum values at point A (see Fig. 6), which appears to be a possible site of fiber failure and debonding. Figures 9 an 10 show that the longitudinal (γ_n) and transverse (γ_p) shear stresses reach their maximum values on the surface of the hole.

Acknowledgments

Fruitful discussions with Professors G. deBotton and P. M. Suquet are gratefully acknowledged. NA and CC acknowledge the support of the Office of Naval Research contract N00014-92-J-1808 through sub-agreement KK3006 from the University of California, Santa Barbara. PPC acknowledges the support of the NSF MRL Program at the University of Pennsylvania under Grant No. DMR-9120668. The ABAQUS finite element code was made available under academic license from Hibbitt, Karlsson and Sorensen, Inc., Providence, RI.

References

[1] Aravas, N., 'Finite elastoplastic transformations of transversely isotropic metals', *Int. J. Solids Struct.*, **29**, 2137–2157 (1992).

[2] Bakhvalov, N. and Panasenko, G., *Homogenisation: Averaging Processes in Periodic Media.* Kluwer Academic Publishers, Dordrecht, The Netherlands (1989).

[3] deBotton, G. and Ponte Castañeda, P., 'Elastoplastic constitutive relations for fiber-reinforced solids', *Int. J. Solids Struct.*, **30**, 1865–1890 (1993).

[4] Christensen, R. M., *Mechanics of Composite Materials.* Wiley, New York (1979).

[5] Green, A. H. and Adkins, J. E., *Large Elastic Deformations.* Clarendon Press, Oxford (1960).

[6] Goto, S. and McLean, M., 'Role of interfaces in creep of fibre-reinforced metal-matrix composites – I. Continuous fibers', *Acta Metall. Mater.*, **39**, 153–164 (1991a).

[7] Goto, S. and McLean, M., 'Role of interfaces in creep of fibre-reinforced metal-matrix composites – II. Short fibers', *Acta Metall. Mater.*, **39**, 165–177 (1991b).

[8] Hibbitt, H. D., 'ABAQUS/EPGEN — A general purpose finite element code with emphasis on nonlinear applications', *Nucl. Eng. Des.*, **77**, 271–297 (1984).

[9] Jansson, S., 'Homogenized nonlinear constitutive properties and local stress concentrations for composites with periodic internal structure', *Int. J. Solids Struct.*, **29**, 2181–2200 (1992).

[10] Johnson, A. F., 'Creep characterization of transversely-isotropic metallic materials', *J. Mech. Phys. Solids*, **25**, 117–126 (1977).

[11] Kelly, A. and Street, N., 'Creep of discontinuous fibre composites II. Theory for the steady state', *Proc. Roy. Soc. Lond. A*, **328**, 283–293 (1972).

[12] Lene, F., 'Damage constitutive relations for composite materials', *Engng Fract. Mech.*, **25**, 713–728 (1986).

[13] Lene, F. and Leguillon, D., 'Homogenized constitutive law for a partially cohesive composite', *Int. J. Solids Struct.*, **18**, 443–458 (1982).

[14] Liu, I.-S., 'On representations of anisotropic invariants', *Int. J. Engng Sci.*, **20**, 1099–1109 (1982).

[15] McLean, M., 'Creep deformation of metal-matrix composites', *Comp. Sci. Tech.*, **23**, 37–52 (1985).

[16] McLean, M., 'Mechanisms and models of high temperature deformation of composites', *Mat. Res. Symp. Proc.*, **120**, 67–79 (1988).

[17] McMeeking, R. M., 'Models for the creep of ceramic matrix composite materials', to appear (1993a).

[18] McMeeking, R. M., 'Power law creep of a composite material containing discontinuous rigid aligned fibers', to appear (1993b).

[19] Mileiko, S. T., 'Steady state creep of a composite material with short fibres', *J. Mat. Sci.*, **5**, 254–261 (1970).

[20] Nagtegaal, J. D., Parks, D. M. and Rice, J. R., 'On numerically accurate finite element solutions in the fully plastic range', *Comp. Methods Appl. Mech. Eng.*, **4**, 153–177 (1974).

[21] Sanchez Palencia, E., *Non-homogeneous media and vibration theory*, Lecture Notes in Physics, Vol. 127. Springer-Verlag, Berlin (1980).

[22] Smith, G. F., 'On isotropic functions of symmetric tensors, skew-symmetric tensors and vectors', *Int. J. Engng Sci.*, **9**, 899–1916 (1971).

[23] Suquet, P. M., *Plasticité et Homogénéisation*, Thèse de doctorat d'Etat, Université Paris VI (1982).

[24] Suquet, P. M., 'Elements of homogenization for inelastic solids', in *Homogenization techniques for composite media*, Edited by E. Sanchez Palencia and A. Zaoui, eds., Lecture Notes in Physics, Vol. 272, pp. 193–278. Springer-Verlag, Berlin (1987).

[25] Wang, C.-C., 'A new representation theorem for isotropic functions: an answer to Professor G. F. Smith's criticism of my papers on representations of isotropic functions. Part 1. Scalar-valued isotropic functions', *Archs Ration. Mech. Anal.*, **36**, 166–197 (1970a).

[26] Wang, C.-C., 'A new representation theorem for isotropic functions: an answer to Professor G. F. Smith's criticism of my papers on representations of isotropic functions.

Part 2. Vector-valued isotropic functions, symmetric tensor-valued isotropic functions, and skew-symmetric tensor-valued isotropic functions', *Archs Ration. Mech. Anal.*, **36**, 198–223 (1970b).

[27] Weber, C. H., Lõfvander, J. P. A. and Evans, A. G., 'The creep behavior of CAS/Nicalon continuous-fiber composites', *Acta Metall. Mater.*, **41**, 2681–2690 (1993).

Appendix A: Transversely isotropic invariants

An alternative set of commonly used transversely isotropic invariants is

$$J_1 = \sigma_p = \frac{1}{2}\boldsymbol{\sigma} : \boldsymbol{\beta}, \tag{118}$$

$$J_2 = \sigma_n = \boldsymbol{\sigma} : \mathbf{a}, \tag{119}$$

$$J_3 = \tau_p^2 = \frac{1}{2}\left[(\boldsymbol{\sigma}\cdot\boldsymbol{\beta}) : (\boldsymbol{\sigma}\cdot\boldsymbol{\beta}) - \frac{1}{2}(\boldsymbol{\sigma} : \boldsymbol{\beta})^2\right], \tag{120}$$

$$J_4 = \tau_n^2 = \boldsymbol{\sigma}^2 : \mathbf{a} - (\boldsymbol{\sigma} : \mathbf{a})^2, \tag{121}$$

$$J_5 = \det(\boldsymbol{\sigma}), \tag{122}$$

where $\mathbf{a} = \mathbf{nn}$, and $\boldsymbol{\beta} = \mathbf{I} - \mathbf{a}$. Physically, $(\sigma_p, \sigma_n, \tau_p, \tau_n)$ correspond to the in-plane hydrostatic stress, the longitudinal stress, the maximum transverse shear stress, and the resolved longitudinal shear stress respectively. A schematic representation of the above invariants is shown in Fig. 11.

For convenience, we also define

$$\sigma_d^2 = (\sigma_p - \sigma_n)^2 = \left(\frac{3}{2}\,\mathbf{n}\cdot\boldsymbol{\sigma}'\cdot\mathbf{n}\right)^2 \qquad \text{and} \qquad \sigma_s^2 = 3\,(\tau_p^2 + \tau_n^2), \tag{123}$$

and note that

$$\sigma_e^2 = (\sigma_p - \sigma_n)^2 + 3\,(\tau_p^2 + \tau_n^2) = \sigma_d^2 + \sigma_s^2. \tag{124}$$

If the fibers are aligned with the x_3 coordinate direction, i.e. $\mathbf{n} = \mathbf{e}_3$ and $\boldsymbol{\beta} = \mathbf{e}_1\mathbf{e}_1 + \mathbf{e}_2\mathbf{e}_2$, then

$$\sigma_p = \frac{1}{2}(\sigma_{11} + \sigma_{22}), \tag{125}$$

$$\sigma_n = \sigma_{33}, \tag{126}$$

$$\tau_p^2 = \sigma_{12}^2 + \frac{1}{4}(\sigma_{11} - \sigma_{22})^2, \tag{127}$$

$$\tau_n^2 = \sigma_{13}^2 + \sigma_{23}^2, \tag{128}$$

and

$$\sigma_d^2 = \left(\frac{3}{2}\,\sigma'_{33}\right)^2. \tag{129}$$

In the following, we state the relationships between (I_1, I_2, I_4, I_5) and $(\sigma_p, \sigma_n, \tau_p, \tau_n)$:

$$\sigma_p = \frac{1}{2}(I_1 - I_4), \tag{130}$$

$$\sigma_n = I_4, \tag{131}$$

$$\tau_p^2 = \frac{1}{2} I_2 - I_5 + \frac{1}{2} I_4^2 - \frac{1}{4}(I_1 - I_4)^2, \tag{132}$$

$$\tau_n^2 = I_5 - I_4^2, \tag{133}$$

and

$$I_1 = \sigma_n + 2\sigma_p, \tag{134}$$

$$I_2 = \sigma_n^2 + 2\sigma_p^2 + 2(\tau_p^2 + \tau_n^2), \tag{135}$$

$$I_4 = \sigma_n, \tag{136}$$

$$I_5 = \sigma_n^2 + \tau_n^2. \tag{137}$$

Appendix B: The unit cell problem

We start with the case where the unit cell occupies the region $-c_1 \leq y_1 \leq c_1$, $-c_2 \leq y_2 \leq c_2$, $-c_3 \leq y_3 \leq c_3$, and then let $c_3 \to \infty$.

In the following we refer to problems 1, 2, 3 and 4 defined in section 6.2.

Problem 1: Longitudinal tension

The only non-z mponents of the macroscopic strain $\mathbf{E}$ are E_{11}, E_{22} and E_{33}. The geometry of the cell and the applied loads are symmetric with respect to $y_3 = 0$ in this case. Let $\mathbf{u}^{(1)}(\mathbf{y})$ be the solution of the unit cell problem and define $\tilde{\mathbf{u}}(\mathbf{y})$ by

$$\tilde{u}_1(y_1, y_2, y_3) = u_1^{(1)}(y_1, y_2, -y_3), \tag{138}$$

$$\tilde{u}_2(y_1, y_2, y_3) = u_2^{(1)}(y_1, y_2, -y_3), \tag{139}$$

$$\tilde{u}_3(y_1, y_2, y_3) = -u_3^{(1)}(y_1, y_2, -y_3). \tag{140}$$

One can readily show that $\tilde{\mathbf{u}}(\mathbf{y})$ satisfies the governing equations and the boundary conditions (97)-(101), i.e. $\tilde{\mathbf{u}}$ is another solution of the unit cell problem. Since the solution is unique,

this implies that $\tilde{\mathbf{u}} = \mathbf{u}^{(1)}$, i.e. $\mathbf{u}^{(1)}$ has the following symmetries

$$u_1^{(1)}(y_1, y_2, -y_3) = u_1^{(1)}(y_1, y_2, y_3), \tag{141}$$
$$u_2^{(1)}(y_1, y_2, -y_3) = u_2^{(1)}(y_1, y_2, y_3), \tag{142}$$
$$u_3^{(1)}(y_1, y_2, -y_3) = -u_3^{(1)}(y_1, y_2, y_3). \tag{143}$$

Therefore,

$$u_3^{(1)}(y_1, y_2, 0) = 0. \tag{144}$$

When $c_3 \to \infty$, there is no way to distinguish the location of $y_3 = 0$; therefore, in view of the above symmetries, $\mathbf{u}^{(1)}$ must be independent of y_3, i.e.

$$u_1^{(1)} = u_1^{(1)}(y_1, y_2), \tag{145}$$
$$u_2^{(1)} = u_2^{(1)}(y_1, y_2), \tag{146}$$
$$u_3^{(1)} = 0. \tag{147}$$

The solution of the unit cell problem can be now written as

$$\hat{u}_1(y_1, y_2) = E_{11}\, y_1 + u_1^{(1)}(y_1, y_2), \tag{148}$$
$$\hat{u}_2(y_1, y_2) = E_{22}\, y_2 + u_2^{(1)}(y_1, y_2), \tag{149}$$
$$\hat{u}_3(y_3) = E_{33}\, y_3. \tag{150}$$

The geometry of the unit cell and the applied loads are also symmetric with respect to $y_1 = 0$ and $y_2 = 0$. Therefore, using arguments similar to those used above, one can readily show that the Y-periodic field $\mathbf{u}^{(1)}$ has the additional symmetries

$$u_1^{(1)}(y_1, -y_2) = u_1^{(1)}(y_1, y_2), \tag{151}$$
$$u_2^{(1)}(y_1, -y_2) = -u_2^{(1)}(y_1, y_2), \tag{152}$$

and

$$u_1^{(1)}(-y_1, y_2) = -u_1^{(1)}(y_1, y_2), \tag{153}$$
$$u_2^{(1)}(-y_1, y_2) = u_2^{(1)}(y_1, y_2). \tag{154}$$

In view (149)-(151), the total displacement $\hat{\mathbf{u}}$ of the unit cell problem has the symmetries stated in (151)-(154) for the Y-periodic displacement $\mathbf{u}^{(1)}$.

Also, since the macroscopic load corresponds to longitudinal tension, the only non-zero component of $< \boldsymbol{\sigma}^{(0)} >$ is $< \sigma_{33}^{(0)} >$.

Taking into account the aforementioned symmetries of $\hat{\mathbf{u}}$ and $\mathbf{u}^{(1)}$, the symmetries of the geometry, and the Y-periodicity of $\mathbf{u}^{(1)}$, we readily conclude that only one quarter of the unit cell needs to be analyzed (see Fig. 2). The corresponding boundary conditions are

$$y_1 = 0: \quad \hat{u}_1 = 0 \quad \text{and} \quad \hat{\sigma}_{12} = 0, \tag{155}$$

$$y_2 = 0: \quad \hat{u}_2 = 0 \quad \text{and} \quad \hat{\sigma}_{21} = 0, \tag{156}$$

$$y_1 = b\sqrt{3}: \quad \hat{u}_1 = E_{11}\, b\sqrt{3}, \quad \hat{\sigma}_{12} = 0 \quad \text{and} \quad \int_0^b \hat{\sigma}_{11}\, dy_2 = 0, \tag{157}$$

$$y_2 = b: \quad \hat{u}_2 = E_{22}\, b, \quad \hat{\sigma}_{21} = 0 \quad \text{and} \quad \int_0^{b\sqrt{3}} \hat{\sigma}_{22}\, dy_1 = 0. \tag{158}$$

The integral conditions in (157) and (158) are consequences of the fact that $< \sigma_{11}^{(0)} >=< \sigma_{22}^{(0)} >= 0$, and are obtained by using equation (106) and taking into account the symmetries of the problem. Using equation (106), one can also show that

$$< \sigma_{33}^{(0)} >= \frac{F_3}{b^2\sqrt{3}} \qquad \text{where} \qquad F_3 = \int_A \hat{\sigma}_{33}\, dA, \tag{159}$$

A being the area of the finite element mesh on the y_1-y_2 plane shown in Fig. 2.

The boundary conditions (155)-(158) can be easily implemented in a standard finite element program. The problem is solved using four-node generalized plane strain elements with 2×2 Gauss integration.

Let h be the thickness of the elements in the y_3-direction. The $\hat{u}_3$ component of the displacement is set to zero at $y_3 = 0$, the value of $\hat{u}_3$ at $y_3 = h$ taken to be equal to $E_{33}h$. The displacement component $\hat{u}_3$ at $y_3 = h$ is a degree of freedom *common* to all nodes, so that $\hat{\epsilon}_{31} = \hat{\epsilon}_{32} = 0$ and $\hat{\epsilon}_{33} = (1/h)(\hat{u}_3)_{y_3=h} = E_{33}$ =constant everywhere in the finite element mesh. In view of the isotropy of the constituents, we also have that $\hat{\sigma}_{31} = \hat{\sigma}_{32} = 0$ everywhere. *Note that the force* F_3, defined in (159b) is work conjugate to $\hat{u}_3$ at $y_3 = h$.

The macroscopic strain component E_{33} is applied, and the corresponding $< \sigma_{33}^{(0)} >$, E_{11} and E_{22} are determined. The average stress $< \sigma_{33}^{(0)} >$ is found using (159).

Problem 2: Transverse tension

The only non-zero components of the macroscopic strain $\mathbf{E}$ are E_{11}, E_{22} and E_{33}. Also, the only non-zero component of $< \boldsymbol{\sigma}^{(0)} >$ is $< \sigma_{11}^{(0)} >$. One can readily show that the solution of

this problem has the same symmetries as that of Problem 1. One quarter of the cross-section of the unit cell is analyzed, and the boundary conditions are

$$y_1 = 0: \quad \hat{u}_1 = 0 \quad \text{and} \quad \hat{\sigma}_{12} = 0, \tag{160}$$

$$y_2 = 0: \quad \hat{u}_2 = 0 \quad \text{and} \quad \hat{\sigma}_{21} = 0, \tag{161}$$

$$y_1 = b\sqrt{3}: \quad \hat{u}_1 = E_{11}\, b\sqrt{3} \quad \text{and} \quad \hat{\sigma}_{12} = 0, \tag{162}$$

$$y_2 = b: \quad \hat{u}_2 = E_{22}\, b, \quad \hat{\sigma}_{21} = 0 \quad \text{and} \quad \int_0^{b\sqrt{3}} \hat{\sigma}_{22}\, dy_1 = 0, \tag{163}$$

$$y_3 = h: \quad \hat{u}_3 = E_{33}\, h \quad \text{and} \quad F_3 = 0. \tag{164}$$

The solution is obtained using four-node generalized plane strain elements with 2×2 Gauss integration. The macroscopic strain component E_{11} is applied, and the corresponding $< \sigma_{11}^{(0)} >$, E_{22} and E_{33} are determined. The average stress $< \sigma_{11}^{(0)} >$ is found using the relationship

$$< \sigma_{11}^{(0)} >= \frac{1}{b} \int_0^b \hat{\sigma}_{11}(b\sqrt{3}, y_2)\, dy_2. \tag{165}$$

Problem 3: Transverse shear

The only non-zero components of the macroscopic strain $\mathbf{E}$ are $E_{12} = E_{21}$. Also, the only non-zero components of $< \boldsymbol{\sigma}^{(0)} >$ are $< \sigma_{12}^{(0)} >=< \sigma_{21}^{(0)} >$.

Using arguments similar to those used in Problem 1, one can readily show that i) $u_3^{(1)} = 0$, ii) $u_1^{(1)}$ and $u_2^{(1)}$ are independent of y_3, and iii) the solution has the following symmetries (or anti-symmetries)

$$u_1^{(1)}(y_1, -y_2) = -u_1^{(1)}(y_1, y_2), \tag{166}$$

$$u_2^{(1)}(y_1, -y_2) = u_2^{(1)}(y_1, y_2), \tag{167}$$

and

$$u_1^{(1)}(-y_1, y_2) = u_1^{(1)}(y_1, y_2), \tag{168}$$

$$u_2^{(1)}(-y_1, y_2) = -u_2^{(1)}(y_1, y_2). \tag{169}$$

One quarter of the cross-section of the unit cell is analyzed, and the boundary conditions are

$$y_1 = 0: \quad \hat{u}_2 = 0 \quad \text{and} \quad \hat{\sigma}_{11} = 0, \tag{170}$$

$$y_2 = 0: \quad \hat{u}_1 = 0 \qquad \text{and} \qquad \hat{\sigma}_{22} = 0, \tag{171}$$

$$y_1 = b\sqrt{3}: \quad \hat{u}_2 = E_{21}\, b\sqrt{3} \quad \text{and} \quad \hat{\sigma}_{11} = 0, \tag{172}$$

$$y_2 = b: \quad \hat{u}_1 = E_{12}\, b \quad \text{and} \quad \hat{\sigma}_{22} = 0. \tag{173}$$

The solution is obtained using four-node plane strain elements with 2×2 Gauss integration and an independent interpolation for the dilatation rate are used in order to avoid artificial constraints on incompressible modes (Nagtegaal et al., 1974). The macroscopic strain component E_{12} is applied, and the corresponding $< \sigma_{12}^{(0)} >$ is determined using the relationship

$$< \sigma_{21}^{(0)} > = \frac{1}{b\sqrt{3}} \int_0^{b\sqrt{3}} \hat{\sigma}_{21}(y_1, b)\, dy_1 = \frac{1}{b} \int_0^{b} \hat{\sigma}_{12}(b\sqrt{3}, y_2)\, dy_2. \tag{174}$$

Problem 4: Longitudinal shear

The only non-zero components of the macroscopic strain $\mathbf{E}$ are $E_{13} = E_{31}$. Also, the only non-zero components of $< \boldsymbol{\sigma}^{(0)} >$ are $< \sigma_{13}^{(0)} > = < \sigma_{31}^{(0)} >$.

Using arguments similar to those used in Problem 1, one can readily show that i) $u_1^{(1)} = u_2^{(1)} = 0$, ii) $u_3^{(1)}$ is independent of y_3, and iii) the solution has the following symmetries (or anti-symmetries)

$$u_3^{(1)}(-y_1, y_2) = -u_3^{(1)}(y_1, y_2), \tag{175}$$

$$u_3^{(1)}(y_1, -y_2) = u_3^{(1)}(y_1, y_2). \tag{176}$$

One quarter of the cross-section of the unit cell is analyzed and the solution is obtained using eight-node three-dimensional brick elements with $2 \times 2 \times 2$ Gauss integration. Let h be the thickness of the elements in the y_3-direction. The following boundary conditions are used

$$\hat{u}_1 = E_{13}\, y_3 \quad \text{and} \quad \hat{u}_2 = 0 \quad \text{everywhere},$$

$$y_1 = 0: \quad \hat{u}_3 = 0 \quad \text{and} \quad \hat{\sigma}_{11} = 0, \tag{177}$$

$$y_2 = 0: \quad \hat{\sigma}_{21} = \hat{\sigma}_{23} = 0, \tag{178}$$

$$y_3 = 0: \quad \hat{\sigma}_{33} = 0, \tag{179}$$

$$y_1 = b\sqrt{3}: \quad \hat{u}_3 = E_{31}\, b\sqrt{3} \quad \text{and} \quad \hat{\sigma}_{11} = 0, \tag{180}$$

$$y_2 = b: \quad \hat{\sigma}_{21} = \hat{\sigma}_{23} = 0, \tag{181}$$

$$y_3 = h: \quad \hat{\sigma}_{33} = 0. \tag{182}$$

The macroscopic strain component E_{13} is applied, and the corresponding $< \sigma_{13}^{(0)} >$ is determined using the relationship

$$< \sigma_{13}^{(0)} >= \frac{1}{b} \int_0^b \hat{\sigma}_{13}(b\sqrt{3}, y_2)\, dy_2 = \frac{1}{A} \int_A \hat{\sigma}_{31}(y_1, y_2)\, dA. \tag{183}$$

Figure captions

1. Hexagonal array of fibers and the corresponding unit cell.
2. Finite element mesh.
3. Longitudinal stress-strain curve.
4. Transverse stress-strain curve
5. Stress-strain curve for transverse shear.
6. Schematic representation of a plate with a hole. The fibers are in the x_2 coordinate direction.
7. Contours of creep strain invariant ϵ_n.
8. Contours of creep strain invariant ϵ_p.
9. Contours of creep strain invariant γ_n.
10. Contours of creep strain invariant γ_p.
11. Transversely isotropic stress invariants.

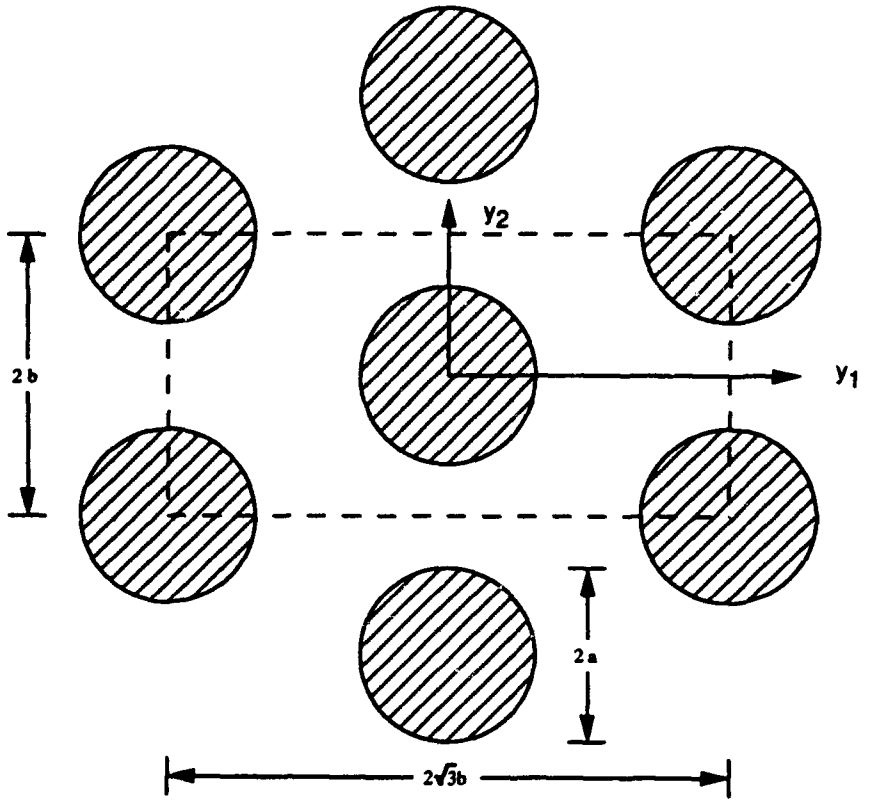

Fig. 1

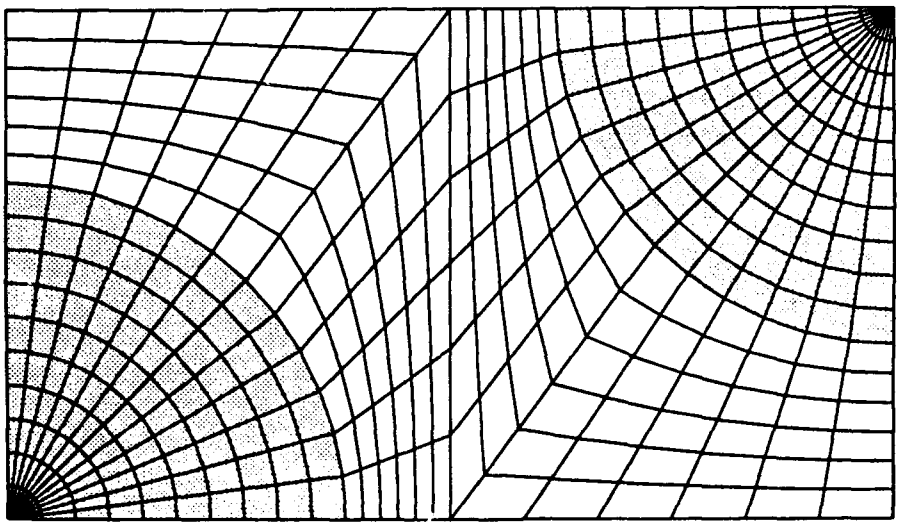

Fig. 2

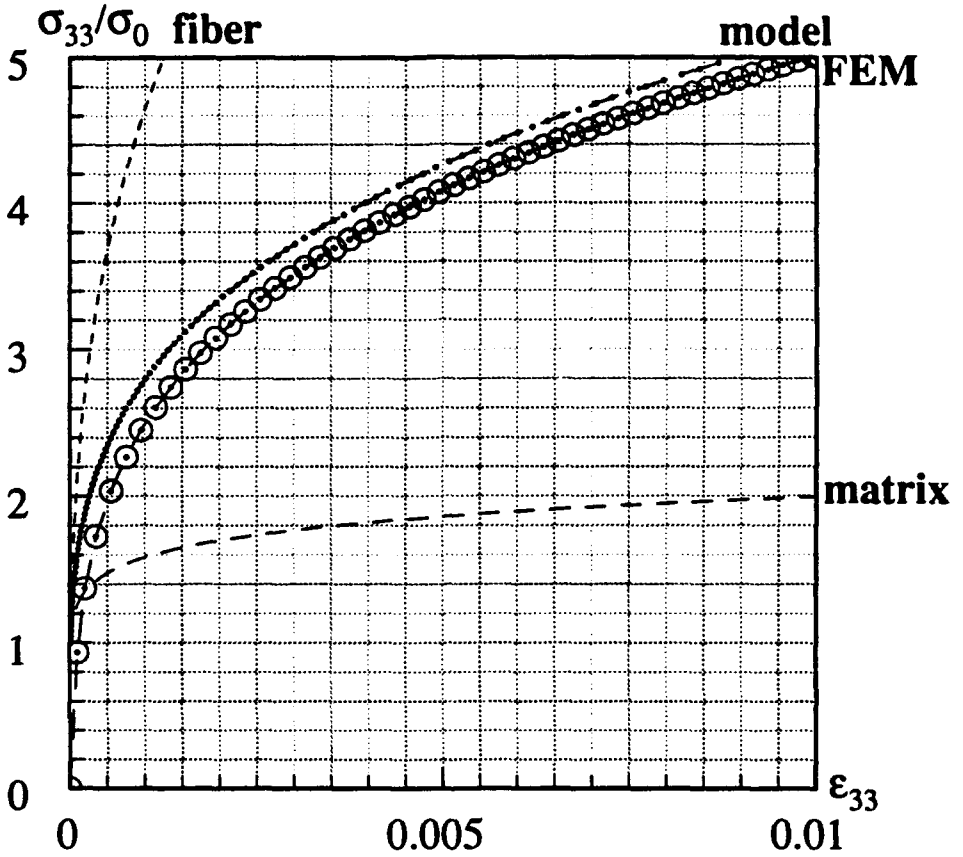
σ_{33}/σ_0 fiber
model
FEM
matrix
5
4
3
2
1
0
0
0.005
0.01
ε_{33}

Fig. 3

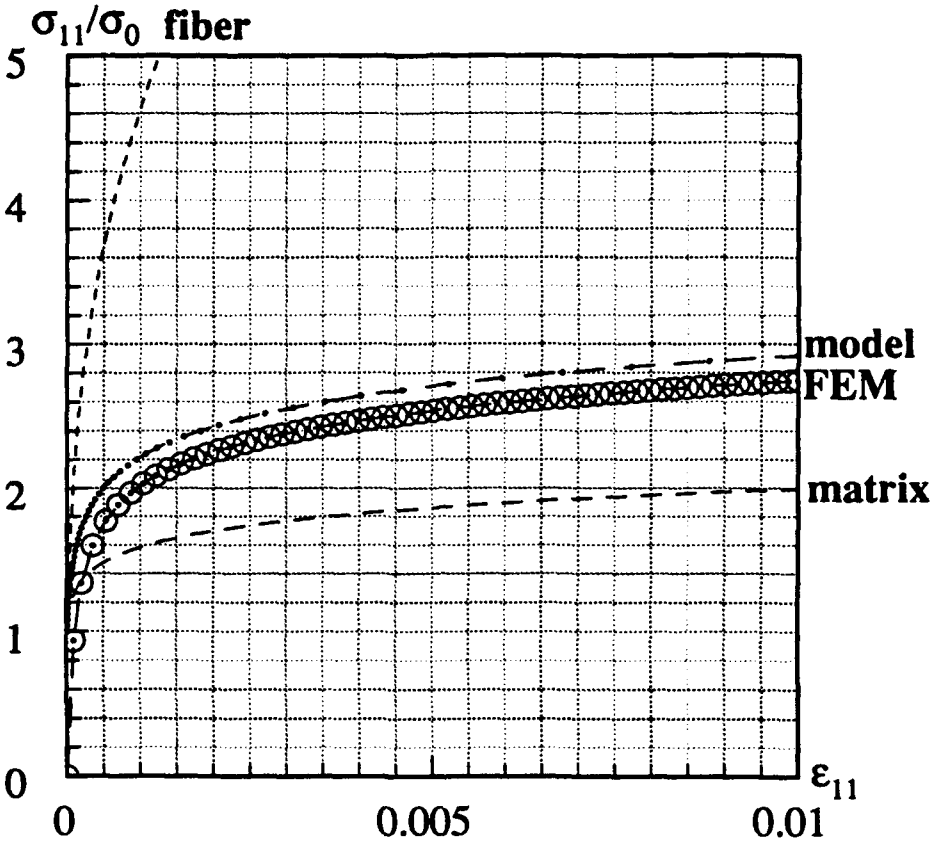
σ_{11}/σ_0 fiber
5
4
3
2
1
0
0
0.005
0.01
ε_{11}
model
FEM
matrix

Fig. 4

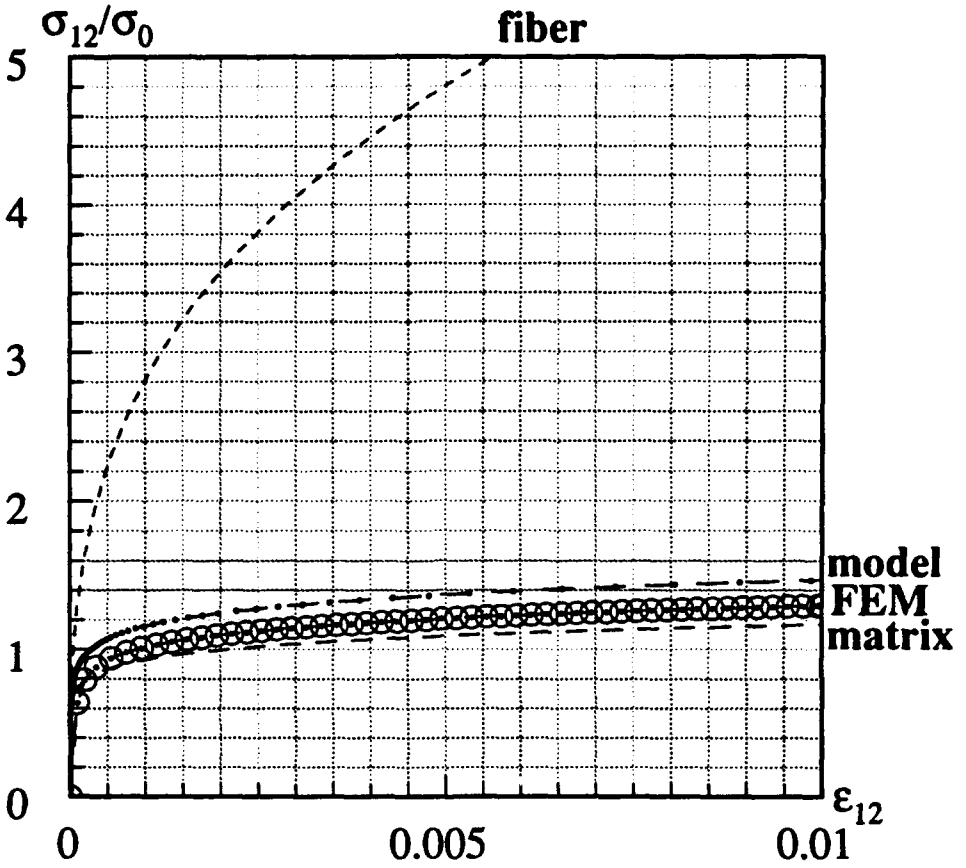

Fig. 5

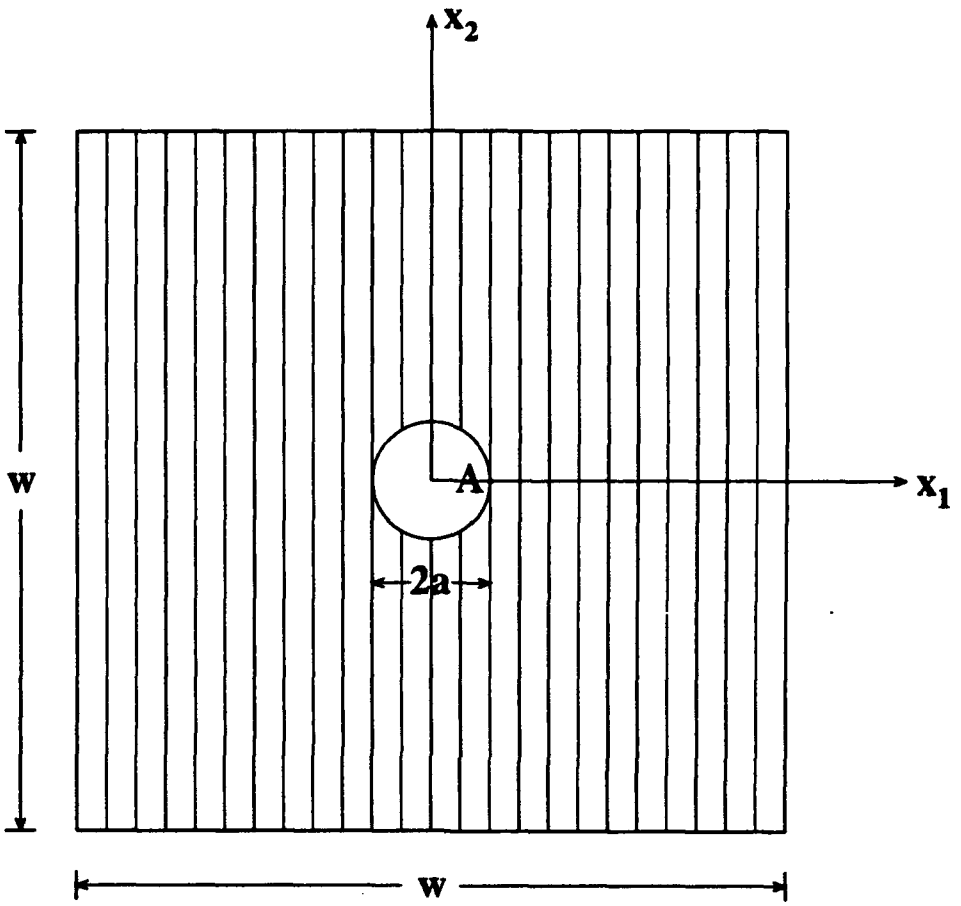

Fig. 6

CONTOURS

1 +0.00E-00
2 +2.00E-03
3 +4.00E-03
4 +6.00E-03
5 +8.00E-03

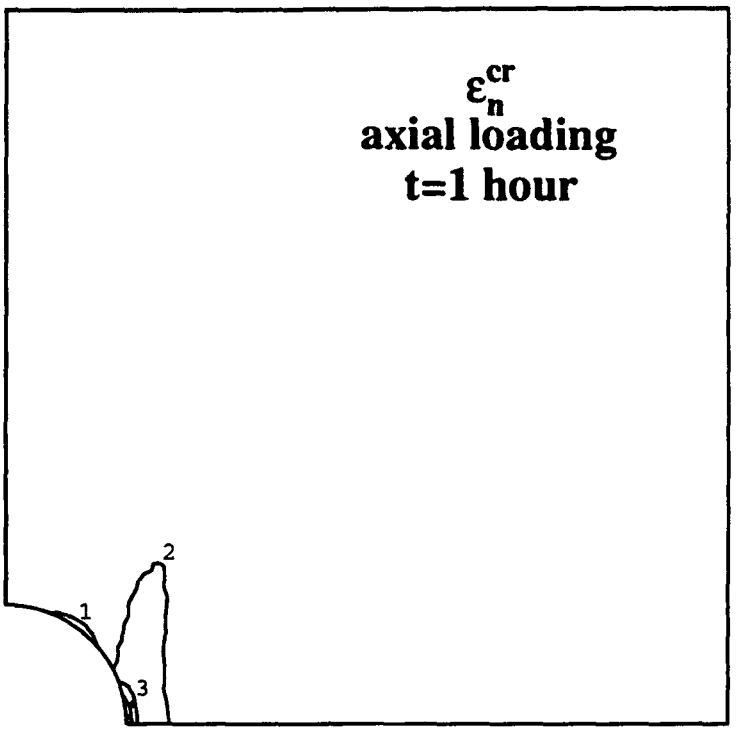

CONTOURS

1 -7.00E-03
2 -5.00E-03
3 -3.00E-03
4 -1.00E-03

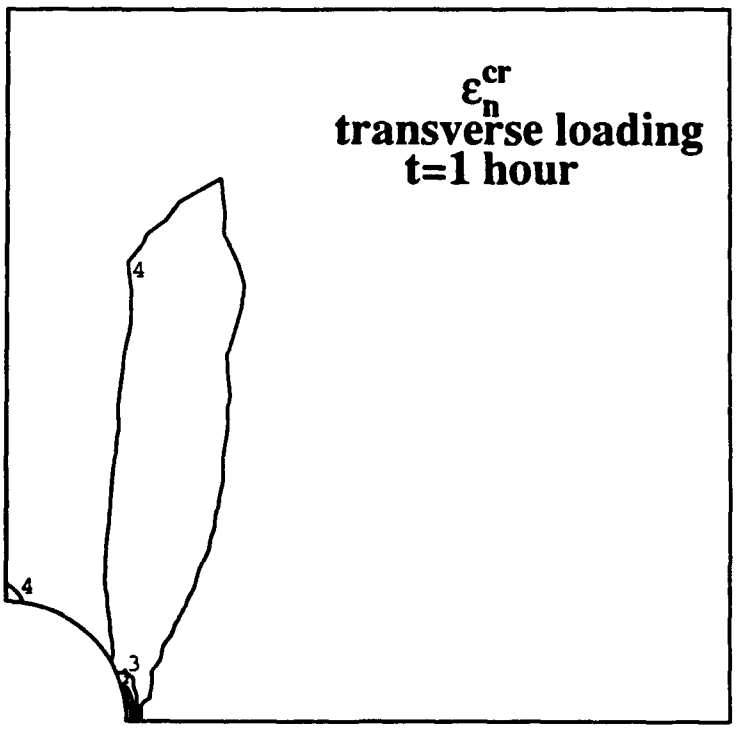

Fig. 7

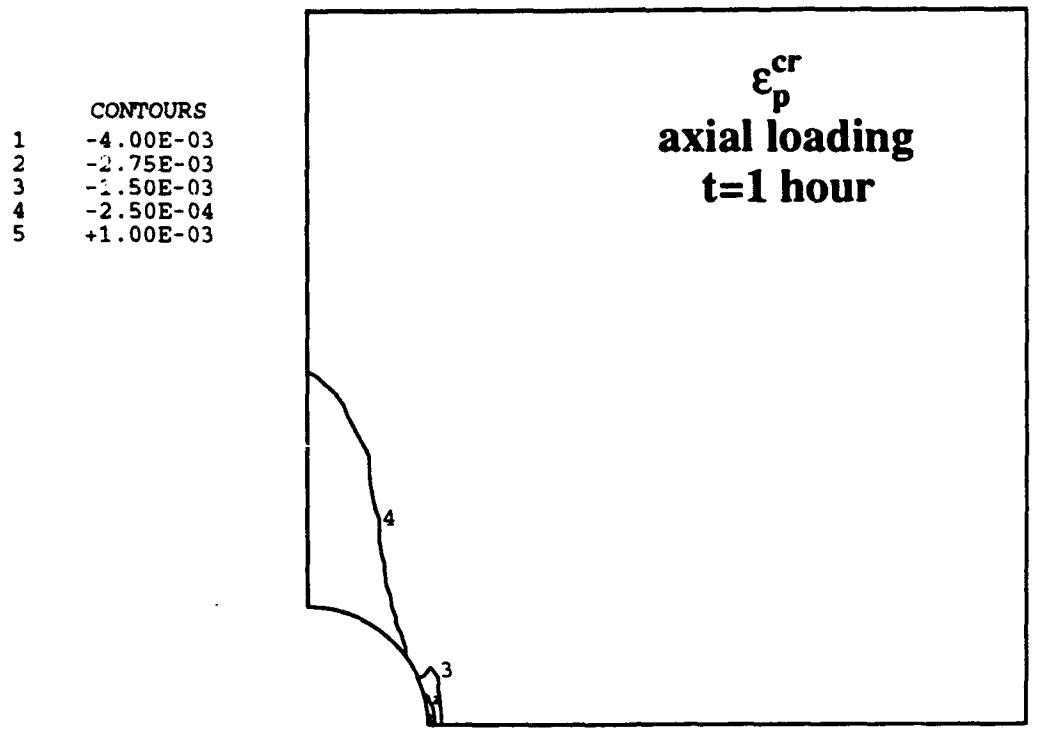
CONTOURS
1 -4.00E-03
2 -2.75E-03
3 -1.50E-03
4 -2.50E-04
5 +1.00E-03
ε_p^{cr}
axial loading
t=1 hour
4
3

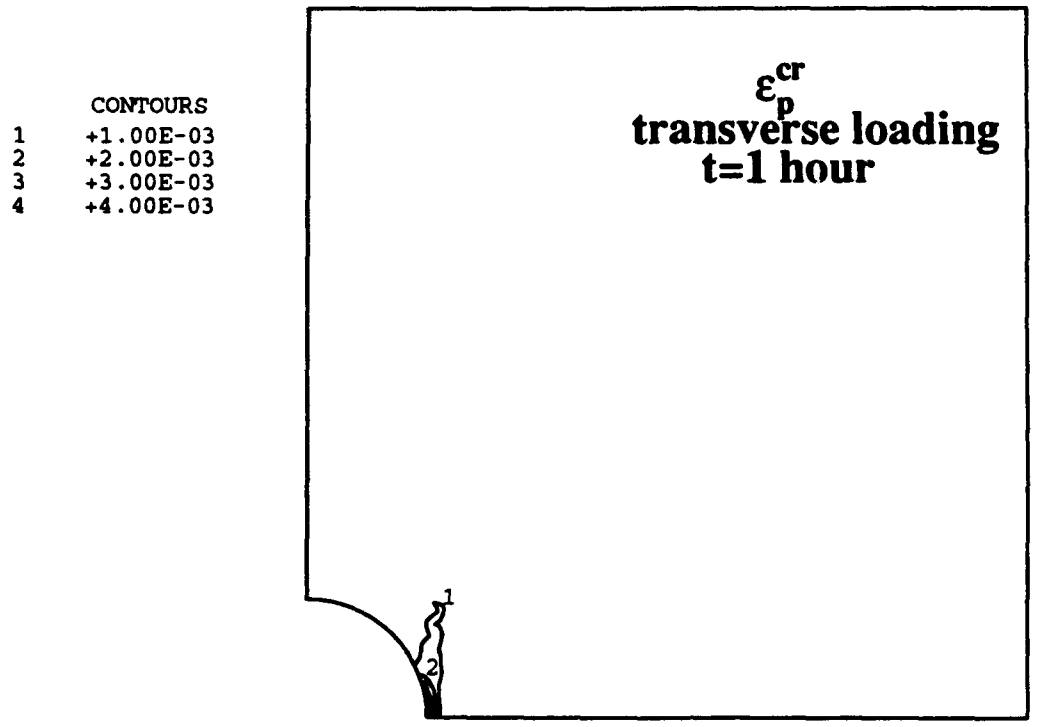
CONTOURS
1 +1.00E-03
2 +2.00E-03
3 +3.00E-03
4 +4.00E-03
ε_p^{cr}
transverse loading
t=1 hour
1
2

Fig. 8

CONTOURS

1	+1.00E-03
2	+3.00E-03
3	+5.00E-03
4	+7.00E-03
5	+9.00E-03

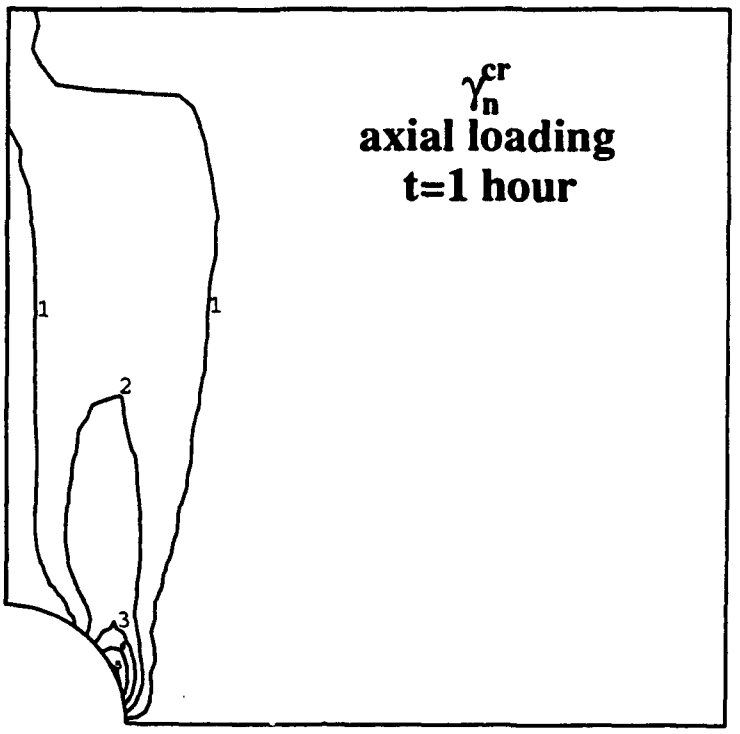

CONTOURS

1	+5.00E-02
2	+7.50E-02
3	+1.00E-01
4	+1.25E-01
5	+1.50E-01
6	+1.75E-01
7	+2.00E-01

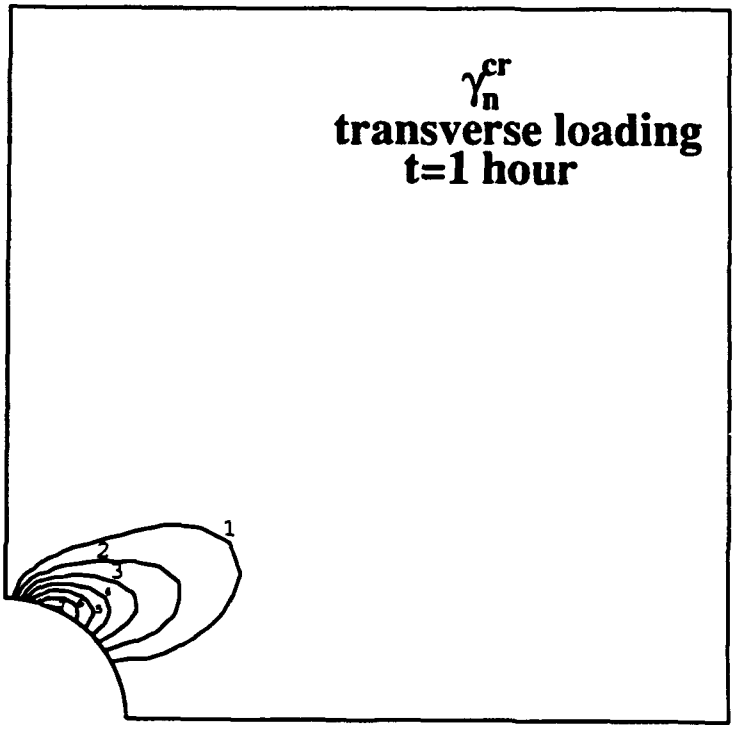

Fig. 9

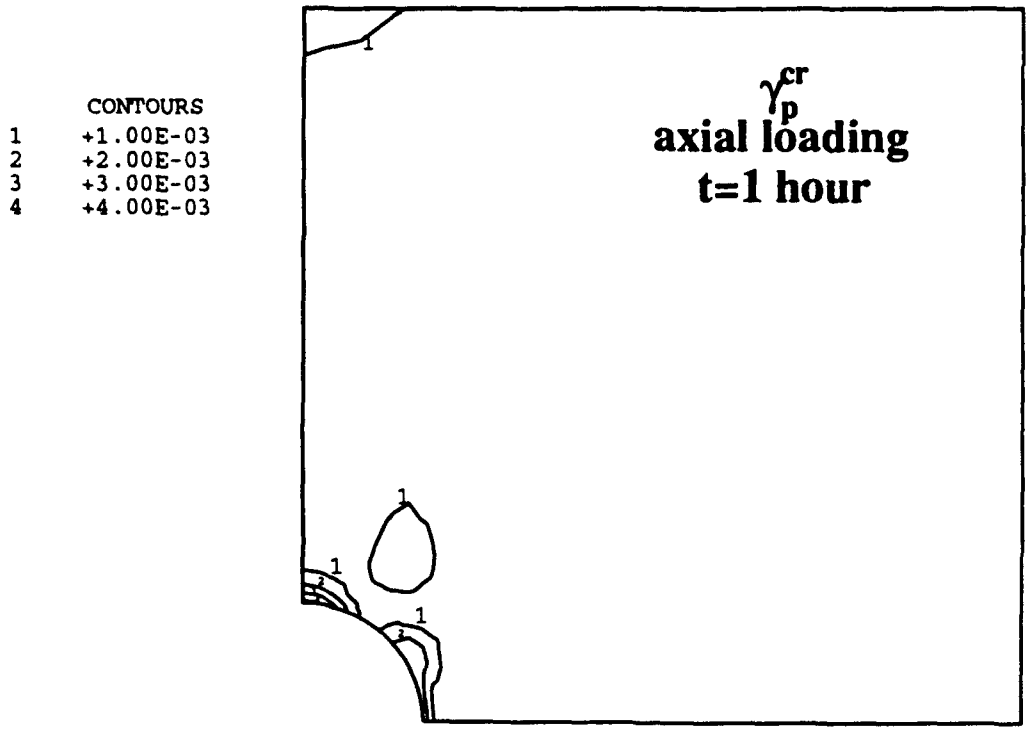
CONTOURS
1 +1.00E-03
2 +2.00E-03
3 +3.00E-03
4 +4.00E-03
γ_p^{cr}
axial loading
t=1 hour

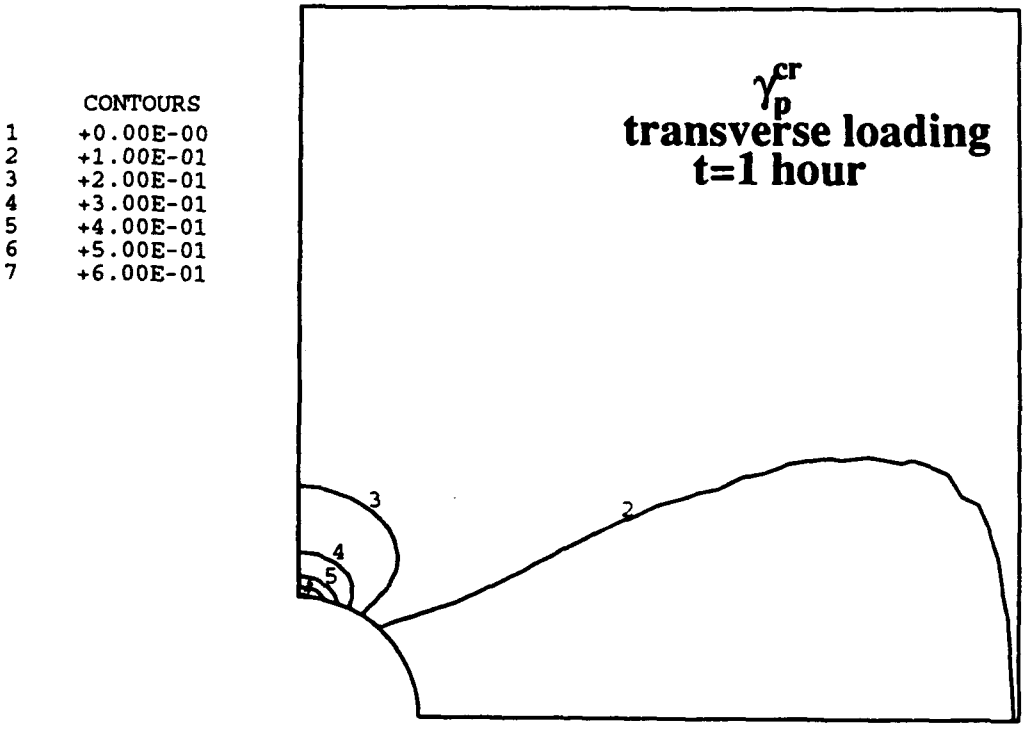
CONTOURS
1 +0.00E-00
2 +1.00E-01
3 +2.00E-01
4 +3.00E-01
5 +4.00E-01
6 +5.00E-01
7 +6.00E-01
γ_p^{cr}
transverse loading
t=1 hour

Fig. 10

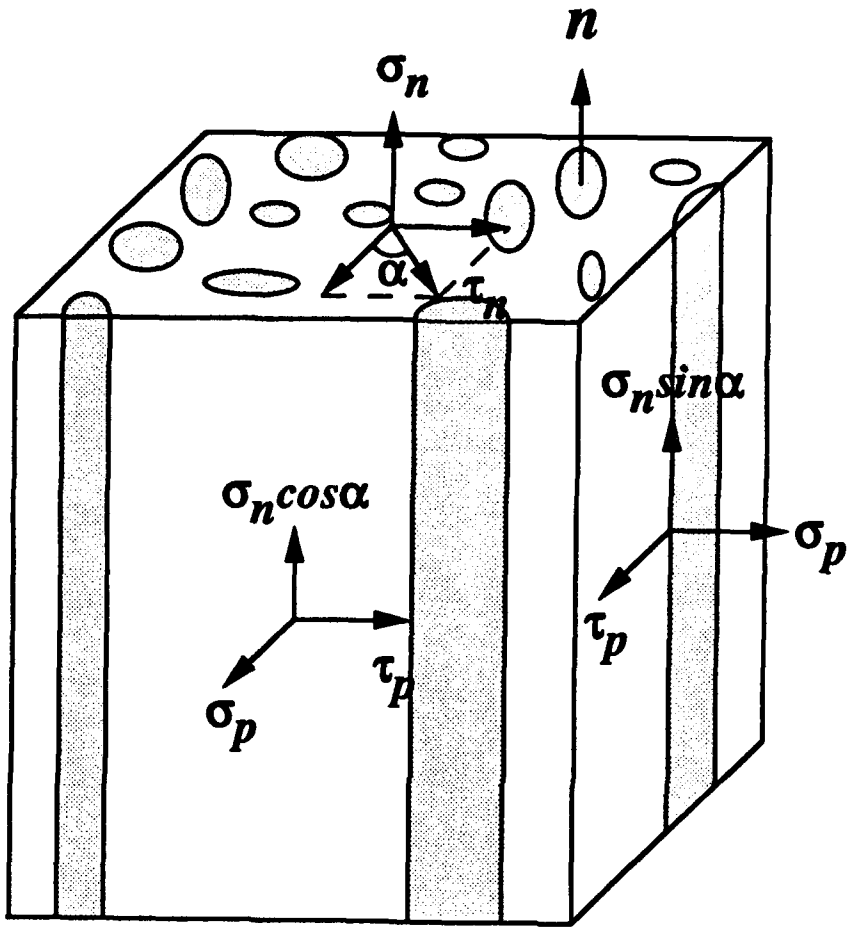

Fig. 11

MATERIALS

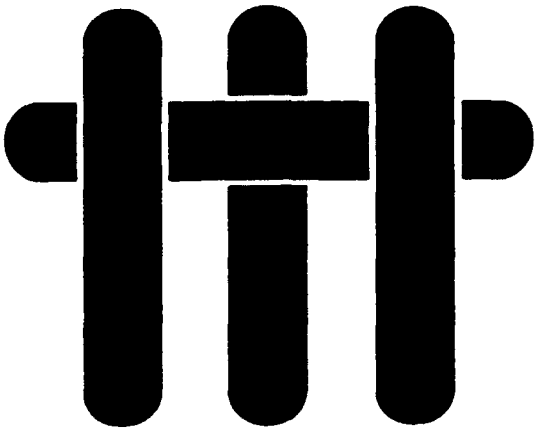

THE CREEP ANISOTROPY OF A CONTINUOUS-FIBER-REINFORCED SiC/CAS COMPOSITE

by

C.H. Weber, J.P.A. Löfvander and A.G. Evans
Materials Department
College of Engineering
University of California, Santa Barbara
Santa Barbara, California 93106-5050

Submitted to the Journal of the American Ceramic Society

KJS 11/4/93

ABSTRACT

Creep studies conducted on a unidirectional SiC/CAS composite indicate that the Nicalon fibers provide longitudinal creep strengthening at 1200°C. The deformation is transient in nature because grain growth in the fibers enhances their creep resistance. The transverse creep strength is considerably smaller, being dominated by the matrix, resulting in appreciable creep anisotropy. This anisotropy leads to severe distortion when off-axis loadings are imposed. Residual stresses develop upon unloading after creep, and cause superficial matrix cracking.

1. INTRODUCTION

Ceramic matrix composites are expected to have a key role in achieving the performance goals of the next generation of advanced aircraft. The intrinsic ceramic properties of high refractoriness, good oxidation resistance and low density have been motivating the development of these materials. Much of the recent effort has been expended in overcoming some of the key limitations of monolithic ceramic materials, particularly their notch sensitivity. This work has led to the development of ceramic matrix composites (CMCs), using fiber reinforcements as a means of controlling damage and redistributing stresses.[1-9] Critical to the success of this approach is the presence of a fiber coating that provides a "weak" interface.[5-7] However, much remains to be addressed at high temperatures, where most of the performance benefit is to be obtained. The presence of fibers can have either beneficial or detrimental influences, depending upon the creep strength of the fibers compared with that for the matrix.[10,11] The situation to be explored in this study represents a CMC in which the fibers have a greater creep strength than the matrix, exemplified by glass ceramics reinforced with silicon carbide fibers. In this case, the fibers should impart creep strengthening.[12-14] The actual magnitude depends on the explicit role of the 'weak' interface.

Another important factor is the creep anisotropy. While creep resistant fibers result in strengthening in the fiber direction, the composite has inferior transverse properties, which may limit structural integrity. It therefore becomes imperative to understand this anisotropy, in order to guide materials development and ensure reliable engineering design.

2. BACKGROUND AND PHILOSOPHY

CMC components typically experience large thermal gradients, but small pressure loads. Such situations result in bending moments and shears, which may cause flexural creep and distortion. The material anisotropy can have a substantial effect on these responses. The philosophy of the present study is to perform flexural creep tests and to provide an interpretation by comparing with compression and tension data. Moreover, the tests are performed at the relatively low stress and strain levels expected in actual applications, wherein distortions > 1–2% are unacceptable.

Anositropy in the creep of CMCs is investigated by using a calcium aluminosilicate (CAS) system, unidirectionally reinforced with SiC (Nicalon™) fibers.‡ In this CMC, the fibers have a greater creep strength than the matrix.[10,15] However, both the fibers and the matrix are susceptible to microstructural changes and transient creep responses. At temperatures above ~ 1200°C, Nicalon *fibers* experience both compositional and microstructural changes.[16-18] These involve the evolution of CO with the resultant creation of an outer sheath of β-SiC, having relatively large grains (~ 15 nm in diameter).[18] As the peripheral grains coarsen, the creep strength of the fibers increases.[15] Within a composite matrix, the role of the Nicalon fibers depends on the actual CO evolution. These effects are examined at a temperature of 1200°C, which represents a compromise between the desire to use CMCs at the highest possible temperature and the need to have microstructural and compositional stability.

Glass ceramics have creep characteristics dominated by the residual amorphous material.[19] The extent of crystallization thus dominates the creep strength of the CAS *matrix*. Moreover, such materials often exhibit creep asymmetry: they deform more rapidly in tension than compression, because of void formation in the amorphous

‡ The material was provided by Corning through K. Chyung.

material.[19] Such asymmetry, when present, has important implications for the interpretation of flexural creep.[20]

3. EXPERIMENTAL PROCEDURES

3.1 Testing Procedures

In SiC/CAS, the presence of a carbon layer at the fiber/matrix interface results in a strong dependence of mechanical properties on the extent of oxidation.[5,6] Consequently, in order to allow separation of the influence of mechanical loading and environment, creep tests were conducted under inert conditions by using a hydraulic testing machine in argon (≈ 0.1 MPa) within a furnace having a 2200°C temperature capability. *Flexural* experiments were performed on beams measuring approximately 3 x 3.5 x 45 mm. A device was constructed which directly and continuously evaluates the curvature over the inner span, by measurement of the displacement, Δ[21] (Fig. 1). Pure bending operates within this region. The normal strains ε are thus axially *uniform* and are related to the displacement Δ in a straightforward manner.‡ The *maximum* normal strain on either the tensile or compressive surface is explicitly related to Δ by,[21]

$$\varepsilon_{max} = h\Delta/\left(\Delta^2 + s^2\right) \qquad (1)$$

where h is the beam thickness and s the span. The device allows strain measurements accurate to within ± 0.01%, and a resolution of ± 0.0005%.

The *stresses* that develop in flexure relate to the applied *moment*, M. Determining exact values is not straightforward (Appendix I). It is established that, at the moments and deflections used in this study, SiC/CAS has minimal creep asymmetry and,

‡ This simple relationship obtains, even at deformations substantially larger than those explored in the present tests ($\varepsilon < 2\%$).

moreover, stress transfer from the matrix results in fiber dominated behavior. Additionally, since the fibers are viscoelastic,[22] *linear* solutions may be used to obtain nominal stresses from the moments. The linear formula for peak stress on the tensile surface is

$$\sigma_{\bullet}^{max} = (3/2)P(L-\ell)/bh^2 \qquad (2)$$

where P is the load, L is the outer span, ℓ the inner span and b the beam width.

The same system was adapted for *compressive* creep measurements. For this purpose, the outer gauging rods (Fig. 1) were attached to the top loading plate, while the central gauging rod (attached to the LVDT) contacted a creep resistant SiC platen directly under the specimen. Deformation of the specimen was measured from the relative displacement of the inner and outer gauging rods from which the strain could be determined directly.

3.2 Characterization Techniques

The materials were examined by both scanning and transmission electron microscopy. For scanning electron microscopy (SEM), specimens were prepared using standard metallographic techniques. Carbon-coated samples were examined in the JEOL SM 848 SEM in secondary mode. The microscope was equipped with a Tracor Northern TN 5500 analysis system. For transmission electron microscopy (TEM), samples prepared by ion milling were examined at 200kV in a JEOL 2000FX TEM equipped with a LINK eXL high take-off angle energy dispersive spectroscopy system. Computer simulations and indexing of selected area diffraction (SAD) patterns were facilitated by the Desktop Microscopist software package (Virtual Labs, Ukiah, CA 95482).

TEM analysis of the composite after creep was impeded by crumbling of the matrix during foil preparation. The following, alternative, procedure was thus used to obtain samples of fibers. Wafers, approximately 2.5 mm square and 300 μm thick, were cut using a slow speed diamond wafering blade, with the fiber orientation in the plane of the wafer. These wafers were then soaked in concentrated hydrofluoric acid for about 3 minutes to remove most of the matrix, leaving the intact fibers behind. These fibers were then extracted using a tweezers, mounted on a copper grid and ion milled prior to TEM analysis.

4. RESULTS

4.1 Material Characterization

The SiC/CAS material has 16 plies, with an average fiber volume fraction $f \approx 0.4$, although local variations are evident (Fig. 2). It has a glass-rich surface layer. During testing, this layer was located at the outer surface of the side faces. Characterization by TEM revealed that the matrix consists primarily of anorthite with a grain size 1 μm. Substantial twinning was evident throughout the matrix. Very fine precipitates (20 nm), probably zirconia, were detected within the CAS grains. The fiber/matrix interface consisted of a 300Å thick carbon layer (Fig. 3), identified by means of scanning EELS micrographs. Electron diffraction analysis of the fibers revealed a characteristic ring pattern, representative of β-SiC with a very fine grain size. Dark-field imaging established a grain size, $d \approx 1$–3 nm.

4.2 Creep Rates

The *flexural* creep experiments with longitudinally oriented fibers, conducted at 1200°C, were performed at moments corresponding to nominal stress levels between 50 to 150 MPa. The strains were limited to ~ 1%. These tests gave the *longitudinal* flexure

creep rates summarized in Fig. 4. The strain is transient, at all applied moments. Tensile creep rates obtained at similar stresses[10] superpose onto the flexural results (Fig. 4). This correspondence between flexure and tension indicates that there is minimal creep asymmetry at small strains (< 1%) and at stresses up to ~ 150 MPa.

Two flexure tests were conducted at the same moment, but with one periodically interrupted. The sample was cooled rapidly upon interruption, in order to limit recovery effects.[10] The strain was then measured from the beam curvature at room temperature.[21] The results demonstrate the history insensitivity of composite creep (Fig. 5).

Transverse compressive creep data are presented in Fig. 6. In contrast to the longitudinal response, the transverse behavior is characterized by a minimum deformation-rate, preceded by an initial transient. The creep rate minimum can be characterized by a power-law, with an exponent, m ≈ 2.4.

A comparison of longitudinal and transverse creep at 50 and 75 MPa (Fig. 7) illustrates the *anisotropy* and provides direct evidence that *longitudinal creep strengthening* is imparted by Nicalon fibers. An alternative demonstration of the creep anisotropy is provided by the cross-sectional profiles of crept flexural samples (Fig. 8). The relatively low (matrix-controlled) shear creep strength of unidirectional fiber composites results in large shear distortions between the inner and outer loading points. These distortions are substantially higher than the (fiber-controlled) longitudinal deformations caused by pure bending between the inner loading points. Such behavior does not occur in isotropic beams because the ratio of the peak shear stress to the peak tensile stress is typically low (≤ 0.1).¶

¶ For elastic or linearly creeping fibers, this ratio is,[23] $\lambda = 2(L - l)/h$.

4.3 Observations

SEM and TEM conducted on the crept samples has established that there is minimal *matrix* damage at small strains ($\lesssim$ 1%). The absence of matrix cracks is consistent with earlier studies conducted at room temperature[9] at the stress levels used in these tests (maximum of 150 MPa) and with the minimal creep asymmetry. However, cracks *were* found in the glass-ceramic *coating*, on those sides that had been subject to compression during creep. Cracking was more prevalent at higher loads. The occurrence of such cracks implies the presence of a *residual tension* after cooling and unloading. Related behavior has been found in monolithic ceramics.[24]

In transverse compressive loading, *transverse matrix* damage initiated, but only at larger strains ($\gtrsim$ 2%). This damage is manifest as voids emanating from the interfaces, at segments perpendicular to the loading axis (Fig. 9). At higher stresses ($\gtrsim$ 50 MPa) squeezing out of the matrix from between fibers resulted in impingement of the fibers. Fragmentation of the fibers then typically occurred at the points of contact. These damage initiation mechanisms were found to be spatially non-uniform and appeared to correlate with locally high concentrations of fibers. Coalescence of damage along well-defined shear bands led to failure of the samples.

TEM revealed significant *microstructural* changes in the *fibers* (Fig. 10). A well-defined outer shell formed, within which substantial grain growth had occurred (grain size, d $\approx$ 10–15 nm) and an inner core in which the grain size remained unaltered (d $\approx$ 1–3 nm) (Fig. 11). This behavior is consistent with that found for Nicalon fibers in the absence of a matrix.[18] The extent of the large grained regions increased with time at temperature. More precise determinations of the kinetics of grain growth and shell evolution are in progress. There were no apparent changes to the C interphase.

5. DISCUSSION

The interpretation of the above results relies on three basic features, each governed by the flexural and compressive characteristics of anisotropic beams. (i) For the pure bending region between the inner loading points, in which the flexural strain measurements have been made (Fig. 1, Eqn. 1), there are no in-plane shear stresses.[23] In consequence, the deformations are controlled by the *longitudinal* properties of the composite. (ii) The similarity of the deformation rates measured in flexure and tension establishes that the deformation is symmetric, within the stress and strain ranges explored in the present study, consistent with the absence of creep induced matrix damage. (iii) The matrix dominated deformation in transverse compression substantially exceeds the longitudinal deformation, verifying that the fibers are considerably more creep resistant than the matrix. This anisotropy is the origin of the beam distortions found in four-point bending (Fig. 8).

These three features provide the logic for the following sequence. The transverse compression data are first used to estimate the creep properties of the matrix. These values are then used with the flexural data to characterize the fiber dominated longitudinal behavior. Finally, the creep properties of the fibers *within the composite* are established.

Both constituents are *assumed to exhibit power law creep*. The steady-state formulae are, for the matrix,

$$\dot{\varepsilon} = \dot{\varepsilon}_{mo}\left(\sigma/\sigma_{mo}\right)^{m} \tag{2}$$

and for the fibers,

$$\dot{\varepsilon} = \dot{\varepsilon}_{fo}\left(\sigma/\sigma_{fo}\right)^{n} \tag{3}$$

where σ_{mo} and σ_{fo} are the reference stresses.

5.1 Matrix Creep Strength

The creep properties of the *matrix* are estimated from the composite steady-state data obtained in transverse compression (Fig. 6), given by,

$$\dot{\varepsilon} = \dot{\varepsilon}_{co}(\sigma/\sigma_{co})^{m} \tag{4}$$

where σ_{co} is the reference stress for the composite. In the absence of significant matrix damage, the power law for the matrix should be the same as that for the composite[25,26] (m = 2.4). Furthermore, the reference stresses should be related by[25,26]

$$\sigma_{mo} = \sigma_{co}\beta(f,m) \tag{5}$$

with f being the fiber volume fraction. The coefficient β has been calculated for perfectly bonded interfaces.[26, 27] For the present composite (m = 2.4 and f = 0.4) the calculations give β = 0.7. Consequently, the data of Fig. 6 can be related to the matrix creep properties by means of a reference stress conversion. Eqn. (3)‡ gives β = 0.7, such that in Eqn. (2): σ_{mo} = 0.7 MPa and $\dot{\varepsilon}_{mo} = 4.0 \times 10^{-11}$ s^{-1}.

5.2 Longitudinal Creep

The longitudinal data are dominated by the fibers (Fig. 4). The lack of significant fiber fracture at small strains suggests that an equi-strain criterion may be used for interpretation.[12] The following procedure is used for this purpose. First, based on the

‡ This conversion is strictly applicable only in steady-state and at small strains, prior to matrix damage.

above matrix creep parameters, a beam analysis yields the fraction of the moment borne by the fibers (Appendix I). This analysis indicates that essentially all of the creep strength is associated with the fibers, except during the initial transient (times, $t \lesssim 5h$). The primary nature of the creep arises because of microstructural changes within the fibers (Figs. 10,11). The most important mechanism appears to be grain growth, which is time dependent. Consequently, by using *time* as an independent variable (rather than strain), it is found that the axial creep data can be uniquely correlated (Fig. 12). The associated constitutive law for the composite closely approaches the form ($t \gtrsim 1h$),

$$\dot{\varepsilon}/\dot{\varepsilon}_{co} \approx (\sigma/\sigma_{co})^{n}(t/\tau)^{\alpha}\eta \qquad (6)$$

with a stress exponent, $n \approx 1$, a time constant $\tau = 5.5 \times 10^{-6}$ s and $\alpha \approx -0.9$. The coefficient η is unity for the composite but becomes f for the fibers. The reference parameters are $\sigma_{co} = 1$ MPa, $\dot{\varepsilon}_{co} = 1/s$. The extent and magnitude of the grain growth are consistent with the observed *creep* strengthening of the fibers (Appendix II), and also with a stress exponent, $n \approx 1$, characteristic of diffusional creep.[27]

There is a similarity between the microstructural changes in the Nicalon fibers found here during creep within a CAS matrix, to those previously found in the absence of a matrix.[18] This indicates that a CO partial pressure having sufficient magnitude to suppress chemical changes does not develop. The evolving CO can presumably escape from the composite. The consequences are that longitudinal creep of the composite is primary in nature and that the creep rates are comparable to those for the fibers in the absence of the matrix.[15] The C interphase remains relatively stable, at least upon testing in an inert environment. Consequently, this phase appears to have minimal effect on the longitudinal creep rates, at the stress levels explored in this study. These stresses are below those needed to cause appreciable fiber failure, such that an influence of the

interphase would not be expected. However, interphase effects are likely at higher stresses, approaching the fiber bundle strength.

5.3 Residual Stress

The cracking of the coating on the compressive side of the flexural specimens after unloading is associated with the development of *residual tensile stresses*. Such cracking may be important in causing exposure of the fibers to environmental attack. The peak value of the residual stress is expected to be proportional to the magnitude of the applied stress during creep (Appendix III), consistent with the greater tendency for such cracking at larger stresses. The mechanism involved is associated with load transfer from the fibers to the matrix and differs from that found in flexure in monolithic ceramics.[24]

6. CONCLUSION

Nicalon fibers have a beneficial effect on the longitudinal creep strength of calcium aluminosilicate (CAS) glass ceramics. Moreover, time-dependent microstructural changes in the fibers result in long-term creep hardening. The transverse creep strength is much smaller, being dominated by the matrix. The composite is thus highly anisotropic. This anisotropy causes extensive distortion with off-axis loadings. Residual stresses resulting from stress redistribution during creep can damage the composite upon cooling and may degrade its subsequent structural integrity.

ACKNOWLEDGEMENTS

Thanks are expressed to Dr. Ken Chung of Corning Inc. for supplying the material and to Dr. Joachim Mayer of the Max-Planck Institut, Stuttgart, Germany for the scanning EELS image of the CAS/Nicalon interface

APPENDIX I

Stress Redistribution in a Creeping Beam

Stress redistribution in flexural beams has been analyzed for a variety of non-linear problems, including power law creep[28] and tension/compression asymmetry.[20] In this appendix, results relevant to fiber composites are derived, subject to symmetric behavior in tension/compression. The new feature concerns the load shedding from the matrix to the fibers and its influence on the flexural deformation. When both constituents have the same creep rates ($m = n, \dot{\varepsilon}_{mo} = \dot{\varepsilon}_{fo}, \sigma_{mo} = \sigma_{fo}$) the steady-state stress distribution is well-known and given by,[28]

$$\frac{\sigma(y)}{\sigma_e} = \left(\frac{2n+1}{3n}\right)\left(\frac{2y}{h}\right)^{\frac{1}{n}} \tag{A1}$$

where y is the distance from the neutral axis and σ_e is the stress expected for a linear beam (Eqn. 2). In the transient, before steady-state is obtained, a much more complex stress distribution exists.

When the fibers have a higher creep strength than the matrix, account must be taken of the redistribution in moment from the matrix to the fibers. In the absence of fiber fracture, the strain-rates in the fibers and matrix are equal.[12] Inserting this equality into Eqns. (2) and (3), the following steady-state relationship is obtained from Eqn. (A1) for the fraction ξ of applied moment carried by the fibers,

$$\frac{\xi^n}{(1-\xi)^m} = \chi\left[\frac{f^n}{(1-f)^m}\right]\sigma_e^{m-n}\left(\frac{2m+1}{3m}\right)^m\left(\frac{3n}{2n+1}\right)^n \tag{A2}$$

where $\chi = [\dot{\varepsilon}_{mo}\sigma_{fo}^{n}/\dot{\varepsilon}_{fo}\sigma_{mo}^{m}]$. The maximum stresses in the matrix and fibers during steady-state creep are respectively,

$$\frac{\hat{\sigma}_m}{\sigma_e} = \left(\frac{2m+1}{3m}\right)\frac{(1-\xi)}{(1-f)} \tag{A3}$$

and

$$\frac{\hat{\sigma}_f}{\sigma_e} = \left(\frac{2m+1}{3m}\right)\frac{\xi}{(1-f)} \tag{A4}$$

The equivalent result for the composite is

$$\frac{\hat{\sigma}_c}{\sigma_e} = \left(\frac{2n+1}{3n}\right)\xi + \left(\frac{2m+1}{3m}\right)(1-\xi) \tag{A5}$$

An evaluation of the composite properties using these formula is achieved by iteration. Initially, it is assumed that the composite properties are controlled exclusively by the fibers in accordance with Eqn. (6). Then ξ is evaluated for Eqn. (A2). The revised distribution of stress between the fiber and matrix is determined from ξ, using Eqns. (A3) and (A4). The procedure is repeated until convergence is achieved. One complication for SiC/CAS is time dependence of the strain rate ratio, χ, caused by the creep hardening of the fibers. This time dependence may be obtained from the actual flexural data, and expressed from Eqn. (6) as

$$\dot{\varepsilon}_{fo} \approx f\dot{\varepsilon}_{\infty}(t/\tau)^{\alpha} \tag{A6}$$

The consequence is a time dependent ξ, which may be estimated from Eqns. (A2) to (A4). Trends in ξ (t), as well as $\hat{\sigma}_c/\sigma_e$ (t) computed from these formulae, using the present data show that (Fig. A1) for $f = 0.4$, most of the load is carried by the fibers ($\xi \approx 1$) except during the early stages. Consequently, with $n \approx 1$, Eqn. (A5) indicates that the elastic formula (Eqn. 2) may be used to evaluate stresses for the conditions used in this study. However, for other testing conditions, this simplification will not apply.

APPENDIX II

Creep Properties of Fibers

Fine-grained polycrystalline ceramics often creep in accordance with a steady-state law,[27]

$$\dot{\varepsilon}/\dot{\varepsilon}_o = (\sigma/\sigma_o)^n (\Omega^{1/3}/d)^{\beta} \quad \text{(B1)}$$

where Ω is the atomic volume, d is the grain size, β a coefficient between 1 and 3 and n is in the range 1–2. In this case, $n \approx 1$.[22] Based on the present microstructural observations (Fig. 10) the fiber is treated as two concentric cylinders, the outer defined by a grain size d_f and the inner by a grain size d_i. The thickness of the outer cylinder is represented by, $\zeta = t/R$, (Fig. 11). The load distribution between the large and fine grained regions is determined from the 'rule-of-mixtures,' by using Eqn. B1. Then the overall creep-rate is

$$\dot{\varepsilon}/\dot{\varepsilon}_o = (\sigma/\sigma_o)^n (\Omega^{1/3}/d^*)^{\beta} \quad \text{(B2)}$$

where $d^* = [(1-\zeta)^2 d_i + \zeta (2-\zeta) d_f]$. By inserting the measured value for $d_i = 2$ nm and $d_f = 15$ nm and noting that $\zeta \approx 0.4$ after 2 h at 1200°C,[18] Eqn. (B2) predicts a creep strengthening of about an order of magnitude. This strengthening level is consistent with the measurements summarized in Fig. 12, as well as the transient nature of the creep found in Nicalon fibers.[15, 22]

APPENDIX III

Residual Stresses

Stress redistribution during creep in the presence of creep resistant fibers causes the *matrix* stress levels to approach zero. Cooling under load to retain this stress condition, followed by elastic unloading, causes residual stresses. The residual matrix stresses, upon unloading, are simply the elastic stress on initial loading, but with opposite sign, as dictated by the relative moduli of the matrix and the fibers:

$$\sigma_m^R = -\sigma_e\left[(1-f) + \frac{E_f}{E_m} f\right]^{-1} \qquad \text{(C1)}$$

Consequently, residual *tensile* stresses may occur in those regions of the matrix initially subject to compression. Note that the reduced stress in the matrix during actual creep contributes to the absence of matrix damage and the consequent creep symmetry.

REFERENCES

[1] K.M. Prewo, "Tension and Flexural Strength of Silicon Carbide Fiber Reinforced Glass Ceramics," *J. Mater. Sci.*, **21** (1986) 3590.

[2] A.G. Evans and D.B. Marshall, "The Mechanical Behavior of Ceramic Matrix Composites, Overview No. 85," *Acta Metall.*, **37** 2657–83 (1989).

[3] R. Kerans and T.A. Parthascratty, *J. Am. Ceram. Soc.*, **76** (1991) 1385.

[4] G. Bao and Z. Suo, "Remarks on Crack-Bridging Concepts," *Appl. Mech. Rev.*, **45** (1992) 355.

[5] H.C. Cao, E. Bischoff, O. Sbaizero, M. Rühle and A.G. Evans, "Effect of Interfaces on the Properties of Fiber-Reinforced Ceramics," *J. Am. Ceram. Soc.*, **73** (1990) 1691–99.

[6] J.J. Brennan, "Tailoring of Multiple Ceramics" (ed. R.E. Tressler *et al.*) Plenum, NY (1986) 549.

[7] J.W. Hutchinson and H. Jensen, "Models of Fiber Debonding and Pull-Out," *Mech. of Mtls.*, **9** (1990) 139.

[8] S.M. Spearing and F.W. Zok, "Stochastic Aspects of Matrix Cracking in Brittle Matrix Composites," *J. Eng. Mater. Tech.*, in press.

[9] D. Beyerle, S.M. Spearing, F. Zok and A.G. Evans, "Damage and Failure in Unidirectional Ceramic-Matrix Composite," *J. Am. Ceram. Soc.*, **75** 2719–25 (1992).

[10] X. Wu and J.W. Holmes, "Creep Recovery Behavior of Nicalon Calcium-Aluminosilicate Composites," *J. Am. Ceram. Soc.*, **76** (1993) 2695.

[11] J.W. Holmes, G.E. Hilmar, R. Bhall and J. DiCarlo, "Tensile Creep and Creep Recovery of Unidirectional SiC/Si_3N_4 Composites," Proceedings 6th Hitemp Review, Cleveland, Oct. 1993.

[12] A. Kelly and K.N. Street, "Creep of Discontinuous Fiber Composites II. Theory for the Steady-State," *J. Mech. Phys. Solids*, **14** 177–86 (1966).

[13] M. McLean, "Creep Deformation of Metal-Matrix Composites," *Comp. Sci. & Tech.*, **23** 37–52 (1985).

[14] D.W. Petrasek, D.L. McDaniels, L.J. Westfall and J.R. Stephens, "Fiber-Reinforced Superalloy Composites Provide an Added Performance Edge," *Met. Progress*, **130** 27–31 (1986).

[15] G. Simon and A.R. Bunsell, "Creep Behavior and Structural Characterization at High Temperatures of Nicalon SiC Fibers," *J. Mat. Sci.*, **19** 3658–70 (1984).

[16] S.M. Johnson, R.D. Brittain, R.H. Lamoreaux and D.J. Rowcliffe, "Degradation Mechanisms of Silicon Carbide Fibers," *J. Am. Ceram. Soc.*, 71 C-132–C-135 (1988).

[17] R. Chaim, A.H. Heuer and R.T. Chen, "Microstructural and Microchemical Characterization of Silicon Carbide and Silicon Carbonitride Ceramic Fibers Produced From Polymer Precursors," *J. Am. Ceram. Soc.*, 71 960–69 (1988).

[18] T. Mah, N.L. Hecht, D.E. McCullum, J.R. Hoenigman, H.M. Kim, A.P. Katz and H.A. Lipsitt, "Thermal Stability of SiC Fibers (Nicalon®)," *J. Mat. Sci.*, 19 1191–201 (1984).

[19] R. Morrell and K.H.G. Ashbee, *J. Mater. Sci.*, 8 (1973) 1253.

[20] T.J. Chuang and S.M. Wiederhorn, *J. Am. Ceram. Soc.*, 71 (1988) 395.

[21] C.H. Weber, J.P.A. Löfvander, J.Y. Yang, C.G. Levi and A.G. Evans, *Acta Metall. Mater.*, 41 (1993) 2681.

[22] R.E. Tressler and J. DiCarlo, *High Temperature Ceramic Matrix Composites* (Ed. R. Naslain) Woodhead (1992).

[23] S. Timoshenko, *Strength of Materials, Part II, 3d ed.*, Van Nostrand-Reinhold, Princeton, (1956) 527.

[24] D.F. Carroll, R.E. Tressler, Y. Tsai and C. Near, *Tailoring Multiphase and Composite Ceramics* (Ed. R.E. Tressler *et al.*) Plenum, NY (1986) pp. 775–82.

[25] G. Bao, J.W. Hutchinson and R.M. McMeeking, "Particle Reinforcement of Ductile Phases Against Plastic Flow and Creep," *Acta Metall. et Mater.*, 8 1871–82 (1991).

[26] D. Zahl, S. Schmauder and R.M. McMeeking, to be published.

[27] A.H. Heuer, R.M. Cannon and N.J. Tighe, "Plastic Deformation in Fine Grained Ceramics, Ultrafine-Grain Ceramics," Eds. J.J. Burke, N.L. Reed and V. Weiss, Syracuse Univ. Press, 1970, 339–65.

[28] G.W. Hollenberg, G. Terwilliger and R.S. Gordon, *J. Am. Ceram. Soc.*, 34 (1971) 196.

FIGURE CAPTIONS

Fig. 1. Schematic of apparatus used for flexural creep assessment. The modification used for transverse compressive creep measurements is shown in the insert.

Fig. 2. Overview of the fiber distribution.

Fig. 3. a) TEM bright field micrograph of interfacial carbon layer. b) EELS spectrum for carbon: brightness correlates with concentration of carbon.

Fig. 4. Longitudinal creep characteristics of the composite at 1200°C obtained in flexure. Also shown are literative data for tension.[10]

Fig. 5. Effects of periodic unloading on flexural creep curves.

Fig. 6. Transverse compressive creep curves at 1200°C.

Fig. 7. A comparison of longitudinal flexure and transverse creep rates at two equivalent stress levels. Longitudinal tensile results at similar stresses are also shown.[10]

Fig. 8. The profile of a flexural specimen after testing at 1250°C and 50 MPa.

Fig. 9. Scanning electron micrograph of matrix and interface damage found upon transverse compression testing: a) $\varepsilon \approx 1\%$, b) $\varepsilon = 2\%$, c) $\varepsilon = 4\%$.

Fig. 10. Transmission electron micrograph of Nicalon fiber after creep testing of SiC/CAS at 1200°C for 50 h.

Fig. 11. Schematic of grain growth behavior in Nicalon fibers at 1200°C.

Fig. 12. Normalized plot of longitudinal creep strength.

Fig. A1. a) Fraction of applied moment carried by the fibers at different times during creep. Dashed line is approximate. b) Maximum composite stress relative to linear result, σ_e.

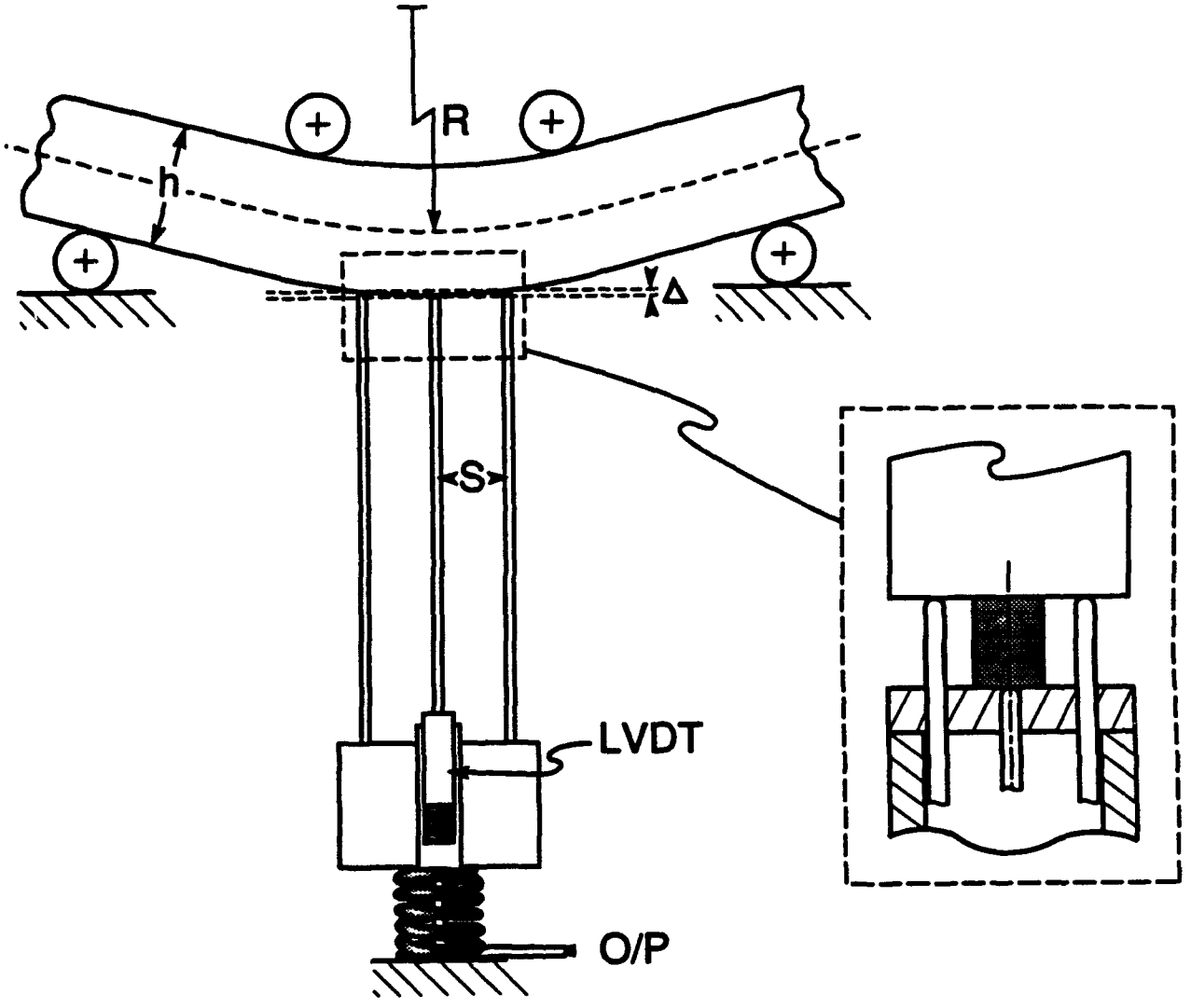

Fig. 1

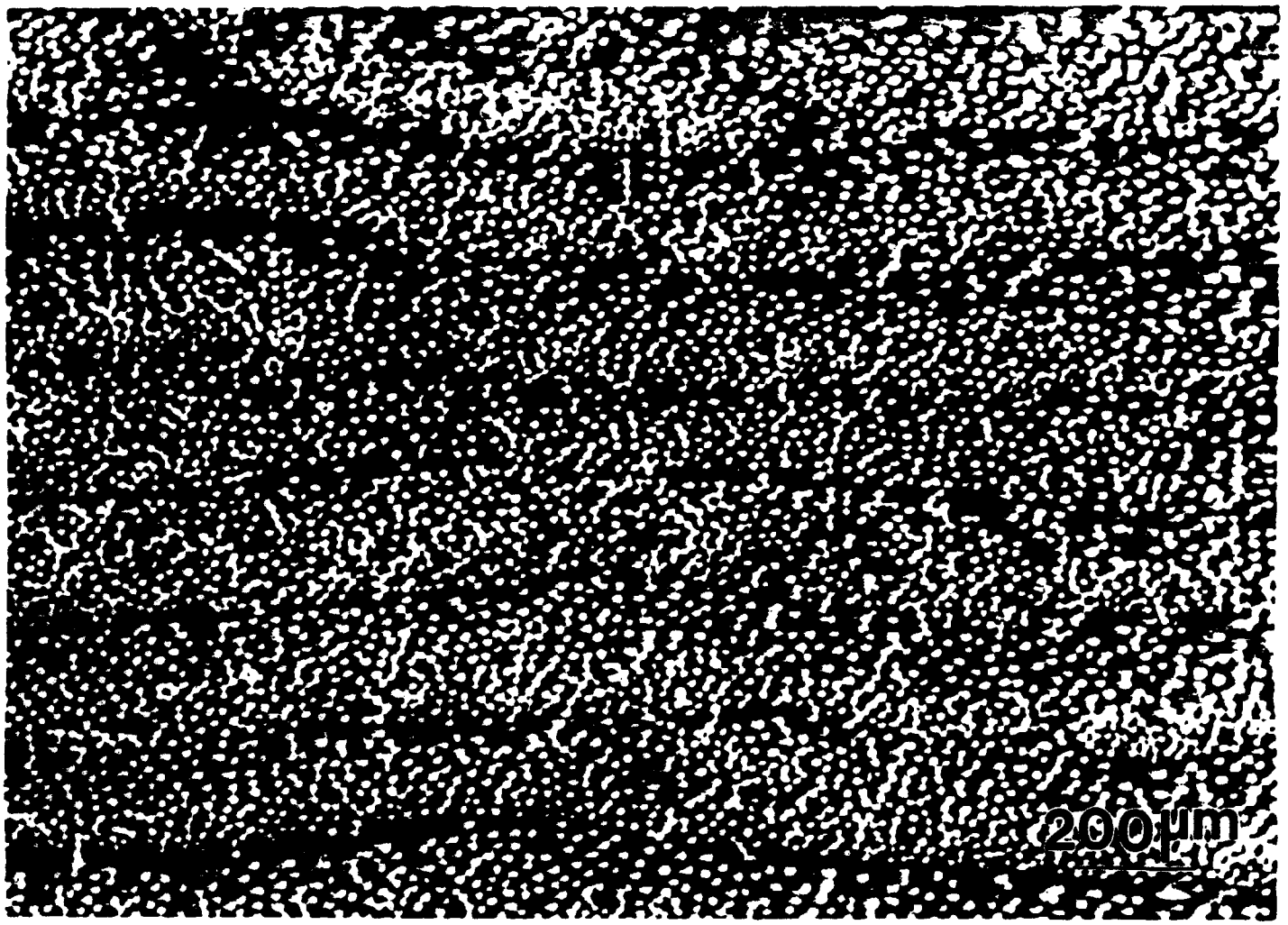

Fig. 2

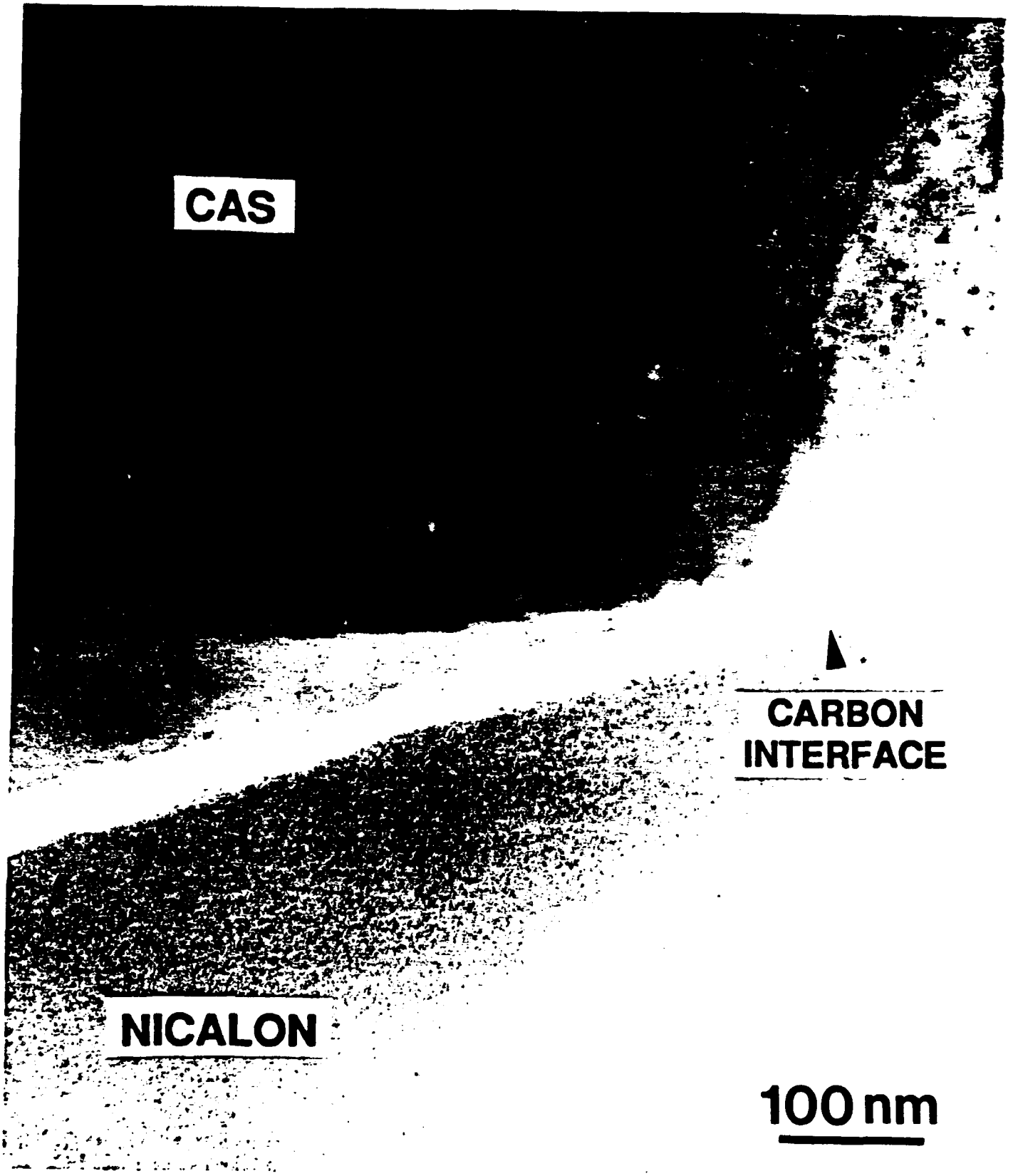

Fig. 3a

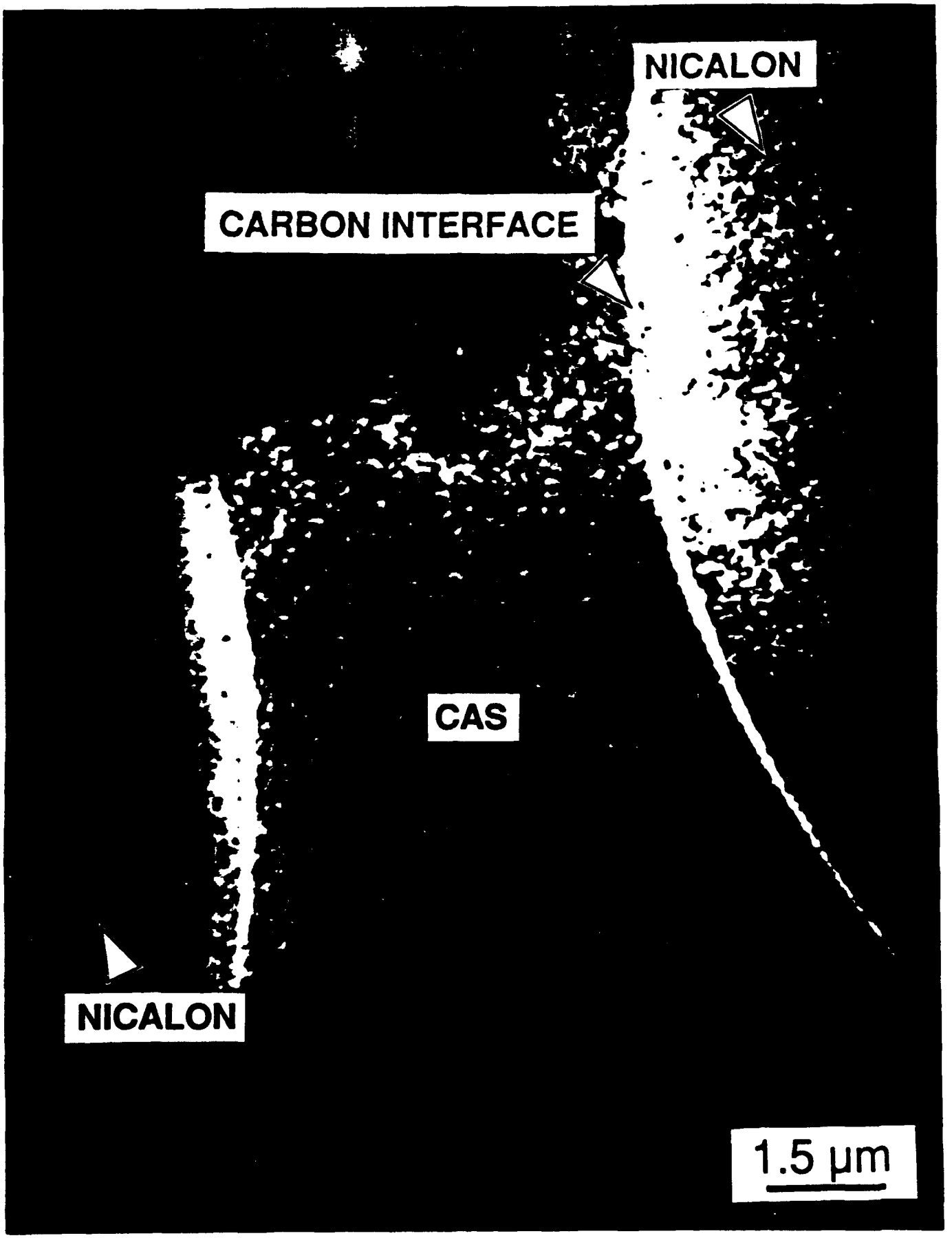

Fig. 3b

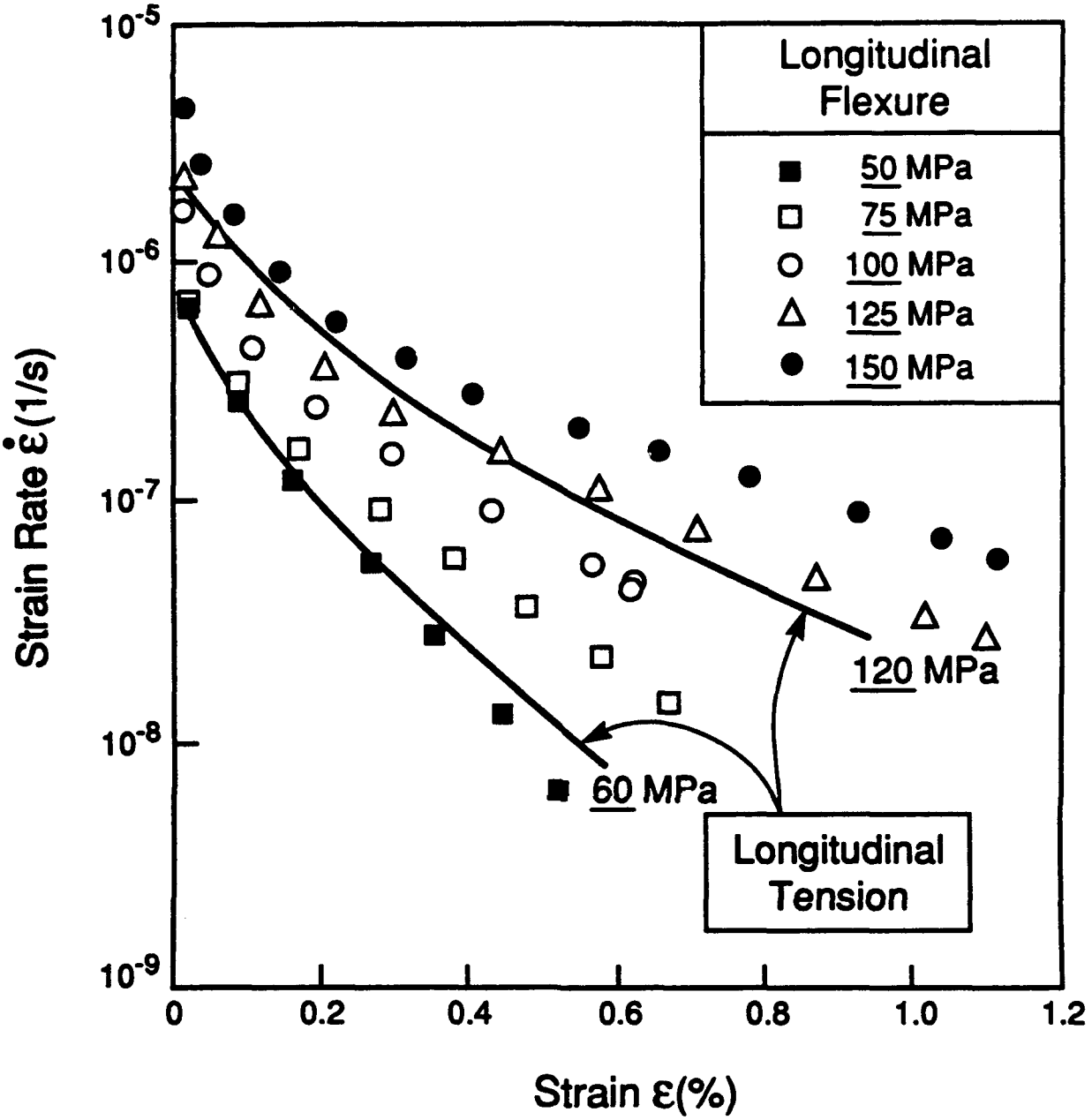
Longitudinal Flexure
50 MPa
75 MPa
100 MPa
125 MPa
150 MPa
120 MPa
60 MPa
Longitudinal Tension
Strain Rate ε̇(1/s)
Strain ε(%)
10-5
10-6
10-7
10-8
10-9
0
0.2
0.4
0.6
0.8
1.0
1.2

FIG 4

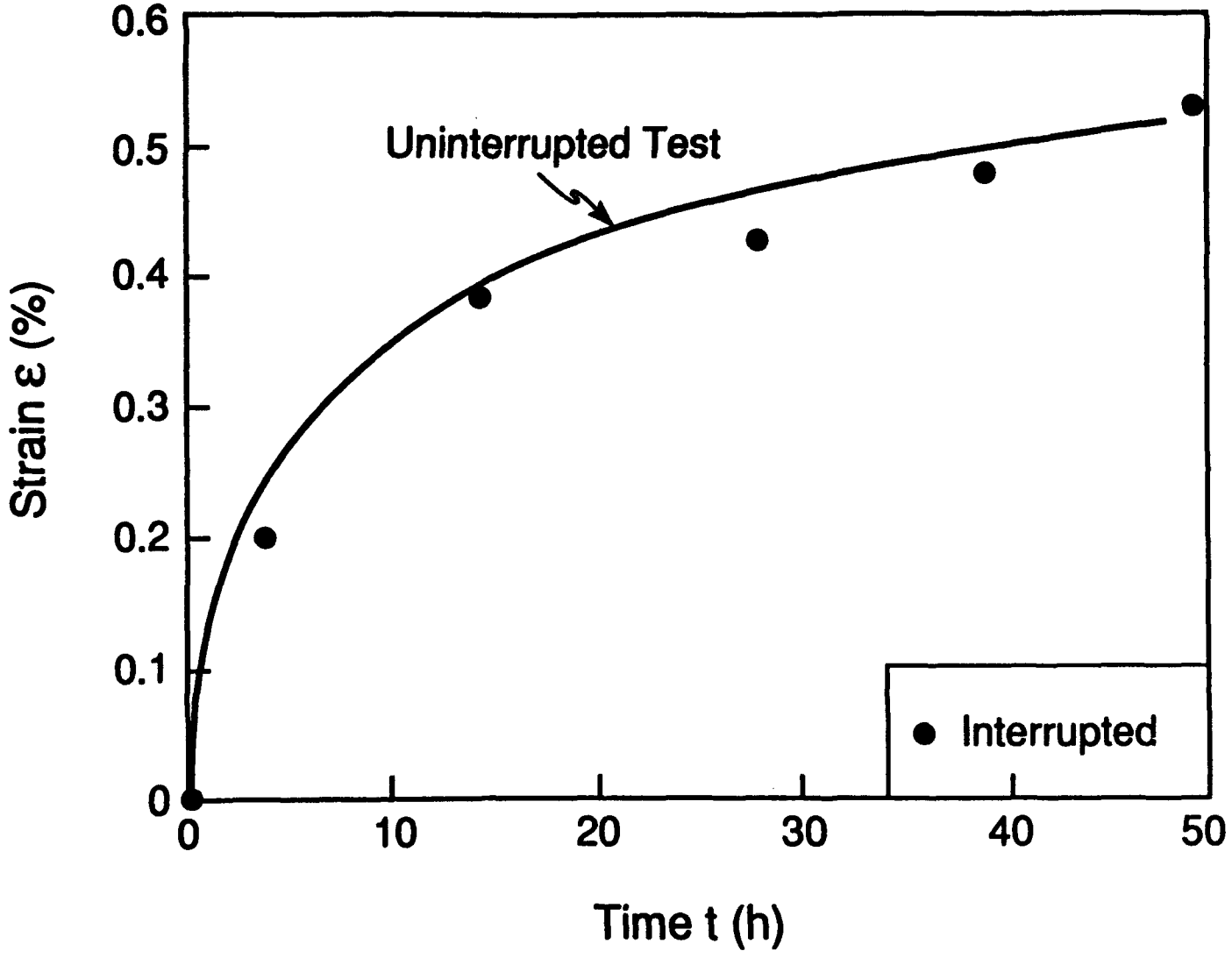
0.6
0.5
0.4
0.3
0.2
0.1
0
Strain ε (%)
Uninterrupted Test
Interrupted
0
10
20
30
40
50
Time t (h)

FIG 5

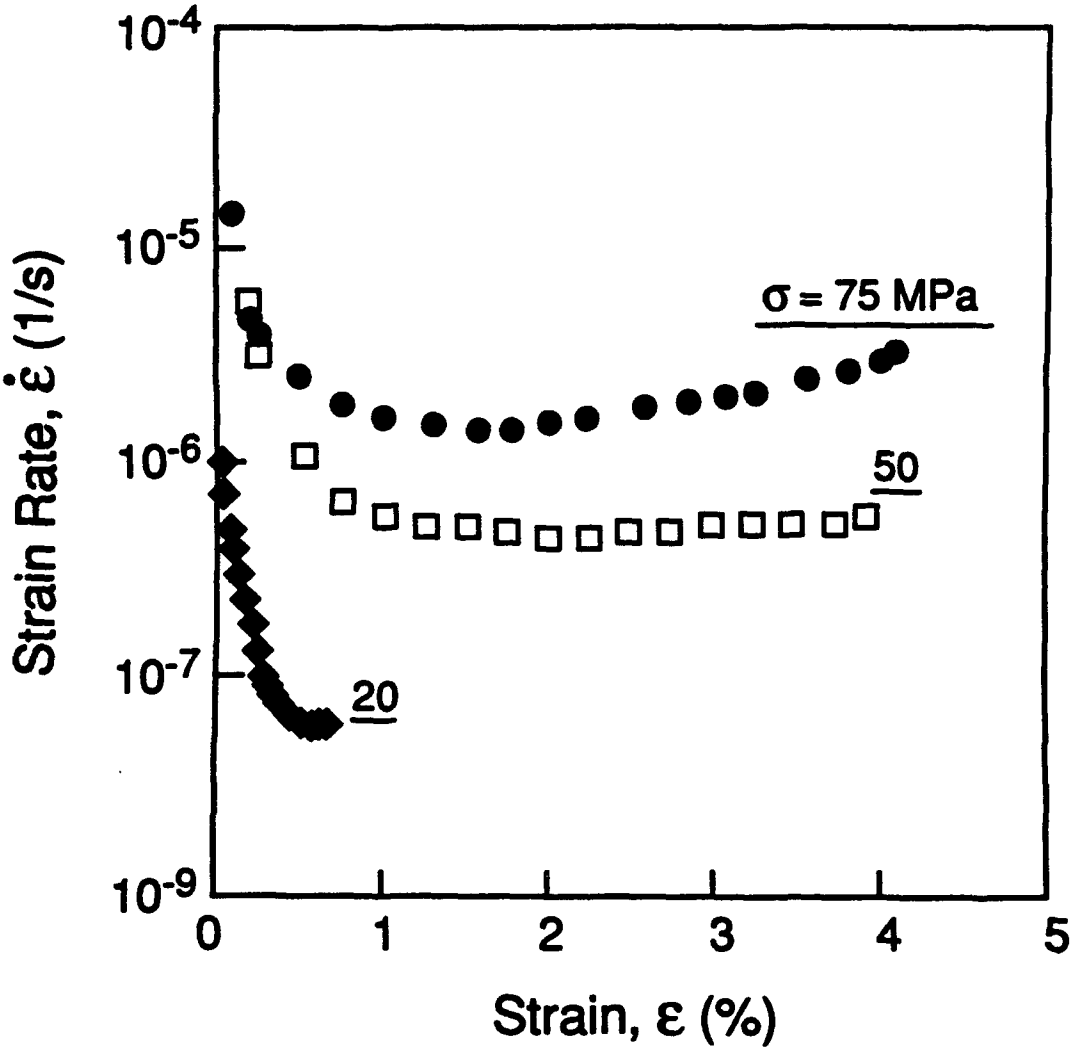
Strain Rate, ε̇ (1/s)
10-4
10-5
10-6
10-7
10-9
σ = 75 MPa
50
20
0
1
2
3
4
5
Strain, ε (%)

Fig. 6

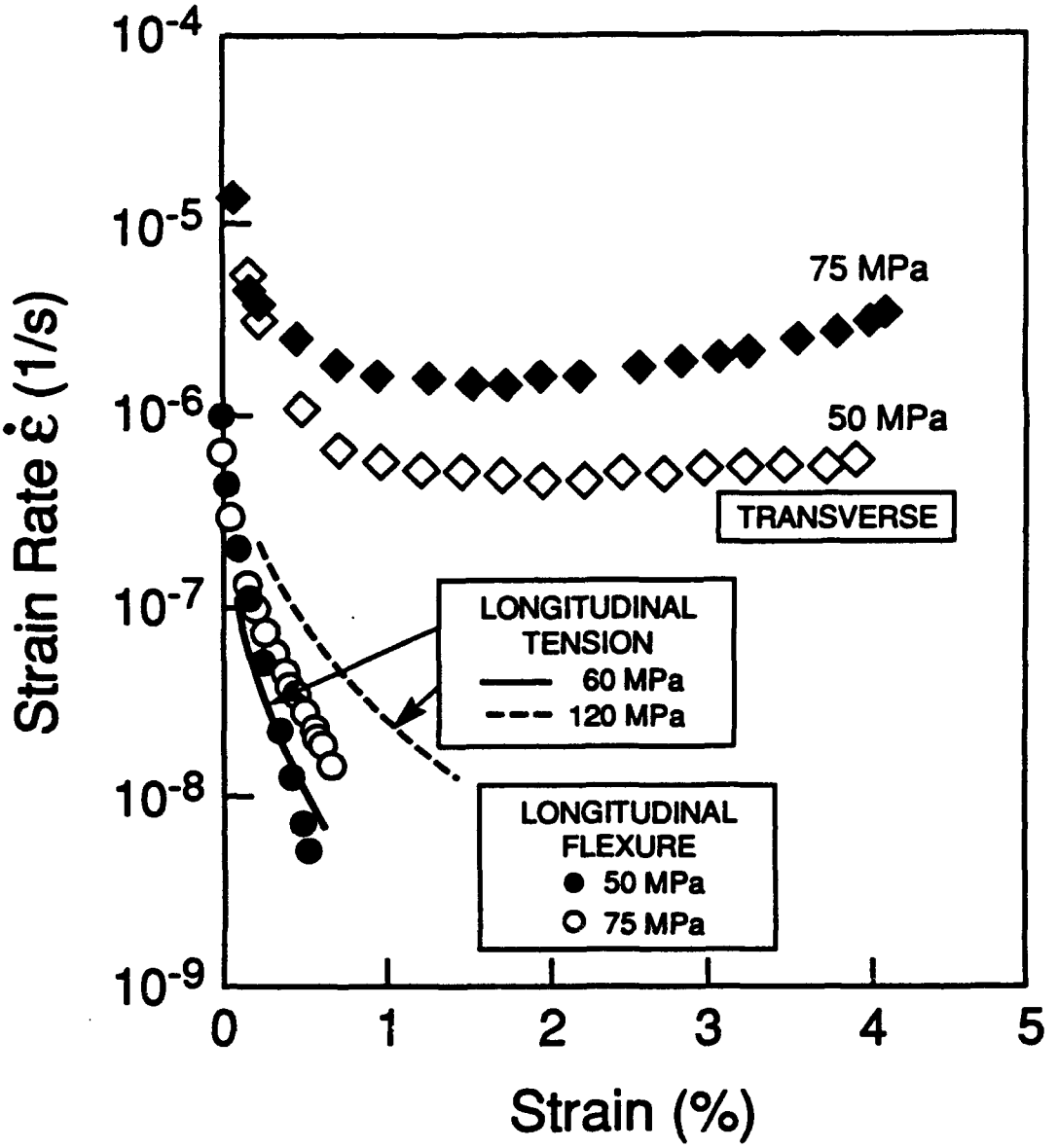

Evans.URI-11/93-amk-D47#1236-2

Fig. 7

10mm

Fig. 8

Fig. 9

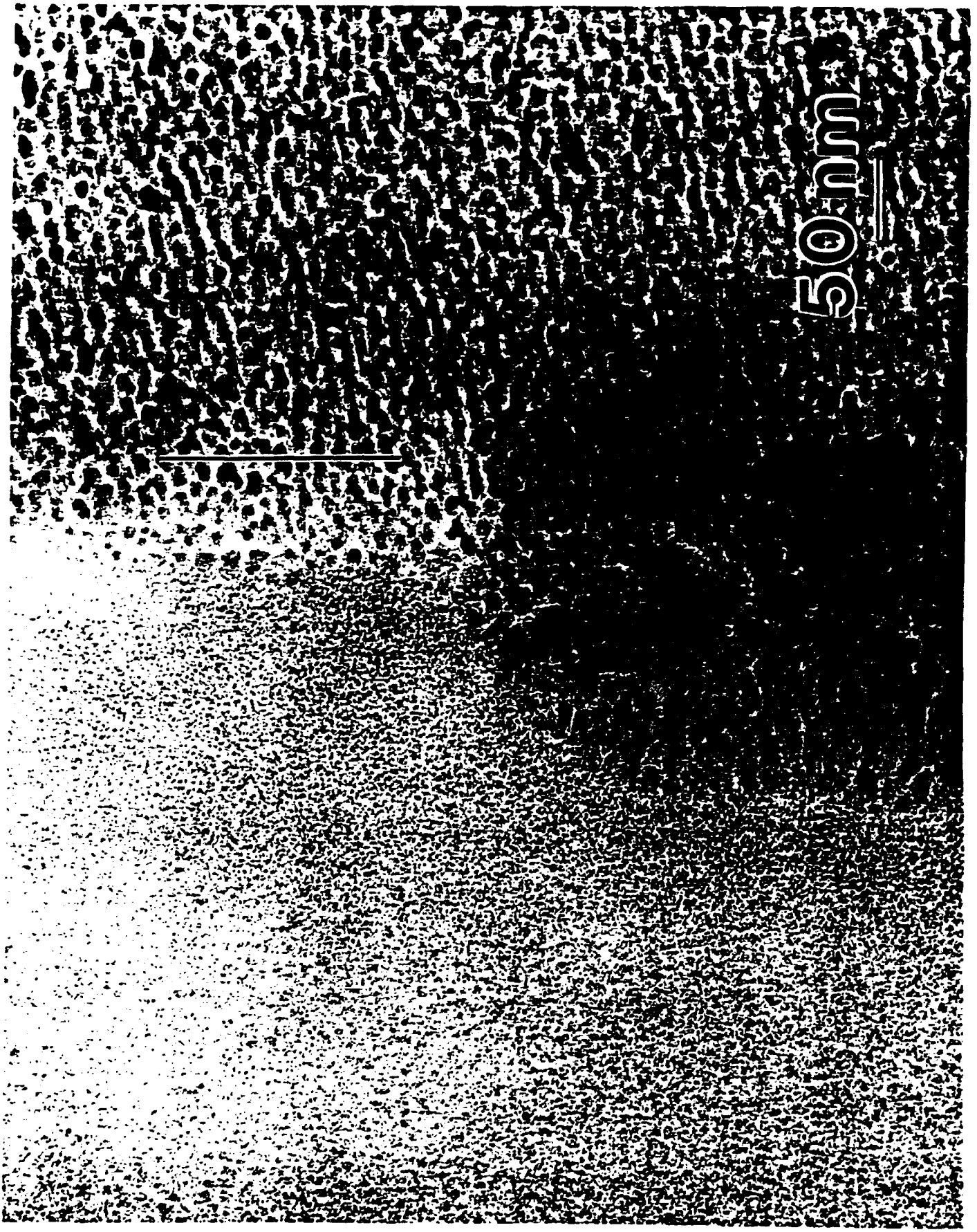

Fig. 10

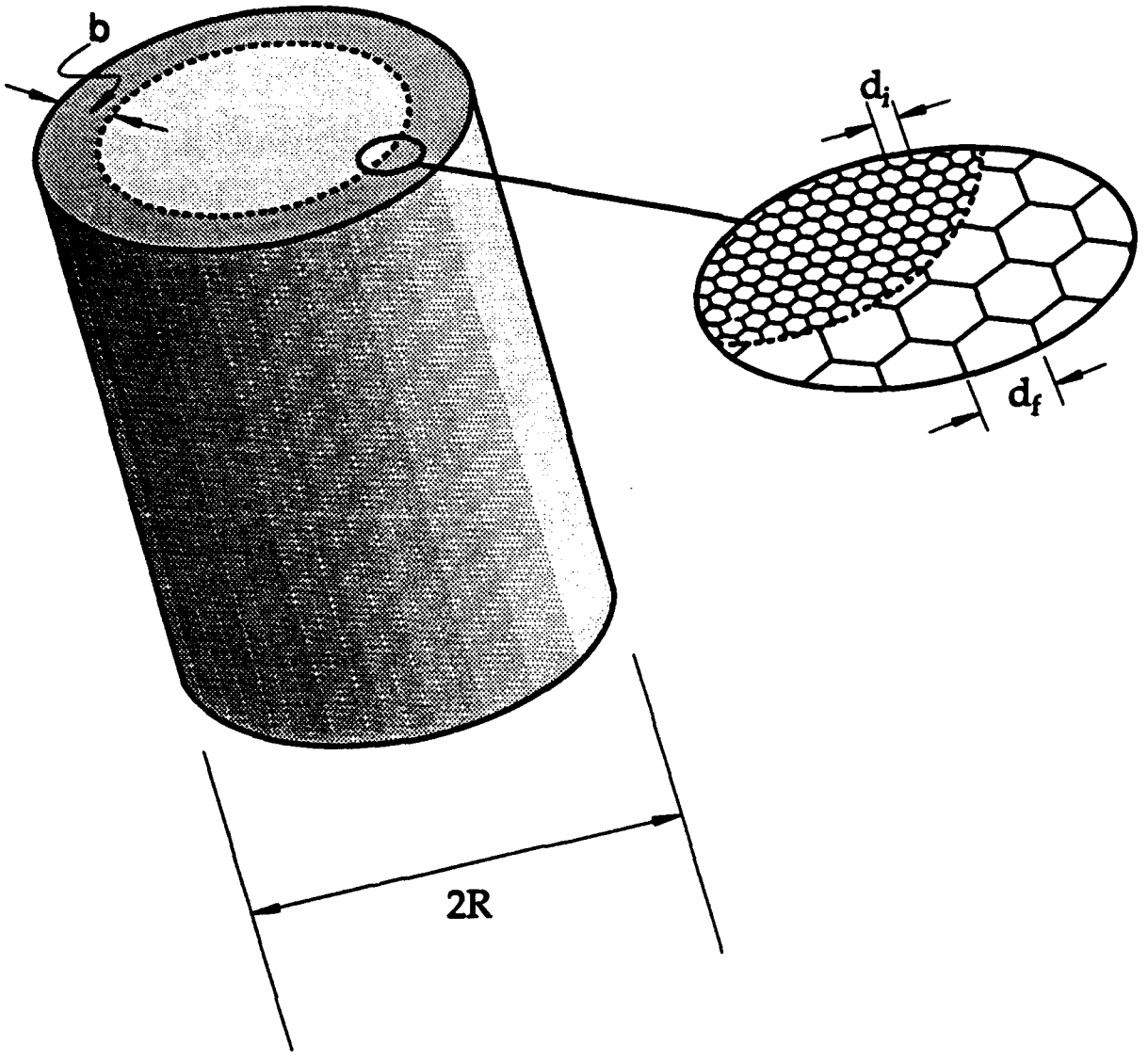

NICALON/GRAINgrwth.1

FIG. 11

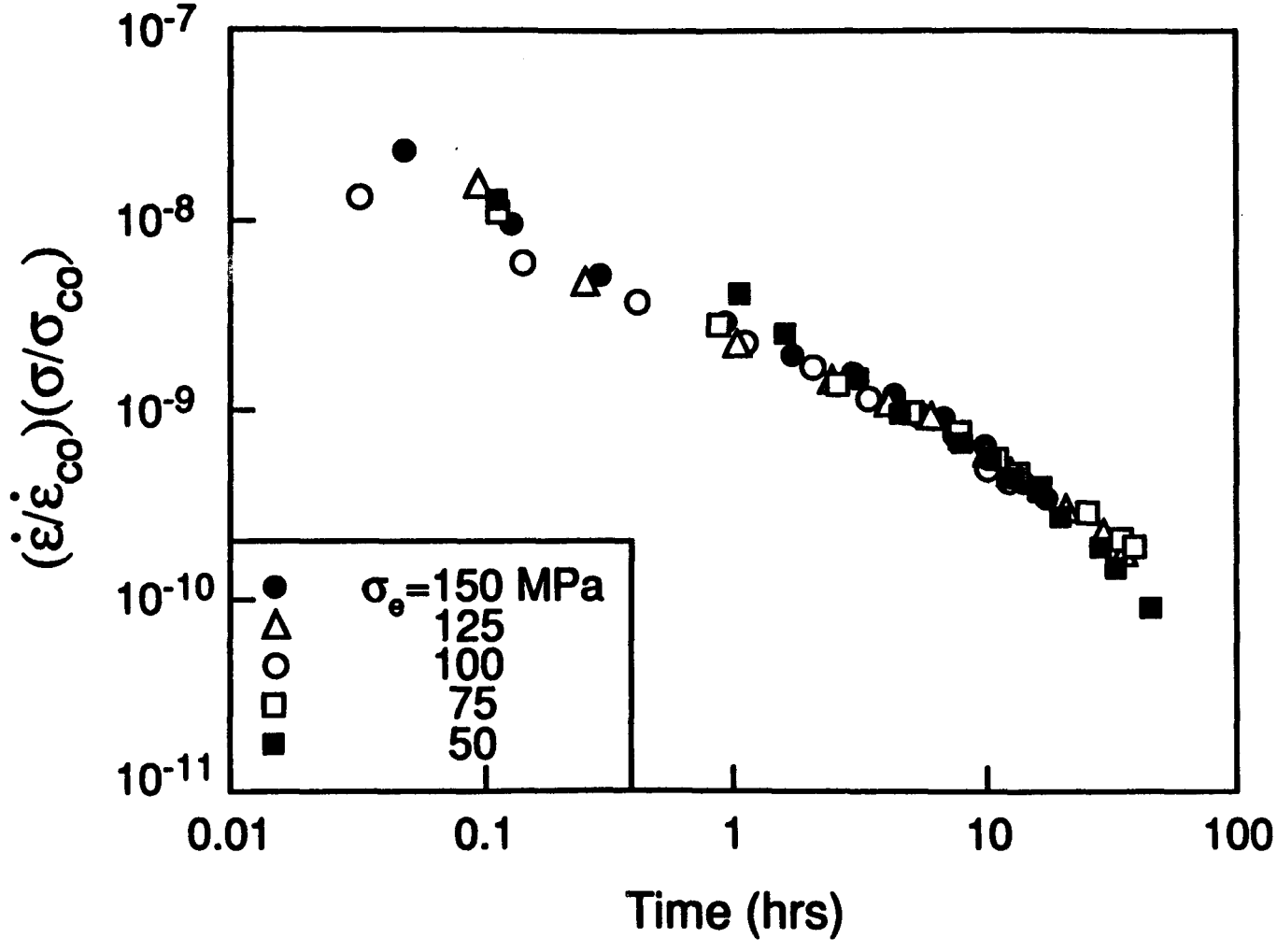

Weber-URI-8/92-amk-D2#648-8

FIG 17

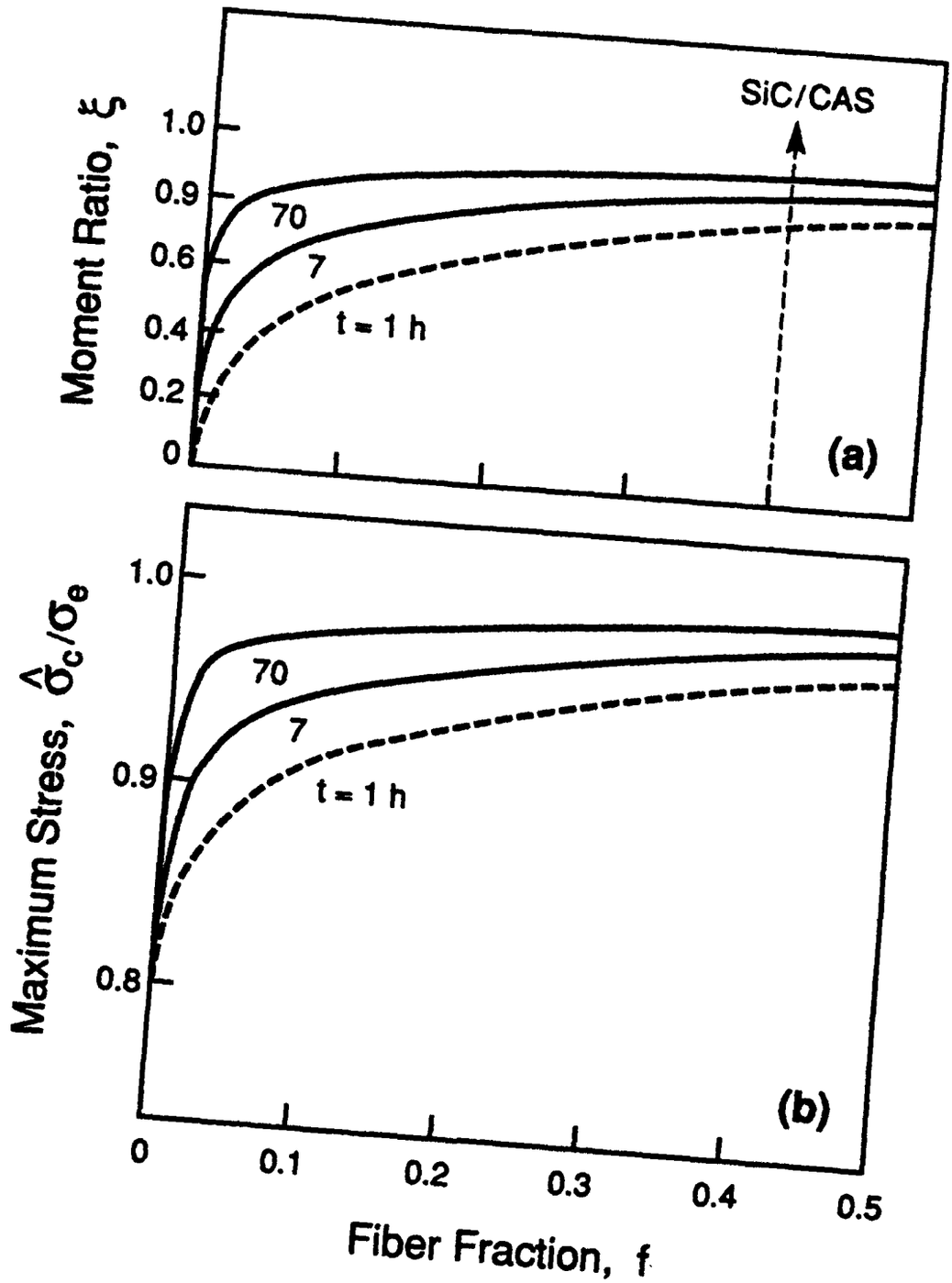

Weber.URI-10/92-emh-D2/9601-1

Fig. A1

Int. J. Solids Structures Vol. 30, No. 13, pp. 1807–1823, 1993
Printed in Great Britain

0020-7683/93 $6.00+.00

POWER LAW CREEP OF A COMPOSITE MATERIAL CONTAINING DISCONTINUOUS RIGID ALIGNED FIBERS

ROBERT M. MCMEEKING
Department of Materials and Department of Mechanical Engineering,
University of California, Santa Barbara, CA 93106, U.S.A.

(*Received* 16 *December* 1991; *in revised form* 24 *September* 1992)

Abstract—An asymptotic analysis is presented for the power law creep of a matrix containing discontinuous rigid aligned fibers. The fibers analysed have a high aspect ratio. As a result, the fiber length is much greater than both the fiber diameter and the spacing between neighboring fibers. For this situation, flow around the fiber ends can be neglected when the creep strength is being calculated. When the matrix is not slipping on the fiber surface or is nearly stuck, shearing flow dominates the behavior. The radial gradient of shear stress is balanced by the axial gradient of hydrostatic stress. Longitudinal, radial and circumferential deviatoric stresses are negligible. The resulting power law creep rate of the composite material is inversely proportional to the fiber aspect ratio raised to the power $1+1/n$ where n is the creep index. The fiber volume fraction also influences the creep rate. When the matrix slips freely on the fiber surface, or nearly so, stretching dominates the matrix flow. In this situation, the composite creep strength is not much better than the unreinforced matrix.

NOMENCLATURE

Note: superposed caret indicates a physical variable; a symbol without a caret is normalized and dimensionless, e.g. $\hat{a}$ is the fiber radius, a is $\hat{a}/\hat{b}$ where $\hat{b}$ is the unit cell radius.

$\hat{a}$	fiber radius
$\hat{b}$	unit cell radius
B	matrix creep rheology parameter
D	function of geometry and creep parameters; controls the creep strength
$\hat{\dot{e}}$	axial strain rate
F	function for radial distribution of axial velocity
G	function controlling hydrostatic stress distribution
$\hat{L}$	fiber half length
m	interface drag exponent
n	matrix creep exponent
N	higher order term in creep strength
$\hat{r}$	radial coordinate
S	relative creep strength of composite material
S_2	scaled creep strength in excess of matrix strength
S_4	same as S evaluated in Bao *et al.* (1991)
$\bar{S}$	average radial stress
$\underline{S}$	stress deviator
$\hat{v}$	velocity
V_f	fiber volume fraction
$\hat{z}$	axial coordinate
α	$\hat{L}/\hat{a}$ fiber aspect ratio
δ	$\hat{b}/\hat{L}$ small parameter
$\dot{\varepsilon}_e$	effective strain rate
η	z/δ
λ	$\hat{L}/\hat{b}=1/\delta$
$\hat{\mu}$	interface drag parameter
ρ	integration variable
$\hat{\sigma}$	hydrostatic stress
$\underline{\hat{\sigma}}$	stress tensor
$\bar{\hat{\sigma}}_a$	macroscopic axial stress
$\hat{\sigma}_f$	fiber axial stress
$\hat{\sigma}_m$	matrix axial stress
$\hat{\sigma}_e$	tensile equivalent stress
$\Sigma=(\hat{\dot{e}}/B\delta)^{1/n}$	parameter for stress normalization
θ	circumferential coordinate.

INTRODUCTION

Cell models are popular and effective for estimating the creep strength of metal matrix fiber reinforced composites and such an approach has been used by Kelly and Street (1972), Dragone and Nix (1990), Goto and McLean (1991) and Bao *et al.* (1991b). For aligned discontinuous fibers, an individual reinforcement is considered embedded in a unit cell of the matrix material such that the volume ratio of fiber to matrix in the unit cell equals the average ratio in the composite material. Boundary conditions to cause the deformation are imposed on the perimeter of the unit cell to enforce periodicity and symmetry. For the creep response to tensile stresses aligned with the axis of circular fibers, it is sufficient to calculate the behavior of an axisymmetric cell such as that shown in Fig. 1. The deformation imposed on the cell forces it to retain its circular cylindrical shape. Each point on the surface of the cell is free of shear traction. The average transverse stress on the cell is zero and appropriate conditions are imposed at the interface between the fiber and the matrix material. In the annotations in Fig. 1 the conditions appropriate to an interface around a rigid fiber without debonds but with a nonlinear viscous sliding behavior are stated. In general, however, any physical assumption can be incorporated into the cell model such as fiber elasticity or creep, debonding of the interface, etc.

Cell models usually require a numerical treatment as undertaken by Dragone and Nix (1990) and Bao *et al.* (1991b). However, in certain circumstances an approximate model is accurate and can be analysed without recourse to complete numerical treatment. This approach has been used by Kelly and Street (1972) and Goto and McLean (1991). One such circumstance is when the fibers are aligned and have an aspect ratio which is high and a volume fraction that is moderate to high. Then the matrix segment around the fiber (with section ABCD in Fig. 1) is slender and can be readily analysed with approximate flow fields. In addition, the flow in the remaining matrix segment at the fiber ends does not need to be analysed accurately because it contributes little to the yield or creep strength compared to the matrix around the fiber. That is, when the fiber aspect ratio is high, the energy dissipation in the fiber end regions during matrix creep is negligible compared to the energy dissipation rate in the matrix surrounding the fiber. The creep strength is directly related to the energy dissipation rate, so it can be analysed by calculating the major contributions to the energy dissipation rate. In this paper, that is achieved by analysing the creeping flow of the matrix adjacent to the fiber sides. If this approach is unsatisfactory in a particular case, it can always be rectified by considering longer fibers, thereby making the fiber end regions relatively less important. In this sense, the analysis can always be justified by taking

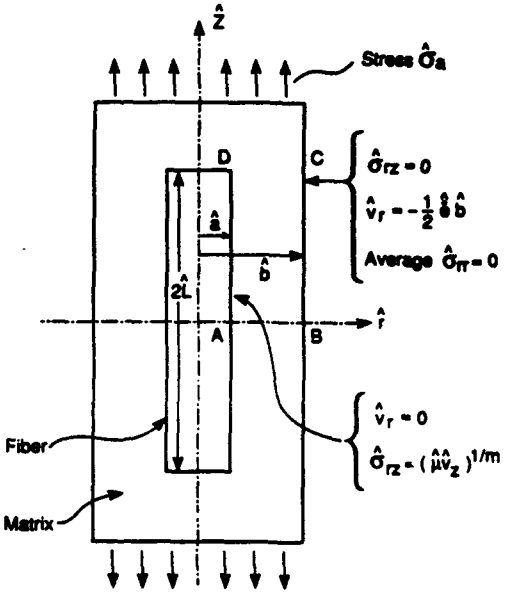

Fig. 1. Unit cell for matrix creep analysis.

the asymptotic limit of extremely long fibers. However, the analysis is proposed as being justifiable for fibers with a range of finite aspect ratios.

The issue has been studied by Bao *et al.* (1991a) for layered composites with perfectly plastic matrices. Bao *et al.* found that less than 10% of the yield strength is due to the end region when the volume fraction of rigid reinforcements is 25% and their aspect ratio is 100. For smaller aspect ratios the contribution from the end region is a higher fraction but can be modeled in an ad hoc manner as was demonstrated by Bao *et al.* (1991a). In addition, the aspect ratio of the cell relative to the aspect ratio of the fiber is known to affect the prediction of strength significantly which was demonstrated by Bao *et al.* (1991b). Thus, it is likely that the choice of aspect ratio of the cell will also influence how much of the strength is due to the matrix material around the fiber compared to the amount due to the material at the fiber ends. For example, choosing the aspect ratio of the cell to be the same as the aspect ratio of the fiber, as Bao *et al.* (1991a) did, is likely to exaggerate the importance of the fiber end region for high aspect ratio cases. A perhaps more sensible choice, in which the distance between the fiber and the cell edge is the same at the end and on the side, is likely to diminish the importance of the matrix at the fiber ends and so the 10% contribution mentioned above is probably an overestimate. At the other extreme of the rheology, namely a linearly viscous matrix, an argument can be made that as well as fiber end regions occupying relatively small volumes of the total composite microstructure, any non-uniformity of flow which they induce will be confined to the fiber end region by a St Venant effect. Thus, for all types of matrix an analysis concerned only with the matrix material surrounding the fibers circumferentially can be justified in certain cases.

In particular, the problem of a high aspect ratio rigid fiber embedded in a power law creeping matrix can be analysed in terms of the matrix material around the fiber. The cell shown in Fig. 1 will be used. The fiber is bonded to the matrix so that the radial velocity at the fiber is zero. However, it is assumed that the bond, or thin layer of interphase material at the interface, has a power law rheology of its own which allows slip of the matrix relative to the fiber. The end of the fiber is bonded strongly to the matrix as well, so that matrix incompressibility forces a net matrix flow parallel to the fiber. The axisymmetric quasistatic creeping response to an axial stress is considered. A power law rheology is assumed so that the analysis represents the steady state creep of metal or ceramic matrices around rigid (e.g. ceramic) fibers.

PROBLEM FORMULATION

The domain of the problem is the axisymmetric region with section ABCD in Fig. 1 ($\hat{a} \leqslant \hat{r} \leqslant \hat{b}$; $0 \leqslant \hat{z} \leqslant \hat{L}$). In cylindrical polar coordinates, the governing equilibrium equations neglecting inertia and body forces are

$$\frac{\partial \sigma_{rr}}{\partial r} + \frac{\sigma_{rr} - \sigma_{\theta\theta}}{r} + \delta \frac{\partial \sigma_{rz}}{\partial z} = 0, \tag{1}$$

$$\frac{\partial \sigma_{rz}}{\partial r} + \frac{\sigma_{rz}}{r} + \delta \frac{\partial \sigma_{zz}}{\partial z} = 0, \tag{2}$$

where σ is a scaled stress such that

$$\hat{\sigma} = \Sigma \sigma, \tag{3}$$

with $\hat{\sigma}$ being the Cauchy stress and Σ a scaling parameter to be discussed later. The components r and z are scaled measures of position defined by

$$\hat{r} = \hat{b} r \tag{4}$$

and

$$\hat{z} = \hat{L}z, \tag{5}$$

where $\hat{r}$, $\hat{z}$, $\hat{b}$ and $\hat{L}$ are specified in Fig. 1. The parameter δ is such that

$$\delta = \hat{b}/\hat{L}, \tag{6}$$

and in the problems to be analysed is much less than 1. The choice of differential scaling for r and z introduces a coordinate stretching transformation (Van Dyke, 1975) which will be useful in the subsequent analysis.

The matrix creeps with a power law incompressible rheology given by

$$\hat{\dot{e}}_{ij} = \tfrac{3}{2}B\hat{\sigma}_e^{n-1}\hat{S}_{ij}, \tag{7}$$

where $\hat{\mathbf{e}}$ is the strain rate, $\hat{\mathbf{S}}$ is the deviatoric stress given by

$$\hat{S}_{ij} = \hat{\sigma}_{ij} - \hat{\sigma}\delta_{ij}, \tag{8}$$

where $\hat{\sigma}(=\hat{\sigma}_{kk}/3)$ is the hydrostatic part of the stress, $\hat{\sigma}_e$ is the effective stress such that

$$\hat{\sigma}_e = \sqrt{\tfrac{3}{2}\hat{S}_{ij}\hat{S}_{ij}}, \tag{9}$$

and B is a material constant which is, however, dependent on temperature. Note that in uniaxial stress the axial strain rate equals B times the nth power of the stress. In terms of scaled variables, the creep law can be written as

$$\frac{\partial v_r}{\partial r} = \tfrac{3}{2}\sigma_e^{n-1}S_{rr}, \tag{10}$$

$$\frac{v_r}{r} = \tfrac{3}{2}\sigma_e^{n-1}S_{\theta\theta}, \tag{11}$$

$$\delta\frac{\partial v_z}{\partial z} = \tfrac{3}{2}\sigma_e^{n-1}S_{zz}, \tag{12}$$

$$\frac{\partial v_z}{\partial r} + \delta\frac{\partial v_r}{\partial z} = 3\sigma_e^{n-1}\sigma_{rz}, \tag{13}$$

where $\hat{\mathbf{v}}$ is the velocity and

$$\hat{\mathbf{v}} = \hat{b}B\boldsymbol{\Sigma}^n\mathbf{v}. \tag{14}$$

On AB ($z = 0$) the boundary conditions by symmetry are

$$v_z(r,0) = 0, \tag{15}$$

$$\sigma_{rz}(r,0) = 0. \tag{16}$$

On AD ($r = a = \hat{a}/\hat{b}$) one boundary condition is

$$v_r(a,z) = 0, \tag{17}$$

while the slip condition (see Fig. 1) becomes

$$v_z(a,z) = \sigma_{rz}^m/\mu, \tag{18}$$

where

$$\mu = \hat{\mu}B\delta\Sigma^{n-m}, \tag{19}$$

and $\hat{\mu}$ is a slip parameter for the interface. It should be noted that the last boundary condition can represent a variety of physical situations. One possibility is that there is a thin but distinct interphase of thickness t so that $V_z(a,z)/t$ is the shear strain rate in the interphase. Equation (18) then implies that the interphase is subject to power law creep but with an exponent m and the coefficient in the creep law is $1/(3^{(m+1)/2}\hat{\mu}t)$ replacing B in eqn (7). Another possibility is that there is no interphase but instead the fiber has a rough surface over which the matrix must flow even though the bond between the matrix and the fiber is relatively weak in shear. In that case, the index m would equal n and the slip parameter $\hat{\mu}$ would depend on the roughness of the fiber surface which would provide drag.

On *BC* ($r = 1$) the boundary conditions are

$$\sigma_{rz}(1,z) = 0 \tag{20}$$

and

$$v_r(1,z) = -\tfrac{1}{2}\delta, \tag{21}$$

where

$$\hat{\dot{e}} = B\Sigma^n\delta \tag{22}$$

is the axial strain rate. The condition in eqn (21) means that the scaled axial strain rate is equal to δ. This choice is arbitrary, though convenient. As a consequence, eqn (22) establishes Σ in terms of $\hat{\dot{e}}$, the axial strain rate in physical variables. The boundary condition, eqn (21), states that the unit cell remains a cylinder of uniform diameter. As a result, the normal stress σ_{rr} is not uniformly zero on $r = 1$. However, the average of σ_{rr} on $r = 1$ can be set to zero so that

$$\int_0^1 \sigma_{rr}(1,z)\,dz = 0 \tag{23}$$

to ensure that the transverse stress is approximately zero. The approximation arises because the cell extends a small distance above *C*, but that portion is neglected. The boundary condition equation (23), can be met through adjustment of the hydrostatic stress.

Note that no explicit boundary conditions are posed for *CD*. The average stress there will be of interest and determines $\hat{\sigma}_a$. The creep strength S of the composite material is defined as the average axial stress in the composite at a given axial strain rate divided by the stress in the matrix alone at the same axial strain rate. That is

$$S = \hat{\sigma}_a(\hat{\dot{e}})/(\hat{\dot{e}}/B)^{1/n}, \tag{24}$$

where $\hat{\sigma}_a$ is a function of the axial strain rate $\hat{\dot{e}}$.

ASYMPTOTIC ANALYSIS

A perturbation series solution will be developed. It will have much in common with the outer solution for a plane strain power law squeeze film due to Johnson (1984). In addition, there are boundary layers, but fully matched solutions will not be established in them. In the outer solution for the fiber problem, the matrix flow is dominated by shearing and the shear stress can be expanded in integer powers of δ, so that

$$\sigma_{rz} = \sigma_{rz}^{(0)} + \delta\sigma_{rz}^{(1)} + O(\delta^2). \tag{25}$$

As a consequence of eqn (13), v_z is $O(1)$ at leading order so

$$v_z = v_z^{(0)} + \delta v_z^{(1)} + O(\delta^2). \tag{26}$$

Incompressibility [i.e. the sum of eqns (10)–(12)] then implies that

$$v_r = \delta v_r^{(1)} + O(\delta^2), \tag{27}$$

and, apart from σ_{rz}, S_{ij} is $O(\delta)$, so

$$S_{rr} = \delta S_{rr}^{(1)} + O(\delta^2), \tag{28}$$

etc. Any gradient of σ_{rz} in the r direction must be balanced by a gradient of σ_{zz} in the z direction. For this to be possible, the stress σ_{zz} must be $O(1/\delta)$ so that the contribution of the longitudinal gradient of σ_{zz} to eqn (2) is $O(1)$ which is the same order of magnitude as the contribution of the shear stress gradient in eqn (2). This suggests

$$\sigma = \frac{1}{\delta}\sigma^{(-1)} + \sigma^{(0)} + O(\delta) \tag{29}$$

so that the hydrostatic stress is an order of magnitude larger than the deviatoric stress.

The leading order governing equations can now be stated. With terms of higher order omitted, it is found that eqn (1) gives

$$\frac{\partial\sigma^{(-1)}}{\partial r} = 0, \tag{30}$$

while eqn (2) provides

$$\frac{\partial\sigma_{rz}^{(0)}}{\partial r} + \frac{\sigma_{rz}^{(0)}}{r} + \frac{\partial\sigma^{(-1)}}{\partial z} = 0. \tag{31}$$

The creep relationship of eqn (13) gives

$$\frac{\partial v_z^{(0)}}{\partial r} = 3(\sigma_e^{(0)})^{n-1}\sigma_{rz}^{(0)}, \tag{32}$$

where

$$\sigma_e^{(0)} = \sqrt{3}\,|\sigma_{rz}^{(0)}|, \tag{33}$$

while incompressibility provides

$$\frac{\partial v_r^{(1)}}{\partial r} + \frac{v_r^{(1)}}{r} + \frac{\partial v_z^{(0)}}{\partial z} = 0. \tag{34}$$

Equations (15)–(23) give the boundary conditions

$$v_z^{(0)}(r,0) = 0, \tag{35}$$

$$\sigma_{rz}^{(0)}(r,0) = 0, \tag{36}$$

$$v_r^{(1)}(a,z) = 0, \tag{37}$$

$$v_z^{(0)}(a,z) = (\sigma_{rz}^{(0)})^m/\mu, \tag{38}$$

$$v_r^{(1)}(1,z) = -\tfrac{1}{2}, \tag{39}$$

$$\sigma_{rz}^{(0)}(1,z) = 0 \tag{40}$$

and

$$\int_0^1 \sigma^{(-1)}(1,z)\,\mathrm{d}z = 0. \tag{41}$$

Solution

Equation (30) shows that $\sigma^{(-1)}$ is independent of r. Therefore, integration of eqn (31) subject to eqn (40) gives

$$\sigma_{rz}^{(0)} = \frac{1}{2}\left(\frac{1}{r} - r\right)\frac{\mathrm{d}\sigma^{(-1)}}{\mathrm{d}z}. \tag{42}$$

It will be confirmed that $\mathrm{d}\sigma^{(-1)}/\mathrm{d}z$ is positive for $z > 0$ and thus so is $\sigma_{rz}^{(0)}$. Consequently eqn (32) shows that

$$\frac{\partial v_z^{(0)}}{\partial r} = \frac{3^{(n+1)/2}}{2^n}\left(\frac{1}{r} - r\right)^n\left(\frac{\mathrm{d}\sigma^{(-1)}}{\mathrm{d}z}\right)^n. \tag{43}$$

Integration of eqn (42) with eqn (37) provides

$$v_z^{(0)} = \frac{1}{\mu 2^m}\left(\frac{1}{a} - a\right)^m\left(\frac{\mathrm{d}\sigma^{(-1)}}{\mathrm{d}z}\right)^m + F(r,a,n)\left(\frac{\mathrm{d}\sigma^{(-1)}}{\mathrm{d}z}\right)^n, \tag{44}$$

where

$$F(r,a,n) = \frac{3^{(n+1)/2}}{2^n}\int_a^r \left(\frac{1}{\rho} - \rho\right)^n \mathrm{d}\rho. \tag{45}$$

Differentiation of eqn (44) with respect to z provides the axial strain rate which is inserted into eqn (34). Integration of eqn (34) with respect to r combined with boundary condition equation (37) then gives

$$v_r^{(1)} = \frac{1}{\mu 2^{m+1}}\left(\frac{1}{a} - a\right)^m\left(\frac{a^2}{r} - r\right)\frac{\mathrm{d}}{\mathrm{d}z}\left(\frac{\mathrm{d}\sigma^{(-1)}}{\mathrm{d}z}\right)^m - \frac{1}{r}\int_a^r \rho F(\rho,a,n)\,\mathrm{d}\rho\,\frac{\mathrm{d}}{\mathrm{d}z}\left(\frac{\mathrm{d}\sigma^{(-1)}}{\mathrm{d}z}\right)^n. \tag{46}$$

The boundary condition specifying the strain rate, eqn (38), then provides the nonlinear differential equation

$$\frac{\mathrm{d}}{\mathrm{d}z}\left[G(a,n)\left(\frac{\mathrm{d}\sigma^{(-1)}}{\mathrm{d}z}\right)^n + \frac{(1-a^2)^{m+1}}{\mu 2^{m+1}a^m}\left(\frac{\mathrm{d}\sigma^{(-1)}}{\mathrm{d}z}\right)^m\right] = \frac{1}{2}, \tag{47}$$

where

$$G(a,n) = \int_a^1 \rho F(\rho, a, n)\, d\rho. \tag{48}$$

This can be integrated once and boundary condition equation (36) along with eqn (42) can be used to give

$$G(a,n)\left(\frac{d\sigma^{(-1)}}{dz}\right)^n + \frac{(1-a^2)^{m+1}}{\mu 2^{m+1} a^m}\left(\frac{d\sigma^{(-1)}}{dz}\right)^m = \frac{z}{2}. \tag{49}$$

This is hard to solve in general when $m \neq n$ except when $n = 2$ and $m = 1$ and vice versa. Substantial insight and a degree of generality can be retained by choosing $m = n$. As discussed previously, this case represents that of a well bonded fiber–matrix interface with a rough fiber surface at a temperature sufficiently high to give rise to a negligible shear strength of the bonded interface. The resistance to slip arises from the drag induced by the creep of the matrix along the rough fiber suface. Alternately, it could represent the case of an interphase with the same creep index as the matrix but with a different creep coefficient. The approach of using $m = n$ permits the study of the effect of a weak interface and some general insights are obtained. With $m = n$, eqn (49) provides

$$\frac{d\sigma^{(-1)}}{dz} = \left(\frac{z}{D}\right)^{1/n}, \tag{50}$$

where

$$D(a,n) = 2G(a,n) + \frac{(1-a^2)^{n+1}}{\mu 2^n a^n}. \tag{51}$$

Integration of eqn (49) and use of eqn (41) reveals that

$$\sigma^{(-1)} = -\frac{z^{1+1/n} - \dfrac{n}{2n+1}}{\left(1+\dfrac{1}{n}\right)D^{1/n}}. \tag{52}$$

The remaining significant terms in the solution are then

$$\sigma_{rz}^{(0)} = \frac{1}{2}\left(\frac{1}{r} - r\right)\left(\frac{z}{D}\right)^{1/n}, \tag{53}$$

$$v_z^{(0)} = \left[\frac{1}{\mu 2^n}\left(\frac{1}{a} - a\right)^n + F(r,a,n)\right]\frac{z}{D}, \tag{54}$$

$$v_r^{(1)} = -\left[\frac{1}{\mu 2^{n+1}}\left(\frac{1}{a} - a\right)^n\left(r - \frac{a^2}{r}\right) + \frac{1}{r}\int_a^r \rho F(\rho, a, n)\, d\rho\right]\frac{1}{D}. \tag{55}$$

Thus the key assumption made by Kelly and Street (1972) that the velocity in the z direction is proportional to z is correct to leading order. However, now the dependence on r has been established too.

Boundary layer

It is possible to proceed with the solution to higher order terms and so establish the small corrections involved but this will not be done here. However, it should be noted that boundary layers are involved at $z = 0$ and at $r = 1$. The shear stress to leading order is zero

at those locations and thus so is the effective stress σ_e. In the pure power law rheology being used in this problem, this makes the matrix rigid to leading order at $z = 0$ and $r = 1$. However, material is deforming at those locations and as a result the higher order terms in the deviatoric stress in the perturbation series diverge there. To correct this, a boundary layer analysis is required. However, the result of Johnson (1984) for the plane strain squeeze film indicates that the boundary layers are passive and so do not disrupt the leading order outer solution. Consequently, the leading order outer solution equations (52)–(55) are valid. The boundary layer analysis provides a significant correction term at higher order in the outer solution. This correction term has not been worked out. However, the boundary layer at $z = 0$ can be analysed and terms for the correction estimated there. An overall axial balance of stress then provides the net resultant stress for the composite material and therefore an estimate to higher order of the creep strength of the composite. The details of the boundary layer results are developed in the Appendix.

COMPOSITE MATERIAL CREEP RESPONSE

We now have an estimate for the average axial stress at $z = 1$ in the cell. This is given by eqn (52) at $z = 1$ divided by δ plus the correction $\delta^{1/n}N$ arising from the analysis of the boundary layer at $z = 0$ [see eqns (A16), (A22) and (A28)]. The correction is required at $z = 1$ to balance the tension in the boundary layer at $z = 0$. Thus, the average stress at $z = 1$ in normalized variables is

$$\frac{n}{\delta(2n+1)D^{1/n}} + \delta^{1/n}N. \tag{56}$$

Clearly, as long as D is not large, the first term will be the largest contribution to $\hat{\sigma}_a$ (see Fig. 1) which represents the creep stress of the composite material. Additional contributions to $\hat{\sigma}_a$ will arise from the effects of matrix flow around the fiber end. This term may be of the same order of magnitude as the boundary layer term N, but the fiber end flow term is difficult to estimate. Although it may be inconsistent, we will simply omit the fiber end flow term but include the boundary term. It is hoped that the result will then be meaningful for low fiber volume fractions where the fiber end flow term will tend to be small. In any case, as long as D is not large, the discrepancy relates only to a higher order term and the creep behavior predicted by the leading order term in eqn (56) is still reliable. The omission will be more serious in the case of low drag fiber–matrix interfaces with moderate to high volume fractions of fibers because D becomes large in that case. Then the fiber end term will be just as significant as the leading term in eqn (56). The validity of the model is then doubtful.

The estimate for $\hat{\sigma}_a$ is obtained from eqn (56) in physical variables. Accordingly

$$\begin{aligned}\hat{\sigma}_a &= \frac{\Sigma \hat{L} n}{\hat{b}(2n+1)D^{1/n}} + \Sigma N \delta^{1/n} \\ &= \left(\frac{\hat{\dot{e}}}{B}\right)^{1/n}\left[\frac{\lambda^{1+1/n}n}{(2n+1)D^{1/n}} + N\right],\end{aligned} \tag{57}$$

where $\lambda = \hat{L}/\hat{b}$. In turn, the creep strength is

$$S = \frac{\lambda^{1+1/n}n}{(2n+1)D^{1/n}} + N. \tag{58}$$

Note that the term S functions as a dimensionless reference stress (Leckie, 1986) for the creep behavior of the composite as in

$$\hat{\dot{e}} = B(\hat{\sigma}_e/S)^n. \tag{59}$$

The results will be left in the form presented in eqns (57) and (58) even though the dependence on parameters like fiber volume fraction and fiber aspect ratio is not apparent. The forms presented, in terms of a and λ, are more versatile with the advantage that there is no asumption dependent conversion from a and λ to volume fraction and fiber aspect ratio. However, such conversions can be made easily by the user of the results. For example, Kelly and Street (1972) neglected the ends of the unit cell and assumed that $\hat{b}$ is half the nearest neighbor center to center spacing in a hexagonal array of fibers. In that case

$$a = \hat{a}/\hat{b} = (2\sqrt{3}V_f/\pi)^{1/2}, \tag{60}$$

where V_f is the fiber volume fraction. On the other hand, if the unit cell is assumed to have the same aspect ratio as the fiber, then

$$a = V_f^{1/3}. \tag{61}$$

Therefore, it is best to avoid any conversion and leave the user of the results to choose an approach which is appropriate to the material of interest.

In any case, since

$$\lambda = \hat{L}/\hat{b} = (\hat{L}/\hat{a})(\hat{a}/\hat{b}) \tag{62}$$

λ will be proportional to the aspect ratio of the fiber $\alpha = \hat{L}/\hat{a}$. Therefore, the creep strength S, eqn (58), depends relatively strongly on the fiber aspect ratio, being proportional to $\alpha^{1+1/n}$. This ranges from a quadratic dependence for linear viscosity to nearly linear for high n. This dependence was identified by Kelly and Street (1972). As the fiber volume fraction increases, a will increase and be around unity for fiber volume fractions around unity. This will cause D to become very small or zero, predicting very large or infinite creep strengths. This locking up is present in the model of Kelly and Street (1972), occurring at $V_f = 0.91$ in that case, which is when fibers in a hexagonal array touch each other.

As the fiber volume fraction approaches zero with μ finite, a will disappear and so will the creep strength predicted by the first term in eqn (58). The second term, N, then provides the creep strength, which will be unity according to eqn (A22). Returning to the general case, consider what happens if $\mu \to 0$. This is the zero drag case and eqn (51) makes it clear that $D \to \infty$. Consequently, the creep strength is then given by N, expressed in this case by eqn (A28). Results for N for several values of n are plotted in Fig. 2. The values are less

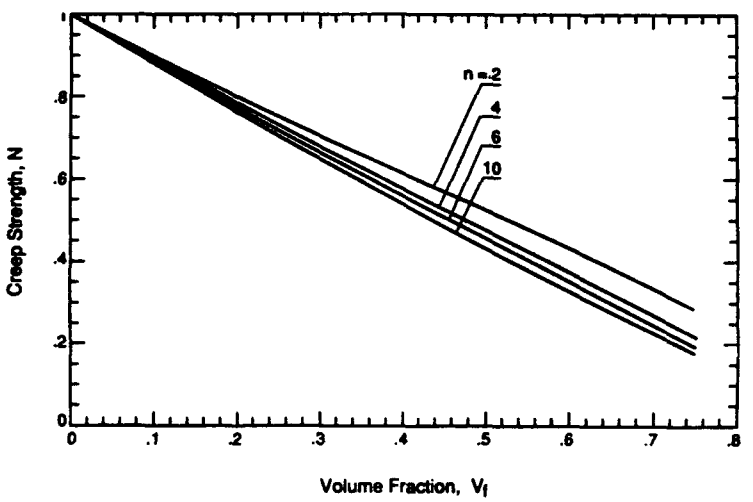

Fig. 2. Creep strength of a material with zero drag between the fiber and the matrix.

than or equal to unity, indicating that the composite will be weaker than the matrix alone. This effect occurs because the fibers act only to fill cylindrical holes in the matrix and the composite behavior represents the creep of a matrix filled with such cylindrical holes. It can be seen in Fig. 2 that N is approximately given by $1-V_f$, confirming this effect. This result is not exact because the effect of flow around the fiber end has been neglected. The true result is probably $1-V_f$ plus a small amount accounting for the fiber end effect. However, the magnitude of the contribution due to flow around the very end of the fiber will not depend to any great extent on the aspect ratio of the fiber. Thus, for long, discontinuous fibers, the creep strength will be modest if the matrix is free to slip without drag relative to the fiber. This effect was apparent, although not emphasized, in the model of Kelly and Street (1972).

It is difficult to know realistic physical values of μ. In addition, the model for interface drag with $m = n$ is of limited value although it is very similar to a form implied in the model of Kelly and Street (1972). As they pointed out (in terms of their interface sliding parameter but the implications are the same), a given value of μ (less than ∞) will have a stronger effect on the creep strength of a material with a low n compared to a high n. This arises because S is controlled by $D^{-1/n}$ and μ enters the creep strength to leading order through D. However, the effect of a more physically realistic slip law remains to be investigated. For example, interface diffusion tends to occur readily in metal matrix composites at creep temperatures. This will tend to induce slipping with a linear rheology, i.e. $m = 1$ in eqn (18).

Finally, we can consider the creep strength in detail for the no slip case $\mu = \infty$. This is accomplished by consideration of $\tilde{S} = (S-1)/\alpha^{1+1/n}$ computed from eqn (58). This parameter is the excess creep strength over the matrix strength normalized to make it independent of α. The result is plotted as a function of a^2 in Fig. 3 for several creep exponents. For comparison, the equivalent parameter from the model of Kelly and Street (1972) is plotted as well. For the latter model, the volume fraction has been converted to a by use of eqn (60). The result has the form

$$\tilde{S}_K = (S-1)/\alpha^{1+1/n} = \left(\frac{2}{3}\right)^{1/n} \frac{n}{2n+1} \left(\frac{a}{1-a}\right)^{1/n} \frac{a^2}{1-a^2}. \tag{63}$$

It can be seen in Fig. 3 that there are significant differences between the two models.

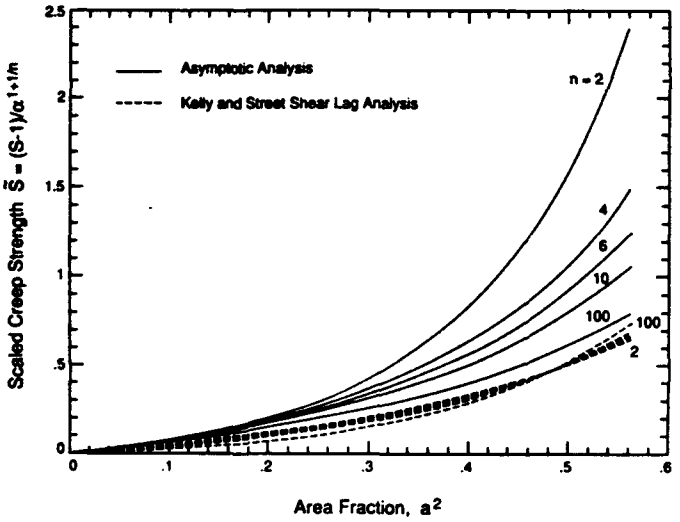

Fig. 3. Excess creep strength of a material with no slip between the fiber and the matrix. The result is normalized by the fiber aspect ratio raised to the power $1+1/n$.

FIBER STRESSES

Fiber stresses are important because the reinforcements can crack and degrade the creep strength when the stress exceeds the fiber strength as observed by Weber *et al.* (1993). In addition, Sancaktar and Zhang (1990) have demonstrated that high shear stresses on the interface can cause interphase and matrix cracking. The shear stress at the interface between the matrix and the fiber is directly related to the gradient of the average axial fiber stress along the fiber. The average axial stress at any point in the fiber can be computed from a net balance of forces in the axial direction. This requires

$$\hat{\sigma}_a = a^2\hat{\sigma}_f(\hat{z}) + (1-a^2)\hat{\sigma}_m(\hat{z}) \tag{64}$$

at any position $\hat{z}$ where $\hat{\sigma}_f$ is the average axial fiber stress at $\hat{z}$ and $\hat{\sigma}_m$ is the average axial matrix stress at $\hat{z}$. From eqn (52) we have

$$\hat{\sigma}_m(\hat{z}) = \left(\frac{\hat{\dot{e}}}{B}\right)^{1/n}\left\{\frac{\left[\left(\frac{\hat{z}}{L}\right)^{1+1/n} - \frac{n}{2n+1}\right]\lambda^{1+1/n}}{(1+1/n)D^{1/n}} + N\right\}. \tag{65}$$

Given eqn (57), it follows that

$$\hat{\sigma}_f(\hat{z}) = \left(\frac{\hat{\dot{e}}}{B}\right)^{1/n}\left\{\frac{\lambda^{1+1/n}}{D^{1/n}}\frac{n}{n+1}\left[\frac{1}{a^2} - \frac{1-a^2}{a^2}\left(\frac{\hat{z}}{L}\right)^{1+1/n} - \frac{n}{2n+1}\right] + N\right\}. \tag{66}$$

The highest value is at $\hat{z} = 0$ where

$$\begin{aligned}\hat{\sigma}_f^{max} &= \hat{\sigma}_f(0)\\ &= \left(\frac{\hat{\dot{e}}}{B}\right)^{1/n}\left[\frac{\lambda^{1+1/n}}{D^{1/n}}\frac{n}{n+1}\left(\frac{1}{a^2} - \frac{n}{2n+1}\right) + N\right].\end{aligned} \tag{67}$$

Neglecting N, which will be small compared to other terms when λ is large, we find

$$\frac{\hat{\sigma}_f^{max}}{\hat{\sigma}_a} = \frac{2n+1-a^2n}{a^2(n+1)}. \tag{68}$$

Thus the maximum axial fiber stress can be obtained approximately by multiplying the composite stress by a factor given by a fairly simple formula. For example, with a^2 equal to a quarter (i.e. the fiber diameter is equal to the fiber spacing), the ratio is $(7n+4)/(n+1)$ which, for example, is equal to 6.4 for $n = 4$. It is interesting that the ratio is independent of the aspect ratio of the fiber. This, however, only applies if the fiber is long enough, say with an aspect ratio of 5 or greater.

A further interesting point is that the minimum matrix stress (at $\hat{z} = 0$) is compressive. Expressed as a fraction of the composite stress, the minimum matrix stress $\hat{\sigma}_m^{min} = \hat{\sigma}_m(0)$ is

$$\frac{\hat{\sigma}_m^{min}}{\hat{\sigma}_a} = -\frac{n}{n+1}, \tag{69}$$

independent of the volume fraction *and* the fiber aspect ratio (given that the fiber aspect ratio is high enough).

COMPARISON WITH FINITE ELEMENT RESULTS

There are few finite element results available in detail for comparison. The most useful is the analysis by Dragone and Nix (1990), who treated an aluminum alloy with 20% by volume of SiC fibers. A unit cell approach was adopted and calculations performed for $n = 4$. The fiber was perfectly bonded to the matrix and so the relevant comparison is with our results when $\mu = \infty$. A number of features found in the asymptotic analysis are apparent in their steady-state solution for $\alpha = 5$, a somewhat lower aspect ratio than we would prefer for comparison. The stress in the matrix around the fiber is dominated by the hydrostatic stress with the hydrostatic component apparently 25 times the longitudinal deviatoric stress. The hydrostatic stress in the matrix varies almost linearly down the length of the fiber. (Our analysis predicts a variation with $\hat{z}^{1.25}$, but it would be difficult to distinguish this from a linear behavior in numerical results.) The hydrostatic stress adjacent to the fiber is independent of distance from the fiber. The axial stress at the fiber end is about 25% higher than the composite stress indicating an effect of flow around the end of the fiber which we have neglected. The aspect ratio of the cell is equal to the aspect ratio of the fiber. Therefore, by eqn (61), $a^2 = V_f^{2/3}$. For $V_f = 0.2$, this gives $a^2 = 0.34$. For this value of a^2, we predict 4.5 for $\hat{\sigma}_f^{max}/\hat{\sigma}_a$ from eqn (68) and -0.8 for $\hat{\sigma}_m^{min}/\hat{\sigma}_a$ from eqn (69). Dragone and Nix (1990) find these ratios at steady state to be 4.9 and -1.2, respectively. Thus even for the low aspect ratio fiber the asymptotic analysis is reasonably good. We suspect that most of the discrepancy is due to the stress arising from flow around the fiber ends. When the difference between the composite stress and the stress at the fiber end is factored out, our ratios predict the Dragone and Nix (1990) stress values almost exactly. Thus, for longer fibers, we believe our estimates will be quite accurate even without adjustment.

The steady-state strain rates computed by Dragone and Nix (1990) at 80 MPa for fibers with aspect ratios 5, 7 and 10 are listed in Table 1. Also given is a strain rate for an aspect ratio of 20 obtained by extrapolation of the transient results. The matrix steady creep law used by Dragone and Nix (1990) is our eqn (7) with $B = 2 \times 10^{-13}$ when strain rate is given in units of s^{-1} and stress in MPa; as noted before, $n = 4$. The finite element creep strength is computed from eqn (24) and the asymptotic result from eqn (58) with $\mu = \infty$ and $a^2 = V_f^{2/3} = 0.34$ as used in the finite element results. N was taken to be 1 in eqn (58); there is reasonable agreement. The Kelly and Street (1972) predictions for creep strength, based on our eqn (63) with $N = 1$, are also given in Table 1 under the heading "shear lag". They are well below the other results. Dragone and Nix (1990) provide additional results in which the aspect ratio of the cell is varied and the asymptotic solution also agrees reasonably well with those.

Another comparison can be made with the finite element results of Bao *et al.* (1991b). The comparison is made in Table 2. One feature in the results of Bao *et al.* (1991b) is the contrast with the results of Dragone and Nix (1990). Bao *et al.* (1991b) predict lower creep strengths as can be seen in the results for $n = 4$ in Table 2. This suggests that either Dragone and Nix (1990) or Bao *et al.* (1991b) are in error. However, the asymptotic analysis consistently predicts higher strengths than Bao *et al.* (1991b). The substantial differences are probably due to the contribution to the creep strength in the finite element results arising from the fiber end region. The cell length in the finite element calculations is $1/V_f^{1/3}$ times the fiber length. The portion of the cell beyond the fiber ends as a fraction of the whole cell

Table 1. Comparison of steady-state creep results from the finite element calculations of Dragone and Nix (1990) and the asymptotic solution. The results are for 20% SiC fibers in 6061 Al at 80 Mpa. (_____) ≡ extrapolated

Fiber aspect ratio α	Steady creep rate	Creep strength S		
	Finite element results (Dragone and Nix)	Finite elements (Dragone and Nix)	Asymptotic analysis	Shear lag (Kelly and Street)
	s^{-1}			
5	3.5×10^{-8}	3.9	4.5	2.7
7	1×10^{-8}	5.3	6.4	3.6
10	1.5×10^{-9}	8.6	9.4	5.0
20	(7×10^{-11})	(18.5)	21	10.5

Table 2. Comparison of creep strength calculated by Bao *et al.* (1991b) by finite elements with the asymptotic solution. The adjusted column lists $\bar{S} = 1 + V_f^{1/3}(S-1)$ based on the asymptotic solution

Fiber volume fraction V_f	Fiber aspect ratio α	Creep index n	Creep strength S		
			Finite elements (Bao *et al.*)	Asymptotic analysis	Adjusted $\bar{S}$
0.1	5	5	1.8	2.5	1.7
0.1	5	10	1.6	2.2	1.5
0.1	10	5	2.4	4.3	2.5
0.1	10	10	2.1	3.5	2.2
0.2	5	4	3.4	4.5	3.1
0.2	5	5	3.3	4.1	2.8
0.2	5	10	2.9	3.3	2.3
0.2	10	4	4.7	9.4	5.9
0.2	10	5	4.5	8.1	5.2
0.2	10	10	3.9	5.8	3.8

length is $1 - V_f^{1/3}$. This region of the cell experiences relatively unconstrained flow compared to the matrix material surrounding the fiber circumferentially. An estimate of the effect can be made by consideration of radial stressing. The portion of the cell around the fiber would require a radial stress S to produce the same strain rate as unit radial stress would produce in an unconstrained end region. Therefore, the average radial stress on the whole cell for the same strain rate is

$$\bar{S} = 1 + V_f^{1/3}(S-1). \tag{70}$$

This can be converted to an axial stress result by addition of hydrostatic stress. Therefore eqn (70) with S given by the asymptotic solution provides an estimate for the axial creep strength of a unit cell with the same aspect ratio as the fiber. In Table 2 it can be seen that $\bar{S}$ agrees better than S with the creep strength of Bao *et al.* (1991b). There are still discrepancies, but the conversion represented by eqn (70) is an approximation at best. It seems safe to conclude that the asymptotic results should be used for cases where the fiber aspect ratio is greater than 20 so that fiber end effects are less important.

CONCLUSION

An asymptotic solution has been presented for power law creep of a composite material containing aligned, rigid, discontinuous, well bonded high aspect ratio fibers. The solution exhibits several of the features assumed by Kelly and Street (1972) for their shear lag model. These features include the linearity of the axial velocity with distance along the fiber and the dominance of the creep strength by the shearing flow in the matrix. However, asymptotically exact forms for the velocity and stress are provided rather than the estimates used in the shear lag model. The asymptotic solution provides a model for the creep law of the composite material. Although the shear lag creep law of Kelly and Street (1972) exhibits several of the characteristics of the more exact asymptotic creep law, the shear lag model underestimates the creep strength of the composite material. We think this arises from a stress averaging procedure used by Kelly and Street (1972) which seems to be faulty.

The dominant characteristic of the creep law predicted by the asymptotic analysis is that the creep strength is proportional to the fiber aspect ratio raised to the power $1 + 1/n$, where n is the creep exponent. In addition, the model shows that fiber–matrix interface slip can have a disastrous effect on the creep strength of discontinuous fiber composites. If the interface has no shear strength, the creep strength of the composite is approximately equal to the creep strength of the matrix alone. This indicates that such a composite material would creep as fast as the unreinforced matrix at the same applied stress. However, modest levels of interface drag can be mitigated by very long fibers. The effect can be identified in eqn (58) where the interplay between interface drag and aspect ratio is evident. A low drag

coefficient, μ, gives rise to a high value of D. However, very long fibers will have a large aspect ratio leading to high values of λ. The resulting combination can lead to significant creep strengths. Thus continuous fibers, even with occasional breaks, can provide good strengthening even when some interface slip can occur.

The asymptotic solution agrees reasonably well with finite element analyses of the problem. The solution features in the matrix are very similar. Some adjustments have to be made to the creep strength for some of the comparisons to account for the fact that the finite element results were obtained typically for low aspect ratio fibers with unit cells containing substantial volumes of relatively unconstrained matrix beyond the fiber ends. With an appropriate adjustment, there is quite good agreement in terms of the creep strength.

Acknowledgement—This research was supported by the DARPA University Research Initiative at the University of California, Santa Barbara (ONR Contract N00014-86-K0753).

REFERENCES

Bao, G., Genna, F., Hutchinson, J. W. and McMeeking, R. M. (1991a). Models for the strength of ductile matrix composites. In *Intermetallic Matrix Composites*, MRS Symposium Proceedings, Vol. 194 (Edited by D. L. Anton, P. L. Martin, D. B. Miracle and R. M. McMeeking), pp. 3–15. MRS, Pittsburgh.

Bao, G., Hutchinson, J. W. and McMeeking, R. M. (1991b). Particle reinforcement of ductile matrices against plastic flow and creep. *Acta Metall. Mater.* **39**, 1871–1882.

Dragone, T. L. and Nix, W. D. (1990). Geometric factors affecting the internal stress distribution and high temperature creep rate of discontinuous fiber reinforced metals. *Acta Metall. Mater.* **38**, 1941–1953.

Goto, S. and McLean, M. (1991). Role of interfaces in creep of fibre-reinforced metal–matrix composites—II. Short fibres. *Acta Metall. Mater.* **39**, 165–177.

Johnson, R. E. (1984). Power-law creep of a material being compressed between parallel plates: A singular perturbation problem. *J. Engng Math.* **18**, 105–117.

Kelly, A. and Street, K. N. (1972). Creep of discontinuous fibre composites II. Theory for the steady-state. *Proc. R. Soc. Lond.* **A328**, 283–293.

Leckie, F. A. (1986). Micro- and macromechanics of creep rupture. *Engng Fract. Mech.* **25**, 505–521.

Sancaktar, E. and Zhang, P. (1990). Nonlinear viscoelastic modelling of the fiber–matrix interphase in composite materials. *Trans. ASME, J. Mech. Design* **112**, 605–619.

Van Dyke, M. (1975). *Perturbation Methods in Fluid Mechanics*. The Parabolic Press, Stanford, CA.

Weber, C. H., Lõfvander, J. P. A., Yang, J. Y., Levi, C. G. and Evans, A. G. (1993). Microstructure and creep of α-TiAl reinforced with Al_2O_3 fibers. *Acta Metall. Mater.* (to appear).

APPENDIX. BOUNDARY LAYER ANALYSIS

According to Johnson (1984), the outer solution velocity equations (54) and (55) prevail into the boundary layer at $z = 0$. Thus in terms of unstretched coordinates with $\eta = z/\delta$ in the boundary layer

$$v_z = \frac{\delta}{D}\left[\frac{1}{\mu 2^n}\left(\frac{1}{a}-a\right)^n + F(r,a,n)\right]\eta \tag{A1}$$

and

$$v_r = -\frac{\delta}{D}\left[\frac{1}{\mu 2^{n+1}}\left(\frac{1}{a}-a\right)^n\left(r-\frac{a^2}{r}\right)+\frac{1}{r}\int_a^r \rho F(\rho,a,n)\,d\rho\right]. \tag{A2}$$

An effective strain rate can be computed as

$$\varepsilon_e = \sqrt{2/3}\left[\left(\frac{\partial v_r}{\partial r}\right)^2+\left(\frac{v_r}{r}\right)^2+\left(\frac{\partial v_z}{\partial \eta}\right)^2+\frac{1}{2}\left(\frac{\partial v_z}{\partial r}\right)^2\right]^{1/2} \tag{A3}$$

and then the constitutive law provides

$$S_{rr} = \tfrac{2}{3}\varepsilon_e^{(1-n)/n}\frac{\partial v_r}{\partial r}, \tag{A4}$$

$$S_{\theta\theta} = \tfrac{2}{3}\varepsilon_e^{(1-n)/n}\frac{v_r}{r}, \tag{A5}$$

$$S_{zz} = \tfrac{1}{3}\varepsilon_e^{(1-n)/n}\frac{\partial v_z}{\partial \eta}, \tag{A6}$$

and

$$\sigma_{rz} = \tfrac{1}{3}\varepsilon_e^{(1-n)/n}\frac{\partial v_z}{\partial r}. \tag{A7}$$

The hydrostatic stress can be computed from the two equilibrium equations

$$\frac{\partial \sigma}{\partial r} = -\frac{\partial S_{rr}}{\partial r} + \frac{S_{\theta\theta} - S_{rr}}{r} - \frac{\partial \sigma_{rz}}{\partial \eta} \tag{A8}$$

and

$$\frac{\partial \sigma}{\partial \eta} = -\frac{\partial \sigma_{zz}}{\partial r} - \frac{\sigma_{rz}}{r}. \tag{A9}$$

According to Johnson (1984), on the scale of the boundary layer, the hydrostatic stress at leading order is uniform and given by eqn (52) with $z = 0$. It is sustained by tractions on the side of the cell enforcing the constraint that $v_r = -\frac{1}{2}\delta$ there. Therefore, the boundary condition for evaluation of the hydrostatic stress is

$$\sigma(1,0) = -\frac{n^2}{\delta(n+1)(2n+1)D^{1/n}} - S_{rr}(1,0), \tag{A10}$$

which ensures that eqn (23) is satisfied at higher order. At higher order, eqn (23) degenerates to a point wise condition on σ_{rr} because S_{rr} is uniform at $r = 1$ which is a boundary layer also.

Thus by solution of eqns (A8) and (A9) subject to eqn (A10), the stresses can be established throughout the boundary layer at $z = 0$. In particular, σ_{zz} can be computed on $z = 0$. This stress at $z = 0$ plus the axial stress in the fiber at $z = 0$ must be balanced at the other fiber end by an appropriate average stress. The leading order term in eqn (52) at $z = 1$ plus a smaller correction arising from terms computed in eqn (A8) is required. This provides an estimate of the creep strength of the composite material to higher order.

The form of v_z is such that on $z = 0$

$$\frac{\partial \sigma_{rz}}{\partial \eta} = \tfrac{1}{3}\varepsilon_e^{(1-n)/n}\frac{\partial^2 v_z}{\partial r\,\partial \eta} \tag{A11}$$

because, through $(\partial v_r/\partial r)^2$, ε_e depends on η^2. Therefore, on $z = 0$, eqn (A8) becomes

$$\frac{\partial \sigma_{rr}}{\partial r} = \tfrac{1}{3}\varepsilon_e^{(1-n)/n}\left[\frac{v_r}{r^2} - \frac{1}{r}\frac{\partial v_r}{\partial r} - \frac{1}{2}\frac{\partial^2 v_z}{\partial r\,\partial \eta}\right]. \tag{A12}$$

Since $\partial v_z/\partial r = 0$ there, on $z = 0$

$$\varepsilon_e = \sqrt{2/3}\left[\left(\frac{\partial v_r}{\partial r}\right)^2 + \left(\frac{v_r}{r}\right)^2 + \left(\frac{\partial v_z}{\partial \eta}\right)^2\right]^{1/2}, \tag{A13}$$

with v_z and v_r given by eqns (A1) and (A2). To compute the higher order terms in σ_{rr} on $z = 0$, eqn (A12) can be integrated subject to

$$\sigma_{rr}(1,0) = 0, \tag{A14}$$

which is equivalent to eqn (A10) with the leading order term (i.e. the first term on the right-hand side) omitted. The result for $\sigma_{rr}(r,0)$ can be used to compute the axial stress from

$$\sigma_{zz}(r,0) = \sigma_{rr}(r,0) + S_{zz}(r,0) - S_{rr}(r,0). \tag{A15}$$

The net resultant in the boundary layer is

$$2\pi\int_0^1 \sigma_{zz}(r,0)r\,dr = \delta^{1/n}N\pi, \tag{A16}$$

which defines N. Two cases can be considered. One situation arises if μ is large or infinite and there is little or no slip at the fiber–matrix interface. This is the high drag case. In that situation N only becomes important in the creep strength at small volume fractions of fibers. The other case is where μ is small or zero so that the matrix is free or almost free to slip against the fiber without drag.

High drag interface

In this case, D in eqn (51) is large only if a is small. With D large, the leading order stress estimate at $z = 1$ can be modest in magnitude and the higher order corrections are significant. Investigation of the velocities in eqns (A1) and (A2) reveals that when a is small, the term containing μ can be neglected and the effective strain rate ε_e on $z = 0$ is almost uniform except when r is just slightly larger than a. However, the strain rates tend rapidly to

zero at $r = a$ and according to eqns (A4)–(A6) so do the deviatoric stresses. Consequently, the small region around the fiber with r slightly larger than a will contribute very little to the stress resultant N. In view of this, a treatment will be reasonably accurate with ε_e taken to be uniform everywhere on $z = 0$ but with the strain rate components allowed to vary otherwise according to eqns (A1) and (A2).

With the strain rates computed from eqns (A1) and (A2) (with $\mu \to \infty$) eqn (A12) becomes

$$\frac{\partial \sigma_{rr}}{\partial r} = -\tfrac{2}{3}\varepsilon_e^{(1-n)/n}\frac{\delta}{D}\left[\frac{2}{r^3}\int_a^r \rho F(\rho,a,n)\,d\rho - \frac{1}{r}F(r,a,n) + \frac{1}{2}\frac{\partial F(r,a,n)}{\partial r}\right]. \tag{A17}$$

With ε_e uniform, this integrates, subject to eqn (A14) to give

$$\sigma_{rr} = \tfrac{2}{3}\varepsilon_e^{(1-n)/n}\frac{\delta}{D}\left[\frac{1}{r^2}\int_a^r \rho F(\rho,a,n)\,d\rho - G(a,n) - \tfrac{1}{2}F(r,a,n) + \tfrac{1}{2}F(1,a,n)\right]. \tag{A18}$$

On $z = 0$, from eqns (A4) and (A6)

$$S_{zz} - S_{rr} = \tfrac{2}{3}\varepsilon_e^{(1-n)/n}\frac{\delta}{D}\left[2F(r,a,n) - \frac{1}{r^2}\int_a^r \rho F(\rho,a,n)\,d\rho\right] \tag{A19}$$

so

$$\sigma_{zz} = \tfrac{2}{3}\varepsilon_e^{(1-n)/n}\frac{\delta}{D}[\tfrac{1}{2}F(r,a,n) + \tfrac{1}{2}F(1,a,n) - G(a,n)] \tag{A20}$$

which is valid for r close to 1 but suspect for r close to a. Calculation of N from eqn (A18) then gives

$$N = \delta^{-1/n}\varepsilon_e^{(1-n)/n}\frac{\delta}{D}[\tfrac{2}{3}(2+a^2)G(a,n) + \tfrac{1}{3}(1-a^2)F(1,a,n)]. \tag{A21}$$

This result is most readily utilized for even integer positive values of n. In that case, calculation of $F(1,a,n)$ and $G(a,n)$ can be carried out by binomial expansion. In addition, the leading terms in ε_e can be computed at $r = 1$. The result to leading terms is

$$N = 1 - \frac{(2n^2-2n-7)(n-1)}{6n(n-3)}a^2 + \cdots. \tag{A22}$$

Low drag interface

In this situation, μ is close to zero. The limiting case of $\mu \to 0$ (no drag) will be considered. As a consequence, the velocities in eqns (A1) and (A2) become

$$v_z = \frac{\eta\delta}{1-a^2} \tag{A23}$$

and

$$v_r = -\frac{\delta}{1-a^2}\frac{1}{2}\left(r - \frac{a^2}{r}\right) \tag{A24}$$

and $D = \infty$. This is a planar flow in the fiber direction, as would be expected when there is no drag. The effective strain rate is

$$\varepsilon_e = \frac{\delta}{1-a^2}\left[1 + \frac{1}{3}\frac{a^4}{r^4}\right]^{1/2} \tag{A25}$$

and integration of eqn (A12) gives, on $z = 0$,

$$\sigma_{rr} = -\frac{2}{3}\left(\frac{\delta}{1-a^2}\right)^{1/n}\int_r^1 \left[1 + \frac{1}{3}\frac{a^4}{r^4}\right]^{(1-n)/2n}\frac{a^2}{r^3}\,dr. \tag{A26}$$

The deviatoric stresses are such that

$$S_{zz} - S_{rr} = \frac{2}{3}\left(\frac{\delta}{1-a^2}\right)^{1/n}\left[1 + \frac{1}{3}\frac{a^4}{r^4}\right]^{(1-n)/2n}\left[\frac{3}{2} + \frac{1}{2}\frac{a^2}{r^2}\right]. \tag{A27}$$

Finally, the stress σ_{zz}, the sum of eqns (A26) and (A27), can be integrated to give

$$N = \frac{4/3}{(1-a^2)^{1/n}}\int_a^1 \left[1 + \frac{1}{3}\frac{a^4}{r^4}\right]^{(1-n)/2n}\left[\frac{3}{2}r + \frac{a^4}{2r^3}\right]dr. \tag{A28}$$

Note that when $a = 0$, $N = 1$, as in eqn (A22).

Diffusive void bifurcation in stressed solid

Z. Suo and W. Wang

Mechanical and Environmental Engineering Department

Materials Department

University of California, Santa Barbara, CA 93106

(January 1994)

Abstract—Interconnects are susceptible to solid diffusion under residual stress, electric current, and elevated temperature. As atoms diffuse, voids nucleate, drift and enlarge. At some point, the voids of rounded shape can collapse to narrow slits and sever the lines. The fatal slits are often found to be transgranular, i.e. each slit cuts across a single grain. They have raised much concerns, but the underlying mechanism has remained unclear. We propose that a void changes shape due to surface diffusion under the combined action of surface energy, elastic energy and electric current. The void will be rounded if surface energy prevails, but will collapse to a slit if the elastic energy or the electric current prevails. This paper analyzes a cylindrical void in an infinite crystal under biaxial stresses but under no electric current. Four things are done. (1) A suitable thermodynamic potential is minimized and maximized to select, among a family of ellipses, equilibrium void shapes. The bifurcation diagram consists of a subcritical pitchfork and two Griffith cracks. (2) A void under biased stresses is analyzed to illustrate the effect of imperfections. (3) Exact initial bifurcation modes are determined. The critical loads for the successive modes are closely separated, indicating that the shape evolution will be sensitive to initial imperfections. (4) A variational principle for shape evolution under stress, current and surface energy is identified. Stress-induced evolution time is estimated by using this variational principle.

I. INTRODUCTION

Making reliable interconnects has been a persistent challenge as integrated circuits evolve. Present-day interconnects are made of aluminum or aluminum-based alloys, and are less than a few microns in width. Submicron lines will be in use around the turn of the century. Copper interconnects have longer lifetimes; they would prevail should fabrication overcome the difficulties. In this paper, data for aluminum are quoted to illustrate various points, but the physical processes apply to any metals. The interconnects operate under severe conditions: high stress, intense current, and temperature exceeding one third of the melting point (933 K for aluminum). Diffusion-mediated degredation is ubiquitous as the *brute forces* act in the *small dimensions*. [1,2]

The stress results from the mismatch in thermal expansion coefficients of the metal lines and the surrounding insulators. Pure aluminum in bulk has low yield strength, below 100 MPa at the room temperature, and usually is not under high stress. Yet high stress prevails in fine lines constrained by stiff insulators. The stress is raised in two ways. First, the thermal expansion mismatch results in a hydrostatic stress which, under triaxial constraint, can not be relieved by plastic flow; for typical thermal history, tensile stress around 400 MPa is found by finite element calculations and X-ray measurements. [3-5] Second, in the small dimensions dislocations are severely bent and can only move under high stress; even without triaxial constraint the stress in thin films may exceed 200 MPa. [6]

In addition to the stress, the interconnects carry intense electric current, sometimes exceeding 10^{10} A/m^2. Both stress and current cause atoms to diffuse, known respectively as stressmigration and electromigration. Evidence has recently accumulated that narrow, transgranular slits can form and sever the lines. [7-9] The sequence of the events has also been revealed: a rounded void nucleates first, enlarging and drifting, and then collapses to a narrow slit. [10] Since forming a slit transfers much less mass than growing a rounded void across the linewidth, a slit can significantly reduce the interconnect lifetime. Consequently, the

transgranular slits have raised much concerns, even though they may not as prevalent as rounded voids, as judged from their less frequent appearance in the published micrographs.

In a previous communication, we have shown how electric current alone can cause the shape instability. [11] Yet most slits form under both electric current and thermal stress. In this paper we focus on the role played by the stress under no electric current. Instability under combined stress and current will be analyzed elsewhere using some of the methods developed here. The interconnects operate in such a temperature range that, within the time of interest, ample atoms diffuse on the void surface but negligible atoms diffuse in the lattice. The void is assumed to reside inside a perfect grain so that grain boundaries are inaccessible for diffusion. Creep is assumed to be slow compared to surface diffusion and therefore neglected. Also neglected is instantaneous dislocation glide, which seems to be a reasonable first approximation, given the high stress in the interconnects. As such, surface diffusion is the only dissipative process included in this analysis.

As diffusion varies the void shape, the solid varies energy by either varying the elastic field or creating the surface. The instability of the void shape is an outcome of the competition between the variation in the elastic and the surface energy. Figure 1 illustrates a small cylindrical void in an elastic solid under biaxial stresses. The two dimensional problem conveys the essence of the competition; the three dimensional version will be treated elsewhere. Focus on the problem of perfect symmetry: a circular void in an infinite isotropic solid under biaxial stresses $\sigma_1 = \sigma_2 = \sigma$. The perfect circle is obviously an equilibrium shape: nothing is unbalanced to drive surface diffusion. However, this equilibrium becomes unstable if the stress is high, as discussed below. Imagine a void perturbed from the circular shape, say, an ellipse in Fig. 1. Now both stress and surface energy drive the atoms to diffuse on the void surface, but in the opposite directions. Let K be the curvature of, and w the elastic energy density on, the void surface. Because $K_A > K_B$, the surface energy strives to move atoms from B to A and restore the circular symmetry. Because $w_A > w_B$, the elastic energy strives to move atoms from A to B and

amplify the asymmetry. The void collapses if the elastic energy prevails over the surface energy.

This picture forms the basis of a dimensional analysis. Let a_0 be the initial radius of the void, σ the thermal stress, γ the surface energy, and E Young's modulus. The relative importance of the elastic energy and the surface energy is described by a dimensionless number

$$\Lambda = \frac{\sigma^2 a_0}{\gamma E}. \tag{1.1}$$

When Λ is small, surface energy dominates, and the void will be rounded. When Λ is large, strain energy dominates, and the void will collapse into a narrow slit. The circular void collapses when Λ exceeds a critical value, Λ_c. The analysis in this paper will show that $\Lambda_c = 3/8$. For aluminum with $E = 7\times10^{10}$ N/m^2 and $\gamma = 1$ N/m, under stress $\sigma = 4\times10^8$ N/m^2 the critical radius is $a_0 = 164$ nm. Any larger void will collapse under this stress level. The mechanism works under both tensile and compressive stress.

The same phenomenon is anticipated for other material systems. A technically important example is residual gas pores inside single crystal oxide fibers, subjected to both high temperatures and mechanical loads. The mechanism can limit the lifetime of the composite materials based on these fibers (Private communication with A.G. Evans). In this paper, however, we will set aside these potential applications and concentrate on the general formulation of the problem, and on the implications for the interconnects.

Surface diffusion mediated instability in elastic solids has been studied by several investigators. [12-15] The lead phenomenon, which has engaged the previous studies, is that an initially flat surface may undulate due to surface diffusion, driven by elastic energy against surface energy. Recent kinetic simulation has shown that crack-like slits may result from such undulation. [15] A dimensionless group similar to Λ has appeared in these studies, with a_0 replaced by the wavelength. In writing this paper, we have been inspired by these studies, and by the recent synthesis of the spatio-temporal complexity on the basis of nonequilibrium thermodynamics and dynamical systems. [16]

In this paper, the void evolution is viewed as an irreversible process, and formulated in a

sufficiently general way that other mechanisms of energy variation or entropy production can be readily incorporated. A variational principle is identified which governs the evolution under combined action of surface energy, elastic energy and electron wind force. Questions typical for any evolutionary process also have direct bearing on the voids in the interconnects. (1) Under what conditions does a circular void become unstable? (2) What is the destination of the evolution, a slit of vanishing thickness, or something still quite rounded? (3) Given nominally the same experimental conditions, why are the slits not always observed? (4) How fast does the shape change? (5) What is the role of stress bias or other imperfections? Energetics and kinetics will be considered separately in two sections; together they illuminate the phenomenon.

II. ENERGETICS

The suitable thermodynamic potential, consisting of both elastic and surface energy, is a functional of the void shape. Approximate equilibrium void shapes are selected, among a family of ellipses, by minimizing and maximizing the potential. The bifurcation diagram is a composite of a subcritical pitchfork and the Griffith cracks. A void under biased stresses is analyzed to illustrate the effect of imperfections.

A. Why does a circular void collapse

Figure 1 illustrates the cross section of a cylindrical void in a solid, subjected to biaxial stresses on the external boundary, but not on the void surface. The cross-sectional shape of the void is arbitrary. The work done by the load either varies energy in the solid, or produces entropy in the diffusion process. The first law of thermodynamics requires that

$$\text{(Energy Rate)} + \text{(Dissipation Rate)} = \text{(Work Rate)}. \tag{2.1}$$

The solid varies energy either in the body or on the surface. Denote w as the strain energy per volume, and γ the surface energy per area. They are taken to be independent from each other for practical purposes. That is, γ is independent of the applied stress, and the strain field in the

body is determined by the elasticity theory neglecting the effect of surface energy. The total elastic energy and surface energy are

$$U_e = \int_{body} w dA, \quad U_s = \int_{surface} \gamma dL. \tag{2.2}$$

For the two dimensional problem, they are energy per length, integrated over the cross-sectional area of the solid, A, and the arclength of the void, L, respectively. Under the fixed mechanical load, the suitable potential is $\Phi = U_e + U_s - (\text{Load} \times \text{Displacement})$. Furthermore, U_e = (Load×Displacement)/2 for linear elastic solids. Thus, the thermodynamic potential for the linear elastic solid under constant load is

$$\Phi = -U_e + U_s. \tag{2.3}$$

The potential is *a functional of void shape*. For a given void shape, U_e is determined by the elasticity problem, and U_s is integrated over the perimeter of the void. The same potential has also appeared in the linear fracture mechanics as a functional of crack size and, in three dimensions, crack shape.

The first law (2.1) becomes

$$d\Phi/dt + (\text{Dissipation Rate}) = 0. \tag{2.4}$$

The second law of thermodynamics requires that the dissipation be nonnegative, and vanish in equilibrium. That is, atoms diffuse to reduce the potential of the system. Of all void shapes, the equilibrium shape minimizes Φ. Because atoms diffuse only on the surface, the void conserves the cross-sectional area as the shape changes. Other kinetic details are unnecessary for equilibrium considerations and are left to the next section.

In Introduction, the shape instability is analyzed by the local states on the surface. Alternatively, it can be analyzed by the global energy. Compare Φ for the circular void and a void with reduced symmetry, say an ellipse having the same area as the circle. Here and later we will use Δ to signify the difference of a quantity for an ellipse and a circle; for example, $\Delta\Phi$ = Φ(ellipse) - Φ(circle). The ellipse has longer perimeter than the circle, so that $\Delta U_s > 0$. The body with the elliptic hole is more compliant to the external load than the body with the circular

hole, so that $\Delta U_e > 0$. Consequently, both the surface and the elastic energy increase when the circle breaks the symmetry; $\Delta\Phi < 0$ if $\Delta U_e > \Delta U_s$. The circular void is unstable when either the elastic energy is large, or the surface energy is small. These considerations also identify Λ in (1.1).

B. To relax or to collapse

The fate of the voids need be clarified. Will a noncircular void relax to a circular void, or will it collapse to a narrow slit? In the following, the potential energy is calculated for ellipses having the constant area, and the ellipse that minimizes it is taken to be in equilibrium. The procedure is that of Rayleigh-Ritz: the potential is a functional of the void shape, but only a restricted family of shapes are searched to minimize it. The procedure usually yields approximate equilibrium shapes, and the accuracy improves as more families are searched. The family of ellipses with the constant area are parameterized by only one number. Yet it will be shown that this family contain two exact asymptotes: the initial bifurcation from the circle, and the slit of vanishing thickness. Thus, it is not unreasonable to expect that the ellipses well approximate the equilibrium shapes between the two asymptotes.

Let a_0 be the radius of the initial circular void. The ellipses have the same area as the circle, πa_0^2. Their shapes are described by

$$X = a_0\sqrt{\frac{1+m}{1-m}}\cos\theta, \quad Y = a_0\sqrt{\frac{1-m}{1+m}}\sin\theta. \tag{2.5}$$

The circle corresponds to $m = 0$, the X-direction slit to $m \to +1$, and the Y-direction slit to $m \to -1$. The ellipses have perimeter

$$P = \frac{a_0}{\sqrt{1-m^2}}\int_0^{2\pi}\left(1+m^2-2m\cos 2\theta\right)^{1/2}\mathrm{d}\theta. \tag{2.6}$$

The elastic solution for the elliptic voids exists in the literature, from which U_e is calculated (Appendix A). For the body with an elliptic hole and the body with a circular hole, the elastic energy differs by

$$\Delta U_e = 4\pi \frac{\sigma^2 a_0^2}{E} \frac{m^2}{1-m^2}. \tag{2.7}$$

Thus U_e increases as the ellipse becomes more elongated, the area and load being constant. This has been stated previously on an intuitive basis that a body with an elliptic hole is more compliant than a body with a circular hole. Combining (2.6) and (2.7), the difference in the potential is

$$\frac{\Delta\Phi}{2\pi a_0 \gamma} = -2\Lambda \frac{m^2}{1-m^2} + \left(\frac{P}{2\pi a_0} - 1 \right). \tag{2.8}$$

Now Φ is a function of the shape parameter m for a given control parameter Λ.

Figure 2a displays the function $\Phi(m)$ at several constant levels of Λ. Each minimum and maximum represents a stable and unstable equilibrium state, respectively. Three types of behaviors emerge depending on the value of Λ, i.e. the relative importance of elastic and surface energy. (1) When $\Lambda = 0$, the stress vanishes; Φ reaches a minimum at $m = 0$, and maxima at $m = \pm 1$. The circular void is stable and the two slits are unstable: any ellipse will relax to the circle. (2) When $\Lambda \in (0, 3/8)$, the stress is finite but surface energy still dominates; Φ reaches a local minimum at $m = 0$, two maxima at some $\pm m_c$, and two minima at $m = \pm 1$. The maxima act as energy barriers: an ellipse of $|m| < m_c$ will relax to the circle, but an ellipse of $|m| > m_c$ will collapse to the slits. (3) When $\Lambda \in (3/8, \infty)$, the stress dominates; Φ reaches the maximum at $m = 0$, and minima at $m = \pm 1$. The circle is unstable but the slits are stable: any elliptic void will collapse to the slits.

The above information is projected onto the (Λ, m) plane, Fig. 2b. The heavy solid and dotted lines correspond to the stable and unstable equilibrium states, respectively. The two slits $m = \pm 1$ are stable for any $\Lambda > 0$, but unstable for $\Lambda = 0$. The circle $m = 0$ is metastable when $\Lambda < 3/8$, but unstable when $\Lambda > 3/8$. The dotted curve is the unstable equilibrium states, referred to as m_c in the preceding paragraph. These lines divide the (Λ, m) plane into four regions. A point in each region corresponds to an ellipse under a constant level of Λ, evolving toward a stable equilibrium state, either the circle or the slits. The evolution direction in each region is indicated

by an arrow. An ellipse below the dotted curve relaxes to the circle, and an ellipse above the dotted curve collapses to a slit. An initially circular void will collapse if Λ exceeds the critical value $\Lambda_c = 3/8$. This value has been used in Introduction to calculate the critical void radius under a given stress.

C. Pitchfork and crack

The bifurcation diagram, Fig. 2b, is better appreciated as follows. First focus on how the perfect circle breaks the symmetry, i.e. the subcritical pitchfork bifurcation at Λ_c. The shape parameter m measures the *order* in the critical point theory. [16] Expand (2.8) in powers of m:

$$\frac{\Delta\Phi}{2\pi a_0 \gamma} = \left(-2\Lambda + \frac{3}{4}\right)m^2 + \left(-2\Lambda + \frac{33}{64}\right)m^4 + \ldots \tag{2.9}$$

Only the two leading terms are retained for small m. When $\Lambda > 3/8$, the coefficient is positive for m^2, so that $m = 0$ maximizes Φ. When $\Lambda < 3/8$, the coefficient is positive for m^2 but negative for m^4, so that $m = 0$ minimizes Φ. Consequently, $\Lambda = 3/8$ is the critical point above which the circle is unstable. Equilibrium requires that $d\Phi / dm = 0$, i.e.

$$2\left(-2\Lambda + \frac{3}{4}\right)m + 4\left(-2\Lambda + \frac{33}{64}\right)m^3 = 0. \tag{2.10}$$

When $\Lambda < 3/8$, Φ reaches the two maxima at

$$m^2 = \frac{64}{15}\left(\frac{3}{8} - \Lambda\right), \quad \Lambda \to \frac{3}{8}. \tag{2.11}$$

This analysis determines the critical point, $\Lambda_c = 3/8$, and the asymptotic behavior of the dotted curve in Fig. 2b as $m \to 0$. Yet the analysis is not rigorous in that the equilibrium shapes are only searched among the ellipse family. This concern will be removed in Section IIIB where the ellipse is shown to be an exact initial bifurcation mode.

The other limiting case, the slit of vanishing thickness, reproduces the Griffith theory of cracks. [17] Keep only the unbounded terms in (2.8) as $m \to \pm 1$:

$$\frac{\Delta\Phi}{2\pi a_0 \gamma} \approx -\frac{2\Lambda}{1-m^2} + \frac{4}{\pi\sqrt{1-m^2}}. \tag{2.12}$$

For a given Λ, the potential attains the maxima when

$$\sqrt{1-m^2} = \pi\Lambda, \quad \Lambda \to 0. \tag{2.13}$$

This is the asymptote in Fig. 2b as $m \to \pm 1$. From (2.5) the crack length is $a = a_0\sqrt{2/(1-m)}$ as $m \to 1$, so that (2.13) becomes

$$\frac{\sigma^2 a}{\gamma E} = \frac{2}{\pi}, \tag{2.14}$$

which is just the Griffith condition for crack growth.

The connection with the Griffith cracks is not fortuitous. Both phenomena are based on the competition between the elastic and the surface energy, i.e. on the potential (2.3), although the kinetic process are different: a void changes the shape by surface diffusion, and a crack extends by atomic decohesion. The energetics coincide of the two phenomena in the limit when the void approaches the crack. The conclusion should apply to other loading configurations if a void is sufficiently elongated to be approximated by a crack. Let $\mathcal{G}$ be the elastic energy releases rate for the crack. As atoms diffuse on the surface, the elongated void will become shorter if $\mathcal{G} < 2\gamma$, but longer if $\mathcal{G} > 2\gamma$. The connection is useful because $\mathcal{G}$ has been solved in fracture mechanics for many configurations.

D. Stress bias and other imperfections

A void in an interconnect deviates from the perfect symmetry in many ways. Surface energy is anisotropic in crystals; for example, the {111} planes in aluminum have the lowest surface energy, and are the preferred void surfaces. The interconnect is finite and encapsulated by insulators; the elastic modulus misfit causes asymmetry. The stresses in two directions are not exactly the same. Given these imperfections, the circular symmetry breaks even at vanishing stress. What use, then, is the perfect problem?

The significance of the perfect problem is understood as follows. If an imperfection is not too large in magnitude, it only changes the potential Φ slightly. Changing with it will be the locations of the minima and maxima. The lines in Fig. 2 will bend somewhat, but the essential

features should remain unchanged. Even for large imperfections there will still be regions, just as in Fig. 2b, where a void will relax to a rounded shape (no longer a perfect circle), and other regions where a void will collapse to a slit.

It is obviously impractical, and often unnecessary, to analyze all the imperfections. To illustrate the general idea, we study a void in an isotropic crystal under a biased stress state, i.e. $\sigma_2 \neq \sigma_1$ in Fig. 1. The potential is

$$\Delta\Phi = -\frac{2\pi a_0^2}{E}\left(\frac{m}{1-m}\sigma_2^2 - \frac{m}{1+m}\sigma_1^2\right) + \gamma(P - 2\pi a_0). \tag{2.15}$$

The first term, the elastic energy, is evaluated in Appendix A. As evident from (2.15), the tensile and the compressive stresses give the identical response. We will consider the case $\sigma_2 > \sigma_1 \geq 0$, and modify the control parameter as $\Lambda = \sigma_2^2 a_0 / E\gamma$.

Figure 3a and 3b are for $\sigma_1/\sigma_2 = 0.8$; they are representative for any stress ratios in the interval $0 < \sigma_1/\sigma_2 < 1$. Several asymmetries are noted when comparing Figs. 2a and 3a. For small Λ, the local minimum no longer occurs at $m = 0$, nor do the two maxima at the same value of $|m|$. At a critical value, still denoted as Λ_c, the minimum and the maximum on the right-hand side annihilate, but the maximum on the left-hand side persists. In Fig. 3b, the values of m minimizing Φ are the heavy solid lines, and the values of m maximizing Φ are the dotted lines. As expected, under the biased stress, the equilibrium shape is noncircular even for a small value of Λ. The heavy solid curve ends at Λ_c, and is continued by the dotted curve.

Figure 4a and 4b are the corresponding diagrams under uniaxial stress state, $\sigma_1 = 0$ and $\sigma_2 \neq 0$, Fig. 1. For a small Λ, Φ has a local minimum and a local maximum. For a large value of Λ, Φ monotonically decreases as m increases. In Fig. 4b, the slit m = -1 is an unstable equilibrium state, and the slit m = 1 is a stable equilibrium state. The heavy solid curve ends at Λ_c, and is continued by the dotted curve. Note that the critical value Λ_c is reached at about m = 0.5, corresponding to an ellipse with axes ratio 3.

An inspection shows that Fig. 3b will degenerate to Fig. 2b as $\sigma_1 / \sigma_2 \to 1$, and to Fig. 4b as $\sigma_1 / \sigma_2 \to 0$. They all have the identical Griffith limit as $m \to 1$, as anticipated. Although

Figs. 2b-4b look very different, they mean practically the same thing. The initial void shape is usually not too different from a circle. It will relax to a more or less rounded void if $\Lambda < \Lambda_c$, but collapse to a slit of vanishing thickness if $\Lambda > \Lambda_c$. Plotted in Fig. 6 is Λ_c as a function of the stress ratio. The critical number does not vary significantly for the entire range of the stress ratio.

III. KINETICS

In this section, kinetic concepts for surface diffusion in elastic solids are reviewed. [12-15] We present them in the language of nonequilibrium thermodynamics, [18] so that other mechanisms of energy variation or entropy production can be added readily. Electromigration is used to illustrate the procedure. Exact initial bifurcation modes of a circular void are determined; the critical loads for successive modes are closely spaced, indicating that complicated void shapes may evolve for slightly different initial imperfections. A variational principle governing shape change is identified and used to estimate the evolutionary rate.

A. Evolution is an irreversible process

Nonequilibrium thermodynamics has three elements: mass conservation, the two thermodynamic laws, and phenomenological kinetic relations. These are examined in turn for the present problem. Conservation of atoms sets a kinematic constraint: at any point the surface recedes if the flux has a positive divergence, i.e.

$$V_n = \Omega \partial J / \partial L. \tag{3.1}$$

On the left-hand side, $V_n = \boldsymbol{n} \cdot \partial \boldsymbol{X} / \partial t$ is the normal velocity of the surface, where t is the time, $\boldsymbol{X}$ the position vector of a point on the surface, and $\boldsymbol{n}$ the unit vector normal to the surface pointing into the solid; $V_n > 0$ if the surface recedes. On the right-hand side, J is the surface atomic flux, i.e. the number of atoms per time across per length, L is the arclength, and Ω is the atomic volume.

Express the first law (2.4) explicitly as

$$d\Phi / dt + \int FJ dL = 0. \tag{3.2}$$

The integral extends over the void perimeter. Everything else having been defined, this equation uniquely defines F as the diffusion driving force on each atom. Furthermore, (3.2) links the global energy variation with the local kinetic process. The first term is the potential energy increase rate, and the second term the dissipation rate associated with surface diffusion. The second law of thermodynamics requires that the dissipation be positive when atoms diffuse, and vanish when an the void attains equilibrium. Consequently, the potential energy decreases as the void evolves toward the equilibrium shape. Equation (3.2) is valid for any *virtual* surface velocity V_n and flux J compatible in the sense of (3.1), even if F and J are *not* connected by any kinetic relation. This rigorous understanding will lead to an explicit formula for F in (3.5), and an evolutionary variational principle in Section IIIC.

When a piece of the void surface recedes, the body becomes more compliant to the constant load and the void has longer perimeter, so that both U_e and U_s increase. Formalizing these observations with Φ defined by (2.2) and (2.3), one can show that

$$d\Phi / dt = -\int (w - \gamma K) V_n dL. \tag{3.3}$$

The elastic energy density is evaluated on the surface; for a traction-free cylindrical void, $w = \sigma_t^2 / 2E$, σ_t being the hoop stress. The curvature, K, is taken to be positive for a convex void. Equation (3.3) shows that the potential changes only when the surface moves, as sensible. The capillary term in (3.3) is the same as the Laplace-Young relation for soap films. Replacing V_n in (3.3) by J using (3.1), and then integrating by parts, one reaches

$$d\Phi / dt = \int J \frac{\partial}{\partial L} (\Omega w - \Omega \gamma K) dL. \tag{3.4}$$

Since (3.2) and (3.4) are valid for any virtual flux, a comparison of them gives

$$F = -\partial (\Omega w - \Omega \gamma K) / \partial L. \tag{3.5}$$

Given a void shape with the prescribed load, w is determined by the elasticity problem and K by the geometry. Atoms diffuse in the direction of F; the void reaches equilibrium when F vanish at every point on the surface. It is sometimes convenient to think in terms of quantity $(\Omega w - \Omega \gamma K)$, the chemical potential. Atoms diffuse toward the position with lower chemical

potential. This forms the basis of the instability argument in Introduction.

The above considerations are applicable for any kinetic relations. In the remainder of the section, a linear kinetic relation is assumed:

$$J = MF. \tag{3.6}$$

The phenomenological constant obeys Einstein's relation $M = D_s \delta_s / \Omega kT$, with D_s the surface diffusivity, δ_s the effective thickness of the surface atomic layers participating in the diffusion process, k Boltzmann's constant, and T the absolute temperature. The crystal is assumed to be isotropic so that M is constant along the void surface.

The following normalizations prevail in the remainder of Section III:

$$[x, l, 1/\kappa] = [X, L, 1/K]/a_0, \quad \Sigma = \sigma_t / \sigma, \quad \tau = t\Omega^2 M\gamma / a_0^4. \tag{3.7}$$

A combination of (3.1), (3.5) and (3.6) gives

$$\boldsymbol{n} \cdot \dot{\boldsymbol{x}} = -\frac{\partial^2}{\partial t^2}\left(\frac{\Lambda}{2}\Sigma^2 - \kappa\right). \tag{3.8}$$

The superimposed dot signifies the derivative with respect to the dimensionless time τ. The right-hand side is completely determined for a given void shape and load; the dimensionless hoop stress Σ is determined by the elasticity theory. Consequently, (3.8) governs the evolution, a moving boundary problem with only one parameter, Λ. Although every individual physical origin is well understood, the evolutionary process can be remarkably complex. In what follows we will concentrate on the aspects that have direct bearing on the voids in interconnects.

B. Initial bifurcation modes

The Rayleigh-Ritz procedure in Section IIB does not warrant that an ellipse is indeed a bifurcation mode. Here we solve, by a semi-inverse approach, the exact initial bifurcation modes of the circular void under biaxial stress $\sigma_1 = \sigma_2 = \sigma$, Fig. 1. The initial bifurcation modes are first guessed, and then confirmed, to be hypotrochoids.

A hypotrochoid is the trajectory of a point fixed on a circular disc which rolls, without

slipping, upon the interior of another fixed circle. It is described by

$$x = \cos\theta + m\cos n\theta, \quad y = \sin\theta - m\sin n\theta, \quad \theta \in [0, 2\pi]. \tag{3.9}$$

Here n is a positive integer; $m(\tau) \ll 1$ measures the small perturbation from the circle. They look like curved polygons; for $n = 1$ an ellipse, for $n = 2$ a triangle etc. To the first power in m, the hypotrochiods defined by (3.9) always have the same area, π.

The elastic solution of a hypotrochoidal hole exists in the literature, as outlined in Appendix B. To the first power in m, the dimensionless hoop stress is

$$\Sigma = 2 + 4mn\cos(n+1)\theta. \tag{3.10}$$

After some manipulations, the first order perturbation of the dimensionless curvature is found to be

$$\kappa = 1 + m\left(n^2 + 2n\right)\cos(n+1)\theta, \tag{3.11}$$

and that of the surface velocity

$$n \cdot \dot{x} = \dot{m}\cos(n+1)\theta. \tag{3.12}$$

Substituting the above into the evolution equation (3.8), and only retaining the terms of first power in m, one obtains that

$$\dot{m} = mn(n+1)^2(8\Lambda - n - 2). \tag{3.13}$$

In the above $\cos(n+1)\theta$ has been canceled from the both sides. That this evolution equation is independent of the position on the surface, θ, is significant: with a small perturbation from the circle, the nth hypotrochoid will grow or shrink only as the nth hypotrochoid. This confirms that hypotrochoids are indeed the initial bifurcation modes. The perturbation grows if $\dot{m} > 0$, and shrinks if $\dot{m} < 0$. The critical load is reached when $\dot{m} = 0$ in (3.13). Thus

$$\Lambda_n = \frac{n+2}{8}. \tag{3.14}$$

For $n = 1$, the bifurcation mode is an ellipse, and the critical load is $\Lambda_1 = 3/8$.

Observe that the critical loads for successive bifurcation modes are not far apart, being spaced by 1/8. If the control parameter Λ is large (large void or high stress), the long term shape will be selected according to the initial imperfection of the hole. The spatio-temporal complexity can be resolved by tracing the evolution governed by (3.8) for various initial imperfections. The

calculation will not be pursued here, but a variational principle identified in the following section will ease the labor.

C. Variational principles for evolution

Numerical computation is inescapable to trace the evolution in general. Given a void shape, the elasticity problem must be solved first, usually numerically, and the void shape is then updated according to (3.8). The whole process is repeated for many time steps. Equation (3.8) has been exclusively used in the previous studies, but it may not be efficient because it involves high order differentiations of the boundary. Instead, variational principles may be used.

Variational principles have been developed for problems such as grain boundary cavitation and powder compaction. [19,20] We find a variational principle governing the shape change in the present problem. Recall that the first law of thermodynamics (3.2) is valid for any compatible virtual velocity and flux. Write this explicitly as

$$\frac{\mathrm{d}}{\mathrm{d}t}(\delta\Phi)+\int F\delta J\mathrm{d}L=0. \tag{3.15}$$

The variation in Φ is due to the shape change. Replacing F in (3.15) by using the kinetic relation $F=J/M$, one obtains

$$\delta\left[\frac{\mathrm{d}\Phi}{\mathrm{d}t}+\int\frac{1}{2M}J^2\mathrm{d}L\right]=0. \tag{3.16}$$

This suggests the following variational principle.

Of all virtual velocities and fluxes compatible in the sense of (3.1), the actual velocity and flux minimize functional

$$\Pi=\frac{\mathrm{d}\Phi}{\mathrm{d}t}+\int\frac{1}{2M}J^2\mathrm{d}L. \tag{3.17}$$

The integral extends over the perimeter of the void. For a given shape, the first term can only vary with the surface velocity, which in turn relates to the flux by (3.1). Consequently, Π can be viewed as a functional of either V_n or J, both being functions of the arclength L. Compared with the grain boundary cavitation problem, [19] a new term, $\mathrm{d}\Phi/\mathrm{d}t$, appears to account for energy

variation. An example in Section IIID will illustrate how this term works.

Using (3.3), one can also write the functional in alternative forms, e.g.

$$\Pi = \int \left[-(w - \gamma\kappa)V_n + \frac{1}{2M} J^2 \right] dL, \tag{3.18}$$

which may be convenient in some circumstances. Rigorously, (3.17) only says that Π is stationary at the actual velocity and flux. A proof of minimum on the basis of (3.18) follows. Let J be the actual flux that satisfies (3.1), (3.5) and (3.6). Because atoms only diffuse on the void surface, the function $J(L)$ is periodic with the perimeter of the void. Let $Q(L)$ be an arbitrary function having the same period, $(J + Q)$ be a virtual flux, and the associated virtual velocity be obtained from (3.1). The virtual flux need not satisfy the kinetic relation (3.6). We now compute the difference $\Pi(J+Q) - \Pi(J)$ using (3.18). Replacing both the virtual and the actual velocity with their associated fluxes by (3.1), the difference in Π becomes

$$\int \left\{ -(w - \gamma\kappa)\Omega \frac{\partial Q}{\partial L} + \frac{1}{2M} \left[(J+Q)^2 - J^2 \right] \right\} dL. \tag{3.19}$$

Integrating the first term by parts, one reaches

$$\int \left\{ \frac{\partial}{\partial L}(\Omega w - \Omega\gamma\kappa) + \frac{J}{M} \right\} Q dL + \int \frac{Q^2}{2M} dL. \tag{3.20}$$

The first integral vanishes because J satisfies (3.5) and (3.6). The second integral is always nonnegative because $M > 0$, which in turn is required by the second law of thermodynamics. Thus, $\Pi(J+Q) - \Pi(J) \geq 0$ for any virtual flux. This proves the variational principle.

We now wish to illustrate the versatility of the variational principle by considering how to include electromigration. As an electric current passes an interconnect, the drifting electrons exert on each atom on the void surface a force $F^* = -q^* E_t$, known as the *electron wind force*. [1] Here q^* (> 0) is a phenomenological constant having the unit of electric charge, and E_t is the electric field tangential to the void surface. The negative sign signifies that the force directs along in the electron flow, which is opposite to the electric field. Including the work done by the electron wind force, the first law (3.2) becomes

$$d\Phi / dt + \int FJ dL = \int F^* J dL. \tag{3.21}$$

As before, J can be any virtual flux, and Φ varies with the virtual V_n compatible with J. It follows that, of all virtual velocities and fluxes that satisfy (3.1), the actual velocity and flux minimize the functional

$$\Pi = \frac{d\Phi}{dt} + \int\left(\frac{1}{2M}J^2 - F^* J\right)dL. \tag{3.22}$$

It also follows from (3.21) that

$$F = F^* - \partial(\Omega w - \Omega\gamma K)/\partial L. \tag{3.23}$$

That is, the diffusion driving force consists of the electron wind force and the thermodynamic forces resulting from the elastic and the surface energy. Let ϕ be the electric potential governed by the Laplace equation. The electric field tangential to the void surface is given by $E_t = -\partial\phi/\partial L$. If q^* is constant along the surface, the diffusion driving force in (3.23) becomes

$$F = -\partial\left(-q^*\phi + \Omega w - \Omega\gamma K\right)/\partial L. \tag{3.24}$$

The quantity in the bracket plays the same role as the chemical potential.

The above variational principles apply to a void subjected to periodic boundary conditions. For other problems such as powder compaction, suitable boundary terms must be added. It is straightforward to extend the variational principles for a surface in the three dimensions. There will be two surface flux components, J_1 and J_2, and (3.1) be replaced by the surface divergence. In (3.17), the line integrals will be replaced by surface integrals, the surface integrals by volume integrals, and J^2 by $J_1^2 + J_2^2$. The variational principle can be used by dividing the surface into *finite elements*, so that surface evolution problems can be readily solved in three dimensions.

D. How fast does a void evolve

In using the variational principles, the void shape is approximately described by a finite number of parameters, all evolving with time. The more parameters, the better the description. As an example, the evolution rate of a void under biaxial stress $\sigma_1 = \sigma_2 = \sigma$ will be estimated. The initial imperfections are such that the void will evolve in the first mode, from a circle to a slit. As before, we will approximate the shapes between the two limits by a family of ellipses, a

choice compromising the accuracy of the prediction and the complexity of the calculation. The family of ellipses are

$$X = a_0 \alpha \cos\theta, \quad Y = a_0 \alpha^{-1} \sin\theta . \tag{3.25}$$

The dimensionless semi-axis, $\alpha(\tau)$, is the parameter that describes the void shape; it is restricted to be $\alpha > 1$. The ellipses conserve the area, elongating and shrinking in the X and Y directions , respectively, at the same rate.

The variational principle of version (3.17) will be used here. The dimensionless velocity is

$$v_n = \boldsymbol{n} \cdot \dot{\boldsymbol{x}} = (\dot{\alpha} / \alpha)(\mathrm{d}\theta / \mathrm{d}l)\cos 2\theta . \tag{3.26}$$

The dimensionless flux j is so defined that (3.1) becomes $v_n = \mathrm{d}j / \mathrm{d}l$. Owing to the symmetry, $j = 0$ when $\theta = 0$. Integrate (3.26) and one obtains

$$j = \frac{\dot{\alpha}}{2\alpha} \sin 2\theta . \tag{3.27}$$

The potential Φ for an ellipse has been given by (2.8); m and α are related by comparing (3.25) and (2.5). The normalized functional takes form

$$\frac{\Pi}{(2\pi a_0 \gamma)\left(\Omega^2 M\gamma / a_0^4\right)} = \left(-\Lambda I_0 + I_1\right)\dot{\alpha} + \frac{1}{2} I_2 \dot{\alpha}^2 . \tag{3.28}$$

The coefficients I's depend on α only. Straightforward calculations yield

$$I_0 = \alpha\left(1 - \alpha^{-4}\right), \tag{3.29}$$

$$I_1 = \frac{2}{\pi} \int_0^{\pi/2} \frac{\sin^2\theta - \alpha^{-4}\cos^2\theta}{\sqrt{\sin^2\theta + \alpha^{-4}\cos^2\theta}} \mathrm{d}\theta , \tag{3.30}$$

$$I_2 = \frac{1}{2\pi\alpha} \int_0^{\pi/2} \sin^2 2\theta \sqrt{\sin^2\theta + \alpha^{-4}\cos^2\theta}\, \mathrm{d}\theta . \tag{3.31}$$

The integrals are computed numerically. Minimizing Π in (3.28) by setting $\partial\Pi / \partial\dot{\alpha} = 0$, one obtains the approximate evolution rate

$$\dot{\alpha} = \left(\Lambda I_0 - I_1\right) / I_2 . \tag{3.32}$$

Two limiting cases are obtained explicitly. For ellipses close to the circle, $\alpha \to 1$, the initial velocity is

$$\dot{\alpha} = 4(\alpha - 1)(8\Lambda - 3), \quad \alpha \to 1^+ . \tag{3.33}$$

The rate $\dot{\alpha}$ is linear with the perturbation (α - 1). This result is consistent with (3.13), noting

$\alpha = 1 + m$ to the first power in m. For very elongated ellipse, $\alpha \gg 1$, neglecting the terms with α^{-4} in I's, one finds that

$$\dot{\alpha} = \frac{15}{2}\alpha\left(\frac{\pi}{2}\Lambda\alpha - 1\right), \quad \alpha \gg 1. \tag{3.34}$$

The rate is quadratic with the semi-axis for a very elongated void, and vanishes when the Griffith condition (2.14) is satisfied.

Equation (3.32) is plotted in Fig. 6. Denote a as the semi-axis of an ellipse and $\alpha = a / a_0 > 1$. The ellipse will elongate further if the velocity is positive, but relax toward a circle if the velocity is negative. Three behaviors emerge for different values of Λ. For $\Lambda = 0$, the rate is negative for any ellipse, which wil' relax to the circle under the action of surface energy alone. For $\Lambda \in (0, 3/8)$, the rate is negative for ellipse not too far from the circle, but positive for very elongated ellipses. For $\Lambda \in (3/8, \infty)$, the rate is positive for any ellipse, which will collapse to a slit.

The evolution time from one ellipse to another is obtained by integrating (3.32). The three types of behaviors are plotted in Figs. 7a, b, c, respectively. Since the evolution is an irreversible process, the time always increases in these figures. When $\Lambda \in (3/8, \infty)$, any ellipse will become more elongated, Fig. 7a. The curves are plotted by arbitrarily assigning the initial value $\alpha =$ 1.01 at $\tau = 0$. One can also read from the diagram the time needed for, say, an ellipse with $\alpha =$ 1.2 to evolve to an ellipse with $\alpha = 2.0$ under load level $\Lambda = 5/8$. When $\Lambda \in (0, 3/8)$, there is an unstable equilibrium shape for each value of Λ, which is marked as the dashed line in Fig. 7b for $\Lambda = 1/8$. More elongated ellipses will collapse to slits, but less elongated ellipses will relax to the circle. When $\Lambda = 0$, any ellipse will relax to the circle, Fig. 7c. This diagram gives the relaxation time of the ellipses after the load is removed. Conversely, the surface kinetic constant, M, can be deduced if the relaxation time is measured experimentally.

Approximate, but explicit formulas can be obtained from (3.33) and (3.34). For example, if both initial and final axes, a_i and a_f, are not too far from the circular radius a_0, the time duration is integrated from (3.33):

$$t_f - t_i = \frac{kTa_0^4}{32\Omega\gamma D_s \delta_s}\left(\frac{\sigma^2 a_0}{E\gamma} - \frac{3}{8}\right)^{-1} \ln\left(\frac{a_f - a_0}{a_i - a_0}\right). \tag{3.35}$$

The formula can also be used to estimate the order of magnitude even when a_f is not very close to a_0.

If the void shape is described by many parameters, (3.28) will consist of a linear and a bilinear forms of their rates. Setting the partial derivatives of Π with respect to the rates to be zero, one obtains simultaneous linear algebraic equations for the rates. They are solved by Gaussian elimination to yield coupled initial value problems, which are then integrated by any standard procedure. Of course, as the void shape evolves, the elasticity problem must be independently solved at each step. The implementation as described is now in progress.

IV. CONCLUDING REMARKS

A void in an elastic solid collapses into a transgranular slit when the dimensionless group $\sigma^2 a_0 / E\gamma$ exceeds a critical value. The mechanism works under both tensile and compressive stress. It is important to examine this mechanism among the related ones. The transgranular slits will dictate the interconnect lifetime only if grain boundary cavitation does not prevail. The latter has been thoroughly studied; [21] the stress to initiate grain boundary cavitation is $\sigma \approx 2\gamma / a_0$, which is substantially lower than the stress to initiate a transgranular slit. Several considerations might explain why the transgranular slits occur in interconnects. First, a void drifts in a line under electric current, so that even a void nucleated at a grain boundary or a triple junction may sever the line inside a grain. [10] Second, for a line having the bamboo-like grain structure, encapsulated by dielectrics, atomic sinks are partially eliminated which, in turn, limits the growth rate of a rounded void. [22] Third, electric current is expected to contribute in causing the shape instability. [11] Fourth, electromigration will redistribute stress in the interconnects. [23]

As discussed in Introduction, surface diffusion is the only dissipative process included in the present analysis. Among other dissipative processes, plastic creep gives rise to the greatest

uncertainty. If operating at sufficiently high rate, creep will relax the thermal stress in the interconnect, and reduce the stress concentration at the tip of an elongated ellipse. Consequently, plastic creep tend to prevent a void from collapsing, or to blunt the tip of an existing elongated void. Creep can be incorporated into the analysis, which adds numerical complexities, but the major uncertainty arises from the lack of precise knowledge of the creep law in submicron dimensions. Some basic development is needed before such numerical analysis is worthwhile.

Although this work has been motivated by the interconnects, the phenomenon is anticipated for other material systems where stress is high and grain boundaries are inaccessible for diffusion. For example, single crystal oxide fibers under mechanical load may suffer delayed fracture due to this mechanism. Unlike the existing stress corrosion cracking mechanisms, this one does not invoke environmental effects. It will cause a pre-existing void inside a well coated material to collapse; general fracture follows when the void is sufficiently elongated. It is hoped that experiments with better controlled systems will soon succeed in sorting out these matters.

ACKNOWLEDGEMENTS

We wish to thank Professor E. Arzt of the Max-Planck-Institut at Stuttgart, and Dr. J.E. Sanchez of Advanced Micro Devices for their generosity of showing us unpublished micrographs. The work was supported by the Defense Advanced Research Projects Agency through the University Research Initiative under the Office of Naval Research contract N-0014-92-J-1808, and by the National Science Foundation through grant MSS-9202165, and through a Young Investigator Award MSS-9258115 for Z. Suo.

REFERENCES

1 P.S. Ho and T. Kwok , Rep. Prog. Phys, **52**, 301 (1989).

2 C.Y. Li, P. Totta, and P. Ho, eds. *Stress-Induced Phenomena in Metallization*, American Institute of Physics, New York (1992).

3 R.E. Jones and M.L. Basehore, Appl. Phys. Lett. **50**, 725 (1987).

4 B. Greenebaum, A.I. Sauter, P. Flinn and W.D. Nix, Appl. Phys. Lett. **58**, 1845 (1991).

5 M.A. Korhonen, C.A. Paszkiet and C.-Y. Li, J. Appl. Phys. **69**, 8083 (1991).

6 W.D. Nix, Metallurgical Trans. **20A**, 2217 (1989).

7 J.E. Sanchez, L.T. McKnelly, and J.W. Morris, J.W. J. Appl. Phys. **72**, 3201 (1992).

8 J.H. Rose, Appl. Phys. Lett. **61**, 2170 (1992).

9 Y.-C. Joo and C.V. Thompson, Mat. Res. Soc. Symp. Proc. In press (1993).

10 O. Kraft, S. Bader, J.E. Sanchez, E. Arzt, Mat. Res. Soc. Symp. Proc. In press (1993).

11 W. Yang, W. Wang and Z. Suo, submitted to J. Mech. Phys. Solids. (1993).

12 R.J. Asaro and W.A. Tiller, Metall. Trans. **3**, 1789 (1972).

13 C.-H. Chiu and H. Gao, Int. J. Solids Structures **30**, 2983 (1993).

14. L.B. Freund, F. Jonsdottir, J. Mech. Phys. Solids. **41**, 1245 (1993).

15 W.H. Yang and D.J. Srolovitz, Phys. Rev. Lett. **71**, 1539 (1993).

16 G. Nicolis and I. Prigogine, *Exploring Complexity*. Freeman Co. New York (1989).

17 A.A. Griffith, Phil. Trans. R. Soc. Lond. **A211**, 163-197 (1921).

18. I. Prigogine, *Introduction to Thermodynamics of Irreversible Processes*, 3rd. ed. Wiley, New York (1967).

19 A. Needleman and J.R. Rice, Acta Metall. **28**, 1315 (1980).

20 R.M. McMeeking and L.T. Kuhn, Acta Metall. **40**, 961 (1992).

21 T.-J. Chuang, K.I. Kagawa, J.R. Rice, L.B. Sills, Acta Metall. **27**, 265 (1979).

22. A.F. Bower and L.B. Freund, J. Appl. Phys. **74**, 3855 (1993).

23. M.A. Korhonen, P. Borgesen, K.N. Tu and C.-Y. Li, J. Appl. Phys. **73**, 3790 (1993).

24 A.H. England, *Complex Variable Methods in Elasticity*, Wiley, London (1971).

APPENDIX A: ELASTIC ENERGY CALCULATION

An infinite body containing an elliptic hole subjected to remote stresses stores infinite amount strain energy. Yet one can compute the energy difference between a body containing an elliptic hole and a body containing a circular hole subjected to the same remote stress state. Denote ΔU_e = U_e(ellipse) - U_e(circle). The ellipse and the circle have the same area, πa_0^2. The hole can be regarded as an elastic medium with vanishing stiffness, so it can have strains. Of course, the stresses inside the hole vanish. For an infinite body containing an elliptic hole under remote stress, it is well known that the strain inside the hole is uniform. Denote the applied remote stresses as σ_{ij}^{∞}, and the strains inside the hole as ε_{ij}^0. We will show that

$$\Delta U_e = \frac{1}{2}\pi a_0^2 \sigma_{ij}^{\infty} \Delta\varepsilon_{ij}^0. \tag{A1}$$

Here $\Delta\varepsilon_{ij}^0$ are the differences in the strains inside the elliptic hole and those inside the circular hole.

To prove (A1), consider a body of external boundary S_∞ containing an arbitrary hole of boundary S_0. Denote n_i as the unit normal vector on the surfaces, pointing away from the solid. Let σ_{ij}^{∞} be a stress tensor independent of position. The body is subjected to the traction vector $\sigma_{ij}^{\infty} n_i$ on the external surface, but free of traction on the void surface. Let u_j be the displacement field in the body. The elastic energy in the body is

$$U_e = \frac{1}{2}\int_{S_\infty} \sigma_{ij}^{\infty} n_i u_j \mathrm{d}S. \tag{A2}$$

Rewrite the above as

$$U_e = \frac{1}{2}\int_{S_\infty + S_0} \sigma_{ij}^{\infty} n_i u_j \mathrm{d}S + \frac{1}{2}\int_{S_0} \sigma_{ij}^{\infty} n_i u_j \mathrm{d}S. \tag{A3}$$

In the second integral, the surface normal is switched to point into the solid.

To understand the first integral in (A3), one needs an auxiliary body with the same geometry as the original body. The auxiliary body is under the uniform stress σ_{ij}^{∞} everywhere, with traction $\sigma_{ij}^{\infty} n_i$ on *both* internal and external surfaces. Consequently, the first integral in (A3) is the virtual work done by the traction on the auxiliary body through the displacement of

the original body. According to the reciprocal theorem, it is the same as the virtual work done by the traction of the original body through the displacement of the auxiliary body. Neither the traction $\sigma_{ij}^{\infty} n_i$ on the original body, nor the displacement of the auxiliary body depends on the hole geometry. Thus, the first integral in (A3) is independent of the hole geometry. Only the second integral makes the difference when the hole changes shape or size.

To take advantage of the fact that strains are uniform in the elliptic hole, one apply the Gauss theorem to the second integral in (A3), which changes the displacement to the strain inside the hole, leading to (A1).

Referring to Fig. 1, for an elliptic hole subjected to remote biaxial stress state, the hoop stresses at point A and B, respectively, are [24]

$$\sigma_t(A) = -\sigma_1 + \frac{3+m}{1-m}\sigma_2, \quad \sigma_t(B) = -\sigma_2 + \frac{3-m}{1+m}\sigma_1. \tag{A4}$$

The corresponding stresses for a circular void are obtained by setting $m = 0$. Because the point on the surface is under uniaxial stress state, the hoop strains are given by the stress divided by Young's modulus E of the solid. Compatibility requires that on the surface the hoop strain in the solid is the same as the hoop strain in the "medium" inside the hole. Thus,

$$\Delta\varepsilon_{xx}^0 = \frac{-4m}{1+m}\frac{\sigma_1}{E}, \quad \Delta\varepsilon_{yy}^0 = \frac{4m}{1-m}\frac{\sigma_2}{E}. \tag{A5}$$

Substituting (A5) into (A1), one finds the elastic energy difference between a body with an elliptic hole and a body with a circular hole:

$$\Delta U_e = \frac{2\pi a_0^2}{E}\left(\frac{m}{1-m}\sigma_2^2 - \frac{m}{1+m}\sigma_2^2\right). \tag{A6}$$

Plane stress conditions are assumed in the above; under plane strain conditions, replace E by $E/(1-\nu^2)$, ν being Poisson's ratio.

APPENDIX B: STRESS AROUND A HYPOTROCHOIDAL HOLE

The hoop stress around a hypotrochoidal hole is obtained from Ref. 24 with some manipulations. For two dimensional elasticity problems, the stress field is solved by two analytic functions $\Omega(z)$ and $\omega(z)$ where $z = x + iy$ and $i = \sqrt{-1}$, namely

$$\sigma_{yy} + \sigma_{xx} = 4\,\mathrm{Re}\left[\Omega'(z)\right], \tag{B1}$$

$$\frac{\sigma_{yy} - \sigma_{xx}}{2} + i\sigma_{xy} = \bar{z}\Omega''(z) + \omega'(z). \tag{B2}$$

The function

$$z = R\left(\zeta + m\zeta^{-n}\right) \tag{B3}$$

conformally maps the exterior of a unit circle on the ζ-plane, $\zeta = \exp(i\theta)$, to the exterior of a hypotrochoid on the z-plane. Here n is a positive integer and $0 \le m < 1/n$. The last restriction ensures that the hypotrochoid does not have loops and only has cusps if $m = 1/n$. A hypotrochoid hole under remote biaxial tension, $\sigma_{xx} = \sigma_{yy} = \sigma$ as $|z| \to \infty$, is solved by

$$\Omega(z) = \frac{\sigma R}{2}\left(\zeta - \frac{m}{\zeta^n}\right), \tag{B4}$$

$$\omega(z) = -\frac{\sigma R}{2}\left(\frac{1}{\zeta} - m\zeta^n + \left(\frac{1 + m\zeta^{n+1}}{\zeta^{n+1} - mn}\right)\left(\zeta^n + \frac{mn}{\zeta}\right)\right). \tag{B5}$$

The hole is traction free so that the hoop stress on the surface is giving by the first invariant of the stress tensor, $\sigma_t = \sigma_{xx} + \sigma_{yy}$. From (B1), (B3) and (B4) one finds that

$$\sigma_t = 4\,\mathrm{Re}\left[\frac{d\Omega / d\zeta}{dz / d\zeta}\right] = \sigma\frac{2 - 2m^2n^2}{1 + m^2n^2 - 2mn\cos(n+1)\theta}. \tag{B6}$$

In the body of the text, (3.10) retains the terms up to m^2 power in m.

FIGURE CAPTIONS

Fig. 1 The cross section of a cylindrical void in an elastic solid under biaxial stresses.

Fig. 2 Biaxial stress state $\sigma_1 = \sigma_2 = \sigma$. a) The potential as a function of the void shape m at several levels of Λ. b) The bifurcation diagram is a combination of a subcritical pitchfork and two Griffith cracks.

Fig. 3 Biased biaxial stress state $\sigma_1/\sigma_2 = 0.8$ a) The potential as a function of the void shape m at several levels of Λ. b) Stability conditions projected on the (m, Λ) plane.

Fig. 4 Uniaxial stress state $\sigma_1 = 0$, $\sigma_2 \neq 0$. a) The potential as a function of the void shape m at several levels of Λ. b) Stability conditions projected on the (m, Λ) plane.

Fig. 5 The critical number Λ_c as a function of the stress ratio.

Fig. 6 The evolution rate of an elliptic void.

Fig. 7 The [illegible]e for one ellipse to evolve to another.

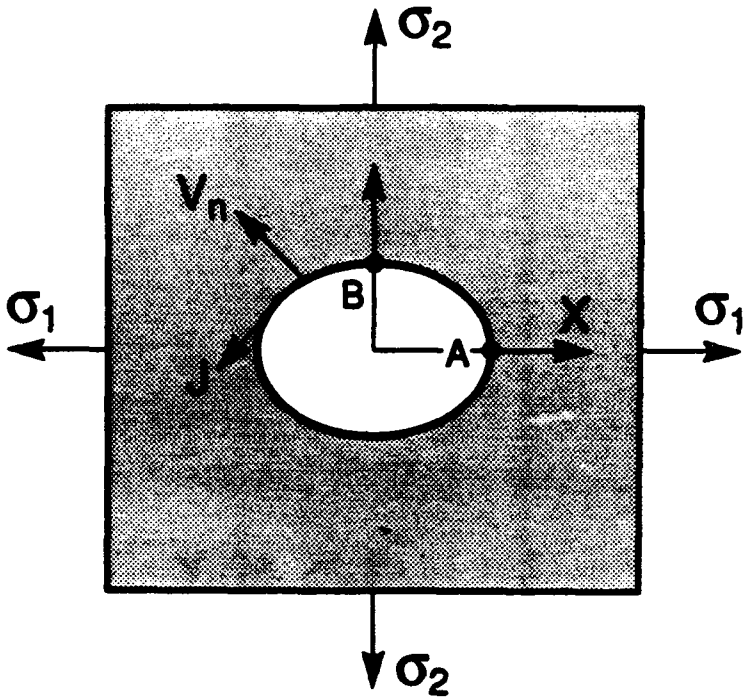

Figure 1

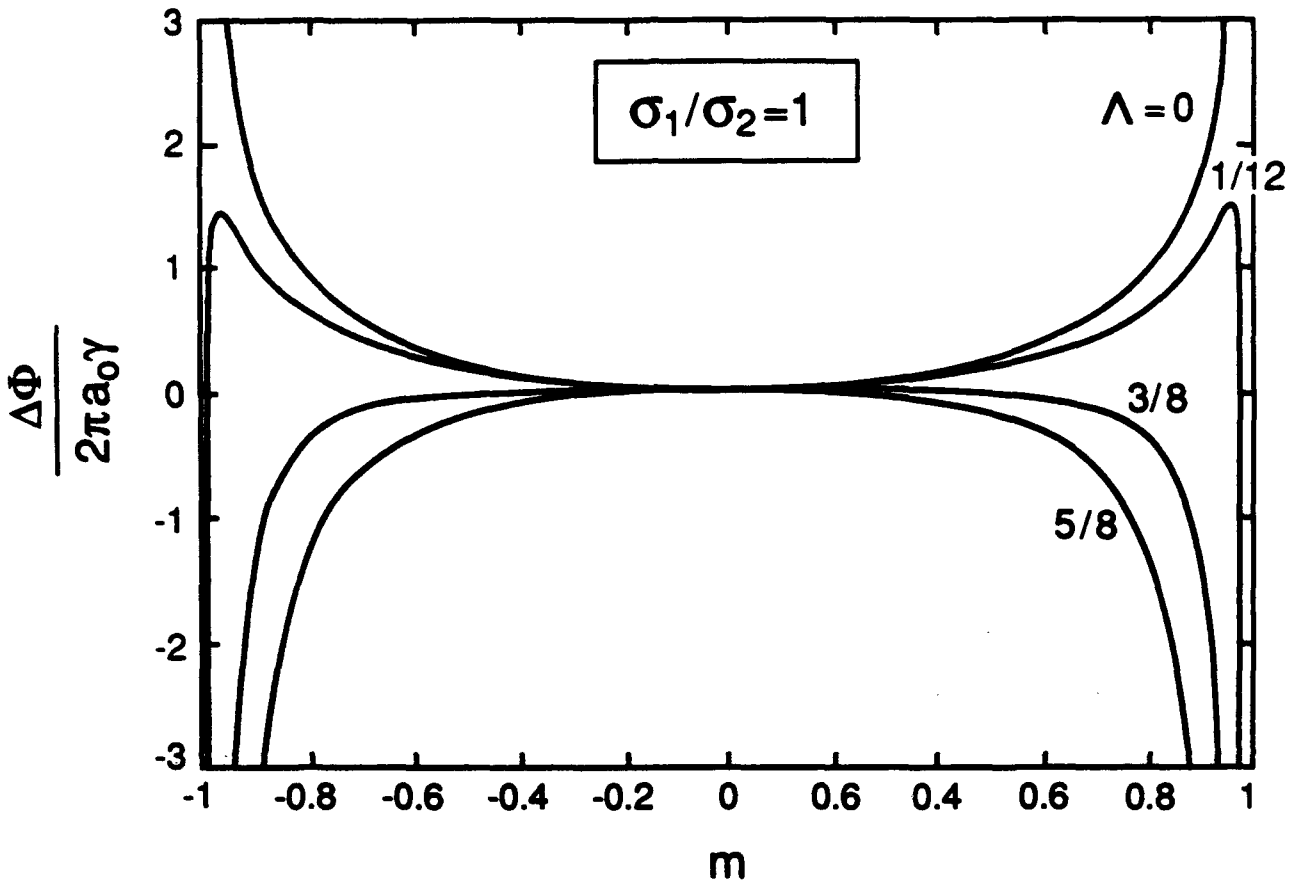
$\sigma_1/\sigma_2=1$
$\Lambda=0$
1/12
3/8
5/8
$\frac{\Delta\Phi}{2\pi a_0\gamma}$
m
3
2
1
0
-1
-2
-3
-1
-0.8
-0.6
-0.4
-0.2
0
0.6
0.4
0.6
0.8
1

Figure 2a

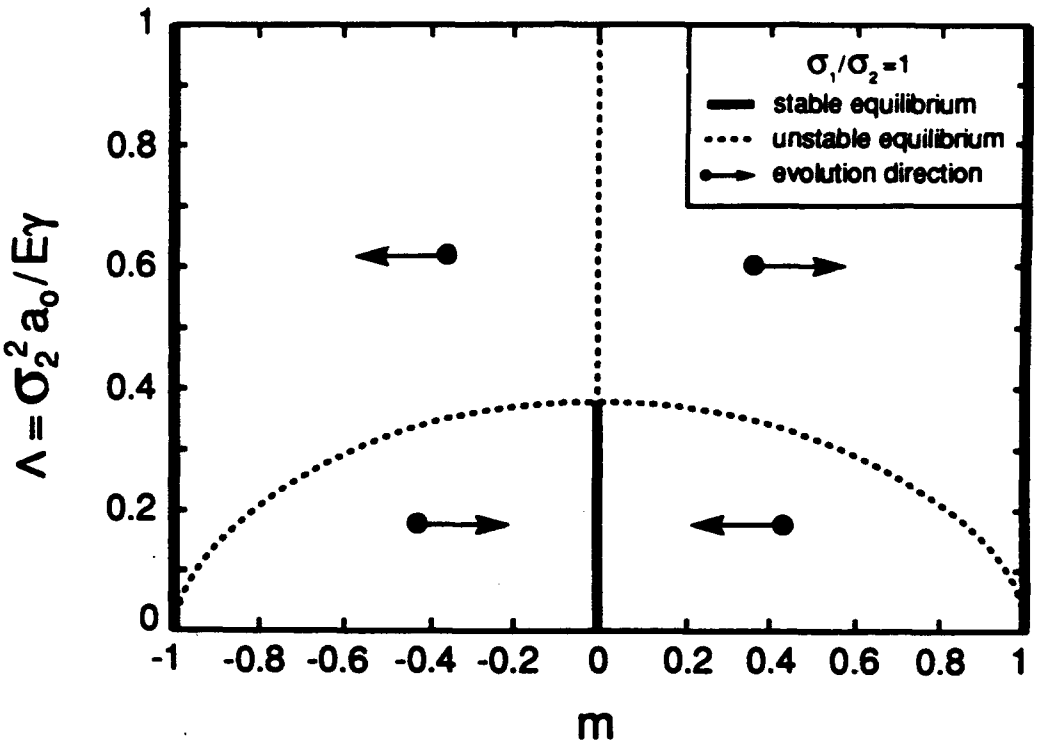
$\sigma_1/\sigma_2=1$
stable equilibrium
unstable equilibrium
evolution direction
$\Lambda = \sigma_2^2 a_0/E\gamma$
1
0.8
0.6
0.4
0.2
0
-1
-0.8
-0.6
-0.4
-0.2
0
0.2
0.4
0.6
0.8
1
m

Figure 2b

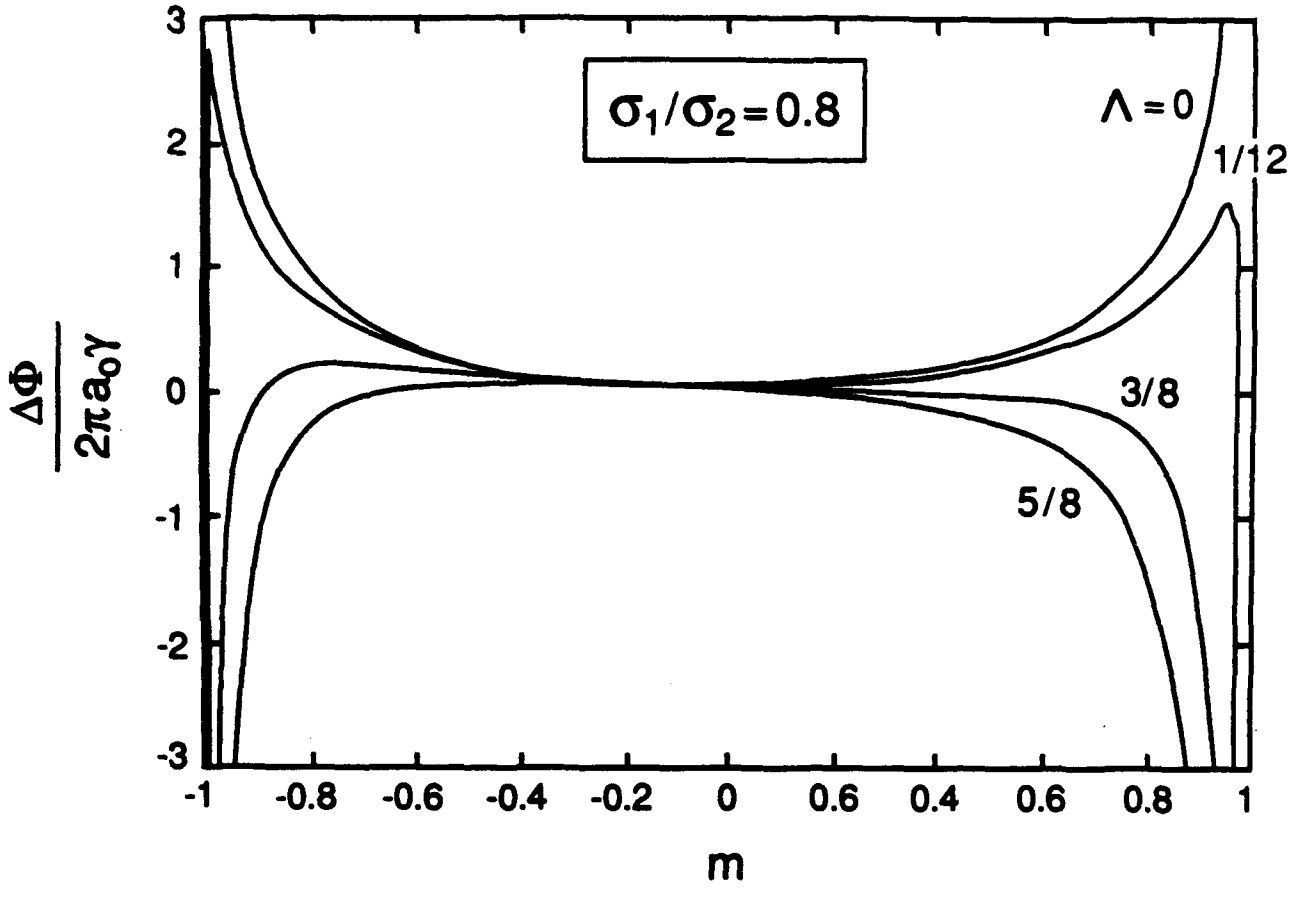
$\sigma_1/\sigma_2=0.8$
$\Lambda=0$
1/12
3/8
5/8
$\frac{\Delta\Phi}{2\pi a_0\gamma}$
m
3
2
1
0
-1
-2
-3
-1
-0.8
-0.6
-0.4
-0.2
0
0.6
0.4
0.6
0.8
1

Figure 3a

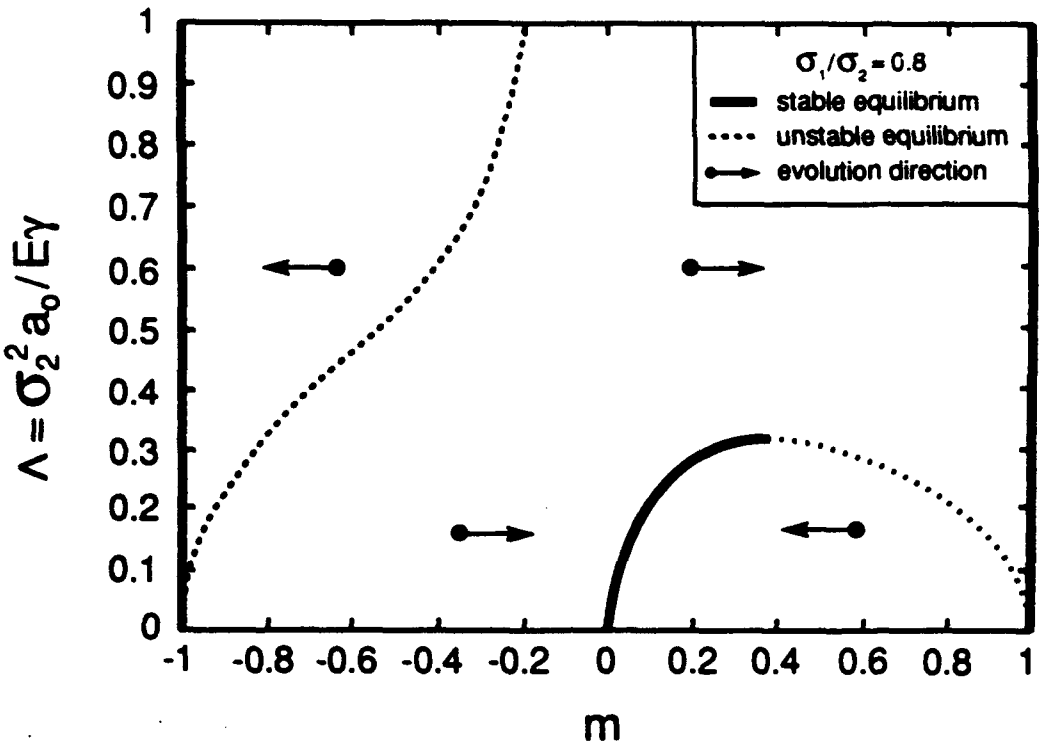
$\sigma_1/\sigma_2 = 0.8$
stable equilibrium
unstable equilibrium
evolution direction
$\Lambda = \sigma_2^2 a_0 / E\gamma$
m
1
0.9
0.8
0.7
0.6
0.5
0.4
0.3
0.2
0.1
0
-1
-0.8
-0.6
-0.4
-0.2
0
0.2
0.4
0.6
0.8
1

Figure 3b

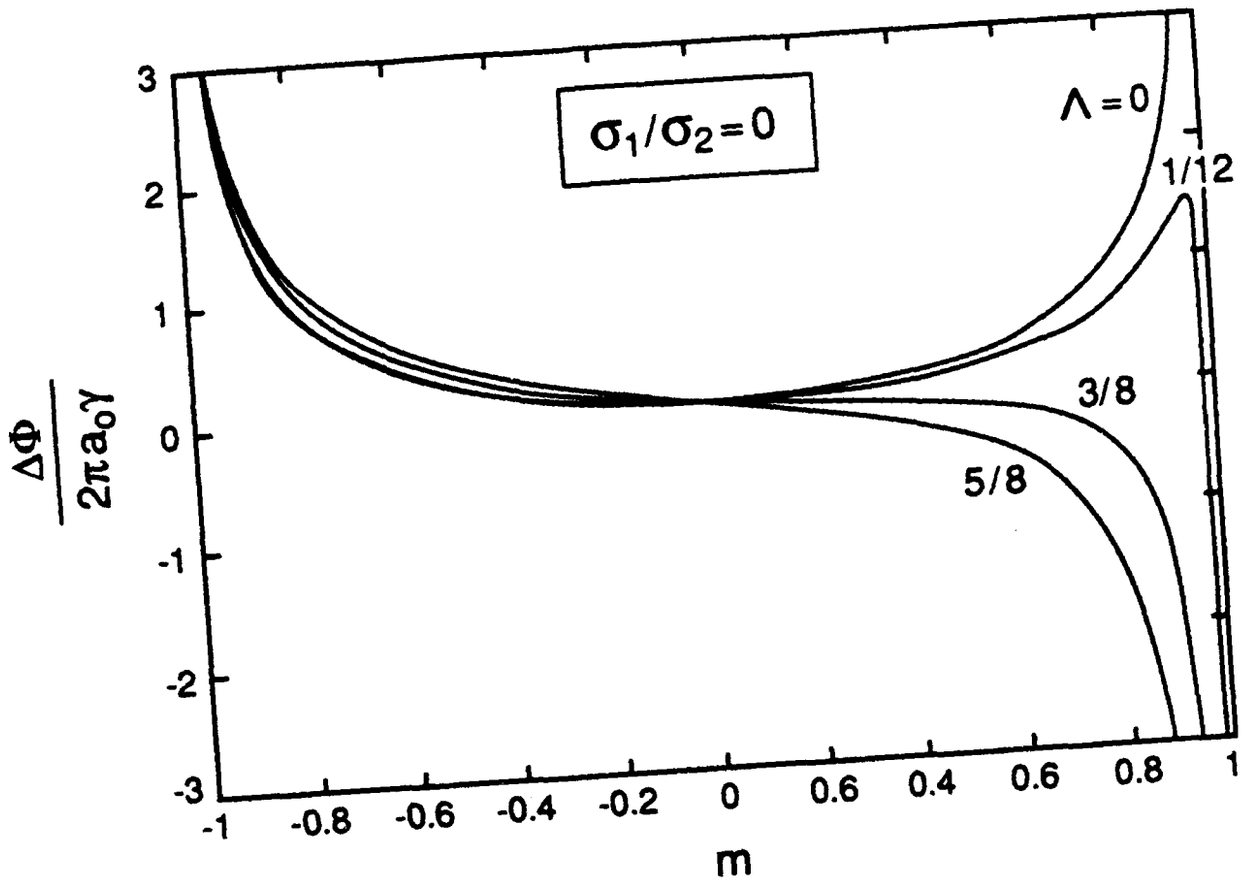
$\sigma_1/\sigma_2=0$
$\Lambda=0$
1/12
3/8
5/8
$\frac{\Delta\Phi}{2\pi a_o\gamma}$
m
3
2
1
0
-1
-2
-3
-1
-0.8
-0.6
-0.4
-0.2
0
0.6
0.4
0.6
0.8
1

Figure 4a

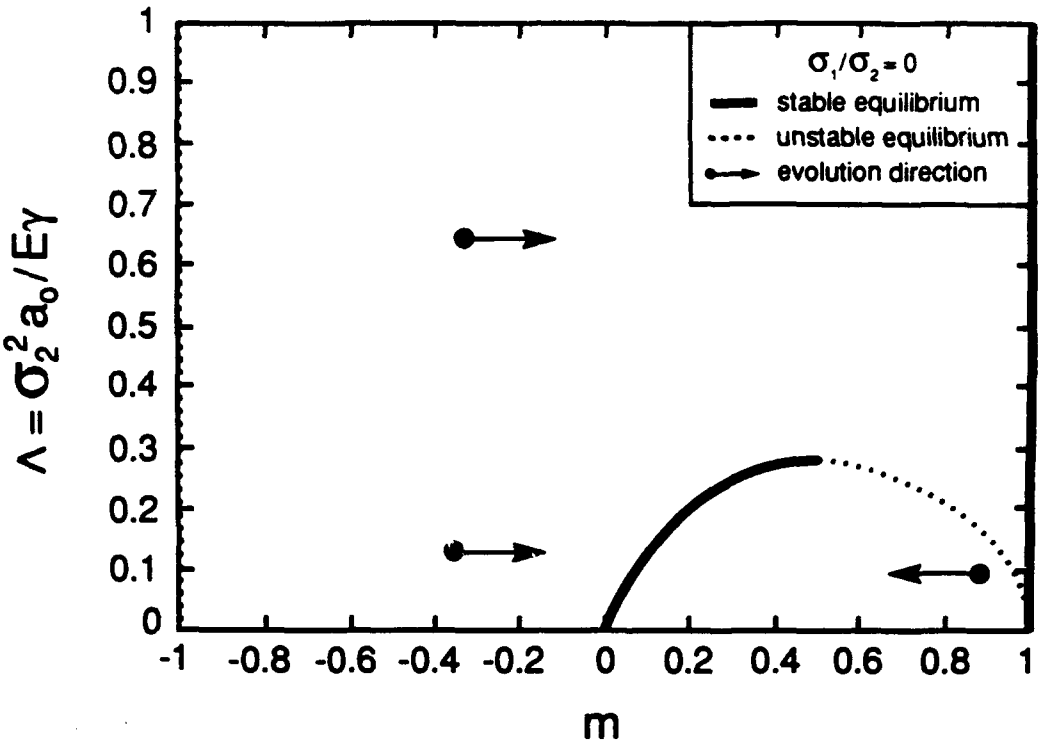
$\sigma_1/\sigma_2 = 0$
stable equilibrium
unstable equilibrium
evolution direction
$\Lambda = \sigma_2^2 a_0/E\gamma$
m
1
0.9
0.8
0.7
0.6
0.5
0.4
0.3
0.2
0.1
0
-1
-0.8
-0.6
-0.4
-0.2
0
0.2
0.4
0.6
0.8
1

Figure 4b

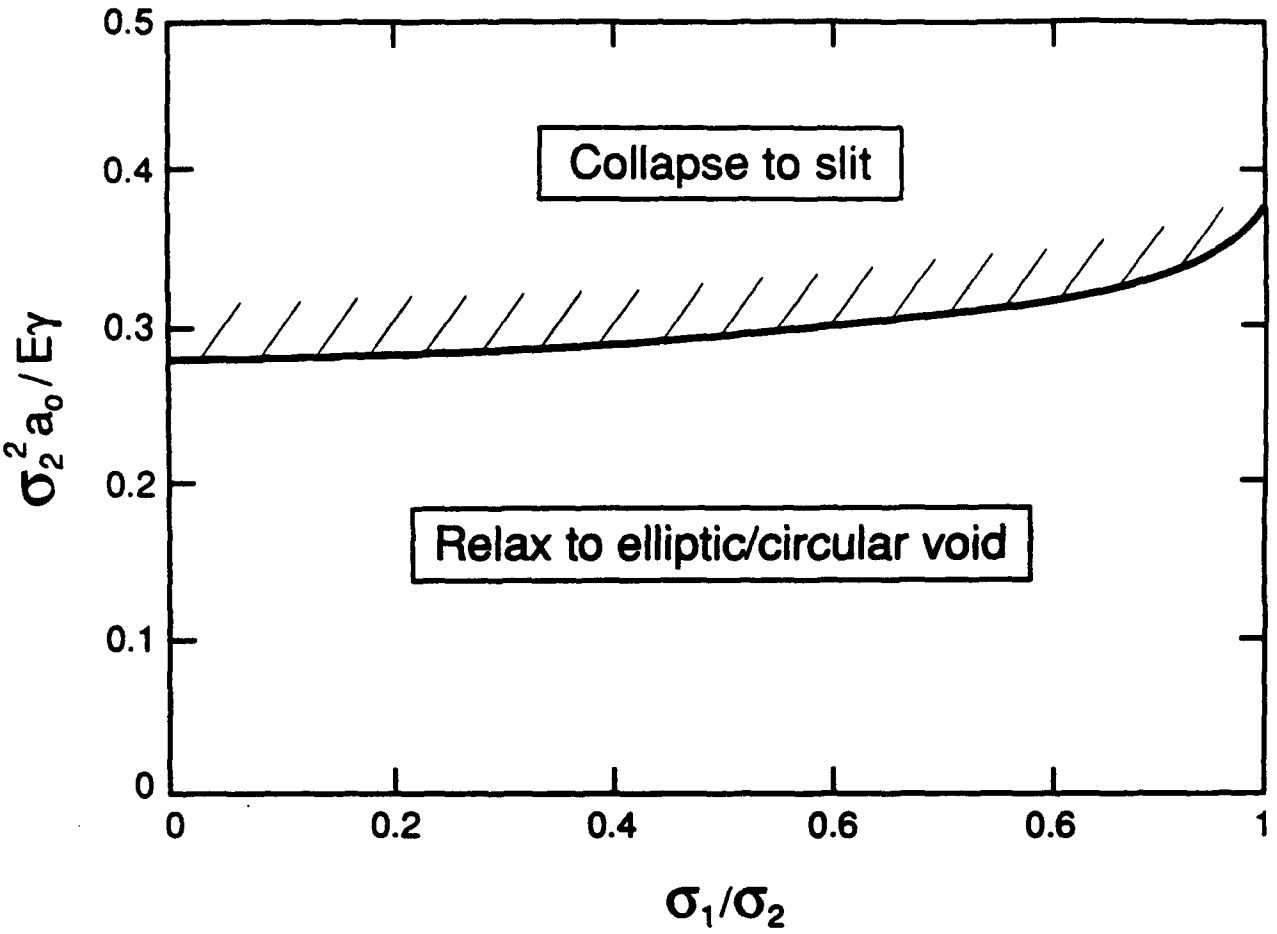
0.5
0.4
0.3
0.2
0.1
0
0
0.2
0.4
0.6
0.6
1
Collapse to slit
Relax to elliptic/circular void
$\sigma_2^2 a_o / E\gamma$
σ_1/σ_2

Figure 5

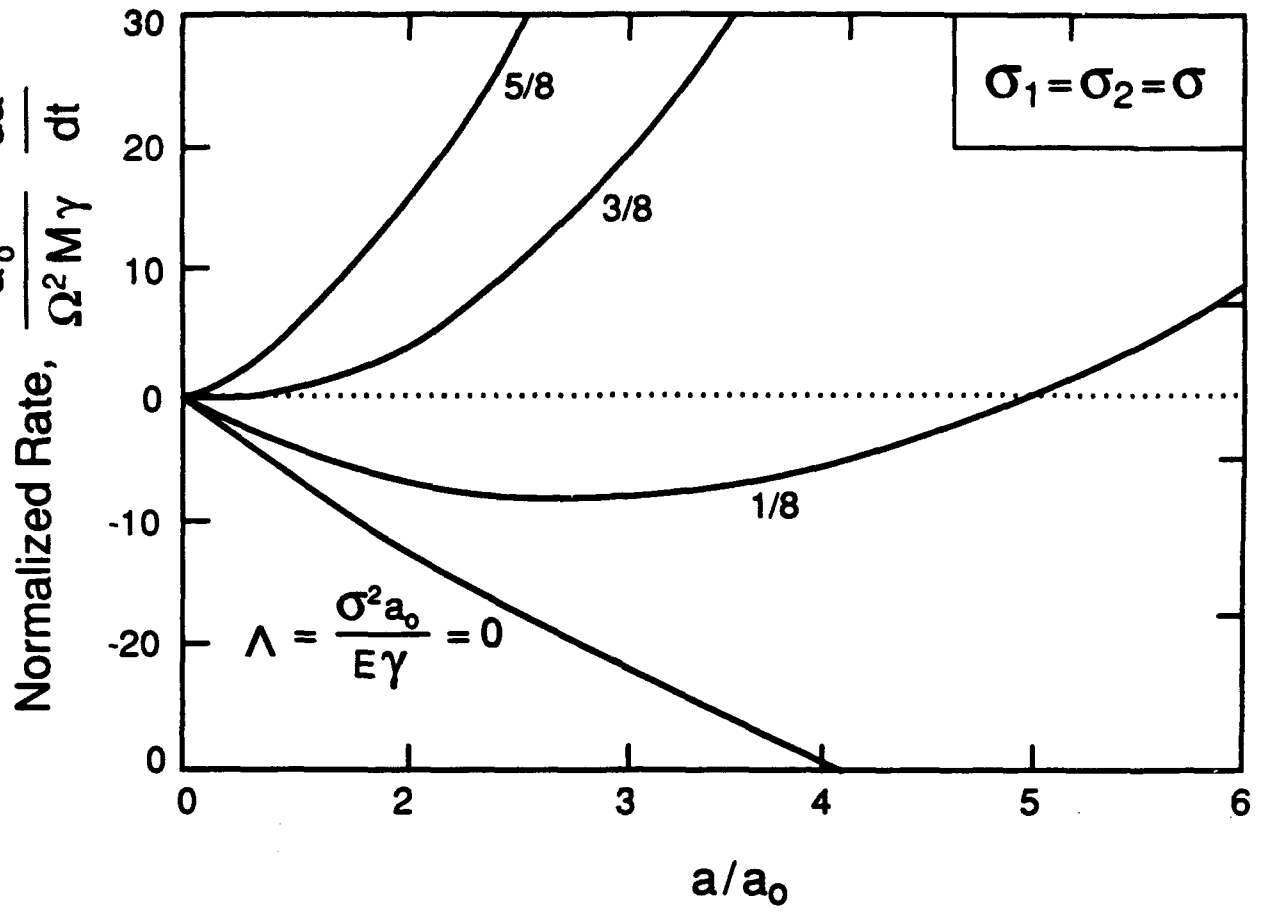
Normalized Rate, $\frac{a_o^3}{\Omega^2 M\gamma}\frac{da}{dt}$
30
20
10
0
-10
-20
0
0
2
3
4
5
6
a/a_o
5/8
3/8
1/8
$\sigma_1=\sigma_2=\sigma$
$\Lambda = \frac{\sigma^2 a_o}{E\gamma} = 0$

Figure 6

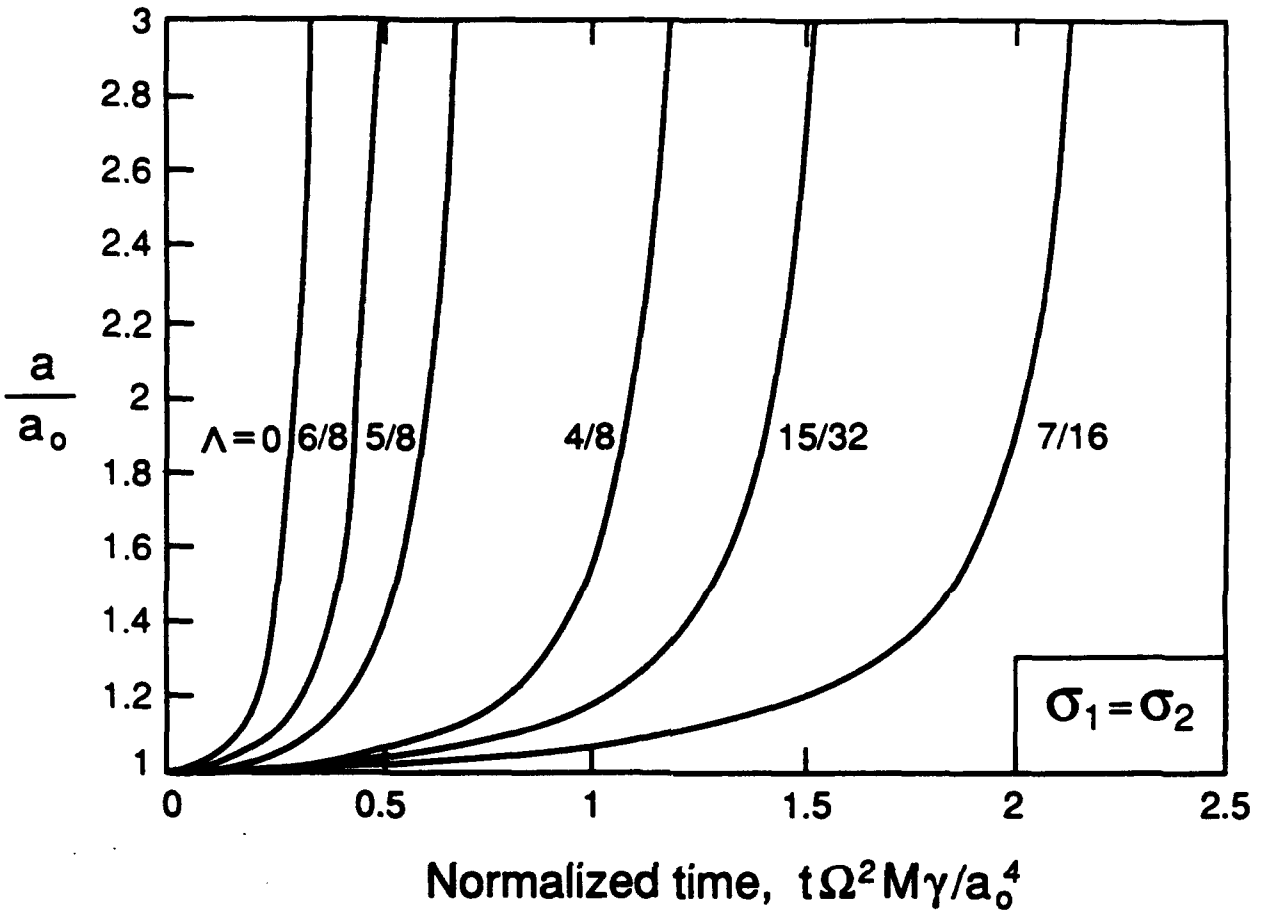
3
2.8
2.6
2.4
2.2
2
1.8
1.6
1.4
1.2
1
a / a_o
Λ=0
6/8
5/8
4/8
15/32
7/16
σ1=σ2
0
0.5
1
1.5
2
2.5
Normalized time, tΩ²Mγ/a_o⁴

Figure 7a

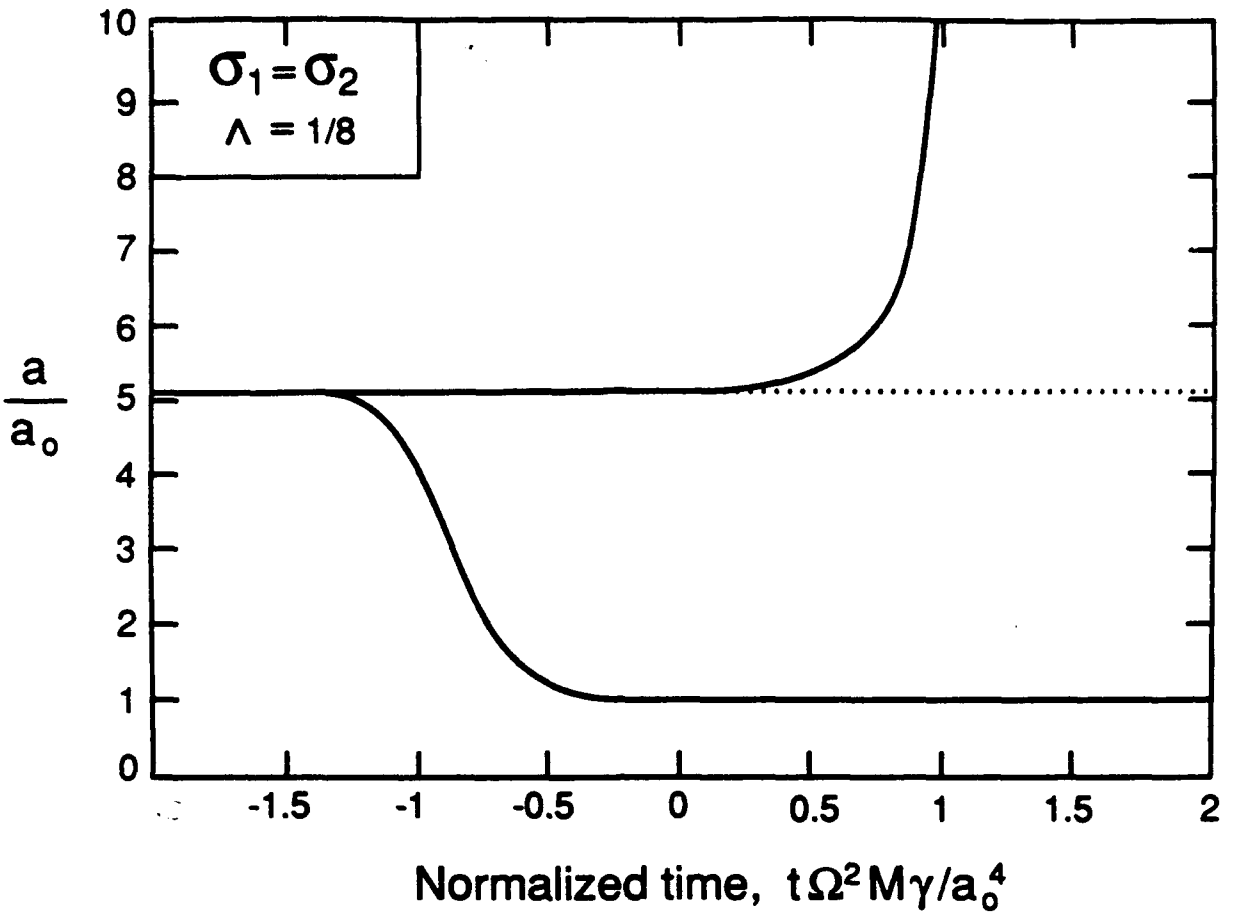
$\sigma_1 = \sigma_2$
$\Lambda = 1/8$
$\frac{a}{a_o}$
10
9
8
7
6
5
4
3
2
1
0
-1.5
-1
-0.5
0
0.5
1
1.5
2
Normalized time, $t\Omega^2 M\gamma/a_o^4$

Figure 7b

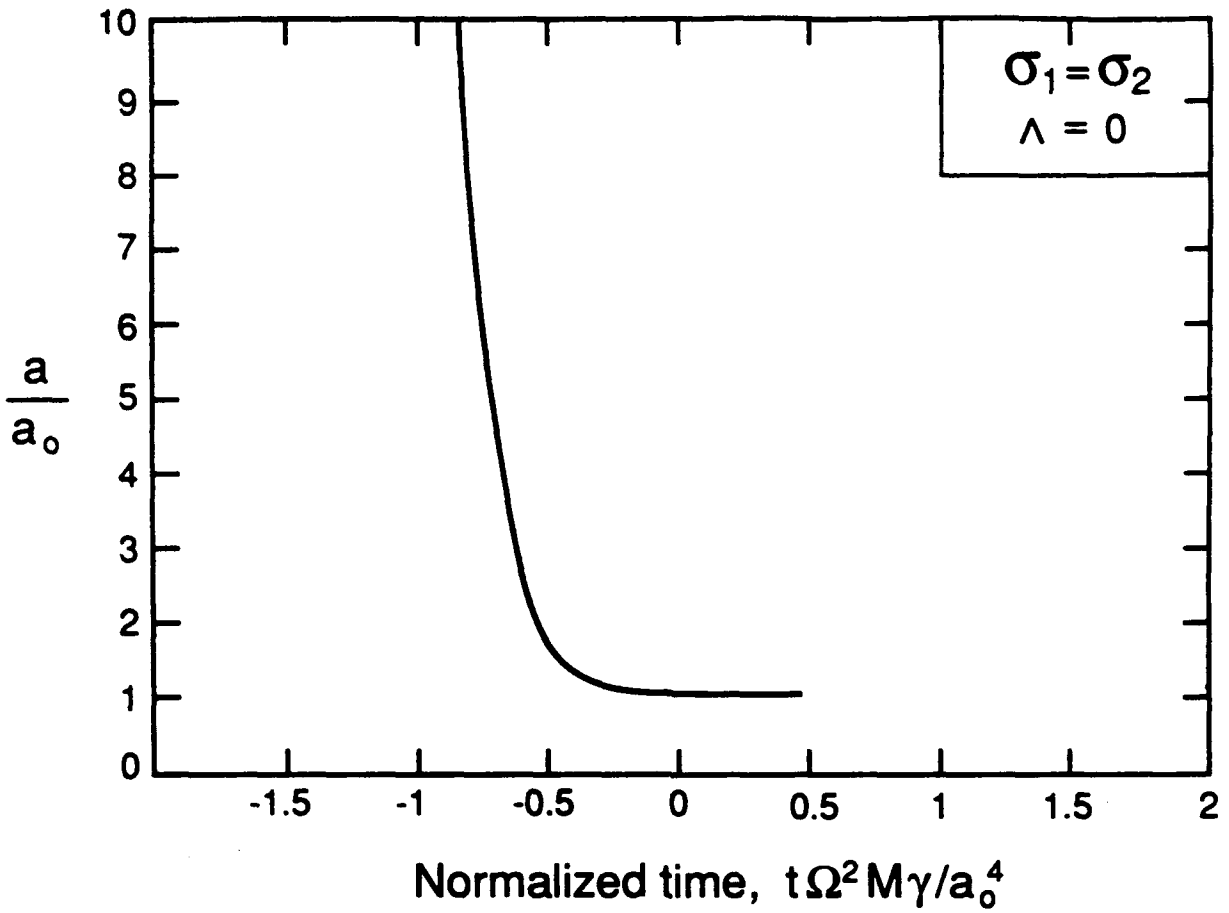
$\sigma_1 = \sigma_2$
$\Lambda = 0$
$\frac{a}{a_o}$
10
9
8
7
6
5
4
3
2
1
0
-1.5
-1
-0.5
0
0.5
1
1.5
2
Normalized time, $t\Omega^2 M\gamma/a_o^4$

Figure 7c